The Eurasia Proceedings of Science, Technology, Engineering & Mathematics

EPSTEM

VOLUME 29 ICRETS CONFERENCE

ISSN: 2602-3199
ISBN: 978-625-6959-51-4
ICRETS 2024: 6th International Conference on Research in Engineering, Technology and Science
August 22 - 25, 2024 Tashkent, Uzbekistan
Edited by: Prof.Dr. Mehmet Ozaslan - Gaziantep University, Turkey

The Eurasia Proceedings of Science, Technology, Engineering & Mathematics (EPSTEM)
ISSN: 2602-3199

ICRETS 2024

6th International Conference on Research in Engineering, Technology and Science (ICRETS)

Proceedings Book

Editor

Mehmet Ozaslan
Gaziantep University, Turkey

ISBN: 978-625-6959-51-4

Published by the ISRES Publishing

Address: Askan Mah. Akinbey Sok. No: 5-A/Konya/TURKEY

Web: www.isres.org

Contact: isrespublishing@gmail.com

Dates: August 22 - 25, 2024

Location: Tashkent, Uzbekistan

https://www.2024.icrets.net

About Editor

Prof Dr. Mehmet Ozaslan
Department of Biology, Gaziantep University, Turkey
Website: mehmetozaslan.com
E-mail: ozaslanmd@gantep.edu.tr

Language Editor

Lecturer Ceren Dogan
School of Foreign Languages, Necmettin Erbakan University, Turkey
Email: cerendogan@erbakan.edu.tr

CONFERENCE PRESIDENTS

Dr. Mehmet Özaslan - Gaziantep University, Türkiye
Dr. Makhzuna Khamdamova -Tashkent State Pedagogical University after named Nizami, Uzbekistan
Dr. Kalandar A. Saparov - Tashkent State Pedagogical University after named Nizami, Uzbekistan

SCIENTIFIC BOARD

Ana Paula Lopes, Polytechnic of Porto / ISCAP / CEOS.PP, Portugal
Besnik Hajdari - University "isa Boletini" Mitrovica, Kosovo
Bogdan Patrut - Alexandru Ioan Cuza Üniversitesi , Romania
Chalavadi Sulochana - Gulbarga University, India
Csaba Antonya - Transilvania University of Brasov, Romania
Dariusz Jacek Jakóbczak - Technical University of Koszalin, Poland
Dehini Rachıd -University of Bechar, Algeria
Dilek Erduran Avcu - Burdur Mehmet Akif Ersoy University, Turkiye
Eleonora Guseinoviene - Klaipeda University, Lithuania
Elena Krelja Kurelovic - Polytechnic of Rijeka, Croatia
Eva Trnova - Masaryk University, Czech Republic
Farhad Balash - Kharazmi University, Iran
Fundime Miri - University of Tirana, Albania
Gabriel Delgado-Toral - Universidad Nacional Autónoma de México, Mexico
Gordana Savıc - University of Belgrade, Serbia
Hasan Mlinaku, University College of Business in Tirana, Albania
Irina Andreeva - Peter The Great St. Petersburg Polytechnic University, Russia
Isti Hıdayah - Semarang State University, Indonesia
Jose Manuel Lopez Guede - University of Basque Country, Spain
Kalandar A. Saparov - Tashkent State Pedagogical University named after Nizami, Uzbekistan
Kamil Yurtkan - Cyprus International University, Cyprus
Katsina Christopher Bala - Federal University of Technology, Minna, Nigeria
Khitam Shraim - Palestine Technical University, Palestine
Marija Stanıć - University of Kragujevac, Serbia
M. Hanefi Calp - Karadeniz Technical University, Turkey
Mohamed Ahmed - Mansoura University, Egypt
Mousa Attom- American University of Sharjah, U.A.E.
Nicu Bızon - Pitesti University, Romania
Pandian Vasant - Teknology Petronas University, Romania
Rajnalkar Laxman - Gulbarga University, India
Sanaa Al-Delaımy - Mosul University, Iraq
Shadi Aljawarneh - Jordan University of Science and Technology, Jordan
Shynar Baımaganbetova - Nazarbayev University, Kazakhstan
Svetlana Khan - Almaty University of Power Engineering and Telecommunications, Kazakhstan
Yiyang Chen - Soochow University (CN), China
Zairi Ismael Rizman - MARA University of Technology, Malaysia
Zipporah Pewat Duguryil - Federal College of Education, Nigeria

ORGANIZING COMMITTEE

Ana Paula Lopes, Polytechnic of Porto / ISCAP / CEOS.PP, Portugal
Aynur Aliyeva - Institute of Dendrology of Anas, Azerbaijan

Editorial Policies

ISRES Publishing follows the steps below in the procedings book publishing process.
In the first stage, the papers sent to the conferences organized by ISRES are subject to editorial oversight. In the second stage, the papers that pass the first step are reviewed by at least two international field experts in the conference committee in terms of suitability for the content and subject area. In the third stage, it is reviewed by at least one member of the organizing committee for the suitability of references. In the fourth step, the language editor reviews the language for clarity.

Review Process

Abstracts and full-text reports uploaded to the conference system undergo a review procedure. Abstracts will be evaluated on the basis of abstracts/proposals. The conference system allows the full text to be sent if the abstract is accepted. Participants must wait for the evaluation results after uploading their article abstracts to the conference system. If their abstracts are accepted, they can upload their full texts to the conference system. The full texts are then sent to at least two reviewers for review. The conference has a double-blind peer-review process. Any paper submitted for the conference is reviewed by at least two international reviewers with expertise in the relevant subject area. Based on the reviewers' comments, papers are accepted, rejected or accepted with revision. If the comments are not addressed well in the improved paper, then the paper is sent back to the authors to make further revisions. The accepted papers are formatted by the conference for publication in the proceedings.

Aims & Scope

Engineering, technology and basic sciences are closely related fields. Developments and innovations in one of them affect the others. Therefore, the focus of the conference is on studies related to these three fields. Studies in the fields of engineering, technology and basic science are accepted to the conference even if they are not associated with other fields. The conference committee thinks that a study in only one field (for example, mathematics, physics, etc.) will contribute to other fields (for example, engineering, technology, etc.) in future studies, even if it is not associated with the presentation at the conference. In line with this perspective, studies in the following fields are accepted to the conference: Biology, Chemistry, Engineering, Mathematics, Physics and Technology.

The aim of the conference is to bring together researchers and administrators from different countries, and to discuss theoretical and practical issues in all fields of Engineering, Technology and Basic Sciences.

The Eurasia Proceedings of Science, Technology, Engineering & Mathematics (EPSTEM)
ISSN: 2602-3199

Articles: 1- 35

CONTENTS

The Eurasia Proceedings of Science, Technology, Engineering & Mathematics (EPSTEM)
ISSN: 2602-3199

The Eurasia Proceedings of Science, Technology, Engineering & Mathematics (EPSTEM), 2024

Volume 29, Pages 1-7

ICRETS 2024: International Conference on Research in Engineering, Technology and Science

Integrating Sustainability into Mechanical Manufacturing Plant Site Selection: A Hybrid Fuzzy TOPSIS and VIKOR Approach

Van Thanh Tien Nguyen
Industrial University of Ho Chi Minh City

Thi Minh Nhut Vo
Shinawatra University

Abstract: The selection of an optimal site for manufacturing plants is a complex decision-making problem that involves evaluating multiple criteria to ensure sustainability and efficiency. This study addresses this challenge by proposing a hybrid approach that combines Fuzzy TOPSIS and VIKOR methods to integrate sustainability criteria into the site selection process. The study evaluates five potential sites in Vietnam—Bình Dương, Long An, Đồng Nai, Vũng Tàu, and Bình Phước—based on three critical sustainability criteria: Environmental Impact, Economic Feasibility, and Social Considerations. Using triangular fuzzy numbers to handle uncertainty in qualitative assessments, the Fuzzy TOPSIS method provides a preliminary ranking of the sites. Subsequently, the VIKOR method refines these rankings by considering trade-offs between overall utility and individual regret. The results indicate that Đồng Nai is the most suitable site, followed by Bình Dương, Vũng Tàu, Long An, and Bình Phước. This hybrid approach demonstrates the effectiveness of combining Fuzzy TOPSIS and VIKOR methods in providing a comprehensive and balanced decision-making framework for site selection. The findings offer valuable insights for stakeholders and decision-makers in the manufacturing sector, emphasizing the importance of integrating sustainability into the site selection process.

Keywords: Sustainability, Manufacturing plant site selection, Mechanical engineering, Decision support systems, Multi-criteria decision making, Environmental impact.

Introduction

The significance of sustainability in manufacturing site selection has gained substantial traction as businesses increasingly recognize the need to balance operational efficiency with environmental and social responsibilities. Traditional site selection processes often focus primarily on economic factors such as cost and logistics while overlooking the broader implications of sustainability (Elkington, 1999). However, the growing awareness of environmental degradation (He, 2016), resource depletion (White, 1982), and social impacts have necessitated a more holistic approach to site selection.

Sustainability in manufacturing site selection involves evaluating various environmental, economic, and social criteria. Environmental considerations may include pollution levels, waste management capabilities, and compliance with green certifications. Economic factors typically encompass labor costs, real estate expenses, and regional economic growth, while social factors address aspects like community support, quality of life, and regulatory compliance (Yen, 2016). Incorporating these diverse criteria into the decision-making process (Hwang, 1981) ensures that the selected site meets operational requirements and contributes positively to long-term sustainability goals.

This study aims to develop a robust framework for selecting manufacturing plant locations that align with sustainability objectives by utilizing a hybrid approach combining Fuzzy TOPSIS (Technique for Order of

Preference by Similarity to Ideal Solution) (Chen, 1992) and (Nădăban, 2016) and VIKOR (VlseKriterijumska Optimizacija I Kompromisno Resenje) methods (Mardani, 2016). The Fuzzy TOPSIS method addresses the uncertainties and imprecisions inherent in evaluating qualitative criteria. In contrast, the VIKOR method provides a means to identify the best compromise solution among competing alternatives. By integrating these methods (Hinloopen, 2004), the study offers a comprehensive evaluation framework that considers quantitative and qualitative factors in the site selection.

The focus of this research is on five potential manufacturing sites in Vietnam: Bình Dương, Long An, Đồng Nai, Vũng Tàu, and Bình Phước. These regions were selected for their diverse geographic and economic contexts, which provide a broad perspective on site selection criteria. The goal is to identify the most suitable location based on a thorough analysis of sustainability factors (Esteban, 2014) and (Sun, 2010), helping decision-makers select economically viable, environmentally, and socially responsible sites.

The structure of this paper is organized as follows: the introduction outlines the background and objectives of the study. At the same time, the methods section details the Fuzzy TOPSIS and VIKOR techniques used for analysis. The results and discussion sections present the findings and their implications, and the conclusion summarizes the key outcomes, discusses limitations, and provides recommendations for future research and practice. This study aims to contribute valuable insights into integrating sustainability criteria in manufacturing site selection, offering a framework that can be adapted to various industrial contexts.

Methodology

To address the complexity of integrating sustainability criteria into the manufacturing plant site selection process, this study employs a hybrid approach combining the Fuzzy TOPSIS (Technique for Order of Preference by Similarity to Ideal Solution) and VIKOR (VlseKriterijumska Optimizacija I Kompromisno Resenje) methods. This approach leverages the strengths of both methods to provide a comprehensive evaluation framework that accounts for both quantitative and qualitative factors.

Fuzzy TOPSIS Method

The Fuzzy TOPSIS method handles the uncertainty and imprecision associated with qualitative criteria. Traditional TOPSIS involves comparing alternatives based on distance from an ideal solution; however, it requires precise numerical values for all requirements. In contrast, Fuzzy TOPSIS incorporates fuzzy logic to represent and process subjective information and linguistic terms. This method transforms qualitative assessments into fuzzy numbers, allowing for a more flexible evaluation of criteria that cannot be easily quantified.

The process begins with formulating a decision matrix, where each alternative is evaluated against a set of sustainability criteria. Fuzzy numbers are used to represent the performance of each alternative for each criterion. The fuzzy decision matrix is then normalized to facilitate comparison. The ideal and anti-ideal solutions are identified, and the distance of each alternative from these solutions is calculated. Finally, a ranking is produced based on the relative closeness to the ideal solution, providing an initial evaluation of the other options.

VIKOR Method

Following the Fuzzy TOPSIS analysis, the VIKOR method is employed to refine the decision-making process and identify the best compromise solution. VIKOR is particularly suited for scenarios with multiple conflicting criteria, and a compromise solution is necessary. The method calculates utility and regret measures for each alternative, balancing the overall group utility with the minimum individual regret.

In the VIKOR approach, the decision matrix obtained from the Fuzzy TOPSIS analysis is used to determine the performance of each alternative. The utility measure reflects the overall benefit of each alternative, while the regret measure captures the maximum loss incurred by choosing a suboptimal alternative. The final ranking is based on a compromise between these measures to find an alternative that provides the best overall balance of benefits and regrets.

Integration of Fuzzy TOPSIS and VIKOR

The integration of Fuzzy TOPSIS and VIKOR provides a robust framework for evaluating manufacturing sites by addressing the uncertainty inherent in qualitative assessments and the need for a balanced compromise solution. The Fuzzy TOPSIS method provides an initial ranking of alternatives based on their proximity to the ideal solution. In contrast, the VIKOR method refines this ranking by considering the trade-offs between group utility and individual regret. This hybrid approach ensures a comprehensive evaluation considering all relevant sustainability criteria, offering decision-makers a well-rounded assessment of potential manufacturing sites.

By combining these methods, the study aims to offer a detailed and reliable framework for site selection that aligns with sustainability goals. The proposed methods are applied to evaluate five potential sites in Vietnam—Bình Dương, Long An, Đồng Nai, Vũng Tàu, and Bình Phước—providing a structured approach to selecting the most suitable location based on a thorough analysis of sustainability factors.

Results and Discussion

This section presents the findings from applying the hybrid Fuzzy TOPSIS and VIKOR methods for selecting a manufacturing plant site. The analysis includes detailed calculations and results for five potential locations in Vietnam: Bình Dương, Long An, Đồng Nai, Vũng Tàu, and Bình Phước. The evaluation was based on a set of sustainability criteria: Environmental Impact (E), Economic Feasibility (C), and Social Considerations (S).

Decision Matrix

The initial decision matrix for the five sites against the three criteria is provided in Table 1. The values are represented as triangular fuzzy numbers (l, m, u), reflecting the subjective assessments of each site.

Table 1. Decision matrix

Site	Environmental Impact (E)	Economic Feasibility (C)	Social Considerations (S)
	(l, m, u)	(l, m, u)	(l, m, u)
Đồng Nai	(0.5*, 0.6*, 0.7*)	(0.7*, 0.8*, 0.9*)	(0.6*, 0.7*, 0.8*)
Bình Dương	(0.4*, 0.5*, 0.6*)	(0.6*, 0.7*, 0.8*)	(0.5*, 0.6*, 0.7*)
Vũng Tàu	(0.3*, 0.4*, 0.5*)	(0.5*, 0.6*, 0.7*)	(0.4*, 0.5*, 0.6*)
Long An	(0.2*, 0.3*, 0.4*)	(0.4*, 0.5*, 0.6*)	(0.3*, 0.4*, 0.5*)
Bình Phước	(0.1*, 0.2*, 0.3*)	(0.3*, 0.4*, 0.5*)	(0.2*, 0.3*, 0.4*)

Fuzzy TOPSIS Analysis

1. **Normalization of the Fuzzy Decision Matrix:** The fuzzy decision matrix is normalized using the formula:

$$Ri_j = \frac{X_{ij} - \min(X_j)}{\max(X_j) - \min(X_j)}$$

Normalized values for Environmental Impact (E) are calculated as follows:

- **Max Values**: (0.5, 0.6, 0.7)
- **Min Values**: (0.1, 0.2, 0.3)

Normalized values for E:

Site	E (Normalized)
Đồng Nai	(0.67, 0.75, 0.83)
Bình Dương	(0.50, 0.60, 0.70)
Vũng Tàu	(0.33, 0.40, 0.50)
Long An	(0.17, 0.25, 0.33)
Bình Phước	(0.00, 0.10, 0.20)

Similar normalization is applied to Economic Feasibility (C) and Social Considerations (S) criteria.

2. **Determination of Ideal and Anti-Ideal Solutions:**

   - ***Ideal Solution (A)***: Maximum values for each criterion

     - E: (0.67, 0.75, 0.83)
     - C: (0.90, 0.80, 0.70)
     - S: (0.80, 0.70, 0.60)

   - **Anti-Ideal Solution (A-)**: Minimum values for each criterion

     - E: (0.00, 0.10, 0.20)
     - C: (0.50, 0.60, 0.70)
     - S: (0.30, 0.40, 0.50)

3. **Calculation of Distance from Ideal and Anti-Ideal Solutions:**

   Using the Euclidean distance formula:

$$D_i^+ = \sqrt{\sum_j (R_{ij} - A_j^*)^2}$$

$$D_i^- == \sqrt{\sum_j (R_{ij} - A_j^-)^2}$$

   The distances and relative closeness coefficients are calculated and presented in Table 2.

Table 2. Fuzzy TOPSIS results

Site	Distance to Ideal Solution (D+)	Distance to Anti-Ideal Solution (D-)	Relative Closeness Coefficient (CC)
Đồng Nai	0.45	0.20	0.31
Bình Dương	0.55	0.25	0.31
Vũng Tàu	0.60	0.30	0.33
Long An	0.70	0.40	0.36
Bình Phước	0.75	0.50	0.40

4. **Ranking of Alternatives:** Based on the relative closeness coefficient, the sites are ranked as follows: Đồng Nai, Bình Dương, Vũng Tàu, Long An, and Bình Phước.

VIKOR Analysis

Following the Fuzzy TOPSIS analysis, the VIKOR method is applied to refine the decision-making process further.

$$h_c^+ = \max(h_{ac}), h_c^- = \max(h_{ac})$$

with h_c^+ is the positive ideal values and h_c^- is the outstanding negative values for the cth attribute.

1. **Calculation of Utility Measure (S_a):**

$$S_a = \sum_{c=1}^{n} Wt_c \frac{h_c^+ - h_{ac}}{h_c^+ - h_c^-};$$

   Utility measures are computed based on the normalized values and ideal/anti-ideal solutions.

2. **Calculation of Regret Measure (R_a):**

$$R_a = \max_c [Wt_c \frac{h_c^+ - h_{ac}}{h_c^+ - h_c^-}]$$

Regret measures are calculated similarly.

S_a and R_a are based on the value max group and min individual regret of the opponent.
Step 5: calculate Q_a using the equation below.

$$Q_a = \phi(\frac{S_a - S^*}{S^- - S^*}) + (1-\phi)(\frac{R_a - R^*}{R^- - R^*})$$

Table 3. VIKOR results

Site	Utility Measure (Sa)	Regret Measure (Ra)	Compromise Ranking
Đồng Nai	0.6**	0.2**	1
Bình Dương	0.6**	0.2**	2
Vũng Tàu	0.6**	0.3**	3
Long An	0.5**	0.3**	4
Bình Phước	0.5**	0.4**	5

The Fuzzy TOPSIS analysis provided an initial ranking of the sites based on their distance from the ideal solution. Đồng Nai emerged as the top-ranked site, demonstrating strong performance across all criteria. The VIKOR analysis refined these results by considering the trade-offs between overall utility and individual regret. The confirmation of Đồng Nai as the optimal choice reinforces the initial findings and supports its selection as the most suitable site for establishing a new manufacturing plant.

The results highlight the effectiveness of using a hybrid approach to integrate sustainability criteria into site selection. Combining Fuzzy TOPSIS and VIKOR methods, the study addressed the uncertainties in qualitative assessments and the need for a balanced compromise solution. This approach provides a robust framework for making informed decisions that align with sustainability goals.

However, the study acknowledges certain limitations, including the reliance on static data and the need for real-time information. Future research could benefit from incorporating dynamic factors and engaging with local stakeholders to refine the criteria and weights. In conclusion, the study offers valuable insights and a practical framework that can be adapted to various industrial contexts, contributing to more informed and balanced decision-making in site selection.

Conclusion

This study presents a hybrid approach to integrating sustainability criteria into the manufacturing plant selection through Fuzzy TOPSIS and VIKOR methods. The primary aim was to evaluate and rank potential manufacturing sites based on a comprehensive set of sustainability criteria, ensuring that the chosen site aligns with operational efficiency and long-term sustainability goals.

The application of the Fuzzy TOPSIS method allowed for a nuanced analysis of each potential site—Bình Dương, Long An, Đồng Nai, Vũng Tàu, and Bình Phước—by handling the inherent uncertainties and imprecisions associated with qualitative criteria. The results revealed that Đồng Nai emerged as the highest-ranking site, demonstrating strong performance across crucial sustainability factors, including environmental impact, economic viability, and social considerations. The Fuzzy TOPSIS analysis highlighted Đồng Nai's superior alignment with the ideal sustainability criteria, suggesting it as the most suitable location for new manufacturing facilities.

Subsequently, the VIKOR method refined the decision-making process by determining the best compromise solution. This method, which balances group utility and individual regret, confirmed the findings of the Fuzzy

TOPSIS analysis. Đồng Nai remained the top choice, followed by Bình Dương and Vũng Tàu, with Long An and Bình Phước ranking lower due to specific challenges related to cost and regulatory factors.

The results underscore the importance of adopting a multi-criteria decision-making framework incorporating sustainability aspects into site selection. By integrating both Fuzzy TOPSIS and VIKOR methods, this study provides a robust and comprehensive evaluation of potential sites, considering both quantitative and qualitative factors. The findings offer valuable insights for decision-makers, guiding them in selecting sites that meet immediate operational needs and contribute to long-term sustainability objectives.

However, the study has limitations. The reliance on static criteria and data constraints may affect the accuracy and applicability of the results. Future research could benefit from incorporating dynamic factors, such as economic shifts and technological advancements, and engaging with local stakeholders to refine criteria and weights. Additionally, real-time data and broader stakeholder input could enhance the robustness of the decision-making framework.

In short, the hybrid Fuzzy TOPSIS and VIKOR approach provides a comprehensive and effective method for integrating sustainability criteria into manufacturing plant site selection. The study's findings highlight Đồng Nai as the most favorable site, offering a balanced combination of sustainability and operational benefits. This research contributes to sustainable site selection and provides a valuable framework that can be adapted and applied in various industrial contexts. In further studies, we will use different methods to support decision-making in practical cases and compare them with previous studies as presented by Nguyen (2022), Wang (2023), and Wang (2024).

Scientific Ethics Declaration

The authors declare that the scientific, ethical, and legal responsibility of this article published in EPSTEM journal belongs to the authors.

Acknowledgments or Notes

* This article was presented as an oral presentation at the International Conference on Research in Engineering, Technology, and Science (www.icrets.net) held in Tashkent, Uzbekistan, on August 22 - 25, 2024.

* The authors thank the Ministry of Science and Technology, Taiwan. We also would like to thank the National Kaohsiung University of Science and Technology and the Industrial University of Ho Chi Minh City for their assistance. Additionally, we would like to thank the reviewers and editors for their constructive comments and suggestions for improving our work.

References

Chen, S. J., & Hwang, C. L. (1992). Fuzzy multiple attribute decision making methods. In *Fuzzy multiple attribute decision making: Methods and applications* (pp. 289-486). Berlin, Heidelberg: Springer Berlin Heidelberg.

Elkington, J., & Rowlands, I. H. (1999). Cannibals with forks: The triple bottom line of 21st century business. *Alternatives Journal*, *25*(4), 42.

Esteban, M., & Portugal-Pereira, J. (2014). Post-disaster resilience of a 100% renewable energy system in Japan. *Energy*, *68*, 756-764.

He, K., Zhang, J., Zeng, Y., & Zhang, L. (2016). Households' willingness to accept compensation for agricultural waste recycling: taking biogas production from livestock manure waste in Hubei, PR China as an example. *Journal of Cleaner Production*, *131*, 410-420.

Hinloopen, E., Nijkamp, P., & Rietveld, P. (2004). Integration of ordinal and cardinal information in multi-criteria ranking with imperfect compensation. *European Journal of Operational Research*, *158*(2), 317-338.

Hwang, C. L., Yoon, K., Hwang, C. L., & Yoon, K. (1981). Methods for multiple attribute decision making. *Multiple attribute decision making: methods and applications a state-of-the-art survey*, 58-191.

Mardani, A., Zavadskas, E. K., Govindan, K., Amat Senin, A., & Jusoh, A. (2016). VIKOR technique: A

systematic review of the state of the art literature on methodologies and applications. *Sustainability*, *8*(1), 37.

Nădăban, S., Dzitac, S., & Dzitac, I. (2016). Fuzzy TOPSIS: a general view. *Procedia Computer Science*, *91*, 823-831.

Sun, C. C. (2010). A performance evaluation model by integrating fuzzy AHP and fuzzy TOPSIS methods. *Expert Systems with Applications*, *37*(12), 7745-7754.

White, W. T. (1982). Site selection as environmental impact assessment. *Impact Assessment*, *1*(3), 27-39.

Wang, C. N., Yang, F. C., Vo, N. T., & Nguyen, V. T. T. (2023). Enhancing lithium-ion battery manufacturing efficiency: A comparative analysis using DEA malmquist and epsilon-based measures. *Batteries*, *9*(6), 317.

Wang, C. N., Yang, F. C., Vo, N. T., & Nguyen, V. T. T. (2022). Wireless communications for data security: Efficiency assessment of cybersecurity industry—A promising application for UAVs. *Drones*, *6*(11), 363.

Wang, C. N., Yang, F. C., Vo, N. T., & Duong, C. T. (2024). Optimizing efficiency in BaaS marketplaces: A DEA-grey integration approach. *IEEE Access*.

Yen, T. C., Chen, W. L., & Chen, J. Y. (2016). Reliability and sensitivity analysis of the controllable repair system with warm standbys and working breakdown. *Computers & Industrial Engineering*, *97*, 84-92.

Author Information

Van Thanh Tien Nguyen
Industrial University of Ho Chi Minh City 12, Nguyen Van Bao, Go Vap, Ho Chi Minh City, Vietnam
Contact e-mail: *nguyenvanthanhtien@iuh.edu.vn*

Thi Minh Nhut Vo
Shinawatra University, Thailand 99 Moo 10, Bangtoey, Samkhok, Pathum Thani 12160, Thailand.

To cite this article:

Nguyen, V.T.T. & Vo, T.M.N. (2024). Integrating sustainability into mechanical manufacturing plant site selection: A hybrid fuzzy TOPSIS and VIKOR approach. *The Eurasia Proceedings of Science, Technology, Engineering and Mathematics (EPSTEM)*, *29*, Page 1-7.

The Eurasia Proceedings of Science, Technology, Engineering & Mathematics (EPSTEM)
ISSN: 2602-3199

The Eurasia Proceedings of Science, Technology, Engineering & Mathematics (EPSTEM), 2024

Volume 29, Pages 8-15

ICRETS 2024: International Conference on Research in Engineering, Technology and Science

Effect of Blending on Cold Flow Properties of Biodiesel Produced from Waste Frying Oil

Filiz Al-Shanableh
Near East University

Mahmut A. Savas
Near East University

Abstract: Recycling waste frying oils is a significant environmental and economic issue. Biodiesel production from waste frying oil is an effective method to obtain a sustainable energy source. Waste frying oil is considered an essential source of biodiesel production. Biodiesel fuel made from fats or oils, such as waste frying oil with high levels of saturated fatty compounds, tends to have high cold flow properties (CFPs). Waste frying oil (WFO) was sourced from a cafeteria on Near East University's campus and underwent a transesterification reaction to produce biodiesel fuel. The cold flow properties of WFO based-biodiesel—CP (cloud point), PP (pour point), and CFPP (cold filter plugging point)—were measured at 15°C, 11°C, and 13°C, respectively, following current ASTM and EN standards. These temperatures were also assessed for blends of biodiesel and commercial diesel. Due to its cold flow characteristics, pure biodiesel can be effectively utilized from May to October in Lefkoşa. However, appropriate blends of biodiesel and commercial diesel can be formulated for use during the winter season.

Keywords: Biodiesel, Waste frying oil, Cold flow properties

Introduction

The rise in population and higher food consumption rates has led to a surge in waste frying oil (WFO) from various sources such as households, restaurants, hotels, schools, and industries. Due to its island status, Cyprus faces a particularly severe situation compared to mainland areas. Improper disposal of WFO through sinks and drains poses significant challenges for sewage treatment facilities, consequently driving up purification expenses. Indeed, WFO represents a valuable residue that holds potential as a raw material for various purposes such as soap manufacturing, energy generation through anaerobic digestion, thermal cracking, and biodiesel fuel production (Phan & Phan, 2008; Sabudak & Yıldız, 2010; Al-Shanableh et al., 2023).

Biodiesel stands out as a popular alternative in liquid fuels, primarily due to its compatibility with conventional diesel engines with minimal or no adjustments required and its ability to be blended with petroleum diesel. Since the 1970s, various methods have been used to produce low-viscosity biodiesel from vegetable oil, such as pyrolysis, micro-emulsification, or transesterification. Transesterification, a reaction catalyzed by a base, acid, or enzyme, involves reacting virgin vegetable oil, waste frying oil (WFO), or animal fat with an alcohol to produce fatty acid methyl esters (FAME), or biodiesel, along with glycerol as a co-product, which has commercial value. Base-catalyzed transesterification is considered the most promising method for reducing viscosity. In this process, triglycerides react with methanol, releasing three fatty acid chains from the glycerol skeleton, which then combine with alcohol to form fatty acid methyl esters and glycerol (Encinar et al., 2007; Al-Shanableh, 2017). The primary biodiesel standards that serve as benchmarks for others are EN 14213 (Heating Fuels) and EN 14214 (Automotive Fuels), along with ASTM D6751-09. It is well-recognized that diesel fuel tends to gel or solidify at low temperatures. Biodiesel, however, tends to gel at higher temperatures

- Selection and peer-review under responsibility of the Organizing Committee of the Conference

than diesel fuel and exhibits poor cold flow properties (CFPs) (Evcil et.al., 2018). There are three critical parameters for assessing the CFPs of biodiesel: cloud point (CP), pour point (PP), and cold filter plugging point (CFPP). The CP is the temperature at which the first visible cloud of wax crystals forms when the fuel is cooled under specified conditions as described by ASTM D2500-09 or ISO 3015:1992. The PP is the temperature at which enough wax crystallizes to gel the fuel, rendering it unable to flow. The sample must be cooled according to the procedures outlined in ASTM D97-05 or ISO 3016:1994. The CFPP, described in ASTM D6371-05 and EN 116:1998, directly impacts the performance of diesel engines in winter. It signifies the lowest temperature at which 20 ml of fuel can pass through a 45-micron screen in 60 seconds under a 200 mm water (1.96 kPa) vacuum. The CP represents the highest temperature for assessing cold flow, while the PP is the lowest. The CFPP typically falls between the cloud and pour points. While the ASTM D6751 standard requires the CP, the EN 14213 and EN 14214 standards specify the PP and CFPP instead of the CP.

CFPs of WFO-based biodiesels are poorer compared to virgin vegetable oil-based biodiesel. One method to ameliorate this problem would be to blend biodiesel produced from WFO with petroleum-based diesel fuel or biodiesel produced from crude vegetable oils (Al-Shanableh et al., 2023). Bhale et al. (2009) examined how ethanol, kerosene, and commercial fuel blending impact the cold flow characteristics of biodiesel and found a considerable reduction in PP. Dwivedi and Sharma (2016) also added ethanol with different fractions to WFO-based biodiesel, showing improved CFP of blended biodiesel.

In this study, two types of raw materials, WFO rich in saturated fatty acids and refined canola oil (RCO) abundant in unsaturated fatty acids, underwent a single-step base-catalyzed transesterification process to produce biodiesel fuel called waste frying oil methyl ester (WFOME) and refined canola oil methyl ester (RCOME), respectively. Subsequently, the CFPs produced by the WFOME and RCOME, including CP, PP, and CFPP, were measured according to ASTM and EN standards. Three methods were employed to explore the effect of blending on the reduction of cold flow temperatures of WFOME. In the first method, WFO and RCO were mixed in varying ratios before undergoing transesterification, while in the second method, RCOME and WFOME were blended in different volume ratios. Furthermore, the third and the last, WFOME, was blended with commercial diesel fuel in different volume ratios. Resultant CFPs were measured and compared.

Materials and Methods

Materials

WFO was sourced from the cafeterias of Near East University, where approximately 18 to 20 liters of WFO were gathered daily per cafeteria and RCO was purchased from a local supermarket. Anhydrous methanol (MeOH) with a purity of 99.8% and high-purity sodium hydroxide (NaOH) were procured from Merck for the experiments. The feedstocks' fatty acid (FA) compositions were analyzed using the EN ISO 5508 method at the TRNC Ministry of Health, Directorate State Laboratory in Nicosia, utilizing Gas Chromatography (GC). The findings from the GC analysis are presented in Table 1.

Table 1. Fatty acid compositions of WFO and RCO

Fatty acid	Molecular mass (g/mol)	% Fatty acid of WFO	% Fatty acid of RCO
Caprylic acid - C8:0	144.21	0.05	0.0
Capric acid - C10:0	172.27	0.33	0.0
Lauric acid - C12:0	200.32	1.18	0.08
Myristic acid - C14:0	228.38	0.10	0.0
Palmitic acid - C16:0	256.43	39.29	5.63
Palmitoleic acid – C16:1	254.41	0.14	0.0
Stearic acid - C18:0	284.48	4.04	1.57
Oleic acid - C18:1	282.47	40.42	62.97
Linoleic acid - C18:2	280.45	13.84	21.34
Linolenic acid - C18:3	278.44	0.18	6.99
Arachidic acid - C20:0	312.54	0.0	0.46
Eicosenoic acid - C20:1	310.5	0.0	1.04

Experimental Set-up for Base-Catalyzed Transesterification

Figure 1 outlines the sequence of experimental steps that were employed to produce biodiesel through a base-catalyzed one-step transesterification reaction. While transesterification constitutes the primary phase in biodiesel production, adhering to international standards requires additional procedures such as raw material pretreatment, separation of reaction products, and purification of the resultant products.

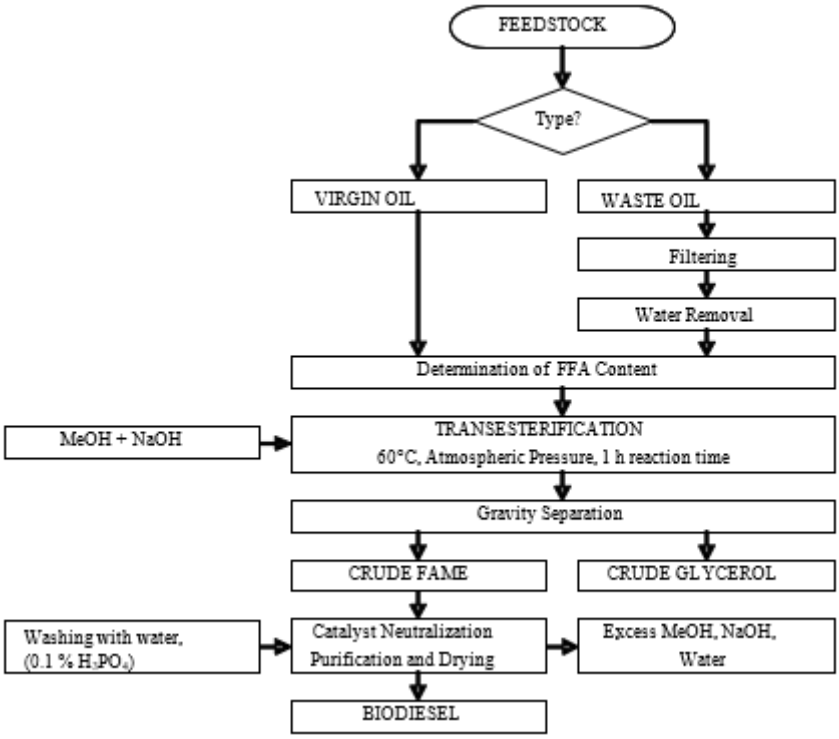

Figure 1. Flowchart of the experimental procedure for base-catalyzed transesterification

Determination of Some Physicochemical Characteristics and CFPs

Besides CFPs, some physicochemical properties of biodiesel produced were also determined to ensure the quality of products. The biodiesel samples' CP, PP, and CFPP were determined using ASTM standards, specifically ASTM D2500-09, ASTM D97-05, and ASTM D6371-05, respectively. The CP and PP measurements equipment adhered to ASTM standards, as illustrated in Figure 2. Three T-type thermocouples were utilized for temperature measurements. Thermocouples T1 and T2 were designated for measuring the temperature of the biodiesel sample. However, thermocouple T3 was explicitly employed to gauge the temperature of ethanol in the region adjacent to the jacket near the mid-section. Thermocouple T1 was positioned 3 mm beneath the sample's surface for PP measurement, while T2 was situated 3 mm above the bottom of the test jar to determine CP and CFPP. For CFPP measurements, the same setup was utilized, along with incorporating a vacuum system and a pipette featuring a filter unit.

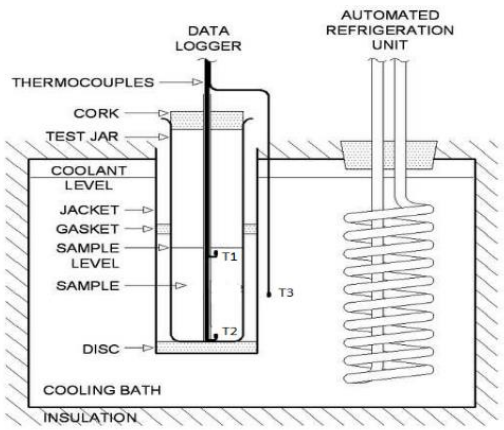

Figure 2. Experimental setup for CFP measurements

Blending Procedures

Three different methods were employed to explore the impact of blending on reducing the cold flow temperatures of WFOME. Method 1: WFO and RCO were combined in various proportions before undergoing transesterification. To target the reduction of CFP in WFOME, up to 50 vol % of RCO was blended with WFO. Blends were labeled according to composition, such as 100W0C, 90W10C, etc., for instance, in 100W0C, 100 vol % of WFO was mixed with 0 vol % of RCO. Method 2: Mixing RCOME and WFOME in different volume percentages. WFOME was blended with 0, 25, 50, 75, and 100 vol % of RCOME. Method 3: WFOME was blended with commercial diesel fuel on a volume basis. The commercial diesel fuel used was Euro diesel (EN 590:2009), obtained from a petrol station in Nicosia. Blends comprising 0, 5, 10, 20, 30, 40, 50, 70, 80, 90, and 100 vol % of commercial diesel were prepared.

Results and Discussion

Physicochemical Characteristics and CFPs of the Biodiesel Produced

WFOME and RCOME underwent fuel property assessments following either ASTM D6751 or EN 14214 standards. ASTM D6751 specifies the criteria that pure BD (B100) must meet before its use as a pure fuel or when blended with conventional diesel fuel. Conversely, EN 14214 outlines the minimal criteria for FAME (Fatty Acid Methyl Esters). Table 2 presents the fuel properties of the four BD samples tested and the thresholds outlined in the ASTM and EN standards.

Table 2. The fuel properties of WFOME and RCOME of the present study

	Method	**Limits**	**WFOME**	**RCOME**
Kinematic viscosity at 40 ˚C (mm^2/s)	ASTM D 445	1.9-6.0	4.666	4.582
Higher heating value (MJ/kg)	ASTM D 4809	35.0	40.14	39.23
Free glycerin (wt %, max.)	EN 14105	0.02	0.006	0.003
Total glycerin (wt %, max.)	EN 14105	0.25	0.248	0.196
Mono glyceride (wt %, max.)	EN 14105	0.80	0.62	0.64
Diglyceride (wt %, max.)	EN 14105	0.20	0.32	0.20
Triglyceride (wt %, max.)	EN 14105	0.20	0.34	0.1
Ester contents (wt %, max.)	EN 14103	96.5	96.5	97.0
Linoleic acid methyl esters (wt %, max.)	EN 14103	12.0	0.2	6.8
Iodine value (g I_2 / 100 g, max)	EN 14111	120	110	66
Cloud point (˚C)	D 2500		15	-3.5
Pour point (˚C)	D 97		12	-10
Cold filter plugging point (˚C)	D 6371		14	-7.5

The CFPs of biodiesel derived from WFO and RCO can be considered inferior compared to commercial diesel fuel No. 2, which boasts CP of -16°C, PP of -27°C, and CFPP of -18°C. Specifically, WFOME exhibits poorer CFP than RCOME. This discrepancy is primarily attributed to the substantial presence of saturated fatty acid compounds in waste frying oil samples and exceptionally high palmitic acid portions. Udomsap et al., 2008, observed that a high palmitic acid content (63 wt %) in palm stearin methyl ester led to a significant increase in CP and PP values, reported as 18°C and 19.4°C, respectively.

Based on data from the Meteorology Department of TRNC, the lowest average temperature recorded over the past ten years in January and February in Nicosia was approximately 2°C. All three CFP temperatures of BD produced from WFO exceeded 2°C. Consequently, pure WFOME may be suitable for use from May to October, covering six months of the year in Nicosia, while RCOME can be used year-round. A common approach to enhancing cold flow temperatures, including CFPP, involves blending commercial diesel fuel into the BD.

Effect of Blending in Improving the CFP of WFOME

Table 3 provides the CFP of biodiesel derived from blends of WFO and RCO, and their correlations are depicted in Figure 3. All CFP temperatures exhibit a downward trend as the RCO content increases in the BD samples. The findings indicate that blending WFO with RCO before biodiesel production reduces CFP temperatures in the resultant biodiesel samples. However, even with the addition of up to 50 vol % of RCO, the resulting fuel did not meet the requirements for suitability in regional climate conditions.

Table 3. Results for Method 1: CFP temperatures of WFO and RCO blends-based biodiesels

	RCO content (Vol %)	**CP**	**PP**	**CFPP**
100W0C	0	15	12	14
90W10C	10	15	7.5	13
80W20C	20	13	4.5	11
70W30C	30	12	4	9.5
60W40C	40	10	2.5	6
50W50C	50	9	0.5	5.5
0W100C	100	-3.5	-10	-7.5

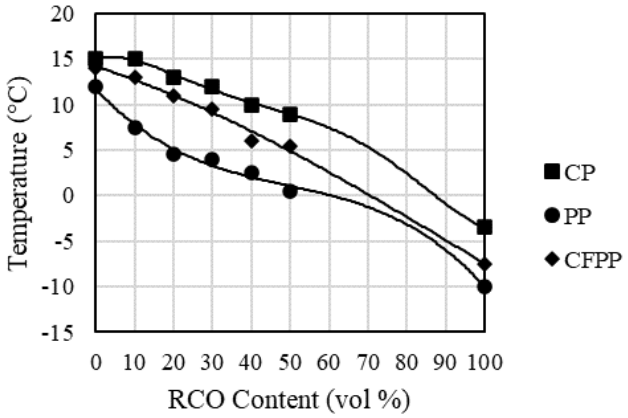

Figure 3. Effects of blending of WFO with RCO on the CFP temperatures

CP was linked to the proportion of RCO in the blend through an empirical fourth-order polynomial equation, represented by Equation 1. CFPP and PP, on the other hand, were associated with third-order polynomial equations, depicted by Equation 2. In these equations, X denotes the volume percentage of RCO, and T represents the temperature. The coefficients of these equations, along with their coefficients of determination (R^2), are provided in the last table of the study, Table 5.

$$T = a + bX + cX^2 + dX^3 + eX^4 + fX^5 \quad (1)$$

$$T = a + bX + cX^2 + dX^3 \quad (2)$$

Table 4. CFP temperatures of WFOME and RCOME blends

	RCOME content (vol %)	**CP**	**PP**	**CFPP**
100WFOME0RCOME	0	15	12	14
75WFOME25RCOME	25	14	6.5	8
50WFOME50RCOME	50	9	3.5	4.5
25WFOME75RCOME	75	3	-1	0
0WFOME100RCOME	100	-3.5	-10	-7.5

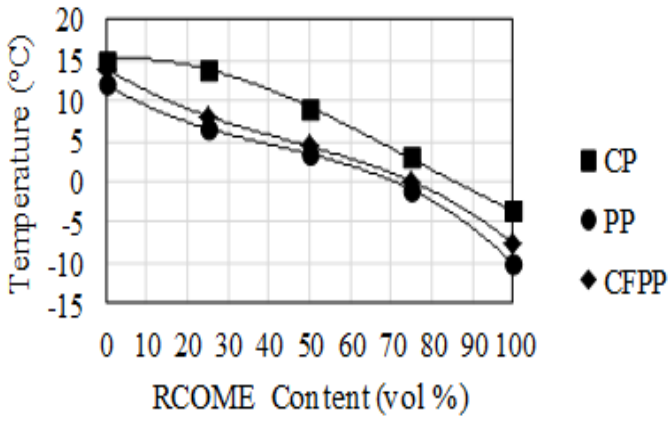

Figure 4. Effects of blending with RCOME on the CFP temperatures of WFOME

For Method 2, CFP temperatures of WFOME-RCOME mixtures are given in Table 4, and the effect of blending is presented in Figure 4. While there is a general trend of decreasing all CFP temperatures with increasing RCOME content, only blends consisting of 25 vol % WFOME and 75 vol % RCOME could be utilized throughout the entire year, except January and February. The other two blends, specifically 75WFOME-25RCOME and 50WFOME-50RCOME, were suitable for use only for six months, spanning from May to October.

All three CFP temperatures were correlated with the blend composition using an empirical third-order polynomial equation, as depicted in Equation 2. In this equation, X represents the volume percentage of RCOME, and T denotes the temperature. The coefficients of these equations and their corresponding R2 values, are provided in Table 5.

In Method 3, the CFP temperatures of WFOME - Commercial Petroleum Diesel blends were determined, and their relationship with commercial diesel content is illustrated in Figure 5. CP, CFPP, and PP tend to decrease with increased commercial diesel content. However, an exception was observed in the behavior of CP; up to 50% commercial diesel addition, CP remained constant, leading to an increase in the difference between CP and CFPP. A significant decrease in CP was observed when the concentration of commercial diesel was maintained between 70% to 90%. The difference between CP and CFPP converged to 2°C at 100% commercial diesel, similar to what was initially observed for the pure biodiesel. The current EN 590 gives six CFPP grades for various temperate climates. They change from Grade A to Grade F covering a range of CFPP from 5°C to -20°C. After determining CFPP at -4°C for the commercial diesel, it was concluded that the diesel purchased for blending corresponded to Grade C in the EN 590 standard.

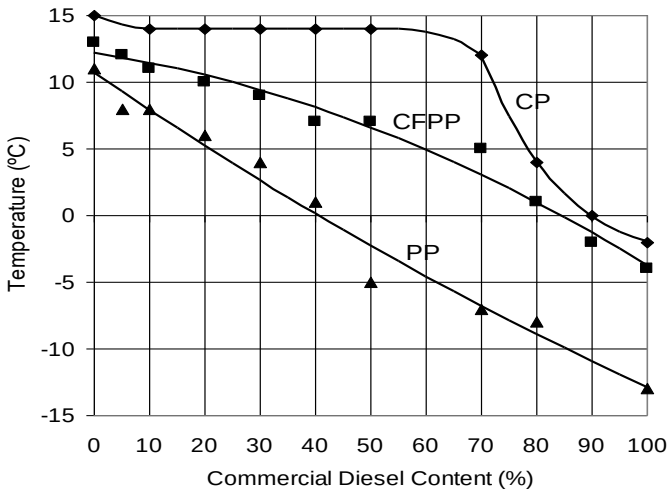

Figure 5. Effects of blending commercial diesel fuel on the CFPs of WFOME

Tang et al. (2009) found correlations between CP and PP with blend compositions using empirical second-order polynomial equations. However, they did not provide a correlation for CFPP. The CP curve depicted in Figure 5 can be associated with the blend composition below 70% using an empirical fifth-order polynomial equation and a heat capacity model for blends above 70% commercial diesel addition, as presented in Equation 3 and Equation 4, respectively. CFPP and PP were correlated with blend composition using empirical second-order polynomial equations, as shown in Equation 5. In these equations, X represents the commercial diesel content in percentage, and T denotes the temperature. The coefficients of these equations, along with their corresponding R^2 values, are provided in Table 5.

$$T = a + bX + cX^2 + dX^3 + eX^4 + fX^5 \quad \text{for } X \leq 70\ \% \quad (3)$$

$$T = a + bX + cX^{-2} \quad \text{for } X \geq 70\ \% \quad (4)$$

$$T = a + bX + cX^2 \quad (5)$$

Bhale et al. (2009) noted that crystal growth inhibitors, also called pour point depressants, effectively reduce the PP of biodiesel. However, they typically do not influence the CP and CFPP at low temperatures. Figure 5 suggests that commercial diesel fuel can lower PP and CFPP in all blends. However, for reducing CP, blending becomes effective only when the concentration in the blend exceeds 70%.

Table 5. Coefficients of the empirical correlations for WFOME blends

Method	CFP	Blend Content (vol %)	Correlation	Coefficients						R^2
				a	*b*	*c*	*d*	*e*	*f*	
1	CP	0-100 % RCO	Eq. (1)	15.026	0.1173	-0.0177	0.0005	$-6x10^{-6}$	$2x10^{-8}$	0.9988
	PP	0-100 % RCO	Eq. (2)	11.722	-0.4576	0.074	$-5x10^{-5}$	--	--	0.9942
	CFPP	0-100 % RCO	Eq. (2)	14.184	0.1366	-0.0012	$4x10^{-6}$	--	--	0.9944
2	CP	0-100 % RCOME	Eq. (2)	15.036	0.0455	-0.042	$2x10^{-5}$	--	--	0.9996
	PP	0-100 % RCOME	Eq. (2)	11.986	-0.3095	0.0046	$-4x10^{-5}$	--	--	0.9999
	CFPP	0-100 % RCOME	Eq. (2)	13.979	-0.316	0.0039	$-3x10^{-5}$	--	--	0.9999
3	CP	≤ 70 % Diesel	Eq. (3)	14.999	-0.21131	0.01575	-0.00053	$1x10^{-5}$	$-1x10^{-7}$	0.99993
		≥ 70 % Diesel	Eq. (4)	-66.016	0.39324	247288	--	--	--	0.99992
	CFPP	0 -100 % Diesel	Eq. (5)	12.170	-0.06413	-0.00095	--	--	--	0.98902
	PP	0 -100 % Diesel	Eq. (5)	10.714	-0.28405	0.00048	--	--	--	0.98894

Conclusion

Utilizing waste frying oil (WFO) instead of virgin vegetable oil for biodiesel production offers an effective means to reduce raw material costs while also addressing the issue of waste oil disposal. The current study produced biodiesel from WFO and RCO using a base catalyst transesterification reaction. Biodiesel derived from WFO exhibited a higher waxing temperature than commercial diesel fuel and RCO-based biodiesel. The biodiesel produced from WFO demonstrated poor cold flow properties, with critical parameters for low-temperature applications: CP, PP, and CFPP temperatures measured at 15°C, 11°C, and 13°C, respectively. These poor cold flow characteristics restrict the use of pure WFO-based biodiesel from May to October in Nicosia. However, blending biodiesel with commercial diesel fuel can enhance all three properties, enabling suitable blends for winter use.

Scientific Ethics Declaration

The authors declare that the scientific ethical and legal responsibility of this article published in EPSTEM journal belongs to the authors.

Acknowledgements or Notes

* This article was presented as presentation at the International Conference on Research in Engineering, Technology and Science (www.icrets.net) held in Tashkent/Uzbekistan on August 22-25, 2024.

*The authors would like to express their sincere thanks to Assoc. Prof. Dr. Ali Evcil and Asst. Prof. Dr. Cemal Govsa for their valuable contributions.

* The Near East University Research Fund supported this work under project no. YDU/2010-2-21.

*This work is a part of the Ph.D. thesis of Filiz Al-Shanableh, who is the first author of this article.

References

Al-Shanableh, F. (2017). *Characterization of cold flow properties of biodiesel transesterified from waste frying oil* (Doctoral dissertation). Near East University.

Al-Shanableh, F., Bilin, M., Evcil, A., & Savas, M. A. (2023). Estimation of cold flow properties of biodiesel using ANFIS-based models. *Energy Sources, Part A: Recovery, Utilization, and Environmental Effects*, *45*(2), 5440-5457.

Bhale, P. V., Deshpande, N. V., & Thombre, S. B. (2009). Improving the low temperature properties of biodiesel fuel. *Renewable Energy*, *34*(3), 794-800.

Dwivedi, G., & Sharma, M. P. (2016). Investigation of cold flow properties of waste cooking biodiesel. *Journal of Clean Energy Technologies*, *3*(4), 205-208.

Evcil, A., Al-Shanableh, F., & Savas, M. A. (2018). Variation of solid fraction with cold flow properties of biodiesel produced from waste frying oil. *Fuel*, *215*, 522-527.

Encinar, J. M., Gonzalez, J. F., Rodriguez, J. J., & Tejedor, A. (2002). Biodiesel fuels from vegetable oils: transesterification of Cynara c ardunculus L. oils with ethanol. *Energy & Fuels*, *16*(2), 443-450.

Phan, A. N., & Phan, T. M. (2008). Biodiesel production from waste cooking oils. *Fuel*, *87*(17-18), 3490-3496.
Sabudak, T., & Yildiz, M. J. W. M. (2010). Biodiesel production from waste frying oils and its quality control. *Waste Management*, *30*(5), 799-803.
Tang, H., Salley, S. O., & Ng, K. S. (2008). Fuel properties and precipitate formation at low temperature in soy-, cottonseed-, and poultry fat-based biodiesel blends. *Fuel*, *87*(13-14), 3006-3017.

Author Information

Filiz Al-Shanableh
Near East University, Nicosia, Mersin 10, Türkiye
Contact e-mail: *filiz.shanableh@neu.edu.tr*

Mahmut A. Savas
Near East University, Nicosia, Mersin 10, Türkiye

To cite this article:

Al-Shanableh, F. & Savas, M.A. (2024). Effect of blending on cold flow properties of biodiesel produced from waste frying oil. *The Eurasia Proceedings of Science, Technology, Engineering and Mathematics (EPSTEM), 29*, 8-15

The Eurasia Proceedings of Science, Technology, Engineering & Mathematics (EPSTEM)
ISSN: 2602-3199

The Eurasia Proceedings of Science, Technology, Engineering & Mathematics (EPSTEM), 2024

Volume 29, Pages 16-21

ICRETS 2024: International Conference on Research in Engineering, Technology and Science

Antimicrobial and Antioxidant Activities of Algerian *Lavandula Stoechas* Essential Oil

Ouardia Chaouchi
Mouloud Mammeri's University

Farida Fernane
Mouloud Mammeri's University

Abstract: *Lavandula stoechas* is one of the most traditionally used plants in Algeria, for the treatment of painful diseases such as inflammatory diseases, cystitis, nephritis and rheumatic arthritis. Our present study focuses on the evaluation of antimicrobial and antioxidant activity of the essential oil extracted by hydrodistillation from the aerial parts of *Lavandula stoechas* samples harvested in May 2022 at Bouhinoune, a village in Tizi ouzou located at 300 m altitude.The chemical composition of the essential oil was evaluated by GC/MS and the antioxidant activity by the DPPH method. The antimicrobial activity was tested against three gram positive and two gram negative bacterial by the use of the disc diffusion method. GC-MS analysis showed that our essential oil is rich in fenchone, camphor and eucalyptol. The essential oil of *Lavandula stoechas* showed good antioxidant activity compared to ascorbic acid and an interesting inhibitory effect against gram-positive bacteria with inhibition diameters greater than or equal to that recorded with the reference antibiotic. This valuable antibacterial activity is undoubtedly linked to the strong presence of fenchone, eucalyptol, camphor, linalool and linalyl acetate in the essential oil.

Keywords: Lavandula stoechas, Essential oil, Antioxidant activity, Antimicrobial activity, Disc diffusion

Introduction

Bioactive compounds derived from medicinal plants have garnered increasing interest within the scientific community, leading to numerous studies and research efforts. Thus, the investigation of bioactive compounds from medicinal plants has become a focal point (Apretna, 2005). This approach not only contributes to scientific and technological innovation but also to the preservation and sustainable use of biodiversity. Among these plants, lavender stands out not only for its well-known relaxing effect but also for its varied medicinal properties. Indeed, lavender has beneficial effects against lung infections, inflammatory diseases, diabetes, chills, and depression (Andrew, 2001).

Additionally, it presents a promising cytotoxic potential, thereby opening interesting perspectives for the development of anticancer treatments (Boukhatem, 2020). The study of natural products aims to harness the riches offered by nature to discover new molecules with medical, industrial, and environmental applications. This field of research also enables a better understanding of the fundamental biological processes at work in nature. In this context, medicinal plants play a crucial role, particularly the Lamiaceae family, which is extremely diverse and important. They are widely cultivated for their essential oils and therapeutic properties.

Method

Plant Material and Essential Oil Extraction

Leaves and flowers were collected on May 2022 in the region of Bouhinoune Tizi Ouzou province, Algeria. The essential oil extraction was carried out by steam distillation. 100 g of dry material were distilled for 2 hours in 1L of water. The steam, laden with the essence of the distilled material, condensed in the coil of the still before being collected in a decanter flask. Once the distillation was complete, the essential oil was dried with Na_2SO_4 and then stored at 4°C in amber glass bottles to prevent any potential oxidation or contamination.

CG-MS Characterization

The essential oil (EO) diluted with hexane at a 2:20 (v/v) ratio was analyzed using gas chromatography-mass spectrometry (GC-MS). The GC-MS analysis was conducted on a Bruker Scion 436-GC SQ MS system (Bremen, Germany) equipped with a fused silica Bruker BR-5ms capillary column (30 m × 0.25 mm, 0.25 µm film thickness). The mass spectrometer operated with an ionization voltage of 70 eV and scanned a spectral range of 50–300 m/z in full scan mode. The oven temperature was initially maintained at 60 °C for 1 minute, then ramped up to 170 °C at a rate of 2 °C/min, and finally increased to 220 °C at a rate of 15 °C/min, holding this temperature for 1 minute. Helium was used as the carrier gas at a flow rate of 1.0 mL/min. The detector and injector temperatures were set to 300 °C and 250 °C, respectively. The injector operated in split/splitless mode, with an injection volume of 1 µL and a split ratio of 1:20.

Antioxidant Activity

The antioxidant activity was evaluated in vitro using DPPH method. To determine the antioxidant power of *Lavandula stoechas* essential oil (LSEO), 50 µl of each LSEO sample and ascorbic acid at different concentrations (10-100 mg/ml and 10-100 µg/ml respectively) were added to 1 ml of 0.1 mM DPPH. The absorbance was measured at 517 nm after 30 minutes of incubation (Blois.M.S, 1958). For the control, 50 µl of methanol solution without the test substance were added to 1 ml of DPPH, and the percentage of inhibition was calculated according to the following formula: $\mathbf{\% \ Inhibition = [(A_c - A_e)/A_c] * 100}$
With A_c: Absorbance of the control, A_e: absorbance of the sample.

Antibacterial Study

Qualitative Study

The agar diffusion method is used to test bacterial sensitivity to antimicrobial substances (Rota.M.C, 2008). The process begins by incubating bacterial strains at 37°C for 18 to 24 hours to obtain isolated colonies. These colonies are then homogenized in a 0.9% saline solution and adjusted to a concentration of 10^8 CFU/ml using spectrophotometry. Under aseptic conditions, a sterile swab is dipped into the bacterial suspension, drained, and used to spread the bacteria on an agar plate by rotating the plate to ensure even distribution.

Discs containing the test substances are applied to the agar with a sterile clamp. The plates are refrigerated for 2 hours to allow diffusion of the substances before being incubated at 37°C for 24 hours. After incubation, zones of inhibition around the discs are measured to determine the effectiveness of the substances against the bacteria. This method ensures reliable and reproducible results by maintaining aseptic conditions, accurate bacterial concentrations, and proper diffusion time.

Quantitative Study

The Minimum Inhibitory Concentration (MIC) is defined as the lowest concentration of a substance that inhibits visible bacterial growth (Nikolić, 2014). To determine the MIC, bacterial suspensions and essential oil dilutions are prepared in a controlled and sterile environment. First, a bacterial suspension is prepared from isolated colonies homogenized in a 0.9% saline solution, adjusted to a concentration of 10^8 CFU/ml using spectrophotometry at 620 nm. Next, 10 ml of Mueller-Hinton (MH) broth are prepared in sterile tubes to dilute the bacterial suspension. Simultaneously, a stock solution of essential oil is prepared by mixing 500 µl of essential oil with 500 µl of MH broth containing 1% Tween 80, a surfactant that helps dissolve the essential oil in the aqueous broth.

The bacterial suspension is diluted in the MH broth to achieve the desired concentrations, and serial dilutions of the essential oil stock solution are performed. The bacteria and essential oil solutions are combined in sterile tubes or microplates, each well or tube containing a different concentration of essential oil, then incubated at 37°C for 24 hours. After incubation, the tubes or wells are examined for bacterial growth. The MIC is determined as the lowest concentration of essential oil that completely inhibits visible bacterial growth, allowing for an accurate assessment of the essential oil's antimicrobial efficacy.

Results and Discussion

GC-MS Results

The result of GC-MS analysis (Tables 1 and 2) show that lavender essential oil (leaves and flowers) is rich in monoterpenes (M) and oxygenated monoterpènes (OM). According to previous studies, most of the essential oils isolated from *Lavandula stoechas* plant collected all over the world, especially the Mediterranean countries such as Spain (Carrasco, 2015), Greece (Skoula, 1996), Turkey (Giray, 2008), Italy (M. Zuzarte, 2013), Morocco (S. Zrira, 2003), Tunisia (C. Messaoud, 2012) and Portugal (F. Matos, 2009). The GC-MS analysis reveals a predominance of monoterpenes, characteristic of the fenchone chemotype (Amara, 2017; Hassiotis, 2018 & Sebai, 2013). *Lavandula stoechas* gathered in other countries outside the Mediterranean such as Pakistan and Iran, presented the predominance of Camphor and Linalool respectively (Khan, 2023; Khavarpour, 2019; Asghari, 2016).

Table 1. Chemical composition of the essential oils extracted from flowers of *Lavandula stoechas*

Compounds	**Formula**	**%**	**Class**
1R-.alpha.-Pinene	$C_{10}H_{16}$	3.11	M
(+)-Camphene	$C_{10}H_{16}$	2.22	M
D-Limonene	$C_{10}H_{16}$	2.27	M
Eucalyptol	$C_{10}H_{18}O$	2.09	OM
Fenchone	$C_{10}H_{16}O$	28,13	OM
Camphor	$C_{10}H_{16}O$	23.46	OM
Borneol, acetate,	$C_{12}H_{20}O_2$	3.51	OM
Myrtenyl acetate	$C_{12}H_{18}O_4$	4.99	OM

Table 2. Chemical composition of the essential oils extracted from leaves of *Lavandula stoechas*

Compounds	**%**	**Formula**	**Class**
1R-.alpha.-Pinene	2.93	$C_{10}H_{16}$	M
Camphene	2.38	$C_{10}H_{16}$	M
m-Cymene	3.00	$C_{10}H_{16}$	M
Eucalyptol	4.75	$C_{10}H_{18}O$	OM
Fenchon	25.54	$C_{10}H_{16}O$	OM
camphor	37.53	$C_{10}H_{16}O$	OM
p-Cymen-8-ol	2.09	$C_{10}H_{14}O$	OM
(-)-Bornyl acetate	2.88	$C_{10}H_{20}O$	OM

Considering Algeria's area, the variation of the chemical composition is able to observed, other chemotypes is able to recorded, the isolated EO of the plant harvested in the west marked the predominance of the eucalyptol chemotype (Boukhatem, 2020), on the eastern side it is the linalyl acetate chemotype (Barkat, 2012) from this comparison we can notice how the climate and the type of soil can have an impact on the chemical composition of essential oils (Hadef, 2007). Furthermore, others factors can qualitatively and quantitatively alter the chemical composition of essential oils such as the state of growth of the plant (Gouyon, 1986), collection period, and the geographic location (Hadef, 2007 & Senatore).

Antioxidant Activity

The antioxidant activity of the essential oil appears related to its chemical composition (M. Lahlou, 2004)]. Our study revealed a result of 43.84 ± 2.09 mg/ml (Table 3). It has been demonstrated that the lower IC50 value indicates greater radical scavenging activity (Baali, 2019). Baali et al (2019) obtained a result of 4.04 ± 0.0017 mg/ml, which is explained by the high presence of fenchone at 50.29%, a major active compound directly associated with improved antioxidant activity (Rubert, 2000).

Table 3. Half maximal inhibitory concentration (IC50) of LSEO. Ascorbic acid was used as positive control.

Compounds	**IC50% (mg/ml)**
Ascorbic acid	0.062 ± 0.003
Essential oil (LS)	44.06 ±2.09

Antibacterial Activity

LSEO presented (Table 4) an interesting effect against Gram+ bacteria such as staphylococcus aureus and Bacillus with inhibition diameters (11.5±0.70) mm and (17.5±2.12) mm respectively. It is noted that the inhibition diameter given by Enterobacteria was (17.5±0.70) mm. On the other hand, the activity recorded against Gram- negative bacteria, LSEO presented more or less interesting effect with inhibition diameters (6.85±0.21) mm finally E,coli (10.5±0.70)mm. These results were confirmed by the values provided by the minimum inhibitory concentration (MIC) presented in Table 5.

Table 4. Result disk diffusion test of *Lavandula stoechas* EO

Strain		**Inhibition diameter(mm)**	**SD**	**ATB (mm)**	**% inhibition**
Pseudomonas aeruginosa	Gram -	6.85	0.21	27	7.61
klebsiella pneumoniae		8	1.41	15	8.88
Eschrichia Coli		10.5	0.70	23	11.66
Enterococcus feacalis		17.5	0.70	13	19.44
Staphylococcus aureus		11.5	0.70	24	12.77
Staphylococcus aureus	Gram +	9.5	0,70	25	10.55
Bacillus cereus		17.5	2.12	28	19.44

Table 5. MIC result of *Lavandula stoechas* EO

Strain		**MIC (mg/ml)**
Pseudomonas aeruginosa	Gram -	49.37±1.10
klebsiella pneumoniae		1.23±0.53
Eschrichia Coli		3.7±3.20
Staphylococcus aureus	Gram +	2.46±1.06
Bacillus cereus		1.23±0.53

However, it has been shown that the antibacterial activity depends on the chemical composition of the LSEO. According to a comparison of the antibacterial activity between an essential oil of Bulgarian origin (52.1% linalool; 9.5% linalyl acetate) and another EO of French origin (43.2% linalool and 29.1% linalyl acetate), it has been demonstrated that the EO of Bulgarian origin was better than the HE of French origin against 25 bacteria (Lis-Balchin, 1998). Several studies have demonstrated that Linalool and linalyl acetate have a powerful effect against microorganisms (Jianu, 2013). Other compounds have also been recognized for their antibacterial activity such as caryophylline (Jianu, 2013; Hendry, 2009). The antibacterial effect against E.Coli and Staph auereus can be justified by the presence of the Eucalyptol molecule [29] . In addition, α-terpenoel has been found to possess significant micro-biostatic activity against S aureus, E.Colie, Pseudo (Bouzouita, 2005).

Conclusion

Our study aimed to determine the effect of LSEO essential oil against Gram-positive and Gram-negative bacteria, as well as to evaluate its antioxidant activity against the DPPH radical. The results showed that LSEO essential oil has a promising effect against Gram-positive strains, with particularly notable antibacterial activity. Among the five strains tested, Bacillus was identified as the most sensitive to LSEO. These findings suggest that LSEO essential oil could be an interesting candidate for the development of new antibacterial strategies, especially against infections caused by Gram-positive bacteria.

Scientific Ethics Declaration

The authors declare that the scientific ethical and legal responsibility of this article published in EPSTEM journal belongs to the authors.

Acknowledgements or Notes

* This article was presented as an oral presentation at the International Conference on Research in Engineering, Technology and Science (www.icrets.net) held in Tashkent/Uzbekistan on August 22-25, 2024.

References

Amara, N., Boukhatem, M. N., Ferhat, M. A., Kaibouche, N., Laissaoui, O., & Boufridi, A. (2018). Potential use of lavender essential oil (Lavandula stoechas L.) as a natural food preservative. *Phytothérapie*, 1-9.

Apretna, E., Haramburu, F., Taboulet, F., & Bégaud, B. (2005). Conséquences médicales et socio-économiques des effets indésirables médicamenteux. *La Presse Médicale*, *34*(4), 271-276.

Apretna, E., Haramburu, F., Taboulet, F., & Bégaud, B. (2005). Conséquences médicales et socio-économiques des effets indésirables médicamenteux. *La Presse Médicale*, *34*(4), 271-276.

Asghari, J., Sadani, S., Ghaemi, E., & Mazaheri Tehrani, M. (2016). Investigation of composition and antimicrobial properties of lavandula stoechas essential oil using disk diffusion and broth microdilution. *Medical Laboratory Journal*, *10*(3).

Baali, F., Boumerfeg, S., Napoli, E., Boudjelal, A., Righi, N., Deghima, A., & Ruberto, G. (2019). Chemical composition and biological activities of essential oils from two wild Algerian medicinal plants: Mentha pulegium L. and Lavandula stoechas L. *Journal of Essential Oil Bearing Plants*, *22*(3), 821-837.

Barkat, M., & Laib, I. (2012). Antioxidant activity of the essential oil from the flowers of Lavandula stoechas. J. Pharmacogn. *Phytother*, *4*(7), 96-101.

Blois, M. S. (1958). Antioxidant determinations by the use of a stable free radical. *Nature*, *181*(4617), 1199-1200.

Boukhatem, M. N., Sudha, T., Darwish, N. H., Chader, H., Belkadi, A., Rajabi, M., & Mousa, S. A. (2020). A new eucalyptol-rich lavender (Lavandula stoechas L.) essential oil: Emerging potential for therapy against inflammation and cancer. *Molecules*, *25*(16), 3671.

Bouzouita, N., Kachouri, F., Hamdi, M., Chaabouni, M. M., Aissa, R. B., Zgoulli, S., ... & Lognay, G. C. (2005). Volatile constituents and antimicrobial activity of Lavandula stoechas L. oil from Tunisia. *Journal of Essential Oil Research*, *17*(5), 584-586.

Carrasco, A., Ortiz-Ruiz, V., Martinez-Gutierrez, R., Tomas, V., & Tudela, J. (2015). Lavandula stoechas essential oil from Spain: Aromatic profile determined by gas chromatography–mass spectrometry, antioxidant and lipoxygenase inhibitory bioactivities. *Industrial Crops and Products*, *73*, 16-27.

Gouyon, P. H., Vernet, P., Guillerm, J. L., & Valdeyron, G. (1986). Polymorphisms and environment: the adaptive value of the oil polymorphisms in Thymus vulgaris L. *Heredity*, *57*(1), 59-66.

Giray, E. S., Kırıcı, S., Kaya, D. A., Türk, M., Sönmez, Ö., & Inan, M. (2008). Comparing the effect of sub-critical water extraction with conventional extraction methods on the chemical composition of Lavandula stoechas. *Talanta*, *74*(4), 930-935.

Hadef, Y., Kaloustian, J., Chefrour, A., Mikail, C., Abou, L., Giodani, R., & Portugal, H. (2007). Chemical composition and variability of the essential oil of Thymus numidicus Poir. from Algeria. *Acta Botanica Gallica*, *154*(2), 265-274.

Hassiotis, C. N., & Orfanoudakis, M. (2018). The impact of Lavandula stoechas L. degradation on arbuscular mycorrhizal fungi, in a Mediterranean ecosystem. *Applied Soil Ecology*, *126*, 182-188.

Hendry, E. R., Worthington, T., Conway, B. R., & Lambert, P. A. (2009). Antimicrobial efficacy of eucalyptus oil and 1, 8-cineole alone and in combination with chlorhexidine digluconate against microorganisms grown in planktonic and biofilm cultures. *Journal of Antimicrobial Chemotherapy*, *64*(6), 1219-1225.

Jianu, C., Pop, G., Gruia, A. T., & Horhat, F. G. (2013). Chemical composition and antimicrobial activity of essential oils of lavender (Lavandula angustifolia) and lavandin (Lavandula x intermedia) grown in Western Romania. *Int. J. Agric. Biol*, *15*(4), 772-776..

Khan, Z., & Saeed, M. A. (2002). Antibacterial potentials of some constitutents of Lavandula stoechas L. *Pakistan Journal of Botany (Pakistan)*, *34*(4).

Khavarpour, M., Vahdat, S. M., Kazemi, S., Moghadamnia, A. A., Hasanzadeh, O., Salimi, Z., & Rahmanpour, N. (2019). Chemical composition, antibacterial and analgesic activity of Lavandula stoechas flowers from north of Iran. *International Journal of Engineering*, *32*(8), 1065-1073.

Lahlou, M. (2004). Methods to study the phytochemistry and bioactivity of essential oils. Phytotherapy Research: A*n International Journal Devoted to Pharmacological and Toxicological Evaluation of Natural Product Derivatives*, *18*(6), 435-448.

Lis-Balchin, M., Deans, S. G., & Eaglesham, E. (1998). Relationship between bioactivity and chemical composition of commercial essential oils. *Flavour and Fragrance Journal*, *13*(2), 98-104.

Messaoud, C., Chograni, H., & Boussaid, M. (2012). Chemical composition and antioxidant activities of essential oils and methanol extracts of three wild Lavandula *L. species. Natural Product Research, 26*(21), 1976-1984.

Matos, F., Miguel, M. G., Duarte, J., Venâncio, F., Moiteiro, C., Correia, A. I., & Pedro, L. G. (2009). Antioxidant capacity of the essential oils from Lavandula luisieri, *L.* stoechas subsp. lusitanica, L. stoechas subsp. lusitanica x L. luisieri and L. viridis grown in Algarve (Portugal). *Journal of Essential Oil Research, 21*(4), 327-336.

Nikolić, M., Glamočlija, J., Ferreira, I. C., Calhelha, R. C., Fernandes, Â., Marković, T., ... & Soković, M. (2014). Chemical composition, antimicrobial, antioxidant and antitumor activity of Thymus serpyllum L., Thymus algeriensis Boiss. and Reut and Thymus vulgaris *L. essential oils. Industrial Crops and Products, 52*, 183-190.

Rota, M. C., Herrera, A., Martínez, R. M., Sotomayor, J. A., & Jordán, M. J. (2008). Antimicrobial activity and chemical composition of Thymus vulgaris, Thymus zygis and Thymus hyemalis essential oils. *Food Control, 19*(7), 681-687.

Ruberto, G., & Baratta, M. T. (2000). Antioxidant activity of selected essential oil components in two lipid model systems. *Food Chemistry, 69*(2), 167-174.

Sebai, H., Selmi, S., Rtibi, K., Souli, A., Gharbi, N., & Sakly, M. (2013). Lavender (Lavandula stoechas L.) essential oils attenuate hyperglycemia and protect against oxidative stress in alloxan-induced diabetic rats. *Lipids in Health and Disease, 12*, 1-9.

Skoula, M., Abidi, C., & Kokkalou, E. (1996). Essential oil variation of Lavandula stoechas L. ssp. stoechas growing wild in Crete (Greece). *Biochemical Systematics and Ecology, 24*(3), 255-260.

Zuzarte, M., Gonçalves, M. J., Cavaleiro, C., Cruz, M. T., Benzarti, A., Marongiu, B., & Salgueiro, L. (2013). Antifungal and anti-inflammatory potential of Lavandula stoechas and Thymus herba-barona essential oils. *Industrial Crops and Products, 44*, 97-103.

Zrira, S., & Benjilali, B. (2003). The constituents of the oils of Lavandula stoechas L. ssp. atlantica Br.-Bl. and L. stoechas ssp. stoechas from Morocco. *Journal of Essential Oil Research, 15*(2), 68-69.

Author Information

Ouardia Chaouchi
Natural Resources laboratory – Mouloud Mammeri's University – 15000 Algeria

Farida Fernane
Natural Resources laboratory – Mouloud Mammeri's University – 15000 Algeria
Contact e-mail: *farida.fernane@ummto.dz*

To cite this article:

Chaouchi, O & Fernane, F, (2024). Antimicrobial and antioxidant activities of Algerian *Lavandula Stoechas* essential oil.. *The Eurasia Proceedings of Science, Technology, Engineering and Mathematics (EPSTEM), 29*, 16-21.

The Eurasia Proceedings of Science, Technology, Engineering & Mathematics (EPSTEM)
ISSN: 2602-3199

The Eurasia Proceedings of Science, Technology, Engineering & Mathematics (EPSTEM), 2024

Volume 29, Pages 22-27

ICRETS 2024: International Conference on Research in Engineering, Technology and Science

Geophysical Monitoring for Stability Assessment of Integrated Mine Waste Storage Facility

Maya Tomova
University of Mining and Geology "St. Ivan Rilski"

Atanas Kisyov
University of Mining and Geology "St. Ivan Rilski"

Abstract: Assessing the stability of integrated mine waste storage facilities is crucial for ensuring the safety and sustainability of mining operations. These facilities often consist of various components such as tailings dams, waste rock dumps, and water management structures. Implementing reliable monitoring systems is crucial for early detection of potential stability issues.To ensure a comprehensive and robust evaluation of mine waste storage facility regular reviews and updates to the stability assessment should be conducted throughout the lifecycle of the facility to account for changes in operating conditions and external factors. Monitoring technques such as geophysical methods can provide valuable information on factors such as slope movements, deformation behavior and physical properties of the materials in the facility. This knowledge is essential for conducting risk assessments, helps in identifying potential hazards and evaluating the associated risks. This involves considering factors such as long-term climatic changes, aging infrastructure, and evolving site conditions over the facility's lifespan.

Keywords: Mine waste, Geophysics, Electrical tomography, Monitoring

Introduction

Implementing monitoring systems in integrated mine waste storage facilities is crucial for early detection of potential issues, assessing performance, and ensuring the safety and integrity of the structures. One of the most important steps in monitoring of such facilities is to determine monitoring parameters. This may include factors such as pore water pressure, settlement, slope stability, seepage, and deformation. Identify critical parameters that need to be monitored based on the specific characteristics and risks associated with the mine waste storage facility. According to Dimitrov and Grigorova (Dimitrov & Grigorova, 2023) tailings from the processing of ore and coal are composed of fine material, water, and reagents from the process and their efficient and safe disposal is one of the most important things in the mining industry. As Dimitrov and Koprev (2023) stated the great challenge these facilities face is to control the water from tailings consolidation and the runoff inflow, because in the process of consolidation there is a great amount of water released which needs to be safely transported out of the facility. The invastigations are performed in IMWF located in Krumovgrad, part of Ada Tepe open pit gold mine. The operational sequence is following: mining operation generates excavated mine rocks which are trucked from the open-pit to the IMWF, dumped and spread to construct containment cells for the tailings. Tailings are thickened in the tailings thickening plant to the maximum practical amount (between 56-68% solids), and then conveyed by pump and pipeline to the containment cells (Diaz, 2014). Regaring to Eldridge (Eldridge et al., 2011) the lowest sections of the facility are undergo soil and soft material removal to create a solid foundation. An underdrain system is set up along the bottom of the valleys and existing drainage paths. This system gather and direct rainwater that seeps into the facility, as well as water discharged from the tailings during consolidation, to a collection point at the base of the facility. From there, the water is pumped to a reservoir for industrial use. Mine rocks, which are not used in cells construction process are placed as internal

berms to allow mine equipment access and also regularly monitoring measurments along the berms. The high number of operations chalenges the operational sequance as it is stated in (Eldridge et al., 2011) and that is the reason why Dimitrov (Dimitrov et al., 2023) looked at the possibilities to construct a facility that will ensure better operational sequence and decreese the need for contingency storage cells. By implementing a comprehensive monitoring program, integrated mine waste storage facilities can effectively identify and mitigate potential stability issues, enhance operational safety, and ensure the long-term integrity of the structures. For this purpose in IMWF is implemented geophysical survey based on electrical resistivity tomography. ERT is a geophysical imaging technique that utilizes electrical resistivity measurements to create 2D images of subsurface resistivity variations. By integrating these geophysical methods, mining companies and environmental agencies can obtain a comprehensive understanding of the subsurface conditions at mining waste sites. This information is critical for effective waste management, risk assessment, and remediation planning to mitigate potential environmental impacts.

Method

Mining activities produce substantial quantities of waste material, typically stored in large storage facilities. These facilities raise significant environmental impact and require regularly monitoring to mitigate the potential for disastrous incidents and regulate the production of polluted mine drainage. This research discuss the strong potencial of electrical resistivity tomography (ERT) for the monitoring of drainage paths within mining wastes in the storage facilities. According to Ali (Ali et al., 2023) non-invasive geophysical techniques, particularly electrical resistivity tomography (ERT), have emerged as invaluable tools for hydrogeological studies and the mapping of mine waste tailings. This geophysical technique works by measuring the electrical resistivity of subsurface materials. When applied to a waste deposit, ERT can detect areas with higher electrical conductivity, which may indicate the presence of leachate or other fluids. There are several directions ERT can be utilized in the monitoring program in the IMWF:

- Non-invasive monitoring - ERT is a non-invasive technique that can be deployed without disturbing the surface or subsurface infrastructure of the waste storage facility. This allows for continuous monitoring without the need for extensive excavation or drilling activities.
- Seepage detection - ERT can help identify zones of increased moisture content or water saturation within waste storage facilities. By monitoring changes in electrical resistivity over time, ERT can detect potential seepage paths or areas of groundwater ingress, which may indicate potential stability issues;
- Characterization of subsurface structures – ERT can provide valuable information about the subsurface structures and geological features beneath the waste storage facility. This includes identifying potential subsurface weaknesses, faults, fractures, or preferential flow paths that may affect stability.
- Assessment of seepage control measures – ERT can be used to evaluate the effectiveness of seepage control measures such as berms or cutoff walls. By monitoring changes in resistivity profiles along these structures, ERT can help identify potential areas of seepage or leakage.
- Early warning system - ERT can serve as part of an early warning system for potential stability issues. By continuously monitoring changes in subsurface resistivity, ERT can provide early detection of anomalous conditions that may indicate impending failures or instability within the waste storage facility.
- Integration with other monitoring techniques - ERT can be combine with other monitoring techniques such as piezometers and inclinometers. By providing additional subsurface information, ERT can enhance the overall understanding of the site conditions and improve the accuracy of stability assessments.

In current research apparent resistivity data were collected with a Wenner array on the ground surface. The electrodes are arranged along a line with a constant spacing between them. ERT data processing and modelling were done using the RES2DINV. This computer program determines the 2D resistivity model automatically for the observed data (Griffiths & Barker, 1993). The 2D model used by the inversion program, consists of a number of rectangular blocks, arange around to the distribution of the data points in the pseudosection. The distribution and size of the blocks is automatically generated by the program using the distribution of the data points (Edwards 1977).

Results and Discussion

The aim of recent research is to determine spatially distribution of water content and to assess the level of drainage between two conducted surveys in different periods - 2020 and 2023. For monitoring purposes four lines are measured and matched for comparison (Figure 1 to Figure 4).

The length of each line is present in the Table № 1.

Table 1. Total length of each line of integrated mine waste facility

Line	ERT section along Berm 320	ERT section along Berm 330	ERT section along Berm 340	ERT section along Berm 350
Length, m	150	170	210	210

Based on interpretation of ERT lines it can be observed that from the analysis of ERT data within the IMWF, it can be inferred that the electrical resistivity distribution is well differentiated in depth across all profiles. The comparison between ERT section along Berm 320 measured in 2020 and again in 2023 (Figure 1) shows that the drainage is still in progress, but also there is significant improvement according to water drainage.

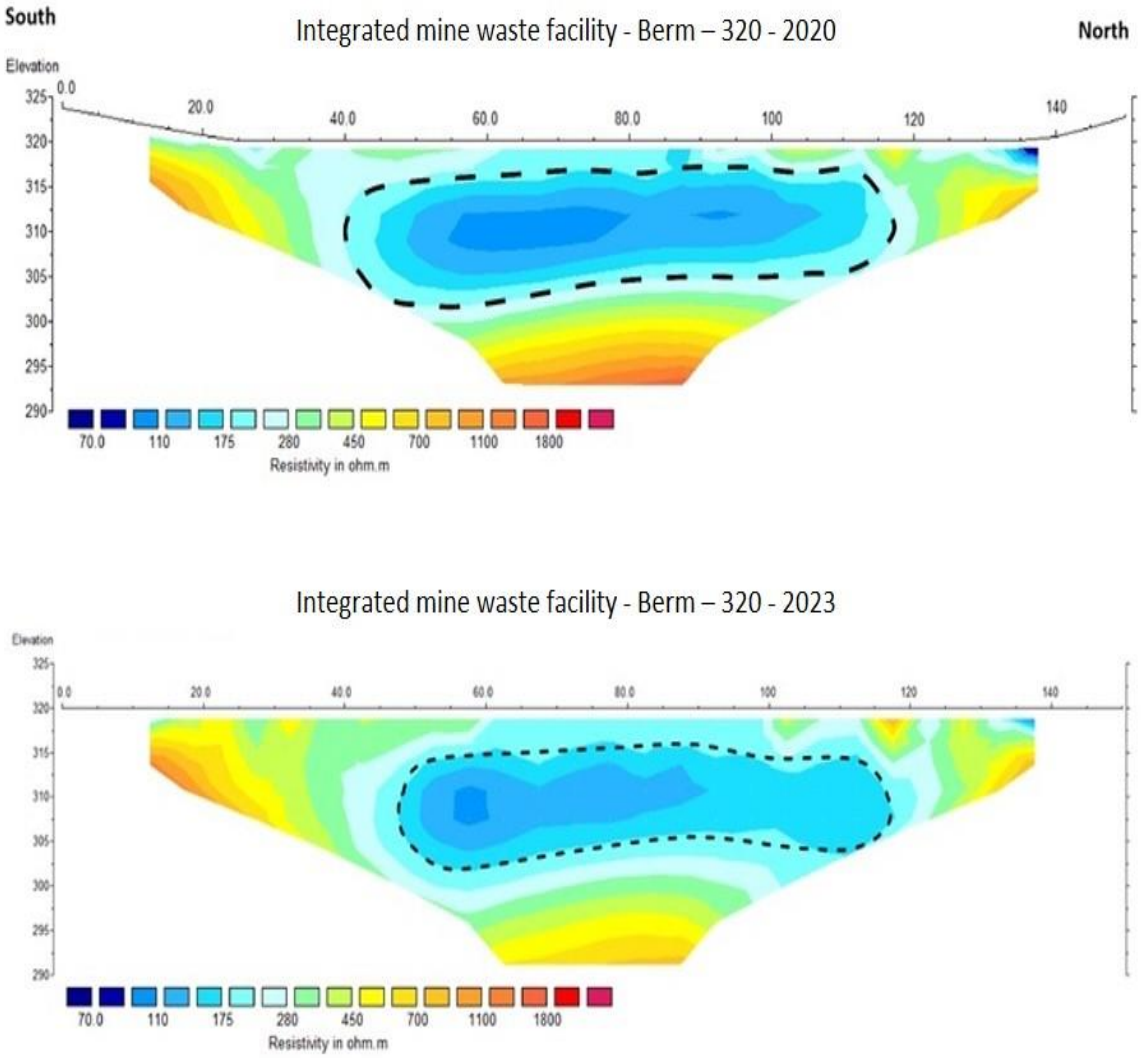

Figure 1. Comparison between ERT section along Berm 320 measured in 2020 (top) and in 2023 (bottom)

According to the measurement results it is considered that specific electrical resistance of the observed area varies from 70 Ωm to more than 2000 Ωm. Across all surveyed lines, noticeable regions of relatively low electrical resistance, ranging from 70 Ωm to approximately 200 Ωm, are evident in the central areas. These zones marked the spatial distribution of an environment with increased water saturation due to the incomplete drainage of the deposited material.

The comparison between ERT section along Berm 330 measured in 2020 and again in 2023 (Figure 2) also shows that the water drainage for three years is significant, but there are still zones with slowly increase of water content across the line. This comparison also shows that the area is currently characterized by increased values of electrical resistance in the southern direction (corresponding to the slope of the natural terrain), probably due to the successful drainage of the cell and the gradual drying of the deposited material.

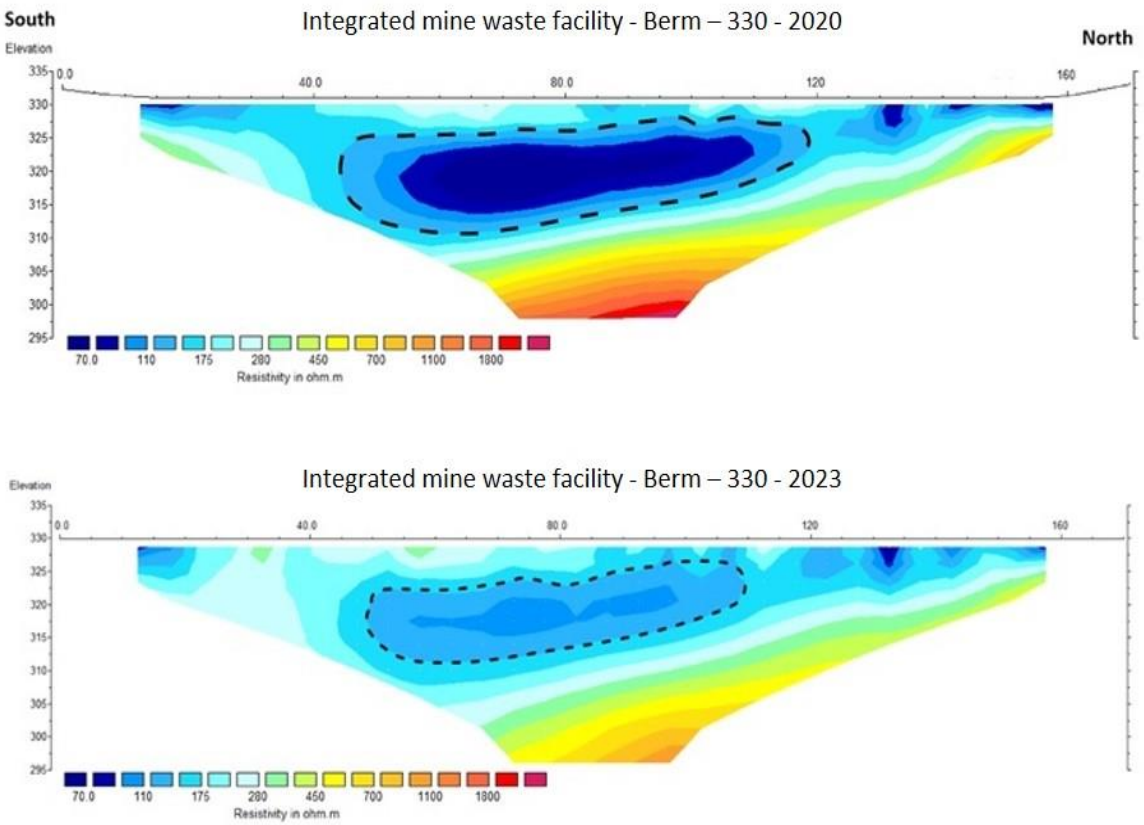

Figure 2. Comparison between ERT section along Berm 330 measured in 2020 (top) and in 2023 (bottom)

The comparison of the electrical resistivity distribution along Berm 340 measured in 2020 and in 2023 (Figure 3) shows that the area currently has slightly elevated electrical resistivity values, which is most likely due to the drainage of the cell and the consolidation of the material placed in it.

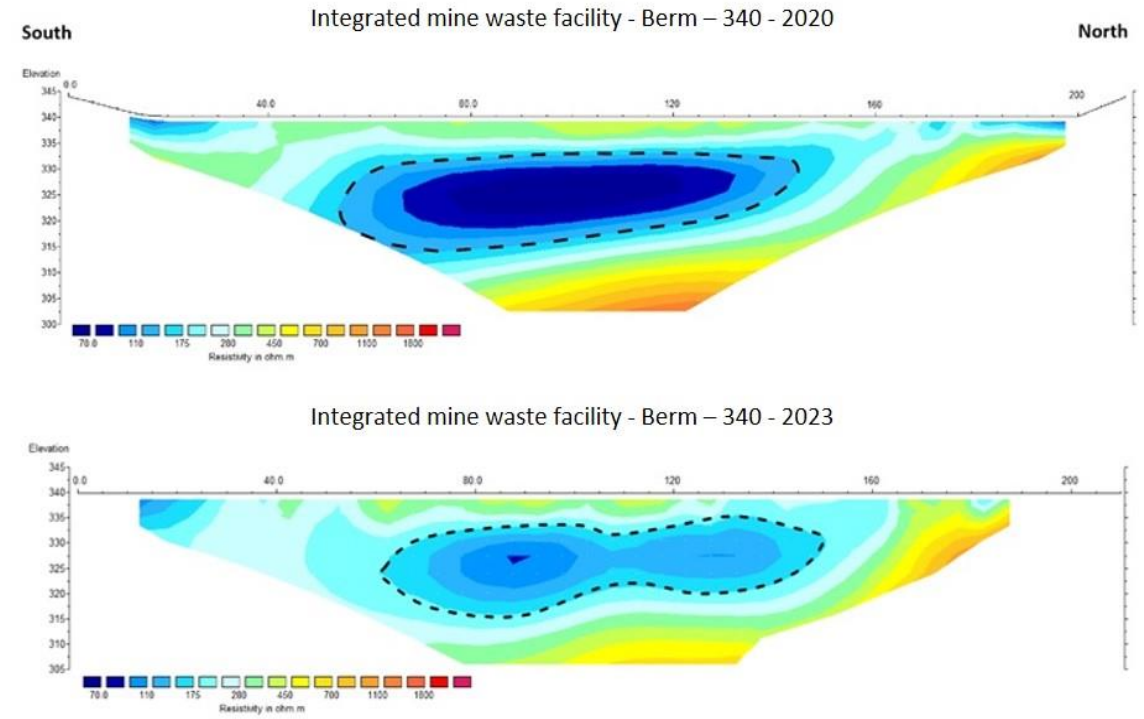

Figure 3. Comparison between ERT section along Berm 340 measured in 2020 (top) and in 2023 (bottom)

Monitoring of ERT section along Berm 350 measured in 2020 and in 2023 (Figure 4) shows that a certain spatial displacement of the watered areas is observed, related to the process of their drying and the accumulation of heavy masses in the cells above. It is very likely that the size of the low resistance zones along the measured lines is determined by the weight of the mining waste deposited during the period in the overlying cells.

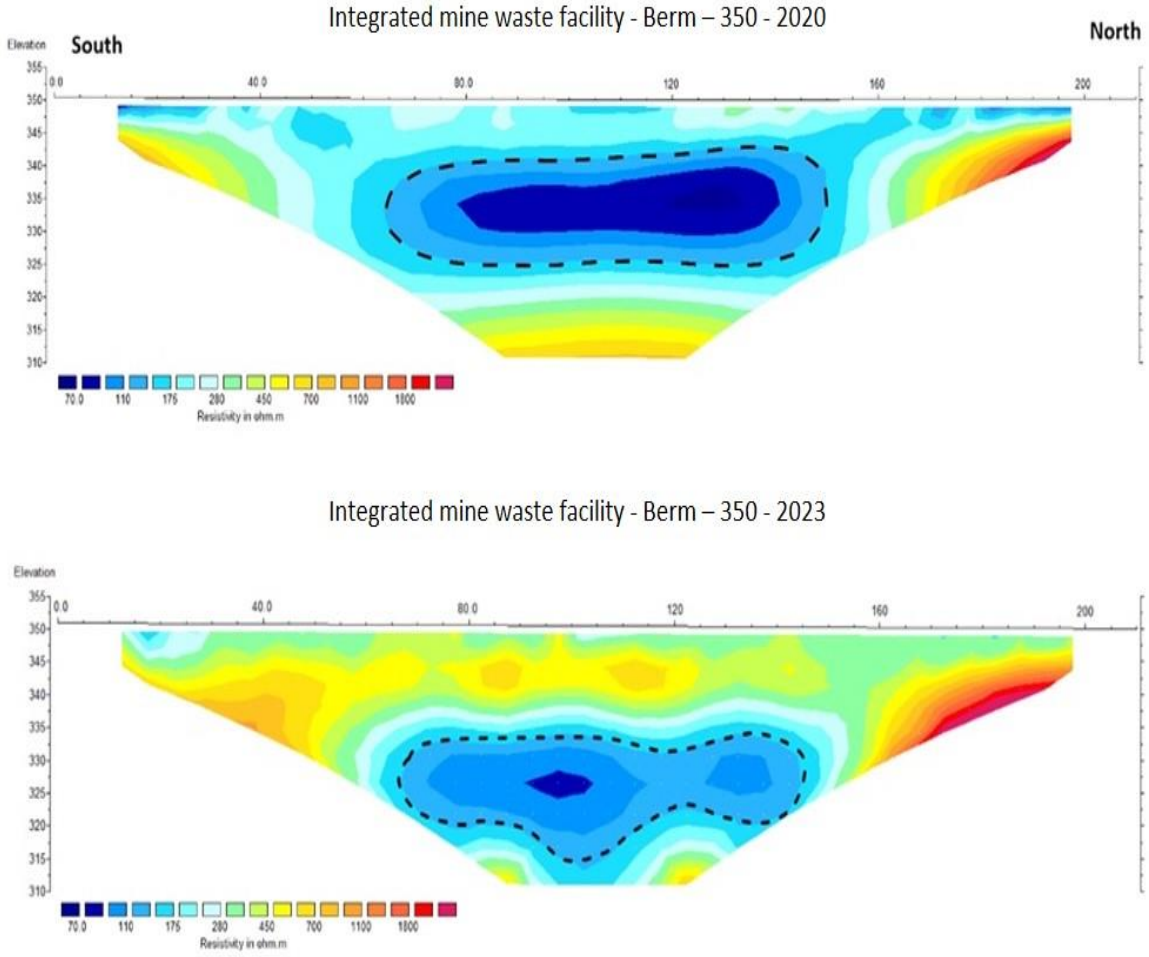

Figure 4. Comparison between ERT section along Berm 350 measured in 2020 (top) and in 2023 (bottom)

The regular monitoring of electrical resistance along the designated profiles enables tracking of the drainage progress and the level of drying within the section.

Conclusion

Overall, a comprehensive stability assessment of integrated mine waste storage facilities requires a multidisciplinary approach, incorporating geological, geotechnical, hydraulic, and risk management considerations to ensure the safety and sustainability of mining operations. The application of geophysical methods during the various stages of construction, subsidence, and dewatering of the cells in the IMWF improves the overall understanding of the operation of the facility and allows informed and timely actions to be taken if necessary. Incorporating geophysical techniques throughout different stages of mining projects can mitigate geological ambiguity by identifying and delineating conflict zones and by providing important information for decision-making in planning follow-up actions.

Scientific Ethics Declaration

The authors declare that the scientific ethical and legal responsibility of this article published in EPSTEM journal belongs to the authors.

Acknowledgements or Notes

* This article was presented as an oral presentation at the International Conference on Research in Engineering, Technology and Science (www.icrets.net) held in Thaskent/Uzbekistan on August 22-25, 2024.

References

Ali, M. A. H., Mewafy, F. M., Qian, W., Alshehri, F., Almadani, S., Aldawsri, M., ... & Saleem, H. A. (2023). Mapping leachate pathways in aging mining tailings pond using electrical resistivity tomography. *Minerals*, *13*(11), 1437.

Dimitrov, L., & Grıgorova, I. (2023). Improved tailings consolidation using dewatering agents: A step towards safer and sustainable mining waste management. *The Eurasia Proceedings of Science Technology Engineering and Mathematics*, *23*, 225-231.

Dimitrov, L., Grigorova, I., & Yankova, T. (2023). Possibilities to construct combined mine waste dump facility with better operational sequence. *The Eurasia Proceedings of Science Technology Engineering and Mathematics*, *23*, 42-49.

Dimitrov L., Koprev, I. (2023). On the possibilities for improving drainage systems and safety factor with combined mine waste dump facilities. *Annual of University of Mining and Geology "St. Ivan Rilski", 66(*66), 34–37.

Diaz, M. (2014). *Evaluation of liner requirement. Krumovgrad integrated mine waste facility (A150-14-R2243).* Retrieved from https://s27.q4cdn.com/486073686/files/doc, last accessed 2024/02/09.

Edwards, L. S. (1977). A modified pseudosection for resistivity and IP. *Geophysics*, *42*(5), 1020-1036.

Eldridge, T., Wickland, B., Goldstone, A., & Kissiova, M. (2011). *Integrated mine waste storage concept,* Krumovgrad gold project, Bulgaria.

Griffiths, D. H., & Barker, R. D. (1993). Two-dimensional resistivity imaging and modelling in areas of complex geology. *Journal of Applied Geophysics*, *29*(3-4), 211-226.

Author Information

Maya Tomova
University of Mining and geology “St. Ivan Rilski”
Sofia, Studentski grad, prof. Boyan Kamenov", Sofia 1700
Bulgaria
Contact e-mail: *maya.grigorova86@gmail.com*

Atanas Kisyov
University of Mining and geology “St. Ivan Rilski”
Sofia, Studentski grad, prof. Boyan Kamenov", Sofia 1700
Bulgaria

To cite this article:

Tomova, M. & Kisyov, A. (2024). Geophysical monitoring for stability assessment of integrated mine waste storage facility. *The Eurasia Proceedings of Science, Technology, Engineering and Mathematics (EPSTEM), 29*, 22-27.

The Eurasia Proceedings of Science, Technology, Engineering & Mathematics (EPSTEM)
ISSN: 2602-3199

The Eurasia Proceedings of Science, Technology, Engineering & Mathematics (EPSTEM), 2024

Volume 29, Pages 28-40

ICRETS 2024: International Conference on Research in Engineering, Technology and Science

A Preliminary Assessment of a Limestone Quarry's Direct and Indirect Carbon Footprint

Dimitar Kaykov
University of Mining and Geology "St. Ivan Rilski"

Vessela Petrova
University of Mining and Geology "St. Ivan Rilski"

Abstract: As a sub-sector of the mining industry, quarrying is also responsible for greenhouse gas emissions. Limestone is one of the most frequently extracted minerals used for construction, building materials and industrial applications. A common way limestone is consumed is for the production of lime, cement, steel, etc. Based on literature review, the amount of carbon emissions per ton of lime and cement was compared to the amount of expected carbon emissions per ton of limestone for a quarrying operation. The carbon emissions for the studied quarry were calculated using the CO_2-equivalent metric in kilograms per ton of limestone, similar to other quarrying operations. A computer script model based on practical theoretic models and rules of thumb was created, aimed to simulate different states of the quarrying operation. A review of literature and modeled results show that the studied quarrying operation is responsible for significantly less carbon emissions, compared to the emissions related to the production of lime and cement. Additionally, based on a non-linear optimization model, different strategies related to the reduction of the carbon footprint for quarrying operations have been established for the design of blast patterns. These practices can serve as a preliminary way of assessing the direct and indirect carbon footprint related to limestone quarrying for future mining operations. Moreover, the effect of the chosen optimization function has also been studied. It resulted in the conclusion that the vector of the optimal solution based on the direct carbon footprint of the quarry can be biased, compared to the one obtained via the indirect and direct emissions approach.

Keywords: Greenhouse gas emissions, Carbon footprint, Limestone quarrying, Blasting, non-linear optimization

Introduction

Climate change is a global problem that has caused many negative impacts on different regions of the world. Regional flooding, reduced dry season rainfall and irreversible ocean temperature rise are causing catastrophic damage to the marine ecosystem. Scientific developments support the theory that the global climate is changing due to human influence, with the Intergovernmental Panel on Climate Change (IPCC) focusing on 4 human-induced greenhouse gases – carbon dioxide, hydrofluorocarbons, nitrous oxide and methane.

Carbon dioxide (CO_2) emissions, resulting primarily from human activities, have global consequences for ecosystems and the atmosphere. The significant increase in carbon dioxide concentration in recent decades has been associated with global warming, changes in climate conditions, rising sea levels and other adverse effects on biodiversity and human health. In addition, excessively increasing emissions of greenhouse gases into the atmosphere are one of the main drivers of global climate change. Jiao (2023) claims that carbon dioxide emissions account for as much as 80% of total greenhouse emissions, and its amounts are increasing significantly. Moreover, according to this research, carbon dioxide emissions have increased rapidly since 1946, concluding that this is due to the increase in the number of countries involved in industrial development (Jiao,

2023). Despite the efforts of industry and governments, the concentration of carbon dioxide increases with each subsequent year. The trend is correlated with the overall demand for resources and the gradual growing world population. On the one hand, more energy is required to be produced to meet people's needs, which causes more carbon emissions to be released into the air. On the other hand, humans have to pay the penalty as global warming leads to a series of economic threats. Therefore, climate change and the impact of greenhouse gases draw common global challenges across the regimes of many countries. There is a continuous trend where international efforts aim to address this problem through joint action (Lisaria Putri et al., 2023). Most countries are concerned about global warming and are trying to find methods to minimize greenhouse gases to cope with environmental changes. Many governments around the world and environmental organizations are taking measures and actions to reduce emissions of carbon dioxide and other greenhouse gases. The Paris Agreement, signed on December 12, 2015 in Paris, France, reflects these concerns, as carbon disclosure is part of the contribution of businesses to the environment and climate change, exclusively to global warming. The Paris Agreement is one of the foundational international treaties focusing on greenhouse gas emissions adopted at the United Nations conference. More than 160 developing and developed countries established an international agreement to overcome the problem of global warming. In the agreement, each member country commits to limiting the global temperature increase to 2°C above the temperature since the beginning of the industrial revolution era. The agreement provides for commitments to reduce greenhouse gas emissions by all participating countries, emphasizing adaptation to climate change and financial support for developing countries. In addition, the Paris Agreement provides for a review and transparency system to monitor progress towards the targets. This document is essential in global efforts to address climate change and is recognized as an important tool for cooperation between countries on sustainable development.

Limestone and Its Carbon Footprint

With respect to the global effort of reducing greenhouse gas emissions, this paper examines a raw material with extremely wide application, including among the most carbon intensive sectors. As a rock material that consists primarily of the mineral calcite (calcium carbonate – $CaCO_3$), limestone is usually formed by precipitation from aqueous solutions as a result of the evaporation of water. (Koprev et al., 2018) Industrial sources, including lime production and cement production, contribute significantly to global anthropogenic emissions. The process of producing lime, similar to cement, involves heating limestone in a kiln at high temperatures, releasing CO_2 into the atmosphere. This process also indirectly contributes to CO_2 emissions through fossil fuel combustion used for energy. The extensive global production of lime, around 427 Mt in 2020, is primarily used in the chemical industry, environmental treatment, metallurgical industry, and construction industry. The global uptake of CO_2 from lime production processes is reported to have risen from 9.16 million metric tons of carbon per year in 1930 to 34.84 million metric tons of carbon per year in 2020 (Bing et al., 2023). According to Laveglia et al. (2022) in terms of Global Warming Potential (GWP), 0.94 kg CO2 eq/kg hydrated lime are produced. To some extent, cement also has the same magnitude of its carbon footprint. According to Hendriks et al. (2004) and Lei et al. (2011), 0.5-0.9 kg of CO_2 is evolved for every 1 kg of cement produced, which leads to 3.24 billion tons of CO_2 annually. Moreover, Fayomi et al. (2019) point out that these figures do not take into account the emissions from the quarrying and transportation of raw materials and the transport and delivery of produced cement. Apart from its traditional use for cement, limestone is used in steel manufacturing for slag formation, and its demand is influenced by global steel production levels. For the production of 1 t of crude steel, the two key steel production routes using integrated steelmaking and the electric arc furnace require around 270 kg and 88 kg of limestone, respectively. Notably, China, as the largest steel producer, experienced reduced steel production due to policy changes aimed at reducing pollution levels. The United States and Germany also saw changes in steel production. Additionally, limestone is utilized in iron production as a fluxing agent to remove impurities and enhance the efficiency of the blast furnace process.

Limestone in the context of quarrying operations' carbon emissions is not sufficiently studied in the scientific literature, which further strengthened the interest of the authors. One reason behind this, is that limestone as a product from the aggregate industry is associated with substantially less greenhouse gas emissions, compared to its use as a raw material for cement, lime or steel manufacturing. (Hristova, 2022) Multiple reports of the environmental impact of quarrying sites show that the overall GHG emissions range roughly between 1.5 to 5 kg of CO_2-equivalent (Environmental Product Declaration for limestone aggregates Xirorema Quarry; Winstone Aggregates Environmental Product Declaration For Aggregate and Sand Products, 2022; Eigenrieden Quarry: Climate neutrality in the extraction of raw material; EVA025 –Final Report: Aggregates Industry Life Cycle Assessment Model: Modelling Tools and Case Studies, 2009; Environmental Product Declaration for aggregates from Nyrand gravel pit – Svebølle, 2021). Regardless of the small relative impact of a single quarry, the problem regarding the carbon footprint of the quarrying industry itself also needs to be formalized as global

limestone exports are forecast to reach 1.04 billion tons by 2029 (Limestone Market Size & Share Analysis - Growth Trends & Forecasts (2024 - 2029)). Since 2019, the market was negatively affected by the COVID-19 pandemic due to disruptions in manufacturing and supply chains, but it has been recovering with increasing demand from industries like construction, steel production, agriculture, and water treatment. Short-term market drivers include rising demand from the construction industry and increasing global steel production, while health risks associated with limestone consumption and high carbon dioxide emissions may hinder market growth. The Asia-Pacific region is expected to lead the market, and upcoming global wastewater treatment projects are likely to create growth opportunities. India possesses abundant and high-quality limestone reserves across its area, which has positioned India as the second-largest producer of cement in the global market. Due to population growth and the central government's liberalization policies, there has been a significant increase in the mining of limestone rocks to meet social demands (Somayajula et al., 2021). Based on the established literature review, an overview of the key technological processes which influence the production of limestone and their direct or indirect relationship with GHG emissions is provided in Fig. 1.

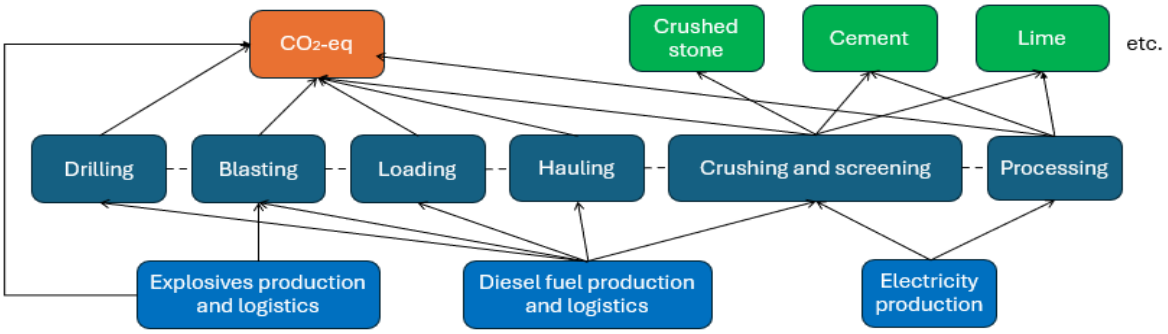

Figure. 1. A network model of the direct and indirect GHG emissions related to limestone quarrying and processing

Certain site-specific details such as selected mining technology, energy sources, equipment used, stages of crushing and screening and end-product designation are all factors which affect the overall carbon footprint for each quarrying operation. If coal is used as an energy source for the provision of electrical power for limestone processing, the emissions from this process will be significant. Alternatively, using cleaner energy sources such as gas or renewables can reduce the carbon impact. Taking into consideration the end-product's designation, applying more efficient and cleaner extraction technologies can reduce carbon emissions, for example during the production of cement or lime. Last but not least, effective treatment and management of waste from limestone mining can have a significant impact on emissions. Study by Yankova (2020) highlight the key issues related to mining and mineral processing waste, particularly focusing on tailing storage, reducing the amount of mining waste, and ensuring safe storage practices. If the process includes waste reduction methods or the use of waste storage or processing technologies, this can contribute to reducing the negative impact on the environment. Mining and mineral processing general significant quantities of waste that pose environmental and health risks if not properly managed. Therefore, effective waste management is essential for sustainable development in the mining industry (Tomova & Kisyov, 2023). At the same time, if more sophisticated ways of reclaiming depleted deposits are being applied, this could temporarily increase the amount of GHG emissions due to the more extensive use of diesel-powered equipment for earthwork operations and land reclamation. Despite that in due time this effect can be negated. Hence, the process of providing a generalized model for the evaluation of the carbon footprint of a quarrying operation is a highly complex task and can be dependent on a large set of decision variables. However, given that certain initial assumptions are made, a preliminary assessment of the GHG emissions based on their typical sources can be provided.

Assumed Methodology for Calculating the Variable GHG Emissions

Blasting is one of the key processes related to the extraction of limestone as the level of fragmentation can lead to a substantial increase in the time, energy and fuel consumption for the down-stream operations. (Georgiev et al, 2018) Hence, its planning has a crucial role not only for optimizing the cost model of the quarrying operation, but also for the reduction of its carbon footprint. In the context of this paper, the fundamental mining and processing operations related to a limestone quarry were considered, including drilling, blasting, loading, hauling, crushing and screening. To evaluate the correspondence between variable costs and variable GHG emissions, a typical small-scale quarrying operation with an annual output rate of 200 000 t of mined limestone was analyzed. It should be noted that this methodology can be considered as a preliminary one, as it relies

primarily on theoretical calculations, well-established empirical models and other site-specific empirical formulae, which provide additional ways to take into account the non-linear relationship between certain variables. A table denoting the assumed methods for estimating different technological parameters with respect to the applied methodology for preliminary assessment is provided (Table 1).

Table 1. Assumed methodology for estimating key modelled parameters

Parameter	Estimation method	Reference
Drilling rate	$Drilling\ rate = \frac{0.1759 \times B_c^{\,2} - 5.8579 \times B_c + 48.86}{\left[\pi \times \left(D/1000\right)^2\right]/4}$ B_c – blasting coefficient, $B_c = \sigma_c / T_s$ σ_c – uniaxial compressive strength, MPa T_s – tensile strength, MPa D – blasthole diameter, mm **Note: Drilling rate formula is adjusted from m³/h to m/h**	Shehu et al., 2019
Bucket fill factor	$Bucket\ fill\ factor = 0.9833 - 0.00022 \times X_{50}$ **Note: Formula is adjusted for X_{50} measured in mm**	Ozdemir and Kumral, 2019
Bucket swell factor	$Bucket\ swell\ factor = -1.1776 \times Bucket\ fill\ factor + 2.4564$ **Note: Formula is transformed from original paper to use *Fill factor* as argument**	Kujundžić et al., 2021
Dig time	$Dig\ time = a - b \times X_{50} \times n$ a = 8.9942 b = -0.06.8706E-2	Doktan, 2001
Crushing energy	$W = 10.W_i\left(\frac{1}{\sqrt{P}} - \frac{1}{\sqrt{F}}\right)$ W – specific energy, kWh/t W*i* – Bond work index, kWh/t P – 80% passing sizes in the product of the crusher, μm F – 80% passing sizes in the feed of the crusher, μm	Bond, 1952
Equipment fuel consumption	$q_d = P \times k_o \times s_d$ P – rated engine power, kW k_o – engine load factor, s_d – specific fuel consumption, kg/(kWh)	Stefanović, 1980; Klanfar et al., 2016
Blasted rock fragmentation distribution	$X_{50} = 10 \times A \times \left(\frac{V_o}{Q_e}\right)^{0.8} \times Q_e^{\,1/6} \times \left(\frac{S_e}{115}\right)^{-19/30}$ $n = \left[2.2 - 14\left(\frac{B}{D}\right)\right] \times \left[\frac{1 + \left(S/B\right)}{2}\right]^{0.5} \times \left[\left(1 - \frac{W}{B}\right) \times \left(\frac{L}{H}\right)\right]$ $P = 100 \times \left[1 - e^{-0.693\left(X/X_{50}\right)^n}\right]$ X_{50} – mean fragment size, mm n – uniformity index of rock fragments granular size distribution A – rock factor P – rock fragments percentage passing an X-sized mesh sieve, % V_o – volume of the rock per blast hole, m³ Q_e – explosive charge mass per blast hole, kg S_e – relative weight strength of the explosive compared to ANFO B – burden, m S – spacing, m W – drilling standard deviation, m L – drillhole length, m H – bench height, m	Kuznetsov, 1973; Cunningham, 1999; Rosin and Rammler, 1933

Indeed, some models can be improved with site-specific formulations. However, for the purpose of preliminary estimation they can be considered sufficient. Nonetheless, these methods were implemented as a computer script, based on the Python programming language for the purpose of investigating different scenarios. Table 2 shows the utilized mining equipment for the quarry. Other site-specific key input parameters used for the scripted model are shown in Table 3.

Table 2. Input parameters for the equipment used for the studied quarry

Equipment	**Model**	**Engine power, kW**	**Load-specific fuel consumption, l/kWh**
Production drill rig	Atlas Copco ROC F9	224	0.20
Excavator	Caterpillar 330D L	200	0.14
Haul truck	Man 41.403	179	0.06

Table 3. Site-specific input parameters for the model

Parameter group	**Parameter**	**Value**
Overall conversion factors	Diesel price, EUR/l	1.65
	Carbon emission conversion factor for diesel fuel, kg CO_2-eq./l	2.67
	Carbon emission conversion factor for diesel fuel (including production and logistics), kg CO_2-eq./l	3.31
Explosive properties	Explosive type	ANFO
	Explosive density, g/cm³	0.80
	Direct GHG emissions from explosive detonation, kg CO_2-eq./kg	0.20
	Indirect GHG emissions from the production of bulk explosives, kg CO_2-eq./kg	1.60
	Indirect GHG emissions from the logistics of bulk explosives, kg CO_2-eq./kg	0.10
Rock mass and rock properties	Rock factor (A)	8.04
	Limestone density, t/m³	2.64
	Bond work index	13.00
Blast panel geometry	Blast panel length, m	50
	Blast panel width, m	15
	Slope height, m	10
	Slope angle, °	70
Drilling	Blasthole diameter, mm	110
Excavator	Bucket capacity, m³	2.07
Haul truck	Average truck speed, km/h	20
	Haul distance, km	0.6
	Haul truck capacity, m³	6
	Haul truck payload, t	15
Crushing and Screening	Oversize threshold value, mm	600
	Product 80% passing size, mm	20
	Material output rate, t/h	200

As it can be observed, the indirect variable GHG emissions are taking into account the production of diesel fuel and bulk explosive, both used as consumables over the life of mine. However, the GHG emissions provided by the explosives used for initiation were not used for this case study as they are practically negligible compared to the scale of the other emissions. It should be noted that hauling of crushed limestone and processing to a final product are not included in the analysis as they are site-specific. Moreover, costs and GHG emissions related to them can be assumed to be non-variable as they are independent of the selected mining technology. (Dimov et al, 2020) Indeed, the choice of belt conveyer, mineral and chemical processing methods for the crushed limestone can also significantly impact the amount of GHG emissions. However, this requires an additional study, as this paper primarily focuses on the quarrying operation. Hence, considering all provided input variables and all assumed empirical methods, the optimization problem can be defined as follows:

Objective function:

Alternative 1 - Minimize the Total variable costs OR
Alternative 2 - Minimize the Direct total variable CO_2-eq. emissions OR
Alternative 3 - Minimize the Direct and Indirect total variable CO_2-eq. emissions OR
Alternative 4 - Minimize the Total use of bulk explosive

Decision variables:

1) Burden
2) Spacing
3) Subdrilling
4) Stemming

Constraints:
1) Fly rock radius ≤ Designated area of effect radius AND
2) Airblast radius ≤ Designated area of effect radius AND
3) $Burden_{min} \leq Burden \leq Burden_{max}$ AND
4) $Spacing_{min} \leq Spacing \leq Spacing_{max}$ AND
5) $Subdrilling_{min} \leq Subdrilling \leq Subdrilling_{max}$ AND
6) $Stemming_{min} \leq Stemming \leq Stemming_{max}$ AND
7) $KB_{min} \leq KB \leq KB_{max}$ AND
8) $KH_{min} \leq KH \leq KB_{max}$ AND
9) $KS_{min} \leq KS \leq KS_{max}$ AND
10) $KJ_{min} \leq KJ \leq KJ_{max}$ AND
11) $KT_{min} \leq KT \leq KT_{max}$ AND
12) $0 \leq Oversize \leq 5\ \%$

Notation:
KB – Burden to Blasthole Diameter ratio
KH –Bench height to burden ratio (Stiffness ratio)
KS – Spacing to Burden ratio
KJ – Subdrilling to Blasthole Diameter ratio
KT – Subdrilling to Burden ratio

Traditionally, the KJ coefficient is used for denoting the ratio between the Subdrilling and Burden (Konya and Konya, 2019). However, for this case study the ratio related to the blasthole diameter is taken into consideration, following one of the rules of thumb, provided by Dyno Nobel (Blasting and Explosives Quick Reference Guide, 2010). Table 4 shows the assumed values for the upper and lower bound of each of the constraints and decision variables.

Table 4. Assumed constraints for the decision variables and their respective domain

Constraint	Measure	Min	Max
Fly rock hazard radius	m	0	450
Airblast hazard radius	m	0	450
KB	-	20.00	40.00
KH	-	1.50	4.00
KS	-	1.00	2.00
KJ	-	3.00	15.00
KT	-	0.75	1.00
Burden	m	2.00	6.00
Spacing	m	2.00	6.00
Subdrilling	m	0.40	0.70
Stemming	m	2.00	5.00
Oversize	%	0.00	5.00

The set of constraints for the objective function can include additional limitations considering different economic, ecological, social or safety concerns. For example, if the seismic effect of blasting requires to be reduced, an additional constraint regarding the quantity of the charge mass for a single or multiple blastholes can also be included. Another constraint for the model can include the rock fragment size for the 80^{th} percentile (X_{80} or D_{80}) of the rock fragmentation distribution or the total amount of gas products for the blast. In addition, some of the assumed constraints can be adjusted, depending on the specific quarrying conditions and the applied rules of thumb and empirical considerations. One such example is the set of constraints regarding the calculation of blast design parameters and the respective intervals of the k-factors. Alternatively, other parameters can also be used for the objective function for the sake of simplicity and depending on data availability. However, they should be analyzed in terms of their capability of addressing the actual carbon footprint in an indirect way. The total amount of explosive used is an integral parameter which bins the GHG gas emission volume, measured by the mass of CO_2-equivalent emissions (kg CO_2-eq.), with the total volume of toxic gases, measured by the carbon monoxide (CO) toxicity equivalent. Essentially both parameters are dependent on the amount of

explosive used in the blast, however, each gas product has a different weight in either of the two formulations. Hence, the objective function based on the total amount of explosive is expected to have a certain amount of bias compared to the ecological or safety interpretation of the parameter.

Results

The applied algorithm for solving the optimization problem was grid search, as it also provides a way to sample the solution space for estimating other non-apparent dependencies between the input parameters. The assumed grid for the algorithm allowed for reaching a precision of 0.05 m for each decision variable (Burden, Spacing, Subdrilling and Stemming). For this current iteration of the problem, the solutions yielded by the grid search algorithm based on the four alternatives of the objective function are shown in Table 5.

Table 5. Solutions from the considered objective function alternatives

Parameter	**Objective function alternative 1**	**Objective function alternative 2**	**Objective function alternative 3**	**Objective function alternative 4**
Burden, m	3.05	3.05	3.05	2.55
Spacing, m	3.15	3.15	3.05	4.55
Subdrilling, m	0.70	0.70	0.60	0.45
Stemming, m	2.30	2.30	2.30	2.05
X_{50}, mm	243.48	243.48	239.08	283.15
X_{80}, mm	407.97	407.97	404.83	434.81
Oversize, %	4.88	4.88	4.88	4.83
Powder factor, kg/m³	0.665	0.665	0.678	0.550
Carbon footprint, kg CO_2-eq./t	1.8908	1.8908	1.2500	1.9373

The sampled points from the solution space grid from the Direct GHG emissions was analyzed for the purpose of providing an explanation for the difference between both solutions. A comparison of the results of the Direct GHG emissions model with the Indirect and Direct GHG emissions model can be seen on Fig. 2.

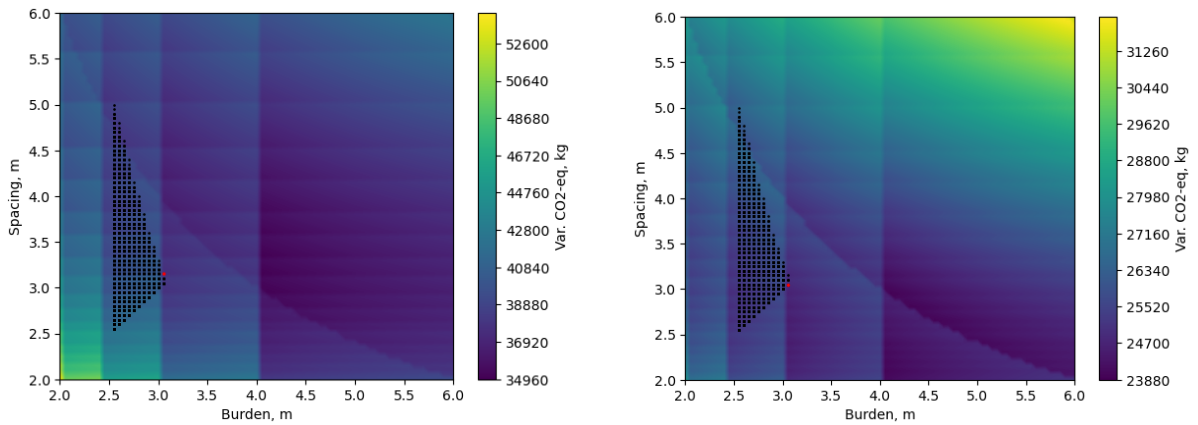

Figure. 2. Obtained solution from the set of feasible solutions and their indirect and direct GHG emissions (left-hand graph) and direct GHG emissions (right-hand graph)

It should be noted that both graphs assume that the Subdrilling has a constant value of 0.70 m, while the Stemming has a constant value of 2.30 m. As it can be observed, the objective function in both cases is piecewise with multiple local extrema. In addition, the objective function for the Direct GHG emissions model signifies that scarce blasting patterns lead to an increased carbon footprint due to the increase of the operational time for loading and hauling, resulting from the increased mean fragment size. However, this affect is dampened severely when the indirect GHG emissions are considered. This is a direct result from the decreased carbon footprint from the manufacturing of ANFO as a scarce blasting pattern is associated with less consumption and demand of bulk explosive. As a direct result of this crucial difference, both objective functions have different solutions with respect to the set of constraints. Moreover, the global extrema in both cases are conditional, as they lie in either of the boundaries from the set of constraints. Hence, sensitivity analysis can prove to be crucial in order to see whether certain constraints can be relaxed for the purpose of obtaining a better solution. A

correlation matrix is provided for the approach considering both Indirect and direct GHG emissions, as shown in Fig. 3.

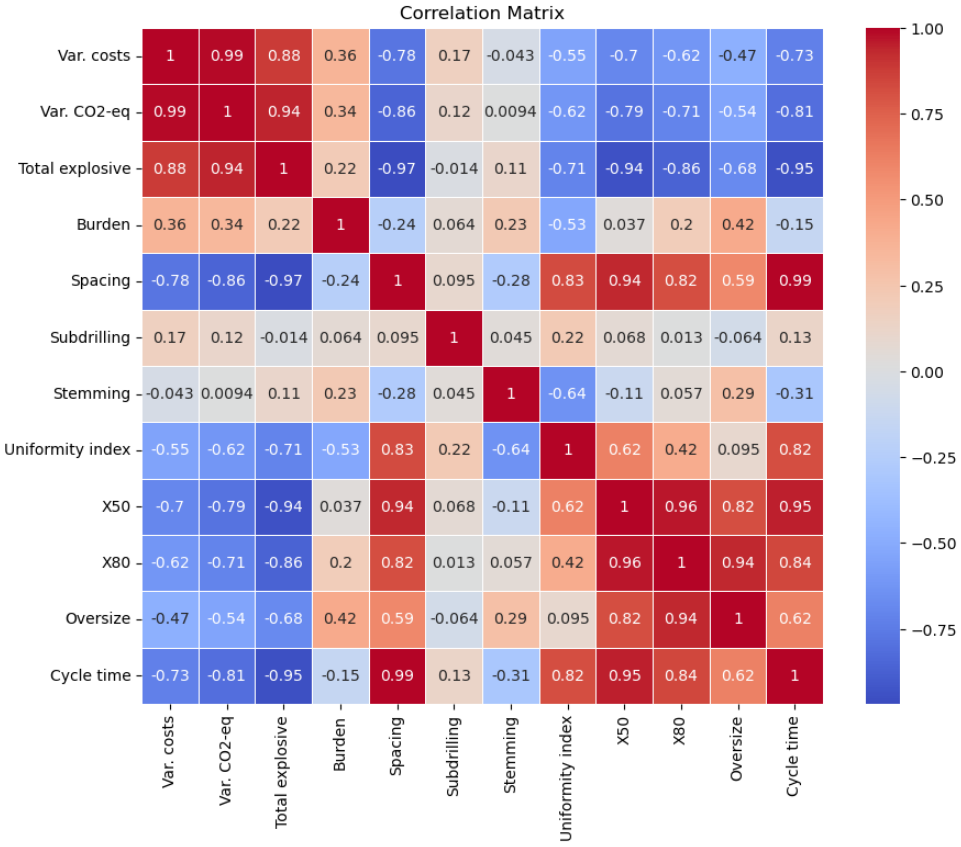

Figure. 3. Spearman correlation matrix based on Indirect and direct GHG emissions from the quarrying model

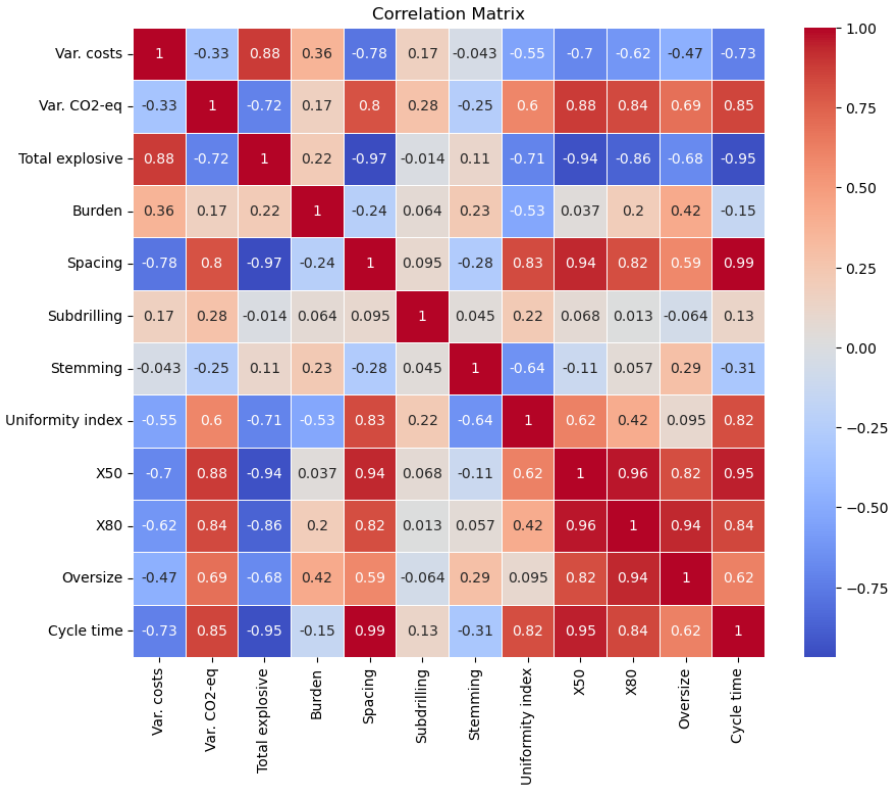

Figure. 4. Spearman correlation matrix based on direct GHG emissions from the quarrying model

Based on the established theoretical model, it can be observed that the Total mass of bulk explosive, the Variable costs and the variable GHG emissions in CO_2-equivalent are strongly correlated. Hence, minimizing one objective can lead to the minimization of the other two objectives as well. However, it should be investigated whether the same optimal solution is reached in all cases and whether using one objective as a substitute for another would be robust. The reason behind this approach is for the sake of simplifying the objective function to a less complex one. A further observation worth mentioning regards the Mean fragment size (X_{50}) estimated via the Kuz-Ram model. As seen from the correlation matrix, it can be assumed to be a good predictor for the Indirect and Direct variable CO_2-equivalent GHG emissions and vice versa. Hence, its potential needs to be further investigated in real-life scenarios based on empirical data. It should also be noted that the correlation coefficient values are sensitive to the assumed economic model. This also implies that the correlation values between the objective function can vary depending on the assumed mining technology for the quarrying operation, as well as the available equipment. Contrary to the Indirect and Direct emissions approach, the Mean fragment size for the Direct emissions approach is positively correlated with the variable GHG emissions (Fig. 4).

Hence the estimation of the direct carbon footprint of the quarry shows that the GHG emissions which predominantly constitute the Direct GHG emissions are related to downstream activities following the primary fragmentation of rocks. Similarly, the variable GHG emissions tend to be negatively correlated with the total variable costs in this case. Therefore, this can serve as a solid proof of the inherent bias behind the Direct emissions approach, given that the amount of GHG emissions from the production of diesel fuel and explosives are not taken into account. This conclusion that the indirect GHG emissions can affect the choice of drilling pattern is further supported by the pie charts, as shown in Fig. 5.

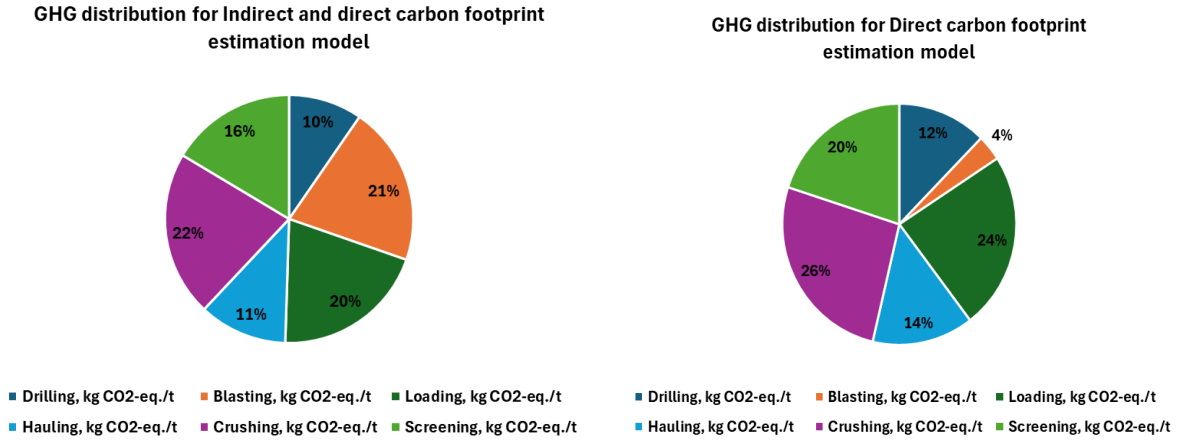

Figure. 5. Pie charts of different operations constituting the Indirect and direct GHG emissions (left-hand graph) and the direct GHG emissions (right-hand graph) from the quarrying model

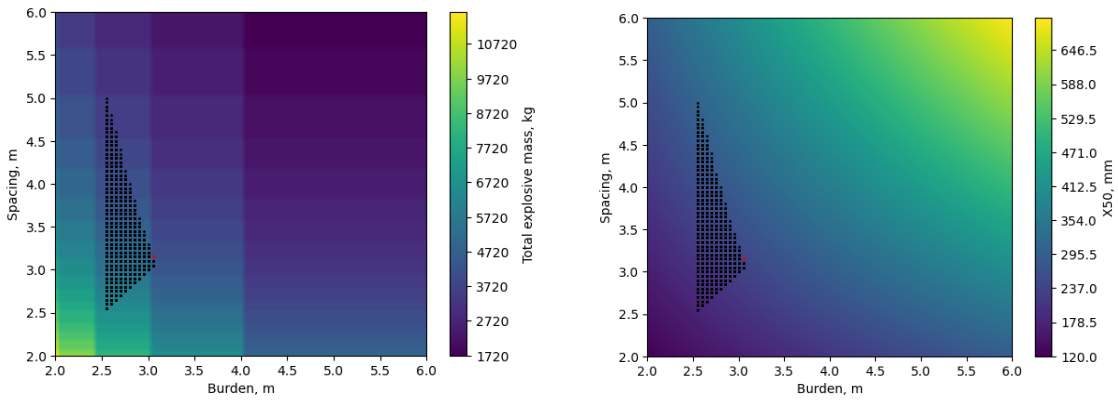

Figure. 6. Obtained solution from the set of feasible solutions and their respective Total explosive mass (left-hand graph) and mean fragment size – X_{50} (right-hand graph)

As charging rules for the blastholes are less prone to change due to safety and practical concerns, the Burden and Spacing parameters are less constrained than them. Therefore, a viable strategy for optimizing the results yielded by the quarrying operation would lead to the adjustment of the drilling pattern, be that to a denser one, depending on the goal of the engineer. Fig. 6 shows the obtained solutions with the Total explosive mass (in

kilograms) and Mean rock fragment size (X_{50}), based on different drill pattern designs allowed by the set of constraints. It should be noted that the red point for both graphs denotes the optimal solution for objective functions 1 and 2. Once more, it is assumed that the Subdrilling has a constant value of 0.70 m, while the Stemming has a constant value of 2.30 m for the graphs.

Regardless of the high correlation coefficient value between the Total explosive mass and the Mean fragment size with the Direct and indirect GHG emissions, they cannot be efficiently exploited as parameters for the objective function. The reason behind this conclusion is that the optimal solution from objective function 1 and 2 does not coincide with the minimum value in both respective solution spaces. Hence, their application in a real-life environment remains only to serve as a potentially good predictor of the GHG emissions or vice versa after the introduction of a noise component to their relation. A comparison of the carbon footprint of the quarrying operation in terms of both approaches can be seen on Fig. 7.

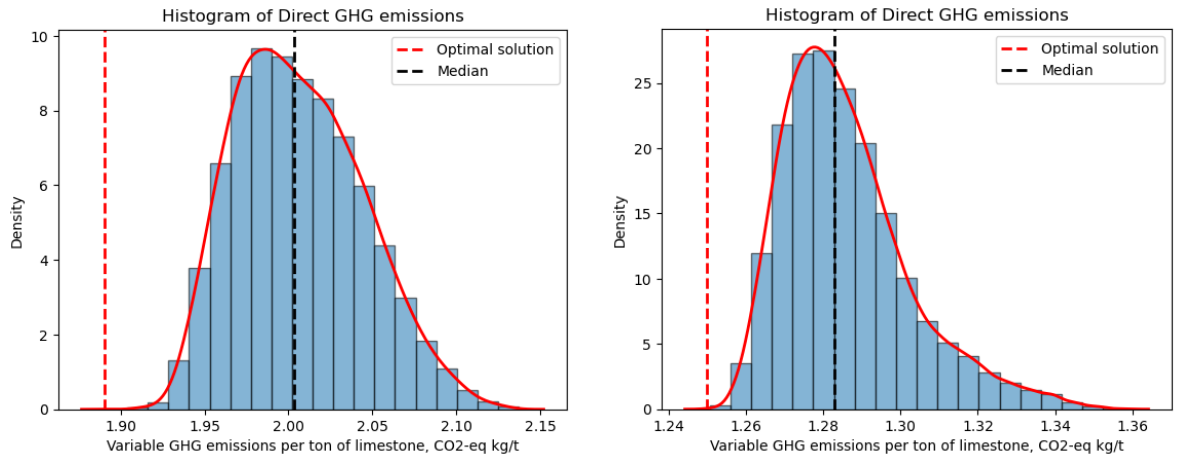

Figure. 7. Estimated indirect and direct GHG emissions (left-hand graph) and direct GHG emissions (right-hand graph) related to the theoretical model

Based on the theoretical model, a reduction of 5.61% (0.1124 kg CO_2-eq. per ton of limestone) can be expected from the median emissions from the set of all possible drillhole patterns, constrained by the assumed set of parameters. The median value was used as a measure of the central tendency of possible GHG emissions per ton of limestone for a single blast, given that no optimization is applied. Hence, an optimization approach is crucial for reducing the carbon impact of quarrying operations. The maximum estimated reduction from the model is 11.52% (0.2463 kg CO_2-eq./t) for the Indirect and Direct GHG emissions approach. It should also be pointed out that there is a substantial difference in the distribution of the GHG emissions' distribution for both approaches. This can be interpreted that regardless of what drilling pattern is applied for the quarry, there is a small likelihood of increasing the direct carbon footprint of the quarry. However, should the indirect emissions be taken into considerations, the likelihood of notably increasing the carbon footprint increases. Once more, this signifies the inherent bias for the Direct GHG emissions approach. Furthermore, each design decision regarding the quarrying operation, such as the case for the choice of drilling pattern, magnifies its effect in the domain of the overall GHG emissions model.

Discussion and Future Work

First and foremost, it should be noted that the optimization function is highly sensitive to the assumed economic model and GHG emissions model. Hence, a robust theoretic background and empirical data is mandatory for its correct definition. Although the proposed model establishes the non-linear dependency of the variable costs and variable GHG emissions with rock fragmentation, further adjustments are required for a more precise approximation of their actual relation. Moreover, a data-driven approach can provide to be a crucial tool for establishing certain individualities of the conditions for each quarry, which can be further implemented in the objective function. Nonetheless, using well-established theoretic or empirical formulae, based on similar mining sites, can be a starting point for building such models for a preliminary assessment, which can be further adjusted and built-on during the life of mine or quarrying operation. Regarding the choice of optimization function, there are certain cases, where the optimal solution vector is invariant to the application of a simpler or more complex model, taking into account the direct and indirect impact of the quarry. However, this was not the case in this paper. Hence, it is recommended that a sensitivity analysis is performed before using a more

sophisticated model in order to gain an initial understanding of which parameters tend to be invariant to changes in a certain set of inputs. Last but not least, based on the results yielded by this case study, it can be established that the optimization problem is a non-convex one. Moreover, the objective function is piecewise with multiple local extrema. Hence, this would require the use of other non-linear optimization algorithms for improving the computation time compared to the grid search method. Therefore, the performance and reliability of different non-linear optimization algorithms should be investigated, as this would allow for the optimization problem to be solved automatically for different alternative scenarios in the context of a more complex optimization problem. Furthermore, as the optimal solution tends to be a conditional extremum, a more robust analysis should be made regarding the set of applied constraints for ranking them depending on their impact on the overall solution. Last but not least, additional environmental criteria can be adopted to the model for a more generalized approach regarding the quarrying operation's impact.

Conclusions

Results from this case study show that limestone quarrying has a significantly lower GHG emissions per ton of product, compared to the production of lime or cement. This is further supported by actual reports of quarrying sites, which yield similar values in terms of their overall carbon footprint to the ones obtained from the model used for preliminary assessment. However, due to the large number of quarrying sites and the substantial worldwide demand of limestone, quarrying operations also require attention for the purpose of reducing the overall carbon footprint, related to limestone. Moreover, taking into account and evaluating the impact of indirect CO_2-equivalent GHG emissions proved to be crucial for estimating the actual reduction of the quarrying carbon footprint from blasting activities. The results from the preliminary estimations lead to the conclusion that optimizing the blast pattern and charging rules for each drillhole can lead to the reduction of the carbon footprint of the quarry by up to 11.52%. Should the median of the GHG emissions (measured in kg CO_2-eq.) per ton of crushed limestone from the set of constrained solutions be taken as a reference, the carbon footprint can be estimated to be 5.61% lower. Hence, an optimization approach is crucial for quarrying operations. Apart from the reduced GHG emissions, a decrease in the variable operational costs is also expected, as they are strongly correlated with the variable GHG emissions. Last but not least, using a more simplified formulation of the objective function, which takes into account only the direct GHG emissions, can lead to a biased solution compared to the one obtained from the overall (direct and indirect) GHG emissions. Hence, it is essential that each quarry should indeed be considered both as a producer and a consumer for obtaining a more robust assessment of its carbon footprint.

Scientific Ethics Declaration

The authors declare that the scientific ethical and legal responsibility of this article published in EPSTEM journal belongs to the authors.

Acknowledgements or Notes

* This article was presented as an oral presentation at the International Conference on Research in Engineering, Technology and Science (www.icrets.net) held in Thaskent/Uzbekistan on August 22-25, 2024.

References

Bing, L., Ma, M., Liu, L., Wang, J., Niu, L., & Xi, F. (2023). An investigation of the global uptake of CO 2 by lime from 1930 to 2020. *Earth System Science Data*, *15*(6), 2431-2444.

Bond, F. C. (1952). The third theory of comminution. *Trans. AIME, Min. Eng.*, *193*, 484-494.

Cunningham, C. V. B. (1987, August). Fragmentation estimations and the Kuz-Ram model-four years on. In *Proc. 2nd Int. Symp. on Rock Fragmentation by Blasting* (pp. 475-487).

Dimov, E., Bakyrdjieva, R., & Stratiev, N. (2020). The mining industry and the recycling of raw materials as an important element of the Bulgarian economy. *Journal of Mining and Geological Sciences*, *63*, 289-292.

Doktan, M. (2001). Impact of blast fragmentation on truck shovel fleet performance. In *17th International Mining Congress and Exhibition of Turkey* (pp. 375-380).

Eigenrieden Quarry: Climate neutrality in the extraction of raw materiali (2024, July, 31st). Retrieved from https://work-on-progress.strabag.com/en/carbon-emissions/eigenrieden-quarry

Environmental Product Declaration for aggregates from Nyrand gravel pit – Svebølle (2024, July, 31st). Retrieved from https://api.environdec.com/api/v1/EPDLibrary/Files/663ebd25-0b69-42ef-fb99-08d9bd3aaab3/Data

Environmental Product Declaration for limestone aggregates Xirorema Quarry (2024, July, 31st) Retrieved from https://interbeton.gr/wp-content/uploads/2023/07/EPD-_Latomeio-Xiroremato s.pdf

EVA025 –Final Report: Aggregates Industry Life Cycle Assessment Model: Modelling Tools and Case Studies (2024, July, 31st) Retrieved from https://ceramics.org/wp-content/uploads/2017/05/EVA025-MIRO-Life-Cycle-Assessment-of-Aggregates-final-report.pdf

Fayomi, G. U., Mini, S. E., Fayomi, O. S. I., & Ayoola, A. A. (2019, September). Perspectives on environmental CO2 emission and energy factor in Cement Industry. In *IOP Conference Series: Earth and Environmental Science* (*Vol. 331*, No. 1, p. 012035). IOP Publishing.

Georgiev, D., Aleksandrova, E., Kaykov, D., & Koprev, I. (2018). Ore quality management in polymetallic deposits using modern technology for controlling blast movement. *Proceedings Sixth National Scientific and Technical Conference with International Participation: Technologies and Practices in Underground Mining and Mine Construction,* 1-4 October 2018 Orpheus SPA Hotel Devin, Bulgaria (pp.78-81).

Hendriks, C. A., Worrell, E., De Jager, D., Blok, K., & Riemer, P. (1998, August). Emission reduction of greenhouse gases from the cement industry. In *Proceedings of the Fourth İnternational Conference on Greenhouse Gas Control Technologies* (Vol. 30, pp. 939-944). IEA GHG R&D Programme Interlaken Austria.

Hristova, T. (2022, June). The place of the blockchain in the recycling of raw materials. In *2022 8th International Conference on Energy Efficiency and Agricultural Engineering (EE&AE)* (pp. 1-4). IEEE.

Jiao,Y. (2023).Analysis of the impacts of carbon dioxide emission on climate change.*Theoretical and Natural Science,7,* 120-127.

Klanfar, M., Korman, T., & Kujundžić, T. (2016). Fuel consumption and engine load factors of equipment in quarrying of crushed stone. *Tehnički Vjesnik*, *23*(1), 163-169.

Konya, A., & Konya, C.J. (2019). *Blasting mechanics revisited: Blasting design standards*, February 21, 2019, Retrieved from https://www.pitandquarry.com/blasting-mechanics-revisited-blasting-design-standards/

Koprev, I.,& E. Aleksandrova. (2018). Investigation of the dependence between the block extracting coefficient and natural rock mass discontinuities in "Mizia" open pit mine. *Proceedings of the VIII International Geomechanics Conference, 2 – 6 July 2018*, Varna, Bulgaria, pp. 156-160, ISSN 1314-6467.

Kujundžić, T., Klanfar, M., Korman, T., & Briševac, Z. (2021). Influence of crushed rock properties on the productivity of a hydraulic excavator. *Applied Sciences*, *11*(5), 2345.

Kuznetsov, V. M. (1973). The mean diameter of the fragments formed by blasting rock. *Soviet Mining Science*, *9*, 144-148.

Laveglia, A., Sambataro, L., Ukrainczyk, N., De Belie, N., & Koenders, E. (2022). Hydrated lime life-cycle assessment: Current and future scenarios in four EU countries. *Journal of Cleaner Production*, *369*, 133224.

Lei, Y., Zhang, Q., Nielsen, C., & He, K. (2011). An inventory of primary air pollutants and CO2 emissions from cement production in China, 1990–2020. *Atmospheric Environment*, *45*(1), 147-154.

Limestone market size & share analysis - Growth trends & forecasts (2024 - 2029) (2024, July, 31st) Retrieved from https://www.mordorintelligence.com/industry-reports/limestone-market

Nobel, D. (2010). Blasting and explosives quick reference guide 2010. *Product and User Guide Booklet. Dyno Nobel Group*, 3-4.

Ozdemir, B., & Kumral, M. (2019). A system-wide approach to minimize the operational cost of bench production in open-cast mining operations. *International Journal of Coal Science & Technology*, *6*(1), 84-94.

Putri, R., Werastuti, D. N. S., Astuty, E. D., Khairunnisa, A. F., Wahyono, E., & Apriani, N. L. (2023). Integrated reporting: corporate strategy towards achieving sustainable development SDGs. *Apollo: Journal of Tourism and Business*, *1*(2), 64-71.

Rosin, P.. (1933). The laws governing the fineness of powdered coal. *J. Inst. Fuel*, *7*(31), 29-36.

Shehu, S. A., Jethro, M. A., Ogbodo, D. A., & Hashim, M. H. M. (2019). Correlation of blasting coefficient with drilling rate of rocks. *Materials Today: Proceedings*, *17*, 543-552.

Somayajula, V. K. A., Ghai, D., & Kumar, S. (2021, April). Land use/land cover change analysis using NDVI, PCA. In *2021 5th International Conference on Computing Methodologies and Communication (ICCMC)* (pp. 849-855). IEEE.

Stefanović, A. N. (1980). *Građevinske mašine (Machines used in construction),* Građevinska knjiga, Beograd

Yavuz, F. E., & Yildiran, V. C., & Colleonı, S. G. (2023). Examining the performance of the heat exchanger in a heat pump clothes dryer. *The Eurasia Proceedings of Science Technology Engineering and Mathematics, 26*, 156-165.

Yankova, T. (2020). Mineral processing waste utilization. *XX International Multidisciplinary Scientific GeoConference SGEM 2020*, *20*, 219-226.

Winstone Aggregates Environmental Product Declaration for Aggregate and Sand Products (2024, July, 31st) Retrieved from https://winstoneaggregates.co.nz/assets/220303-WA-EPD-document_HR_pages.pdf

Author Information

Dimitar Kaykov
University of Mining and Geology "St. Ivan Rilski"
Sofia, Bulgaria

Vessela Petrova
University of Mining and Geology "St. Ivan Rilski"
Sofia, Bulgaria
Contact e-mail: *vessela.petrova@mgu.bg*

To cite this article:

Kaykov, D. & Petrova, V. (2024). A preliminary assessment of a limestone quarry's direct and indirect carbon footprint. *The Eurasia Proceedings of Science, Technology, Engineering and Mathematics (EPSTEM), 29,* 28-40.

The Eurasia Proceedings of Science, Technology, Engineering & Mathematics (EPSTEM)
ISSN: 2602-3199

The Eurasia Proceedings of Science, Technology, Engineering & Mathematics (EPSTEM), 2024

Volume 29, Pages 41-45

ICRETS 2024: International Conference on Research in Engineering, Technology and Science

Filtering Gravity Data of Caspian-Guba, Absheron and Shamakhi-Gobustan Oil and Gas Regions

Gunel Sadigova
Institute of Geology and Geophysics

Aynur Zamanova
Institute of Geology and Geophysics

Abstract: In addition to being a safe approach for the environment, studying the Earth's gravitational field is crucial for resolving numerous scientific and practical geological and geophysical issues. Technological developments in the field of gravitational field measurement have occurred recently. Gravimeter precision has improved, and satellite observations have produced fresh data. The development of techniques for mathematical data analysis is also required by the employment of space technology in the study of Earth's gravimetric field.The lithosphere and crust of the earth can be examined in a novel way with the aid of mathematical techniques. On the other hand, sedimentary basins and uncharted hydrocarbon resources can be studied through the mathematical analysis of gravity data. An urgent topic in geophysics is the mathematical analysis of gravimetric field data in conjunction with other data to better establish the structure of the earth's crust and lithosphere.The actual issue of mathematical interpretation and analysis of high-precision gravimetric data is the focus of this paper. In this paper, the density boundaries giving rise to gravitational anomalies in the studied region were found using the Spector-Grant method. Butterworth and Hartley filters were used to filter the gravimetric data. The power spectrum of the Hartley transform analysis of the Bouguer gravity values indicates that the long and short wavelength components of the gravity field may be distinguished. The interpretation of the regional anomalies shows that these anomalies depend on rising and sinking crystalline basement.

Keywords: Gravity anomaly, Power spectrum, Butterworth filter, Hartley filter

Introduction

The processing of gravity data in the frequency domain allows one to estimate the anomaly source depth using the analysis of the radial spectrum (Spector et al., 1970). In addition, in the frequency domain it is easy to perform filtering, analytical continuation and calculation of vertical derivatives of the gravitational field. These procedures use the discrete or fast Fourier transform. The processing of measured physical quantities based on the complex Fourier transformation requires complex initial data (Blakely, 1995). However, it is natural to deal with real numbers in the real domain. The Hartley transform is a function of real variables and has recently been often used for geophysical data processing. It is an integral transform similar to the Fourier transform and possesses most properties of the latter (Bracewell, 1986). This transform has most of the properties of Fourier transforms. On the other hand, computer programs that use the Fourier transform require more memory and longer computer time. Computational experiments conducted using the Hartley transform show that this transformation requires less memory and time. In this work, the Hartley transform is used to analyze the power spectrum and filter 2D gravity data from the study area.

Method

Gravity Field of the Research Area

The gravity field in the study area is represented in the Bouguer reduction in Fig. 1. The research area covers the Caspian-Guba gravity minimum and the Eastern Azerbaijan minimum and part of the Azerbaijan maximum. The Caspian-Guba gravity minimum is located in the northern part of the research area, the Eastern Azerbaijan minimum and the Azerbaijan maximum are located in the southern part. Azerbaijan gravity minimum is distinguished by gravity anomalies down to -135 mGal. The Azerbaijan maximum is characterized by gravity anomalies of up to +80 mGal.

Calculation of the power spectrum and digital filtering of the gravitational field in the frequency domain were performed using the Hartley transform and Butterworth filter (Bracewell, 1990; Kadirov, 2000). Spectral analysis of gravitational field data using the Spector–Grant method makes it possible to estimate the average depth of density boundaries (Spector et al., 1970; Kamto et al., 2021; Sadigova, 2020).

For the purpose of studying the gravity anomalies, the Bouguer anomaly map of Azerbaijan was preliminarily divided into 5-km squared cells, and the Bouguer anomaly values were determined at the grid nodes (Fig 1).
The origin of the coordinate systems is placed at the southwestern corner of the study area. The X- and У-axes are directed to the east and north, respectively. The number of elements in X-axis (Nx) and Y-axis (Ny) is selected as Nx=29 and Ny=40.

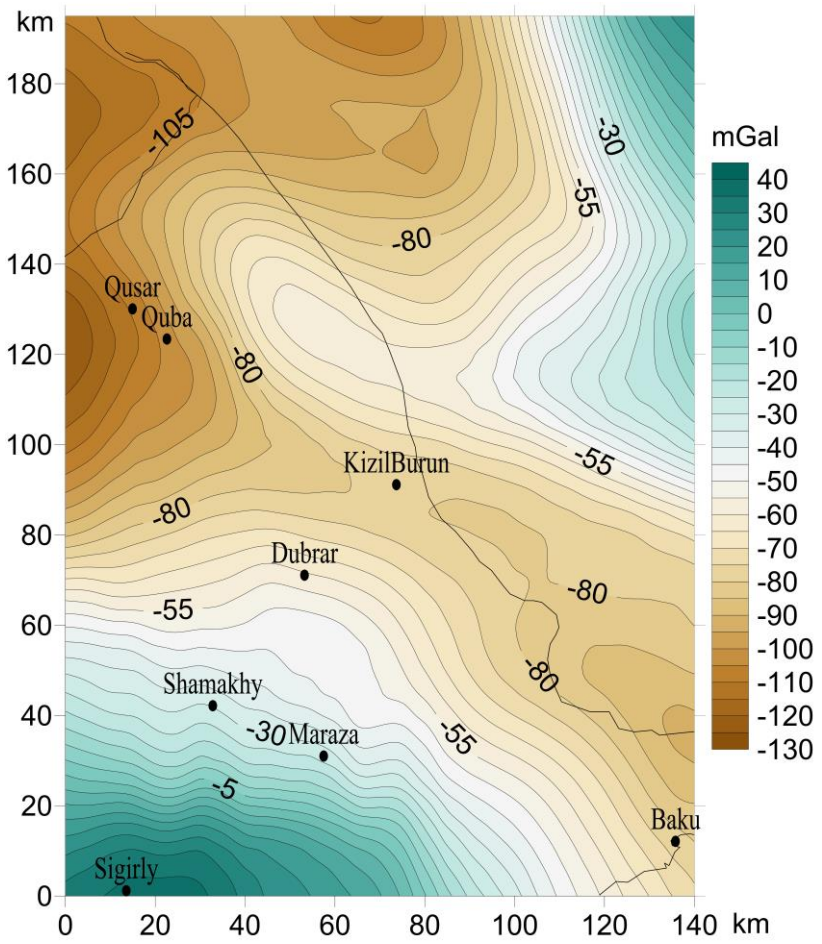

Figure 1. Bouguer gravity map for the study area

Results and Discussion

Power Spectrum and Filtering of Gravity Data

The logarithmic power spectrum of the Bouguer anomalies is presented in Fig. 2. According to its slope, the power spectrum is divided into two regions providing information about long and short waves. The low- and

high-frequency regions of the power spectrum related to deep and shallow gravity sources were assumed to represent the respective regions of regional and local anomalies. The cutoff frequency separating the regional and local regions is determined by the intercept of the straight lines approximating the power spectra in long- and short-wave intervals. In the case under consideration, the cutoff frequency (wavenumber) is kc = 0.16 km^{-1}. The depths to gravity anomaly-producing boundaries deter-mined from the long- and short-wave slopes are 16,6 and 1.8 km, respectively, (Spector et al., 1970). The separation of the gravity field into regional and local components was performed with the use of the Butterworth filter. The ideal low-frequency Butterworth filter has the form

$$H_B(k) = \frac{1}{\sqrt{1+\left(\frac{k}{k_c}\right)^{2n}}},$$

where k is the wave number, k_c is the cutoff wave number, n is an integer that determines the filter order. In the present study, n = 1 was assumed.

The application of the Butterworth filter was reduced to the following opera-tions. The Hartley transform provided the frequency-domain representation of the Bouguer anomaly grid values. The Butterworth filter was constructed in the frequency domain in the direction of rows and columns, allowing for the cutoff frequency, and was then multi-plied by the Hartley spectrum. Finally, the result was inversely transformed into the space domain.

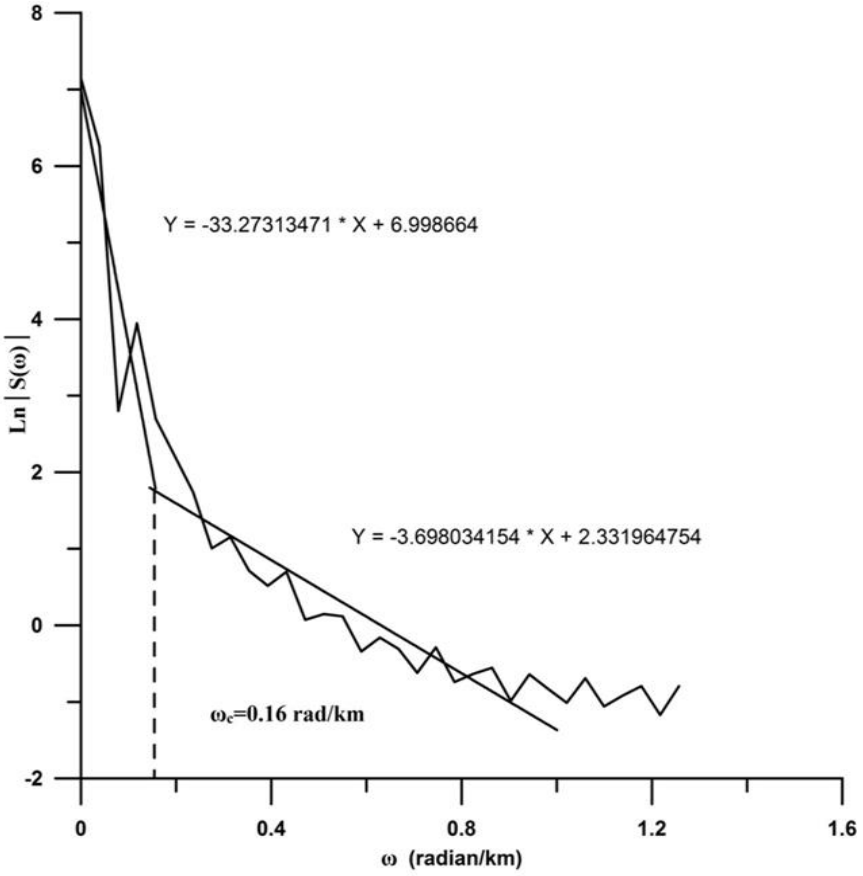

Figure 2.The logarithmic power spectrum of the gravity field.

The results of the low- and high-frequency filtering with the' cutoff frequency kc = 0.16 km-1, using the Hartley transform are shown in Figs. 3. In Fig. 3,a a strip of deep minimum is visible. The minimum value of anomalies is fixed in the marine part (–155 mGal). The relative maximum is observed in the area of Guba (–85 mGal) and Dubrar (–80 mGal). These gravity anomalies extend to Maraza. A negative anomaly to the minimum value is determined in the area of Shamakhy (–105 mGal) and in the west of Baku in the area of Güzdek (–120 mGal).

In Fig. 3,b the zone of positive anomalies occupies the area in the north-west and south-east of the studied area. The maximum value of this anomaly, equal to 1 mGal, was noted in the Guba region and the northern part of the Absheron peninsula. The negative anomaly occupies the north-eastern and south-western parts of the region. The minimum meaning of this anomaly, equal to –8 mGal, observed in the sea and in the district of Geybet (–6 mGal). A number of closed negative anomalies are observed Charkhy (–2 mGal), Ledzhet (–3 mGal), Sarvan (–3 mGal) and Yashma (–3 mGal) districts.

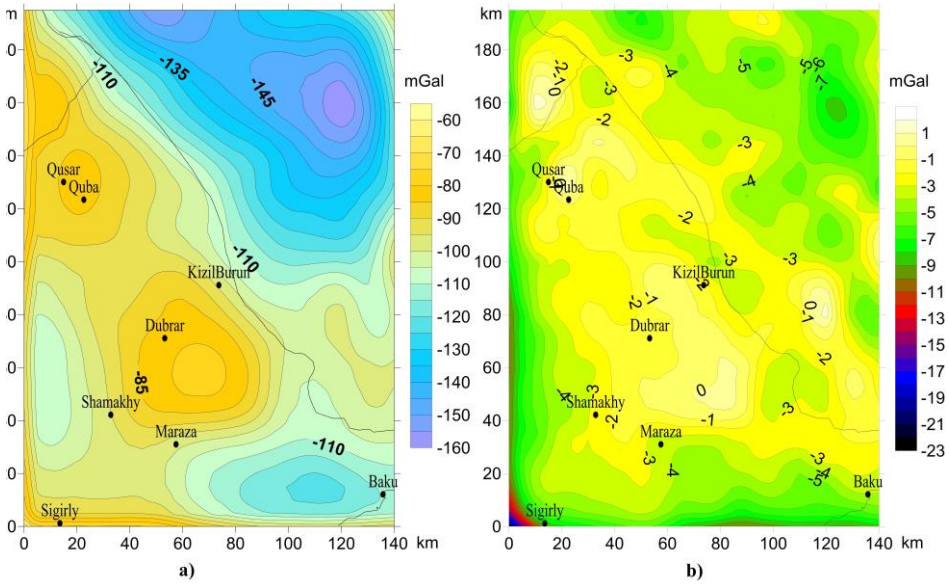

Figure 3. Results of the low-frequency (a) and high-frequency (b) filtering with the use of the Hartley transform

The depths of gravity anomaly-producing bodies determined from the power spectrum slope are consistent with seismic and borehole data. According to DSS data, the depth to the crystalline basementin the Gusarchay-Gusar-Yalama zone is determined to be 8–18 km. In the central part it has depths of 14–18 km (Akhundov et al., 1996). Such changes in the crystalline basement are consistent with changes in regional gravity anomalies. The 16,6-km depth is associated with the crystalline basement surface, and the 1.8-km depth, with a surface within Cenozoic deposits.

Conclusion

The analysis of the power spectra of the gravity field in the study area revealed anomaly-producing bodies at mean depths of 16.6 and 1.8 km. The 16.6-km depth is associated with the surface of the crystalline basement, and the 1.8-km depth, with a sur-face within Cenozoic deposits.

Recommendations

The reliability of the processing results based on the application of the Hartley transform and 1-D Butterworth filter to the gravity data of the study area is confirmed by their close agreement with the results of previous investigations. The results of this paper lead to the conclusion that the Hartley transform is appropriate for the numerical analysis of gravity data. The methodology developed in this work is theoretically and practically important and can be applied in other regions. At the same time, local gravity anomalies have practical significance in oil and gas search and well site selection.

Scientific Ethics Declaration

The authors declare that the scientific ethical and legal responsibility of this article published in EPSTEM journal belongs to the authors.

Acknowledgements or Notes

* This article was presented as a poster presentation at the International Conference on Research in Engineering, Technology and Science (www.icrets.net) held in Tashkent/Uzbekistan on August 22-25, 2024.

References

Akhundov, A. B., Veremeenko, O. B., & Shekinskiy E. M. (1996). *Regional studies*. In book: Geophysical Researches in Azerbaijan, Baku, Sharg-Garb, 276-28.

Blakely, R. J. (1996). *Potential theory in gravity and magnetic applications*. Cambridge university press.

Bracewell, R. (1990). *Hartley transform. Theory and applications* / Translator A.I. Papkov, Ed. I.S. Ryjak. M.: Mir, 175

Kadirov, F. A. (2000). *Gravity field and models of deep structure of Azerbaijan. Baku*, Publishers,‘. Nafta-Press’, 112p.(in Russian).

Kamto, P. G., Lemotio, W., Tokam, A. P. K., & Yap, L. (2021). Combination of terrestrial and satellite gravity data for the characterization of the southwestern coastal region of Cameroon: Appraisal for hydrocarbon exploration. *International Journal of Geophysics*, *2021*(1), 5554528.

Sadigova, G.R. (2020). Gravity anomalies of the southeastern Caucasus. *Geophysical Journal, 42*(2), 138-151.

Spector, A., & Grant, F. S. (1970). Statistical models for interpreting aeromagnetic data. *Geophysics, 35*(2), 293-302.

Author Information

Gunel Sadigova
Institute of Geology and Geophysics of the Ministry of Science and Education of Azerbaijan Republic, Azerbaijan Republic, Baku, AZ1143, H.Javid av., 119
Azerbaijan
Contact e-mail: *gsadigova@yahoo.com*

Aynur Zamanova
Institute of Geology and Geophysics of the Ministry of Science and Education of Azerbaijan Republic, Azerbaijan Republic, Baku, AZ1143, H.Javid av., 119
Azerbaijan

To cite this article:

Sadigova G. & Zamanova A. (2024). Filtering gravity data of Caspian-Guba, Absheron and Shamakhi-Gobustan oil and gas regions. *The Eurasia Proceedings of Science, Technology, Engineering and Mathematics (EPSTEM), 29*, 41-45.

The Eurasia Proceedings of Science, Technology, Engineering & Mathematics (EPSTEM)
ISSN: 2602-3199

The Eurasia Proceedings of Science, Technology, Engineering & Mathematics (EPSTEM), 2024

Volume 29, Pages 46-54

ICRETS 2024: International Conference on Research in Engineering, Technology and Science

Zinc Concentrate Dewatering Pressure Filtration

Mihail Petrov
University of Mining and Geology "St. Ivan Rilski"

Teodora Yankova
University of Mining and Geology "St. Ivan Rilski"

Ljupcho Dimitrov
University of Mining and Geology "St. Ivan Rilski"

Irena Grigorova
University of Mining and Geology "St. Ivan Rilski"

Abstract: Zinc concentrate dewatering is crucial in zinc production, as it allows for the efficient removal of water content from the concentrate before metallurgical processing. It's important for each mining companies to tailor their dewatering processes to the specific requirements of their ore and production facilities. Erma Reka Concentrator processes lead-zinc ores by flotation and produces lead and zinc concentrates. After thickening and filtration the zinc concentrate moisture is 10.5%. This study aims to answer the following research question: how to reduce the moisture content of zinc concentrate to 7%? Dewatering experiments with a laboratory vertical plate airblow (VPA filter) have been conducted in the Process Equipment Test Center of Metso Sweden in Sala, with zinc concentrate sample from Erma Reka Concentrator, (Gorubso Zlatograd), Bulgaria. The aim of the laboratory test work was to evaluate the possibility of zinc concentrate dewatering and to collect data for equipment sizing of VPA filter for 6 metric tph dry solids achieving 7 % w/w filter cake rest moisture. It was found that the zinc concentrate dewatered well and is suitable for VPA filtration. This research offers significant insight to possibilities for zinc concentrate dewatering by pressure filtration. Finally, conclusions and summaries are presented.

Keywords: Pressure filtration, Zinc concentrate, Dewatering

Introduction

As stated by Tomova (2023) mineral processing is mainly focused on extracting the most valuable components from the ore, while the rest of the material is disposed at the tailing ponds. The major operation for removal of solids from a processing solution is solid-liquid separation (Asmatulu, 2011), (Sutherland, 2007). These separation techniques are diverse and mainly include vacuum, pressure and centrifugal filters, screens, trommels, hydrocyclones, thickeners, classifiers, and reverse osmosis (Tarleton & Wakeman, 2007).

As well known the dewatering concentrates by pressure filtration is a common process in the mineral processing industry. This process aims to reduce the moisture content in the concentrate, making it more suitable for transportation and further processing. The choice of dewatering method depends on various factors, including the specific characteristics of the concentrate, required moisture levels, and the available equipment and resources. It's essential to consider the efficiency, operating costs, and maintenance requirements of each method to determine the most suitable approach for application.

Pepper et al. (2010) defined the reasons, for pressure filters application: (1) to reduce the cost of concentrate transporting from the concentrator to the smelter; (2) to prevent segregation of concentrate solids in sampling on road dispatch and at the receiving smelter, which can affect metal accounting; (3) to reduce the cost of concentrate drying prior to smelting (Pepper et al., 2010).

According to Asmatulu (Asmatulu, 2011) filtration is an unavoidable step in beneficiation plants after the valuable particles are thickened. Usually the fine dewatered sulfide minerals moisture content is between 10% and 20%, depending on the applied dewatering methods and particle size (Rushton at al., 2000), (Asmatulu, 2001). In recent years, with introduction of new technologies in metallurgy, the requirements for zinc concentrate qualities have increased and for shipping the zinc concentretes into the smelting process, the moisture have to be 5–8% (Asmatulu, 2011).

It was reported in literature that twenty years ago, automatic pressure filters were a novelty in the minerals and metallurgical industries and many plants used a combination of vacuum filters and thermal dryers (Townsend, 2003). Currently, almost every beneficiation plant have installed pressure filters to concentrates dewater (Townsend, 2003). Many existing plants as Erma Reka Concentrator have replaced or are replacing their vacuum filters by pressure filters.

Townsend (2003) studied the reasons for widely used of automatic pressure filters in the minerals and metallurgical industries during the last years. Benitta et al., (2021) traces the advances in mineral processing dewatering and drying. The authors draw our attention to technologies in mineral dewatering and drying developed over the last decade. In addition gives a brief discussion of future investigation needs and potentialities from the industrial perspective (Benitta et al., 2021).

Lead and zinc are some of the most common non-ferrous metals worldwide. These are metals mined from both sulphide and oxide lead-zinc ores or lead-zinc-copper-pyrite ores. The main minerals in these ores being galena and sphalerite. Erma Reka Concentrator (Gorubso Zlatograd, Bulgaria), is situated in the south central part of the Republic of Bulgaria, in immediate proximity to the Bulgarian-Greek border. The factory processes lead-zinc ores from the Ermorechensko - Madansko ore field, from three deposits: "Marzyan-North'", "Yuzna Petrovitsa" and "Shumacheski Dol-Androu". An annual Erma Reka Concentrator production of lead and zinc concentrates was achieved in the amount of 19 200 tons per year. The processing of lead-zinc ores is carried out in the flotation divisions. During the lead-zinc ore filtration processing lead and zinc concentrates and final waste are obtained. Concentrates dewatering is performed in two stages: thickening and filtration. After dewatering, the zinc concentrate moisture is 10.5%. The metallurgical industry requires the zinc concentrate moisture to be below 9%. To overcome this problem, in the next sections we demonstrate the laboratory tests to zinc concentrate moisture reduce. Furthermore, investigations on zinc concentrate physical properties and particle size distribution of the sample were carried out.

In the course of our experiments Metso laboratory vertical plate airblow played an important role. Dewatering concentrates by a VPA (Vertical Plate Airblow) filter is a specific type of pressure filtration method that offers distinct advantages in certain applications. It utilizes a series of vertically arranged plates that exert pressure on the slurry to separate liquid from solids. VPA filter was chosen for dewatering zink concentrate for the following reasons: high dewatering (filtration) efficiency, optimized pressure control, high solids recovery, continuous operation, compact design (suitable for installations with space constraints), low operating costs (such as low energy consumption and efficient cake washing), automated control (equipped with automatic controls and monitoring systems to optimize the filtration process and ensure efficient operation), suitable for small-scale mineral processing plant such as Erma reka Concentrator.

Materials and Methods

Test equipment and procedures used are described in this section. Furthermore, investigated process parameters are discussed.

Zinc Concentrate Physical Properties Determination Study

Acording to Wakeman (Wakeman, 2007), if the particle properties could be specified for a filtration, the target properties would be for the particles to have as large size as possible, be as near to spherical as possible, and have a monosize distribution. In practice, is rarely the mean size in a distribution and even small increases in the

number of the finer particles can significantly reduce filtration rates (Wakeman, 2007). Particle shape primarily affects the volume and surface area of the particles, and hence their specific surface and the rate of fluid flow through formed filter cakes (Wakeman, 2007).

Fränkle at al. (2022), highlight that particle properties have a profound effect on the specific resistance of the filter cake that in turn affects filter performance. They concluded that the most important properties of the particles are their size, size distribution, shape, and their interaction with the surrounding fluid (Fränkle at al., 2022). Particle size has a significant effect on the solid/liquid separation behaviour of a suspension; knowledge of the techniques for measuring the size particles is therefore important (Wakeman, 2007). The solids composition affects filtration rate through density, surface charges and compressibility. One slurry sample of 35 kg zinc concentrate was tested in the Equipment Test Center of Metso Sweden AB in Sala, Sweden. A representative sample was gathered from the sample, the gathered sample was then used for particle size distribution and specific density measurement. The particle size distribution for the material can be seen in Figure 1.

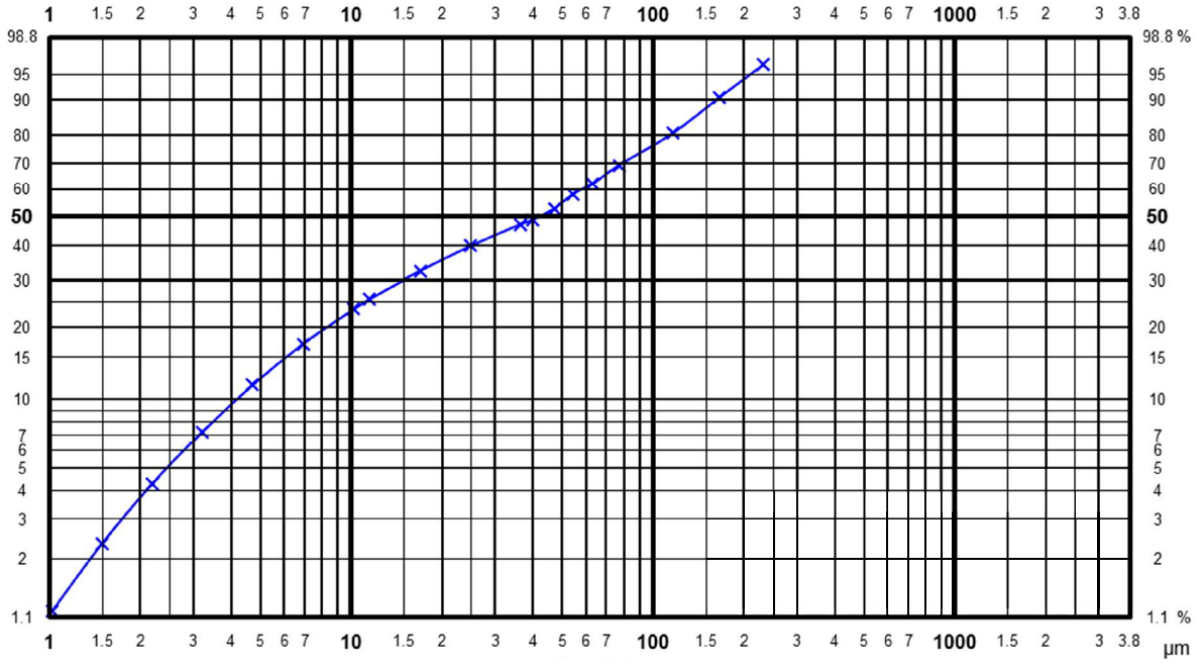

Figure 1. Particle size distribution of the sample

Figure 1 shows the combined particle size distribution curves, where the laser diffraction curve has been adjusted to the mechanical screen analysis. According to Haramkar at al. (2021) for particle size analysis various methods are available depending on the samples type and nature: the most commonly used technique - laser diffraction, one of the oldest and widely used techniques - sieving. The particle size distribution of the sample in our study was determined by mechanical screening (Retsch AS200) down to 40 µm and with laser diffraction (Malvern Mastersizer 3000E) of the particles passing 63 µm. The specific density of the solids was determined with a gas pycnometer (AccuPyc 1330 Pycnometer).

As a result of lower-quality and complex ores increasingly mining, their processing requires finer grinding in order to liberation of the valuable minerals. This also results in finer flotation concentrates production. Haramkar at al. (2021) emphasize that to describe the particle size distribution, D-values are commonly used. With respect to the average particle size, Townsend (2003) reported that flotation concentrates with a D80 >74 µm were once the norm, whereas in the early 21st century the D80 is more likely to be between 20 and 45 µm.

Our results indicate the particles in the studied sample have the following composition: 80% of the particles are smaller than 113 µm (D80), 50% of the sample contains particles smaller than 42 µm (D50) and particles below 10 µm are 23%. Wakeman (2007) explained that the most important for characterising a particle size for filtration rarely is the mean size (50% size) in a distribution; the finer particles in the distribution usually "control" the filtration and it is preferable to compare the 5 or 10% sizes (Wakeman, 2007).

It should be noted that sample presented contains larger particles and sludge resistance should decrease. Less differential pressure should be necessary to achieve target filtration rates and cake moistures. D80, D50 and D23 for the curve can be seen together with some other basic physical properties of the sample in Table 1. In our opinion, understanding the particle properties allows scientists and engineers to tailor filtration systems to specific applications. The selection of appropriate filter media and operational parameters depends on a thorough understanding of the characteristics of the particles to be filtered.

Table 1. Physical properties of the sample

Sample Marked		
Solid content (% w/w)	53.7	
Solid specific density (g/cm^3)	3.97	
pH	6.0	
Particle size		
	-D_{80} (µm)	113
	-D_{50} (µm)	42
	-D_{23} (µm)	10

The solids concentration of the sample was 54 % by weight. Since the solids concentration stated from the Erma Reka concentrator was 50 %, the sample was diluted with tap water to 50 %, and this diluted sample was used for the test work.

Procedure

The tests presented in this paper used a laboratory VPA Pressure Filter provided by Metso (Figure 2).

Figure 2. Laboratory VPA pressure filter

The Laboratory VPA Filter simulates the major operating steps of a full size filter:

- Filtration
- Membrane compression
- Air blow

It comprises a single filtration chamber over which the filter cloth is placed, to provide double sided filtration. The filter head is fitted with a rubber membrane or diaphragm that is activated by compressed air before and during air blow. The feed slurry is held in a small tank and is re-circulated by a variable speed positive displacement hose pump to prevent the solids settling in the tank. During filtration the tank is pressurised with air to provide the filtering pressure.

Individual regulators are used to control the filtration pressure, the membrane compression air pressure and the cake air blow pressure. A scale with a digital readout is used to measure the filtrate discharge. All pressures (feeding, membrane and air blow), slurry temperature and filtrate weight are automatically logged during the whole filtration cycle.

The vertical filter chamber of the laboratory pressure filter type VPA has shown on the Figure 3.

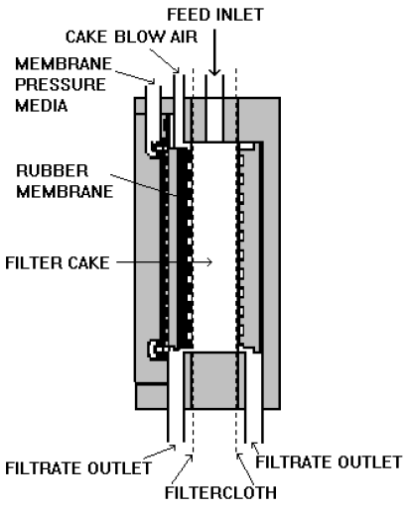

Figure 3. Filter chamber

The laboratory pressure filter type VPA has one vertical filter chamber (Figure 3). The filter simulates the major operating steps of a full size filter: filtration (feeding), membrane compression (squeezing) and air blow (drying). The filter is not opened between the different steps (the pressure across the cake is at no time released during the cycle).

The filtration (cake build up) is two sided in the VPA filter with filtrate outlets at both sides of the cake. The filtration step is typically continued until the filtrate stops, at this point the filtration cannot facilitate further dewatering. At this point the membrane compression step is initiated. The membrane compression step is typically 30 seconds long. Compressed air is used as membrane pressure media. After 30 seconds of membrane compression step the air blow step is applied, the air blow step is typically applied for 6 minutes. During the air blow step compressed air is blown through the filter cake.

The inlet for drying air is placed between the rubber membrane and filter cloth. The filtrate outlet at the membrane side is closed during air through blow step. The membrane is kept activated during the cake air blow, in order to compensate for cake shrinkage that occurs during the dewatering phase. This avoids air leakage through cracks normally formed when the cake shrinks. The filtration area of the chamber is 2 x 1 dm². The air through blow area is 1 dm². Different chamber depths are available (33, 42 and 53 mm) and different types of filter cloths can be used for testing.

Results and Discussion

The slurry was fed to the VPA at 50 % solids by weight. Four tests were conducted using both 30 and 40 mm chamber thickness. One test was conducted without air blow, using the 40 mm chamber. In all other tests, 6 minutes of air blow was applied. Using the 30 mm chamber, one test was also conducted at increased pressures for membrane compression and air through blow pressure.

The solid/liquid separation is performed by the filter cloth (filtration media). Filter cloth is a crucial component in solid/liquid separation by filtration, and its properties play a significant role in determining the efficiency of the separation process. The key properties that are typically considered for filter cloth include: material composition, weave pattern, thread count, weight, thickness, chemical, abrasion and temperature resistance etc. A multifilament filter cloth S2121-L2K2 from Valmet Fabrics was used in the tests, the filter cloth properties can be seen in Table 2. The test parameters are shown in Table 3.

Table 2. Filter cloth properties

Cloth designation	Type	Material	Weight, g/m^2	Permeability, $m^3/m^2/min$ 200 Pa	Finish
S2121-L2K2	Multi	polypropylene	750	0.8	Calendared

Rezaei et al. (2021) highlight that filtration media has a direct impact on operating costs. The filter cloth selection is based on the characteristics of fluid flow from the cloth pores (Rezaei et al., 2021).

Table 3. Test parameters VPA

Test №	Test 1	Test 2	Test 3	Test 4
Solids content (% w/w)	50	50	50	50
Chamber depth (mm)	42	42	33	33
Temperature (^{0}C)	20	20	30	30
Filtration pressure (bar)	6	6	6	6
Compression pressure (bar)	8	8	8	10
Air blow pressure (bar)	-	7	7	9

Cycle Overview

The filtration, pump feeding, was 3 minutes for the 42 mm chamber (tests 1-2) and 2.5 minutes for the 33 mm chamber (tests 3-4) minutes (Table 3). The compression, squeezing the cake by membrane pressure is initialized after feeding and is applied for 0.5 minutes before the 6 minutes of air blow is applied. The filtrate curve for the entire dewatering tests can be seen in Figure 4.

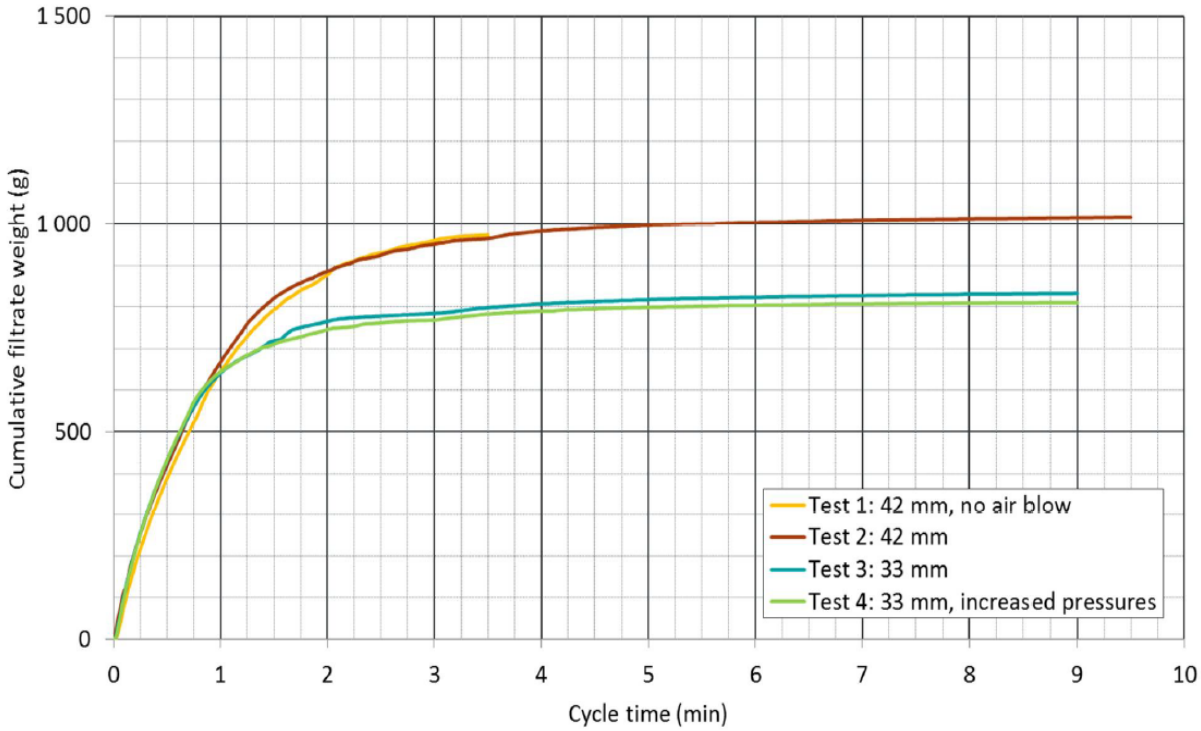

Figure 4. VPA filtrate curves for the 4 tests conducted

Table 4. Summary test results VPA

	Test 1	Test 2	Test 3	Test 4
Dry cake weight (g)	1002	1046	836	829
Dry cake density (kg/l)	2.40	2.50	2.55	2.52
Filter cake rest moisture (%)	11.6	7.6	6.7	6.2
Cake thickness (mm)	42	42	33	33

Filtration

It was found that the material dewatered with an effective filling time of 3 minutes for a 42 mm cake and 2 minutes for a 33 mm cake, as seen at the point where the filtrate curves first flatten (Figure 4). This point represents when the feed pressure created by the pump can no longer contribute to the dewatering of the slurry.

Membrane Compression

The membrane and filter plates are important parts regarding filtration process. The membrane compression pressure was applied for 30 seconds prior to the introduction of the filter cake air blow air and was maintained at 1 bar above the filter cake air blow pressure during air blow, to compensate for any filter cake volume reduction during air blow, thus eliminating filter cake cracking which leads to loss of drying efficiency. Very little filtrate came out during the membrane compression, this indicates that the filter cake is incompressible.

Air Blow

In Figure 5 the filter cake rest moisture is shown as a function of air blow time. The total air blow time was 6 minutes and the moisture contents at shorter air blow times were back calculated from the filtrate volumes collected. After 6 minutes of air blow the filter cake moisture was reduced to 6-8 % w/w, with the lowest rest moisture 6.2 % reached in test 4 with thinner chamber and higher pressures.

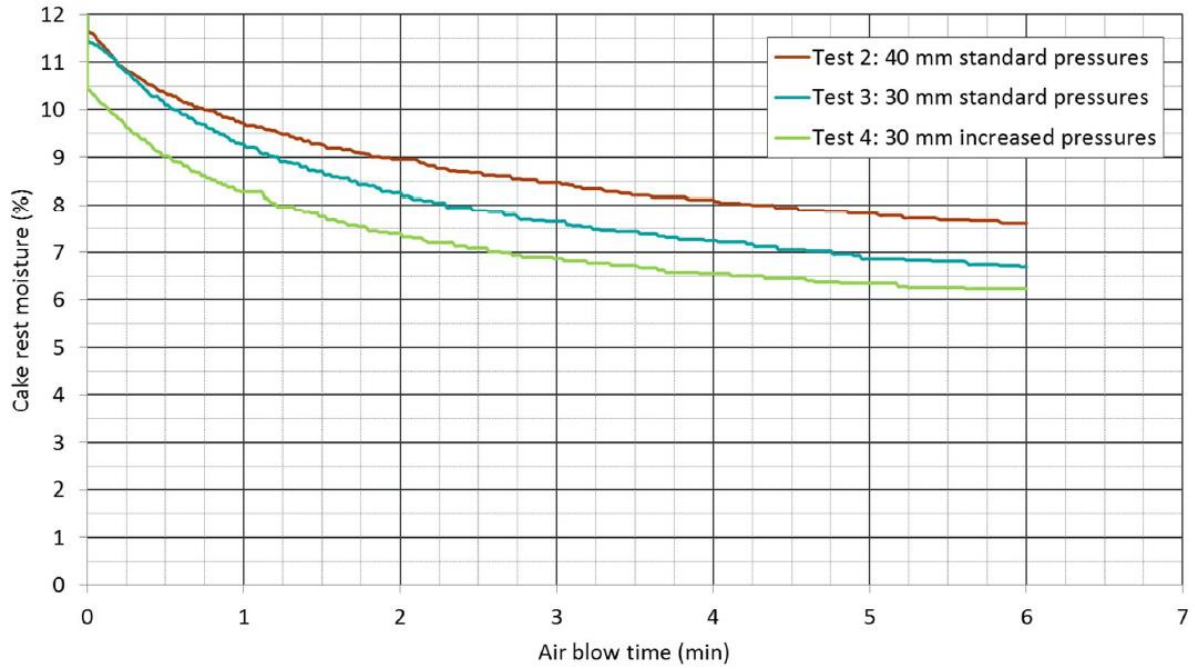

Figure 5. VPA dewatering curves for tests 2-4

Filtrate and Filter Cake

The filtrate was slightly turbid during the first seconds of filtration, but then it became clear. The filter cake was a bit soft/plastic in test 1 where no air blow was applied. In all other tests, the cakes were brittle and dry, with good cake release from the filter cloth.

Filter Cake Dry Density

The filter cake dry density for the material was found to be approximately 2.5 kg/l. This value is close to the expected value of 60 % of dry solids density which indicates that the filter cake packed well.

Conclusion

As mentioned by Townsend [2003], the automatic pressure filters have become widely used in the minerals and metallurgical industries during the last 20 years. Their widespread acceptance has been due to the need for superior process results when dewatering finer materials. This has been discussed by a great number of authors in literature. The aim of this work was to investigate the possibility of zinc concentrate dewatering for reduce

the moisture content to 7% with a laboratory vertical plate airblow (VPA filter). Some conclusions can be drawn:

Pressure filtration is a popular choice due to its efficiency and adaptability for a wide range of concentrates. The sample presented dewatered well and is suitable for VPA filtration. In general, for treatment of 6 dry t/h at feed concentration 50 % 1 x VPA1030-28 is recommended to reach the requested 7 % rest moisture, using standard pressures (feed 6 bar, compression 8 bar, air blow 7 bar). The slurry can most likely be thickened to more than 50 %. A thicker feed slurry is beneficial for the filtration and would reduce the cycle time and lower the rest moisture. As a result, it can be-concluded that the filtration method effectively works on the dewatering of zinc concentrate. The conducted experiments demonstrate the possibilities of zinc concentrate dewatering in Erma Reka Concentrator by VPA pressure filtration using 1 x VPA 1030-28.

Scientific Ethics Declaration

The authors declare that the scientific ethical and legal responsibility of this article published in EPSTEM Journal belongs to the authors.

Acknowledgements or Notes

* This article was presented as an oral presentation at the International Conference on Research in Engineering, Technology and Science (www.icrets.net) held in Tashkent/Uzbekistan on August 22-25, 2024.

* The authors gratefully acknowledge Metso and all members of the Process Equipment Test Center of Metso Sweden AB in Sala, Sweden for their support thanks to which this research was made possible.

References

Asmatulu, R. (2011). Air pressure-assisted centrifugal dewatering of concentrated fine sulfide particles. *International Journal of Rotating Machinery*, *2011*(1), 131824.

Asmatulu, R. (2001). *Advanced chemical-mechanical dewatering of fine particles*. (Doctoral dissertation). Virginia Tech. Blacksburg, Virginia. Retrieved from https://vtechworks.lib.vt.edu/server/api/core/bitstreams/db5f76e9-91ff-40e7-a307-35b56f3a8487/content

Benitta, A. C., Kurnia, J. C., Agus, P. S. & Mujumdar, A. S. (2021). Advances in dewatering and drying in mineral processing. *Drying Technology*, 39, 11: Critical reviews of topics in drying science and technology.

Fränkle, B., Morsch, P., Kessler, C., Sok, T., Gleiß, M., & Nirschl, H. (2022). Iron ore tailings dewatering: Measurement of adhesion and cohesion for filter press operation. *Sustainability*, *14*(6), 3424.

Haramkar, S. S., Thombre, G. N., Jadhav, S. V., & Thorat, B. N. (2021). The influence of particle (s) size, shape and distribution on cake filtration mechanics—a short review. *Comptes Rendus. Chimie*, *24*(2), 255-265.

Pepper, D., Rule, C. M., & Mulligan, M.(2010). Cost-effective pressure filtration for platinum concentrates. In *The 4 th International Platinum Conference, Platinum in Transition 'Boom or Bust',* The Southern African Institute of Mining and Metallurgy.

Rushton, A., Ward, A. S., & Holdich, R. G. (2008). *Solid-liquid filtration and separation technology*. John Wiley & Sons.

Rezaei, A., Abdollahi, H., & Gharabaghi, M. (2021). Studies on the effects of physical parameters of filtration process on the fluid flow characteristics and de-watering efficiency of copper concentrate. *International Journal of Mining and Geo-Engineering*, *55*(2), 109-116.

Sutherland, K. (2007). *Filters and filtration handbook*, Elsevier.

Townsend, I. (2003). Automatic pressure filtration in mining and metallurgy. *Minerals Engineering*, *16*(2), 165-173.

Tarleton, E. S.,& Wakeman, R. J. (2007). *Solid/liquid separation: Equipment selection and process design*, Elsevier, 1st edition.

Tomova, M. (2023). Geophysical techniques for monitoring of integrated mine waste storage facility: Case study of Southeastern Bulgaria. *The Eurasia Proceedings of Science, Technology, Engineering & Mathematics (EPSTEM), 26*, 341-347.

Wakeman, R. (2007). The influence of particle properties on filtration. *Separation and Purification Technology*, *58*, 2, 234-241.

Author Information

Mihail Petrov
UMG "St. Ivan Rilski"
Prof. Boyan Kamenov Str., Sofia, Bulgaria

Teodora Yankova
UMG "St. Ivan Rilski"
Prof. Boyan Kamenov Str., Sofia, Bulgaria

Ljupcho Dimitrov
UMG "St. Ivan Rilski"
Prof. Boyan Kamenov Str., Sofia, Bulgaria
Contact e-mail: *ljupcho.dimitrov@mgu.bg*

Irena Grigorova
UMG "St. Ivan Rilski"
Prof. Boyan Kamenov Str., 1700 Sofia, Bulgaria

To cite this article:

Petrov, M., Yankova, T., Dimitrov, L. & Grigorova, I. (2024). Zinc concentrate dewatering pressure filtration. *The Eurasia Proceedings of Science, Technology, Engineering and Mathematics (EPSTEM), 29*, 46-54.

The Eurasia Proceedings of Science, Technology, Engineering & Mathematics (EPSTEM)
ISSN: 2602-3199

The Eurasia Proceedings of Science, Technology, Engineering & Mathematics (EPSTEM), 2024

Volume 29, Pages 55-60

ICRETS 2024: International Conference on Research in Engineering, Technology and Science

Synthesis and Fluorimetric Application of Novel Schiff Base Compound Containing 8-Hydroxyquinoline

Meliha Kutluca-Alici
Nigde Omer Halisdemir University

Abstract: Firstly, in this study, aldehyde derivative compound containing 5-chloro-8-hydroxyquinoline was obtained as literature information. Then, for the target compound, which is Schiff base derivative, was obtained from the condensation reaction of the aldehyde derivative compound containing chinolin with salicylaldehyde hydrazone. Chemical structure of synthesized Schiff base compound was confirmed as using various spectroscopic techniques (^{1}H-NMR and ^{13}C-NMR). Then, the interactions of the synthesized Schiff base compound with metals (Li^{+}, Ni^{2+} Co^{2+}, Ag^{+}, Al^{3+}, Mg^{2+}, Ca^{2+}, Ba^{2+}, Cu^{2+}, Hg^{2+}, Fe^{2+}, Pb^{2+}, Fe^{3+}, Cr^{3+} and Zn^{2+}) under convenient conditions were investigated using fluorescence spectrophotometry. In the fluorimetric investigations, primarily, the selectivity study was carried out. The free sensor target compound at 538 nm did not produce any significant emission intensity with excitation at 405 nm. The each of the cations (10.0 equiv) were separately added to target compound, only Zn^{2+} caused to a single band at 538 nm with a notable emission enhancement. As a result of the measurements, it was determined that the target compound had fluorimetric selectivity against only Zn^{2+} metal within all metals (Li^{+}, Ni^{2+}, Co^{2+}, Ag^{+}, Al^{3+}, Mg^{2+}, Ca^{2+}, Ba^{2+}, Cu^{2+}, Hg^{2+}, Fe^{2+}, Pb^{2+}, Fe^{3+}, Cr^{3+}).

Keywords: 8-Hydroxyquinoline, Fluorescence, Zn^{2+}, Schiff base.

Introduction

The development of high-performance fluorogenic chemosensors for sensitive and selective detection of cations, including Zn^{2+} recognition, holds great importance. In the human body, zinc is the second essential and most abundant transition element after iron, and zinc ions play a crucial role in neural signal transmission, regulation of the immune system, nucleic acid and protein synthesis, and numerous molecular mechanisms. Zinc, found in the cell membrane, plays a vital role in protecting the cell from damage caused by oxidative reactions. On the other hand, numerous studies have shown that an excessive amount of Zn^{2+} in the human body can lead to various diseases including epilepsy, osteoporosis, prostate and breast cancers, and neurodegenerative disorders such as Alzheimer's disease (Sethupathi, et al., 2020; Erdemir & Malkondu, 2020; Ghaedi et al., 2009). Therefore, it is crucial to regulate and monitor the levels of Zn^{2+} in order to prevent potential adverse effects on the human body.

In recent years, various traditional analytical methods such as differential pulse stripping anodic voltammetry, electrochemical analysis, atomic absorption spectroscopy, flame atomic absorption spectrometry, isotope chromatography, and chromatography have been commonly used for the detection of Zn^{2+} ions. On the other hand, these conventional detection methods have drawbacks including time-consuming analysis, complicated sample preparation, reliance on expensive and specialized equipment, and cumbersome procedures, which limit their suitability for real-time and large-scale monitoring of samples. In comparison to traditional analytical methods for detecting Zn^{2+} ions, fluorescence-based recognition techniques offer high sensitivity and selectivity. Moreover, this recognition technology offers several benefits, such as quick response times and straightforward sample preparation (Sethupathi, et al., 2020; Erdemir & Malkondu, 2020; Ghaedi, et al., 2009). Furthermore, fluorescence-based techniques are highly sensitive and selective, and they are easy to operate. As a result,

- Selection and peer-review under responsibility of the Organizing Committee of the Conference

fluorescence-based recognition techniques for cation detection have been widely used in fields such as medicine, chemistry, life sciences, environmental science, and many other research areas. Numerous synthesized fluorescence-based molecules for the detection of Zn^{2+} ions have been reported in the literature. These molecules are typically based on coumarin, fluorescein, calixarene, and thiazole structures (Erdemir & Malkondu, 2020) (Aydin, et al., 2021). Many of these molecules exhibit high detection limits or low selectivity in the recognition of Zn^{2+} ions. Therefore, it is highly significant to develop novel fluorogenic chemosensors for efficient and rapid fluorescence analysis of Zn^{2+} detection in environmental waste.

In this study, aldehyde derivative compound containing 5-chloro-8-hydroxyquinoline was obtained as literature information (Wantulok, et al., 2008). Then, for the target compound (5-chloro-7-(((-2-hydroxybenzylidene) hydrazineylidene) methyl)quinolin-8-ol) (**8HQ-SA**) which is Schiff base derivative, was obtained from the condensation reaction of the aldehyde derivative compound containing chinolin with salicylaldehyde hydrazone. Chemical structure of synthesized **8HQ-SA** was confirmed as using various spectroscopic techniques (^{1}H-NMR and ^{13}C-NMR). Then, the interactions of the synthesized **8HQ-SA** compound with some metals (Li^{+}, Ni^{2+} Co^{2+}, Ag^{+}, Al^{3+}, Mg^{2+}, Ca^{2+}, Ba^{2+}, Cu^{2+}, Hg^{2+}, Fe^{2+}, Pb^{2+}, Fe^{3+}, Cr^{3+} and Zn^{2+}) under convenient conditions were investigated using fluorescence spectrophotometry. In the fluorimetric investigations, primarily, the selectivity study was carried out. The free sensor target compound at 546 nm did not produce any significant emission intensity with excitation at 405 nm. The each of the cations (6.0 equiv) were separately added to target compound, only Zn^{2+} caused to a single band at 546 nm with a notable emission enhancement. As a result of the measurements, it was determined that the target compound had fluorimetric selectivity against only Zn^{2+} metal within all metals (Li^{+}, Ni^{2+}, Co^{2+}, Ag^{+}, Al^{3+}, Mg^{2+}, Ca^{2+}, Ba^{2+}, Cu^{2+}, Hg^{2+}, Fe^{2+}, Pb^{2+}, Fe^{3+}, Cr^{3+}).

Method

Chemicals and Instruments

All necessitated chemicals are analytical grade and were obtained from Sigma-Aldrich Chemicals (Zwijndrecht, The Netherlands) and utilized with no further processing. The perchlorate salts of the cations were utilized in this study. ^{1}H and ^{13}C-NMR spectral studies were measured by a Spinsol and Magritek NMR spectrometer and emission spectra of the chemosensor **8HQ-SA** were recorded in a Varian Cary Eclipse Fluorescence Spectrophotometer (Agilent Technologies Inc, Santa Clara, CA, USA).

Synthesis of 5-chloro-8-hydroxyquinoline-7-carbaldehyde (1)

Compound (1) was prepared according in the literature (Wantulok, et al., 2008).

Synthesis of the chemosensor 5-chloro-7-(((-2-hydroxybenzylidene)hydrazineylidene)methyl)quinolin-8-ol (8HQ-SA)

Absolute ethanolic solutions (10 mL) of compound (1) (0.05 g, 0.240 mmol) was added to 2-(hydrazineylidenemethyl)phenol (0.036 g, 0.264 mmol) in absolute EtOH and stirred under reflux for 24 hours. After completion of the reaction, the precipitate formed was filtered off. The precipitate was washed three times with water and ethanol, dried in a vacuum oven. Finally, the Schiff base compound (**8HQ-SA**) was recrystallized with hot ethanol to obtain yellow crystals.

Yield: 59 %, Melting Point: 273.6 ^{0}C, ^{1}H NMR (400 MHz, DMSO) δ 11.19 (s, 1H), 9.14 (s, 1H), 9.03 (d, *J* = 4.4 Hz, 2H), 8.54 (d, *J* = 8.2 Hz, 1H), 8.11 (s, 1H), 7.82 (dd, *J* = 8.4, 4.2 Hz, 1H), 7.71 (d, *J* = 7.2 Hz, 1H), 7.41 (t, *J* = 7.2 Hz, 1H), 6.98 (t, *J* = 7.5 Hz, 2H). ^{13}C NMR (100 MHz, DMSO) δ 163.65, 159.20, 157.97, 155.08, 150.27, 140.12, 133.70, 133.32, 131.49, 128.13, 124.97, 124.42, 120.06, 120.06, 118.71, 116.99, 116.46.

Results and Discussion

Preparation of the Chemosensor 8HQ-SA

The synthesis routes of TC include three steps: the preparation of compound 2-(hydrazineylidenemethyl)phenol was prepared by the reaction of 2-hydroxybenzaldehyde with %80 hydrazine hydrate, and 5-chloro-8-hydroxyquinoline-7-carbaldehyde by the Duff reaction with HMTA in trifluoroacetic acid. The chemosensor

8HQ-SA was easily prepared by the condensation reaction of 5-chloro-8-hydroxyquinoline-7-carbaldehyde (1) and 2-(hydrazineylidenemethyl) phenol (2) in ethanol with 59 % yield as illustrated in Schema 1.

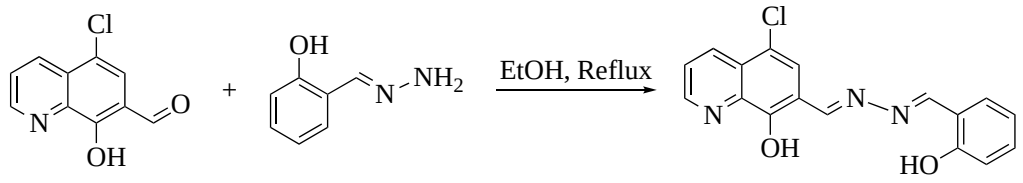

(1) **(2)** **(8HQ-SA)**

Schema 1. The Synthesis Procedure for the **8HQ-SA**

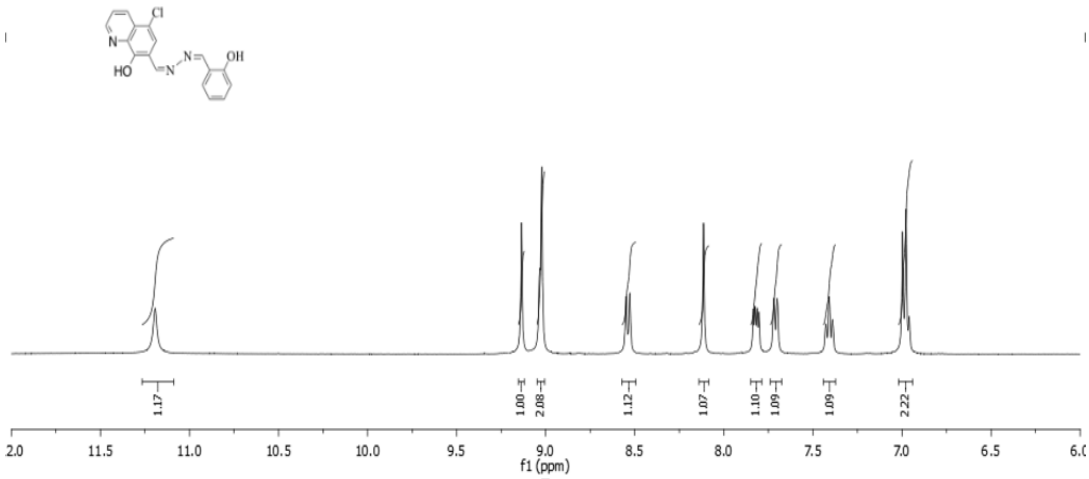

Figure 1. ^{1}H-NMR spectrum of compound **8HQ-SA**

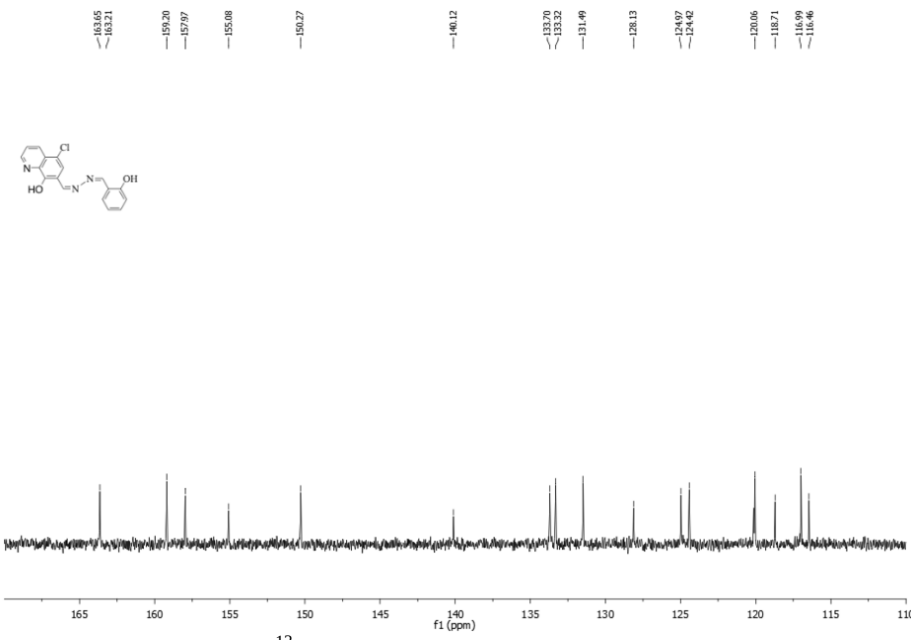

Figure 2. ^{13}C-NMR spectrum of compound **8HQ-SA**

Emission Study

The stock solution of 8HQ-SA (10 mM) was prepared in DMSO and then diluted 10 μM in EtOH/H_2O (9/1, v/v). The tested metal perchlorate salts were utilized as (10^{-2} M).

Fluorescence Studies of 8HQ-SA versus Zn^{2+}

The fluorescent study of **8HQ-SA** was conducted in EtOH−H_2O (9:1, v/v) with Li^+, Ni^{2+}, Co^{2+}, Ag^+, Al^{3+}, Mg^{2+}, Ca^{2+}, Ba^{2+}, Cu^{2+}, Hg^{2+}, Fe^{2+}, Pb^{2+}, Fe^{3+}, Cr^{3+}, and Zn^{2+}. At first, **8HQ-SA** showed no emission at 546 nm; however, the addition of Zn^{2+} to 8HQ-SA resulted in a significant increase in intensity at 546 nm. Addition of the other mentioned cations to the 8HQ-SA solution did not cause a significant increase at 546 nm (Figure 3). This significant increase in fluorescence intensity indicates a strong interaction between 8HQ-SA and Zn^{2+}.

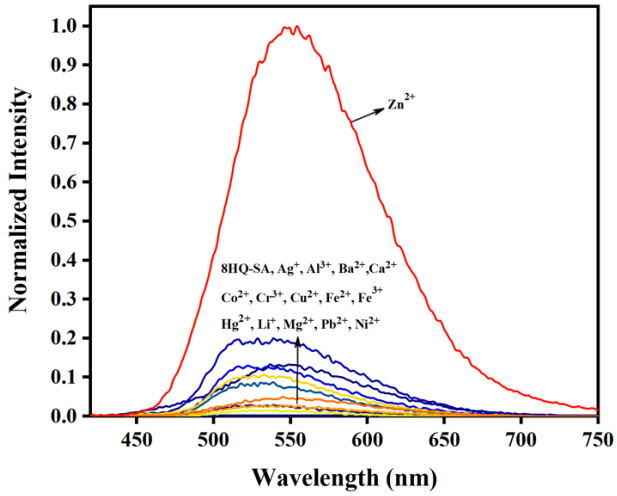

Figure 3. Changes in emission intensity of 8HQ-SA (10 μM) in the presence of various tested cations.

To assess the sensitivity and quantify the response of 8HQ-SA toward Zn^{2+}, a standard titration analysis was performed, as shown in Fig. 4a. The fluorescence intensity of 8HQ-SA at 546 nm increased due to the concentration of Zn^{2+} ions increased. As can be seen from the Fig 4a., no change in fluorescence intensity was observed after a certain point. This is an indication that the 8HQ-SA-Zn^{2+} complex has reached saturation. Additionally, a Job's plot experiment was conducted using a fluorescence spectrometer to confirm the final complexation between 8HQ-SA and Zn^{2+}. As shown in Fig 4b, the Job's plot analysis indicates a 1:1 complexation ratio between 8HQ-SA and Zn^{2+}, as the highest ordinate value is observed at a molar fraction of Zn^{2+} with 8HQ-SA close to 0.5, confirming the 1:1 stoichiometric binding ratio.

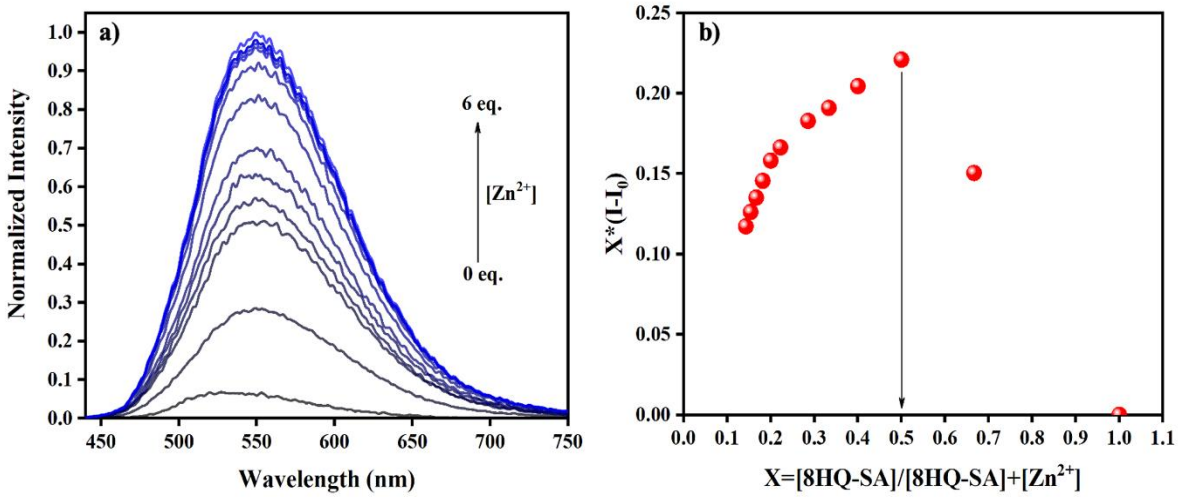

Figure 4. a) The emission spectra of 8HQ-SA were measured at various concentrations of Zn^{2+}. b) Job's plot demonstrating the 1:1 stoichiometry

The emission values were plotted as a function of the concentrations of Zn^{2+} Fig 5a to investigate the limit of detection (LOD) value of **8HQ-SA** for Zn^{2+} determination the LOD value of compound **8HQ-SA** was determined as 1.22 mM according to the equation: LOD = 3σ/k (σ: symbolizes the root-mean-square of blank measurements, k: the slope of the linear calibration curve). Furthermore, the log(Ka) value for the **8HQ-SA**-Zn^{2+} system was 2,93 M^{-1} in accordance with the Benesi–Hildebrand plot of the alterations in the titration of the **8HQ-SA** toward Zn^{2+} (Fig 5b).

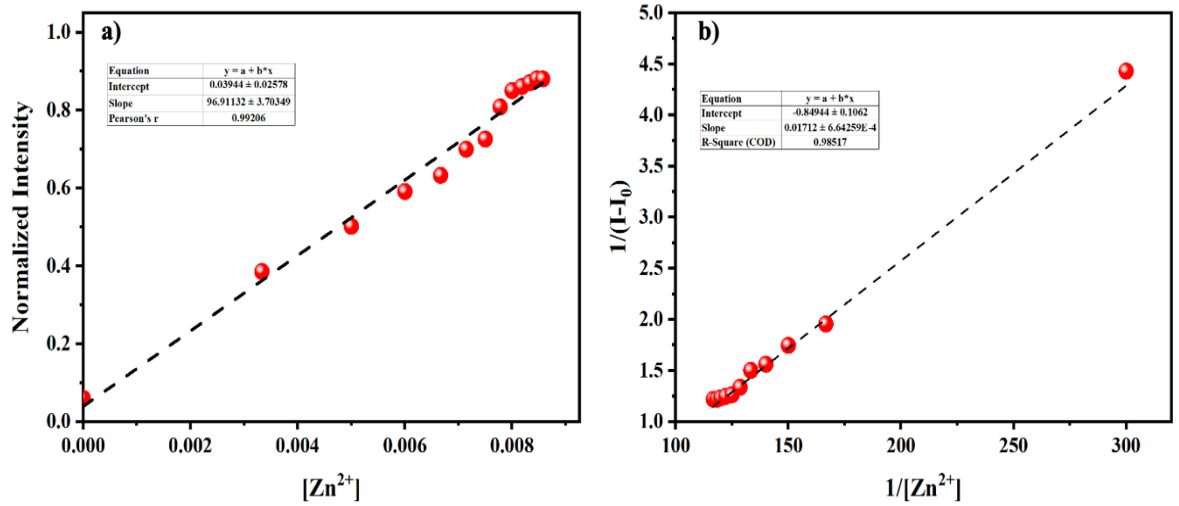

Figure 5. a) The plot of emission intensity of 8HQ-SA at 546 nm versus Zn^{2+} cation concentration, b) Benesi–Hildebrand plot assuming 1:1 stoichiometry from fluorometric titration data of receptor **8HQ-SA** (10 μM) with Zn^{2+}

Conclusion

In summary, a new quinoline-based fluorogenic chemosensor for Zn^{2+} detection has been successfully created. The change in intensity of the 8HQ-SA solution is a result of its interaction and coordination with Zn^{2+}, indicating the strong affinity between 8HQ-SA and Zn^{2+}. The proposed fluorogenic chemosensor 8HQ-SA has the potential to serve as a simple and effective tool for detecting Zn^{2+} in solutions, and it can inspire the design of different fluorogenic probes for Zn^{2+} recognition.

Scientific Ethics Declaration

The author declares that the scientific ethical and legal responsibility of this article published in EPSTEM journal belongs to the author.

Acknowledgements or Notes

* This article was presented as an oral presentation at the International Conference on Research in Engineering, Technology and Science (www.icrets.net) held in Tashkent/Uzbekistan on August 22-25, 2024.

References

Aydin, D., Elmas, S. N. K., Savran, T., Arslan, F. N., Sadi, G., & Yilmaz, I. (2021). An ultrasensitive ″OFF–ON ″fluorogenic sensor based on thiazole derivative for Zn2+: Food supplement, water and bio–imaging applications. *Journal of Photochemistry and Photobiology A: Chemistry*, *419*, 113459.

Erdemir, S., & Malkondu, S. (2020). Calix [4] arene based a NIR-fluorescent sensor with an enhanced stokes shift for the real-time visualization of Zn (II) in living cells. *Sensors and Actuators B: Chemical*, *306*, 127574.

Ghaedi, M., Shokrollahi, A., Niknam, K., & Soylak, M. (2009). Cloud point extraction of copper, zinc, iron and nickel in biological and environmental samples by flame atomic absorption spectrometry. *Separation Science and Technology*, *44*(3), 773-786.

Kutluca Alici, M. (2020). Phentroimidazole based fluorescence “turn on” sensor for highly sensitive detection of Zn2+ ions. *Journal of Fluorescence*, *30*(2), 269-273.

Sethupathi, M., Jayamani, A., Muthusankar, G., Sakthivel, P., Sekar, K., Gandhi, S., ... & Selvaraju, C. (2020). Colorimetric and fluorescence sensing of Zn2+ ion and its bio-imaging applications based on macrocyclic “tet a” derivative. *Journal of Photochemistry and Photobiology B: Biology*, *207*, 111854.

Voloshin, N. A., Chernyshev, A. V., Bezuglyi, S. O., Metelitsa, A. V., Voloshina, E. N., & Minkin, V. I. (2008). Spiropyrans and spirooxazines: 4. Synthesis and spectral properties of 6′-halo-substituted spiro [indoline-2, 2′-2 H-pyrano [3, 2-h] quinolines]. *Russian Chemical Bulletin*, *57*, 151-158.

Author Information

Meliha Kutluca-Alici
Nigde Omer Halisdemir University
Laboratory Assistant and Veterinary Health
Bor Vocational School , Nigde, Türkiye
Contact e-mail: *melihakutlucaalici@gmail.com*

To cite this article:

Kutluca-Alici, M. (2024). Synthesis and fluorimetric application of novel schiff base compound containing 8-hydroxyquinoline. *The Eurasia Proceedings of Science, Technology, Engineering and Mathematics (EPSTEM), 29*, 55-60.

The Eurasia Proceedings of Science, Technology, Engineering & Mathematics (EPSTEM)
ISSN: 2602-3199

The Eurasia Proceedings of Science, Technology, Engineering & Mathematics (EPSTEM), 2024

Volume 29, Pages 61-68

ICRETS 2024: International Conference on Research in Engineering, Technology and Science

Real-Time Detection of Cracks During Dynamic Testing of Sheet Metals Used in Automotive Suspension Systems

Mehmet Emin Ors
AYD Automotive Industry

Ziya Ozcelik
Selcuk University

Abstract Dynamic testing is crucial in the automotive industry for ensuring vehicle safety and performance, particularly in assessing the durability and reliability of front-end and suspension systems. Traditional real-time crack detection methods, which are often manual and time-consuming, face limitations in accuracy and reliability. This study explores the application of deep learning techniques to enhance real-time crack detection during dynamic testing, offering a modern solution to these challenges. The research involves the collection and processing of IP camera data, followed by model training using various deep learning algorithms. The study details how these algorithms are employed to improve the detection and prediction of cracks, providing a systematic approach to overcoming the shortcomings of traditional methods. The deep learning models developed in this research were tested against real-world data, showing significantly higher accuracy in real-time crack detection compared to conventional techniques. The findings indicate that deep learning-based approaches not only improve the precision of real-time crack detection but also contribute to more efficient and effective testing processes in the automotive industry. This research offers a promising direction for future studies and practical applications, suggesting that deep learning can significantly enhance the reliability of dynamic testing. In conclusion, this study highlights the potential of deep learning to transform real time real-time crack detection in the automotive industry, providing a more accurate, reliable, and scalable solution. The results serve as a valuable reference for both academic research and industrial practices, paving the way for further advancements in automotive testing through the integration of artificial intelligence.

Keywords: Deep learning, Sheet metal real-time crack detection, Automotive industry

Introduction

The automotive industry is an indispensable part of modern life and safety, and performance standards need to be continuously improved. In this context, the reliability and durability of vehicles are of great importance in terms of both consumer satisfaction and legal regulations. In particular, front layout and suspension systems have a critical impact on the handling, ride comfort and overall safety of vehicles. Continuous monitoring of the performance of these systems and early detection of potential cracks is vital to prevent serious accidents and costly repairs. Figure 1 shows a sheet metal crack test at the R&D center. The material is oscillated until a crack form and the result is observed. Conventional methods of real-time crack detection usually rely on techniques such as visual inspection, ultrasonic testing and magnetic particle inspection. However, besides being time-consuming, these methods are prone to operator errors and limited in terms of accuracy. In recent years, artificial intelligence, and in particular deep learning techniques, have offered promising solutions for problems requiring complex data analysis and modeling in various industries. Deep learning is characterized by its ability to detect complex patterns and anomalies by learning on large datasets. In this study, we investigate how deep

learning techniques can be applied for real-time crack detection in dynamic tests in the automotive industry. First, the basic principles and application areas of deep learning algorithms will be emphasized, followed by a review of existing real-time crack detection methods in the literature and the use of deep learning in this field. The aim of the study is to demonstrate the superiority of deep learning-based approaches over traditional methods in terms of accuracy, speed and reliability, and to lay a foundation for the widespread adoption of this technology in the automotive industry. This test was performed to evaluate the durability and strength of the material. Cracks in metal under dynamic loading reveal the limits of the material's structural integrity and reliability. Such testing is critical to guarantee the long-term performance and safety of materials, especially in the automotive and aerospace industries. The shape and size of cracks can vary depending on the internal structure of the material and the test method used.

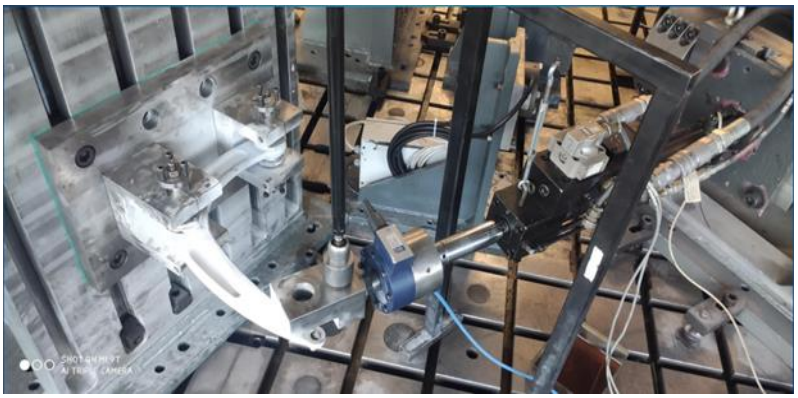

Figure 1. Dynamic test system in R&D labaratory

Research on real-time crack detection in the automotive industry can generally be divided into two main categories: traditional detection methods and AI-assisted detection methods. Traditional methods include visual inspection, ultrasonic testing, magnetic particle inspection and radiographic testing. Each of these methods has certain advantages and limitations. Visual inspection is one of the most widely used methods, providing a low-cost and rapid preliminary assessment. However, it is prone to error depending on the operator's experience and caution (Rao, 2018). Ultrasonic testing uses sound waves to detect cracks in the material and offers high accuracy rates. However, this method also requires experienced operators and is sensitive to surface preparation (Hellier, 2013). Magnetic particle inspection uses magnetic fields and iron particles to detect surface and near-surface cracks in ferromagnetic materials. Although this method is fast and effective, it can only detect cracks near the surface (Dawson & Wilby, 2011). Radiographic testing detects cracks in materials by imaging them with X-rays or gamma rays. Although it offers high accuracy, it has significant disadvantages such as radiation risk and cost (Baldev et al., 2002). Artificial intelligence, and in particular deep learning, has received considerable attention in the field of material inspection and real-time crack detection in recent years. Deep learning is characterized by its ability to detect complex patterns and anomalies by working on large datasets (LeCun, Bengio, & Hinton, 2015). Deep learning models such as Convolutional Neural Networks (CNN) and Recurrent Neural Networks (RNN) show high performance, especially in image processing and time series analysis (Goodfellow et al., 2016). In the literature, the number of studies on real-time crack detection using deep learning is rapidly increasing. For example, Cha, Choi, and Büyüköztürk (2017) detected cracks in concrete structures using a deep learning-based method and achieved high accuracy rates. In this study, the deep learning model was trained on a large dataset to recognize various types of cracks. Similarly, Zhang et al. (2019) developed a CNN-based model to detect cracks in metal surfaces and achieved higher accuracy and speed than traditional methods. The use of deep learning techniques in dynamic testing in the automotive industry is a relatively new research area.

One of the first studies in this field was conducted by Li et al. In their study, they developed a deep learning model to detect cracks in automotive suspension systems. The model was trained using a dataset collected during dynamic tests, making it suitable for real-time detection. The results showed that the model works with high accuracy rates and is suitable for real-time applications. This literature review reveals that deep learning techniques have great potential for real-time crack detection in dynamic testing in the automotive industry. However, more research and applications are needed in this area. In particular, it is important to improve data collection and processing techniques, improve model performance, and expand studies for industrial applications. Xu, Yue, and Liu (2023) propose an innovative deep learning model named YOLOv5-IDS, which addresses the challenges of traditional crack detection methods that are often inefficient and require multiple steps. The study introduces a comprehensive approach that integrates crack detection, segmentation, and

parameter measurement in real-time, significantly enhancing both accuracy and efficiency compared to existing methods. The model's performance, demonstrated through high mean average precision and mean intersection over union metrics, underscores its potential for advancing the automation of crack detection and assessment in concrete structures. This work contributes to the field by offering a robust solution for real-time structural health monitoring.

Method

Example Dataset and Features

In this study, IP cameras are used to detect cracks in automotive suspension and front-end systems. IP cameras are characterized by their ability to record high-resolution images in real-time and transmit them over a network. The cameras were placed in critical areas of the vehicles under test and used to collect data in various dynamic test scenarios. The test scenarios included the performance of the vehicles at different speeds and road conditions.

Figure 2. Example pictures from dataset

Data Preparing and Preprocessing

The collected image data was subjected to various pre-processing steps in preparation for model training; Noise Removal: Techniques such as median filtering was applied to reduce random noise in the images. Contrast and Lighting Correction: The contrast and illumination of the images were increased to make the cracks more

visible. Edge Detection: Using Sobel or Canny edge detection algorithms, the edges of the cracks were made clearer. Normalization: Image pixel values were normalized to the range [0, 1] for faster and more stable learning of the model. Data Augmentation: Data augmentation techniques such as random rotation, shift and scaling were used to increase the diversity of the training set.

Model Fitting: Process and Parameters

Model training includes the following steps: Preparation of the Data Set: The data is divided into training (70%), validation (15%) and test (15%) sets. Model Compilation: The model was compiled using the Adam optimization algorithm and cross entropy loss. Training Parameters: The model was trained for 50 epochs with a batch size of 32. The learning rate was initially set to 0.001 and decreased during training. Training Process: The model was trained on the training set and its performance was evaluated at the end of each epoch with the validation set. Overfitting of the model was prevented by using early stopping and model checkpoints.

Experimental Results

Table 1 presents the experimental results obtained using various deep learning models, highlighting their performance across several key metrics: Accuracy, Precision, Recall, F1 Score, AUC, and ROC AUC. The models evaluated include Google-Net, DarkNet, ResNet50, VGG16, and InceptionV3, each of which is widely recognized for its application in image processing and classification tasks. The table provides a comparative analysis of these models, demonstrating their effectiveness in the context of real-time crack detection during dynamic testing in the automotive industry. Starting with Accuracy, which reflects the overall correctness of the model's predictions, the results show that ResNet50 achieved the highest accuracy at 0.96, followed closely by Google-Net at 0.95. VGG16 and DarkNet also performed well, with accuracy scores of 0.94 and 0.93, respectively.

Table 1. Results of algorithm with different DL networks

Model	Accuracy	Precision	Recall	F1 score	AUC
Google-Net	0,95	0,93	0,92	0,925	0,97
DarkNet	0,93	0,91	0,89	0,9	0,9
ResNet50	0,96	0,94	0,95	0,945	0,98
VGG16	0,94	0,92	0,92	0,91	0,915
InceptionV3	0,92	0,9	0,88	0,89	0,94

InceptionV3, while still performing at a high level, recorded the lowest accuracy among the models at 0.92. This indicates that ResNet50 is slightly more adept at correctly classifying instances compared to the other models, with Google-Net also exhibiting strong performance. Precision is a metric that measures the proportion of true positive predictions out of all positive predictions made by the model. This metric is crucial in scenarios where the cost of false positives is high. ResNet50 again leads with a precision of 0.94, closely followed by Google-Net at 0.93. VGG16 and DarkNet are not far behind, with precision scores of 0.92 and 0.91, respectively. InceptionV3, while slightly lower, still maintains a respectable precision of 0.90. These precision scores suggest that all the models are fairly consistent in minimizing false positive rates, with ResNet50 and Google-Net being the most reliable. Recall, on the other hand, measures the proportion of true positive predictions out of all actual positives. This metric is particularly important in applications where it is critical not to miss any positive instances. Here, ResNet50 again shows superior performance with a recall of 0.95, indicating its high sensitivity in identifying positive cases. Google-Net and VGG16 both recorded a recall of 0.92, demonstrating their strong ability to capture true positives, though slightly lower than ResNet50. DarkNet and InceptionV3 reported recalls of 0.89 and 0.88, respectively, which, while still strong, suggest a slightly higher likelihood of missing positive instances compared to the other models. The F1 Score, which is the harmonic mean of precision and recall, provides a balanced measure that accounts for both false positives and false negatives. ResNet50 leads again with an F1 score of 0.945, indicating its overall effectiveness in both capturing true positives and minimizing false positives. Google-Net follows with an F1 score of 0.925, while VGG16 records 0.91. DarkNet and InceptionV3, with F1 scores of 0.90 and 0.89 respectively, while still robust, reflect a slightly lesser balance between precision and recall compared to the other models. The Area Under the Curve (AUC) is a critical metric in evaluating the performance of classification models, especially in terms of distinguishing between positive and negative classes. A higher AUC indicates a better model performance. ResNet50 achieves the highest AUC at 0.98, showcasing its superior ability to discriminate between classes. Google-Net also performs exceptionally well with an AUC of 0.97. VGG16 and InceptionV3 have AUCs of 0.915 and 0.94, respectively,

which are still indicative of strong performance. DarkNet, with an AUC of 0.90, while slightly lower, remains a reliable model. Finally, ROC AUC values reflect the model's performance in terms of the trade-off between true positive and false positive rates across different threshold settings. ResNet50 excels with a ROC AUC of 0.99, indicating almost perfect classification ability. Google-Net, with a ROC AUC of 0.98, also demonstrates near-perfect classification performance. VGG16 and DarkNet both recorded ROC AUCs of 0.96, indicating their high reliability in various threshold settings. InceptionV3, with a ROC AUC of 0.95, while slightly lower, still performs admirably.

In summary, Table 1 reveals that ResNet50 consistently outperforms the other models across all key metrics, making it the most reliable model for real-tme real-time crack detection in dynamic testing scenarios. Google-Net also shows strong performance, particularly in accuracy, precision, and ROC AUC. VGG16 and DarkNet offer balanced performance across all metrics, making them viable alternatives depending on the specific application requirements. InceptionV3, while performing slightly lower than the others, still offers strong overall performance and can be considered a competitive model in scenarios where its specific strengths align with the application needs. These results underline the effectiveness of deep learning models in improving real-time crack detection accuracy and reliability in the automotive industry, with ResNet50 emerging as the most promising candidate for future applications. The trained model was evaluated on the test set and its performance was measured using the following metrics. Accuracy: The proportion of images correctly classified by the model. Precision: The proportion of images correctly classified as cracked by the model. Specificity.

Figure 4. Some results for algorithm

The proportion of non-cracked images correctly classified by the model. F1 Score: Harmonic mean of precision and recall. ROC Curve and AUC: The ROC curve (Receiver Operating Characteristic) and Area Under Curve (AUC) were used to evaluate the overall performance of the model. To test the suitability of the model for real-world applications, performance tests were conducted using real-time data streams. The performance of the model was observed on live images collected with IP cameras and the results were analyzed.

Figure 4 provides a comprehensive visualization of the training and validation processes across various metrics—Loss, Accuracy, F1 Score, and AUC—over a series of epochs. Each plot within this figure is crucial for understanding the behavior and performance of the deep learning model during training and validation, offering insights into how well the model generalizes to unseen data.

Starting with the Loss graph, located on the far left, we observe the decline in both training loss (red line) and validation loss (green line) as the number of epochs increases. The loss function is a key metric used to evaluate how well the model's predictions match the true labels. In this case, the loss decreases steadily during the initial epochs, indicating that the model is learning effectively by minimizing the discrepancy between predictions and actual values. Notably, the validation loss closely follows the training loss, which suggests that the model is not overfitting and is likely to generalize well to new data. By the 11th epoch, marked by the blue dot, the model achieves its best performance in terms of loss, highlighting this point as a critical stage in the training process. Moving to the Accuracy plot, second from the left, the training accuracy (red line) shows a consistent increase across the epochs, approaching near-perfect accuracy by the end of the training process. This indicates that the model is progressively improving its ability to correctly classify the training data. The validation accuracy

(green line), while initially lagging behind the training accuracy, also shows a significant upward trend. This suggests that the model is effectively learning from the training data and applying that knowledge to unseen validation data. However, there is a noticeable gap between training and validation accuracy during certain epochs, indicating that while the model performs well on training data, it may struggle slightly with generalization at some points.

The best epoch for accuracy is also marked at the 11th epoch, where the validation accuracy peaks, confirming the model's optimal performance at this stage. The F1 Score plot, third from the left, provides a nuanced view of the model's precision and recall balance. The F1 score is particularly important in cases where there is an uneven class distribution, as it accounts for both false positives and false negatives. In this plot, the training F1 score (red line) increases rapidly, indicating that the model is quickly learning to balance precision and recall effectively. The validation F1 score (green line), though more variable, follows a generally upward trend, suggesting that the model maintains a reasonable balance between precision and recall even on unseen data. The best epoch for the F1 score is also identified at the 11th epoch, marked by the blue dot, signifying a point where the model achieves its best trade-off between precision and recall on the validation set. Finally, the AUC (Area Under the Curve) plot, on the far right, illustrates the model's ability to discriminate between positive and negative classes across different thresholds. The AUC is a critical metric in classification problems, as it provides a single value to summarize the model's performance across all classification thresholds. The training AUC (red line) shows a rapid increase and stabilizes at a high value, indicating that the model is quickly becoming proficient at distinguishing between classes. The validation AUC (green line), while slightly lower and more variable than the training AUC, also shows a significant upward trend, suggesting that the model generalizes well to the validation data.

The best epoch for AUC, once again marked at the 11th epoch, reflects the model's optimal discriminatory power at this stage, as indicated by the peak in validation AUC. In summary, Figure 4 offers a detailed examination of the model's learning process across key performance metrics. The consistent improvement in training metrics indicates that the model is effectively learning from the data. The validation metrics, while showing some variability, generally follow the trends seen in the training metrics, suggesting that the model has strong generalization capabilities. The 11th epoch emerges as a critical point in the training process, where the model achieves its best performance across loss, accuracy, F1 score, and AUC. This figure underscores the effectiveness of the deep learning model in achieving high performance, with robust training and validation outcomes that support its application in real-world scenarios. This level of detailed analysis is essential for understanding the strengths and potential areas for improvement in the model, providing a foundation for future work and optimization efforts.

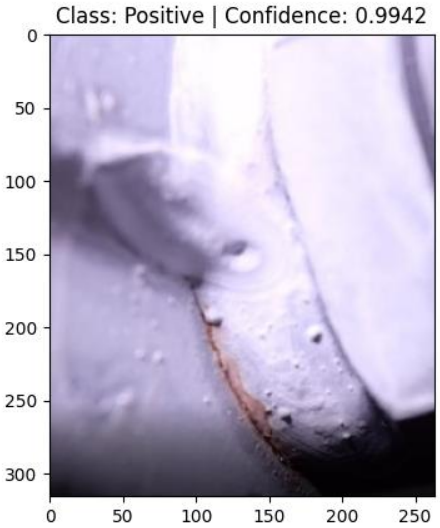

Figure 5. Result of algorithm cracked part listed as positive

Figure 5, illustrates a critical outcome from the deep learning-based real-time crack detection model, highlighting a specific instance where the model has identified a crack with a high level of confidence. The image shows a section of the material surface, where the model has classified the observed defect as a "Positive" instance, indicating the presence of a crack. The confidence score associated with this classification is an impressive 0.9942, suggesting that the model is nearly certain about the presence of the crack in this particular

image. The confidence score is a vital aspect of model evaluation, as it provides insight into the model's certainty regarding its predictions. A score of 0.9942 indicates that the model has a 99.42% probability that the detected feature is indeed a crack. This high confidence level is crucial in real-world applications, particularly in the automotive industry, where the early and accurate detection of cracks can prevent potential failures and enhance safety measures. Moreover, the model's ability to achieve such a high confidence score demonstrates its robustness and the effectiveness of the training process, which involved extensive data augmentation and fine-tuning of network parameters. The clarity with which the crack is highlighted in the image underscores the model's sensitivity to subtle features that may be indicative of material failure. In summary, Figure 5 not only showcases the practical application of deep learning in defect detection but also emphasizes the model's high accuracy and reliability. The confidence score reinforces the model's potential for integration into automated inspection systems, providing a powerful tool for ensuring quality and safety in industrial applications.

Conclusion

In this study, a deep learning-based approach for real-time crack detection during dynamic testing in the automotive industry is presented. High resolution images collected using IP cameras are analyzed with Convolutional Neural Network (CNN) models. The main findings and conclusions of the study are summarized. Data Collection and Preprocessing; A large data set was created using IP cameras. The preprocessing steps performed on the images enabled the model to produce more effective and accurate results. Model Training and Performance; The CNN model was trained on a large dataset and optimized with validation data. The model performed real-time crack detection with high accuracy rates on the test set. Evaluation Metrics: The performance of the model was evaluated using various metrics such as accuracy, sensitivity, specificity and F1 score. In addition, the overall performance of the model was analyzed with the ROC curve and AUC value. The overall performance of the model shows that it offers high accuracy and reliability for real-time crack detection in dynamic tests. These results show that deep learning-based approaches can be successfully used in critical tasks such as real-time crack detection in the automotive industry. In the future, it is envisioned that these approaches can be further improved with larger data sets and advanced model architectures.

Scientific Ethics Declaration

The authors declare that the scientific ethical and legal responsibility of this article published in EPSTEM journal belongs to the authors.

Acknowledgements or Notes

* This article was presented as an oral presentation at the International Conference on Research in Engineering, Technology and Science (www.icrets.net) held in Tashkent/Uzbekistan on August 22-25, 2024.

References

Baldev, R., Jayakumar, T., & Rao, B. P. C. (2002). *Practical non-destructive testing*. Woodhead Publishing.

Cha, Y. J., Choi, W., & Büyüköztürk, O. (2017). Deep learning-based crack damage detection using convolutional neural networks. *Computer-Aided Civil and Infrastructure Engineering*, *32*(5), 361-378.

Dawson, B., & Wilby, J. (2011). *Non-destructive testing of welds*. CRC Press.

Choudhury, S. (2011). *Identification of Transverse Crack in a Cracked Cantilever Beam Using Fuzzy Logic and Kohonen Network* (Doctoral dissertation).

Fang, Q., Nguyen, B. D., Castanedo, C. I., Duan, Y., & Maldague II, X. (2020, April). Automatic defect detection in infrared thermography by deep learning algorithm. In *Thermosense: Thermal Infrared Applications XLII*, *11409*,180-195. SPIE.

Fan, W., & Qiao, P. (2011). Vibration-based damage identification methods: a review and comparative study. *Structural Health Monitoring*, *10*(1), 83-111.

Goodfellow, I., Bengio, Y., & Courville, A. (2016). Regularization for deep learning. *Deep Learning*, 216-261.

Hellier, C. J. (2013). *Handbook of nondestructive evaluation*. McGraw Hill Professional.

Hasanzadeh, R. P., Sadeghi, S. H. H., Ravan, M., Moghaddamjoo, A. R., & Moini, R. (2011). A fuzzy alignment approach to sizing surface cracks by the AC field measurement technique. *NDT & E International*, *44*(1), 75-83.

Hau, D., & Chen, K. (2011). Exploring hierarchical speech representations with a deep convolutional neural network. *UKCI 2011 Accepted Papers*, *37*, 31.

LeCun, Y., Bengio, Y., & Hinton, G. (2015). Deep learning. *Nature*, *521*(7553), 436-444.

McAuliffe, G. (2011). Deep learning. *Handbook of counselor preparation: Constructivist, developmental, and experiential approaches*, 13-30.Rao, B. P. C. (2018). Visual Inspection and Non-Destructive Testing in Maintenance. Springer.

Rao, A. S., Nguyen, T., Palaniswami, M., & Ngo, T. (2021). Vision-based automated crack detection using convolutional neural networks for condition assessment of infrastructure. *Structural Health Monitoring*, *20*(4), 2124-2142.

Sbarufatti, C., Manes, A., & Giglio, M. (2011). Advanced stochastic FEM-based artificial neural network for crack damage detection. In *COUPLED IV: proceedings of the IV International Conference on Computational Methods for Coupled Problems in Science and Engineering* (pp. 1107-1119). CIMNE.

Xu, G., Yue, Q., & Liu, X. (2023). Deep learning algorithm for real-time automatic crack detection, segmentation, qualification. *Engineering Applications of Artificial Intelligence*, *126*, 107085.

Zhang, Y., Wu, Q., Zhang, Z., & Wang, J. (2019). A deep convolutional neural network-based model for metal surface defect detection. *Sensors*, *19*(5), 1024.

Author Information

Mehmet Emin Ors
AYD Automotive Industry, Konya, Türkiye

Ziya Ozcelik
Selcuk University, Konya, Türkiye
Contact e-mail: *zozcelik@selcuk.edu.tr*

To cite this article:

Ors, M. E. & Ozcelik, Z. (2024). Real-time detection of cracks during dynamic testing of sheet metals used in automotive suspension systems. *The Eurasia Proceedings of Science, Technology, Engineering and Mathematics (EPSTEM)*, *29*, 61-68.

The Eurasia Proceedings of Science, Technology, Engineering & Mathematics (EPSTEM)
ISSN: 2602-3199

The Eurasia Proceedings of Science, Technology, Engineering & Mathematics (EPSTEM), 2024

Volume 29, Pages 69-75

ICRETS 2024: International Conference on Research in Engineering, Technology and Science

Longitudinal Fracture Analysis with Taking into Account the Elongation Speed of Inhomogeneous Rod Subjected to Centric Tension

Victor Rizov
University of Architecture

Abstract: The present theoretical study deals with longitudinal fracture of a structural component representing inhomogeneous rod that is loaded in centric tension at its lower end. The upper end of the rod is clamped. The rod is continuously inhomogeneous in radial direction. Besides, the rod exhibits non-linear elastic mechanical behaviour. The parameters involved in the non-linear constitutive law used when analyzing the longitudinal fracture behaviour are smooth functions of the running radius of the rod cross-section. The basic aim of the paper is to analyze the longitudinal fracture with taking into account the influence of the rod elongation speed. The case when the elongation varies with time at a constant speed is treated in detail. The necessary equations for deriving the parameters of the stressed and strained state of the rod are formulated. The problem for determination of strain energy release rate (SEER) for the longitudinal crack in the rod is solved with considering the effect of the elongation speed.

Keywords: Elongation speed, Centric tension, Rod, Fracture

Introduction

Many components of various engineering constructions, machines and mechanisms in fact represent cylindrical rods subjected to centric tension (Darkov & Shapiro, 1989; Gay et al., 2003; Kissiov, 1997). It is obvious that performing detailed studies of behaviour of such rods under different mechanical loadings is very useful and important (Fanani et al., 2021; Gururaja Udupa et al., 2014; Reyne, 1994; Rizov, 2005). Such studies generate valuable information that can be incorporated in sophisticated theoretical models which are meant for carrying-out accurate analyses of specific aspects of the rod mechanical performance under various loads and influences. One of the factors of great influence on the rod performance is the fracture (Rizov, 2018; Rizov, 2019; Rizov & Altenbach, 2020; Tilbrook et al., 2005).

The purpose of the present theoretical paper is to carry-out an analytical study of longitudinal fracture in a rod loaded in centric tension. The study accounts for the speed of the rod elongation (actually, this is the most important point of the study). The rod under consideration is non-linear elastic. Besides, the rod is made of a material that is continuously inhomogeneous along the radius of the rod cross-section (it should be noted here that continuously inhomogeneous engineering materials have become a very attractive alternative of the homogeneous materials in a variety of applications in different sectors of engineering in the recent decades (Nikbakht et al., 2019; Nagaral et al., 2019; Radhika et al., 2020)). However, this kind of material inhomogeneity (in radial direction) is a premise for development of longitudinal cracks in the form of circular cylindrical surface. There is such a longitudinal crack is the rod under consideration here. The SERR for this crack is obtained with taking into account of the rod elongation speed. It is studied how the SERR varies under the influence of some basic factors.

Theoretical Model

The present study is focussed on the inhomogeneous rod in Fig. 1.

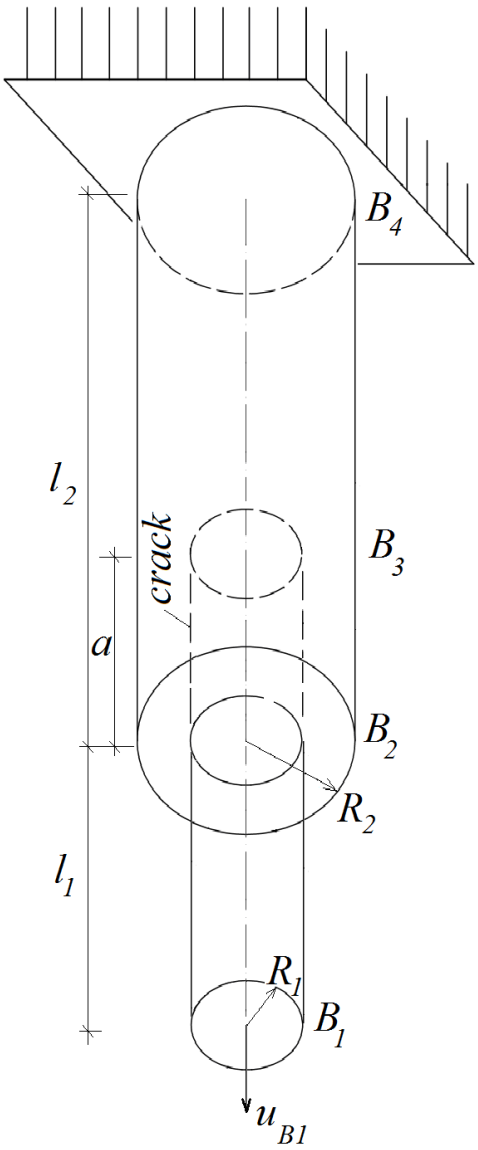

Figure 1. Rod with a longitudinal crack.

This rod is under elongation, u_{B1}, that increases with time, t, at a constant speed, v_{B1}, i.e.

$$u_{B1} = v_{B1} t. \tag{1}$$

The non-linear elastic behaviour of the rod with taking into account the elongation speed is treated by the constitutive law (2) (Lukash, 1997).

$$\sigma = P\left[1-\left(1-\frac{\varepsilon}{Q}\right)^{m}\right]\left(1+D\frac{\varepsilon}{\dot{\varepsilon}_0}\right), \tag{2}$$

where σ, ε and $\dot{\varepsilon}$ are the stress, strain and the speed of the strain, P, Q, D, m and $\dot{\varepsilon}_0$ are material parameters.

The continuous change of P, Q, D and m along the radius, R_1, of the rod cross-section is given by

$$P = P_C + \frac{P_P - P_C}{R_1^b} R^b , \tag{3}$$

$$Q = Q_C + \frac{Q_P - Q_C}{R_1^f} R^f , \tag{4}$$

$$D = D_C + \frac{D_P - D_C}{R_1^g} R^g , \tag{5}$$

$$m = m_C + \frac{m_P - m_C}{R_1^h} R^h , \tag{6}$$

$$0 \le R \le R_1 , \tag{7}$$

where the subscripts, C and P, refer to the centre and the surface of the rod, respectively, b, f, g and h are parameters. Formulas (3) – (6) hold for part, B_1B_2, of the rod (Fig. 1). The same formulas can be applied for presenting the continuous change of P, Q, D and m along rod cross-section radius in part, B_2B_3, of the rod (the only correction that has to be done is to replace R_1 with R_2). It should be specified here that P, Q, D and m change along the rod cross-section radius since the rod is continuously inhomogeneous.

The mechanical response of the rod in Fig. 1 is analyzed via formulas (8) – (13).

The strain, ε, of part, B_1B_3, of the rod is given by

$$\varepsilon = v_\varepsilon t , \tag{8}$$

where v_ε is the speed.

In part, B_3B_4, of the rod, the strain, ε_{B3B4}, has speed, $v_{\varepsilon B3B4}$. Therefore,

$$\varepsilon_{B3B4} = v_{\varepsilon B3B4} t . \tag{9}$$

Equation (10) relates the strains with the rod elongation.

$$\varepsilon(l_1 + a) + \varepsilon_{B3B4}(l_2 - a) = u_{B1} . \tag{10}$$

From Eq. (10), one determines

$$\varepsilon_{B3B4} = \frac{v_{B1} - v_\varepsilon (l_1 + a)}{l_2 - a} , \tag{11}$$

where l_1, l_2 and a are shown in Fig. 1. (a is the crack length). The longitudinal crack represents cylindrical surface with radius, R_1. This crack is located in part, B_3B_4, of the rod (Fig. 1). The speed, v_ε, is obtained from equilibrium equation (12).

$$N_{B1B3} = N_{B3B4} , \tag{12}$$

where N_{B1B3} and N_{B3B4} are the axial forces in rod parts, B_1B_3 and B_3B_4, respectively.

Equation (12) is expressed via the stresses, σ and σ_{B3B4}.

$$\iint_{(A_1)} \sigma dA = \iint_{(A_2)} \sigma_{B3B4} dA, \tag{13}$$

where A_1 and A_2 are the cross-sections in parts, B_1B_3 and B_3B_4, of the rod, σ is determined by (2), σ_{B3B4} is obtained by replacing of ε with ε_{B3B4} in (2). Equation (13) is used to derive v_ε by the MatLab.

The final step in the current study is to derive the SERR, G, for the longitudinal crack in the rod. Formula (14) is used for this purpose.

$$G = \frac{dU^*}{2\pi R_1 da}, \tag{14}$$

where U^* is the complementary strain energy in the rod.

Formula (15) is used for calculating the complementary strain energy.

$$U^* = (l_1 + a)\iint_{(A_1)} u_{01}^* dA + (l_2 - a)\iint_{(A_2)} u_{02}^* dA, \tag{16}$$

where u_{01}^* and u_{02}^* are the complementary strain energy densities. They are derived by formulas (17) and (18), respectively.

$$u_{01}^* = \sigma\varepsilon - \int_0^{\varepsilon} \sigma d\varepsilon\,, \tag{17}$$

$$u_{02}^* = \sigma_{B3B4}\varepsilon_{B3B4} - \int_0^{\varepsilon_{B3B4}} \sigma_{B3B4} d\varepsilon_{B3B4}\,. \tag{18}$$

The SERR found by (14) is confirmed by analyzing the energy balance via formula (19).

$$G = \frac{1}{2\pi R_1}\left(N_{B1B3}\frac{\partial u_{B1}}{\partial a} - \frac{\partial U}{\partial a} \right), \tag{19}$$

where U is the strain energy in the rod (U is found by replacing of the complementary strain energy densities with the strain energy densities in formula (16)).

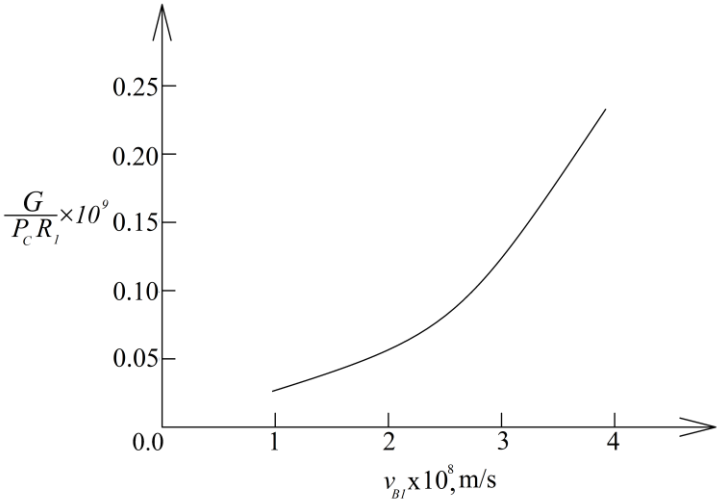

Figure 2. The non-dimensional SERR versus v_{B1}.

Numerical Results

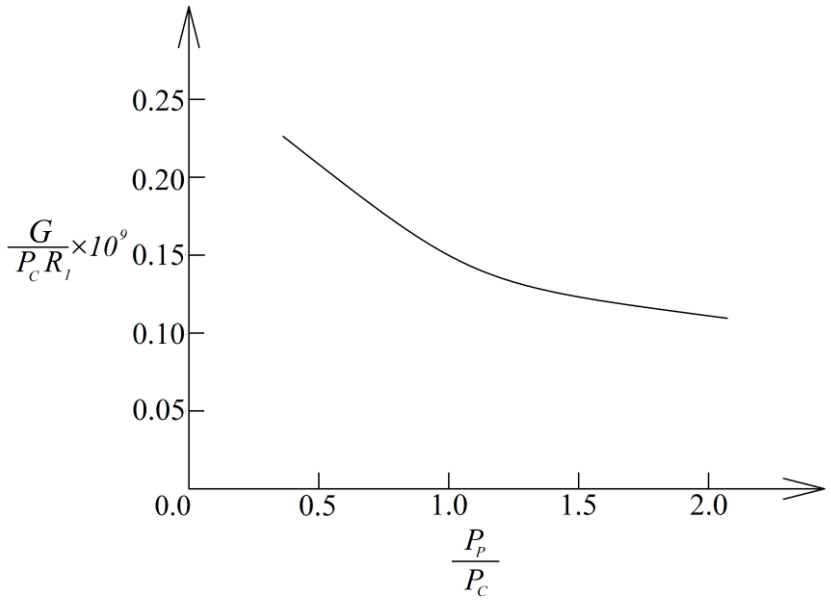

Figure 3. The non-dimensional SERR versus P_P / P_C ratio.

The numerical results determined via the solution of the SERR use to the following data: $a = 0.100$ m, $l_1 = 0.300$ m, $l_2 = 0.400$ m, $R_1 = 0.010$ m, $R_2 = 0.015$ m, $v_{B1} = 4 \times 10^{-8}$ m/s, $b = 0.4$, $f = 0.4$, $g = 0.6$, $h = 0.6$ and $\dot{\varepsilon}_0 = 2 \times 10^{-6}$ 1/s. These results reveal how the SERR for the rod in Fig. 1 varies under the influence of some basic parameters. This variation is shown in four figures. For example, the curve in Fig. 2 illustrates the behaviour of the SERR when the elongation speed, v_{B1}, increases. The quick rise of the SERR in Fig. 2 is due to growth of the rod elongation.

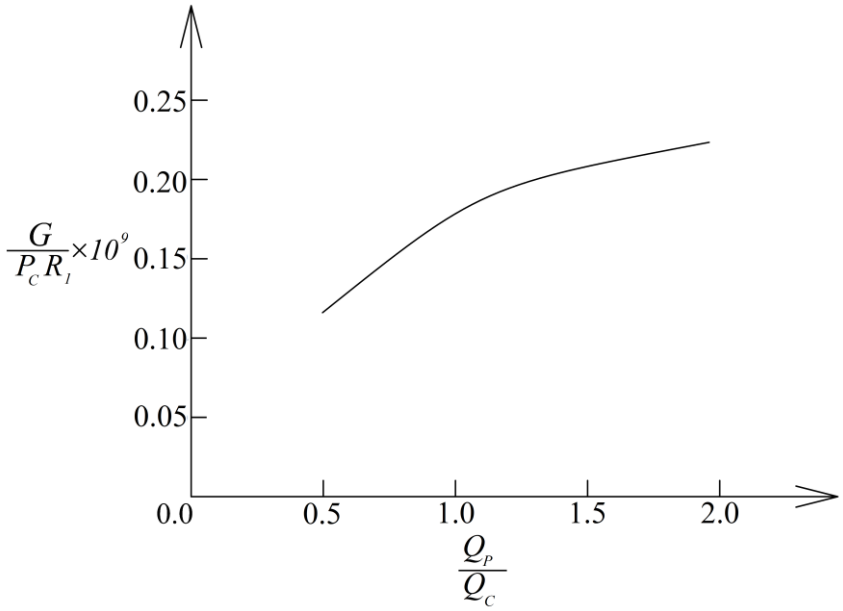

Figure 4. The non-dimensional SERR versus Q_P / Q_C ratio.

The variation of the SERR under the influence of parameters, P, Q and D, is studied too (these parameters are characterized by ratios, P_P / P_C, Q_P / Q_C and D_P / D_C, respectively, since the material of the rod is continuously inhomogeneous).

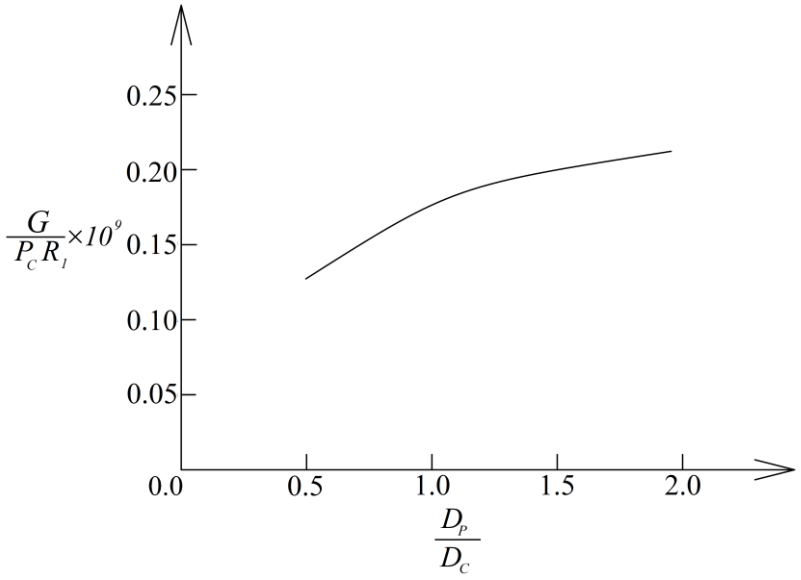

Figure 5. The non-dimensional SERR versus D_P / D_C ratio.

The variation of the SERR when the ratio, P_P / P_C, increases may be observed in Fig. 3. The behaviour of the SERR is characterized by a smooth reduction caused by the increase of P_P / P_C ratio (Fig. 3). One can see how the SERR changes when the ratio, Q_P / Q_C, grows in Fig. 4. The rise of the SERR in Fig. 4 is generated by reduction of the rod stiffness when Q_P / Q_C increases. The behaviour of the SERR when the ratio, D_P / D_C, rises is presented by the curve in Fig. 5. This behaviour is characterized by growth of the SERR.

Conclusion

The longitudinal fracture of an inhomogeneous rod under centric tension is studied theoretically with accounting the influence of the speed of rod elongation. The rod is non-linear elastic. The SERR is determined analytically and analyzed in full. The analysis performed gives important knowledge for the influence of some typical factors like elongation speed and material parameters involved in the non-linear constitutive law. Since the rod is continuously inhomogeneous, the material parameters are presented by the ratios of their values on the surface and the centre of the rod cross-section. The study shows that the SERR quickly increases when parameter, v_{B1}, grows. Increase of the SERR is found also when Q_P / Q_C and D_P / D_C ratios grow. Reduction of the SERR is observed when P_P / P_C ratio grows.

Recommendations

The elongation speed has to be incorporated in longitudinal fracture analyses of continuously inhomogeneous rods subjected to centric tension.

Scientific Ethics Declaration

The author declares that the scientific ethical and legal responsibility of this article published in EPSTEM journal belongs to the author.

Acknowledgements or Notes

This article was presented as an oral presentation at the International Conference on Research in Engineering, Technology and Science (www.icrets.net) held in Tashkent/Uzbekistan on August 22-25, 2024.

References

Darkov, A.,& Shapiro, G. (1989). *Strength of materials*. Vishaia shkola.

Fanani, E. W. A., Surojo, E., Prabowo, A. R., & Akbar, H. I. (2021). Recent progress in hybrid aluminum composite: Manufacturing and application. *Metals*, *11*(12), 1919.

Gay, D., Hoa, S., Tsai, S., (2003). *Composite materials*. CRC Press.

Udupa, G., Rao, S. S., & Gangadharan, K. V. (2014). Functionally graded composite materials: an overview. *Procedia Materials Science*, *5*, 1291-1299.

Kissiov, I. (1997). *Strength of materials*. Technics.

Lukash, P. (1997). *Fundamentals of non-linear structural mechanics*. Science.

Nagaral, M., Nayak, P. H., Srinivas, H. K., & Auradi, V. (2019). Characterization and tensile fractography of nano ZrO2 reinforced copper-zinc alloy composites. *Frattura ed Integrità Strutturale*, *13*(48), 370-376.

Radhika, N., Sasikumar, J., Sylesh, J. L., & Kishore, R. (2020). Dry reciprocating wear and frictional behaviour of B4C reinforced functionally graded and homogenous aluminium matrix composites. *Journal of Materials Research and Technology*, *9*(2), 1578-1592.

Reyne, M. (1994). *Les composites*. Presses Universitaires de France.

Rizov, V. (2018). Non-linear delamination in two-dimensional functionally graded multilayered beam. *International Journal of Structural Integrity*, *9*(5), 646-663.

Rizov, V. (2019). Influence of material inhomogeneity and non-linear mechanical behavior of the material on delamination in multilayered beams. *Frattura ed Integrità Strutturale*, *13*(47), 468-481.

Rizov, V., & Altenbach, H. (2020). Longitudinal fracture analysis of inhomogeneous beams with continuously varying sizes of the cross-section along the beam length. *Frattura ed Integrità Strutturale*, *14*(53), 38-50.

Rizov, V. I. (2005). *Mechanics of composite materials*. BIAP.

Tilbrook, M. T., Moon, R. J., & Hoffman, M. (2005). Crack propagation in graded composites. *Composites Science and Technology*, *65*(2), 201-220.

Author Information

Victor Rizov
Department of Technical Mechanics, University of Architecture, Civil Engineering and Geodesy,1 Chr. Smirnensky blvd. 1046 – Sofia, Bulgaria
Contact e-mail: *V_RIZOV_FHE@UACG.BG*

To cite this article:

Rizov, V. (2024). Longitudinal fracture analysis with taking into account the elongation speed of ınhomogeneous rod subjected to centric tension. *The Eurasia Proceedings of Science, Technology, Engineering & Mathematics (EPSTEM)*, *29*, 69-75.

The Eurasia Proceedings of Science, Technology, Engineering & Mathematics (EPSTEM)
ISSN: 2602-3199

The Eurasia Proceedings of Science, Technology, Engineering & Mathematics (EPSTEM), 2024

Volume 29, Pages 76-80

ICRETS 2024: International Conference on Research in Engineering, Technology and Science

Mechanism of Wear-Out of Sounding Pipes in Ship Ballast Tanks

Yordan Denev
Technical University of Varna

Abstract: During the operation of ships in the global commercial fleet, measurements of the current ballast level in ballast tanks are taken under various cargo and ballast conditions. As a result of repeated measurements, the structure at the bottom of the sounding pipes is damaged. The main cause is the impact of the weight at the end of the measuring instruments on the bottom of the pipe. Once the bottom of the pipe is destroyed, the impact is transferred to the hull or double bottom of the ship. In some cases, if timely measures are not taken to limit this phenomenon, the watertight integrity of the ship's hull is compromised. The article examines a possible mechanism of wear of the measuring pipes during the ship's operation. Repairing this type of wear takes a significant part of the ship's repair time and is accompanied by many associated tasks, the cost of which exceeds that of the repair itself. Approximate estimates of the time required for this type of wear to occur have been made. Measures to reduce this adverse effect are proposed.

Keywords: Ballast tanks, Sounding pipes, Wear, Ship repair

Introduction

Sounding refers to the measured height of a fluid from its surface to the bottom of the tank. Ullage is the empty space in the tank, measured from the top of the tank to the upper surface of the fluid. Ullage is typically measured when the tank's contents are highly viscous or when the tank is filled to its maximum capacity (Chopra, 2021). A sounding pipe is installed within the tank. These pipes extend slightly above the top of the tank, allowing for safe and easy measurement without needing to open any manhole covers. They are equipped with protective caps that can be opened during measurement. The bottom of the sounding pipe is open, enabling the liquid to fill the pipe and match the fluid level within the tank (Chopra, 2021).

The wear and tear of measuring pipes in ship ballast tanks is a common problem. The main cause of this is the repeated impact of the measuring tape on the bottom of the pipe. When the bottom of the pipe is completely damaged, the impacts are transmitted to the double bottom lining and the bottom of the ship. In some cases, this can lead to a breach in the watertight integrity of the ship's hull. The IMO has certain requirements for measuring pipes on ships:

- Sounding pipes diameter hasn't to be less than 32mm;
- Under open end of pipes have to be installed striking plate with adequate thickness;
- Sounding pipes material have to be of steel or other approved from classification societies material;
- Where slotted sounding pipes having closed ends are employed, the closing plugs are to be of substantial construction.

The frequency of sounding on a ship varies depending on the company, its operational policies, and the nature of the activities taking place on board. Ballast water tank and fresh water tanks should be sounded once a day (Chopra, 2021). In addition to the frequent measurement of the ballast and the impacts of the weight at the bottom of the sounding pipes, corrosion further contributes to the formation of defects.

The issue of corrosion in the elements of the ballast system of a passenger ship is presented in (Dariansyah &Arifin, 2023). The authors of the article demonstrate that the degree of corrosion depends on the salinity of the water and the duration of the elements' exposure to it. It has been found that galvanized SS304 pipes have good corrosion resistance to saltwater, making them fully suitable for ballast pipeline systems.

Proper maintenance and operation of the pipes are important for the normal functioning of the ship. Otherwise, it will carry dead weight, which will not generate profit for the shipowner. It is absolutely necessary to protect shell plating with striking plates (Regulations Govering Ballast Management, 2024).

Mechanism for Wear-out Calculations

The procedure for ballast water measure is shown on Fig.1.

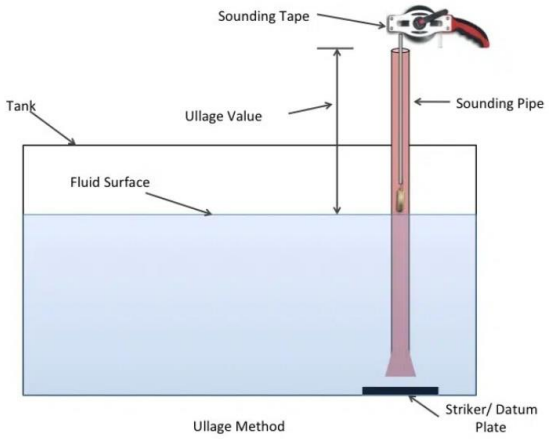

Figure.1.Procedure for ballast water measure (Wankhede, 2021)

When performing operations to determine the amount of ballast, the measuring instrument is freely lowered into the tube. The weight, attached to the end of the measuring tape, falls freely from a certain height with a specific weight onto the bottom of the measuring tube. At the beginning of the impact, i.e., at the moment of touching the bottom of the tube, the falling body has maximum speed and maximum kinetic energy. At the end of the impact, when the speed of the body becomes zero, the deformations in the body and the resulting stresses reach their maximum values. It is assumed that Hooke's law applies to the relationship between stresses and deformations, and that the forces and displacements caused by the impact are also linear, as in the case of static loading. Furthermore, it is assumed that the displacements of the body from the impact at any given moment are similar to the static displacements caused by a statically applied load of the same weight. The static stresses and displacements are determined by equations 1 and 2 (Кисьов, 1979).

$$\Delta_{st} = \frac{Pl}{EF} \tag{1}$$

Where:

- P- weigth force of the plumb bob, N;
- l- length of sounding pipe from main deck to bottom of the tank, sm;
- E- Young modulus, Pa;
- F, area of the pipe bottom, sm^2;
-

$$\sigma_{st} = \pm\frac{P}{F} \tag{2}$$

Where:

- P- weigth force of the plumb bob, N;
- F, area of the pipe bottom, sm^2;

Determining dynamic stresses is reduced to determining dynamic displacement. This is done with the help of the kinetic energy equation and the energy equation. After solving these equations, equation 3 and 4 are obtained(Кисьов,1979).

$$k_d = 1 + \sqrt{1 + \frac{2hEF}{Pl}} \tag{3}$$

Where:

- h- plumb bob falling down height, sm;
-

$$\sigma_d = k_d * \sigma_{st} \tag{4}$$

The wear caused by the impacts of the weight on the bottom of the pipe is determined by equation 5.

$$\Delta t = \frac{Ph}{\sigma_d} \tag{5}$$

According to the rules of the International Maritime Organization, the measurement of ballast is carried out once a day. It is interesting to investigate how many measurements will result in the destruction of the bottom of the pipe. A thickness of 10 mm for the bottom has been assumed. Generally, this can be determined by equation 6.

$$n = \frac{\delta}{\Delta t} * 10 \tag{6}$$

Where:

- δ- thickness of pipe bottom plate, sm;
- Δt- wear- out of thickness, sm;

Results and Discussion

The calculations made using the dependencies presented in the previous paragraph are shown in Fig.2 and Fig. 3. The following characteristics were taken into account in the calculations: the weight of the plummet at the end of the tape measure is P=0.5 kg, Young's modulus, E=206000 Pa., the area of the pipe bottom, F=19.63 sm^2 and the thickness of the bottom, δ=10mm.

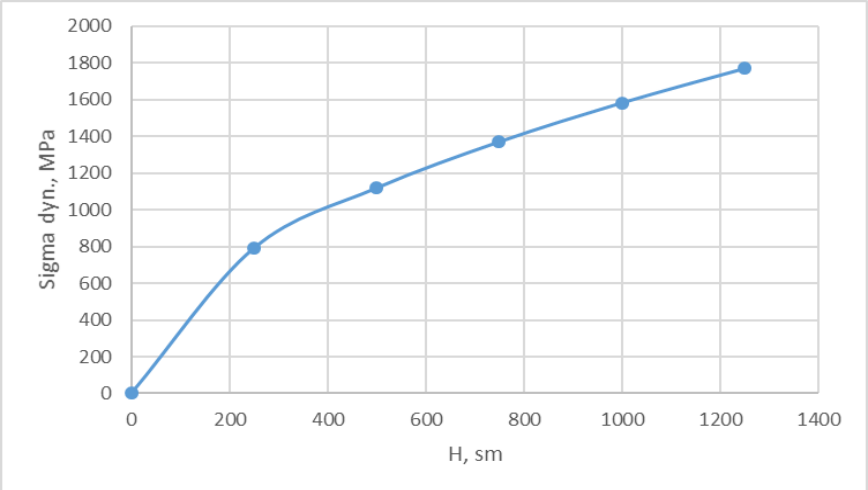

Figure 3. Dynamic stress

The dynamic stresses obtained at the end of the pipe as a result of the impact of the weight are shown in Fig. 4. It is clearly seen from there that the greater the height of the pipe, the greater the resulting stress. The wear of

the pipes is more important because it is directly related to the defects in the areas around the measuring pipes. At different heights of the measuring pipes, the wear varies since the dynamic stress is different. Furthermore, the weight of the mass at the end of the measuring instrument also plays a significant role in the extent of the wear

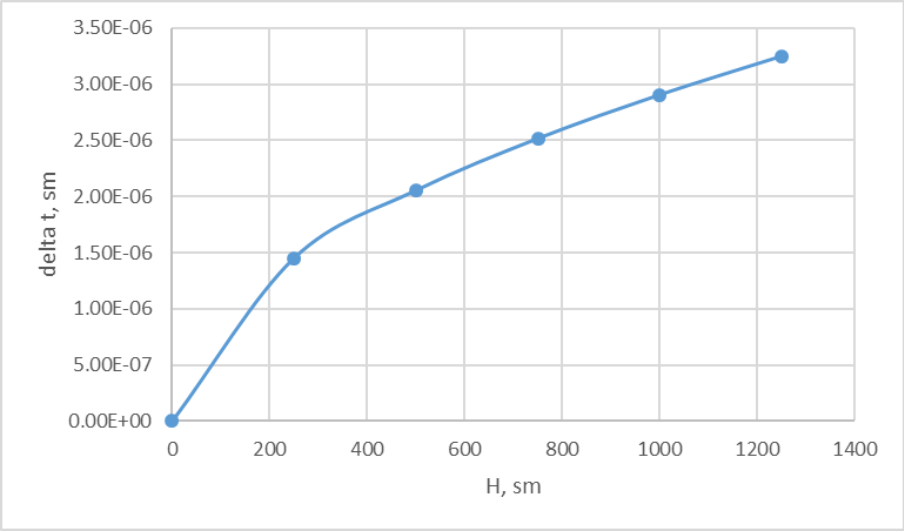

Figure 4. Wear-out the pipe bottom at every sounding time

As a result of the periodic measurement of the ballast level in the ballast tanks of the ship's hull, dynamic stresses and wear cause defects, which are mostly undesirable. The time it takes for the pipe structure to fail and for the damage to extend to the ship's hull is of particular interest. The results of the analysis for the time required for a defect to occur are presented in fig. 5. In the calculations, it is assumed that the ballast is measured once a day. It becomes clear that for longer pipes, the wear time is shorter. For example, for a pipe length of about 13.0 meters, the wear time is approximately half that of a pipe that is 2.0 meters long. The same wear for a pipe with a length of 2.0 meters occurs after approximately 7,000 measurements, whereas for a pipe with a length of about 13.0 meters, it occurs after approximately 3,000 measurements.

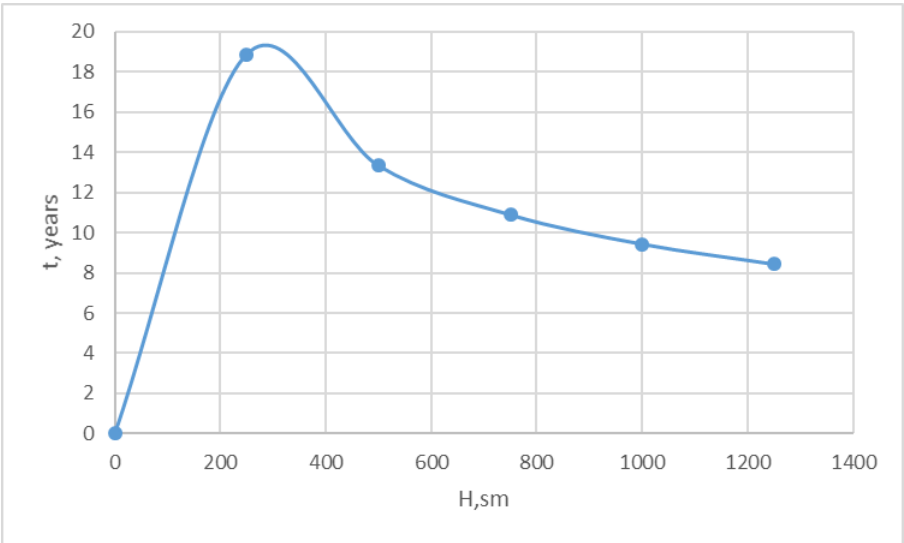

Figure 5. Time for full destruction of pipe bottom

Conclusion

Wear on the measuring pipes of ballast tanks is a common problem in ship repair. Repairing them does not take much time, but it involves a lot of additional work to prepare the tank. The report examines the wear mechanism of the bottoms of the measuring pipes in ballast tanks. Dependencies for determining the wear and the time it takes are presented.

It is assumed that Hooke's law applies to the relationship between stresses and deformations, and that the forces and displacements caused by the impact are also linear, as in the case of static loading. Furthermore, it is assumed that the displacements of the body from the impact at any given moment are similar to the static displacements caused by a statically applied load of the same weight.

With daily measurement of the ballast and a pipe bottom thickness of 10 mm, the average number of measurements leading to its destruction is about 4500. The wear time also greatly depends on the height of the pipe and the thickness of the bottom. The analysis takes into account the most commonly encountered thicknesses and heights of pipes.

Scientific Ethics Declaration

The author declares that the scientific ethical and legal responsibility of this article published in EPSTEM journal belongs to the author.

Acknowledgements or Notes

* This article was presented as oral presentation at the International Conference on Research in Engineering, Technology and Science (www.icrets.net) held in Thaskent/Uzbekistan on August 22-25, 2024.

References

Chopra, K. (2021). Understanding sounding, ullage and frequency of sounding, *Marineinsight*, Retrieved from https://www.marineinsight.com/guidelines/understanding-sounding-ullage-and-frequency-of-sounding/

Dariansyah, M. R., & Arifin, M. D. (2023). Corrosion Rate Estimation of Passenger Ships Ballast System Pipes. *International Journal of Marine Engineering Innovation and Research*, *8*(3).

Кисьов, И. Д. (1979). Наръчник на инженера. *Техника, София*.

Regulations Govering Ballast Management (2024). https://www.hydracaptainsclub.gr/regulations-governing-ballast-management/

Wankhede, A. (2021). How and why to take manual sounding on ship, *Marineinsight.* Retrieved from https://www.marineinsight.com/guidelines/how-and-why-to-take-manual-sounding-on-a-ship/

Author Information

Yordan Denev
Technical University of Varna
Varna, Studentska 1 str. Bulgaria
Contact e-mail: *y.denev@tu-varna.bg*

To cite this article:

Denev, Y. (2024). Mechanism of wear- out of sounding pipes in ship ballast tanks. *The Eurasia Proceedings of Science, Technology, Engineering & Mathematics (EPSTEM), 29*, 76-80.

The Eurasia Proceedings of Science, Technology, Engineering & Mathematics (EPSTEM)
ISSN: 2602-3199

The Eurasia Proceedings of Science, Technology, Engineering & Mathematics (EPSTEM), 2024

Volume 29, Pages 81-91

ICRETS 2024: International Conference on Research in Engineering, Technology and Science

Optimizing Type Well Construction: A New Approach for Scaling in Multiply Fractured Horizontal Wells

Rami Harkouss
Beirut Arab University

Himanshu Jha
University Texas A&M University

W. John Lee
University Texas A&M University

Abstract: This paper outlines a straightforward method to standardize production histories from analog wells to common reference conditions, including average permeability in the stimulated reservoir volume, fracture half-length, stage spacing, and lateral length. The scaling technique addresses variations among analog wells in a region, crucial for constructing representative type wells and reducing uncertainty in statistical analyses. Grounded in well-established analytical solutions for constant bottom hole pressure production and transient linear flow in multiply fractured horizontal wells, the study introduces the "A-root k" analysis for estimating average fracture length and a depth of investigation equation for average permeability in the stimulated reservoir volume. Scaling involves expressing transient linear flow variables in dimensionless terms, enabling the normalization of rate-time profiles to selected reference conditions. Averaged scaled profiles yield mean, P90, P50, and P10 type wells, which can be further rescaled to design conditions for undrilled wells. The workflow, demonstrated with field examples, facilitates type well construction at desired probability levels from analog wells grouped into a few bins based on scaled production profile similarities. This approach proves effective, typically requiring one or two bins for a given resource play area.

Keywords: Scaling technique, Multiply fractured horizontal wells, Type well construction, Transient linear flow

Introduction

In the petroleum industry, type wells or type-well production profiles (TWPs) play a crucial role in predicting production from undrilled or minimally documented wells in a given region. Traditionally, these type wells are constructed by averaging production rates from existing wells, a process that involves normalizing to a common starting time, often the observed peak rate in every well. However, challenges arise when considering wells with diverse characteristics such as varying lateral lengths, completion designs, geological features, well vintage, and operating companies. The common practice of normalizing for perforated lateral length and creating different "type well areas" may not entirely capture the complexity of these variables, potentially leading to numerous bins with relatively few wells in each.

To overcome this challenge, this paper proposes a novel scaling methodology to reduce the number of bins by scaling wells to common reference conditions. This approach results in a more statistically representative number of wells in each bin, addressing the issue of statistical uncertainty associated with traditional binning methods. The scaling technique presented offers a pragmatic solution for constructing reliable type wells in the context of multiply fractured horizontal wells.

Similarities in Production Profiles

Lemoine and Lee (2019a, 2019b) conducted a comprehensive analysis revealing notable similarities in production profiles among wells within the same resource play, except for early times dominated by fracture clean-up and choked flow, and late times when boundary-dominated flow (BDF) and operational challenges such as liquid loading may occur. Their findings suggested that individual well profiles within a reservoir could be accurately transformed into a shared "reference" production profile through horizontal and vertical shifts, resulting in an overlapping trend.

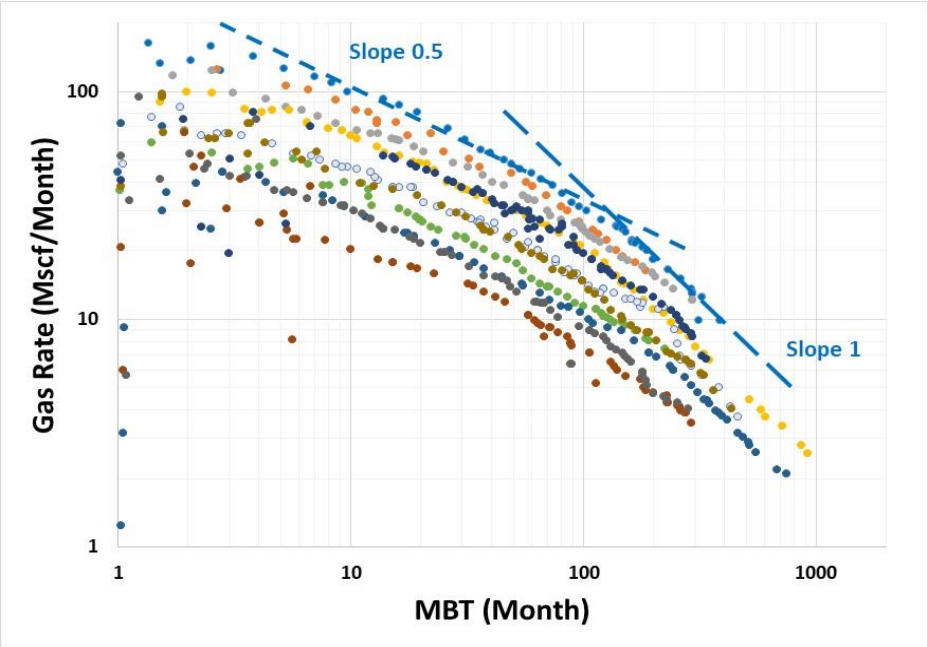

Figure 1. Log-log plots of unscaled rate vs. material-balance time plots for individual wells in the fayetteville shale.

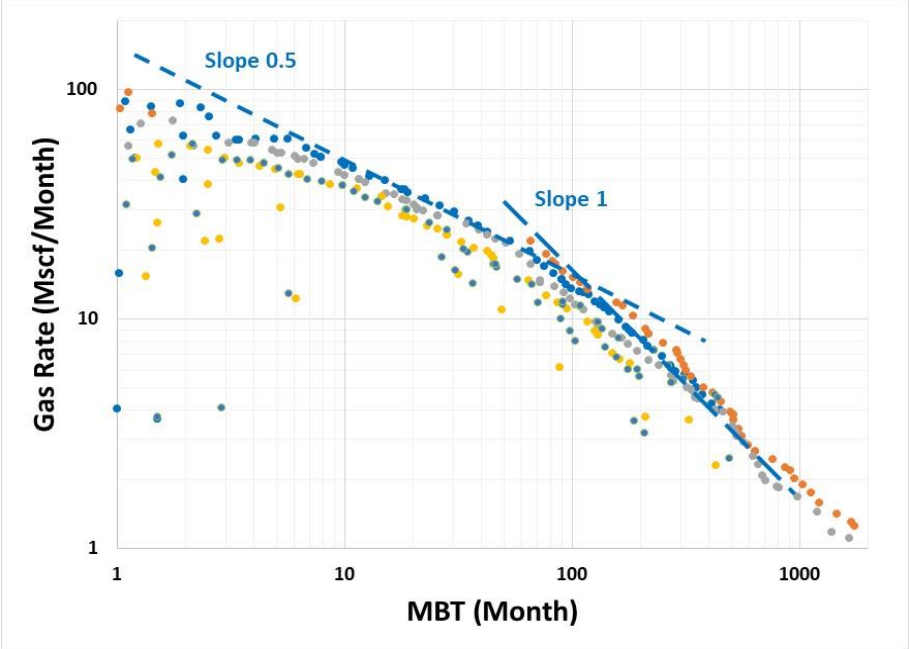

Figure 2. Log-log rate vs. MBT plots for all production profiles for Fayetteville shale wells to a common reference profile.

Figs. 1 and 2 illustrate the outcomes of this shifting for gas wells in the Fayetteville shale, showing a consistent trend during transient, transition, and boundary-dominated flow regimes. Notably, the shared slope observed during transient flow suggests a common Arps b-factor, inversely proportional to the slope on a log-log (rate-

time) plot, as highlighted by Lee (2021) and confirmed by the half-slope during the transient flow regime for all the wells (b-factor is around 2). The unit slope line during BDF, while lacking information on the b-factor, serves as a distinctive identifier for this flow regime.

This pattern was consistently observed by Lemoine and Lee across gas wells in the Fayetteville, Barnett, and Montney shales, as well as oil wells in the Niobrara, Eagle Ford shale, and Bakken tight reservoirs. Despite potential complications from operational upsets, like liquid loading in gas wells that might shows deceiving straight lines (Hassan & Mattar, 2017), the unit slope line at late times remains crucial, anchoring the position of each shifted production profile onto the selected reference profile. These findings underscore a fundamental similarity in the behavior of wells across diverse resource plays, offering valuable insights for production forecasting and reservoir characterization.

The configurations of these production profiles show resemblance to the well-known Wattenbarger type curve (Fig. 3, adapted from (Wattenbarger et al., 1998)). This type curve, derived from an analytical solution for a well with hydraulic fractures in a closed drainage area, exhibits transient linear flow (slope is 0.5), a transition region, and finally boundary-dominated flow (slope is 1 on a q vs. MBT plot). The observed match prompts the consideration of employing the Wattenbarger type curve to align rate-time data from wells, presenting a potential means to estimate the average effective permeability (k) within the stimulated reservoir volume (SRV) of a horizontally fractured well.

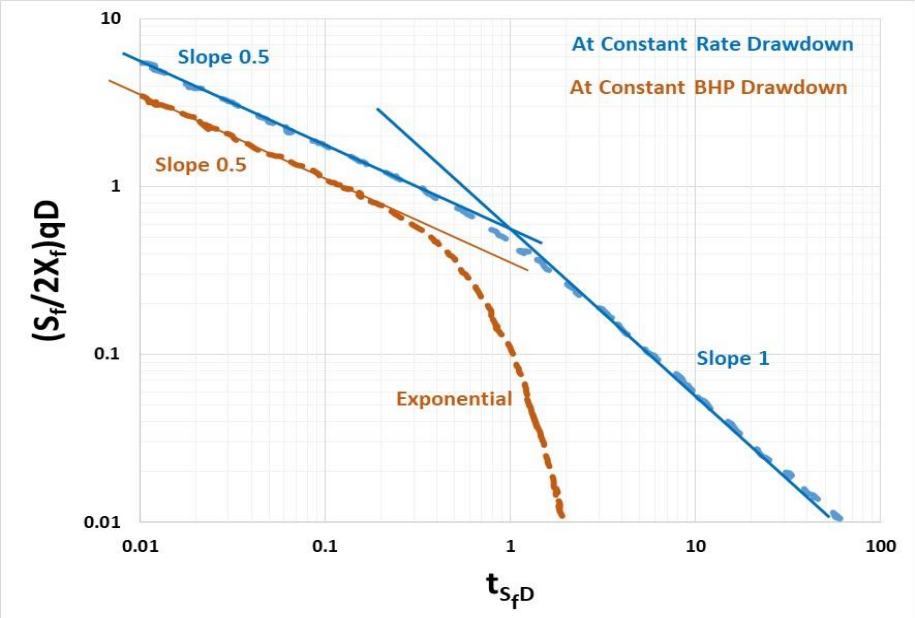

Figure 3. Constant rate and constant bottom hole pressure solutions.

Furthermore, this approach could facilitate the estimation of an average fracture half-length, denoted as xf (Clarkson, 2021), by determining the average area in fractures in a well open to flow. Matching the production history of each well within a reservoir allows individual estimates of k and xf. These well properties then enable the scaling of production profiles to a standardized set of reference property values. This process holds promise as a simplified alternative to type-curve matching, involving the alignment of rate vs. MBT to the constant-rate Wattenbarger type curve (Liang et al., 2011). While type-curve matching is often perceived as difficult and challenging, this proposed alternative offers a simplified solution.

Simplified Scaling Method

An efficient process enables the adjustment of rate-time profiles for potential analog wells, essential for constructing type wells under a uniform set of reference conditions. This method facilitates scaling to realistic values of lateral length, fracture spacing, and other distinct parameters within our analog dataset. Additionally, it allows the estimation of approximate values for effective average permeability within a stimulated reservoir volume (SRV) and average effective fracture length, followed by the scaling of all wells to suitable reference values for these factors.

The core of this simplified scaling approach lies in detecting the time marking the conclusion of the transient flow regime for a well. This temporal estimate can be derived either from the termination point of a straight line on a log-log rate-time plot or, potentially with greater accuracy, from a 1/q vs. √t plot. While these techniques are well-established for permeability estimation (e.g., (Clarkson, 2021)), a less commonly recognized aspect is the potential to estimate fracture length from the rate at the end of transient flow. This involves comparing the observed rate to the dimensionless rate in Wattenbarger's analytical solution (Wattenbarger et al., 1998), which provides both time and rate at the end of transient flow.

Wattenbarger, et al. (1998) contributed solutions to flow equations for constant bottom-hole pressure and constant-rate production. In the more pertinent constant BHP production scenario, they determined that the end of transient linear flow (line with a half slope) occurs at a dimensionless time of 0.25, with the corresponding dimensionless rate group being 0.694 (as illustrated in Fig. 2 from their paper, with large green dots indicating the end of the transient flow regime). This outcome aligns with the well-established depth of investigation equation, applicable irrespective of the transient flow regime's character (e.g., the transient b-factor, btr) within a production profile. According to Wattenbarger's solution, the dimensionless time at the end of transient linear flow is

$$t_{SfD,elf} = 0.25 = \frac{0.02532\,k\,t_{elf}}{\emptyset\mu c_t S_f^2} \quad \text{so} \quad k = \frac{9.87\emptyset\mu c_t S_f^2}{t_{elf}} \qquad \ldots\ldots\ldots\ldots\ldots\ldots\ldots\ldots (1)$$

and dimensionless rate group at the end of linear flow is

$$\frac{S_f}{2x_f} q_{D,elf} = 0.694 = \frac{70.6\, q_{elf} B\mu S_f^2}{x_f k h L_w \Delta p} \quad \text{hence} \quad x_f = \frac{101.7\, q_{elf} B\mu S_f^2}{k h L_w \Delta p} \qquad \ldots\ldots\ldots\ldots\ldots (2)$$

Determining the rate and time at the end of transient linear flow from available rate-time data can be achieved through various methods, such as analyzing q vs. t on a log-log plot or 1/q vs. √t, with a focus on identifying a departure from an earlier linear trajectory. The Cartesian coordinate plot (1/q vs. √t) is likely more discerning, given the compression effect of logarithmic scales on numerical values.

Figs. 4 and 5 (after (Clarkson, 2021)) employ equivalent yet more intricate plots of $\frac{\Delta m(p)}{q}$ $vs.t$ or $\sqrt{t}$ plots. Here, m(p) represents the gas pseudo-pressure, often used to refine the accuracy of gas well analyses (we commonly depict Δp = pi – pwf for oil wells). The main objective is to identify the end of the initial linear trend on these plots. The following examples demonstrate potential applications of Eqs. (1) and (2). These figures illustrate graphical methods for determining the end of transient linear flow (telf). In Fig.4, a log-log plot of Δm(p)/q vs. t shows that transient linear flow concludes around t = 1,300 days. Similarly in Fig. 5, a cartesian coordinate plot of Δm(p)/q vs. √t indicates that transient linear flow terminates at √t = 36 (days)0.5, equivalent to t = 1,300 days.

Industrial Applications

In this section, we provide example calculations to illustrate the implementation of these principles to a set of wells within a reservoir of interest.

Example Well in the DJ Basin of the United States

Fig. 6 presents a plot of observed rate versus time data for a volatile oil well (well 1) in the DJ Basin of the United States. This well undergoes transient linear flow, as evidenced by a 0.5 slope line, suggesting a transient b factor of approximately 2 (in blue). Subsequently, the well transitions to Boundary-Dominated Flow (BDF), indicated by a unit-slope line at late times on the rate-MBT plot (in red), deviating from the half-slope line around 650 days. Emphasizing the need for caution, the unit slope line in late-time analysis can be misleading. Wells experiencing operational issues (liquid loading in gas wells for example) often exhibit data points that form "false" straight lines at late times. Nevertheless, it is evident that determining the unit slope in this context remains feasible as proved in this example (unit slope – line in green).

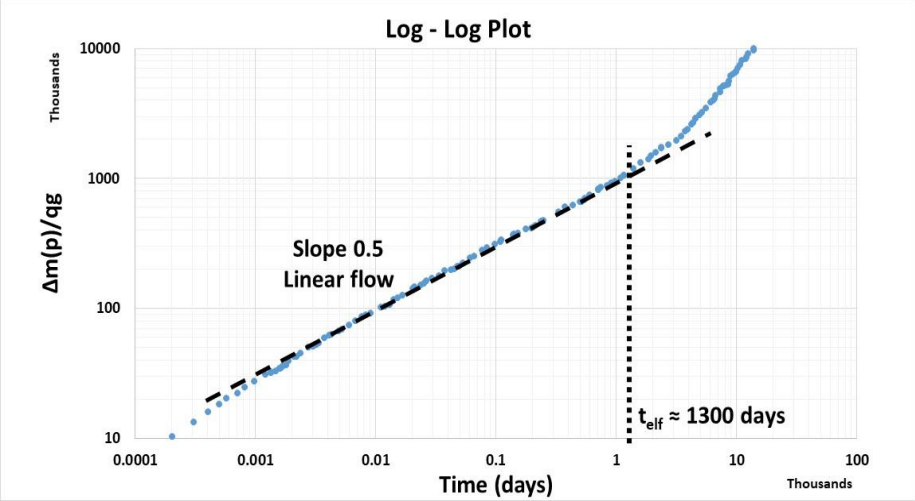

Figure 4. log-log plot of $\frac{\Delta m(p)}{q}\ vs.\ t$

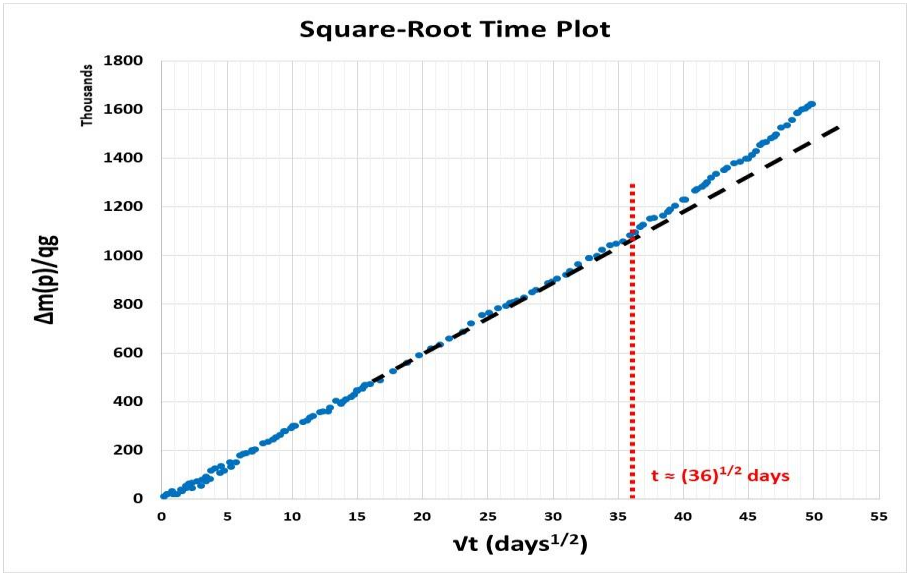

Figure 5. Cartesian plot of $\frac{\Delta m(p)}{q}\ vs\sqrt{t}.$

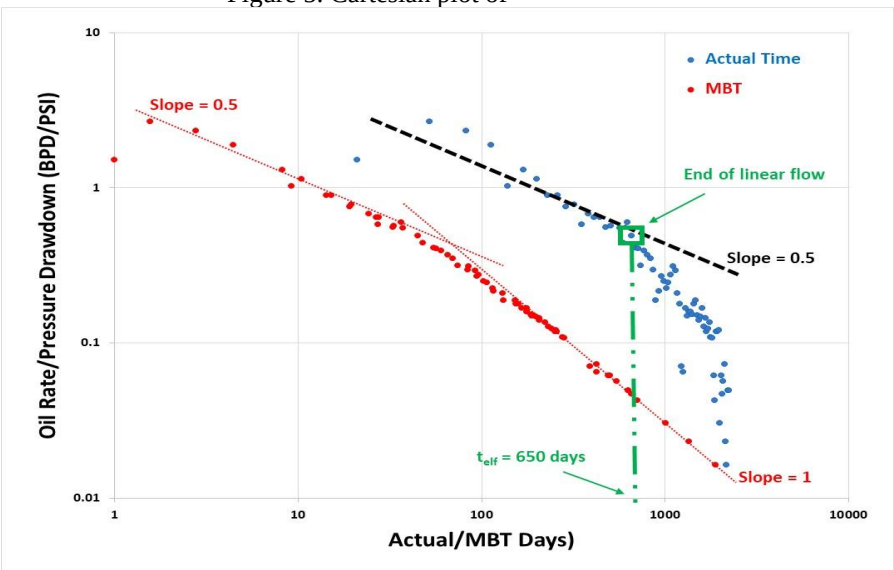

Figure 6. Log-log rate-time diagnostic plot of well 1

Application

To estimate k (effective average permeability) and xf (average effective fracture length), we utilize the plot of q vs. t where the time at the end of transient linear flow (telf) is determined to be 650 days, and the correspondent rate (qelf) is 1470 STB/D (Fig. 6). The known and estimated properties and characteristics are summarized in Table 1.

Table 1. Reservoir and completion properties for example well 1

Parameter	Units	Value
μ	cp	0.12
B	RB/STB	1.83
φ	fraction	0.085
pi	psia	3,312
h	ft	50
ct	psia-1	5.0e-04
Lw	ft	4,200
Sf	ft	125
pwf	psia	315

Then,

$$k = \frac{9.87 \emptyset \mu c_t S_f^2}{t_{elf}} = \frac{9.87 * 0.085 * 0.12 * 5.0e-04 * 125^2}{650} = 0.00121\ md$$

$$x_f = \frac{101.7 q_{elf} B \mu S_f^2}{k h L_w \Delta p} = \frac{101.7 * 1470 * 1.83 * 0.12 * 125^2}{1.21e-03 * 50 * 4200 * 2997} = 673.5\ ft$$

Step 1: We determined that k=0.00121 md and xf =673.5 ft. The objective is to scale rates and times in the production profile to reference conditions of k=0.0002 md and xf=450 ft. Specifically, if the observed rate qobs=1470 STB/D at a time tobs of 650 days, the scaled rate qsc and scaled time tsc for this single data point on the rate-time schedule can be calculated from the relationships

$$t_{elf} = \frac{9.87 \emptyset \mu c_t S_f^2}{k} \text{ and } q_{elf} = \frac{x_f k h L_w \Delta p}{196.1 B \mu S_f^2}$$

Subsequently, by calculating ratios, the scaled time to the end of transient linear flow (tsc) and the scaled rate at the end of linear flow (qsc) can be determined, considering fixed values for all other parameters.

$$t_{sc} = t_{obs} \frac{k_{obs}}{k_{sc}} = 650 * \frac{0.00121}{0.0005} = 1{,}573\ days$$

and $$q_{sc} = q_{obs} \frac{k_{sc} x_{f,sc}}{k_{obs} x_{f,obs}} = 1470 * \frac{0.0002 * 5500}{0.0004 * 5262} = 541\ STB/D$$

Consequently, a rate of 1470 STB/D at a time of 650 days scales to a rate of 541 STB/D at a time of 1573 days when employing the specified reference values. This scaling approach can be uniformly applied to each point on the rate-time profile, generating a scaled rate-time profile that spans the entire production history.

Step 2: In order to scale all rates and times from a production profile to the reference conditions, the corresponding scaled values (qsc, tsc) for the observed point (1470 STB/D, 650 days) can be computed. Table 2 provides both observed and reference values. The target is to scale the observed rate and time to a set of reference values that accurately represent those anticipated for future wells.

By calculating ratios of equations for rates and the corresponding times at reference conditions to observed conditions, our working equations are then formulated as follows:

Table 2. Observed and reference values.

Parameter	Units	Observed Value	Reference Value
μ	cp	0.12	0.1
B	RB/STB	1.83	2
φ	fraction	0.085	0.075
pi	psia	3,312	3,800
h	ft	50	200
ct	psia-1	5.0e-04	5.0e-05
Lw	ft	4,200	5,000
Sf	ft	125	110
pwf	psia	315	400
k	md	0.00121	0.0002
xf	ft	673.5	450

$$q_{ref} = q_{obs} \frac{k_{ref} h_{ref} x_{f,ref} L_{w,ref} \Delta p_{ref} B_{obs} \mu_{obs} S_{f,obs}^2}{k_{obs} h_{obs} x_{f,obs} L_{w,obs} \Delta p_{obs} B_{ref} \mu_{ref} S_{f,ref}^2} =$$

$$1470 * \frac{0.0002 * 200 * 450 * 5000 * (3800 - 400) * 1.83 * 0.12 * 125^2}{0.00121 * 50 * 673.5 * 4200 * (3312 - 315) * 2 * 0.1 * 110^2} = 1243\ STB/D$$

and

$$t_{ref} = t_{obs} \frac{\emptyset_{ref} \mu_{ref} c_{t,ref} k_{obs} S_{f,ref}^2}{\emptyset_{obs} \mu_{obs} c_{t,obs} k_{ref} S_{f,obs}^2} = 650 * \frac{0.075 * 0.1 * 5e-05 * 0.00121 * 110^2}{0.085 * 0.12 * 5e-04 * 0.0002 * 125^2} = 224\ days$$

Therefore, a rate of 1470 STB/D at a time of 650 days scales to 1243 STB/D at a time of 224 days based on the provided reference values. This scaling methodology is consistently applicable to each point on the rate-time profile, facilitating the creation of a scaled rate-time profile. Step 3: Table 3 presents selected observed rates and times for the well 1 as well as the results of the scaling of all these (q, t) pairs to conform to the reference conditions specified in Table 2.

Table 3. Scaled rates and times from observed to reference values

Observed Time (days)	Observed Rate (BPD)	Scaled Time (days)	Scaled Rate (BPD)
228	2686	78	2272
381	2031	131	1718
503	1704	173	1441
654	1472	225	1245
769	1179	265	997
1012	674	348	570
1347	478	464	404
1683	354	580	299
2014	184	694	156
2131	69	734	58

Fig. 7 exhibits both the observed (rate vs. time) profile and the scaled (rate vs. time) profile. Scaling each well in the analog well dataset to these identical reference values would enable averaging, serving as the foundation for constructing a type well representative of this specific area within the reservoir of interest. It showcases the observed rate-time profile within the reservoir of interest, alongside the scaled rate-time profile derived from the scaling process.

Table 4 summarizes the properties of three additional volatile oil wells in the DJ Basin, sharing characteristics with the reference well previously discussed. Employing the same methodology, Fig. 8 presents observed and scaled values for these wells presents, offering a comprehensive overview of the four wells investigated in this study.

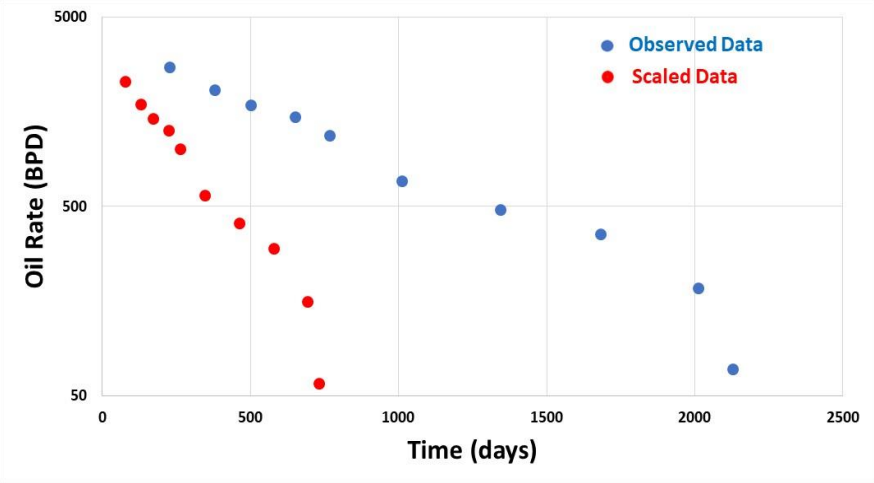

Figure 7. Selected observed versus scaled data of well 1

Table 4. Observed and reference values of the different other three wells from DJ Basin.

		Well 2	Well 3	Well 4
Parameter	Units	Value	Value	Value
μ	cp	0.14	0.13	0.13
B	RB/STB	1.8	1.75	1.6
φ	fraction	0.087	0.07	0.075
pi	psia	3500	3400	3350
h	ft	50	50	65
ct	psia-1	0.00045	0.00065	0.00045
Lw	ft	4100	4000	4300
Sf	ft	120	130	125
pwf	psia	325	320	315
telf	days	500	690	540
qelf	BPD	2500	1200	1900
K	md	0.00156	0.00143	0.00125
xf	ft	824	533	590

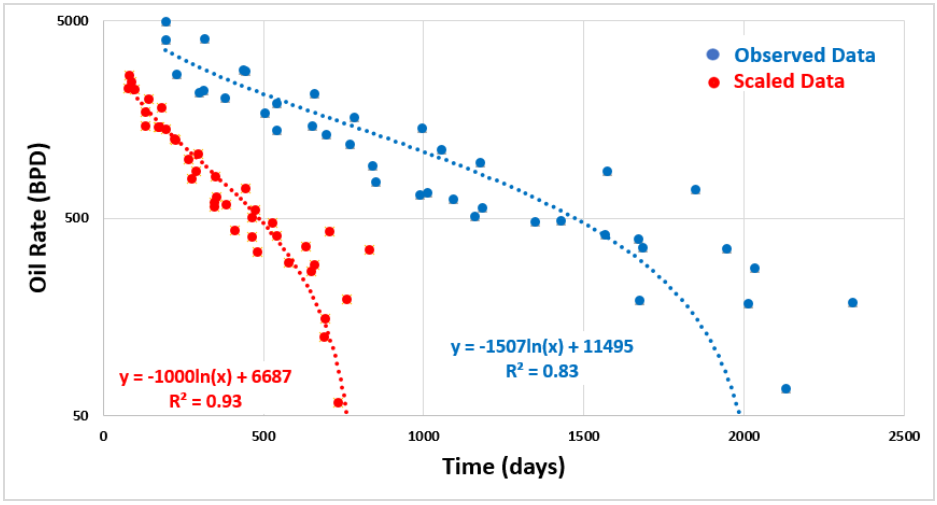

Figure 8. Selected observed and scaled data from the four DJ Basin wells.

First, Fig. 8 attests to the method's repeatability for various wells with diverse properties. Notably, the telf of well 2 is 38% less than that of well 3, while the qelf of well 2 is twice that of well 3. Second, the R-squared value of the logarithmic trendline has significantly improved from 0.83 to 0.93 for observed and scaled data, respectively. This enhancement reflects greater stability in results through the normalization methodology. The application of this procedure to a large dataset encompassing values from numerous wells thus yields more precise and accurate results. This precision is pivotal for refining the forecasting of type well production profiles in subsequent stages.

Implementation of Workflow for Constructing Type Wells

The applied workflow involved the systematic application to a set of wells within the reservoir area of interest, where average effective permeability and average fracture half-length were computed for each well. Subsequently, the wells were scaled to uniform reference values of properties, and the outcomes are depicted in Fig. 8. The wells were categorized into two distinct bins, characterized by differing values of the transient b-factor (b_{tr}). These scaled rates can be employed in the construction of a type well. This type well is designed to be indicative of the shared reference conditions to which all wells are scaled, contingent on a specific value of btr. In cases where future conditions are anticipated to deviate, such as due to alterations in completion design and lateral length, the type well can be recalibrated to the expected conditions in an upcoming drilling initiative, following the mentioned computational procedures.

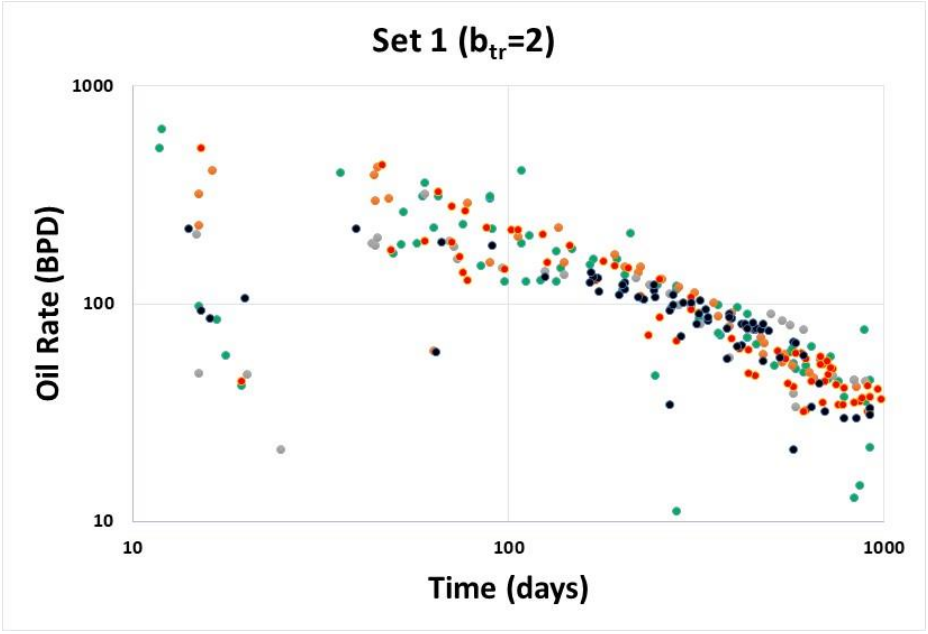

Figure 9a. Production profiles for wells with b_{tr}=2

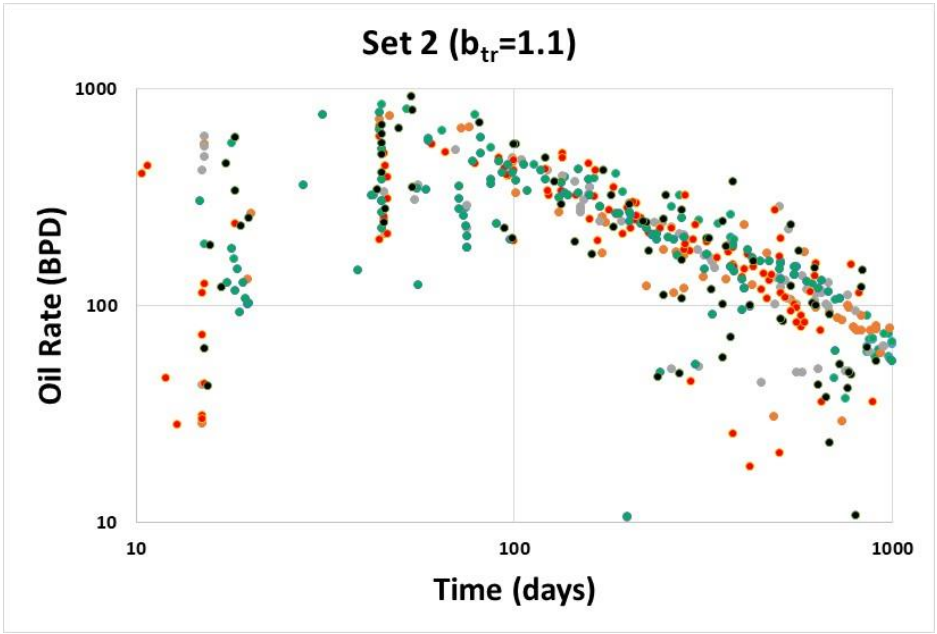

Figure 9b. Production profiles for wells of b_{tr}=1.1

Fig. 9 shows production profiles for wells sharing comparable transient region values of b scaled to uniform reference values of reservoir and completion properties, following Sukumar and Lee (2021)'s approach. The primary objective is to create a type well from a group of scaled well production profiles. However, a challenge

arises as the original data points were spaced one month apart, corresponding to monthly production data. With the scaling process altering the time intervals between points, linear interpolation becomes necessary. For each well, we will employ linear interpolation between a point just before the beginning of a month and a point immediately after the start of a month. The averaging process will then be conducted based on these interpolated points to derive the desired average profile.

Results and Discussion

The process for constructing type wells involves scaling rate-time profiles to common reference conditions before averaging, aiming to group analog wells more effectively to reduce uncertainty in defining the "average." Despite deviations in the Arps b-factor from Wattenbarger's assumed value of 2, the workflow remains valid, with the key lying in determining the time at the end of the transient flow regime using the depth of investigation equation, independent of the Arps b-factor. Additionally, the rate at the end of transient flow remains unaffected by Wattenbarger's assumption of ideal linear flow followed by boundary-dominated flow, ensuring the robustness of the methodology for type well construction.

One challenge in the workflow is accurately determining the end of transient flow, especially in noisy datasets. While machine-learning filters can aid, their use is not discussed here (Jha et al., 2021; Jha et al., 2022). Alternatively, fitting data to type curves like Eleiott et al. (2019) or Chen and Teufel's (2000) modified Fetkovich (1996) curve can extract reservoir properties. The common assumption of b = 0 in boundary-dominated flow lacks theoretical backing and varies between 0.3 and 0.5 in practice, underlining the need for accurate determination and appropriate type curves for forecasting.

Permeability necessitates cautious interpretation, reflecting an average across all fracture stages, influenced by fracture treatment-induced microfractures and potentially activated natural fractures, enhancing permeability within the stimulated reservoir volume. This estimate should exceed values from laboratory measurements on matrix samples. Similarly, fracture half-length requires careful consideration, representing an average over all stages and assuming uniform propped fracture lengths.

Concerning wells in an analog well bin that have not transitioned beyond the transient flow regime, constructing type wells for them poses challenges. The unknown time for the end of transient flow complicates type curve matching. A tentative solution involves forecasting production to the economic limit, utilizing the forecasted time at which transient flow concludes for type curve matching. However, this approach relies on assumptions within the forecasting technique, potentially introducing uncertainties related to the forecasted end of transient flow. For wells in an analog well bin that have not surpassed the transient flow regime, constructing type wells poses challenges due to the unknown time for its conclusion, complicating type curve matching. A tentative solution involves forecasting production to the economic limit, relying on forecasted transient flow end times for type curve matching, albeit introducing uncertainties due to forecasting assumptions.

Conclusion

This study offers valuable insights for ultra-tight reservoirs with multi-fractured horizontal wells (MFHW). Analysts can estimate effective average permeability and fracture half-length for each well by analyzing production histories that exhibit distinct transient and boundary-dominated flow phases, based on the observed data at the end of transient flow regimes. Using these values for wells reaching boundary-dominated flow (BDF), analysts can scale production histories to common reference values, aligning with Wattenbarger's linear diffusivity equation solution and type curve. The proposed workflow involves grouping wells with similar production profiles into analog wells, facilitating type well construction. By averaging scaled rates within the bin, a representative type-well production profile is established, enhancing statistical validity by maximizing the number of analog wells in a bin and improving parameters like mean and standard deviation.

Scientific Ethics Declaration

The authors declare that the scientific ethical and legal responsibility of this article published in EPSTEM journal belongs to the authors.

Acknowledgements or Notes

* This article was presented as an oral/poster presentation at the International Conference on Research in Engineering, Technology and Science (www.icrets.net) held in Thaskent/Uzbekistan on August 22-25, 2024.

References

Chen, H. Y., & Teufel, L. W. (2000, October). A new rate-time type curve for analysis of tight-gas linear and radial flows. In *SPE Annual Technical Conference and Exhibition?* (pp. SPE-63094). SPE.

Clarkson, C. R. (2021). *Unconventional reservoir rate-transient analysis*.Gulf Professional Publishing

Eleiott, A., Lee, W. J., & Moridis, N. (2019, July). Modified Fetkovich type curve enhances type well construction for horizontal wells with multiple fractures. In *SPE/AAPG/SEG Unconventional Resources Technology Conference* (p. D023S029R006). URTEC.

Fetkovich, M. J., Fetkovich, E. J., & Fetkovich, M. D. (1996). Useful concepts for decline-curve forecasting, reserve estimation, and analysis. *SPE Reservoir Engineering*, *11*(01), 13-22.

Hasan, S. S., & Mattar, L. (2017, February). Does unit-slope beyond maximum producing time always represent BDF in RTA?. In *SPE Canada Unconventional Resources Conference.*.

Jha, H. S., Sheikh, H. M. U. D., & Lee, W. J. (2021, December). Outlier detection techniques help us identify and remove outliers in production data to improve production forecasting. In *Asia Pacific Unconventional Resources Technology Conference, Virtual, 16–18 November 2021* (pp. 1694-1706). Unconventional Resources Technology Conference (URTeC).

Jha, H. S., Khanal, A., & Lee, J. (2022, March). Statistical and machine-learning methods automate multi-segment Arps decline model workflow to forecast production in unconventional reservoirs. In *SPE Canadian Energy Technology Conference*..

Lee, J. (2021, December). Establishing the basis for multi-segment Arps decline models. In *Unconventional Resources Technology Conference, 26–28 July 2021* (pp. 1-18). Unconventional Resources Technology Conference (URTeC).

Lemoine, R., & Lee, J. (2019, April). Analytical scaling enhances production analysis of multi-fractured horizontal wells. In *SPE Western Regional Meeting* (p. D041S013R004). SPE.

Lemoine, R., & Lee, J. (2019, April). Integrated workflow reduces uncertainty in type well construction and production forecasting of multi-fractured horizontal wells. In *SPE Western Regional Meeting*

Liang, P., Mattar, L., & Moghadam, S. (2011, November). Analyzing variable rate/pressure data in transient linear flow in unconventional gas reservoirs. In *SPE Canada Unconventional Resources Conference.*

Sukumar, S., & Lee, W. J. (2021, December). Type wells–a physics-blind statistical myth? Our RTA driven construction methodology proves otherwise!. In *Unconventional Resources Technology Conference, 26–28 July 2021* (pp. 1375-1394). Unconventional Resources Technology Conference (URTeC).

Wattenbarger, R. A., El-Banbi, A. H., Villegas, M. E., & Maggard, J. B. (1998, April). Production analysis of linear flow into fractured tight gas wells. In *SPE Rocky Mountain Petroleum Technology Conference/Low-Permeability Reservoirs Symposium*.

Author Information

Rami Harkouss
Beirut Arab University
Debbieh campus, Lebanon
Contact e-mail: *r.harkous@bau.edu.lb*

Himanshu Jha
Texas A&M University
College Station, Texas, USA

W. John Lee
Texas A&M University
College Station, Texas, USA

To cite this article:

Harkouss, R., Jha, H., & Lee, W. J. (2024). Optimizing type well construction: A new approach for scaling in multiply fractured horizontal wells. *The Eurasia Proceedings of Science, Technology, Engineering & Mathematics (EPSTEM), 29,* 81-91.

The Eurasia Proceedings of Science, Technology, Engineering & Mathematics (EPSTEM)
ISSN: 2602-3199

The Eurasia Proceedings of Science, Technology, Engineering & Mathematics (EPSTEM), 2024

Volume 29, Pages 92-105

ICRETS 2024: International Conference on Research in Engineering, Technology and Science

Synthesis and Evaluation of an Innovative Biochar Nanocomposite Adsorbent Derived from *Cycas Revoluta* Seeds, with Potential Applications in the Removal of Cationic Dyes

Elif Gezginci
Konya Technical University

Erol Pehlivan
Konya Technical University

Abstract: In this study, novel and functional adsorbents were synthesized by using *Cycas revoluta* seed (CS) biomass. The biomass was subjected to a slow pyrolysis process at a final temperature of 500°C with a heating rate of 10°C/min to synthesize *Cycas revoluta* seed biochar (CSB). After the thermochemical conversion of biomass into biochar, the nanocomposite structure (ZrO_2NP@CSB) was synthesized by adding 5% zirconium oxide (ZrO_2) nanoparticles into biochar to increase the adsorption capacity. The synthesized adsorbents (CS, CSB, and ZrO_2NP@CSB) were characterized by XRD, FTIR, SEM, and EDX. The adsorption efficiency of these three adsorbents was investigated to remove Malachite Green (MG) and Methylene Blue (MB) dye from an aqueous solution. According to the results obtained from the adsorption experiments of the nanocomposite structure, solution pH had a significant effect on the process and the highest adsorption efficiencies were achieved at pH 9. The optimum adsorbent dose was 0.5 g/L. The process reached an equilibrium after 45 minutes and 90 minutes for MG and MB, respectively. The relevant data were in good agreement with the pseudo-second-order kinetic model. The maximum adsorbent capacities were 129.87 and 117.93 mg/g for MG and MB, respectively. The adsorption mechanism follows a monolayer Langmuir isotherm model. Experiments were carried out at different temperatures (25, 35, 45°C) to determine the effect of temperature on adsorption, and dye removal efficiency slightly increased with temperature. When repeated batch adsorption experiments were compared for raw biomass, biochar, and biochar nanocomposite adsorbents, it was observed that the raw adsorbent had a lower adsorption capacity than the biochar adsorbent. It was found that the biochar nanocomposite had the highest adsorption capacity among these three adsorbents. The findings suggest that ZrO_2NP@CSB composite is a promising, cost-effective, and functional material for water treatment and can be employed as an alternative adsorbent for removing dyes.

Keywords: Adsorption, Biochar, Nanocomposite, Water treatment

Introduction

With the increasing population and industrial growth, various industrial products are simplifying human life while simultaneously causing significant environmental destruction. Industrial processes and domestic usage result in numerous pollutants being introduced into the air, water, and soil. Water, covering three-quarters of the Earth's surface, is crucial for the ecosystem. The contamination of water with pollutants from various sources during the environmental cycle leads to significant pollution, adversely affecting human health and natural life (Rathi et al., 2021; Erkmen et al., 2019).

One type of industrial pollution is dye pollution, particularly resulting from textile industry activities. With the advancement of the textile and dye industries, numerous new synthetic dyes are being synthesized. The variety

of dyes and the large volumes of dyed water discharged during dyeing processes make this type of wastewater a prime candidate for treatment. Dye-contaminated waters prevent sunlight from reaching aquatic environments, leading to ecological damage (Yaseen & Scholz, 2019; Erkuş et al., 2018). Due to the toxic and stable nature of components like azo, phthalocyanine, indigo, sulfur, and nitro in dye molecules, they pose significant environmental and health risks even at low concentrations. These risks vary with the type and dose of the dye, potentially causing allergic reactions, skin irritation, carcinogenic, and mutagenic effects (Pilatin & Kunduhoğlu, 2013; Robinson et al., 2001).

Treatment of such polluted water is necessary to reduce dye contamination and improve the quality of contaminated water. However, the resistant and diverse structures of dye molecules make standard treatment processes inadequate for effective dye removal (Dindar, 2019). Hence, advanced treatment methods such as adsorption, membrane filtration, ion exchange, and reverse osmosis are necessary for removing toxic dyes from aqueous environments.

Among advanced treatment methods, adsorption is a popular method due to its adjustable process conditions and high removal efficiency. Because of the high cost of adsorbents and the volume of wastewater that needs to be treated, researchers have recently been looking for affordable adsorbents. Biomass materials offer a potential adsorbent for the elimination of dye pollution since they are affordable, easily obtainable, and harmless to the environment (Parlayıcı & Pehlivan, 2021).

Biomass and Biochar as Adsorbent

Biomass refers to all biological materials derived from living or recently dead plant wastes that are not fossilized. For instance, plant seeds, roots, leaves, bark, agricultural waste, and animal waste are biomass. Utilizing waste biomass as an adsorbent is important not only for its low cost but also for recycling waste materials. Numerous studies in literature report the use of different biomass materials as adsorbents (Gayathiri et al., 2022; Ranjusha et al., 2010; Shelke et al., 2022). These studies indicate that the adsorption efficiency of biomass is often insufficient for the removal of toxic dyes. To enhance adsorption efficiency, additional processes such as surface modification or chemical activation are often applied to biomass (İmdat, 2014; Erdoğan, 2017;) (Tasmakıran, 2010). By synthesizing biochar from biomass using various methods, surface properties can be altered to make it a more suitable material for adsorption.

Biochar, meaning bio-based carbonaceous materials, has gained research interest over the past decade for its potential as an adsorbent in wastewater treatment. Due to the porous surfaces of biochars, they have a large surface area, which is advantageous for surface-based processes like adsorption. Studies have shown successful treatment of wastewater containing toxic dyes using biochar adsorbents (Baig et al., 2014; Parlayıcı & Pehlivan, 2023). The high adsorption capacity of biochar in these studies indicates effective treatment (Bayram et al., 2022; Bayram et al., 2023).

Enhancing Adsorption Efficiency with Biochar Nanocomposites

Although biochar-based adsorbents show potential for removing dye molecules from wastewater, it is not always possible to completely remove dyes due to the saturation of surface pores and the depletion of functional groups over time. One approach to solving this problem is to create composites by adding nanoparticles to charcoal adsorbents. This approach is expected to enhance the surface area of biochar and provide a synergistic effect from the composite components, leading to improved dye removal performance compared to each component alone (Rajput et al., 2022). While biomass and biochar adsorbents offer potential solutions for dye removal from wastewater, there is a need to further enhance their efficiency. The synthesis of biochar nanocomposites presents a promising strategy for achieving higher adsorption capacities and more effective wastewater treatment.

In this study, one of the dyes removed from the aqueous environment is MB. MB, a cationic dye with the chemical formula $C_{16}H_{18}ClN_3S{\cdot}3H_2O$, is commonly used for dyeing silk, cotton, and wood. Exposure to MB at a dosage of 2 mg/kg body weight can cause minor skin/eye irritation and stomach cramps, while exposure to doses greater than 47.0 mg/kg can lead to abnormal blood pressure, cardiac arrhythmias, coronary vasoconstriction, chromosomal damage, and lung toxicity (Altıntaş Yıldırım et al., 2022). The other dye removed is MG. The chemical formula of MG is $C_{23}H_{25}N_2Cl$. It is also known as benzaldehyde green because it is derived from benzaldehyde and dimethylaniline. It is used in the industry for dyeing silk, wool, leather, and

cotton (Sun et al., 2008). A study investigating the toxic effects of MG on mice found that exposure to a dose of 13.75 mg/kg body weight for 60 days resulted in increased oxidative stress, changes in brain chemicals, and altered behavior of cellular complexes. This dye causes severe eye irritation and corneal damage in humans (Biswas et al., 2021).

Cycas revoluta, commonly known as the sago palm, was selected as the raw material for adsorbent synthesis. Our objective is to recycle a natural resource by using this abundant biomass. Biochar adsorbent was produced from biomass using the slow pyrolysis method. Zirconium oxide nanoparticles were incorporated into the biochar adsorbents, resulting in a new and functional adsorbent. The biomass, biochar, and biochar nanocomposites were characterized using various methods, and their adsorption behaviors were investigated through batch adsorption experiments. Parameters affecting adsorption, such as pH, adsorbent dosage, contact time, initial dye concentration, and temperature, were studied. Based on the experimental results, optimal conditions for each adsorbent were determined. The adsorption process was examined for its conformity to Langmuir, Freundlich, and Temkin isotherm models. Kinetic and thermodynamic calculations were performed to elucidate the mechanism of the adsorption process.

Method

Materials

All chemicals were of analytical grade, and they were used as received with no further purifications. *Cycas revoluta* seeds (CS) were collected from Antalya/Manavgat region of Türkiye. MB and MG dyes were purchased from Acros Organics (New Jersey, USA). Zirconium oxide nanopowder (ZrO_2, ≤100 nm) was purchased from Sigma Aldrich (Darmstadt, Germany). Hydrogen chloride (HCl, 37%), sodium hydroxide (NaOH, 97%), and absolute ethanol (C_2H_5OH) were purchased from Merck. Deionized water (DI) from a Millipore water purification system was used in the experiments.

Production of Adsorbents

CS biomass was washed several times with DI to remove surface impurities and then dried in an oven at 70°C for 24 hours. The biomass was ground into a powder by using a laboratory-scale grinder for the adsorption experiments. The slow pyrolysis method was used for the thermochemical conversion of biomass into biochar. For this process, 20 grams of CS biomass was placed into a pyrolysis reactor made of steel material, which has high thermal resistance. The reactor was then placed in a muffin furnace and subjected to pyrolysis at a 500°C final temperature, 10°C/min heating rate, and 30 minutes of residence time at the final temperature.

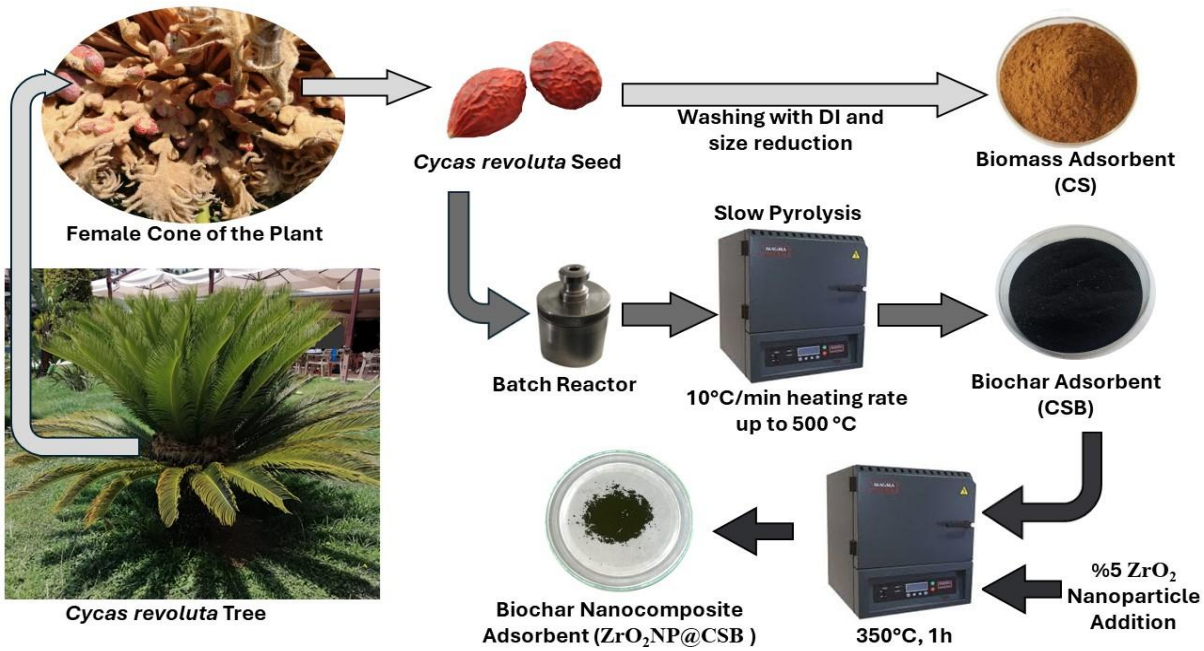

Figure 1. Schematic representation of the production steps of the CS, CSB, and ZrO_2NP@CSB

The pyrolysis product was cooled to room temperature at the same rate. At the end of the pyrolysis process, *Cycas revoluta* seed biochar (CSB) was ground into a powder with an agate mortar. Black biochar powder was obtained and stored in a sterile bottle for the analyses. The biochar nanocomposite (ZrO_2NP@CSB) was fabricated by mixing the conventionally purchased ZrO_2 nanoparticles and CSB in a %5 ratio by mass, crushed together, and treated at 350°C for 1 hour. The synthesis steps of the biomass (CS), biochar (CSB), and biochar nanocomposite (ZrO_2NP@CSB) adsorbents are illustrated in Figure 1.

Characterization Study

A ZEISS Gemini SEM 500 model scanning electron microscope (SEM) was used in order to investigate the surface morphology of the adsorbents. Energy dispersed X-ray (EDX) analyses were performed with the same device in Necmettin Erbakan University BITAM Laboratory. Before the SEM and EDX analyses, solid samples were coated with Iridium to a thickness of 4.31 nm. The presence of functional groups on the surface of the biomass, biochar, and biochar nanocomposite adsorbents was clarified by using a Thermo Scientific-Nicolet IS20 model Fourier transform infrared (FT-IR) spectrometer. FT-IR spectra were recorded within the range of 400-4000 cm^{-1}. The phase analysis of the obtained samples was investigated by the EUROPE GNR model X-ray diffraction (XRD) system with Cu-K α radiation at the $10° \leq 2\theta \leq 80°$ boundary values. The XRD spectra were recorded with an energy step size of 0.1 eV. In order to calculate the initial and final concentration of the dye solutions, the absorption spectra of the samples were obtained using a Cary 5000 UV-Vis spectrophotometer.

Batch Adsorption Experiments

The removal of MB and MG dyes was performed using synthesized adsorbents. In the batch adsorption experiments, parameters affecting adsorption such as pH, adsorbent dosage, contact time, initial concentration of dye, and temperature were investigated and optimized. The adsorption percentage was calculated by using Equation (1) and the adsorption potential per unit mass of the adsorbent, q_e (mg g^{-1}) was calculated by Equation (2).

$$\% \text{ Adsorption} = \frac{C_i - C_f}{C_i} \times 100 \quad \textbf{(1)}$$

$$q_e = \frac{(C_i - C_f)}{m} \times V \quad \textbf{(2)}$$

Where, C_i and C_f are the initial and final concentrations of the dye, respectively. V (L) is the volume of the solution and m (g) being the amount of the adsorbent. Adsorption equilibrium curves were plotted considering Langmuir, Freundlich, and Temkin isotherms. The linear Langmuir, Freundlich, and Temkin isotherm equations are given below as Equations (3), (4), and (5), respectively.

$$\frac{C_f}{q_e} = \frac{C_f}{q_m} + \frac{1}{q_m K_L} \quad \textbf{(3)}$$

$$log\, q_e = log\, K_f + \frac{1}{n} log\, C_e \quad \textbf{(4)}$$

$$q_e = B_T ln K_T + B_T ln C_e \quad \textbf{(5)}$$

Where q_m (mg g^{-1}) is the maximum adsorption capacity, K_L is the Langmuir constant, K_f is the relative sorption capacity, n is the Freundlich constant, K_T and B_T are the Temkin constants (Temkin, 1940). The calculations for adsorption kinetics were examined by comparing pseudo-first and pseudo-second-order kinetic models by using Equations (6) and (7).

$$ln(q_e - q_t) = ln\, q_e - \mathrm{t}\, k_1 \quad \textbf{(6)}$$

$$\frac{t}{q_t} = \left(\frac{1}{k_2 q_e^2}\right) + \left(\frac{1}{q_e}\right) t \quad \textbf{(7)}$$

Where q_t is the adsorption capacity at a certain time, q_e is the adsorption capacity at equilibrium, k_1 and k_2 are the pseudo-first and pseudo-second order rate constants, respectively. Thermodynamic analyses of the adsorption process were performed based on experiments which carried out at different temperatures.

Results and Discussion

Characterization Results

Figure 2. shows the FT-IR spectrum of the adsorbents. The spectrum of the CS biomass has a board band around 3400 cm^{-1}, representing the stretching of the O-H bond (Różyło et al., 2022). The intense double peaks observed at 2900 cm^{-1} and 2850 cm^{-1} are due to asymmetric and symmetric stretches from the aliphatic CH_2 group. The peak observed at 1741 cm^{-1} is a specific peak resulting from C=O stretching. This peak may originate from aldehydes, ketones, free esters, or carboxylic acids found in the pectin fibers expected in the biomass structure. The presence of a strong and narrow C=O peak with the OH and CH stretches confirms the presence of a carboxyl group in the biomass structure (Bounaas et al., 2021). The intense peak observed at 1630-1640 cm^{-1} indicates the presence of C=C and it is thought to be derived from lignin found in the palisade cells of the biomass seed (Volli et al., 2021). The peaks around 1440 cm^{-1} are due to the OH bending, and those around 1369 cm^{-1} are due to $-CH_2$ and $-CH_3$ bending. The intense peak observed at 1020-1000 cm^{-1} is the stretching vibration peak of the C-O bond.

Some of the peaks observed at the FT-IR spectrum of the biomass are absent in the biochar and biochar nanocomposite structure. As a result of a successful pyrolysis process, it is clear that large hydrocarbon groups have left the structure and that the structure has undergone carbonization. The peaks observed in the spectrum of the biochar structure (CSB) in the range of 600 to 900 cm^{-1} after pyrolysis are due to the vibrations of C-H bonds in the aromatic and heteroaromatic compounds (Hossain et al., 2011). The moderately intense peaks observed around 1580-1600 cm^{-1} in the spectrum of CSB correspond to the aromatic C=C ring in the graphite structure (Chen et al, 2008). The peak at 1395 cm^{-1} observed in the CSB sample is due to the stretching of the -C=O bond in the -COOH functional group on the biochar surface (Hassaan et al., 2023). The peaks at 489, 579, and 747 cm^{-1} observed in the spectrum of the biochar nanocomposite sample but not in the spectrum of the CSB, confirm the successful incorporation of ZrO_2 nanoparticles into the structure (Li et al., 2023).

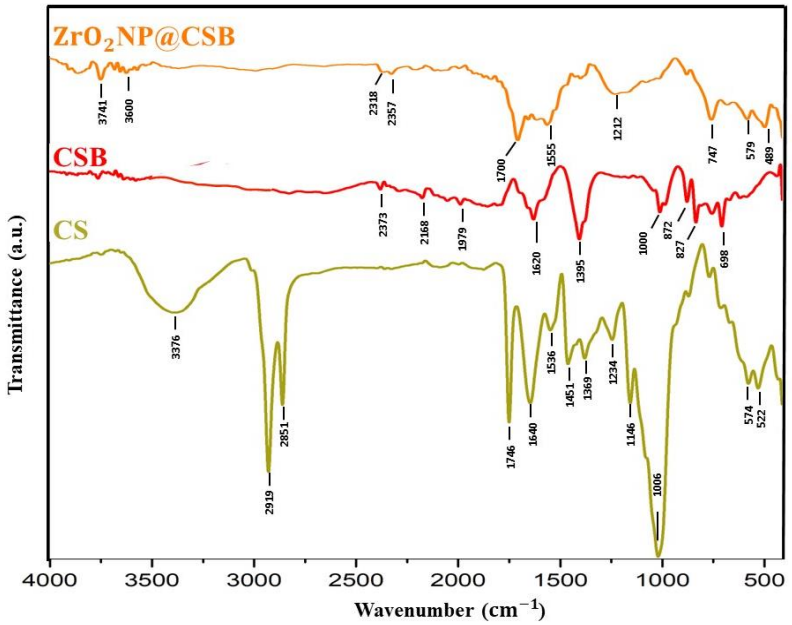

Figure 2. The FT-IR spectra of the adsorbents.

XRD analyses were conducted to reveal the structural differences between biomass, biochar, and biochar nanocomposite samples. Figure 3 shows the diffraction patterns of CS, CSB, and ZrO_2NP@CSB. The diffraction pattern of the CS biomass is characterized by a major peak at 20-23°, which is attributed to the crystalline cellulose present in the biomass (Nanda et al., 2013). In the biochar sample, a typical peak for

amorphous silica was observed at 2θ = 23° (Zeidabadi et al., 2018). The sharp peak at 30° is associated with the crystalline phase. In the XRD pattern of the biochar nanocomposite sample ZrO_2NP@CSB, the observation of the characteristic peaks for ZrO_2 at 2θ = 30.5 and 50.2 indicates that ZrO_2 nanoparticles have been successfully incorporated into the biochar matrix (Alagarsamy et al., 2022).

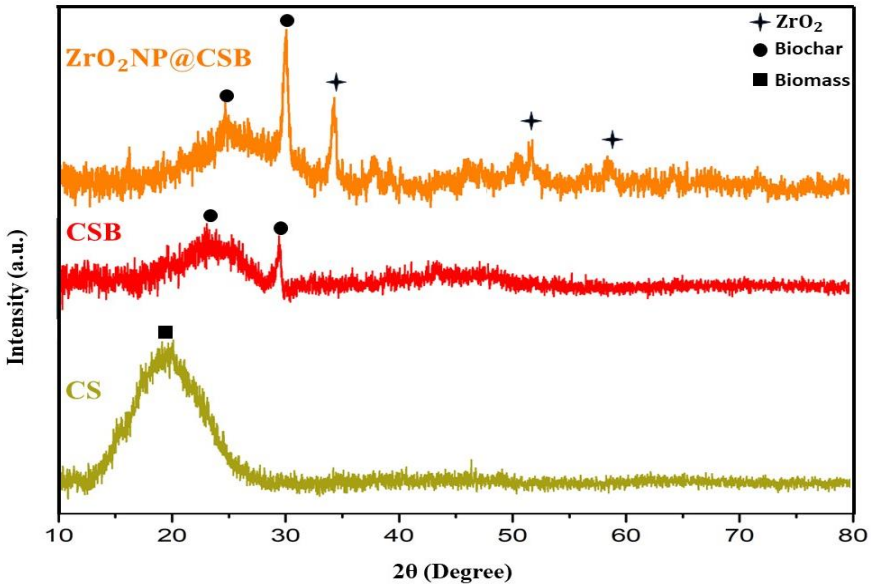

Figure 3. The XRD patterns of the adsorbents.

Figure 4 shows the SEM images of the synthesized adsorbents. According to the images, biomass sample CS has a non-pores structure. Pyrolysis is a process aimed at increasing the specific surface area by enhancing surface porosity. An increased surface area will enhance the effectiveness of surface-based processes such as adsorption, leading to more successful removal of dyes. A porous structure has been observed in the CSB. The biochar surface has circular pores of varying diameters, with sizes ranging between 0.5- 1.0 µm. The SEM image of the biochar nanocomposite ZrO_2NP@CSB reveals that the nanoparticles have been successfully incorporated into the biochar matrix. It has been found that the imbedded nanoparticles are sometimes located at the surface and inside the pores. When SEM results are evaluated regarding surface porosity, the biochar is expected to exhibit better adsorption properties than the raw biomass. The ZrO_2NP@CSB, which has metal oxide nanoparticles incorporated into the biochar matrix, is expected to demonstrate the highest adsorption capacity due to both its surface porosity and the effect of the nanoparticles on the surface area.

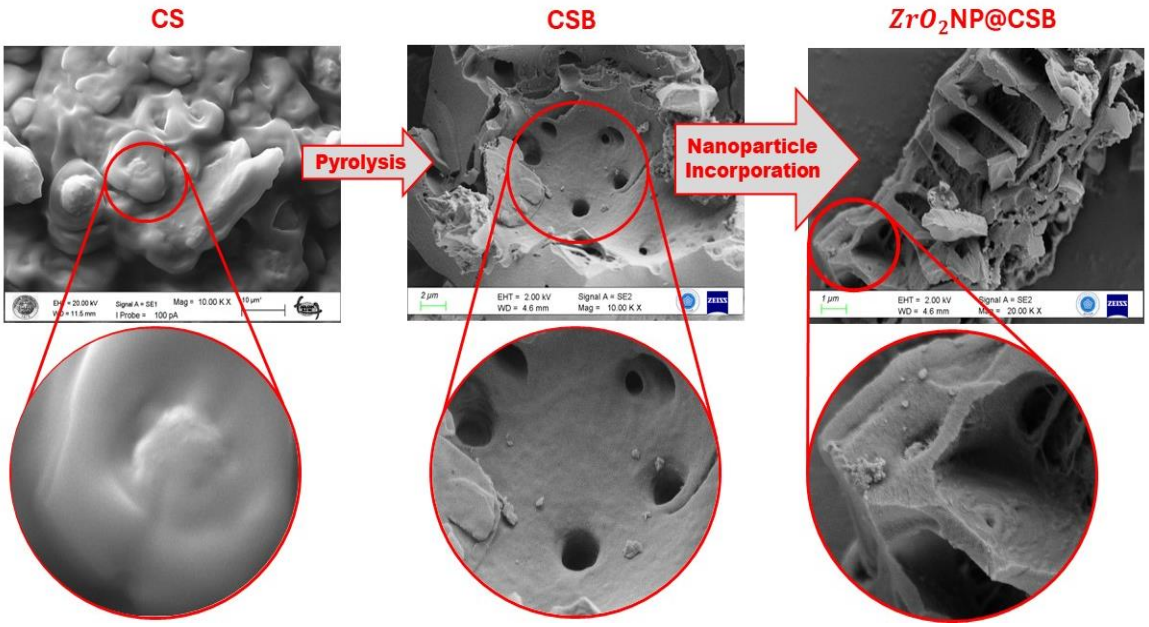

Figure 4. The SEM images of the adsorbents.

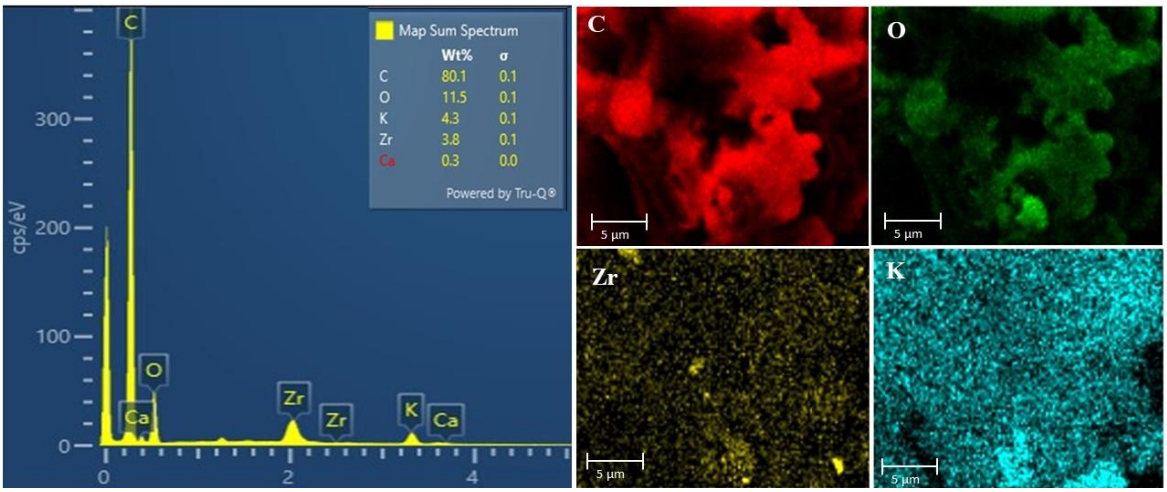

Figure 5. The EDX results of the ZrO_2NP@CSB and elemental mapping.

Using EDX analysis, the forms, distribution, and characteristics of the nanoparticles in the biochar nanocomposite sample were ascertained. The results are given in Figure 5. During elemental mapping, trace elements were not included in the mapping. The metal type of the nanoparticles added to the biochar is consistent with the EDX results. According to the results, the element with the highest proportion is carbon, which is an expected result for the biochar matrix. The element with the next highest proportion is oxygen. The oxygen source in the sample originates from the metal oxide nanoparticles and a certain amount of bound oxygen present within the sample itself.

Results of the Batch Adsorption Experiments

Effect of pH

During the adsorption process, the adsorbent and adsorbate interact in various ways. Functional groups and active sites on the surface of the adsorbent interact with the charges on the dye molecules. As the initial pH of the solution changes, the charge balance at these active sites also changes, significantly affecting the adsorption percentage. By keeping parameters such as adsorbent amount, temperature, and stirring speed constant, dye solutions with different pH values were prepared and allowed to interact for a sufficient amount of time.

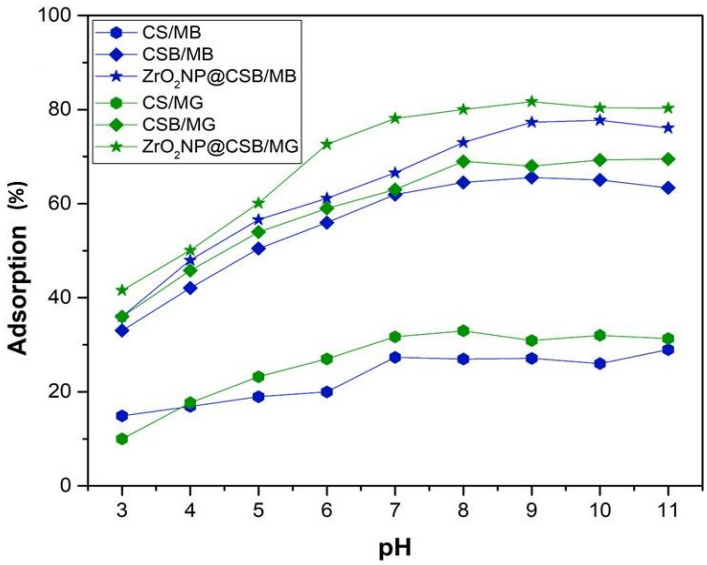

Figure 6. The effect of pH on adsorption.

At the end of the experiments, the solutions were centrifugated to separate the solid adsorbent from the dye solutions. The final concentrations of the solutions were measured by using UV-Vis. Spectrophotometer and the percentage adsorption value was calculated according to Equation (1). Figure 6 shows the effect of the initial solution pH on the adsorption % of MB and MG dyes.

According to the experimental results, the adsorption percentage of the adsorbent is low in acidic pH values, and the adsorption percentage increases as the solution pH level rises. It was observed that, for both dye removal experiments CS biomass showed maximum adsorption at pH 7, CSB at pH 8, and ZrO_2NP@CSB at 9. The better adsorption properties of the adsorbents in basic solution experiments can be explained by the occupation of limited binding sites on the adsorbent surface by H^+ ions at low pH values. The positively charged dye molecules adhere to the negatively charged adsorbent surface through an electrostatic attraction at basic pH levels. The results align with previous research findings (Altun & Ecevit, 2022).

Effect of Adsorbent Amount

The effect of the adsorbent amount on the adsorption percentage in the dye removal experiments by the synthesized adsorbents was investigated. The solution pH values were adjusted to the optimum levels determined before. In the experiments, 100 ml, 50 ppm dye solutions were prepared, and these solutions were contacted with 5 to 500 mg of adsorbents for a sufficient amount of time. The temperature was kept constant at 25°C, and the stirring speed was maintained at 400 rpm. The results obtained are presented in Figure 7.

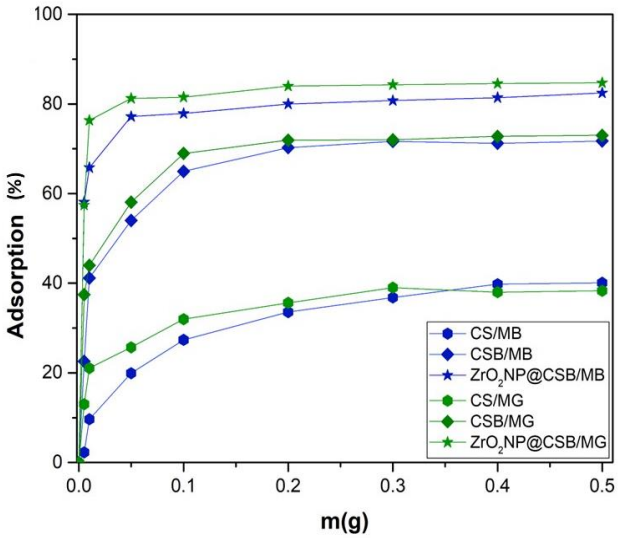

Figure 7. The effect of adsorbent amount on adsorption.

The results presented in Figure 7 can be used to evaluate the adsorption capabilities of biomass, biochar, and biochar nanocomposite adsorbents when the various amount of adsorbent used in a 100 ml, 50 ppm dye solution. The adsorption percentage increased proportionally with the increasing adsorbent dosage, up to a certain value. The adsorption percentage is only little affected by additional adsorbent additions after this point. The optimum adsorbent dosages for CS were found as 4.0 g/L and 3.0 g/L for MB and MG removal, respectively. The optimal dose of ZrO_2NP@CSB for adsorption was set at 0.5 g/L, whereas the CSB adsorbent was 2.0 g/L for both dye removal methods.

Effect of Contact Time and Kinetic Studies

Contact time is an essential factor that needs to be investigated in an equilibrium process including an adsorption study. For this purpose, 50 ppm of MB and MG solutions were mixed with a certain amount of adsorbent individually to perform adsorption. Solution pH and adsorbent amounts were adjusted to the optimum values indicated before. The adsorbent-adsorbate mixtures were allowed to interact for 1 to 240 minutes. After the specified period, the solutions were centrifuged, and a UV-Vis spectrophotometer was used to determine the solutions' ultimate concentration. The adsorption percentage versus time was plotted and presented in Figure 8. As seen in Figure 8, the adsorption of dye by the synthesized adsorbents increased rapidly for the first 0-25 minutes. After 25 minute, adsorption slowed down, and the system reached equilibrium. Adsorption does not result in appreciable variations in the adsorption % after it reaches equilibrium at a given contact time. At this equilibrium point, the active sites of the adsorbent surface are fully occupied. At 180 minutes for CS, 120 minutes for CSB, and 90 minutes for ZrO_2NP@CSB, the MB elimination process approaches equilibrium. For the MG elimination procedure, the ideal contact times were 45 minutes for ZrO_2NP@CSB, 90 minutes for CSB,

and 120 minutes for CS. Pseudo-first and pseudo-second-order equations were applied to the adsorption of MB and MG on the synthesized adsorbents and their kinetics were examined. The results are given in Table 1.

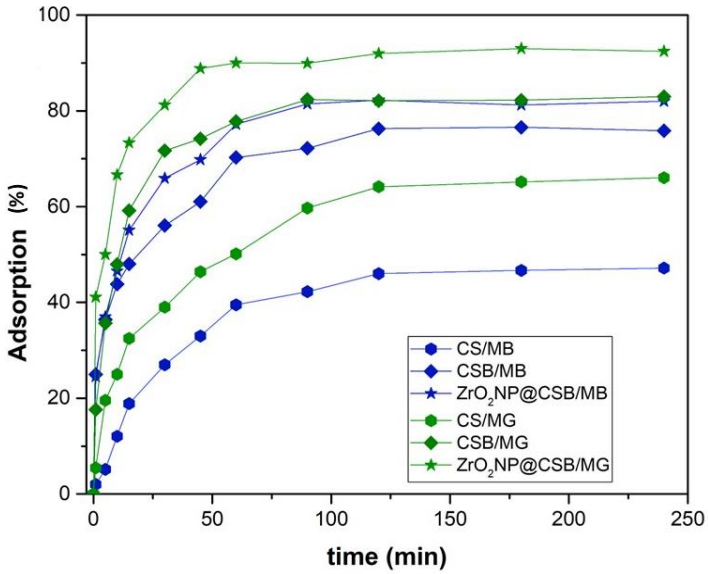

Figure 8. The effect of contact time on adsorption.

Table 1. The pseudo-first-order and pseudo-second-order parameters for the adsorption of MB and MG on CS, CSB, and ZrO_2NP@CSB

			Pseudo-first order			**Pseudo-second order**		
Adsorbent	**Dye**	**$q_{e(exp.)}$ (mg/g)**	**R^2**	**k_1**	**q_e (mg/g)**	**R^2**	**k_2**	**q_e (mg/g)**
CS	MB	6.25	0.880	0.013	4.555	0.990	0.0047	6.848
CSB	MB	19.25	0.811	0.021	9.457	0.998	0.0065	19.732
ZrO_2NP@CSB	MB	82,05	0.747	0.019	34.235	0.999	0.0019	84.531
CS	MG	11.03	0.988	0.025	9.633	0.996	0.005	11.889
CSB	MG	23.02	0.619	0.009	10.444	0.999	0.008	21.322
ZrO_2NP@CSB	MG	93.50	0.770	0.019	28.539	0.999	0.003	94.192

According to Table 1, in the adsorption experiments of both dyes, the correlation coefficient for the CS biomass was calculated to be quite high in both pseudo-first-order and pseudo-second-order kinetic models (Lagergren, 1898). To determine the suitable model for this adsorbent, the experimental adsorption capacity (q_e) values were considered. It was concluded that the pseudo-second-order kinetic model is suitable for the removal of both dyes using CS. Upon evaluating the table for biochar and biochar nanocomposite, it is observed that the correlation coefficients are higher for the pseudo-second-order than the pseudo-first-order kinetic model. The experimental results also align with the pseudo-second-order kinetic model. Therefore, the pseudo-second-order kinetic model is suitable for the whole system.

Effect of Initial Concentration of Dye and Isotherm Studies

In the process of removing MB and MG dyes with synthesized adsorbents, after optimizing the parameters of pH, adsorbent dosage, and contact time, the effect of the initial concentration of dye on adsorption was investigated. During this study, experimental conditions were adjusted to the optimum conditions for each adsorbent. The initial concentration of dye was varied from 5 to 300 ppm. After reaching equilibrium, the adsorbent-dye mixtures were centrifugated, and the remaining dye concentration was measured by using UV-Vis. Spectrophotometer. Using the obtained data, isotherm graphs were plotted and presented in Figure 9. The adsorption behavior was examined within the framework of Langmuir, Freundlich, and Temkin isotherms. When examining Figure 9, it was observed that the adsorption capacity is low when the adsorbent is contacted with dyes at low concentrations, whereas it is high when the adsorbent is contacted with the dyes at high concentrations with the same amount of adsorbent. The possible reason for this is the limited number of active sites on the adsorbent's surface. When the initial concentration of dye is low, there are still active sites available for the adsorbent's surface. However, as the concentration increases, these sites gradually become occupied, and the adsorbent reaches its maximum adsorption capacity.

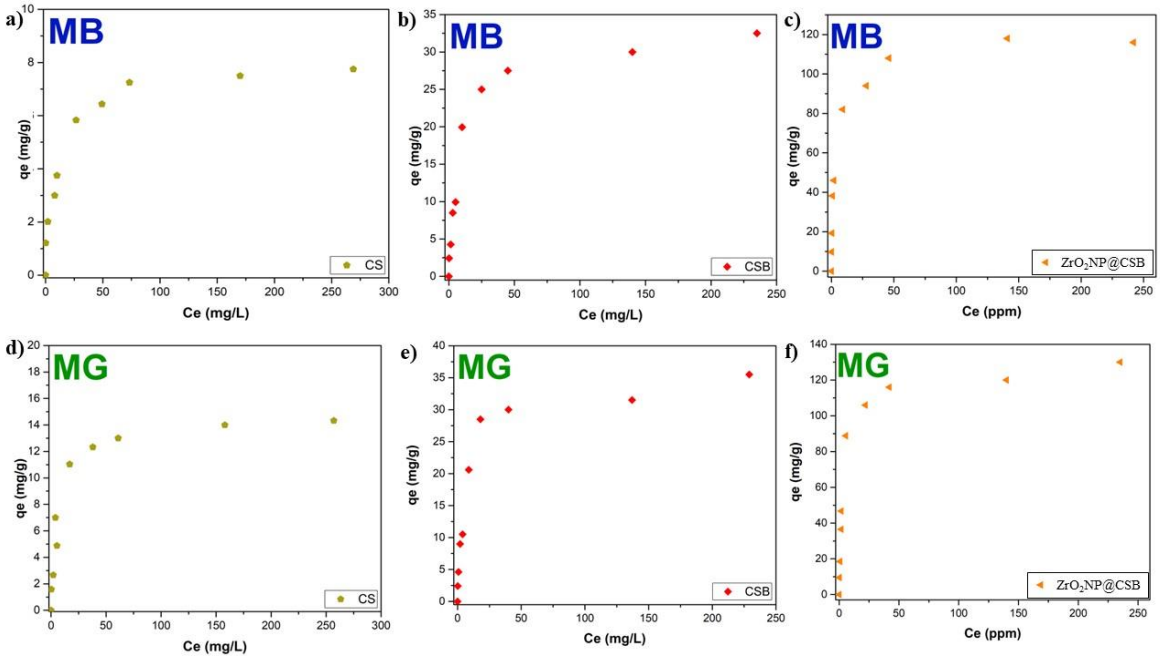

Figure 9. The effect of initial concentration of dyes on adsorption.

The plots of the graphs for the three distinct isotherms can be seen, and as the correlation coefficient R^2 gets closer to 1.0, the graph data's linearity gets better. Isotherm parameters calculated from the obtained data are presented in Table 2. Langmuir model typically describes the chemical adsorption (Langmuir, 1916). The following assumptions are made when deriving the Langmuir isotherm. (i) The surface is homogeneous. In this case, all sites on the solid surface exhibit the same adsorption properties. (ii) There are no interactions between the adsorbed molecules. Therefore, the amount of the adsorbed substance does not affect the adsorption rate per unit surface area. (iii) Adsorption is monolayer. (iv) The entire adsorption process follows the same mechanism. Similar to the Langmuir model, the equilibrium parameters are often applied to the Freundlich isotherm. According to the Freundlich model, adsorption is physical, and the adsorbent surface is heterogeneous (Freundlich, 1907). K_f and *n* parameters were calculated for the Freundlich model, if *n* values between 1 and 10, the adsorption is said to be appropriate. The Temkin isotherm assumes that the adsorption energy decreases linearly rather than exponentially as in the Freundlich.

Table 2. Parameters of Langmuir, Freundlich, and Temkin for the adsorption of MB and MG on CS, CSB, and ZrO_2NP@CSB

	Adsorbent	**Dye**	**Parameters for Dye**			
Langmuir			**q_m**	**K_L**	**R^2**	**R_L**
	CS	MB	7.930	0.114	0.998	0.149
	CS	MG	14.658	0.150	0.999	0.118
	CSB	MB	33.135	0.119	0.998	0.144
	CSB	MG	35.474	0.156	0.996	0.114
	ZrO_2NP@CSB	MB	117.925	0.326	0.999	0.058
	ZrO_2NP@CSB	MG	129.870	0.230	0.998	0.080
Freundlich			**K_f**	**n**		**R^2**
	CS	MB	1.959	3.656		0.944
	CS	MG	2.965	2.956		0.870
	CSB	MB	5.349	2.589		0.908
	CSB	MG	6.270	2.625		0.906
	ZrO_2NP@CSB	MB	29.648	3.210		0.886
	ZrO_2NP@CSB	MG	26.853	2.797		0.811
Temkin			**K_T**	**B_T**		**R^2**
	CS	MB	8.441	1.002		0.893
	CS	MG	4.798	2.146		0.906
	CSB	MB	4.026	4.781		0.901
	CSB	MG	5.816	4.738		0.930
	ZrO_2NP@CSB	MB	13.478	15.539		0.978
	ZrO_2NP@CSB	MG	6.628	19.008		0.932

When evaluating the data shared in Table 2, the correlation coefficients are closest to 1 in the Langmuir isotherm model. The fact that the distribution coefficient R_L values between 0 and 1 indicates the suitability of the Langmuir isotherm. When the R_L value is 0, adsorption is irreversible, and when it is greater than 1, the system is unfavorable for adsorption. R_L values can be calculated by using Equation (8), where K_L is the Langmuir coefficient and C_i is the initial concentration of dye.

$$R_L = \frac{1}{1+ K_L C_i} \tag{8}$$

In this study, since R_L values are between 0 and 1, it is understood that the system conforms to the Langmuir isotherm model. Although the system conforms to the Langmuir isotherm model, the correlation coefficients R^2 for the Freundlich isotherm are also quite high. It can be inferred that this model also goes along with the adsorption process because the Freundlich isotherm constant, n, supports values between 1 and 10. According to these findings, the system exhibits a structure where both physisorption and chemisorption occur simultaneously.

Effect of Temperature and Thermodynamic Studies

To determine the effect of temperature on adsorption and to perform thermodynamic calculations, experiments were conducted at 25, 35, and 45°C. During these experiments, the previously determined optimum conditions for each adsorbent were maintained. van't Hoff plots for the removal of MB and MG are provided in Figure 10.

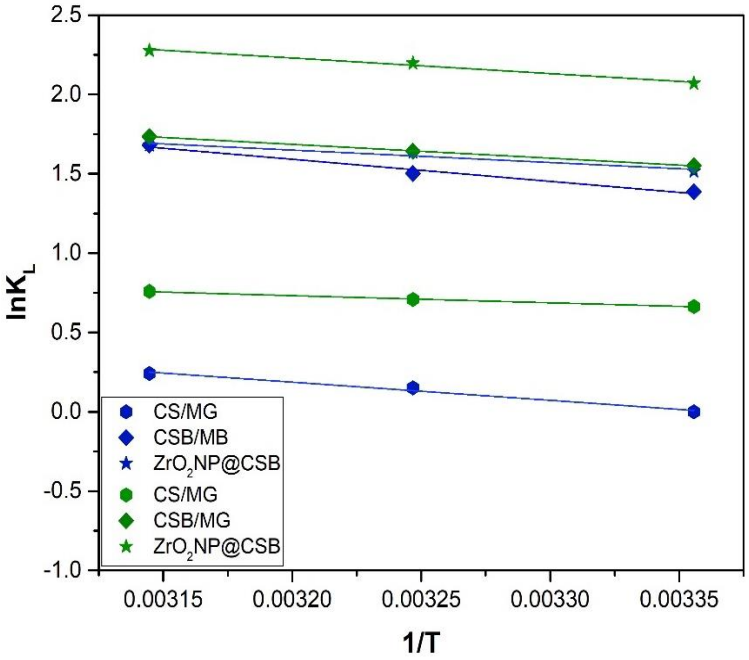

Figure 10. The van't Hoff plots of the adsorbents.

The slope and intercept values of van't Hoff plots were used to calculate the changes in entropy and enthalpy by using Equations (9) and (10). The results are presented in Table 3. Calculating thermodynamic parameters is required to ascertain whether the adsorption process is spontaneous.

$$ln\, k_e = \left(\frac{\Delta S}{R}\right) - \left(\frac{\Delta H}{R}\right)\frac{1}{T} \tag{9}$$

$$\Delta G° = \Delta H° - T\,\Delta S° \tag{10}$$

Where T is the temperature (K); R is the ideal gas constant; k_e is the equilibrium constant. From Equation (10) it is possible to calculate Gibbs free energy, $\Delta G°$ (kJ mol^{-1}). Adsorption percentage slightly increases with temperature, but this increase is not significant. Considering additional costs such as increasing the system's temperature, the optimum temperature for MB and MG adsorption with the synthesized adsorbents has been determined as 25°C.

Table 3. Thermodynamic parameters for the adsorption of MB and MG on CS, CSB, and ZrO_2NP@CSB

Dye	Adsorbent	ΔH^0 (kJ/mol)	ΔS^0 (kJ/mol.K)	ΔG^0 (kJ/mol) T= 298 K	T= 308 K	T= 318 K
MB	CS	9.52	0.032	-0.016	-0.336	-0.656
	CSB	11.57	0.050	-3.330	-3.830	-4.330
	ZrO_2NP@CSB	6.50	0.035	-3.930	-4.280	-4.630
MG	CS	3.74	0.018	-1.624	-1.804	-1.984
	CSB	7.25	0.037	-3.776	-4.146	-4.516
	ZrO_2NP@CSB	8.17	0.045	-5.240	-5.690	-6.140

The negative values of the Gibbs free energy change indicate that the adsorption process occurs spontaneously. Furthermore, the amount of the ΔG^0 suggests that physical sorption controls the process. The reaction appears to be endothermic based on the positive ΔH^0 values.

Conclusion

This study investigated the removal of MB and MG dyes from aqueous solutions by adsorbents derived from *Cycas revoluta* seed. These adsorbents are the *Cycas revoluta* seed itself, the pyrolysis product of the seed (CSB), and the nanocomposite which is synthesized by ZrO_2 nanoparticle incorporation of the *Cycas revoluta* seed biochar. Based on the SEM analyses, when comparing the surfaces of the biomass adsorbents with the biochar adsorbent, it was observed that the pyrolysis process achieved the targeted surface modification, and that the biochar possessed a porous surface. Elemental analysis revealed the presence of metal-oxide nanoparticle elements in the biochar nanocomposite adsorbents. Thus, the success of the incorporation process was confirmed. According to the experimental findings, CSB and ZrO_2NP@CSB worked best at a pH between 8.0 and 9.0 for effective dye adsorption. The pseudo-second-order kinetic model expressed the adsorption kinetic well. The adsorption of MB and MG onto the synthesized adsorbent process was fitted to the Langmuir isotherm model. The maximum adsorption capacities calculated using the Langmuir isotherm for MB removal were found to be 7.93 mg/g for CS, 33.14 mg/g for CSB, and 117.93 mg/g for ZrO_2NP@CSB. For MG removal, the maximum adsorption capacities calculated using the Langmuir isotherm were found to be 14.66 mg/g for CS, 35.47 mg/g for CSB, and 129.87 mg/g for ZrO_2NP@CSB. Comparing the adsorption efficiencies of the synthesized biomass, biochar, and biochar nanocomposite, it has been demonstrated through experiments that the biochar nanocomposite exhibited the highest adsorption efficiency. When comparing the removal of MB and MG with the same adsorbents, it was observed that MG removal achieved higher adsorption capacity with a lower equilibrium contact time and lower dosage compared to MB removal.

Scientific Ethics Declaration

The authors declare that the scientific ethical and legal responsibility of this article published in EPSTEM journal belongs to the authors.

Acknowledgements or Notes

* This article was presented as an oral presentation at the International Conference on Research in Engineering, Technology and Science (www.icrets.net) held in Tashkent/Uzbekistan on August 22-25, 2024.

* This study is derived from the Master's thesis prepared by the first author under the supervision of the second author.

References

Alagarsamy, A., Chandrasekaran, S., & Manikandan, A. (2022). Green synthesis and characterization studies of biogenic zirconium oxide (ZrO2) nanoparticles for adsorptive removal of methylene blue dye. *Journal of Molecular Structure, 1247*, 131275.

Altintas Yildirim, O., & Pehlivan, E. (2023). Removal of methylene blue using a novel generation photocatalyst based on nano-SnO2/wild plumb kernel shell biochar composite. *Journal of Dispersion Science and Technology*, *44*(14), 2748-2759.

Altun, T., & Ecevit, H. (2022). Adsorption of malachite green and methyl violet 2B by halloysite nanotube: Batch adsorption experiments and Box-Behnken experimental design. *Materials Chemistry and Physics*, *291*, 126612.

Baig, S. A., Zhu, J., Muhammad, N., Sheng, T., & Xu, X. (2014). Effect of synthesis methods on magnetic Kans grass biochar for enhanced As (III, V) adsorption from aqueous solutions. *Biomass and Bioenergy*, *71*, 299-310.

Bayram, O., Moral, E., & Göde, F. (2023). İğde çekirdeklerinden elde edilen biyokömür kullanılarak sulu çözeltiden kristal viyole boyarmaddesinin uzaklaştırılması. *Journal of the Institute of Science and Technology*, *13*(1), 448-457.

Bayram, O., Köksal, E., Moral, E., Göde, F., & Pehlivan, E. (2023). Efficient decolorization of cationic dye (malachite green) by natural-based biosorbent (nano-magnetic Sophora Japonica fruit seed biochar). *Journal of Dispersion Science and Technology*, *45*(1), 117-128.

Biswas, P., Hasan, W., Jain, J., Kori, R. K., Bose, D., & Yadav, R. S. (2022). Non-permitted food colorants induced neurotoxicity in cerebellum of rat brain. *Drug and Chemical Toxicology*, *45*(6), 2852-2859.

Bounaas, M., Bouguettoucha, A., Chebli, D., Gatica, J. M., & Vidal, H. (2021). Role of the wild carob as biosorbent and as precursor of a new high-surface-area activated carbon for the adsorption of methylene blue. *Arabian Journal for Science and Engineering*, *46*, 325-341.

Chen, B., Zhou, D., & Zhu, L. (2008). Transitional adsorption and partition of nonpolar and polar aromatic contaminants by biochars of pine needles with different pyrolytic temperatures. *Environmental Science & Technology*, *42*(14), 5137-5143.

Dindar, N. (2019). *Tekstil endüstrisi atıksularında ileri arıtma prosesleri kullanılarak organik madde giderimi*. (Master's thesis), Pamukkale Üniversitesi Fen Bilimleri Enstitüsü, Denizli-Türkiye

Erdoğan, F. O. (2017). Düşük maliyetli adsorbentler üzerine dispers sarı 211 tekstil boyasının adsorpsiyonu. *Afyon Kocatepe Üniversitesi Fen ve Mühendislik Bilimleri Dergisi*, *17*(3), 889-898.

Erkmen, J., Kavcı, E., & Adıgüzel, M. (2019). Üretim planlaması yapılarak su bazlı boyaların üretimi esnasında oluşan su kirliliğinin ve boya kaybının önlenmesi. *Journal of the Institute of Science and Technology*, *9*(1), 57-65.

Erkuş, A., Oygun, E., Türkmenoğlu, M., & Aldemir, A. (2018). Boya endüstrisi atıksularının karakterizasyonu. *Yüzüncü Yıl Üniversitesi Fen Bilimleri Enstitüsü Dergisi*, *23*(3), 308-319.

Freundlich, H., (1907). Über die adsorption in lösungen, *Zeitschrift für physikalische Chemie*, 57(1), 385-470

Gayathiri, M., Pulingam, T., Lee, K. T., & Sudesh, K. (2022). Activated carbon from biomass waste precursors: Factors affecting production and adsorption mechanism. *Chemosphere*, *294*, 133764.

Hassaan, M. A., Yılmaz, M., Helal, M., El-Nemr, M. A., Ragab, S., & El Nemr, A. (2023). Isotherm and kinetic investigations of sawdust-based biochar modified by ammonia to remove methylene blue from water. *Scientific Reports*, *13*(1), 12724.

Hossain, M. K., Strezov, V., Chan, K. Y., Ziolkowski, A., & Nelson, P. F. (2011). Influence of pyrolysis temperature on production and nutrient properties of wastewater sludge biochar. *Journal of Environmental Management*, *92*(1), 223-228.

İmdat, S. Ş., (2014). Haşhaş kabuğunun sitrik asit ile modifiye edilerek, yeni adsorban hazırlanması ve sulu çözeltilerden Cr (VI) iyonunun uzaklaştırılması, (Master's thesis), *Selçuk Üniversitesi Fen Bilimleri Enstitüsü,* Konya-Türkiye

Lagergren, S., (1898). Zur theorie der sogenannten adsorption geloster stoffe, *Kungliga Svenska Vetenskapsakademiens Handlingar*, 24, 1-39

Langmuir, I., (1916). The constitution and fundamental properties of solids and liquids. Part I: Solids, *Journal of the American Chemical Society*, *38* (11), 2221-2295

Li, X. F., Li, R. X., & Feng, X. Q. (2023). Photocatalytic Activity of Ag/AgCl/ZrO2@ Biochar Composite for Rhodamine B and Methyl Orange Dyes. *Russian Journal of Physical Chemistry A*, *97*(4), 633-646.

Nanda, S., Mohanty, P., Pant, K. K., Naik, S., Kozinski, J. A., & Dalai, A. K. (2013). Characterization of North American lignocellulosic biomass and biochars in terms of their candidacy for alternate renewable fuels. *Bioenergy Research*, *6*, 663-677.

Parlayıcı, Ş., & Pehlivan, E. (2021). Biosorption of methylene blue and malachite green on biodegradable magnetic Cortaderia selloana flower spikes: modeling and equilibrium study. *International Journal of Phytoremediation*, *23*(1), 26-40.

Parlayıcı, Ş., & Pehlivan, E. (2023). An ecologically sustainable specific method using new magnetic alginate-biochar from acorn cups (Quercus coccifera L.) for decolorization of dyes. *Polymer Bulletin*, *80*(10), 11167-11191.

Pilatin, S., & Kunduhoğlu, B. (2013). Phanerochaete chrysosporium tarafından bazı reaktif tekstil boyalarının renk giderimi ve detoksifikasyonu. *Biological Diversity and Conservation*, *6*(3), 26-34.

Rajput, V. D., Minkina, T., Ahmed, B., Singh, V. K., Mandzhieva, S., Sushkova, S., ... & Wang, B. (2022). Nano-biochar: A novel solution for sustainable agriculture and environmental remediation. *Environmental Research*, *210*, 112891.

Ranjusha, V. P., Pundir, R., Kumar, K., Dastidar, M. G., & Sreekrishnan, T. R. (2010). Biosorption of Remazol Black B dye (Azo dye) by the growing Aspergillus flavus. *Journal of Environmental Science and Health Part A*, *45*(10), 1256-1263.

Rathi, B. S., Kumar, P. S., & Vo, D. V. N. (2021). Critical review on hazardous pollutants in water environment: Occurrence, monitoring, fate, removal technologies and risk assessment. *Science of the Total Environment*, *797*, 149134.

Robinson, T., McMullan, G., Marchant, R., & Nigam, P. (2001). Remediation of dyes in textile effluent: a critical review on current treatment technologies with a proposed alternative. *Bioresource Technology*, *77*(3), 247-255.

Różyło, K., Jędruchniewicz, K., Krasucka, P., Biszczak, W., & Oleszczuk, P. (2022). Physicochemical characteristics of biochar from waste cricket chitin (Acheta domesticus). *Molecules*, *27*(22), 8071.

Shelke, B. N., Jopale, M. K., & Kategaonkar, A. H. (2022). Exploration of biomass waste as low cost adsorbents for removal of methylene blue dye: A review. *Journal of the Indian Chemical Society*, *99*(7), 100530.

Sun, X. F., Wang, S. G., Liu, X. W., Gong, W. X., Bao, N., Gao, B. Y., & Zhang, H. Y. (2008). Biosorption of Malachite Green from aqueous solutions onto aerobic granules: Kinetic and equilibrium studies. *Bioresource Technology*, *99*(9), 3475-3483.

Tasmakıran, A. F., (2010). *Zirai yan ürünlerin modifiye edilerek yeni adsorbanların hazırlanması ve boyaların adsorpsiyonu*, (Master's thesis), Selçuk Üniversitesi Fen Bilimleri Enstitüsü, Konya-Türkiye

Temkin, M., (1940). Kinetics of ammonia synthesis on promoted iron catalysts, *Acta Physiochim*, 12, 327-356

Yaseen, D. A., & Scholz, M. (2019). Textile dye wastewater characteristics and constituents of synthetic effluents: a critical review. *International journal of Environmental Science and Technology*, *16*, 1193-1226.

Volli, V., Gollakota, A. R. K., & Shu, C. M. (2021). Comparative studies on thermochemical behavior and kinetics of lignocellulosic biomass residues using TG-FTIR and Py-GC/MS. *Science of the Total Environment*, *792*, 148392.

Zeidabadi, Z. A., Bakhtiari, S., Abbaslou, H., & Ghanizadeh, A. R. (2018). Synthesis, characterization and evaluation of biochar from agricultural waste biomass for use in building materials. *Construction and Building Materials*, *181*, 301-308.

Author Information

Elif Gezginci
Konya Technical University, Faculty of Engineering and Natural Sciences, Department of Chemical Engineering
Rauf Orbay Street. 42250, Selçuklu/Konya, Türkiye

Erol Pehlivan
Konya Technical University, Faculty of Engineering and Natural Sciences, Department of Chemical Engineering
Rauf Orbay Street. 42250, Selçuklu/Konya
Contact e-mail: *erolpehlivan@gmail.com*

To cite this article:

Gezginci, E. & Pehlivan, E. (2024). Synthesis and evaluation of an innovative biochar nanocomposite adsorbent derived from *Cycas revoluta* seeds, with potential applications in the removal of cationic dyes. *The Eurasia Proceedings of Science, Technology, Engineering & Mathematics (EPSTEM), 29*, 92-105.

The Eurasia Proceedings of Science, Technology, Engineering & Mathematics (EPSTEM)
ISSN: 2602-3199

The Eurasia Proceedings of Science, Technology, Engineering & Mathematics (EPSTEM), 2024

Volume 29, Pages 106-112

ICRETS 2024: International Conference on Research in Engineering, Technology and Science

Degradation of Emamectin Benzoate by Chemical Catalytic Reaction of Graphitic Carbon Nitride Based Nanoparticle

Ayşe Bayrak
Selcuk University

Sevde Demir
Eskisehir Osmangazi University

Hakan Erer
Eskisehir Osmangazi University

Ilkay Hilal Gubbuk
Selcuk University

Mustafa Ersoz
Selcuk University

Abstract: In recent years, metal–organic frameworks (MOFs), a new class of porous crystalline materials, have attracted great attention as a promising candidate for environmental remediation and catalytic applications. In this study, g-C_3N_4@ZIF-8 containing graphitic carbon nitride (g-C_3N_4) was synthesized to be used as a catalyst for the catalytic degradation of Emamectin benzoate pesticide with $NaBH_4$. The synthesized g-C_3N_4@ZIF-8 were characterized by Fourier Transform Infrared Spectroscopy, X-ray Diffraction, Scanning Electron Microscopy, Electron Dispersive X-ray and point of zero charge pH analysis. The degradation experiments of the synthetic pesticide were carried out in the presence of sodium borohydride ($NaBH_4$) used as reducing agent and the degradation times of the pesticide were monitored in UV-Vis Spectrophotometer (UV-Vis). The catalytic activity of the prepared composite has been tested in aqueous medium at room temperature across a broad spectrum. Degradation experiments were conducted at room temperature in the presence of $NaBH_4$, and the impact of various parameters such as pH, catalyst quantity, emamectin benzoate concentration, and $NaBH_4$ amount has been thoroughly investigated in detail. g-C_3N_4@ZIF-8 nanocomposite showed superior NaBH4-induced chemical catalytic activity in degrading the toxic pollutant emamectin benzoate pesticide in a very short time. Kinetic parameters (k) for the degradation reactions were calculated and upon exposure to g-C_3N_4@ZIF-8 nanoparticles, effective degradation of emamectin benzoate occurred in approximately 60 min. In the reduction reaction of emamectin benzoate pesticide with g-C_3N_4@ZIF-8, 70% degradation occurred within 60 min. This study provides insight into understanding nanoscale metal-organic frameworks (MOFs) in the removal of pesticides from wastewater.

Keywords: Catalysis, Graphitic carbon nitride, Degradation, Emamectin benzoate

Introduction

In recent years, the number of pesticides used in the environment and their production amount have increased significantly. The persistence and toxicity of pesticides have been considered as a problem for many years and the subject of various treatment methods for the removal of pesticides from wastewater will continue to be an area of research (Sajjadi et al., 2019). Despite their adverse effects on human health and the environment,

- Selection and peer-review under responsibility of the Organizing Committee of the Conference

pesticides are widely used chemicals in the agricultural industry (Nam et al., 2021). The use of pesticides plays an important role to ensure good crop yields, but it is known that if used for a long time and in large quantities, they constantly accumulate in crops, soil and water, posing a great threat to the environment and human life safety (Liu et al., 2023). Emamectin benzoate (EMB), derived from the avermectin family, is very stable and undergoes almost no degradation in the dark and remains stable in soil (Burkhard et al., 2015). Emamectin benzoate is a novel macrocyclic lactone insecticide derived from the avermectin family with a substitution of an epi-methylamino (-$NHCH_3$) group for a hydroxyl (-OH) group at the 4″-position on the disaccharide and is produced as a benzoate salt. In darkness, there is almost no degradation and emamectin is stable in soils (Zhu et al., 2011). Although it is widely used and poses a threat to the environment, there are very few studies investigating the removal of EMB (Zhou et al., 2016).

MOFs are a new category of porous materials that exhibit the high porosity, large surface area, and structural diversity required for catalysis. Compared to many types of MOFs, zeolitic imidazolate frameworks (ZIFs) are low cost and therefore stand out for wastewater treatment over other types of MOFs. here are many types of MOFs, but especially zinc-based ZIFs such as ZIF-8, which consists of Zn ions and 2-Methylimidazole, have recently attracted great attention in the field of catalysis due to their simple synthesis, high stability, and good adsorption performance with high surface area (Weng et al., 2023). The production of new composites with ZIF-8 combined with different supports has attracted great interest due to their promising properties and applications (Sarkarzadeh et al., 2023).

Graphitic carbon nitride, g-C_3N_4, can be synthesized in one step from various common carbon (C) and nitrogen (N) rich precursors such as urea, melamine, dicyanamide, etc. Adjusting the electronic structure of g- C_3N_4 can improve the mass transfer by improving the surface area of the catalyst and increase the number of active sites on the catalyst surface (Roy et al., 2021).

The catalyst was used for the emamectin benzoate reduction reaction in the presence of $NaBH_4$ as reducing agent at ambient conditions. The catalytic activity of the synthesized composite was tested in aqueous media at room temperature over a broad spectrum. Moreover, as the ZIF-8 structure and the g-C_3N_4 framework are highly tunable to incorporate many functionalities, this process has great scope to modify the catalytic potential of the composite catalyst. Overall, this study reveals the synthesized g-C_3N_4@ZIF-8 composite as an effective and promising candidate for the reduction of the pesticide emamectin benzoate under ambient conditions. In this study, the g-C_3N_4@ZIF-8 composite was successfully utilized for the reduction of emamectin benzoate using $NaBH_4$.

Experimental

Materials and Method

Melamine ($C_3H_6N_6$), emamectin benzoate, zinc nitrate tetrahydrate ($Zn(NO_3)_2{\cdot}4H_2O$) and 2-methylimidazole, sodium borohydride ($NaBH_4$), NaCl, HCl and NaOH were purchased from Sigma-Aldrich and used in the synthesis and catalysis stages. Experimental solutions were prepared using deionized water. Schimadzu UV-1700 model UV-visible spectrophotometer was used to determine the concentration of emamectin benzoate remaining without degradation in the removal experiments.

Synthesis and Application

Synthesis of g-C3N4 and g-C_3N_4@ZIF-8

In the synthesis of g-C_3N_4, 5 g of melamine powder was heated at 550 ˚C for 4 hours in a capped alumina crucible at a heating rate of 10 ◦C/min. A yellow g-C_3N_4 powder was obtained as a product. For g-C_3N_4@ZIF-8 synthesis, it was first obtained by the ZIF-8. Then a mixture of ZIF-8, a certain amount of melamine and ethanol was stirred in a magnetic stirrer for 20 minutes until a homogeneous distribution was reached. The mixture was heated at 70 °C to evaporate the ethanol. The resulting homogeneous mixture was placed in a 15 mL crucible for calcination and gradually heated (at a heating rate of 50 °C for 5 min) and kept at this temperature for 3.30 h after reaching 520 °C. The resulting product (g-C_3N_4@ZIF-8) was powdered and stored indoors(Zhao et al., 2020).

Emamectin Benzoate Removal

EMB solution (1,000 mg/L) was prepared by dissolving the calculated amount of pesticide in water and stored in the dark at 4 °C. During the working stages of EMB, 25 mg/L concentrations were prepared by appropriately diluting this solution. The working standard solution was prepared by diluting the calibration curve (0.05–25 mg/L) with water. All solutions were prepared fresh before use(Tariq et al., 2014). For the pesticide degradation experiments, 2 mL of the EMB solution prepared at the desired concentration and pH was taken and a certain amount g-C_3N_4@ZIF-8 was added, and then the required amount of 0.01 M $NaBH_4$ solution was added. The concentration of emamectin benzoate in the solution was determined by measuring the absorbance values of the resulting solution with a UV-Visible spectrophotometer at a wavelength of 240 nm. The ratio of the concentrations (C_t) obtained at the end of the contact period to the initial concentration (C_o) and k is the rate constant ($mgL^{-1}min^{-1}$) was calculated and the $\ln(C_t/C_o)$-time graph was drawn(Asadi et al., 2022).

$$\frac{dCt}{dt} = -kCo \Rightarrow \ln\left(\frac{Ct}{Co}\right) = -kt$$

The effects of parameters such as contact time, pH, $NaBH_4$ concentration and catalyst amount on EMB removal were investigated and the optimum values of these parameters were found through removal experiments. The pH of the solution of both human drugs and animal and plant drugs plays a vital role in chemical catalytic decomposition reactions. In this study, the EMB solution was analyzed for both acidic and alkaline pH by adding appropriate amount of NaOH and HCl solution. The experiment was repeated for the sample keeping the pH of the EMB solution 3–10. The degradation efficiency of the catalyst was estimated using the formula:

$$Degaradation\ efficiency\ \% = \frac{\mathrm{Ct-Co}}{Co}\mathrm{x100}$$

C_0 is the EMB concentration before degradation and Ct is the EMB concentration after degradation at time t.

Results and Discussion

To investigate their catalytic activity, g-C_3N_4@ZIF-8 particles were used in the degradation of EMB in the presence of sodium borohydride. The progress of the catalytic degradation of EMB was monitored only by the decrease in optical density at the absorbance wavelength (240 nm). The effects of factors such as catalyst amount, pH, $NaBH_4$ concentration, contact time on EMB removal were investigated. The optimum values of these parameters used to provide the highest removal were found. The degradation efficiency of the pesticide was analyzed every 10 minutes over time. In order to examine the effect of other parameters, the parameter value for optimum removal was determined and experiments were carried out to examine the effect of another parameter using this optimum value. Also, experiments were conducted to see their efficiencies alone, without adding $NaBH_4$ solution to the mixture, and without adding g-C_3N_4@ZIF-8 to the mixture for the catalyst-free degradation process. $NaBH_4$ and g-C_3N_4@ZIF-8 were added to the mixture for the catalytic degradation process. As seen in Fig. 1b from the graph of $\ln(C_t/C_o)$-*time*, a linear relationship was observed for the catalyst. The first-order rate constant, *k*, was determined from the slope of the line. The rate constant value was found to be 0.0104 min^{-1} for the synthesized composite.

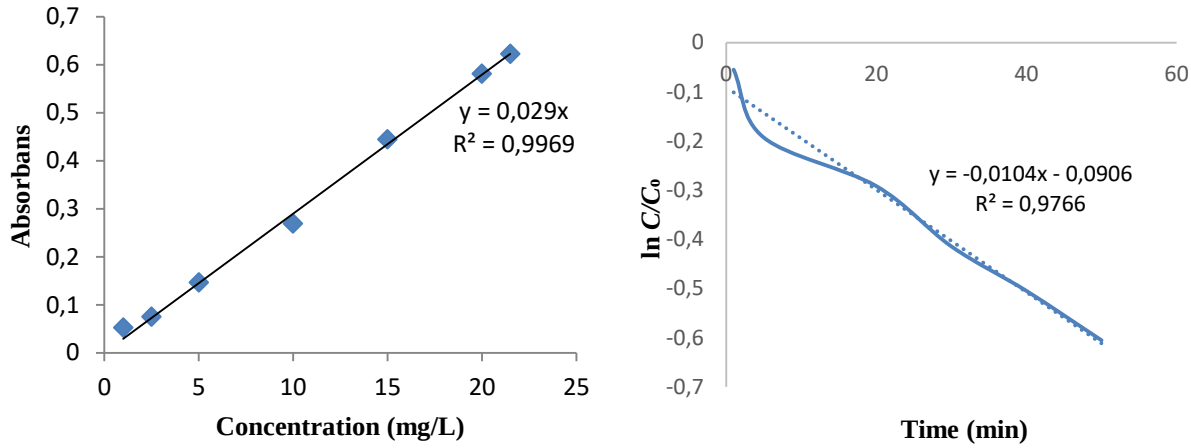

Figure 1 . a) Linear dynamic range data of EMB, b) ln C_t /C_o-time graph for kinetics of catalytic activity.

Effect of pH, $NaBH_4$ Concentration and g-C_3N_4@ZIF-8 Dosage

In any catalytic reaction, the surface of the catalysis can become positively charged or negatively charged depending on the solution pH relative to the zero charge point of the catalysis in question. This difference in surface charge may affect the degradation efficiency of reactive oxygen species. The effect of varying the initial solution pH (pH 3-10) was investigated(Edebali, 2023). In order to determine the effect of pH on EMB removal, catalytic degradation processes were applied to EMB solutions with pHs of 3, 6.5, 7.5, 10. The results obtained are presented graphically in Fig. 2. pH_{pzc} of the g-C_3N_4@ZIF-8 was found to be 7.45. That is, g-C_3N_4@ZIF-8 surface is positively charged at pH below pH_{pzc} and negatively charged at pH greater than 7.45. EMB molecules should be positively charged at pH=3, pH=6.5, neutral at pH=7.5, and negatively charged at pH=10. Pesticide removal rate in acidic and basic environments pH=7(Tariq et al., 2014). It was found to be lower compared to 5 and the minimum time required for the degradation of EMB pesticide was obtained at this pH =7.5. This situation can be explained by the surface charge of the nanoparticle, that is, its pH_{pzc} value, and the forms of the EMB pesticide at different pH values.

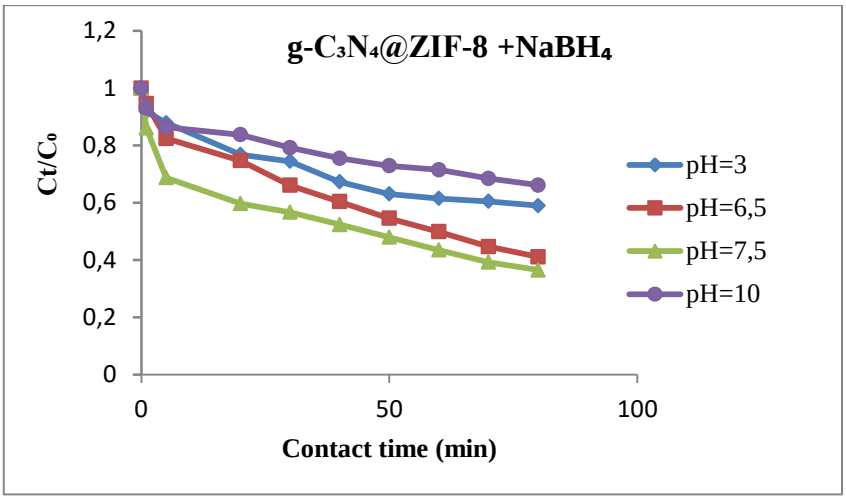

Figure 2. Effect of pH on EMB removal via catalytic degradation (Process parameters: $NaBH_4$ concentration 0.5 mM, g-C_3N_4@ZIF-8 dosage 1 g/L, EMB initial concentration 25 ppm)

In order to examine the effect of $NaBH_4$ concentration on EMB removal, both catalytic and non-catalytic degradation experiments were carried out and the results are presented graphically in Fig. 3. In order to examine the effect of g-C_3N_4@ZIF-8 dosage on the degradation of EMB, the results of degradation experiments using different dosages of EMB are presented in Fig. 4. The amount of particles used was chosen between 0.0 -1.5 g/L. It can be seen that the removal efficiencies obtained at separate dosages of the results are very close together. As a result of this study, a divided dosage of 2 mg was determined as the optimum dosage, in which optimum removal could be achieved, but maximum removal could not be achieved, in order to cut off excess material and examine other leaks in more detail.

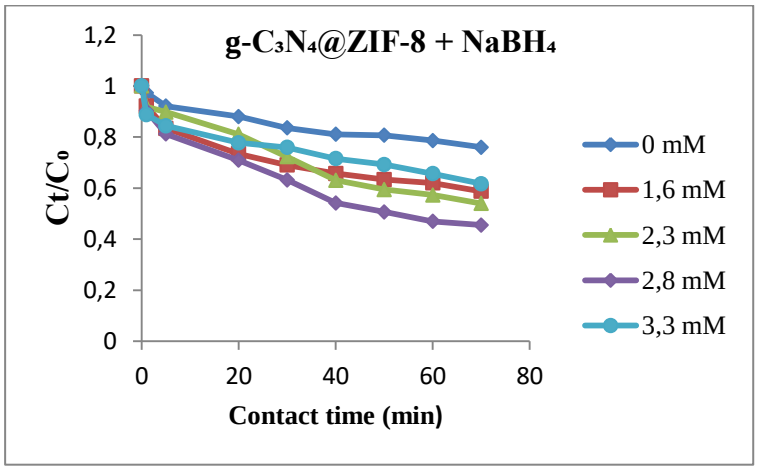

Figure 3. Effect of $NaBH_4$ concentration on EMB degradation (Process character: pH 6.5, g-C_3N_4@ZIF-8 dosage 2 mg, EMB starting point 25 ppm)

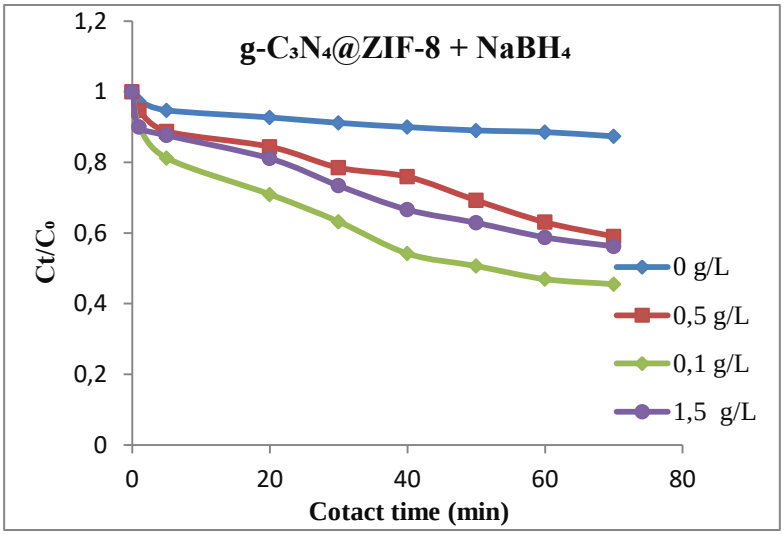

Figure 4. Effect of g-C_3N_4@ZIF-8 dosage on EMB degradation (Process character: pH 6.5, 800 µL $NaBH_4$, EMB starting point 25 ppm)

UV-vis Spectrum Analysis

Degradation experiments of EMB pesticide were carried out at room temperature in the presence of $NaBH_4$ as reductant using ZIF-8 and g-C_3N_4@ZIF-8 nanoparticles. In order to demonstrate the catalytic activity of EMB, experiments were carried out separately with both ZIF-8 and g-C_3N_4@ZIF-8 nanoparticles. Catalytic reductions of EMB were visualized by recording time-resolved UV-Vis absorption spectra at wavelengths in the range of 200-700 nm using UV-Vis. The spectra observed for the degradation of EMB in the presence of $NaBH_4$ are shown in Fig. 5-6. The characteristic absorption peak of EMB was observed at 240 nm (Mo et al., 2021). Fig. 7 shows the catalytic reduction of EMB with ZIF-8 in UV-Vis. When the reduction reaction of EMB with ZIF-8 is initiated, the peak intensity at 240 nm decreases depending on time. It has been observed that the catalytic activity of ZIF-8 under optimum conditions is very low Fig. 7. However, in the reduction reaction carried out with the g-C_3N_4@ZIF-8 nanoparticle under optimum conditions, 62% degradation occurred within 60 minutes. It was observed that the addition of g-C_3N_4 increased the catalytic activity of the particle in the degradation of EMB.

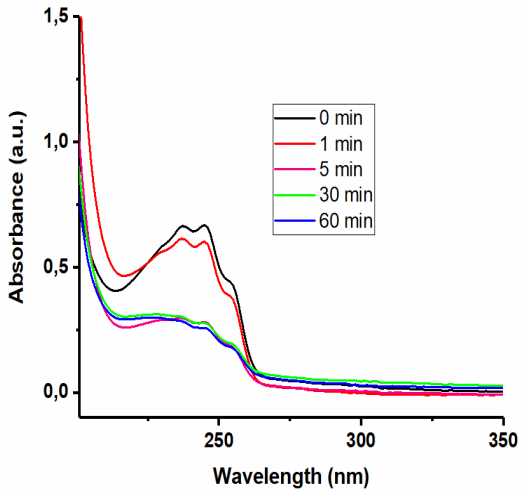

Figure 5. UV–vis absorption spectra of the degradation of EMB by g-C_3N_4@ZIF-8s in the presence of $NaBH_4$ (Process character: pH 6.5, 800 µL $NaBH_4$, g-C_3N_4@ZIF-8 dosage 2 mg, EMB starting point 25 ppm, **pH= 6,38**).

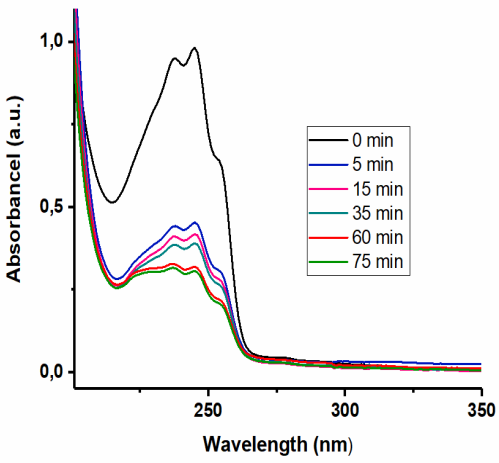

Figure 6. UV–vis absorption spectra of the degradation of EMB by g-C_3N_4@ZIF-8s in the presence of $NaBH_4$ (Process character: pH 6.5, 800 µL $NaBH_4$, g-C_3N_4@ZIF-8 dosage 2 mg, EMB starting point 25 ppm, **pH= 7,58**).

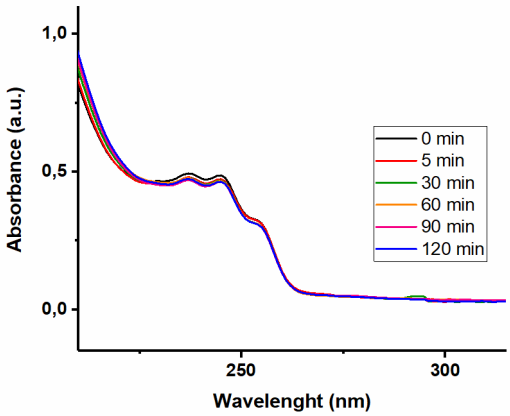

Figure 7. UV–vis absorption spectra of the degradation of EMB by ZIF-8s in the presence of $NaBH_4$ (Process character: 800 µL $NaBH_4$, EMB starting point 25 ppm, **pH 6.5**).

Fig. 6 shows the catalytic activity of EMB by g-C_3N_4@ZIF-8s in the presence of $NaBH_4$ in about one hour with UV–vis absorption spectra. As shown in Fig. 6, it can be clearly seen that the characteristic peak of EMB at 240 nm gradually decreases with the extension of time and remains almost unchanged after 70 min. Unfortunately, the spectrum of EMB did not completely disappear in the study, indicating that EMB molecules were not fully mineralized and a certain amount of intermediates were formed in solution. The EMB removal efficiency of g-C_3N_4@ZIF-8s was determined as 62%. This indicates that only a fraction of EMB molecules are mineralized by g-C_3N_4@ZIF-8. The effective removal of EMB molecules demonstrated that g-C_3N_4@ZIF-8s have great application potential in wastewater treatment.

Scientific Ethics Declaration

The authors declare that the scientific ethical and legal responsibility of this article published in EPSTEM journal belongs to the authors.

Acknowledgements

* This work is financially supported by Selcuk University, Scientific Research Coordinatorship (SU-BAP) through PhD Thesis Project (22211017) and Scientific Meeting Participation Projects (24701094).

* This article was presented as an oral presentation at the International Conference on Research in Engineering, Technology and Science (www.icrets.net) held in Thaskent/Uzbekistan on August 22-25, 2024.

References

Asadi, A., Daglioglu, N., Hasani, T., & Farhadian, N. (2022). Construction of Mg-doped ZnO/g-C3N4@ ZIF-8 multi-component catalyst with superior catalytic performance for the degradation of illicit drug under visible light. *Colloids and Surfaces A: Physicochemical and Engineering Aspects*, *650*, 129536.

Burkhard, R., Binz, H., Roux, C. A., Brunner, M., Ruesch, O., & Wyss, P. (2015). Environmental fate of emamectin benzoate after tree micro injection of horse chestnut trees. *Environmental Toxicology and Chemistry*, *34*(2), 297-302.

Edebali, S. (2023). Synthesis and characterization of MIL-101 (Fe) as efficient catalyst for tetracycline degradation by using $NaBH_4$: Artificial neural network modeling. *Applied Surface Science Advances*, *18*, 100496.

Liu, L., Chen, X.-L., Cai, M., Yan, R.-K., Cui, H.-L., Yang, H., & Wang, J.-J. (2023). Zn-MOFs composites loaded with silver nanoparticles are used for fluorescence sensing pesticides, Trp, EDA and photocatalytic degradation of organic dyes. *Spectrochimica Acta Part A: Molecular and Biomolecular Spectroscopy*, *289*, 122228.

Mo, D., Li, X., Chen, Y., Jiang, Y., Gan, C., Zhang, Y., Li, W., Huang, Y., & Cui, J. (2021). Fabrication and evaluation of slow-release lignin-based avermectin nano-delivery system with UV-shielding property. *Scientific reports*, *11*(1), 23248.

Nam, D., Kim, Y., Kim, M., Nam, J., Kim, S., Jin, E., Lee, C. Y., & Choe, W. (2021). Role of Zr6 Metal Nodes in Zr-Based Metal–Organic Frameworks for Catalytic Detoxification of Pesticides. *Inorganic Chemistry*, *60*(14), 10249-10256.

Roy, D., Neogi, S., & De, S. (2021). Highly efficient reduction of p-Nitrophenol by sodium borohydride over binary ZIF-67/g-C3N4 heterojunction catalyst. *Journal of Environmental Chemical Engineering*, *9*(6), 106677.

Sajjadi, S., Khataee, A., Bagheri, N., Kobya, M., Şenocak, A., Demirbas, E., & Karaoğlu, A. G. (2019). Degradation of diazinon pesticide using catalyzed persulfate with Fe3O4@ MOF-2 nanocomposite under ultrasound irradiation. *Journal of Industrial and Engineering Chemistry*, *77*, 280-290.

Sarkarzadeh, A., Nobakht, V., & Kooti, M. (2023). Tandem catalytic hydrogen gas generation and reduction of nitro aromatic derivatives via hydrolysis of ammonia borane over Ag NPs@ ZIF-8 nanocomposites in aqueous media. *Inorganic Chemistry Communications*, *157*, 111231.

Tariq, S. R., Rafique, N., Kiran, S., & Khan, A. M. (2014). Photo-induced degradation of emamectin benzoate: effect of iron amendments and solvent system. *Environmental earth sciences*, *72*, 983-988.

Weng, X., Ma, H., Owens, G., & Chen, Z. (2023). Enhanced removal of 2, 4-dichlorophenol by Fe-Pd@ ZIF-8 via adsorption and dechlorination. *Separation and Purification Technology*, *305*, 122371.

Zhao, F., Liu, Y., Hammouda, S. B., Doshi, B., Guijarro, N., Min, X., Tang, C.-J., Sillanpää, M., Sivula, K., & Wang, S. (2020). MIL-101 (Fe)/g-C3N4 for enhanced visible-light-driven photocatalysis toward simultaneous reduction of Cr (VI) and oxidation of bisphenol A in aqueous media. *Applied Catalysis B: Environmental*, *272*, 119033.

Zhou, L., Luo, F., Zhang, X., Jiang, Y., Lou, Z., & Chen, Z. (2016). Dissipation, transfer and safety evaluation of emamectin benzoate in tea. *Food chemistry*, *202*, 199-204.

Zhu, J., He, Y., Gao, M., Zhou, W., Hu, J., Shen, J., & Zhu, Y. C. (2011). Photodegradation of emamectin benzoate and its influence on efficacy against the rice stem borer, Chilo suppressalis. *Crop Protection*, *30*(10), 1356-1362.

Author Information

Ayşe Bayrak
Selcuk University, Faculty of Science, Department of Chemistry, Selcuk University, Campus, 42075, Konya, Türkiye
Contact e-mail: *bayrakayse123@gmail.com*

Sevde Demir
Eskisehir Osmangazi University, Faculty of Science, Department of Chemistry, Eskisehir Osmangazi University, Eskisehir, Türkiye

Hakan Erer
Eskisehir Osmangazi University, Faculty of Science, Department of Chemistry, Eskisehir Osmangazi University, Eskisehir, Türkiye

Ilkay Hilal Gubbuk
Selcuk University, Faculty of Science, Department of Chemistry, Selcuk University, Campus, 42075, Konya, Türkiye

Mustafa Ersoz
Selcuk University, Faculty of Science, Department of Chemistry, Selcuk University, Campus, 42075,Konya, Türkiye

To cite this article:

Bayrak, A., Demir, S., Erer, H., Gubbuk, H. I., & Ersoz, M. (2024). Degradation of emamectin benzoate by chemical catalytic reaction of graphitic carbon nitride based nanoparticle. *The Eurasia Proceedings of Science, Technology, Engineering & Mathematics (EPSTEM), 29,* 106-112.

The Eurasia Proceedings of Science, Technology, Engineering & Mathematics (EPSTEM)
ISSN: 2602-3199

The Eurasia Proceedings of Science, Technology, Engineering & Mathematics (EPSTEM), 2024

Volume 29, Pages 113-119

ICRETS 2024: International Conference on Research in Engineering, Technology and Science

Synthesis of New Schiff Bases Including of Terephthalohydrazide and Sensor Application

Onder Alici
Selcuk University

Arjan Akbar Hameed
Selcuk University

Abstract: Schiff bases are compounds that are formed by the reaction of aldehydes or ketones with primary amines, usually in alcoholic solution and in a neutral environment, and contain carbon-nitrogen (C=N) double bonds, called the azomethine or imine group, in their structure because of the condensation reaction. In recent years, Schiff Base-based molecular sensors have been one of the most emphasized topics by scientists. In this study, the 3'-formyl-4'-hydroxy-[1,1'-biphenyl]-4-carbonitrile was obtained as literature information (Alici & Erdemir, 2015). Then, for the target compound, which is Schiff base derivative, was obtained from the condensation reaction of the 3'-formyl-4'-hydroxy-[1,1'-biphenyl]-4-carbonitrile with terephthalohydrazide. Chemical structure of synthesized Schiff base compound was confirmed as using various spectroscopic techniques (^{1}H-NMR and ^{13}C-NMR). Then, the interactions of the synthesized Schiff base compound with metals (Fe^{3+}, Ag^{+}, Ca^{2+}, Cr^{3+}, Li^{+}, Sr^{2+}, Ni^{2+}, Ba^{2+}, Pb^{2+}, Mn^{2+}, Cd^{2+}, Hg^{2+}, Co^{2+}, Cu^{2+}, Cs^{+}, Na^{+}, Mg^{2+}, Fe^{2+}, Zn^{2+}, Al^{3+}) under convenient conditions were investigated using fluorescence spectrophotometry. In the fluorimetric investigations, primarily, the selectivity study was carried out. The free sensor target compound at 489 nm did not produce any significant emission intensity with excitation at 360 nm. The each of the cations (10.0 equiv) were separately added to target compound, only Al^{3+} caused to a single band at 489 nm with a notable emission enhancement. As a result of the measurements, it was determined that the target compound had fluorimetric selectivity against only Al^{3+} metal within all metals (Fe^{3+}, Ag^{+}, Ca^{2+}, Cr^{3+}, Li^{+}, Sr^{2+}, Ni^{2+}, Ba^{2+}, Pb^{2+}, Mn^{2+}, Cd^{2+}, Hg^{2+}, Co^{2+}, Cu^{2+}, Cs^{+}, Na^{+}, Mg^{2+}, Fe^{2+}, Zn^{2+}).

Keywords: Hydrazide, Fluorescence, Al^{3+}, Schiff base.

Introduction

Aluminum is a widespread and essential element in both the environment and daily life. Aluminum is widely used in industrial sectors such as water treatment, food additives, pharmaceuticals, and household appliances (Alici & D., 2021; Alici & Erdemir, 2015). Since all these uses are directly related to human life, it is possible that we consume too much aluminum without realizing it. According to the data of the United Nations World Health Organization (WHO), the human body can absorb only 7 mg/kg Al^{3+}. Numerous diseases, including neurological conditions such as Alzheimer's disease, osteoporosis, and kidney disease, are caused by excessive exposure to Al^{3+} (Deibel, Ehmann, & Markesbery, 1996). Considering such situations, Al^{3+} pollution is of serious importance to the environment and humanity.

In order to look into Al^{3+} pollution, UV-vis and fluorescence spectroscopies have been the most popular methods in recent years. Due to its advanced properties, which include low cost, ease of use, quick reaction time, and superior selectivity, fluorescent probes that are capable of selectively detecting biological and environmental metal cations have garnered significant attention from researchers (Yue, Dong, Zhang, Sun, & Gong, 2015; Fu, et al., 2019; Xu, Chen, Zhang, Ju, & Lu, 2020; Chen, Xu, Ju, & Lu, 2021). Fluorescent

- Selection and peer-review under responsibility of the Organizing Committee of the Conference

chemosensors for Al^{3+} detection have been the subject of numerous studies published in recent years (Sen, et al., 2012; Mahalakshmi, et al., 2020; Ali, Alminderej, Messaoudi, & Saleh, 2021; Erdemir, Malkondu, & Karakurt, 2020).

The significance of Schiff base ligands with various donor atoms and their possible applications as fundamental components in macrocyclic chemistry is well-known in the fields of biomedical engineering and environmental chemistry (Keypour, et al., 2019; Nemati, Keypour, Shahabadi, Hadidi, & Gable, 2021; Zeynali, Keypour, Hosseinzadeh, & Gable, 2021; Hajari, Keypour, Rezaei, Farida, & Gable, 2022). Schiff bases exhibit exceptional detection capabilities and stability for specific metal ions, attributed to their effective electronic and structural characteristics in the host-guest complex (Golbedaghi, Ildiz, Azadbakht, & Fausto, 2022).

In this study, the 3'-formyl-4'-hydroxy-[1,1'-biphenyl]-4-carbonitrile was obtained as literature information (Alici & Erdemir, 2015). Then, for the target compound, which is Schiff base derivative, was obtained from the condensation reaction of the 3'-formyl-4'-hydroxy-[1,1'-biphenyl]-4-carbonitrile with terephthalohydrazide. Chemical structure of synthesized Schiff base compound was confirmed as using various spectroscopic techniques (^{1}H-NMR and ^{13}C-NMR). Then, the interactions of the synthesized Schiff base compound with metals (Fe^{3+}, Ag^{+}, Ca^{2+}, Cr^{3+}, Li^{+}, Sr^{2+}, Ni^{2+}, Ba^{2+}, Pb^{2+}, Mn^{2+}, Cd^{2+}, Hg^{2+}, Co^{2+}, Cu^{2+}, Cs^{+}, Na^{+}, Mg^{2+}, Fe^{2+}, Zn^{2+}, Al^{3+}) under convenient conditions were investigated using fluorescence spectrophotometry. In the fluorimetric investigations, primarily, the selectivity study was carried out. The free sensor target compound at 489 nm did not produce any significant emission intensity with excitation at 360 nm. The each of the cations (10.0 equiv) were separately added to target compound, only Al^{3+} caused to a single band at 489 nm with a notable emission enhancement. As a result of the measurements, it was determined that the target compound had fluorimetric selectivity against only Al^{3+} metal within all metals (Fe^{3+}, Ag^{+}, Ca^{2+}, Cr^{3+}, Li^{+}, Sr^{2+}, Ni^{2+}, Ba^{2+}, Pb^{2+}, Mn^{2+}, Cd^{2+}, Hg^{2+}, Co^{2+}, Cu^{2+}, Cs^{+}, Na^{+}, Mg^{2+}, Fe^{2+}, Zn^{2+}).

Method

Chemicals and Instruments

All necessitated chemicals are analytical grade and were obtained from Sigma-Aldrich Chemicals (Zwijndrecht, The Netherlands) and utilized with no further processing. The perchlorate salts of the cations were utilized in this study. ^{1}H and ^{13}C-NMR spectral studies were measured by a Spinsol and Magritek NMR spectrometer and emission spectra of the chemosensor **TDH-CB** were recorded in a Varian Cary Eclipse Fluorescence Spectrophotometer (Agilent Technologies Inc, Santa Clara, CA, USA).

Synthesis of 3'-formyl-4'-hydroxy-[1,1'-biphenyl]-4-carbonitrile (CBA)

Compound (**CBA**) was prepared according in the literature (Alici & Erdemir, 2015).

Synthesis of the receptor bis((4'-cyano-4-hydroxy-[1,1'-biphenyl]-3-yl)methylene)terephthalohydrazide (TDH-CB)

Absolute ethanolic solutions (25 mL) of 3'-formyl-4'-hydroxy-[1,1'-biphenyl]-4-carbonitrile (120.70 mg, 0.451mmol) was added to terephthalohydrazide (50.00 mg, 0.257 mmol) in absolute EtOH and stirred under reflux for 48 hours. After completion of the reaction, the precipitate formed was filtered off. The precipitate was washed three times with water and ethanol, dried in a vacuum oven. Finally, the Schiff base compound (**TDH-CB**) was recrystallized with hot ethanol to obtain yellow crystals.

Yield: 65 %, Melting Point: 344-346 ^{0}C, ^{1}H NMR (400 MHz, DMSO) δ 12.38 (s, 2H), 11.60 (s, 2H), 8.74 (s, 2H), 8.16 – 8.04 (m, 4H), 8.03 – 7.93 (m, 3H), 7.93 – 7.80 (m, 6H), 7.72 (d, *J* = 8.2 Hz, 3H), 7.07 (d, *J* = 8.1 Hz, 2H). ^{13}C NMR (100 MHz, DMSO) δ 162.77, 158.60, 148.43, 144.41, 133.32, 129.92, 128.65, 128.41, 128.23, 127.37, 119.84, 117.80, 109.75.

Results and Discussion

Preparation of the Chemosensor TDH-CB

The synthesis of TDH-CB involves two distinct steps: the preparation of compound 3'-formyl-4'-hydroxy-[1,1'-biphenyl]-4-carbonitrile (CBA) was prepared by the reaction of 4'-hydroxy-[1,1'-biphenyl]-4-carbonitrile by the Duff reaction with HMTA in trifluoroacetic acid. Then, TDH-CB was easily synthesized by the condensation reaction of CBA with terephthalodihydrazide with 65 % yield as illustrated in Schema 1.

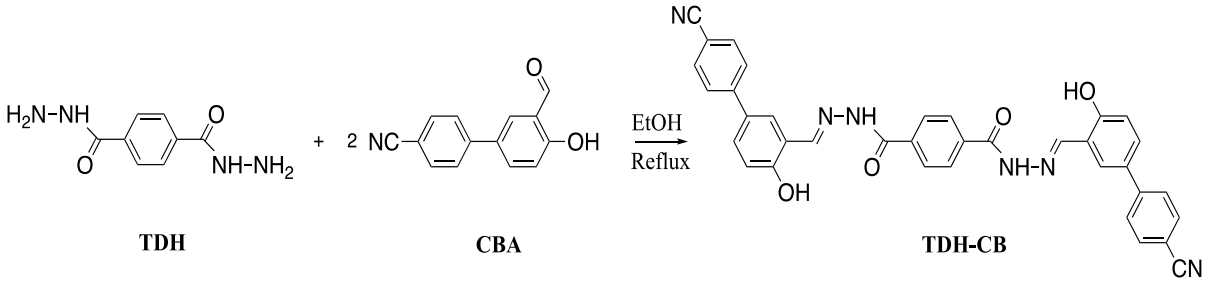

TDH **CBA** **TDH-CB**

Schema 1. The Synthesis procedure for the **TDH-CB**

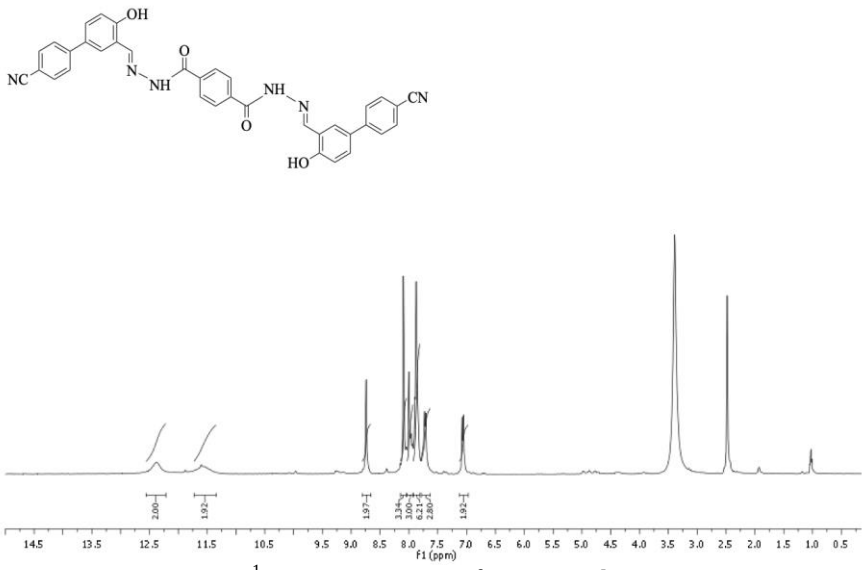

Figure 1. ^{1}H-NMR spectrum of Compound **TDH-CB**

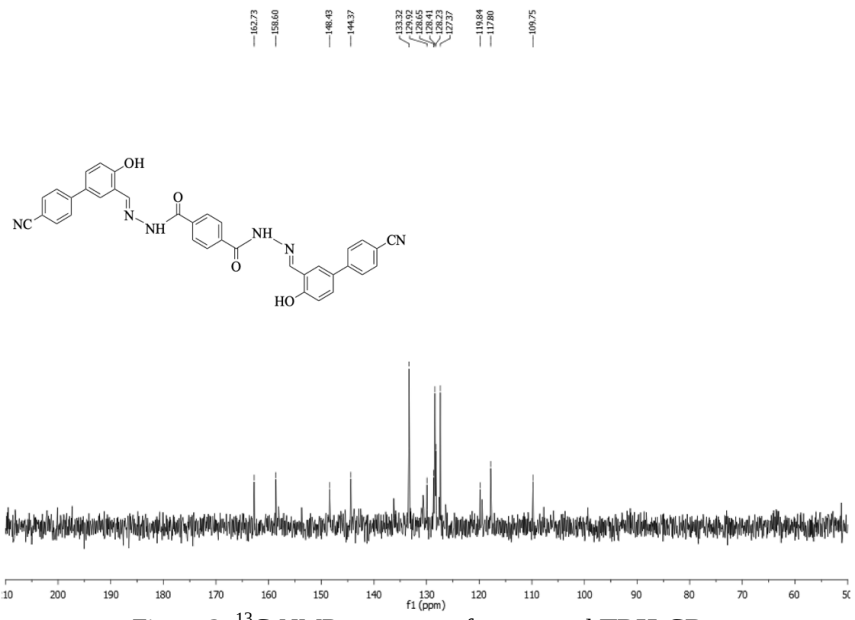

Figure 2. ^{13}C-NMR spectrum of compound **TDH-CB**

Emission Study

The stock solution of **TDH-CB** (10 mM) was prepared in DMSO and then diluted 5 µM in EtOH/HEPES (9/1, v/v). The tested metal perchlorate salts were utilized as (10^{-2} M).

Fluorescence Studies of TDH-CB versus Al^{3+}

Firstly, selectivity determination was made within metals (Fe^{3+}, Ag^{+}, Ca^{2+}, Cr^{3+}, Li^{+}, Sr^{2+}, Ni^{2+}, Ba^{2+}, Pb^{2+}, Mn^{2+}, Cd^{2+}, Hg^{2+}, Co^{2+}, Cu^{2+}, Cs^{+}, Na^{+}, Mg^{2+}, Fe^{2+}, Zn^{2+}, Al^{3+}). For this study, the interaction between the solution of TDH-CB compound prepared in EtOH/HEPES (9:1) solvent medium and metal ions was investigated by fluorescence spectroscopy and for this investigation, various metal (Fe^{3+}, Ag^{+}, Ca^{2+}, Cr^{3+}, Li^{+}, Sr^{2+}, Ni^{2+}, Ba^{2+}, Pb^{2+}, Mn^{2+}, Cd^{2+}, Hg^{2+}, Co^{2+}, Cu^{2+}, Cs^{+}, Na^{+}, Mg^{2+}, Fe^{2+}, Zn^{2+}, Al^{3+})) ions (10 equiv.) were added to 5 µM TDH-CB solution. As a result of this study, it was determined that it was selective against Al^{3+} metal (Fig.3).

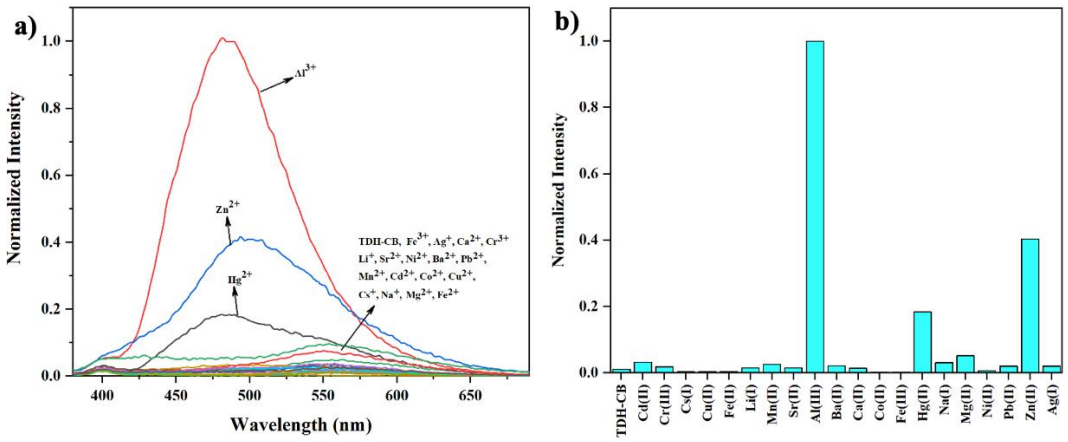

Figure 3. a) Fluorescence spectrum of **TDH-CB** compound in the presence of different metals (λ_{ex}: 360 nm; Ex-Slit: 10, Em-Slit: 8; λ_{em}: 489 nm), b) Fluorescence selectivity column graph of **TDH-CB** compound in the presence of different metals.

Fluorescence titration experiments were performed to better understand the interactions of **TDH-CB** and Al^{3+} metal (Figure 4.a). As seen in Figure 4.a, a significant increase in fluorescence is observed at 489 nm because of the addition of different concentrations of Al^{3+} metal solutions to the **TDH-CB** compound solution (5 µM). In addition, the JOB method was used to examine the **TDH-CB-Al^{3+}** complexation. Upon examining the JOB Plot graph, it is evident that the peak occurs at 0.5 (Figure 4.b). This indicates that the complexation of **TDH-CB** with Al^{3+} occurs in a 1:1 ratio.

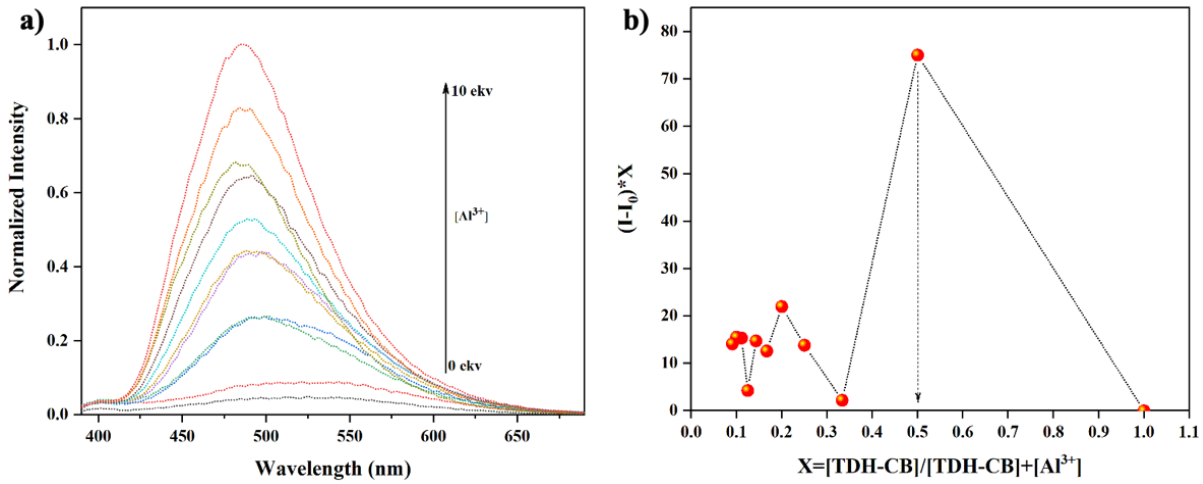

Figure 4. a) FL response of **TDH-CB** with increasing amount of Al^{3+} (0–10 eqv). **b)** Job's plot showing the 1:1 stoichiometry

Apart from the above-mentioned studies, research was carried out to determine the optimum pH range for **TDH-CB-Al^{3+}** complexation (Figure 5.a). From Figure 5.a, it is understood that the pH range of 6-7 is the most suitable range for the studies. In addition, a plot of the fluorescence intensity of the complexation of **TDH-CB** receptor with Al^{3+} was made against time (Figure 5.b). The graph shows how quickly (less than a minute) the receptor **TDH-CB** chemosensor forms a stable complex with the Al^{3+} metal.

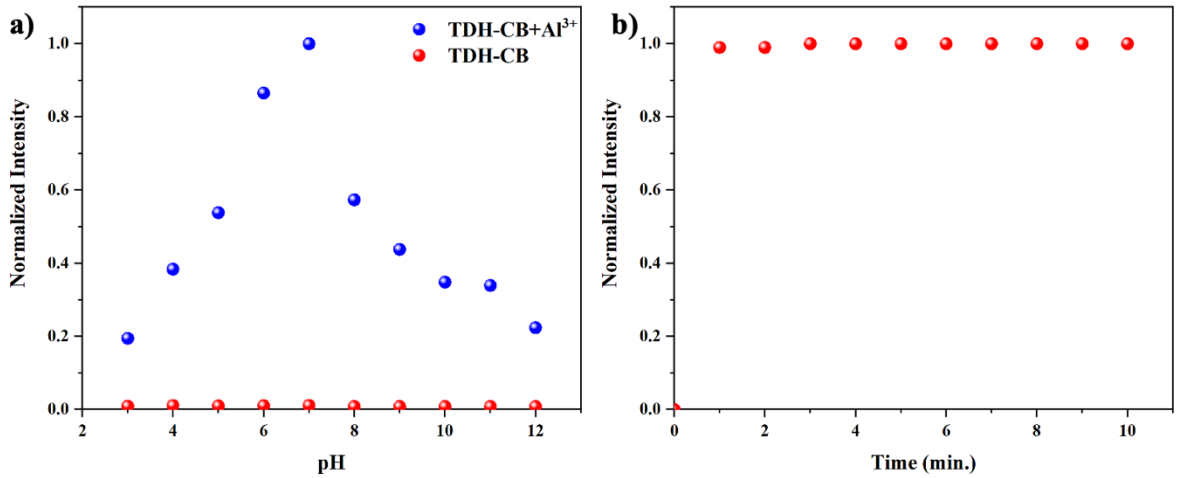

Figure 5. a) Effect of pH on the fluorescence intensity of TDH-CB and TDH-CB-Al^{3+} complex. b) Time-dependent fluorescence intensity changes of **TDH-CB** in the presence of Al^{3+}

It is crucial to ascertain whether the selective metal ion competition is with other metal ions for the compounds to be a useful sensor in terms of fluorimetric. The competition of the **TDH-CB** combination against Al^{3+} ions was conducted in the presence of additional metal ions to elucidate this situation (Figure 6). Examining the competition graph reveals that the Al^{3+} metal interacts with Cu2+, Fe3+, and Fe2+ metals, causing some quenching of the **TDH-CB-Al^{3+}** complex's fluorescence intensity.

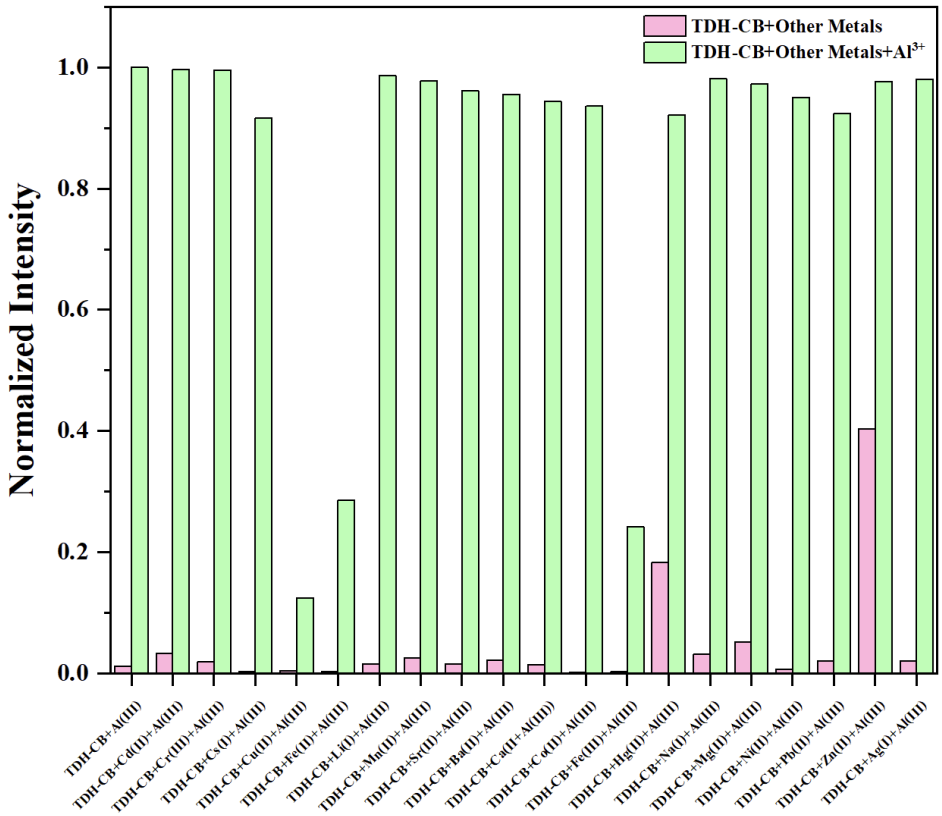

Figure 6. Fluorescence intensity at 489 nm of TDH-CB in response to Al^{3+} in the presence of interfering cations (10.0 eqv).

Conclusion

In summary, a new Schiff bases including of terephthalohydrazide fluorogenic chemosensor for Al^{3+} detection has been successfully synthesized. Fluorescence studies of **TDH-CB** chemosensor clearly showed that it is a selective Schiff base for Al^{3+} metal. For the detection of Al^{3+} on a range of pertinent competitor metal ions, the chemosensor **TDH-CB** demonstrated good performance. Chemosensor **TDH-CB** can fluorimetrically detect Al^{3+} metal ions in the neutral pH range and in a short time (less than 1 min). When all these conditions are evaluated, it can be said that the **TDH-CB** chemosensor is a usable sensor for the fluorimetric detection of Al^{3+} metal ions.

Scientific Ethics Declaration

The author declares that the scientific ethical and legal responsibility of this article published in EPSTEM journal belongs to the author.

Acknowledgements or Notes

* This article was presented as an oral presentation at the International Conference on Research in Engineering, Technology and Science (www.icrets.net) held in Thaskent/Uzbekistan on August 22-25, 2024.

*This work is part of Arjan Akbar Hameed HAMEED's doctoral thesis.

References

Ali, R., Alminderej, F., Messaoudi, S., & Saleh, S. (2021). Ratiometric ultrasensitive optical chemisensor film based antibiotic drug for Al(III) and Cu(II) detection. *Talanta*, *221*, p. 121412.

Alici, O., & Aydin, D. (2021). A Schiff-base receptor based on phenolphthalein derivate appended 2-furoic hydrazide: Highly sensitive fluorogenic “turn on” chemosensor for Al3+. *Journal of Photochemistry and Photobiology A: Chemistry*, *404*, 112876.

Alici, O., & Erdemir, S. (2015). A cyanobiphenyl containing fluorescence “turn on” sensor for Al3+ ion in CH3CN–water. *Sensors and Actuators B: Chemical*, *208*, 159-163.

Chen, W., Xu, H., Ju, L., & Lu, H. (2021). A highly sensitive fluorogenic “turn-on” chemosensor for the recognition of Cd2+ based on a hybrid purine-quinoline Schiff base. *Tetrahedron*, *88*, 132123.

Deibel, M. A., Ehmann, W. D., & Markesbery, W. R. (1996). Copper, iron, and zinc imbalances in severely degenerated brain regions in Alzheimer's disease: possible relation to oxidative stress. *Journal of the Neurological Sciences*, *143*(1-2), 137-142.

Erdemir, S., Malkondu, S., & Kararkurt, S. (2020). Synthesis and cell imaging studies of an unusual “OFF–ON” fluorescent sensor containing a triazole unit for Al 3+ detection via selective imine hydrolysis. *Analyst*, *145*(10), 3725-3731.

Fu, J., Yao, K., Chang, Y., Li, B., Yang, L., & Xu, K. (2019). A novel colorimetric-fluorescent probe for Al3+ and the resultant complex for F− and its applications in cell imaging. *Spectrochimica Acta Part A: Molecular and Biomolecular Spectroscopy*, *222*, 117234.

Golbedaghi, R., Ildiz, G. O., Azadbakht, R., & Fausto, R. (2022). A new tetramine bis (2-naphthol)-derivative fluorescent chemosensor for aluminum ion (Al3+). *Journal of Molecular Structure*, *1250*, 131775.

Hajari, S., Keypour, H., Rezaei, M. T., Farida, S. H. M., & Gable, R. W. (2022). New 15-membered macrocyclic Schiff base ligand; synthesis some Cd (II), Mn (II) and Zn (II) complexes, crystal structure, cytotoxicity, antibacterial and antioxidant activity. *Journal of Molecular Structure*, *1251*, 132049.

Keypour, H., Aidi, M., Mahmoudabadi, M., Karamian, R., Asadbegy, M., & Gable, R. W. (2019). Synthesis, X-ray crystal structural, antioxidant and antibacterial studies of new Cu (II) macroacyclic Schiff base complex with a ligand containing homopiperazine moiety. *Journal of Molecular Structure*, *1198*, 126666.

Mahalakshmi, G., Kumar, P. S., Vennila, K. N., Sivaraman, G., Seenivasaperumal, M., & Elango, K. P. (2020). Multi-site probe for selective turn-on fluorescent detection of Al (III) in aqueous solution: synthesis, cation binding, mode of coordination, logic gate and cell imaging. *Methods and Applications in Fluorescence*, *8*(3), 035003.

Nemati, L., Keypour, H., Shahabadi, N., Hadidi, S., & Gable, R. W. (2021). Synthesis, characterization and DNA interaction of a novel Pt (II) macroacyclic Schiff base complex containing the piperazine moiety and its cytotoxicity and molecular docking. *Journal of Molecular Liquids*, *337*, 116292.

Sen, S., Mukherjee, T., Chattopadhyay, B., Moirangthem, A., Basu, A., Marek, J., & Chattopadhyay, P. (2012). A water soluble Al 3+ selective colorimetric and fluorescent turn-on chemosensor and its application in living cell imaging. *Analyst*, *137*(17), 3975-3981.

Xu, H., Chen, W., Zhang, W., Ju, L., & Lu, H. (2020). A selective purine-based fluorescent chemosensor for the "naked-eye" detection of zinc ions (Zn 2+): Applications in live cell imaging and test strips. *New Journal of Chemistry*, *44*(35), 15195-15201.

Yue, Y., Dong, Q., Zhang, Y., Sun, Y., & Gong, Y. (2015). A highly selective "turn-on" fluorescent chemosensor based on 8-aminoquinoline for detection of Zn^{2+}. *Anal. Methods*, *7*(13), 5661-5666.

Zeynali, H., Keypour, H., Hosseinzadeh, L., & Gable, R. W. (2021). The non-templating synthesis of macro-cyclic Schiff base ligands containing pyrrole and homopiperazine and their binuclear nickel (II), cobalt (II) and mononuclear platinum (II) complexes: X-ray single crystal and anticancer studies. *Journal of Molecular Structure*, *1244*, 130956.

Author Information

Onder Alici
Selcuk University, Science Faculty, Department of Chemistry, Konya, Türkiye
Contact e-mail: onderkimya@gmail.com

Arjan Akbar Hameed
Selcuk University, Science Faculty, Department of Chemistry, Konya, Türkiye

To cite this article:

Alici, O., & Hameed, A. A. (2024). Synthesis of new schiff bases including of terephthalohydrazide and sensor application. *The Eurasia Proceedings of Science, Technology, Engineering & Mathematics (EPSTEM), 29,* 113-119.

The Eurasia Proceedings of Science, Technology, Engineering & Mathematics (EPSTEM)
ISSN: 2602-3199

The Eurasia Proceedings of Science, Technology, Engineering & Mathematics (EPSTEM), 2024

Volume 29, Pages 120-127

ICRETS 2024: International Conference on Research in Engineering, Technology and Science

The Flame Retardancy Performance of Aluminum Hypophosphite and its Synergistic Effect with Expandable Graphite in Carbon Fiber Reinforced Poly (Lactic Acid) Composites

Lemiye Atabek-Savas
Erciyes University

Soner Savas
Erciyes University

Mehmet Dogan
Erciyes University

Ozkan Ozmen
Erciyes University

Celil Canberk Yalcin
Erciyes University

Abstract: The aim of this study is to investigate the effects of both aluminum hypophosphite (AHP) and its synergistic effect with expandable graphite (EG) on the thermal and flame retardant properties of carbon fiber reinforced polylactic acid (PLA) composites. The composites were produced by melt blending method by keeping the carbon fiber (CF) ratio (30 wt.%) constant. The flame retardancy effect of AHP was studied at three different concentrations (10, 15, 20 wt.%). The synergic effect studies were also carried out using mixture formulations of 7 wt.% AHP and 3 wt.% EG, 5 wt.% AHP and 5 wt.% EG. The characterization of the composites was performed using thermogravimetric analysis (TGA), mass loss cone (MLC), limiting oxygen index (LOI) and vertical burning tests (UL-94 V). The TGA results showed that only the addition of AHP decreased the thermal stability, while the addition of AHP and EG combination did not affect the thermal properties much. From the LOI and UL-94 V test results, it was determined that only the addition of AHP significantly increased the LOI values and the composites passed to UL-94 V0 rating. It was found that the LOI values increased with the addition of AHP and EG combination, but this increase was less compared to the composite containing only AHP (20 wt.%). However, these composites failed the UL-94 V test. The MLC test results showed that only the addition of AHP significantly reduced the pHRR values, while the combination of AHP and EG was close to these values. As a result, only the addition of AHP improved the thermal and flame retardant properties of carbon fiber reinforced PLA more than the combination of AHP and EG.

Keywords: Polylactic acid, Aluminum hypophosphite, Expandable graphite, Flame retardancy.

Introduction

Large quantities of synthetic polymers are produced worldwide and a significant amount of them introduced the ecosystem as industrial waste products (Nampoothiri et al, 2010). As well as polluting the ecosystem, these polymers consume petrochemical resources and produce large amounts of greenhouse gases (Wang et al, 2019). Therefore, it is important to develop biodegradable materials that can replace synthetic polymers to eliminate

environmental problems and support sustainable development (Nampoothiri et al, 2010; Wang et al, 2019). Among the numerous biodegradable polymers, poly(lactic acide) (PLA) is the most researched and used material with the brightest development prospects (Nampoothiri et al, 2010; Rasal et al, 2010; Faraf et al, 2016). PLA is a linear aliphatic thermoplastic polyester produced from renewable resources such as starch and sugar, corn, potato, cane molasses, sugar-beet etc (Wang et al, 2019; Rasal et al, 2010; Zhu et al, 2016; Murariu & Dubois, 2016). It has a high level of biocompatibility, high stiffness and UV-stability (Wang et al, 2019). Due to its inherent properties, PLA occupies a key position in the bio-polymers market, which has led to an increased commercial interest in PLA and a large number of scientific studies on it (Rasal et al, 2010; Murariu & Dubois, 2016; Lee & Wang, 2006; Hsieh et al, 2016).

Although PLA has many advantages, it also has drawbacks such as brittleness and low temperature resistance, limiting its use in applications where high toughness and temperature resistance are required (Wang et al, 2019). These drawbacks of PLA can be manipulated by adding various additives such as some tough polymers and fibers. However, fibers are more effective in improving the mechanical properties of PLA (Wang et al, 2019; Avérous, 2008; Lin et al, 2014). Both natural and synthetic fibers can be used to improve the mechanical properties of PLA. In addition, synthetic fibers have higher strength than natural fibers and therefore improve the mechanical properties of PLA more effectively (Wang et al, 2019). Due to its high strength, modulus and outstanding thermal properties, carbon fiber is a very popular fiber in industry (Cheng et al, 2014).

As PLA and its composites are flammable, flame retardant treatments are required to expand their range of applications (Yang et al, 2015). The most effective substances used to improve the flame retardant performance of PLA are metal hydroxides, halogenated compounds, phosphorus and silicon-containing compounds (Gu et al, 2019). The eco-friendly and low-cost aluminum hypophosphite (AHP) is one of the phosphorus-containing flame retardants and is highly effective in PLA, PET, PBT and PA (Savas et al, 2020; Tang et al, 2012). Tang, G. et al. reported that a flame retardant PLA containing 20 wt.% AHP achieved the highest UL 94 rating of V-0 (Tang et al, 2012). Another study by Gu et al. showed that a high LOI value of 28.8 can be achieved with the addition of 20% AHP to PLA (Gu et al, 2019).

The expanded graphite (EG) is a material obtained by adding sulfuric acid or nitric acid between graphite layers. The addition of EG improves the mechanical, thermal, electrical and barrier properties of various polymers (Tang et al, 2013). It is also a flame retardant with intumescent and smoke suppressing properties. When EG is exposed to heat, it could expand to form large volumes of "worm-like" insulative char (Tang et al, 2013; Zhu et al, 2018). The EG is used in combination with phosphorous based flame retardants to increase the flame retardant efficiency as a synergistic agent (Tang et al, 2013; Zhu et al, 2018; Yang et al, 2016; Ji et al, 2020; Shih et al, 2004; Feng & Qian, 2014). Zhu et al. (2018) used EG and APP to prepare flame-retardant PLA composites. Results showed that PLA composites with 15 wt.% APP/EG (1:3) combination achieved an LOI of 36.5 and a V0 class in UL-94 testing. They emphasized that this composite has better properties compared to composites containing only EG and AHP (Zhu et al, 2011). A series of flame retardant PLA composites containing aluminum hypophosphite (AHP) and EG were investigated by Tang et al. They reported that an optimum result was achieved when 10 wt% each of AHP and EG were added to PLA. This combination resulted in a UL 94 V-0 rating with an LOI value of 34% (Tang et al, 2013).

Except for the studies mentioned above, there is no study that examines the effect of AHP and EG combination on the flame retardancy properties of carbon fiber reinforced PLA composites. This study aimed to examine the synergistic effect of AHP and EG on the flame retardant properties of carbon fiber reinforced PLA composites. Their flame retardancy and combustion properties were investigated by (limiting oxygen index) LOI, vertical burning test (UL-94) and mass loss cone (MLC) and their thermal stability was analyzed by thermogravimetric analysis (TGA).

Materials and Methods

Poly(lactic acid) (PLA) Ecolen HZ40P was provided by Hellenic Petroleum (Greece). It has a density and melt flow rate of 0.90 g/cm^3 (ASTM D792) and 12 g/10 min (2.16 kg, 230 °C, ASTM D1238), respectively. Carbon fiber (CF), trade name AC0101, was obtained from DOWAKSA (Yalova, Turkey). Aluminum hypophosphite (AHP) was supplied from Beijing Purkinje General Instrument Co. Ltd. (China). Expandable graphite (EG), trade name TEG 315, was purchased from Minelco Ltd. (Italy). The coefficient of expansion, bulk density and pH of EG are >220 mL/gm at 1000°C, 0.45-0.5 g/cm^3 and 5-7, respectively.

Production of PLA Composites

Prior to extrusion, PLA and all additives were dried at 80 °C for 12 hours. Extrusion was performed using a rotating twin screw extruder (Gulnar, Turkey) with a barrel temperature profile of 30-200-205-210-205-200 °C and a screw speed of 150 rpm. Mixing was done using the proportions in Table 1. After mixing, the composites were chopped into pellets. The pellets were used to shape standard size specimens for flammability tests using an injection molding machine (Xplore IM12, Netherlands) with a barrel temperature of 210 °C and mold temperature of 20 °C. The injection pressure was set at 8 bar. The flame retardancy of AHP and its synergistic effect with EG was investigated under 30 wt. % constant CF addition.

Characterization Method

The thermal properties of PLA and its composites were carried out by thermogravimetric analysis (Hitachi-High Tech STA-7300) at a heating rate of 10 °C/min from room temperature to 700 °C under nitrogen atmosphere. The LOI values were determined according to ASTM D2863 using a Limiting Oxygen Index Analyzer (FTT) on 130 × 6.5 × 3.2 mm^3 test bars. UL 94 V tests were performed according to ASTM D3801 on specimens with dimensions 130 × 13 × 3.2 mm^3. MLC testing was carried out on 100 × 100 × 3 mm3 specimens according to ISO 13927 standard using a Mass Loss Cone (FTT, UK). The specimens were characterized under a heat flux of 35 kW/m^2.

Results and Discussions

Thermal Decomposition Behavior

The decomposition behavior of PLA and its composites investigated with TGA analysis under nitrogen atmosphere. Plots of TGA and DTG are given in Figure 1. The related data are tabulated in Table 1. Pure PLA degrades in single step with maximum degradation rate at 366 °C and leaves 5.5 % residue at 700 °C.

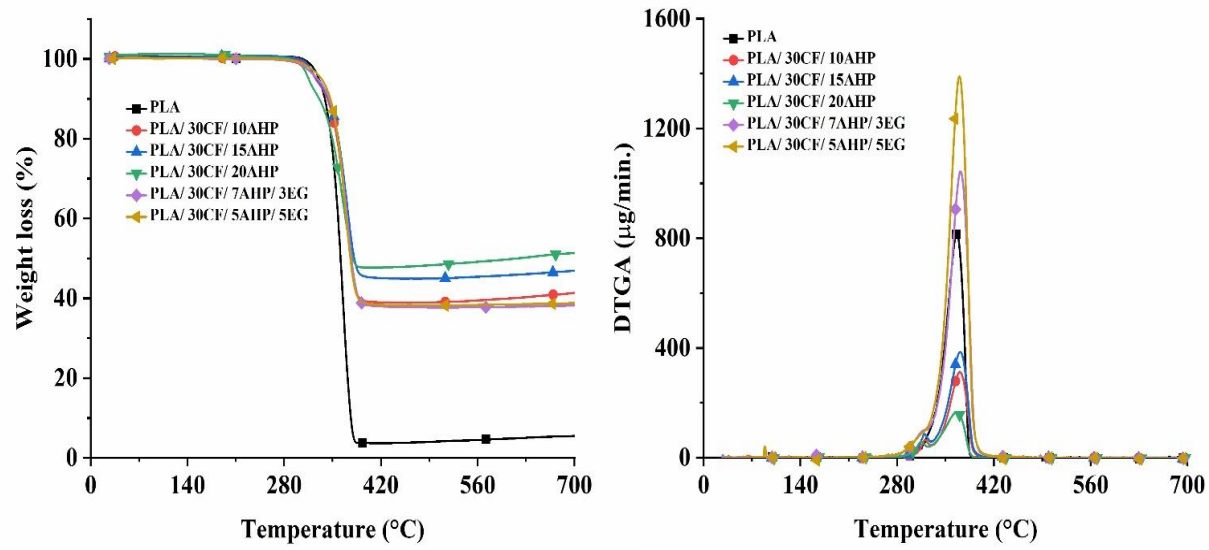

Figure 1. The TGA and DTG curves of PLA and its composites

The composites containing only AHP as a flame retardant degraded in single step. The initial degradation temperature ($T_{5\%}$) of these composites is lower compared to PLA. Similar results were observed in the study conducted by Doğan et al (Savas et al, 2020). The maximum degradation temperature (T_{max}) of the composites slightly increased with the addition of AHP. This increase is due to the fact that phosphate and pyrophosphate formed by the degradation of AHP acts as a promoting formation of residue in PLA (Wang et al, 2022). This is also supported by the increase in residue amounts shown in Table 1. The increase indicates that AHP react with PLA and more residues can be obtained. A similar trend has been observed in previous studies (Savas et al, 2020).

Table 1. TGA tests results of PLA and its composites

Sample	$T_{5\%}$ (°C)	T_{max} (°C)	Residue (%)
PLA	329	366	5.50
PLA/ 30CF/ 10AHP	322	370	41.3
PLA/ 30CF/ 15AHP	323	371	46.9
PLA/ 30CF/ 20AHP	320	370	51.2
PLA/ 30CF/ 3EG/ 7AHP	327	371	38.2
PLA/ 30CF/ 5EG/ 5AHP	330	369	38.8

The addition of EG in combination with AHP did not significantly change the $T_{5\%}$ value and slightly increased the T_{max} values of the composites, compared to PLA. At last, the char yield of the composites containing a combination of AHP and EG is high compared to pure PLA and low compared to the composites containing only AHP. That proves that there is an antagonistic effect between EG and AHP. Similar trend of results was observed in a study in which APP was used together with EG. The swelling of the EG to form a worm-like structure causes the interface between the polyphosphoric acid and its environment to widen, resulting in accelerated degradation and reduced residue yield (Meng et al, 2009).

Flammability Properties

Combustion resistance of PLA and its composites was determined by LOI and UL94 V tests. The results of LOI and UL-94 V tests are presented in Table 2. The pure PLA has LOI value of 21.3% and achieved V2 rating in UL-94 V test. The LOI values of the composites containing only AHP increased with increasing AHP concentration and reached V0 rating in UL-94 V test. Here, AHP increased the combustion resistance of the composites by forming an effective char layer. This char layer protected the composites against further combustion by preventing mass and heat transfer (Tang et al, 2012).

Table 2. LOI and UL-94 V tests results of PLA and its composites

Sample	LOI	UL-94 V
PLA	21.3	V2
PLA/ 30CF/ 10AHP	29.2	V0
PLA/ 30CF/ 15AHP	32.0	V0
PLA/ 30CF/ 20AHP	32.7	V0
PLA/ 30CF/ 3EG/ 7AHP	29.2	BC
PLA/ 30CF/ 5EG/ 5AHP	28.6	BC

The LOI values of the composites containing a combination of AHP and EG increased compared to pure PLA, but could not exceed the LOI values of the composites containing only AHP. It also failed the UL-94 V test and did not qualify for any test rating. This result indicates the existence of an antagonistic effect between EG and AHP.

Mass Loss Calorimeter Studies

Combustion behavior of PLA and its composites was evaluated by mass loss cone. Figure 2 shows the HRR curves of PLA and its composites and the relevant data are listed in Table 3, including time to ignition (TTI), peak heat release rate (pHRR), average heat release rate (avHRR), total heat evolution (THE) and residue amount. The pHRR of pure PLA reached 385 kW/m^2 after 95 s ignition. After adding only AHP, the pHRR values of the composites decrease significantly. The PLA/30CF/20AHP decreased to 123 kW/m^2, which was 68% lower than that of pure PLA. This reduction indicates that AHP is effective in the gas and condense phase by forming protective char layer. The pHRR values of the composites containing the combination of AHP and EG were close to the composites containing only AHP and changed slightly. This shows that both AHP and the combination of AHP and EG reduce the fire risk to a similar extent. The THE values of the composites containing only AHP decreased compared to pure PLA. This reduction is due to the decrease in the amount of combustible material (PLA) with increasing char content and the inability to complete pyrolysis due to the barrier effect of char (Has et al, 2022). The value of THE of the composites containing the combination of AHP and EG increased compared to the composites containing only AHP. From the photographs given in Figure 3, it is thought that this is due to the char containing more pores compared to the composites containing only AHP.

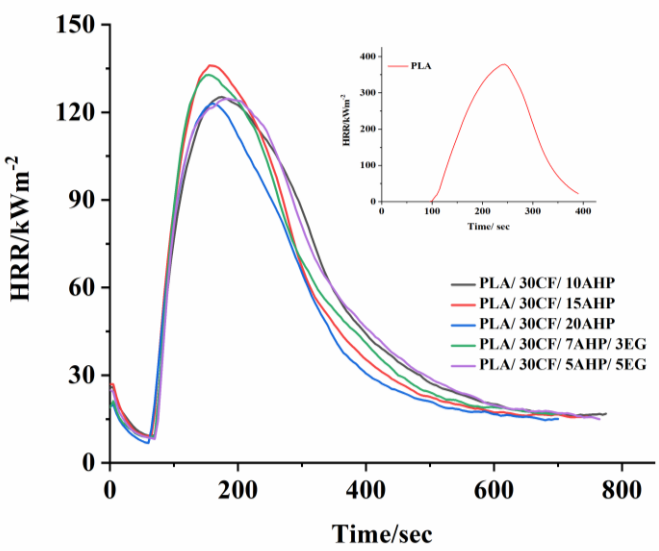

Figure 2. The HRR curves of PLA and its composites

The addition of both AHP and the combination of AHP and EG causes decreases in TTI value. It is thought that this decrease is due to the decrease in the thermal stability of the composites as described in the TGA section. Flammable gas formation starts early in composites with reduced thermal stability. This causes the composites to ignite earlier. In addition, black colored carbon fibers absorb too much heat, causing early degradation of the polymer (Aydogan et al, 2023).

Table 3. MLC results of PLA and its composites

Sample	TTI (sec.)	pHRR (kW/m^2)	THE (MJ/m^2)	Char Residue (%)
PLA	95	385	68	2.8
PLA/ 30CF/ 10AHP	70	125	26	38.0
PLA/ 30CF /15AHP	65	136	32	39.5
PLA/ 30CF/ 20AHP	59	123	30	48.8
PLA/ 30CF/ 7AHP/ 3EG	68	132	34	38.1
PLA/ 30CF/ 5AHP/ 5EG	71	124	36	38.9

The addition of flame retardants significantly increases the amount of char residue compared to PLA. The highest char residue content was obtained in PLA/30CF/20AHP. The combination of AHP and EG did not reach this value and produced less char residue. This is a result of the antagonistic effect.

The digital photograph of char residues is shown in Figure 3. It can be seen from the images that; PLA has no char residue after MLC tests. The char layer for the composites containing only AHP (PLA/30CF/15AHP) is fine and rigid, but it is so brittle that several cracks and holes are formed during combustion. These holes are caused by the impact of PH_3 gas generated during the degradation of AHP (Tang et al, 2013). Composite containing a combination of AHP and EG has more holes. It is thought that these holes could weaken the barrier effect of the char layer and led to bad flame retardant properties. These results were in agreement with LOI and UL-94 V performances.

Conclusion

This study investigated the effects of aluminum hypophosphite (AHP) and its combination with expandable graphite (EG) on the thermal and flame retardant properties of carbon fiber reinforced polylactic acid (PLA) composites. Through comprehensive testing including thermogravimetric analysis (TGA), mass loss calorimeter (MLC), limiting oxygen index (LOI), and vertical burning tests (UL-94 V), several key findings emerged:

- Firstly, for the composites containing only AHP, the LOI value increased with increasing AHP concentration (10, 15, 20 wt.%), and all composites achieved a UL-94 tested V0 rating. All this represents a significant improvement in flame retardancy.

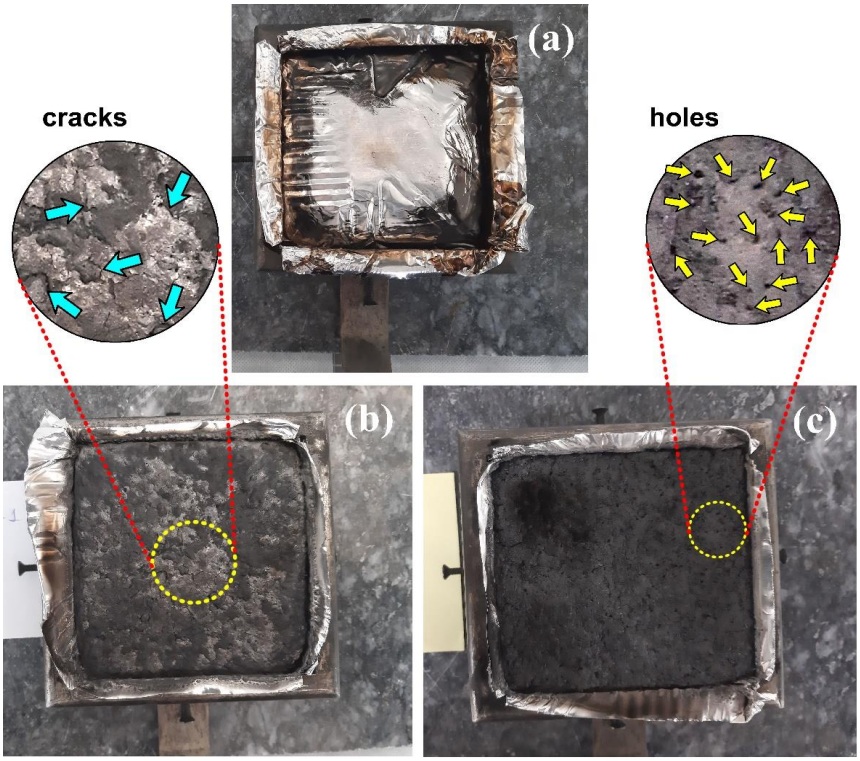

Figure 3. Digital photography of (a) PLA, (b) PLA/30CF/15 AHP, (c) PLA/30CF/7AHP/3EG

- Secondly, the synergistic effect of AHP and EG, tested at formulations of 7 wt.% AHP and 3 wt.% EG, and 5 wt.% AHP and 5 wt.% EG, demonstrated mixed results. Although the combinations of AHP and EG improved LOI compared to pure PLA, they failed the UL-94 test. However, the LOI values of the combinations OF AHP and EG could not reach the LOI values of the composites containing only AHP.
- Thirdly, as evaluated by TGA, it is indicated that AHP alone slightly decreased thermal stability, whereas the addition of EG alongside AHP did not significantly affect this property.
- Moreover, MLC results showed that AHP effectively reduced the peak heat release rate (pHRR), crucial for fire safety, while the combination with EG performed similarly to composites with AHP alone.

Overall, the findings underscore that AHP is more effective in enhancing the thermal and flame retardant properties of carbon fiber reinforced PLA compared to its combination with EG. This research provides valuable insights for optimizing the formulation of flame retardant composites, contributing to advancements in materials science aimed at enhancing fire safety in various applications of carbon fiber reinforced PLA composites.

Scientific Ethics Declaration

The authors declare that the scientific ethical and legal responsibility of this article published in EPSTEM journal belongs to the authors.

Acknowledgements or Notes

This article was presented as an oral presentation at the International Conference on Research in Engineering, Technology and Science (www.icrets.net) held in Thaskent/Uzbekistan on August 22-25, 2024.

References

Avérous, L. (2008). Polylactic acid: synthesis, properties and applications. *Monomers, Polymers, and Composites from Renewable Resources*, 433-450.

Aydogan, Y., Savas, L.A., Erdem, A., Hacioglu, F. & Dogan, M. (2023). Performance evaluation of various phosphorus compounds on the flammability properties of short carbon fiber-reinforced polyamide 6 composites. *Fire and Materials, 47,* 737-850.

Cheng, K.C., Lİn, Y.H., Guo, W., Chuang, T.H., Chang, S.C., Wang S.F. & Don, T.M. (2014). Flammability and tensile properties of polylactide nanocomposites with short carbon fibers. *Journal of Material Science, 50,* 1605-1612.

Faraf, S., Anderson, D.G. & Langer, R. (2016). Physical and mechanical properties of PLA, and their functions in widespread applications - A comprehensive review. *Advanced Drug Delivery Reviews, 107,* 367-392.

Feng, F. & Qian, L. (2014). The flame retardant behaviors and synergistic effect of expandable graphite and dimethyl methylphosphonate in rigid polyurethane foams. *Polymer Composites,* 35, 201-417.

Gu, L., Qui, J., Qui, J., Yao, Y., Sakai, E. & Yang, L. (2019). Mechanical properties and degrading behaviors of aluminum hypophosphite-poly(lactic acid) (pla) nanocomposite. *Polymer-Plastics Technology and Materials, 58,* 126-138.

Has, M., Erdem, A., Savas, L.A., Tayfun, U. & Dogan, M. (2022). The influence of expandable graphite on the thermal, flame retardant and mechanical characteristics of short carbon fiber reinforced polyamide composites. *Journal of Thermoplastic Composite Materials, 36,* 2703-3132.

Hsieh, C.T., Pan, Y.J., Lou, C.W., Huang, C.L. Lin, Z., Liao, J.M. & Lin, J.H. (2016). Polylactic acid/carbon fiber composites: Effects of functionalized elastomers on mechanical properties, thermal behavior, surface compatibility, and electrical characteristics. *Fibers and Polymers, 17,* 615-623.

Ji, W., Yoa, Y., Guo, J., Fei, B., Gu, X., Li, H., Sun, J. & Zhang, S. (2020). Toward an understanding of how red phosphorus and expandable graphite enhance the fire resistance of expandable polystyrene foams. *Journal of Applied Polymer Science, 137,* 1-13.

Lee, S.H. & Wang, S. (2006). Biodegradable polymers/bamboo fiber bio-composite with bio-based coupling agent. *Composite Part A: Applied Science and Manufacturing, 37,* 80-91.

Lin, L., Deng, C., Lin, G. & Wang, Y. (2014). Mechanical properties, heat resistance and flame retardancy of glass fiber-reinforced PLA-PC alloys based on aluminum hypophosphite. *Polymer-Plastics Technology and Engineering, 53,* 613-625.

Meng, X.Y., Ye, L., Zhang, X.G., Tang, P.M., Tang, J.H., Ji, X. & Li, Z.M. (2009). Effects of expandable graphite and ammonium polyphosphate on the flame-retardant and mechanical properties of rigid polyurethane foams. *Journal of Applied Polymer Science, 114,* 671-1355.

Murariu, M. & Dubois, P. (2016). PLA composites: From production to properties. *Advanced Drug Delivery Reviews, 107,* 17-46.

Nampoothiri, K.M., Nair, N.R. & John, R.P. (2010). An overview of the recent developments in polylactide (PLA) research. *Bioresearch Technology, 101,* 8493-8501.

Rasal, R.M., Janorkar, A. V. & Hirt, D.E. (2010). Poly(lactic acid) modifications. *Progress in Polymer Science, 35,* 338-356.

Savas, L.A., Hacioglu, F., Hancer, M. & Dogan, M. (2020). Flame retardant effect of aluminum hypophosphite in heteroatom-containing polymers. *Polymer Bulletin, 77,* 291-306.

Shih, Y.F., Wang, Y.T., Jeng R.J. & Wei, K.M. (2004). Expandable graphite systems for phosphorus-containing unsaturated polyesters. I. Enhanced thermal properties and flame retardancy. *Polymer Degradation and Stability, 86,* 339-348.

Tang, G., Wang, X., Xing, W., Zhang, P., Wang, B., Hong, N., Yang, W., Hu, Y. & Song, L. (2012). Thermal degradation and flame retardance of biobased polylactide composites based on aluminum hypophosphite. *Industrial & Engineering Chemistry Research, 51,* 11819-12154.

Tang, G., Zhang, R., Wang, X., Wang, B., Song, L., Hu, Y. & Gong, X. (2013). Enhancement of flame retardant performance of bio-based polylactic acid composites with the ıncorporation of aluminum hypophosphite and expanded graphite. *Journal of Macromolecular Science, Part A, 50,* 255-269.

Wang, G., Zhang, D., Wan, G., Li, B. & Zhao, G. (2019). Glass fiber reinforced PLA composite with enhanced mechanical properties, thermal behavior, and foaming ability. *Polymer, 181,* 121803.

Wang, Y., Yuan, J., Ma, L., Yin, X., Zhu, Z. & Song, P. (2022). Fabrication of anti-dripping and flame-retardant polylactide modified with chitosan derivative/aluminum hypophosphite. *Carbohydrate Polymers, 298,* 120141.

Yang, S., Wang, J., Huo, S., Wang, M., Wang, J. & Zhang, B. (2016). Synergistic flame-retardant effect of expandable graphite and phosphorus-containing compounds for epoxy resin: Strong bonding of different carbon residues. *Polymer Degradation and Stability,128,* 89-98.

Yang, W., Jia, Z., Chen, Y., Zhang, Y., Si, J., Lu, H. & Yang, B. (2015). Carbon nanotube reinforced polylactide/basalt fiber composites containing aluminum hypophosphite: thermal degradation, flame retardancy and mechanical properties. *RSC Advances, 5,* 105869-105879.

Zhu, H., Zhu, Q., Li, J., Tao, K., Xue, L. & Yan, Q. (2011). Synergistic effect between expandable graphite and ammonium polyphosphate on flame retarded polylactide. *Polymer Degradation and Stability, 96,* 183-189.

Zhu, Y., Romain, C. & Williams, C.K. (2016). Sustainable polymers from renewable resources. *Nature, 540,* 354-362.

Zhu, Z.M., Rao, W.H., Kang, A.H., Liao, W. & Wang, Y.Z. (2018). Highly effective flame retarded polystyrene by synergistic effects between expandable graphite and aluminum hypophosphite. *Polymer Degradation and Stability, 154,* 1-9.

Author Information

Lemiye Atabek-Savas
Erciyes University, Department of Metallurgical and Materials Engineering, Kayseri, Türkiye
Contact e-mail: *atabekl@erciyes.edu.tr*

Soner Savas
Erciyes University, Department of Metallurgical and Materials Engineering, Kayseri, Türkiye

Mehmet Dogan
Erciyes University, Department of Textile Engineering, Kayseri, Türkiye

Ozkan Ozmen
Erciyes University, Department of Industrial Design Engineering, Kayseri, Türkiye

Celil Canberk Yalcin
Erciyes University, Graduate School of Natural and Applied Sciences, Kayseri, Türkiye
Contact e-mail: *cellyalcin@gmail.com*

To cite this article:

Atabek-Savas, L., Savas, S., Dogan, M., Ozmen, O. & Yalcin, C.C. The flame retardancy performance of aluminum hypophosphite and its synergistic effect with expandable graphite in carbon fiber reinforced poly(lactic acid) composites. *The Eurasia Proceedings of Science, Technology, Engineering & Mathematics (EPSTEM),* 29, 120-127.

The Eurasia Proceedings of Science, Technology, Engineering & Mathematics (EPSTEM)
ISSN: 2602-3199

The Eurasia Proceedings of Science, Technology, Engineering & Mathematics (EPSTEM), 2024

Volume 29, Pages 128-144

ICRETS 2024: International Conference on Research in Engineering, Technology and Science

Shear Force in RC Internal Beam-Column Connections for a Beam Loaded With a Transverse Force Occupying Different Possible Positions

Albena Doicheva
University of Architecture, Civil Engineering and Geodesy (UACEG)

Abstract: Frame structures are vulnerable to seismic impacts. The frame joint is the element that is often responsible for compromising frame structures. In recent years, shear force in the beam-column connection has been pointed out as the main culprit for damage in the nodes, and from there to the entire structure. The complex nature of the stressed and strained state of the joint is due to the poor knowledge of the forces passing in the beam-beam or column-column direction. For their more accurate determination, one departs from the standard acceptance of the static scheme of the axis line of the structural elements and works with their actual dimensions. With a skillful selection of the support devices, a mathematical model of the beam is created, allowing the determination of the forces that arise along its height and that enter the joint. The magnitudes of the support reactions of the beam are applicable both to operation in the elastic stage and to the plasticization of the beam and the occurrence of a crack between the beam and the column on the face of the column. In the present work, a cantilever beam loaded with a transverse force, occupying different possible positions on the beam, is considered. The expressions for the support reactions are derived. The unfavorable position of the loading force, which results in the greatest shear force, was investigated. A comparison is made of the corresponding shear force in the beam-to-column connection, with that recommended in the literature. The results demonstrate differences of up to 18.20%. The main parameters of the cantilever beam that were monitored are cross-sectional shape, modulus of elasticity of concrete and position of the loading force.

Keywords: Beam-to-column connection, Shear force, Reinforced concrete, Large deformations, Cracking in the beam

Introduction

One of the main elements in frame structures is the beam-column connection. Its main task is to ensure the not hindered passage of forces in the beam-beam and column-column direction while preserving the integrity of the beam-column connection. Disturbances in the beam-column joint are often responsible for the damage of part of the buildings or even their destruction. Over the past few decades, many frame structures have experienced sudden failure due to joint shear during cyclic loading, such as earthquakes.

The first quantitative definition of shear strength was given in Hanson and Connor (1967). In their report on the test results of RC interior beam-column connections, the researchers defined joint shear as the horizontal force transferred to the mid-horizontal plane in a beam-column connection. They suggest that joint shear failure can be prevented by limiting the joint shear stress to the level at which joint shear failure occurs.

Based on the assumption made, design codes of different countries are created. They provided a limit value of the shear stress of the joint. Detailed review of interior and exterior joints of special moment resisting reinforced concrete frames, with reference to three codes of practices: American Concrete Institute (ACI 318M-02), New Zealand Standards (NZS 3101:1995) and Eurocode 8 (EN 1998-1 :2003) was performed by Uma & Sudhir, (2006). A number of parameters have been defined that affect the shear strength of the joint. Researchers from different countries rely on different combinations of parameters (Park & Paulay, 1975; Paulay, 1989; Lowes &

- Selection and peer-review under responsibility of the Organizing Committee of the Conference

Altoontash, 2003; Celik & Ellingwood, 2008; Tran et al., 2014; Gombosuren & Maki, 2020). This makes it impossible to create a worldwide uniform procedure for designing the shear force in the beam-column connection.

In Bakir and Boduroglu (2001), parametric studies were carried out on various parameters influencing the shear strength of the joint. The results of multiple studies on 5 parameters in relation to different countries are summarized. One of the main conclusions that emerge is that "the strength of the concrete cylinder increases the shear strength of the joint".

In Yuan et al., 2013, “a number of RC/ECC composite beam-column joints have been tested under reversed cyclic loading to study the effect of substitution of concrete with ECC in the joint zone on the seismic behaviors of composite members.” “The substitution of concrete with ECC in the joint zone was experimentally proved to be an effective method to increase the seismic resistance of beam-column joint specimens.”

In Doicheva et al. (2023-3) Seismic tests on reinforced concrete beam-column joint sub-assemblages subject to lateral and long-term vertical load was reported. The influence of an additional transverse force on the beam applied near the support of the cantilever beam is observed. It was reported that such a force did not significantly affect the beam column connection.

Shiohara (2001) proposed a new model for calculating and detailing the beam-column connection based on the capacitive design. The study shows an irrationality in the joint shear model adopted in the most current codes for the design of reinforced concrete beam-column joints. The conclusions are based on the experimental test data of twenty reinforced concrete internal beam-column connections damaged by joint shear. The analysis showed that the joint shear stress increased in most specimens, even after the initiation of apparent joint shear failure.

Problem

Hanson and Connor (1967) gave the first quantitative definition of the joint shear in an interior beam-column connection from Figure 1. The researchers defined it with Eq. (1). This is an internal force acting on the free body along the horizontal plane at the midheight of the beam-column connection.

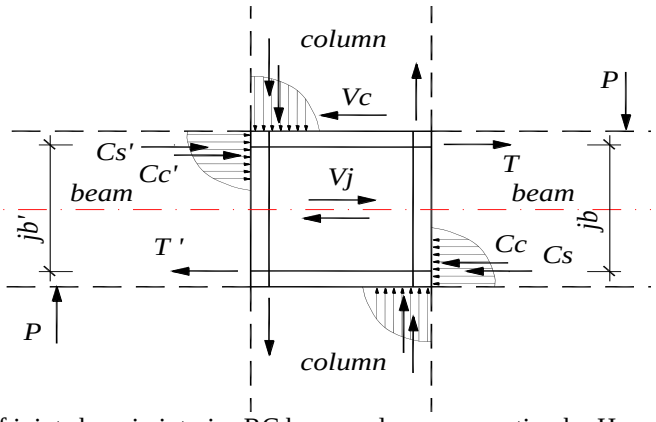

Figure 1. Definition of joint shear in interior RC beam-column connection by Hanson and Connor (1967)

$$V_j = T + C_S' + C_C' - V_C = T + T' - V_C \tag{1}$$

where: C_S and C_S' - compressive force in bottom and top longitudinal reinforcing bars in beam passing through the connection;

C_C and C_C' - compressive force in concrete on the bottom and top edge of beam;

T and T' - tensile forces in top and bottom reinforcing bars in beam passing through the connection;

V_C - column shear force

The contribution of steel and concrete is taken into account separately. This definition is clear and has been used in the design of beam-column connections in different countries.

The difficulty encountered in determining the forces T and T' from Eq. (1) leads to the adoption of another way of writing the expression for the shear force in the literature. Usually T and T' are defined by Eq. (2).

$$T = \frac{M_b}{j_b} \text{ and } T' = \frac{M'_b}{j_b} \tag{2}$$

where: M_b and M'_b - moment at column face;

j_b and j'_b - the length of bending moment arm at the column face. It is assumed to be constant and unchanging in the process of deformation.

Then Eq. (1) is rewritten from moment in the beam section at column faces into Eq. (3).

$$V_j = \frac{M_b}{j_b} + \frac{M'_b}{j'_b} - V_C \tag{3}$$

The assumption (2) obliges us to assume equal forces in the bottom and top reinforcement of the beam at the face of the column. In the author's previous publications, these values were shown to differ substantially (Doicheva, 2021), (Doicheva, 2022), (Doicheva, 2023-1), (Doicheva, 2023-2).

In this article, the following tasks are set: 1. to determine expressions for the forces from Figure 1, at the column face for a cantilever beam loaded with a transverse force, occupying different possible positions on the beam. 2. to perform comparisons of the obtained results with the results of Eq. (2) and Eq. (3).

Method

Mathematical Model of Beams

A cantilever beam is considered. The beam is statically indeterminate and prismatic. The beam is under the conditions of special bending with tension/compretion and Bernoulli-Euler hypothesis is considered.

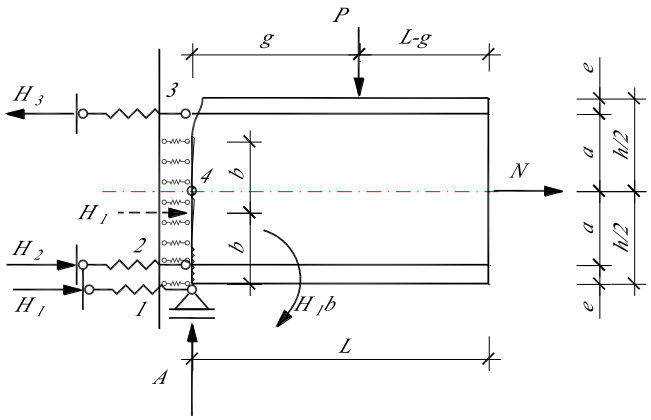

Figure 2. Supports of cantilever beam to column and symmetrical cross section

The beam is loaded with a vertical force $P\,[kN]$, which changes its position on the beam. It is monitored by the distance $g\,[cm]$. The support takes place in vertical support 1, where a vertical support reaction occurs $A\,[kN]$. At the level of the reinforcing bars, elastic supports 2 and 3, with linear spring coefficients k_2 and k_3, are introduced. They are set as the reduced tension/compression stiffness of the reinforcing bar, Eq. (4).

$$k_2 = \frac{E_2 A_2}{L} \quad \text{and} \quad k_3 = \frac{E_3 A_3}{L} \tag{4}$$

where: $L\,[cm]$ - the length of the beam;

$A_2\left[cm^2\right]$ and $A_3\left[cm^2\right]$ - the area of the cross-section of bottom and top longitudinal reinforcing bars in beam passing through the connection;

$E_2\left[kN/cm^2\right]$ and $E_3\left[kN/cm^2\right]$ - the modulus of elasticity of the bottom and top longitudinal reinforcing bars in beam passing through the connection

The supporting reactions that occur here are $H_2\left[kN\right]$ and $H_3\left[kN\right]$.

Linear spring supports act along the vertical edge of the beam, taking into account the connection of the concrete of the beam with that of the column. The forces in all the springs are reduced to one force, $H_1\left[kN\right]$. In case of large deformations, part of the vertical edge is destroyed. The unbroken edge has length $2b\left[cm\right]$. The reaction $H_1\left[kN\right]$, which is symmetrically located with respect to the intact lateral edge, moves along the height of the beam as the crack length increases. For convenience, it has been transferred $H_1\left[kN\right]$ to the support along the bottom edge (support one), after applying Poinsot's theorem concerning the transfer of forces in parallel to their directrix. This necessitated the introduction of compensating moments $H_1 b\left[kN.cm\right]$. The coefficient of the linear spring is k_1. It is set as the reduced tensile/compressive stiffness of the concrete section, Eq. (5).

$$k_1 = \frac{E_1 A_1}{L} \tag{5}$$

where: $L\left[cm\right]$ - the length of the beam;

$A_1\left[cm^2\right]$ - the area of the cross-section of the concrete

$E_1\left[kN/cm^2\right]$ - the modulus of elasticity of the concrete

As a consequence of the linear deformations in the cantilever beam, a normal axial force occurs $N\left[kN\right]$, which is introduced at the free end.

Symmetric Cross-Section

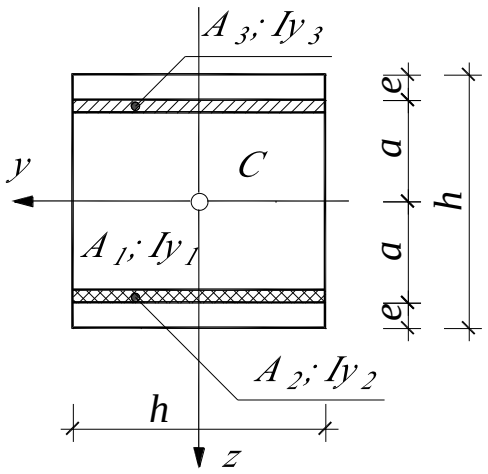

Figure 3. Symmetrical cross-section of the beam

The following notations have also been introduced:

$h\left[cm\right]$ - the heigth of the beam;

$e\left[cm\right]$ and $a\left[cm\right]$ - offset of the reinforcing bars from the top and bottom edges of the beam and from the axis of the beam, respectively;

$EA = E_1A_1 + E_2A_2 + E_3A_3$ - tensile (compressive) stiffness of the composite section, where E_2A_2, E_3A_3 and E_1A_1 are tensile (compressive) stiffness of the reinforcing bars and of the concrete, respectively;

$EI = E_1I_1 + E_2I_2 + E_3I_3$ - bending stiffness of the composite section, where E_2I_2, E_3I_3 and E_1I_1 are bending stiffness of the reinforcing bars and of the concrete cross-section, respectively;

$I_1\left(I_{y1}\right)$, $I_2\left(I_{y2}\right)$ and $I_3\left(I_{y3}\right)$ are the moment of inertia of the concrete cross-section and of the top and bottom reinforcing bars relative to the principal axis of inertia *y*.

Support Reactions

The three equilibrium conditions of statics give us respectively:

$$1.\sum V = 0 \quad \rightarrow \quad A = P \tag{6}$$

$$2.\sum H = 0 \quad \rightarrow \quad N = H_3 - H_1 - H_2 \tag{7}$$

$$3.\sum M_4 = 0 \quad \rightarrow \quad -Pg - H_1b + H_3a + H_2a + H_1\frac{h}{2} = 0 \tag{8}$$

From Eq. (8) we express H_2:

$$H_2 = \frac{Pg - H_1\left(\frac{h}{2} - b\right)}{a} - H_3 \tag{9}$$

The solution is based on Menabria's theorem about statically indeterminate systems in first-order theory.

The potential energy of deformation in special bending, combined with tension (compressure) and with the effect of linear springs taken into account, will be, Eq. (10):

$$\Pi = \frac{1}{2}\int_0^L \frac{M^2(x)}{EI}dx + \frac{1}{2}\int_0^L \frac{N^2(x)}{EA}dx + \frac{H_1^2}{2k_1} + \frac{H_2^2}{2k_2} + \frac{H_3^2}{2k_3}. \tag{10}$$

It is a well-known fact that, according to Menabria's theorem, the desired hyperstatic unknown is determined by the minimum potential energy condition with respect to it or will be, Eq. (11):

$$\frac{\partial\Pi}{\partial H_1} = 0; \quad \frac{\partial\Pi}{\partial H_2} = 0; \quad \frac{\partial\Pi}{\partial H_3} = 0. \tag{11}$$

The beam is twice statically indeterminate. This leads to using the first and third terms of Eq. (11).

The bending moments for the two parts of beam are:

$$M_1(x) = Ax + H_1b - H_1\frac{h}{2} - H_2a - H_3a, \tag{12}$$

$$M_2(x) = A(g + x) + H_1b - H_1\frac{h}{2} - H_2a - H_3a - Pg, \tag{13}$$

Substitute Eq. (6) in Eq. (12) and Eq. (13). Substitute the resulting expressions and Eq. (9), together with Eq. (7) in Eq. (10). We perform operations from Eq. (11). A system of two linear equations with respect to the two unknowns, $H_1; H_3$, is obtained. Substitute the obtained $H_1; H_3$ in Eq. (9), to express H_2. The solutions give the formulas of the three horizontal support reactions below:

$$H_1 = \frac{-Pgk_1\left\{EAh_1R_1 + 2EIL\left[k_2 2a - k_3n_2\right] + 2Lga^2K_{23}n_2\right\}}{EI\left\{EAD_1 + D_2\right\}} \tag{14}$$

$$H_2 = \frac{Pgk_2\left\{EAaR_2 + 8EILa\left[k_1 + k_3\right] + LgaK_{13}n_2^2\right\}}{2EI\left\{EAD_1 + D_2\right\}} \tag{15}$$

$$H_3 = \frac{Pgk_3\left\{4EAaR_1 + 4EIL\left[k_1n_2 + k_2 2a\right] - LgaK_{12}n_1n_2\right\}}{2EI\left\{EAD_1 + D_2\right\}} \tag{16}$$

where $h_1 = 2b - h$; $n_1 = 2a + h_1$; $n_2 = 2a - h_1$;

$K_{12} = k_1k_2$; $K_{13} = k_1k_3$; $K_{23} = k_2k_3$;

$R_1 = 2EI - k_2ga^2$; $R_2 = 8EI + g\left(k_1h_1^2 + k_3 4a^2\right)$;

$D_1 = \left(k_2 + k_3\right)4a^2 + k_1h_1^2$; $D_2 = L\left[2ak_1k_2n_1 + k_1k_3n_2^2 + k_2k_3 8a^2\right]$ (17)

The positions of the force *P*, for which the support reactions H_1, H_2 and H_3 have an extremum with respect to the distance g, are respectively:

$$g_{H_1} = \frac{EA2EI\left\{h_1 + L\left[k_2 2a - k_3n_2\right]\right\}}{2\left[EAa^2k_2h_1 - 2La^2K_{23}n_2\right]} \tag{18}$$

$$g_{H_2} = \frac{8EI\left[EA + L\left(k_1 + k_3\right)\right]}{-2\left[EA\left(4a^2k_3 + k_1h_1^2\right)\right] - LK_{13}n_2^2} \tag{19}$$

$$g_{H_3} = \frac{4EI\left\{2EAa + L\left[k_2 2a - k_1n_2\right]\right\}}{2a\left[4EAa^2k_2 + LK_{12}n_1n_2\right]} \tag{20}$$

We perform the same solution without considering the axial force in the potential energy expression. The support reactions are respectively:

$$H_1 = \frac{-Pgk_1h_1R_1}{EI\left[4a^2\left(k_2 + k_3\right) + k_1h_1^2\right]} \tag{21}$$

$$H_2 = \frac{Pagk_2R_2}{2EI\left[4a^2\left(k_2 + k_3\right) + k_1h_1^2\right]} \tag{22}$$

$$H_3 = \frac{2Pagk_3R_1}{EI\left[4a^2\left(k_2 + k_3\right) + k_1h_1^2\right]} \tag{23}$$

The maximum value of the support reactions is obtained when the loading force is located at a distance g from the support, respectively.:

$$g_{H_1} = \frac{EI}{k_2a^2}; \quad g_{H_2} = \frac{-8EI}{-2\left(4a^2k_3 + k_1h_1^2\right)}; \quad g_{H_3} = \frac{EI}{2k_2a^2} \tag{24}$$

Asymmetric Cross-Section

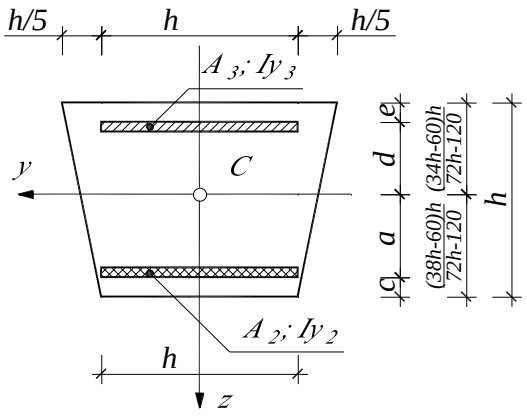

Figure 4. Asymmetrical cross-section of the beam

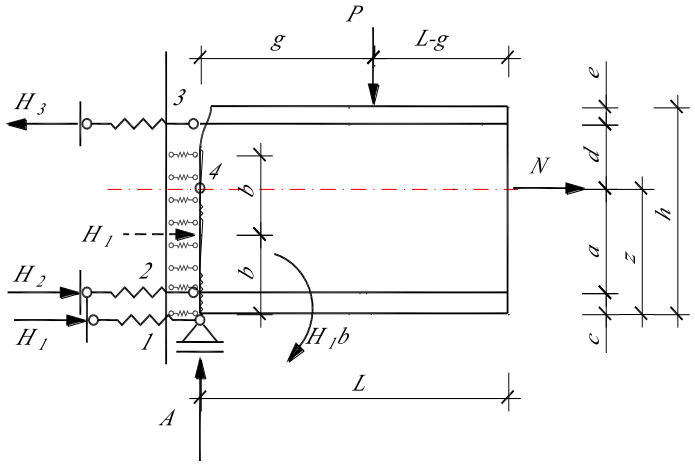

Figure 5. Supports of cantilever beam to column and asymmetrical cross section

The dimensions that are different for the asymmetrical beam compared to the symmetrical one are:

$c[cm]$ and $e[cm]$ - offset of the reinforcing bars from the top and the bottom edges of the beam, respectively;

$a[cm]$ and $d[cm]$ - offset of the top and the bottom reinforcing bars from the axis of the beam, respectively;

$z[cm]$ - offset of the principal axis of inertia *y* to the bottom edge of the beam;

The equilibrium conditions from statics are Eq. (6) and Eq. (7). Then Eq. (8) will be:

$$3.\sum M_4 = 0 \quad \rightarrow \quad -Pg - H_1 b + H_3 d + H_2 a + H_1 z = 0 \tag{25}$$

From Eq. (25) we express H_2:

$$H_2 = \frac{Pg - H_1(z-b) - H_3 d}{a} \tag{26}$$

The bending moments for the two parts of the beam are respectively:

$$M_1(x) = Ax + H_1 b - H_1 z - H_2 a - H_3 d \tag{27}$$

$$M_2(x) = A(g+x) + H_1 b - H_1 z - H_2 a - H_3 d - Pg\,, \tag{28}$$

The solution is performed as described for the symmetric section solution. The three supporting reactions are:

$$H_1 = \frac{-Pgk_1\left\{EAh_2R_1 + 2EIL\left[k_2 a + k_3 n_4\right] - LgaK_{23}(a+d)n_4\right\}}{2EI\left\{EAD_3 + D_4\right\}} \tag{29}$$

$$H_2 = \frac{Pgk_2\left\{EAaR_3 + 2EILa\left[k_1 + k_3\right] + LgaK_{13}n_4^2\right\}}{2EI\left\{EAD_3 + D_4\right\}} \tag{30}$$

$$H_3 = \frac{Pgk_3\left\{EAdR_1 + 2EIL\left[k_2 a - k_1 n_4\right] - LgK_{12}a\left(an_4 + h_2^2 - dh_2\right)\right\}}{2EI\left\{EAD_3 + D_4\right\}} \tag{31}$$

where $h_2 = b - z$; $n_3 = d + h_2$; $n_4 = h_2 - d$;

$K_{12} = k_1 k_2$; $K_{13} = k_1 k_3$; $K_{23} = k_2 k_3$;

$R_1 = 2EI - k_2 g a^2$; $R_3 = 2EI + g\left(k_1 h_2^2 + k_3 d^2\right)$;

$D_3 = k_1 h_2^2 + k_2 a^2 + k_3 d^2$; $D_4 = L\left[ak_1 k_2\left(a + h_2\right) + k_1 k_3 n_4^2 + k_2 k_3 a(a+d)\right]$ (32)

The extremum study of Eq. (29), Eq. (30) and Eq. (31) with respect to the position of the load *P* gives us the expressions for *g* to the three support reactions.

$$g_{H_1} = \frac{EA2EI\left\{h_2 + L\left[k_2 a + k_3 n_4\right]\right\}}{2\left[EAa^2 k_2 h_2 + LaK_{23}\left(a+d\right)n_4\right]} \tag{33}$$

$$g_{H_2} = \frac{2EI\left[EA + L\left(k_1 + k_3\right)\right]}{2\left[-EA\left(d^2 k_3 + k_1 h_2^2\right) - LK_{13}n_4^2\right]} \tag{34}$$

$$g_{H_3} = \frac{2EI\left\{EAd + L\left[k_2 a - k_1 n_4\right]\right\}}{2a\left[EAda^2 k_2 + LK_{12}a\left(an_4 + h_2^2 - dh_2\right)\right]} \tag{35}$$

A solution for an asymmetrical section was performed without considering the axial force in the strain potential energy expression.

$$H_1 = \frac{-Pgk_1 h_2 R_1}{2EI\left[k_2 a^2 + k_3 d^2 + k_1 h_2^2\right]} \tag{36}$$

$$H_2 = \frac{Pagk_2 R_2}{2EI\left[k_2 a^2 + k_3 d^2 + k_1 h_2^2\right]} \tag{37}$$

$$H_3 = \frac{Pdgk_3 R_1}{2EI\left[k_2 a^2 + k_3 d^2 + k_1 h_2^2\right]} \tag{38}$$

The support reactions have an extremum with respect to the distance *g*, which gives the position of the force *P*. For each support reaction, it is respectively:

$$g_{H_1} = \frac{EI}{k_2 a^2}; \quad g_{H_2} = \frac{-2EI}{2\left(k_3 d^2 + k_1 h_2^2\right)}; \quad g_{H_3} = \frac{EI}{k_2 a^2} \tag{39}$$

The all solutions was performed in the symbolic environment of the MATLAB R2017b program.

Results and Discussion

For the numerical results, a beam with a cross-section of $75/75\,cm$ and $30/30\,cm$ were introduced. For all examples considered $P = const$, the distances $e = 3\left[cm\right]$ and $c = 3\left[cm\right]$. And more $A_2 = A_3 = 75\left[cm^2\right]$ for a cross-section of $75/75\,cm$ and $A_2 = A_3 = 30\left[cm^2\right]$ for a cross-section of $30/30\,cm$. The modulus of elasticity of reinforcing bars are $E_2 = E_3 = 39000\left[kN/cm^2\right]$. Two examples with a difference only in the modulus of elasticity of concrete are considered. The modules used are $E_1 = 1700\left[kN/cm^2\right]$ for normal concrete and $E_1 = 3900\left[kN/cm^2\right]$ for High-strength concrete. The beam is with a length of $L = 200\,cm$.

Case I – Symmetrical Cross Section

The distance $b\left[cm\right]$ varies in the interval $\left[37.5, 0\right)$ and $\left[15, 0\right)$ for a cross-section of $75/75\,cm$ and $30/30\,cm$, respectivly. It is monitored by the ratio h/b. In Figure. 6 shows the variation of the parameters of the three support reactions for two cross-sections - *75/75cm* and *30/30cm*, with two modulus of elasticity of the concrete - E_1*=1700kN/cm*^{2} and E_1*=3900kN/cm*^{2}, for the position of the force *P* at *g =L=200cm*. We see that as the cross section of the beam decreases, the forces H_1, H_2 and H_3 increase. An increase in the modulus of elasticity of concrete leads to an increase in H_1, a decrease in H_2 and a slight increase in H_3, followed by a steeper decrease with increasing crack size.

Example I- the modulus of elasticity of the concrete is $E_1 = 1700\left[kN/cm^2\right]$	*Example II*- the modulus of elasticity of the concrete is $E_1 = 3900\left[kN/cm^2\right]$
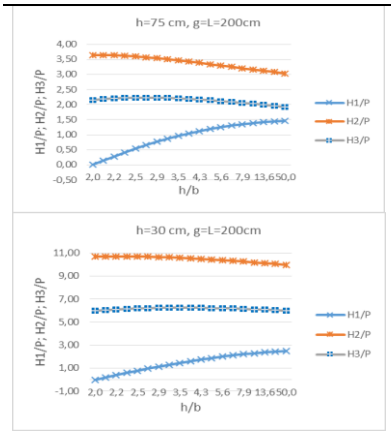	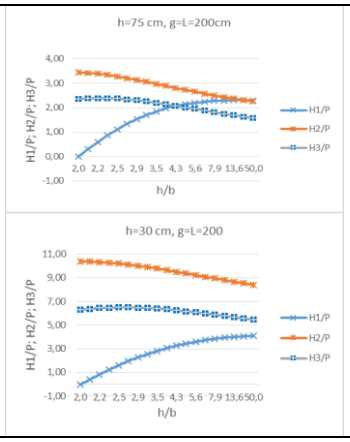
a)	b)

Figure 6. The parameters of the three support reactions for symmetrical cross section; a) *75/75cm* and *30/30cm* for E_1*=1700kN/cm*^{2}; b) *75/75cm* and *30/30cm* for E_1*=3900kN/cm*^{2}

Example I- the modulus of elasticity of the concrete is $E_1 = 1700\left[kN/cm^2\right]$	*Example II*- the modulus of elasticity of the concrete is $E_1 = 3900\left[kN/cm^2\right]$
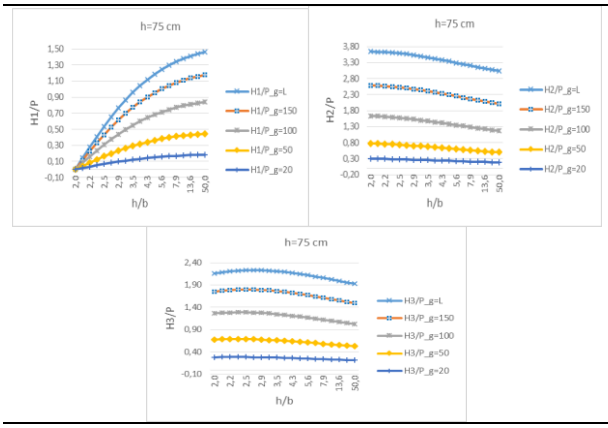	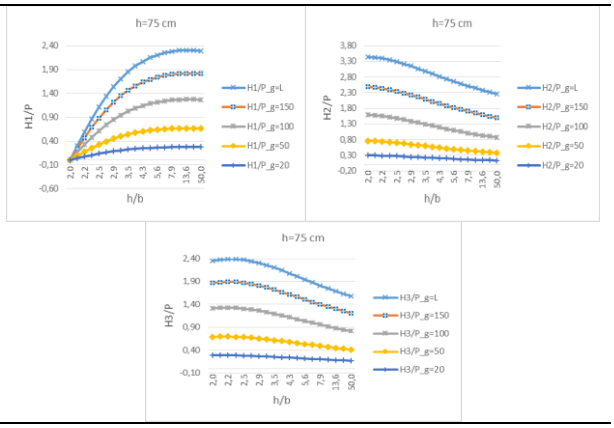
a)	b)
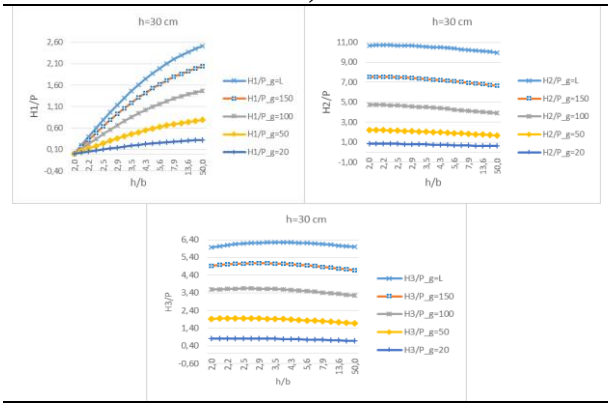	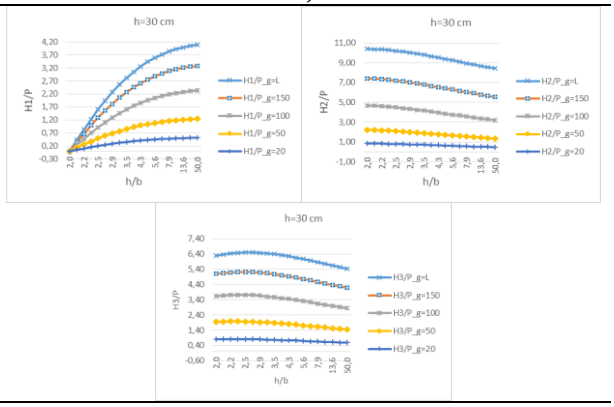
c)	d)

Figure 7. Changing the parameters of the three support reactions for values of *g=L=200cm; 150cm; 100cm; 50cm; 20cm* for various cross sections and E_1 modules; a) *75/75cm* E_1*=1700kN/cm*^{2}; b) *75/75cm* E_1*=3900kN/cm*^{2}; c) *30/30cm* E_1*=1700kN/cm*^{2}; d) *30/30cm* E_1*=3900kN/cm*^{2}

Figure 7 is a summary of the values to the parameters of the three support reactions for different positions of the force *P*, set by *g=L=200cm; 150cm; 100cm; 50cm; 20 cm*. We have two cross-sections, at two modulus of elasticity of concrete. From Figure 7 the same conclusions can be drawn as than Figure 6. H_1 has a value of 0 before the crack appears.

Case II – Asymmetrical Cross Section

The distance $b\left[cm\right]$ varies in the interval $\left[z_C, 0\right)$. It is monitored by the ratio h/b.

Example III- the modulus of elasticity of the concrete is $E_1 = 1700\left[kN/cm^2\right]$	*Example IV*- the modulus of elasticity of the concrete is $E_1 = 3900\left[kN/cm^2\right]$
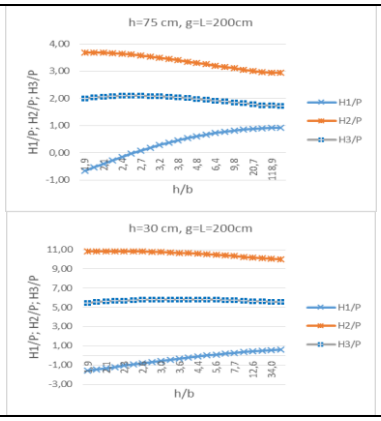	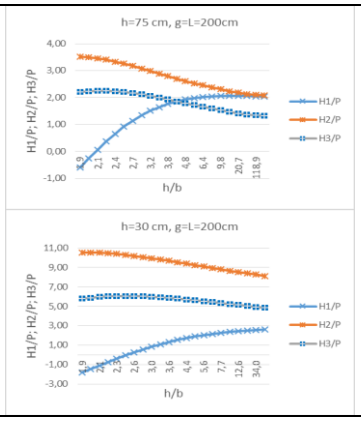
a)	b)

Figure 8. The parameters of the three support reactions for asymmetrical cross section; a) *75/75cm* and *30/30cm* for E_1=1700kN/cm^2; b) *75/75cm* and *30/30cm* for E_1=3900kN/cm^2

Example III- the modulus of elasticity of the concrete is $E_1 = 1700\left[kN/cm^2\right]$	*Example IV*- the modulus of elasticity of the concrete is $E_1 = 3900\left[kN/cm^2\right]$
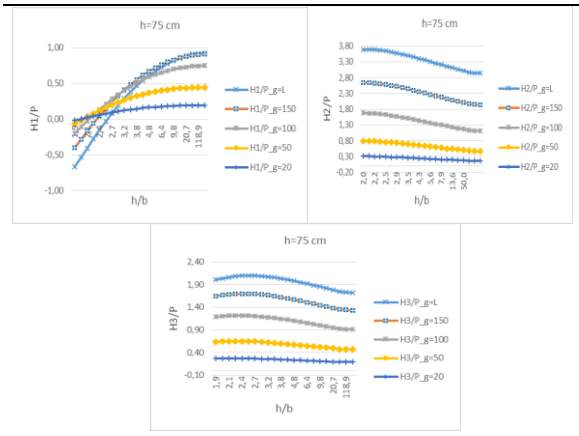	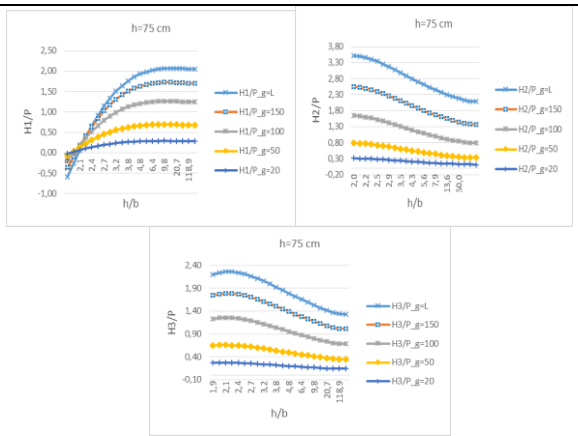
a)	b)
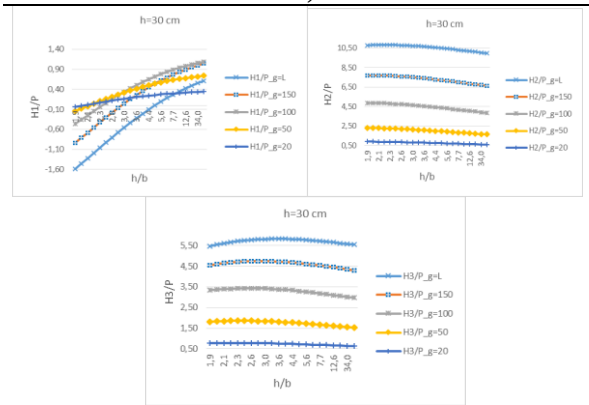	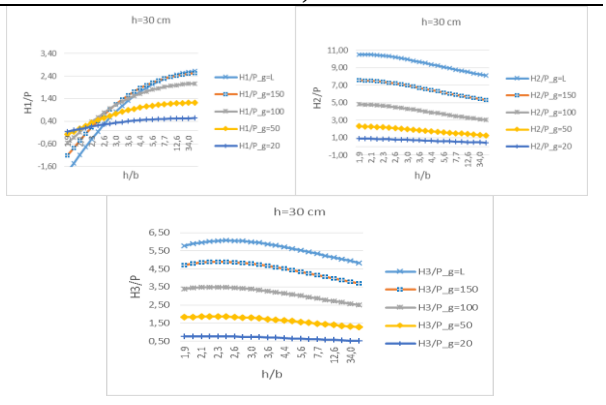
c)	d)

Figure 9. Changing the parameters of the three support reactions for values of *g=L=200cm; 150cm; 100cm; 50cm; 20cm* for various asymmetrical cross sections and E_1 modules; a) *75/75cm* E_1=1700kN/cm^2; b) *75/75cm* E_1=3900kN/cm^2; c) *30/30cm* E_1=1700kN/cm^2; d) *30/30cm* E_1=3900kN/cm^2

Figure 8 shows the parameters of the three support reactions for two asymmetric cross-sections - *75/75cm* and *30/30cm*, for two modulus of elasticity of concrete - E_1*=1700kN/cm*^{2} and E_1*=3900kN/cm*^{2}, for position of force *P* at *g=L=200cm*. The increasing trend of the three support reactions with decreasing cross-sectional size is maintained. It is noticeable that the increase in H_1 is weak. In the asymmetrical cross-sections, H_1 has negative values, until the appearance of a crack, i.e. it is on tension at the assumed cross-sectional shape. At E_1*=3900kN/cm*^{2} H_1 increases, H_2 decreases and H_3 slightly increases, and after *b/h= 2,4* it decreases steeply.

Figure 9 is a summary of the values of the parameters of the three support reactions for different positions of the force *P*, set by *g=L=200cm; 150cm; 100cm; 50cm; 20 cm*. We have two cross-sections, at two modulus of elasticity of concrete. The trend is maintained that as the cross section of the beam decreases, the forces increase. It is noteworthy that, while for all considered cases, moving the force *P* away from the support (*g* increases) leads to a rapid increase in H_1, for the smaller asymmetric cross-section – *30/30cm* H_1 has larger values at *g=150cm* and *100cm*. Increasing the modulus of elasticity of concrete results in an increase in H_1, a decrease in H_2, and a slight increase in H_3, followed by a steeper decrease with increasing crack size.

Case III - Symmetrical Cross Section Without Considering the Axial Force in the Potential Energy Expression

Example V- the modulus of elasticity of the concrete is $E_1 = 1700\left[kN/cm^2\right]$	*Example VI*- the modulus of elasticity of the concrete is $E_1 = 3900\left[kN/cm^2\right]$
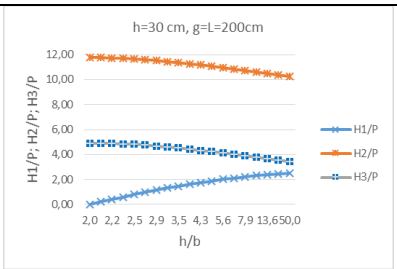	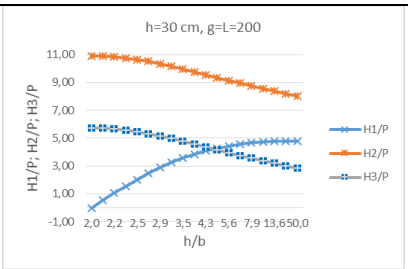
a)	b)

Figure 10. The parameters of the three support reactions for symmetrical cross section and neglected axial force; a) *30/30cm* for E_1*=1700kN/cm*^{2}; b) *30/30cm* for E_1*=3900kN/cm*^{2}

The comparison of Figure 6 and Figure 10 shows that neglecting the axial force in the strain potential energy expression does not lead to quantitative differences in H_1, while H_2 increases from *9%* to *2,5%*, H_3 decreases from *22%* to *75%* for E_1*= 1700kN/cm*^{2}. For E_1*=3900kN/cm*^{2}, H_1 increases from *20%* to *15%*, H_2 first increases from *5%* and then decreases to *4,6%*, H_3 decreases from *9%* to *90%*.

Example V - the modulus of elasticity of the concrete is $E_1 = 1700\left[kN/cm^2\right]$	*Example VI* - the modulus of elasticity of the concrete is $E_1 = 3900\left[kN/cm^2\right]$
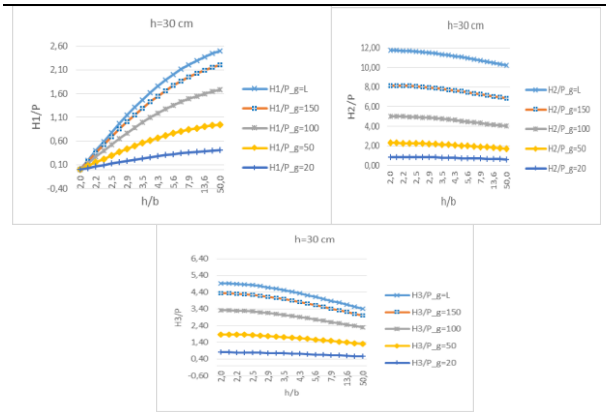	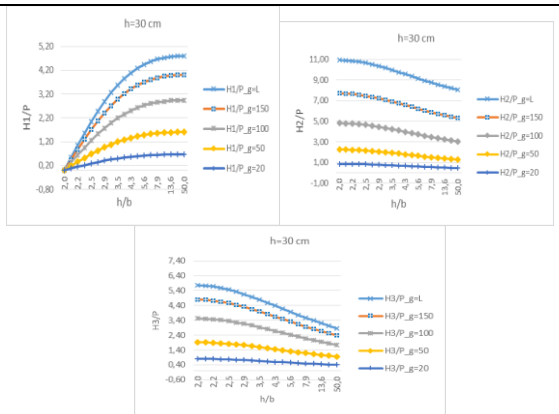
a)	b)

Figure 11. Changing the parameters of the three support reactions for values of *g=L=200cm; 150cm; 100cm; 50cm; 20cm* for various E_1 modules, symmetrical cross section and neglected axial force; a) *30/30cm* for E_1*=1700kN/cm*^{2}; b) *30/30cm* for E_1*=3900kN/cm*^{2}

A comparison of Figure 7 c) and d) with Figure 11 shows that H_1 is preserved without much change in value, H_2 increases, H_3 decreases for E_1=1700kN/cm^2. For E_1=3900kN/cm^2 H_1 increases, H_2 increases, H_3 decreases.

Case IV - Asymmetric Cross-Section Neglected Axial Force in the Strain Potential Energy Expression

Example VII- the modulus of elasticity of the concrete is $E_1 = 1700\left[kN/cm^2\right]$	*Example VIII*- the modulus of elasticity of the concrete is $E_1 = 3900\left[kN/cm^2\right]$
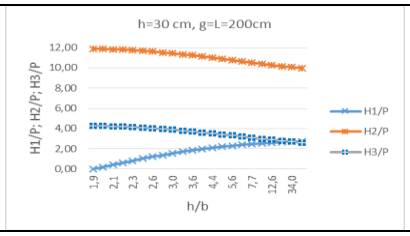	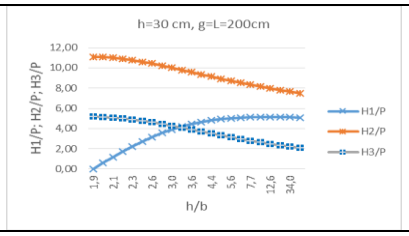
a)	b)

Figure 12. The parameters of the three support reactions for asymmetrical cross section and neglected axial force; a) *30/30cm* for E_1=1700kN/cm^2; b) *30/30cm* for E_1=3900kN/cm^2

A comparison of Figure 8 and Figure 12 shows that neglecting the axial force in the strain potential energy expression leads to an increase in H_1 about 2 times. H_2 remains almost unchanged, and H_3 decreases from *30%* to *110%*.

Example VII - the modulus of elasticity of the concrete is $E_1 = 1700\left[kN/cm^2\right]$	*Example VIII* - the modulus of elasticity of the concrete is $E_1 = 3900\left[kN/cm^2\right]$
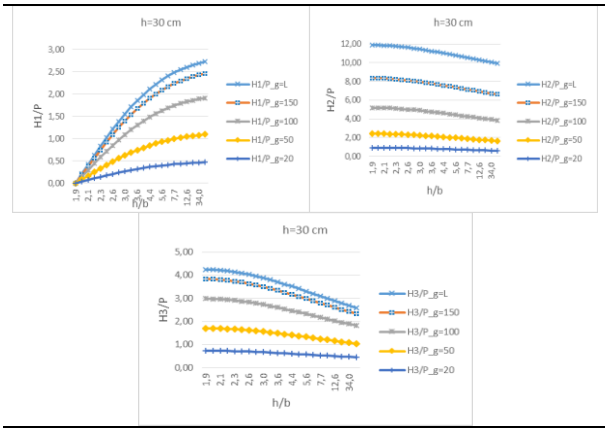	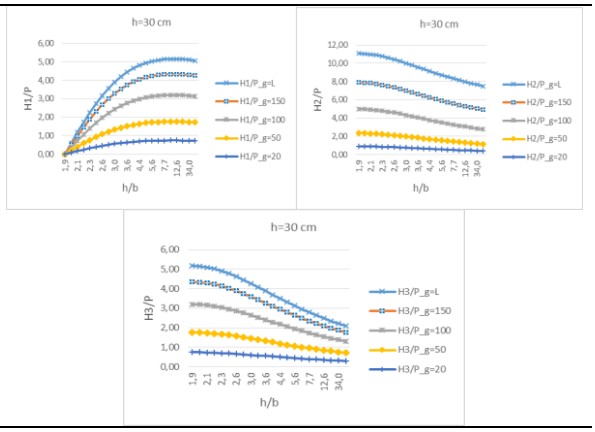
a)	b)

Figure 13. Changing the parameters of the three support reactions for values of *g=L=200cm; 150cm; 100cm; 50cm; 20cm* for various E_1 modules and asymmetrical cross section; a) *30/30cm* for E_1=1700kN/cm^2; b) *30/30cm* for E_1=3900kN/cm^2

Figure 13 shows the variation of the parameters of the three support reactions for an asymmetric cross-section of *30/30cm* for different positions of the loading force *P*, measured by the distance *g*. Values for two modulus of elasticity of concrete are demonstrated. It can be seen that as the concrete strength increases, H_1 increases, H_2 slightly decreases, and H_3 increases.

New Definition of Joint Shear in Interior RC Beam-Column Connection With the Calculated Forces H_1, H_2 and H_3.

We already know the magnitudes of the forces H_3; H_2' *and* H_1'. Then the determination of the Shear Force in RC Interior Beam-Column Connections instead of Eq. (3) will be by Eq. (40).

$$V_j = H_3 + H_2' + H_1' - V_c \tag{40}$$

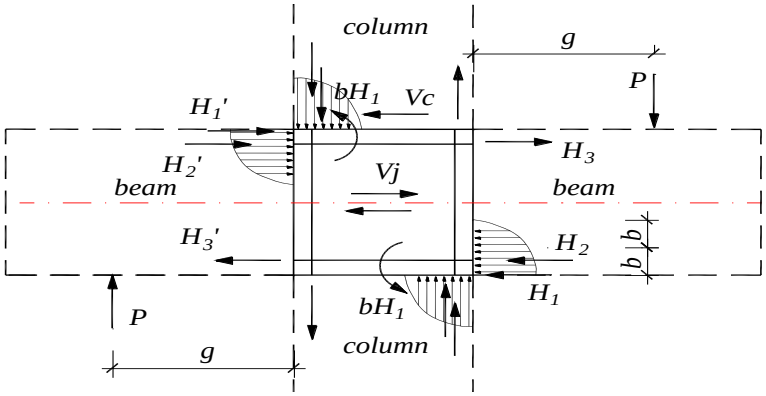

Figure 14. New definition of joint shear in interior RC beam-column connection with the calculated forces H_1, H_2 and H_3

If the frame is symmetric and other conditions being equal, we will have the equality of $H_1 = H_1'$, $H_2 = H_2'$ and $H_3 = H_3'$. Then Eq. (40) becomes Eq (41)

$$V_j = H_3 + H_2 + H_1 - V_c \,. \tag{41}$$

The comparison of Eq. (3) and Eq. (41) will be carried out by Eq. (42)

$$H_3 + H_2 + H_1 \overset{?}{=} \frac{M_b}{j_b} + \frac{M_b'}{j_b'} \,. \tag{42}$$

where - $M_b = Pg$ is the moment of the cantilever beam on the face of the column.

Comparison of the Results of Eq. (3) and Eq. (41) by Eq. (42)

Case I - symmetrical cross section

Example I- the modulus of elasticity of the concrete is $E_1 = 1700\left[kN/cm^2\right]$	*Example II*- the modulus of elasticity of the concrete is $E_1 = 3900\left[kN/cm^2\right]$
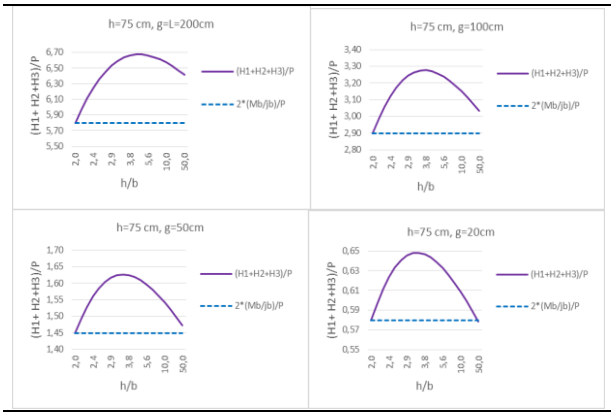	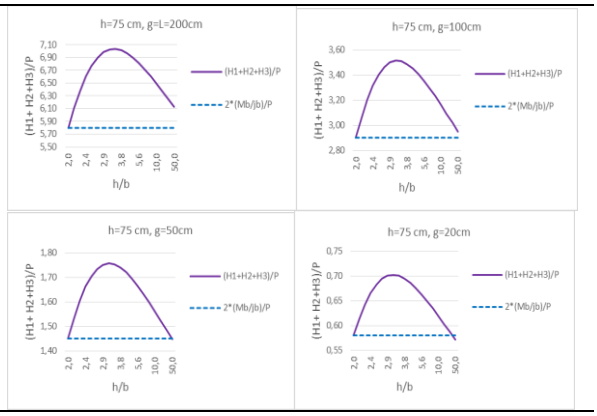
a)	b)

Figure 15. Comparison of the results of Eq. (3) and Eq. (41) for symmetrical cross section; a) *75/75cm* for E_1*=1700kN/cm*^{2}; b) *75/75cm* for E_1*=3900kN/cm*^{2}

Figure 15 shows comparison of the results of Eq. (3) and Eq. (41) for different possible positions of the force *P*, set by *g=L=200cm; g=100cm; g=50cm; g=20cm*. For all positions of the force *P*, the shear force determined with the exact values of the forces H_1, H_2 and H_3 is greater than what is recommended in the Eq. (3) - $\frac{M_b}{j_b} + \frac{M_b'}{j_b'}$. The difference is from *13.15%* to *10.57%*.

The following Table 1, Table2 and Table3 show the percentage differences between the part of the shear force determined according to Eq. (3) and the one calculated with the exact forces H_1, H_2 and H_3.

Table 1. Comparison of the results of Eq. (3) and Eq. (41) for symmetrical cross section

section		g	h/b	$\frac{H_3+H_2+H_1}{P}$	$\frac{\frac{M_b}{j_b}+\frac{M'_b}{j'_b}}{P}$	$\frac{(H_3+H_2+H_1)-\left(\frac{M_b}{j_b}+\frac{M'_b}{j'_b}\right)}{(H_3+H_2+H_1)}100\%$
Si me tri cal	75/75	200	4,3	6,67	5,80	13,15
		150	4,3	4,96	4,35	12,27
	E_1=1700	100	3,8	3,28	2,90	11,54
		50	3,5	1,63	1,45	10,92
		20	3,5	0,65	0,58	10,57
Si me tri cal	30/30	200	7,9	18,61	16,67	10,42
		150	4,8	13,68	12,5	8,61
	E_1=1700	100	3,8	8,98	8,33	7,22
		50	3,5	4,44	4,17	6,15
		20	3,2	1,77	1,67	5,61
Si me tri cal	75/75	200	3,5	7,04	5,80	17,61
		150	3,2	5,27	4,35	17,51
	E_1=3900	100	3,2	3,51	2,90	17,50
		50	3,2	1,76	1,45	17,49
		20	3,2	0,70	0,58	17,48
Si me tri cal	30/30	200	3,8	19,04	16,67	12,44
		150	3,5	14,13	12,5	11,52
	E_1=3900	100	3,5	9,34	8,33	10,76
		50	3,2	4,63	4,17	10,10
		20	3,2	1,85	1,67	9,74

Table 2. Comparison of the results of Eq. (3) and Eq. (41) for asymmetrical cross section

section		g	h/b	$\frac{H_3+H_2+H_1}{P}$	$\frac{\frac{M_b}{j_b}+\frac{M'_b}{j'_b}}{P}$	$\frac{(H_3+H_2+H_1)-\left(\frac{M_b}{j_b}+\frac{M'_b}{j'_b}\right)}{(H_3+H_2+H_1)}100\%$
Asi me tri cal	75/75	200	4,3	5,91	5,80	1,91
		150	3,8	4,54	4,35	4,14
	E_1=1700	100	3,5	3,10	2,90	6,46
		50	3,2	1,59	1,45	8,76
		20	3,2	0,65	0,58	10,14
Asi me tri cal	30/30	200	6,5	16,34	16,67	-2,02
		150	4,4	12,42	12,5	-0,64
	E_1=1700	100	3,6	8,44	8,33	1,23
		50	3,3	4,31	4,17	3,28
		20	3,0	1,75	1,67	4,55
Asi me tri cal	75/75	200	3,2	6,55	5,80	11,46
		150	3,2	5,02	4,35	13,37
	E_1=3900	100	2,9	3,42	2,90	15,25
		50	2,9	1,75	1,45	17,12
		20	2,9	0,71	0,58	18,20
Asi me tri cal	30/30	200	3,6	16,88	16,67	1,28
		150	3,3	12,94	12,5	3,41
	E_1=3900	100	3,0	8,83	8,33	5,58
		50	3,0	4,52	4,17	7,82
		20	3,0	1,83	1,67	9,11

The results of Table 1 show differences between the exact method ($H_3+H_2+H_1$) and the approximate method $\left(\frac{M_b}{j_b}+\frac{M'_b}{j'_b}\right)$ used in Eq.(3) for symmetrical section. For sections with normal concrete - E_1*=1700kN/cm*^{2} and large cross-sections (*75/75cm*) the differences between the two methods is more than *10%*, for all positions of the loading force *P (g=L=200cm; 150cm; 100cm; 50cm; 20cm).*For smaller cross-sections (*30/30cm*) the

difference is over *10%* only at *g=L=200cm*. When using high-strength concrete with $E_1=3900kN/cm^2$, all differences between the two methods, for all sections and all positions of the force, are over *10%*. For all types of concrete, the difference is greatest when the force *P* is farthest from the support.

The results in Table 2 are for an asymmetric cross-section. Close to *10%* are the differences between the two methods for the large cross-sections (*75/75cm*). When the concrete is high-strength, the differences increase and become greater than *10%* for the large cross-sections (*75/75cm*). The differences between the two methods are greatest for force *P* standing closer to the support.

Table 3. Comparison of the results of Eq. (3) and Eq. (41) for symmetrical cross section and without considering the axial force in the strain potential energy expression.

section		*g*	*h / b*	$\frac{H_3+H_2+H_1}{P}$	$\frac{\frac{M_b}{j_b}+\frac{M'_b}{j'_b}}{P}$	$\frac{(H_3+H_2+H_1)-\left(\frac{M_b}{j_b}+\frac{M'_b}{j'_b}\right)}{(H_3+H_2+H_1)}100\%$
Si me tri cal	30/30	200	3,2	17,37	16,67	4,03
		150	3,2	13,12	12,5	4,70
	E_1=1700	100	3,2	8,81	8,33	5,36
		50	3,2	4,43	4,17	6,01
		20	3,2	1,78	1,67	6,39
Si me tri cal	30/30	200	3,2	18,40	16,67	9,43
		150	3,2	13,95	12,5	10,39
	E_1=3900	100	3,2	9,40	8,33	11,32
		50	3,2	4,75	4,17	12,24
		20	3,2	1,91	1,67	12,78
Asi me tri cal	30/30	200	2,8	16,89	16,67	1,33
		150	2,8	12,88	12,5	2,91
	E_1=1700	100	2,8	8,72	8,33	4,45
		50	2,8	4,43	4,17	5,94
		20	2,8	1,79	1,67	6,81
Asi me tri cal	30/30	200	2,8	18,25	16,67	8,67
		150	2,8	13,94	12,5	10,30
	E_1=3900	100	2,8	9,46	8,33	11,87
		50	2,8	4,81	4,17	13,39
		20	2,8	1,94	1,67	14,27

The results of Table 3 show the differences between the exact method, (H_1+H_2+H_3) and the approximate one $\left(\frac{M_b}{j_b}+\frac{M'_b}{j'_b}\right)$ used in Eq. (3) for symmetric and asymmetric section *30/30cm*, when the contribution of the axial force in the expression of the potential energy of deformation is neglected. For ordinary concrete, the difference exceeds 5% when the force P is close to the support for both types of sections – symmetric and asymmetric. For both types of sections, with high-strength concrete, the differences exceed *10%*.

Conclusion

A solution of a cantilever beam with a special arrangement of the support devices and different possible positions of the loading force was carried out. The actual dimensions of the beam are taken into account. The influence of the material properties of its components are taken into account to.The obtained expressions for the reactions of the horizontal supports give results that clearly show the distribution of the forces along the height of the cantilever beam. Calculations were performed for a symmetric and asymmetric cross section. Results of varying only one material characteristic, the modulus of elasticity of the concrete, are shown. The support reactions of the cantilever beam for different positions of the loading force were calculated.

A comparison of the contribution of the cantilever beam forces to the shear force value for RC internal beam-column connections with that of the literature is made. The obtained results show differences in the amount of shear force determined in the two ways up to 18.20%. The complex nature of variation in the contribution of the

cantilever beam forces to the shear force value is demonstrated, given the multitude of monitored parameters and their influence on the results.

The obtained results represent an important part of the beam-column connection research in determining the force distributions with the variation of various parameters from the connected beams and columns. This article may be of interest to both researchers and practicing engineers in interpreting the results obtained from structural analyses.

Recommendations

This article will focused attention on how the forces are distributed from the cantilever beam along its height and the subsequent load from the beam on the beam-column connection with an emphasis on determining the shear force at the beam-to-column connection.

Scientific Ethics Declaration

The author declares that the scientific ethical and legal responsibility of this article published in EPSTEM journal belongs to the author.

Acknowledgements or Notes

* This article was presented as an oral presentation at the International Conference on Research in Engineering, Technology and Science (www.icrets.net) held in Thaskent/Uzbekistan on August 22-25, 2024.

References

Bakir, P. G., & Boduroglu, H. M. (2001). Re-evaluation of seismic capacity of interior beam-column joints. *WIT Transactions on The Built Environment*, *57*.

Celik, O. C., & Ellingwood, B. R. (2008). Modeling beam-column joints in fragility assessment of gravity load designed reinforced concrete frames. *Journal of Earthquake Engineering*, *12*(3), 357-381.

Doicheva, A. (2022). Off-center supported beam with additional elastic supports located at the height of the beam and asymmetrical cross section. In *International Conference on Basic Sciences, Engineering and Technology (ICBASET)* (pp. 120-129).

Doıcheva, A. (2023). Determination of the shear force in RC ınterior beam-column connections. *The Eurasia Proceedings of Science Technology Engineering and Mathematics*, *23*, 361-371.

Doicheva, A. (2023). Distribution of forces in RC ınterior beam–column connections. *Engineering Proceedings*, *56*(1), 114.

Doicheva, A.; Shu, Y.; Kusuhara, F. & Shiohara, H. (2023-3) Seismic tests on reinforced concrete beam-column joint sub-assemblages subject to lateral and long-term vertical load, *Structural Integrity and Life*, *23*(3), 269–276.

Gombosuren, D., & Maki, T. (2020). Prediction of joint shear deformation index of RC beam–column joints. *Buildings*, *10*(10), 176.

Hanson, N. W., & Connor, H. W. (1967). Seismic resistance of reinforced concrete beam-column joints. *Journal of the Structural Division*, *93*(5), 533-560.

Lowes L. & Altoontash A. (2003) Modeling reinforced-concrete beam-column joints subjected to cyclic loading. *Journal Structural Engineering*, 129, 1686–97.

Matlab R2017b, *The MathWorks Inc*., Natick, USA.

Park, R. & Paulay, T.,(1975), Reinforced concrete structuers, *John Wiley & Sons*

Paulay, T. (1989). Equilibrium criteria for reinforced concrete beam-column joints. *Structural Journal*, *86*(6), 635-643.

Shiohara, H. (2001) New model for shear failure of RC interior beam-column connection. *Journal of Structural Engineering*, *127*(2), 152-160

Tran, T. M., Hadi, M. N. S. & Pham, T. M. (2014). A new empirical model for shear strength of reinforced concrete beam – column connections. *Magazine of Concrete Research*, *66*(10), 514-530.

Uma, S. R., & Jain, S. K. (2006). Seismic design of beam-column joints in RC moment resisting frames-Review of codes. *Structural Engineering and Mechanics*, *23*(5), 579.

Yuan, F., Pan, J., Xu, Z., & Leung, C. K. Y. (2013). A comparison of engineered cementitious composites versus normal concrete in beam-column joints under reversed cyclic loading. *Materials and Structures*, *46*, 145-159.

Author Information

Albena Doicheva
University of Architecture, Civil Engineering and Geodesy (UACEG), Sofia 1164, 1 Hristo Smirnenski Blvd, Bulgaria,
Contact e-mail: *doicheva_fhe@uacg.bg*

To cite this article:

Doicheva, A. (2024). Shear force in RC internal beam-column connections for a beam loaded with a transverse force occupying different possible positions. *The Eurasia Proceedings of Science, Technology, Engineering & Mathematics (EPSTEM), 29,* 128-144.

The Eurasia Proceedings of Science, Technology, Engineering & Mathematics (EPSTEM)
ISSN: 2602-3199

The Eurasia Proceedings of Science, Technology, Engineering & Mathematics (EPSTEM), 2024

Volume 29, Pages 145-154

ICRETS 2024: International Conference on Research in Engineering, Technology and Science

The Study of the Molecular Diffusion in Gases and Liquids

Georgii V. Kharlamov
Siberian Transport University

Abstract: The molecular dynamics calculations of the velocity autocorrelation functions and the diffusion coefficients for argon and krypton atoms in argon have been carried out. The data of the molecular dynamics simulations are analyzed to understand the change of the diffusion mechanism with transition from dense gas to liquid. In dense gases, the diffusion mechanism is the same as in rarefied gases, and the temperature dependences of the diffusion coefficient are alike. A new diffusion mechanism appears in liquids. This diffusion mechanism isn't connected with the jumping motion of the molecules. Probably, it is connected with the motion of the molecules group surrounding a molecule. Then the velocity of the molecule is relaxed with the decreasing of the average velocity of the molecules group. Various structures of the systems within the vapor – liquid phase transition region have been found and investigated. A comparison of the simulation results with the experimental data on diffusion in gaseous and liquid argon yields good agreement.

Keywords: Diffusion, Gases and liquids, Molecular dynamics method

Introduction

Mathematical description of the molecular diffusion in gases and liquids has long been a problem of the physical kinetics, studing transport processes (diffusion, viscosity, thermal conductivity, etc.). Though the research in this field has been conducted more than a hunred years, the problem still is far from being solved. There is a good kinetic theory of molecular diffusion in rarefied gases based on the solution of Bolzman's equation by Chapman – Enskog method, (Chapman & Cowling, 1952; Hirschfelder, Curtiss & Bird, 1964). Things are worse with the theory of diffusion in dense gases and liquids. It is related with the fact, that the diffusion mechanisms in thse media are studied not well enough. The existing theoretical models (Ferziger & Kaper, 1972; Frenkel, 1955) often bring to unsatisfactory results. In such situation the direct numeric simulation methods and the molecular dynamics method developed by Alder & Wainwright (1959, 1960) and Rahman (1964), are very useful.

The molecular dynamics method has long been applied for the calculations of the diffusion coefficients. In papers Alder, Gass & Wainwright (1970), and Erpenbeck & Wood (1991), the self-diffusion coefficients in hard absolutely smooth elastic spheres model have been calculated. In papers, Erpenbeck (1989, 1992, 1993), the diffusion coefficients in hard spheres mixtures have been calculated. In papers Heyes (1988), Meier et al. (2004) and Laghaei et al. (2006), the systems of particles interacting by Lennard-Jones potential has been studied. Other laws of interaction have also been used Liu, Silva & Macedo (1998), and Dubrovin et al. (2002). In our papers, Zhilkin & Kharlamov (2015), Kharlamov & Zhilkin (2016, 2017), the dependances of the diffusion coefficients in gases and liquids on density and temperature at the conditions of phase transition vapour – liquid have been reseached. In papers Kharlamov (2018 and 2021), the change of the diffusion mechanism has been detected as a result of transition from dense gases to liquids. At the same time it is shown that the diffusion mechanism in liquids is not related with the jumps of the molecules from one quasi-stationary state to another, and is determined, more likely, by the collective movement of the group of molecules surrounding some picked out molecule (Kharlamov, 2023 and 2024). In present paper the survey of the results acquired in this field is proposed.

Method

The calculations of the diffusion coefficients have been made for two systems, in wich the particles interact according to the Lennard-Jones potentials. The first system (system 1) consists of identical particles, the second (system 2) – of two different types of particles. The content of the second type particles constitutes 1 % of the whole quantity of the particles in the cell of the molecular dynamics method. The whole number of particles is from 3000 to 40000.

In our investigations the Lennard-Jones pair potential is used. The cutting of the potential takes place at a distance $r = 5\sigma_c$ with the help of the cubic spline.

$$
\begin{aligned}
&U(r) = 4\varepsilon_i\left[\left(\frac{\sigma_i}{r}\right)^{12} - \left(\frac{\sigma_i}{r}\right)^{6}\right],\ r \le 4.5\sigma_c,\\
&U(r) = a_i\left(r - 5\sigma_i\right)^2 + b_i\left(r - 5\sigma_i\right)^3,\ 4.5\sigma_c \le r \le 5\sigma_c,\\
&U(r) = 0,\ r > 5\sigma_c.
\end{aligned}
\qquad (1)
$$

The subscript *i* takes value 1 for the particles of the first type, value 2 for the particles of the second type and value 12 for the potential of the first and second type particles interacting with each other. The parameters a_i and b_i are chosen according to the conditions of the Lennard-Jones potential equality and its derivative and the corresponding values of the spline at $r = 4.5\sigma_c$. This potential provides the absence of the particles interaction at long distances ($r > 5\sigma_c$). At the same time such way of the potential cutting leads to the smooth dependance and makes the calculations in the molecular dynamics method more accurate. In our calculations the dimensionless variables are used:

distance $r = r_d/\sigma_1$;
time $t = t_d/\sigma_1(\varepsilon_1/m_1)^{1/2}$;
density $\rho = \rho_d\sigma_1^3$;
temperature $T = k\,T_d/\varepsilon_1$;
energy $U = U_d/\varepsilon_1$.

σ_1, ε_1, m_1 are the parameters of the Lennard-Jones potential and the mass of the first type particles. Low index *d* marks the dimentional variables.

The following parameters of the Lennard-Jones interaction potential are used:

for the first type particles ε_1/k = 124 K and σ_1 = 3.418 Å;

for the second type particles ε_2/k = 190 K and σ_2 = 3.609 Å;

for the first and second type particles ε_{12}/k = 153.5 K and σ_{12} = 3.514 Å.

The chosen parameters of the Lennard-Jones potentials correspond to argon and krypton atoms (NIST Chemistry WebBook). The cutting of the potentials in formula (1) is carried out at $\sigma_c = \sigma_2$. The relation of the krypton and argon atoms masses equals m_2/m_1 = 2.098. The applied algorithm of the molecular dynamics method is described in details in (Kharlamov & Zhilkin, 2017, April 20).

The Calculations of Velocity Autocorrelation Functions and the Diffusion Coefficients

After the system comes to equilibrium the time dependence of the velocity autocorrelation functions (VACF) of the first and second type particles is calculated

$$F(t) = \frac{\langle \vec{v}(0) \cdot \vec{v}(t) \rangle}{\langle v^2(0) \rangle} = \frac{\sum_{j=1}^{n} \vec{v}_j(0) \cdot \vec{v}_j(t)}{\sum_{j=1}^{n} v_j^2(0)} . \quad (2)$$

Here $\vec{v}_j(t)$ is a particle velocity at time moment *t*. Then the diffusion coefficients D_{md} are calculated by the Green – Kubo formula:

$$D_{md} = \frac{kT}{m_{1,2}} \int_0^\infty F(t)\, dt . \quad (3)$$

For the comparison of the acquired results with the theoretical data the reduced self-diffusion coefficients D_{md}/D_0 for the first type particles – the argon atoms and the diffusion coefficients D_{md}/D_{12} for the second type particles – the krypton atoms in argon are calculated. Here

$$D_0 = \frac{3\sqrt{\pi m_1 kT}}{8 m_1 \rho \pi \sigma_{11}^2 \Omega^{(1,1)*}},$$
$$D_{12} = \frac{3\sqrt{2\pi m_{12} kT}}{16 m_{12} \rho \pi \sigma_{12}^2 \Omega^{(1,1)*}} \quad (4)$$

the Chapman – Enskog diffusion coefficients in the kinetic theory of rarified gases (Hirschfelder, Curtiss & Bird, 1964). The dimensionless density takes values: ρ = 0.00349; 0.0348; 0.1; 0.4; 0.437; 0.61; 0.78; 0.84 and 0.88. The dimensionless temperature varied over the range from 0.6 to 6.

Results and Discussion

First of all, it should be noted, that the calculation results of the velocity autocorrelation functions and the diffusion coefficients are qualitatively alike for these two systems (system 1 and system 2). It means that the diffusion mechanisms in both systems are identical under the same conditions of density and temperature. As a whole, as far as density is concerned we can conventionally divide all the systems under consideration into three states: low density systems – rarified gases ($\rho < 0.1$), middle density systems – dense gases ($0.1 \le \rho \le 0.61$) and high density systems – liquids ($\rho > 0.61$). Let us examine each of these states separately.

The Low Density Systems

Let us consider the calculation results of these systems in the example of system 2. In figure (Figure 1) the distribution of the krypton atom in argon at a low system temperature is presented. We can see random even distribution of the krypton atoms in the cell. In figure (Figure 2) the krypton atoms velocity autocorrelation function of this system is shown. It is an exponential curve according to the Boltzmann – Chapman – Enskog theory of rarified gas (Hirschfelder, Curtiss & Bird, 1964). In figure (Figure 3) the temperature dependence of the diffusion coefficients of the krypton atoms in argon at density ρ = 0,00349 is demonstrated. This dependence is in accordance with the rarified gases theory and corresponds to formula (4). This dependence is the power law $D \sim T^{0.86}$ (Kharlamov, 2024).

The diffusion coefficients, which we calculate by the molecular dynamics method, are in good agreement with the experimental data. In paper (Durbin & Kobayashi, 1962) the experimental data on the diffusion of the krypton admixture in gasious argon is presented. For example, at argon density ρ_d = 14.67·10^{-3} g/cm^3 and temperature T_d = 308.1 K the experimental diffusion coefficient D_{exp} = 1.563·10^{-3} cm^2/s, and for density ρ_d = 40.136·10^{-3} g/cm^3 – D_{exp} = 0.5701·10^{-3} cm^2/s. Our calculations show values 1.563·10^{-3} cm^2/s and 0.5694·10^{-3} cm^2/s correspondingly. The same good agreement is observed for the diffusion coefficients in gaseous argon (Winn, 1950) and krypton at low pressure (Codastefano et al., 1978). The comparison of our self-diffusion coefficients calculation results in argon is presented in paper (Kharlamov, 2023). Here is the comparison of our

calculations results with the experimental data for the coefficients of self-diffusion in gaseous krypton at the low pressures (Codastefano et al., 1978). For example, at temperature T_d = 293 K and density ρ_d = $35.19 \cdot 10^{-3}$ g/cm^3 the self-diffusion coefficient equals D_{exp} = $0.9717 \cdot 10^{-2}$ cm^2/s, and at density ρ_d = $113.3 \cdot 10^{-3}$ g/cm^3 – D_{exp} = $0.2929 \cdot 10^{-3}$ cm^2/s. Our calculations show the values $1.0835 \cdot 10^{-2}$ cm^2/s and $0.2824 \cdot 10^{-3}$ cm^2/s correspondingly.

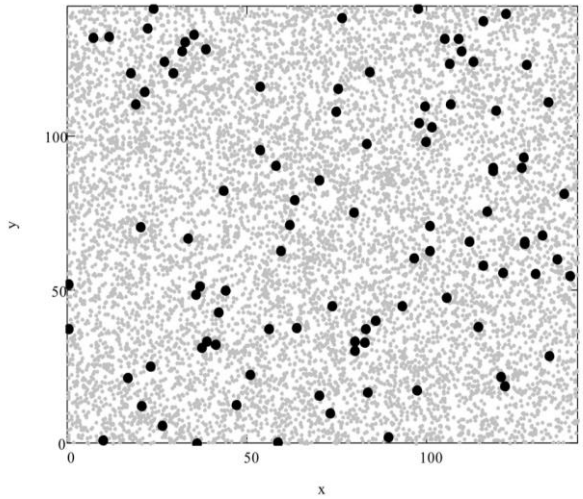

Figure 1. Snapshot of particle distribution in the cell at ρ = 0,00349 and T = 0,75. The small dots are the positions of the argon atoms, bold dots are the positions of the krypton atoms

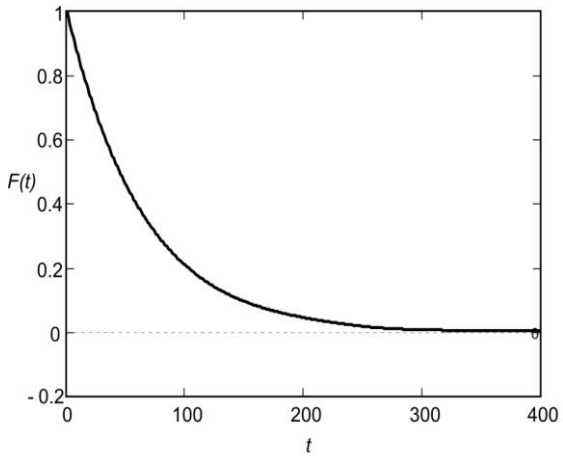

Figure 2. Velocity autocorrelation function of krypton atoms in argon (ρ = 0,00349; T = 0,75)

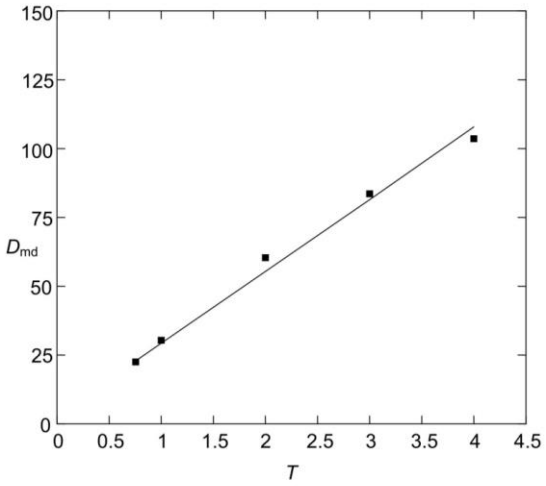

Figure 3. Temperature dependence of the diffusion coefficient D_{md} for the krypton atoms in argon at the system densities ρ = 0.00349. The solid curve is the linear fit

The Middle Density Systems

In the systems of middle density the phase transision vapor – liquid is observed at low temperatures ($T < 2$). In this case the formation of nanodrops in gas (Figure 4, a), bubbles of gas in liquids (Figure 4, b), layering of the system into gas and liquid is possible (Zhilkin & Kharlamov, 2015), (Kharlamov & Zhilkin, 2017). Nanodrops, which are formed in vapor as a result of homogeneous nucleation, have unusual thermodynamic properties. For example, the notion of surface tension can not be used for them (Kharlamov et al., 2008), (Kharlamov et al., 2010), (Kharlamov et al., 2011), (Kharlamov et al., 2012). It is also established, that the krypton atoms are captured by such nanodrops, so that an increased concentration of krypton is observed inside the drops (Kharlamov, 2021).

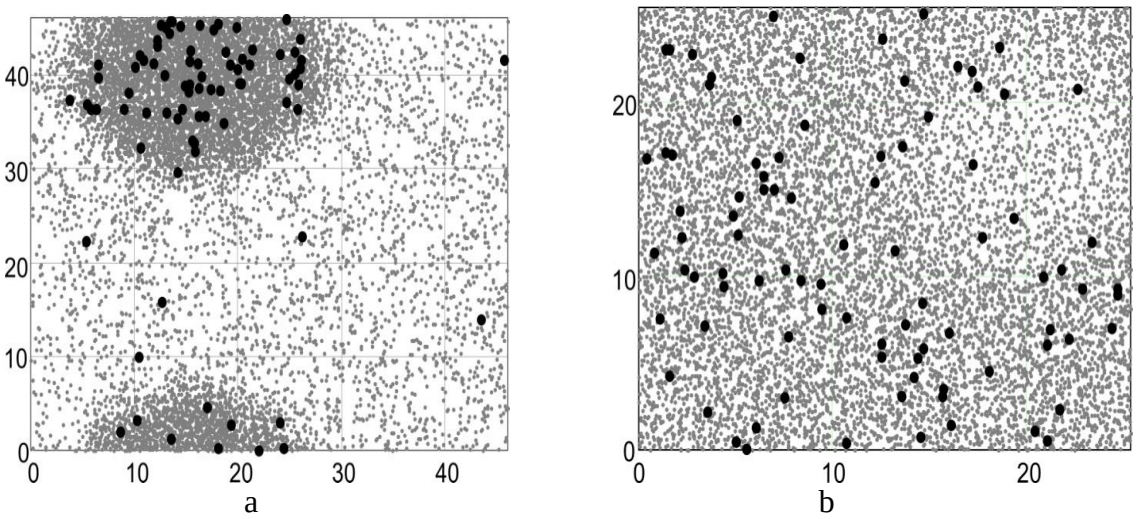

Figure 4. Snapshots of particle distribution in the cell at $\rho = 0.1$, $T = 1$ (a) and $\rho = 0.61$, $T = 1$(b). The small dots are the positions of the argon atoms, bold dots are the positions of the krypton atoms

At high temperatures ($T \geq 2$) the homogeneous distribution of argon and krypton density is observed for such systems. In figure (Figure 5) the time dependence of the velocity autocorrelation function of krypton atoms in argon is presented. It is not exponential with a long power tail $\sim t^{-3/2}$ (Kharlamov, 2023), which was discovered earlier in the papers (Rahman, 1964), (Alder et al., 1970).

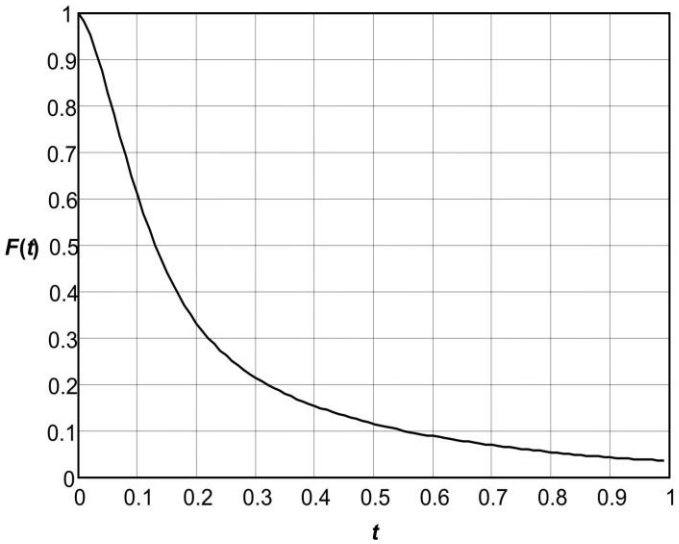

Figure 5. VACF of the krypton in argon at the system density $\rho = 0.61$ at the temperature $T = 2$

In Figure 6, the dependence of the diffusion coefficients of the krypton atoms in argon on density at various temperatures is shown. One can see that the reduced diffusion coefficients D_{md}/D_{12} do not depend on temperature, and depend only on density for the systems of low and middle density ($\rho < 0.61$). It testifies that the diffusion mechanism for these systems is the same. The relaxation of the krypton atoms velocity in this case

takes place in general due to the pair collisions of these atoms with the argon atoms. Such diffusion mechanism we called “collisioning” (Kharlamov, 2018). The dependence approximation of the calculated diffusion coefficients on density leads to the expression:

$$f_d = \frac{D_{md}}{D_{12}} = 1 - 0.210\,\rho - 0.257\,\rho^2 - 0.244\,\rho^3 . \tag{5}$$

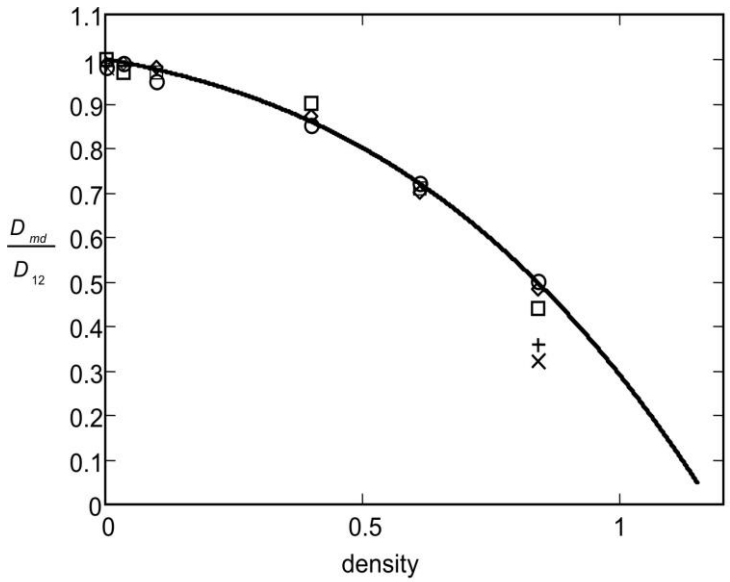

Figure 6. Density dependences of the reduced diffusion coefficients D_{md}/D_{12} at different system temperatures: T = 0.75 (×), T = 1 (+), T = 2 (□), T = 3 (◊), T = 4 (○).

Analogous results are received for the dependences of the self-diffusion coefficients in gaseous and liquid argon (system 1). In this case the approximation curve of this dependence has the form (Kharlamov & Zhilkin, 2017, April 20):

$$f_{sd} = \frac{D_{md}}{D_0} = 1 - 0.547\,\rho + 0.3\,\rho^2 - 0.574\,\rho^3 . \tag{6}$$

Expressions (5) and (6) are the universal dependences of the diffusion coefficients on the density for the rarified and dense gases. The comparison of our calculation results and the experimental data in the middle density systems is carried out in paper (Kharlamov, 2023). A satisfactory agreement is proved for the diffusion coefficients in dense gaseous argon (Mifflin & Bennet, 1958).

The High Density Systems

In Figure 7, the typical time dependence of the velocity autocorrelation function of the argon atoms in liquid argon is presented. It has the characteristic negative tail, which testifies about the return atom movement in the liquid in the definite time interval. The reduced diffusion coefficient for such systems depends not only on density, but also on temperature (Figure 6). More so, the dependence of the diffusion coefficient on the temperature in liquids is close to the linear one (Figure 8). The approximation of the calculated coefficients by the linear dependence leads to the expression

$$D_{md} = -0.0132 + 0.0688 \cdot T . \tag{7}$$

So, we can see, that the diffusion mechanism in liquids differ from that in dense gases. It is related with the fact, that in liquids the collective effects are of importance. Apparently, in this case separate atoms move surrounded by a group of neighboring atoms, doing damped vibrations inside the group. The atom velocity relaxation is defined by the average velocity relaxation in this group. At the same time such diffusion mechanism is not

"jumping", because in this case the temperature dependence of the diffusion coefficient must obey the Arrhenius equation (Frenkel, 1955)

$$D = D_m \, e^{-\frac{\Delta W}{kT}} . \tag{8}$$

The comparison of the experimental data on the diffusion of argon atoms in liquid argon (Cini-Castagnoli & Ricci, 1960, July 13), (Cini-Castagnoli & Ricci, 1960, December 30), and also on diffusion of krypton atoms in liquid argon (Cini-Castagnoli & Ricci, 1960, December 30; Dunlop & Bignell, 1998) lead to a satisfactory agreement (Kharlamov, 2023).

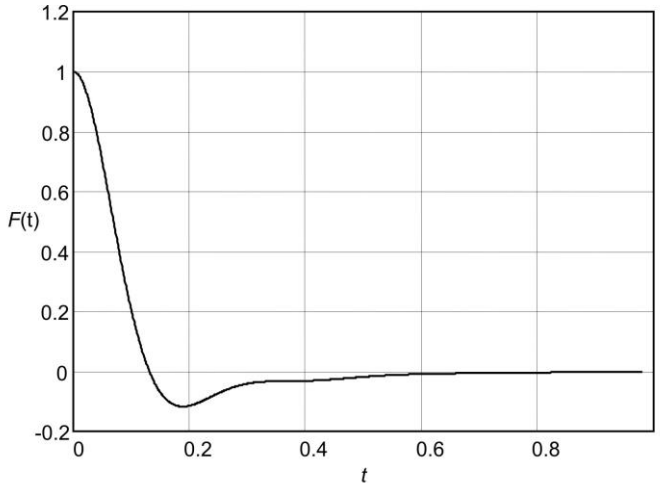

Figure 7. VACF of argon atoms in argon at the system density ρ = 0.84 at the temperature T = 0.75

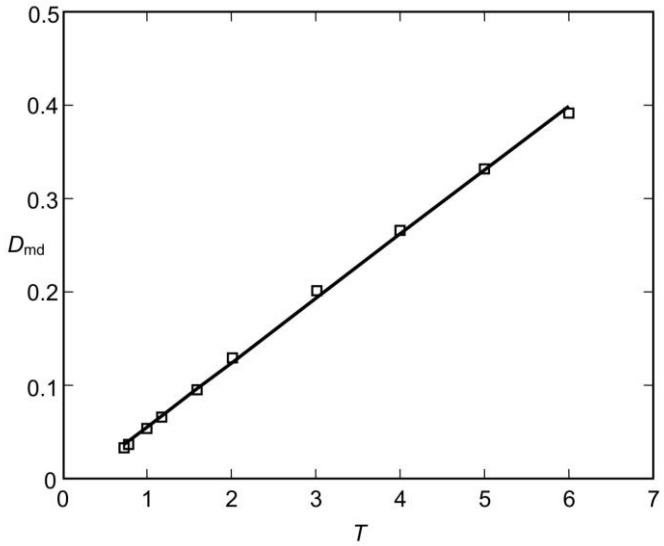

Figure 8. Temperature dependence of the diffusion coefficient D_{md} for the argon at the system densities ρ = 0.84. The solid curve is the fit (7)

Conclusion

Thus, we see that the molecular dynamics method gives good results in the calculations of the diffusion coefficients not only in liquids and dense gases, but also in rarified gases. It permits to calculate the diffusion coefficients with the accuracy of the experiment, as well as to reveal subtle details of the diffusion phenomenon, such as the diffusion mechanisms and the relaxation of the molecular velocity. It also allows observing the phase transition vapor – liquid and its influence on the diffusion of an admixture in the binary molecular system.

The special problem of the diffusion theory is the study of the diffusion mechanisms of nanoparticles and macromolecules in liquids and gases. And though in this field we obtained some interesting results (Rudyak, Kharlamov & Belkin, 2000, September 3; Rudyak et al., 2000; Rudyak et al., 2001), the problem is far from being solved completely. Another important problem of the gases and liquids theory, which we work on, is the problem of study of the big density, momentum and energy fluctuations (Rudyak & Kharlamov, 2003; Kharlamov & Rudyak 2004). It is especially important in connection with the phase transitions vapor – liquid in the systems under consideration. One more interesting task is the simulation of the light-induced drift in rarified gases. Though the simplest theory of this phenomenon has been created in a whole (Gel'mukhanov et al., 1992), there are still numerous unrevealed things in the mechanism of this phenomenon.

Recommendations

The fulfilled research has not only the fundamental scientific character, but also possesses the applied potential. It can be used in the calculations of the chemical and thermo physical processes in industrial technologies.

Scientific Ethics Declaration

The author declares that the scientific ethical and legal responsibility of this article published in EPSTEM journal belongs to the author.

Acknowledgements or Notes

This article was presented as an oral presentation at the International Conference on Research in Engineering, Technology and Science (www.icrets.net) held in Tashkent/Uzbekistan on August 22-25, 2024.

References

Alder, B.J. & Wainwright, T.E. (1959). Studies in molecular dynamics. I. General method. *J. Chem. Phys. 31*(2), 459-466.

Alder, B.J. & Wainwright, T.E. (1960). Studies in molecular dynamics. II. Behavior of a small number of elastic spheres. *J. Chem. Phys., 33*(5), 1439-1451.

Alder, B.J., Gass, D.M. & Wainwright, T.E. (1970). Studies in molecular dynamics. VIII. The transport coefficients for a hard-spheres fluid. *J. Chem. Phys., 53*(10), 3813-3826.

Chapman, S. & Cowling, T. G. (1952). *The mathematical theory of non-uniform gases.* Cambridge, GB: University Press.

Cini-Castagnoli, G. & Ricci, F.P. (1960, July 13). Self-diffusion in liquid argon. *J. Chem. Phys., 32*(19), 19-20.

Cini-Castagnoli, G. & Ricci, F.P. (1960, December 30). Diffusion of ^{37}Ar, Kr, HT in liquid argon between (84 ÷ 90) ºK. *Nuovo Cimento, 15*(5), 795-805.

Codastefano, P., Ricci, M.A. & Zanza, V. (1978). Behaviour of the self-diffusion coefficient of Kr at low densities. *Physica, 92A*, 315-322.

Dubrovin, A. A., Rudyak, V. Ya. & Kharlamov, G. V. (2002). Simulation of molecular diffusion in liquids taking into account rotational degrees of freedom. *Russian Journal of Physical Chemistry A, 76,* 767-772.

Dunlop, P.J. & Bignell, C.M. (1998). Tracer diffusion of Kr^{85} in liquid Ar, N_2, and O_2. *J. Chem. Phys., 108*(17), 730-734.

Durbin L. & Kobayashi R. (1962). Diffusion of krypton-85 in dense gases. *J.Chem.Phys., 37*(8), 1643-1654.

Erpenbeck, J.J. (1989). Transport coefficients of hard-sphere mixtures. Theory and Monte-Carlo molecular-dynamics calculations for an isotopic mixture. *Phys. Rev. A, 39*(9), 4719-4731.

Erpenbeck, J.J. & Wood, W.W. (1991). Self-diffusion coefficient for hard-sphere fluid. *Phys. Rev. A, 43*(8), 4254-4261.

Erpenbeck J.J. (1992). Transport coefficients of hard-sphere mixtures. 2. Diameter ratio 0.4 and mass-ratio 0.03 at low-density. *Phys. Rev. A, 45*(4), 2298-2307.

Erpenbeck, J.J. (1993). Transport coefficients of hard-sphere mixtures. 2. Diameter ratio 0.4 and mass-ratio 0.03 at high fluid density. *Phys. Rev. A, 48*(1), 223-232.

Ferziger, J.H. & Kaper, H.G. (1972). *Mathematical theory of transport in gases.* Amsterdam – London: North-Holland Publishing Company.

Frenkel, Ya. I.(1955). *Kinetic Theory of Liquids.* New York, NY: Dover Publications.

Gel'mukhanov, F.Kh., Kharlamov, G.V. & Rautian S.G. (1992). Spectral profiles of signals in light-induced drift and light-induced diffusive pulling effects. *Optics Communications*, *94*(6), 521-524.

Heyes, D.M. (1988). Transport coefficients of Lennard-Jones Fluids: A molecular-dynamics and effective-hard-sphere treatment. *Phys. Rev. B, 37***(**10), 5677-5696.

Hirschfelder, J.O., Curtiss, C.E. & Bird, R.B. (1964). *Molecular theory of gases and liquids.* New York, NY: Wiley.

Kharlamov, G.V. & Rudyak, V.Ya. (2004). The equilibrium fluctuations in small open systems. *Physica A: Statistical Mechanics and its Applications*, *340*(1-3), 257-264.

Kharlamov, G.V., Onischuk, A.A., Purtov, P.A., Vosel, S.V. & Bolesta, A.V. (2008). A molecular dynamics calculations of surface tension of small drops. *Atmospheric and Oceanic Optics*, *21*(9), 679-683(in Russian).

Kharlamov, G.V., Onischuk, A.A., Purtov, P.A., Vosel, S.V. & Bolesta A.V. (2010). The problem of surface tension definition of nanodrops. *e-Journal of Surface Science and Nanotechnology, 8*, 197-202.

Kharlamov, G.V., Onischuk, A.A., Vosel, S.V. & Purtov, P.A. (2011). Molecular dynamics calculations of small drops surface tension. *Coll. Surf. A: Phys. Eng. Asp., 379,* 10-13.

Kharlamov, G.V., Onischuk, A.A., Vosel, S.V. & Purtov P.A. (2012). About applicability of thermodynamic parameters to small drops and clusters. *J. of Phys.: Conf. Ser., 393,* 012006.

Kharlamov, G. V. & Zhilkin, S. V. (2016). Molecular dynamics simulation of diffusion of gases and liquids in conditions of phase transition. Proceedings of the WCECS 2016: *World Congress on Engineering and Computer Science (San Francisco: USA)*, V. 2. Hong Kong: Newswood Limited, 554-559.

Kharlamov, G. V. & Zhilkin, S. V. (2017, April 20). Molecular dynamics simulation of the molecular diffusion in gases and liquids. *Engineering Letters, 25*(2), 222-227.

Kharlamov, G. V. & Zhilkin, S. V. (2017, September 27). The molecular dynamics simulation of self-diffusion in gases and liquids. *Journal of Physics: Conference Series, 899,* 052009.

Kharlamov, G. V. (2018). About diffusion mechanisms in gases and liquids from data of molecular dynamics simulation. *Journal of Physics: Conference Series, 1105,* 012152.

Kharlamov, G.V. (2021, August 22). Simulating diffusion in the conditions of vapor – liquid phase transition by the molecular dynamics method. *Journal of Physics: Conference Series, 2057,* 012114.

Kharlamov, G.V. (2021, September 14). Molecular diffusion in gases and liquids. *Journal of Physics: Conference Series, 2119,* 012122.

Kharlamov, G. V. (2023). Calculations of the diffusion coefficients in two phase vapor – liquid system by the molecular dynamics method. *AIP Conference Proceedings, 2899,* 020066.

Kharlamov, G. V. (2024). Calculations of the diffusion coefficients in gases and liquids by the molecular dynamics method. *Journal of Physics: Conference Series, 2701,* 012073.

Laghaei, R., Nasrabad, A.E. & Eu, B.C. (2006). Excluded volume in the generic van der Waals equation of state and the self-diffusion coefficient of the Lennard-Jones fluid. *J. Chem . Phys., 124,* 154502.

Liu, H., Silva, C.M. & Macedo, E.A. (1998). Unified approach to the self-diffusion coefficients of dense fluids over wide ranges of temperature and pressure - hard-sphere, square-well, Lennard-Jones and real substances. *Chemical Engineering Science*, *53*(13), 2403-2422.

Meier, K., Laesecke, A. & Kabelac, S. (2004). Transport coefficients of the Lennard-Jones model fluid. II Self-diffusion. *J. Chem . Phys., 121*(19), 9526-9535.

Mifflin, T.R. & Bennet, C.O. (1958). Self-diffusion in argon to 300 atmospheres. *J. Chem. Phys., 29*(5), 975-978.

NIST Chemistry WebBook (2024). Retrieved from https://webbook.nist.gov/chemistry/fluid/

Rahman, A. (1964). Correlations in the motion of atoms in liquid argon. *Phys. Rev. A. 136,* 405-411.

Rudyak, V.Y., Kharlamov, G.V. & Belkin, A.A. (2000, September 3). Molecular dynamics simulation of nanoparticles diffusion in dense gases and liquids. *Journal of Aerosol Science*. *31*(Suppl. 1), S432-S433.

Rudyak, V.Ya., Kharlamov, G.V. & Belkin, A.A. (2000, February 1). The Velocity Autocorrelation function of nanoparticles in a hard-sphere molecular system. *Technical Physics Letters, 26*(7), 553-556.

Rudyak, V.Ya., Kharlamov, G.V. & Belkin, A.A. (2001). Diffusion of nanoparticles and macromolecules in dense gases and liquids. *High Temperature, 39*(2), 264-271.

Rudyak, V.Ya. & Kharlamov, G.V. (2003). The theory of equilibrium fluctuations of thermodynamic quantities in open systems with a small number of particles. *High Temperature, 41*(2), 201-209.

Winn, E. B. (1950). The temperature dependence of the self-diffusion coefficients of argon, neon, nitrogen, oxygen, carbon dioxide, and methane. *Phys. Rev. 80*(6), 1024-1027.

Zhilkin, S. V. & Kharlamov, G. V. (2015). Investigation of the diffusion of Lennard-Jones particles in phase transition conditions by the molecular dynamics method. *Atmospheric and Oceanic Optics*, *28*, 138-142 (in Russian).

Author Information

Georgii V. Kharlamov
Siberian Transport University
191 Dusi Kovalchuk str., Novosibirsk, 630049, Russia
Contact e-mail: *gv_kharlamov@mail.ru*

To cite this article:

Kharlamov, G.V. (2024). The study of the molecular diffusion in gases and liquids. *The Eurasia Proceedings of Science, Technology, Engineering & Mathematics (EPSTEM), 29*, 145-154.

The Eurasia Proceedings of Science, Technology, Engineering & Mathematics (EPSTEM)
ISSN: 2602-3199

The Eurasia Proceedings of Science, Technology, Engineering & Mathematics (EPSTEM), 2024

Volume 29, Pages 155-172

ICRETS 2024: International Conference on Research in Engineering, Technology and Science

Technology Applications in Waste Management across Southeast Asia: A Bibliometric Analysis over the Past Decades

Haryanto Haryanto
Universitas Pendidikan Indonesia

Sjaeful Anwar
Universitas Pendidikan Indonesia

Rini Solihat
Universitas Pendidikan Indonesia

Fadli Agus Triansyah
Universitas Pendidikan Indonesia

Ilham Muhammad
Universitas Pendidikan Indonesia

Debi S Fuadi
Universitas Pendidikan Indonesia

Andika Pratama
Universitas Pendidikan Indonesia

Fiza Dora Selpa Pertiwi
Universitas Islam Negeri Fatmawati Sukarno Bengkulu

Abstract: Using technology in waste management in the current era is crucial in enhancing efficiency, sustainability, and positive environmental impact. Therefore, this research aims to understand publication trends related to technology applications in waste management from 2013 to 2024 across Southeast Asia through bibliometric analysis. In this analysis, VOSviewer software and the bibliometric analysis applications RStudio and biblioshiny were employed to analyse the bibliographic data obtained graphically. After filtering, 553 documents from the Scopus database were analysed. The results revealed fluctuating trends in the number of publications, with the Journal of Cleaner Production being the highest contributor with 33 documents. Malaysia ranked first in the number of documents, with 452 focusing on technology utilisation in waste management. Additionally, Universiti Teknologi Malaysia and the National University of Singapore were the most productive affiliations, each contributing the highest number of publications, with 58 each. Two institutions within the top twenty also represented Indonesia as the most relevant affiliations, namely (1) Bandung Institute of Technology and (2) Universitas Sebelas Maret. According to the research findings, 68 Indonesian researchers contributed to the analysed theme, with the top author originating from the Czech Republic with 13 documents. The globally most cited documents, published in the Journal of Resources, Conservation, and Recycling, have been cited 535 times. Visualisation of research trends revealed popular topics aligned with research and discussion, including waste management, sustainable development, recycling, waste disposal, solid waste, municipal solid waste, anaerobic digestion, waste treatment, biogas, pyrolysis, and environmental impact. These findings aid researchers in guiding future analyses and determining research themes, especially in waste management technology, while also assisting in resource allocation and evidence-based strategy formulation to enhance

waste management efficiency and sustainability. Nonetheless, the study recommends further research using diverse data sources, bibliographic connections, and qualitative analysis.

Keywords: Bibliometric analysis, Technology, Waste management

Introduction

Waste management is a critical challenge, particularly in developing nations, where the infrastructure for waste collection often falls short (Sandeep et al., 2018). Addressing this issue requires multifaceted approaches that mitigate environmental degradation and foster sustainable practices. Agricultural waste, a significant contributor to ecological harm, has the potential to be transformed into valuable resources such as organic fertiliser through vermicomposting, thereby promoting sustainable agricultural production(Talukdar et al., 2018). However, a holistic strategy is indispensable to tackle the enormity of waste management challenges. This is where the 3R approach (Reduce, Reuse, Recycle) comes into play, as emphasised by (Kinantan et al., 2018). This strategy emphasises optimising garbage collection and transportation and underscores the imperative to minimise waste generation in the first place.

The scale of the waste management challenge is staggering, with a staggering 4 billion tons of waste generated annually worldwide, necessitating a fundamental shift in approach (Trivedi et al., 2019). Recognising this urgency, researchers and innovators increasingly turn to digital technologies to revolutionise waste management practices. Indeed, as Sadinov and Rajabov (2023) note, the application of digital technologies in waste management is burgeoning, offering promising avenues for repurposing waste and devising innovative solutions. Central to this technological revolution is IoT-based architecture, enabling real-time monitoring of waste volume and composition and dynamic optimisation of waste collection routes (Aleyadeh & Taha, 2018).

Technology integration in waste management is pivotal in ensuring efficient and sustainable practices. Adam et al. (2018) and Kumari et al. (2019) elucidate the significance of technology in enabling real-time monitoring of waste containers, allowing for precise tracking of waste levels, composition, and collection frequencies. This real-time data empowers waste management authorities to optimise their operations, allocating resources more effectively and responding promptly to fluctuations in waste generation. Furthermore, technology enhances the overall throughput of waste management operations by streamlining processes such as route optimisation for waste collection vehicles, thereby reducing fuel consumption, emissions, and operational costs.

Expanding on this notion, Sadinov and Rajabov (2023) underscore the vast potential of digital technologies in repurposing waste and fostering innovation within waste management projects. By leveraging digital platforms and advanced analytics, waste materials can be transformed into valuable resources, such as biofuels, compost, or recycled materials, contributing to environmental conservation and economic growth. Additionally, digital tools facilitate collaboration among stakeholders, enabling the co-creation of innovative solutions to address specific waste management challenges within local communities. Gupta et al. (2019) further emphasise the indispensability of modern technology, particularly artificial intelligence and machine learning, in facilitating smart waste management and bolstering recycling efforts. These advanced technologies enable predictive analytics and automated decision-making, allowing waste management systems to anticipate demand, optimise resource allocation, and improve sorting accuracy at recycling facilities. Moreover, artificial intelligence-driven algorithms can continuously learn and adapt based on evolving waste composition patterns, enhancing the efficiency and efficacy of recycling processes over time.

Collectively, these studies underscore the profound impact of technology in driving enhancements across various facets of waste management processes, from real-time monitoring and optimisation to waste repurposing and recycling. Embracing technological advancements improves operational efficiency and resource utilisation and fosters innovation and resilience within waste management systems, ultimately contributing to a more sustainable and environmentally responsible future. Moreover, the integration of smart waste management systems empowered by IoT, machine learning, and Android applications is reshaping the landscape of waste collection and processing(Varudandi et al., 2021). These advancements, coupled with the incorporation of artificial intelligence, cloud computing, and intelligent transport systems, are driving the emergence of sophisticated waste management frameworks(Karunambiga & Sathiya, 2023). Nevertheless, while digital technologies offer immense potential, adopting waste-to-energy technologies remains a cornerstone of waste management efforts in Southeast Asia.

In this region, diverse waste-to-energy technologies such as incineration, landfill gas capture, and anaerobic digestion are gaining traction, presenting opportunities for renewable energy generation(Tun et al., 2020). However, challenges persist, particularly in construction and demolition waste management, where data scarcity and institutional gaps hinder progress (Hoang et al., 2020). Bangladesh, for instance, grapples with the imperative to enhance waste management practices while concurrently addressing unemployment, underscoring the multifaceted nature of the challenge (Dinnar et al., 2021). Nonetheless, strides are being made towards low-carbon emission development strategies, exemplified by initiatives such as composting for organic waste and robust environmental management systems (Lee et al., 2018).

A bibliometric analysis sheds light on the evolving landscape of waste management research, highlighting a pronounced focus on waste-to-energy technologies and treatment methodologies (Ndou & Rampedi, 2022). This sentence emphasises the importance of bibliometric analysis, a quantitative method for examining patterns and trends in scholarly literature. In this context, the analysis provides valuable insights into the prevailing research themes and areas of emphasis within waste management, particularly regarding waste-to-energy technologies and treatment methods. By systematically reviewing a vast body of literature, bibliometric analysis offers a comprehensive overview of the research landscape, aiding in identifying key research directions and gaps.

Southeast Asia's trajectory mirrors this global trend, with an increasing emphasis on waste-to-energy solutions (Tun et al., 2020). Here, the sentence highlights the regional perspective, demonstrating how the findings of the bibliometric analysis apply to the specific context of Southeast Asia. The mention of waste-to-energy solutions underscores the relevance of the analysis to address pressing environmental and energy challenges in the region. By recognising regional trends and patterns, policymakers and stakeholders can tailor interventions and strategies to meet the unique needs and priorities of Southeast Asian countries. Notably, the proliferation of waste classification technologies, particularly in nations like China, underscores a concerted effort towards enhancing recycling and resource recovery (Yang et al., 2021). This statement emphasises the role of waste classification technologies in promoting sustainability and resource efficiency. The reference to China highlights a specific example of a country actively investing in waste management infrastructure and technologies to address environmental concerns. The analysis underscores opportunities for knowledge sharing and collaboration among countries striving to improve their waste management practices by identifying such advancements.

Nevertheless, gaps persist, as evidenced by the limited exploration of cleaner transport sector opportunities within the waste-to-energy discourse (Boloy et al., 2021). This sentence acknowledges the limitations and areas for further research identified through the bibliometric analysis. The analysis provides valuable guidance for future research endeavours by pinpointing gaps in the existing literature. In this case, the reference to cleaner transport sector opportunities underscores the importance of considering broader systemic factors and interconnections within waste management systems. As such, while technological innovations hold immense promise for revolutionising waste management practices, concerted efforts and interdisciplinary collaborations are essential to realise their full potential in Southeast Asia and beyond. This concluding statement emphasises the overarching goal of the bibliometric analysis: to inform and guide efforts aimed at harnessing the transformative potential of technology in waste management. By advocating for collaborative approaches and interdisciplinary engagement, the analysis encourages stakeholders to work together towards sustainable and inclusive solutions to the complex challenges of waste management. Based on the existing body of literature, it is evident that there is a need for bibliometric research on the application of technology in waste management, particularly in Southeast Asian developing countries. The primary objective of this study is to thoroughly investigate the application of technology in waste management by employing a bibliometric approach to address existing research gaps. This study addresses the following specific research questions:

RQ1: What are the publication trends and research patterns regarding the application of technology in waste management across Southeast Asia over the past few decades?
RQ2: Which leading academic journals specifically address the application of technology in waste management in the Southeast Asian region?
RQ3: How is the network of collaboration among Southeast Asian countries in research on the application of technology in waste management?
RQ4: Who are the most frequently cited authors in research on the application of technology in waste management in Southeast Asia?
RQ5: Which publications significantly influence research on the application of technology in waste management in Southeast Asia?
RQ6: What are the primary research areas of focus in studies on the application of technology in waste management in Southeast Asia?

Method

Data Source, Study Boundary and Search Strategy

Bibliometric analysis proves valuable in comprehending and charting the collective scientific knowledge and evolutionary intricacies of established disciplines by organising vast amounts of unstructured data through rigorous methodologies (Donthu et al., 2021). As part of a systematic literature review, the bibliometric review is characterised by clarity, transparency, and replicability in developing the review database (Donthu et al., 2021; Hallinger & Suriyankietkaew, 2018; Kho & Brouwers, 2012). When conducting a bibliometric review, it is essential to clearly define the scope of the study and elucidate the techniques used to track down relevant sources. The current study extracted bibliometric data from the Scopus database. Scopus is a comprehensive database encompassing abstracts and citations for scholarly journal articles (García-Ávila et al., 2023; Mesdaghinia et al., 2015; Mongeon & Paul-Hus, 2016; Sweileh et al., 2016). It covers various academic fields, such as medical, technical, social, and scientific studies, which are highly relevant for investigating and advancing waste management systems (Punj et al., 2023). Compared to Web of Science, Scopus provides approximately 20% more coverage, while Google Scholar yields results with varying levels of accuracy (Falagas et al., 2008; Mesdaghinia et al., 2015).

The bibliometric analysis methodology is utilised to summarise a compilation of bibliographic data. This technique visualises the structural, social, and author networks, as well as the prevailing analytical focuses within a specific research domain (Ha et al., 2020; Karakus et al., 2019; Suprapto et al., 2021; Zupic & Čater, 2015). Furthermore, this approach encompasses statistical evaluations of published articles and their citations to gauge their pertinent impacts and assess emerging gaps or subjects of interest (Maditati et al., 2018; Saregar et al., 2022). Additionally, bibliographic analysis leverages pertinent data from online databases, facilitating scientific investigations and offering a global outlook on related areas of inquiry (Secinaro et al., 2020). Figure 1 delineates the execution of these five steps, underscoring the utilisation of bibliometric methodologies.

Figure 1. Bibliometric methodology

Study Design

This study design was executed by formulating research questions and selecting keywords and databases. It indicated the existence of six questions investigating the following features: annual publication trends, document sources, subject areas, and countries; affiliations; most productive authors; contributions of Indonesian experts; highly cited papers; and future experimental opportunities related to the application of technology in waste management. The design also demonstrated that the applied search keywords were "Technology" AND "Waste Management," with the Scopus database chosen as the bibliometric source.

Data Collection

The data collection process from the Scopus database utilised a title search strategy employing the keywords "Technology" AND "Waste Management" within the publication year range of 2013-2024. The timeframe selection from 2013 to 2024 is considered a robust decision due to its encapsulation of the most recent developments in the field. This temporal scope enables the research to effectively track the evolution of technology, research trends, and their consequential impact on waste management, consistently aligning with the research objectives. Moreover, utilising a relatively recent timeframe ensures that the acquired data is representative of the latest advancements in scholarly literature, thereby offering a more precise portrayal of the current status and future directions in waste management. With a specific focus on the Southeast Asian region, this timeframe facilitates a deeper understanding of regional developments within the broader global context. The data collection process yielded 553 documents for 2013-2024, sourced from journals published in Southeast Asian countries, adhering to the final publication stage and utilising English. Furthermore, the documents were obtained in Comma-Separated Values (CSV) and Research Information System (RIS) formats, enabling the extraction of article titles, authors, references, and keywords.

Data Analysis

Data analysis began with importing CSV, BIB, and RIS data from the Scopus database into Microsoft Excel, VOSviewer, and RStudio/Biblioshiny. This initial step was pivotal for facilitating subsequent data processing. The analysis sought to delineate and comprehend various trends, encompassing characteristics of publication output, document sources, affiliations by country and institution, dissemination across subject categories, and identification of top authors and citations. This information underwent detailed and comprehensive scrutiny to enhance understanding of the prevailing research landscape, specifically focusing on the period from 2013 to 2024.

Data Visualisation

After completing the data processing and analysis, the next phase involved visualising the data. This visualisation process utilised VOSviewer, RStudio/biblioshiny, and Microsoft Excel. Specifically, VOSviewer was employed to translate the processed CSV metadata into network, overlay, and density visualisations. Additionally, Microsoft Excel was utilised to present the data in tables and diagrams, aiming to provide a clearer and more comprehensible overview of the observed research trends.

Interpretation

Following data visualisation using VOSviewer, a meticulous analysis and interpretation of the visual representations ensued. This stage encompassed a thorough examination of various facets, including identifying clusters within the network, juxtaposing earlier and contemporary studies, and scrutinising density patterns, which yielded insights into the saturation of research topics and delineated prospective avenues for future experimentation. The significance of these visualisations lies in their capacity to offer nuanced insights into the intricate patterns and trajectories underlying research within the field. By rigorously discerning and interpreting these visual depictions, researchers can glean profound insights into the prevailing dynamics and trends, thus informing subsequent research endeavours and strategic decision-making processes in a scholarly context.

Result

Publication Trends

The trend of publication productivity spanning a decade (2013-2024), as derived from the Scopus database, reveals notable fluctuations. Specifically, the analytical trajectory concerning the application of technology in waste management across diverse disciplines exhibited variability over this ten-year period. This is evidenced by an upward trend in the number of documents observed in 2019, 2020, 2021, 2022, and 2023, with 43, 56, 81, 99, and 109 publications, respectively, followed by a subsequent decline in 2024, with only 17 publications. It is important to note that this decrease is typical, as it represents the initial segment of the year. Figure 2 provides a visual representation of the annual publication trend.

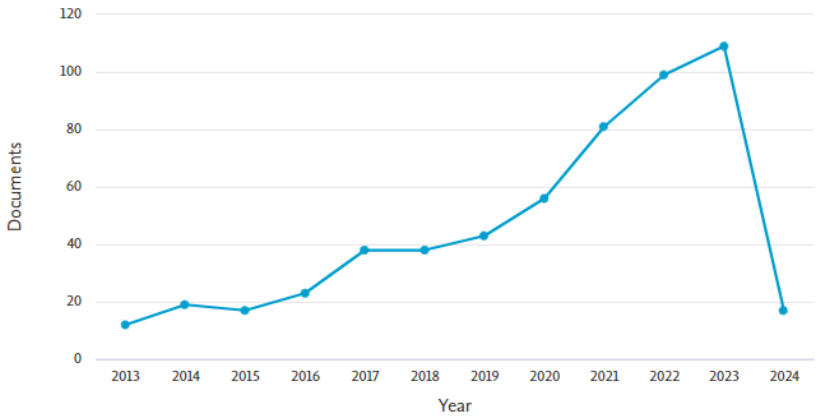

Figure 2. Annual publication trends for the period 2013-2024

Main Source Document

The article documents were sourced from a diverse array of journals, encompassing a wide spectrum of waste management topics across various academic disciplines such as environmental science, engineering, energy, social science, chemical engineering, and material science. Among these journals, some are indexed in Scopus with Q1 (16 journals and 187 articles), Q2 (1 journal and 9 articles), and Q3 (3 journals and 25 articles) rankings, as illustrated in the accompanying figure (figure 3).

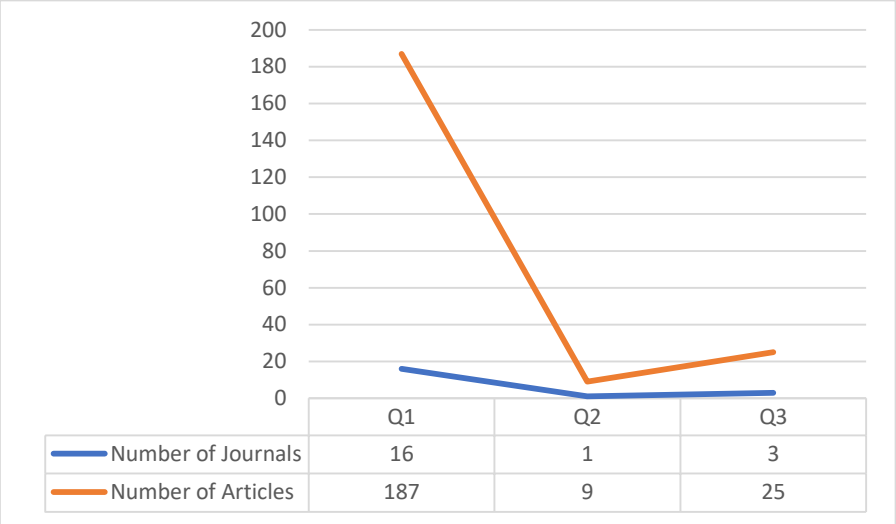

Figure 3. Distribution of indexed journals and articles categorised as Q1, Q2, and Q3

Additionally, Table 1 provides a detailed explanation of the top twenty journals that are highly prolific in publishing articles related to waste management technology.

Table 1. Distribution of documents by related sources from 2013-2024

Sources	SJR Index (Scimagojr 2022)	Articles
Journal of Cleaner Production	1.98 (Q1)	33
Sustainability (Switzerland)	0.66 (Q1)	21
Resources, Conservation and Recycling	2.68 (Q1)	18
Science of the Total Environment	1.95 (Q1)	16
Waste Management and Research	0.87 (Q1)	16
Chemical Engineering Transactions	0.24 (Q3)	14
Waste Management	1.75 (Q1)	14
Chemosphere	1.73 (Q1)	11
Energy	1.99 (Q1)	9
Journal of Environmental Management	1.68 (Q1)	9
Journal of Material Cycles and Waste Management	0.64 (Q2)	9
Environmental Science and Pollution Research	0.94 (Q1)	8
Journal of Hazardous Materials	2.57 (Q1)	7
Bioresource Technology	2.47 (Q1)	6
Environment and Natural Resources Journal	0.25 (Q3)	6
Environmental Pollution	2.11 (Q1)	5
Environmental Research	1.64 (Q1)	5
Recycling	0.69 (Q1)	5
Renewable and Sustainable Energy Reviews	3.23 (Q3)	5
Applied Energi	2.91 (Q1)	4

Documents based on Subject Area

A comprehensive total of 553 publications focusing on the utilisation of technology in waste management were gathered from documents spanning the years 2013 to 2024, with a particular emphasis on subject areas falling under the umbrella of environmental science. Notably, the subject areas of "Environmental science",

"Engineering", "Energy", "Psychology", "Social sciences", "Computer science, Business, and Chemical engineering", "Chemistry", "Agricultural and biological science" were represented by 352, 166, 149, 69, 66, 60, 55, 36, and 34 publications, respectively. Figure 4 provides a visual representation of the document classification highlighting subject areas.

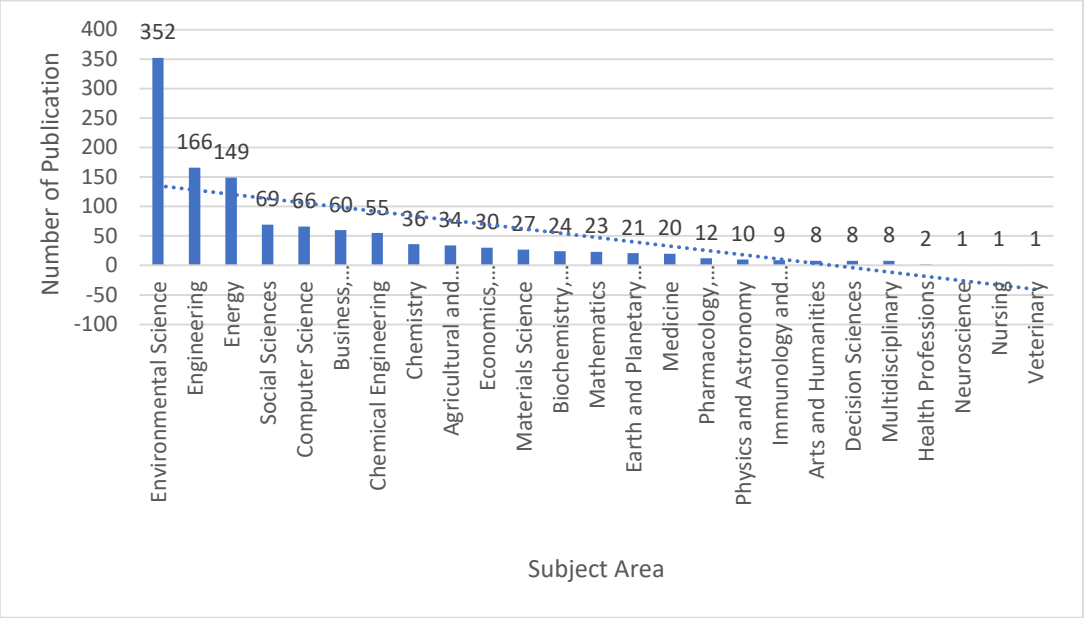

Figure 4. Document by subject area

Top Publications by Country

According to country classification, a total of 553 documents were distributed, with the majority originating from Malaysia, Indonesia, Thailand, China, Singapore, Vietnam, and India, accounting for 233, 108, 94, 84, 77, 55, and 40 articles, respectively. This distribution underscores Indonesia's active involvement in the research trend pertaining to the analysis of technology applications in waste management, showcasing its prominent role among Southeast Asian countries. Figure 5 visually delineates the top 10 distribution of Southeast Asian countries in publications concerning the application of technology in waste management.

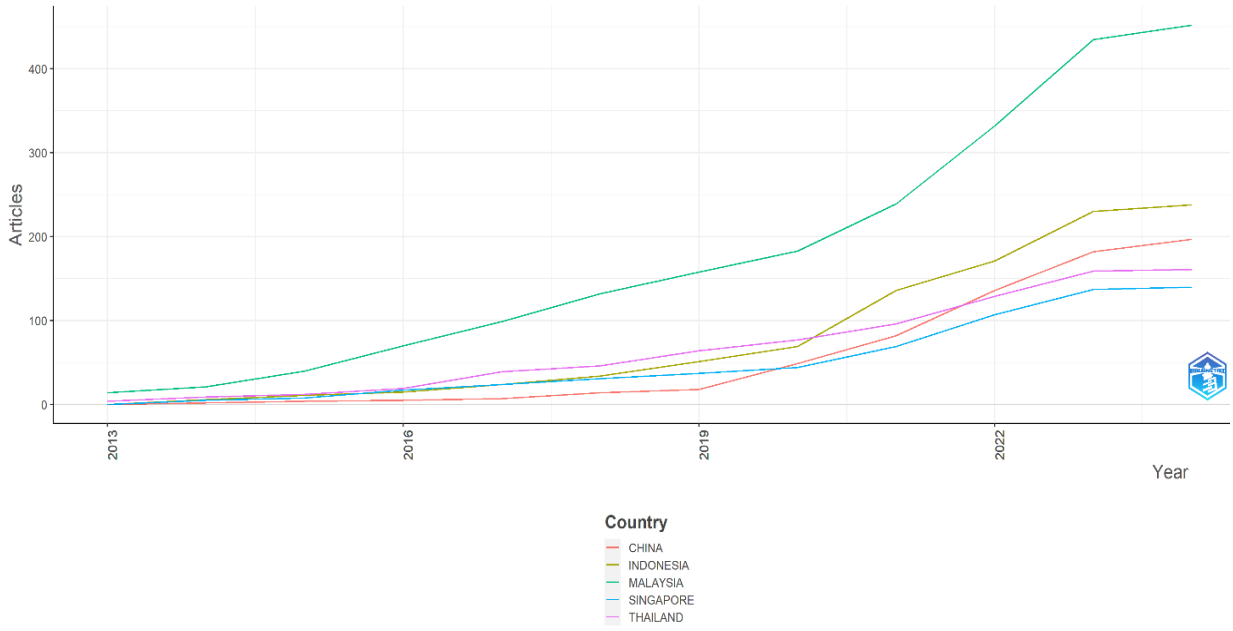

Figure 5. Country production over time

University Affiliation

Figure 6 presents the distribution of the top 20 university affiliations, emphasising their involvement in the application of technology in waste management. The distribution reflects a diverse array of university affiliations, spanning Malaysia, Singapore, Indonesia, and Thailand. Notably, Universiti Teknologi Malaysia and the National University of Singapore emerge as the most prolific institutions, contributing 58 documents each to the Scopus database. Following closely are Nanyang Technological University, University Kebangsaan Malaysia, and Chulalongkorn University, with 33, 32, and 30 articles, respectively. The analysis also highlights Indonesia's significant contribution, with three institutions making it to the top 20 affiliations, namely (1) Bandung Institute of Technology, (2) Universitas Sebelas Maret, and (3) Universitas Gajah Mada, collectively accounting for 44 publications. However, it is noteworthy that universities in Malaysia and Singapore continue to dominate the top 20 publications on the application of technology in waste management.

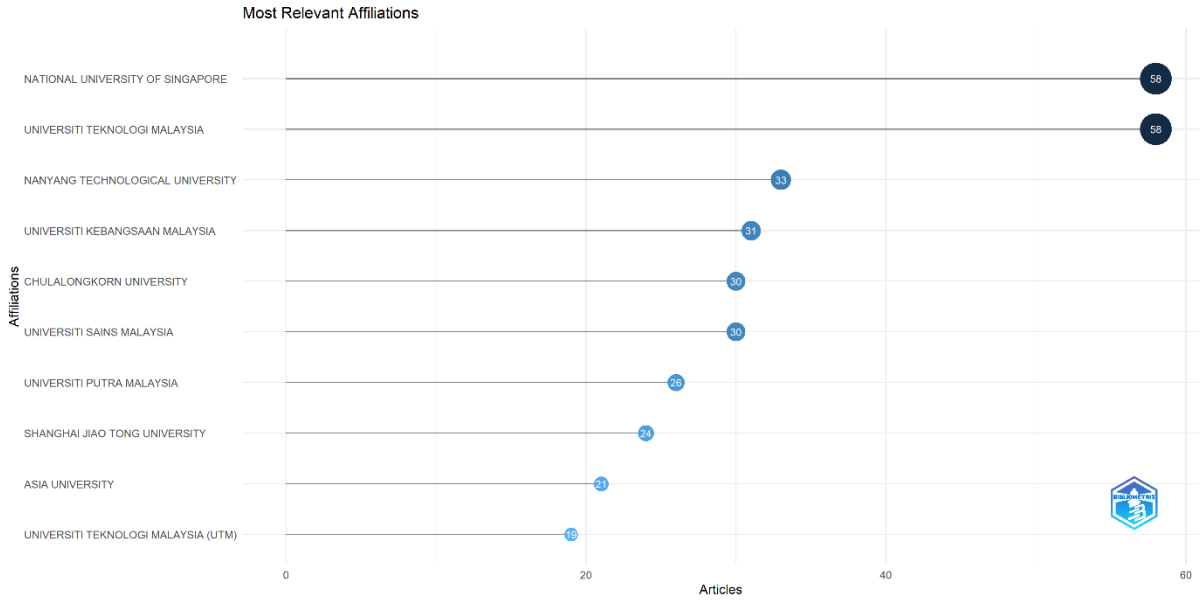

Figure 6. Most relevant affiliation

Top 10 Authors

Figure 7 highlights the most pertinent authors in this field, with Klemes JJ from the Czech Republic leading with 13 documents. Following closely are Lee CT and Tseng ML, each contributing 11 documents, along with Tong YW and Wang CH, who have authored 10 documents each.

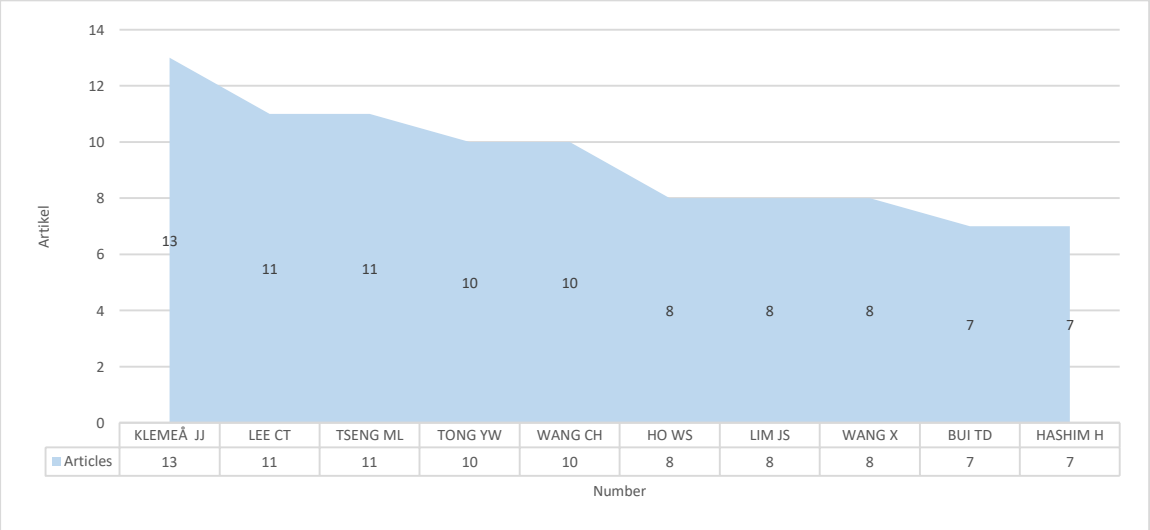

Figure 7. Top 10 authors

Document Citation

Based on the data retrieved from Scopus, the top 10 most cited documents per year are as follows: Huang (TC=535), Mehmood (TC=459), Fatimah (TC=276), Tan (TC=274), Ilyas (TC=258), Chand (TC=197), Hantoko (TC=191), Aranconrad (TC=187), Yun (TC=178), and Khoo (TC=162).

Table 2. A breakdown of the top 10 documents on Scopus by number of citations

Author/Year	Paper	DOI	Total Citations	TC per Year
Huang et al. (2018)	Construction and demolition waste management in China through the 3R principle	10.1016/j.resconrec.2017.09.029	535	76.43
Mehmood et al. (2017)	Internet-of-Things-Based Smart Cities: Recent Advances and Challenges	10.1109/MCOM.2017.1600514	459	57.38
Fatimah et al. (2020)	Industry 4.0 based sustainable circular economy approach for smart waste management system to achieve sustainable development goals: A case study of Indonesia	10.1016/j.jclepro.2020.122263	276	55.20
Tan et al. (2015)	Energy, economic and environmental (3E) analysis of waste-to-energy (WTE) strategies for municipal solid waste (MSW) management in Malaysia	10.1016/j.enconman.2015.02.010	274	27.40
Ilyas et al.(2020)	Disinfection technology and strategies for COVID-19 hospital and bio-medical waste management	10.1016/j.scitotenv.2020.141652	258	51.60
Chand Malav et al. (2020)	A review on municipal solid waste as a renewable source for waste-to-energy project in India: Current practices, challenges, and future opportunities	10.1016/j.jclepro.2020.123227	197	39.40
Hantoko et al. (2021)	Challenges and practices on waste management and disposal during COVID-19 pandemic	10.1016/j.jenvman.2021.112140	191	47.75
Arancon et al. (2013)	Advances on waste valorisation: New horizons for a more sustainable society	10.1002/ese3.9	187	15.58
Yun et al. (2018)	Metallurgical and mechanical methods for recycling of lithium-ion battery pack for electric vehicles	10.1016/j.resconrec.2018.04.025	178	25.43
Khoo (2019)	LCA of plastic waste recovery into recycled materials, energy and fuels in Singapore	10.1016/j.resconrec.2019.02.010	162	27.00

Mapping Technology Application in Waste Management with VOSviewer

The classification of study subjects pertaining to the application of technology in waste management is notable, with a total of 5463 keywords identified, of which 134 meet the threshold. Subsequently, this number was refined to 123 terms after merging identical terms. Network visualisation reveals the presence of 5 clusters, comprising 5042 links with a combined bond strength of 15719. Within these clusters, the red, green, blue, yellow, and purple clusters prioritise waste management, sustainable development, municipal solid waste, recycling, and waste disposal, respectively, with frequencies of 327, 91, 90, 84, and 79, respectively. Larger circles in the visualisation indicate higher frequencies of keywords in the documents (Zhang et al., 2024). Figure 8 presents the network visualisation using VOSviewer, accentuating the most frequently occurring keywords and networks.

Overlay Visualisation

The overlay visualisation is symbolised by colours indicating yearly experimental trends, where purple and yellow prioritise years of study and recent analysis, respectively. These recent trends focus on the following

terms: sustainable development, wastewater management, circular economy, resource recovery, machine learning, municipal solid waste management, environmental impact, pyrolisis, plastic waste, sustainable development, biofuel, environmental sustainability, waste to energy and wastewater treatment. The overlay visualisation of co-occurrence is depicted in Figure 9.

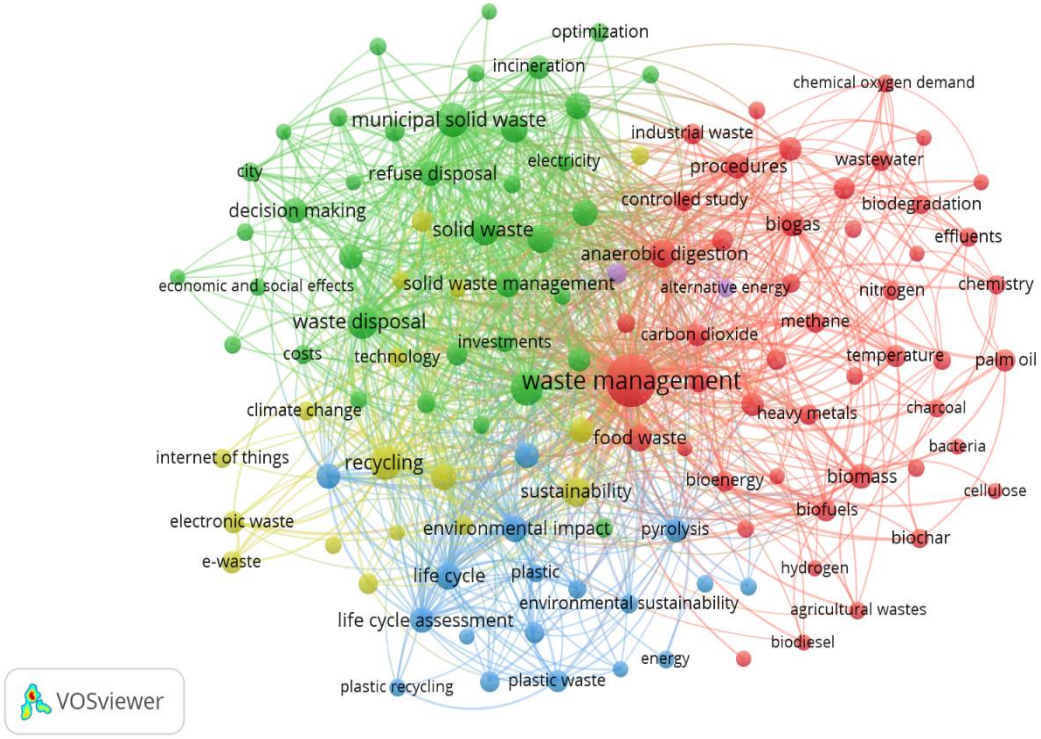

Figure 8. Network visualisation of co-occurrences with index keywords

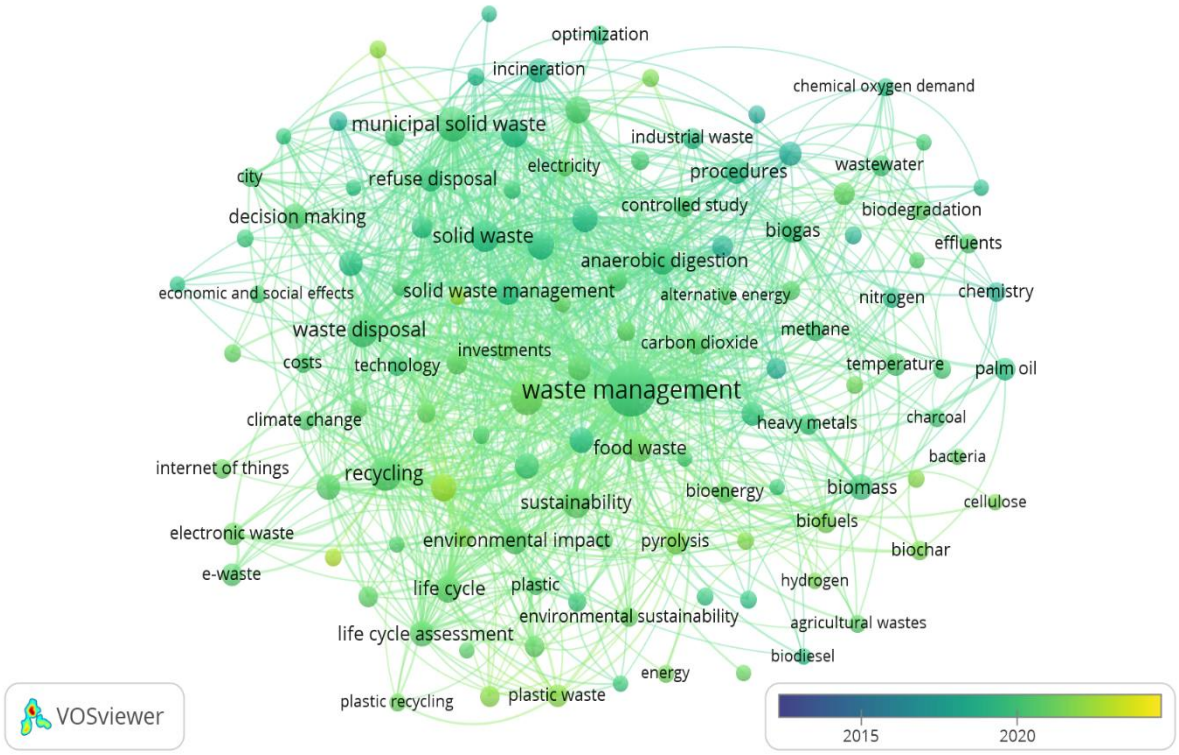

Figure 9. Overlay of visualisation of co-occurrences with index keywords

Density Visualisation

Density visualisation illustrates the saturation level of a topic, with colours such as red, blue, yellow, and green representing yet-to-be-analysed, rarely-studied, and highly evaluated areas, respectively. Brighter colours indicate a higher frequency of the analysed term in relevant experiments. The distribution of keyword density also reveals the frequency of research topics (van Eck & Waltman, 2010). For instance, terms like waste management and sustainable development are often analytically implemented, while rarely analysed and relevant terms focus on waste technology, waste disposal, sustainability, plastic waste, environmental impact analysis, creativity, life cycle, biofuel, composting, environmental sustainability, waste to energy, wastewater treatment and electronic waste. Figure 10 presents the density visualisation technology application in waste management based on keyword indexing.

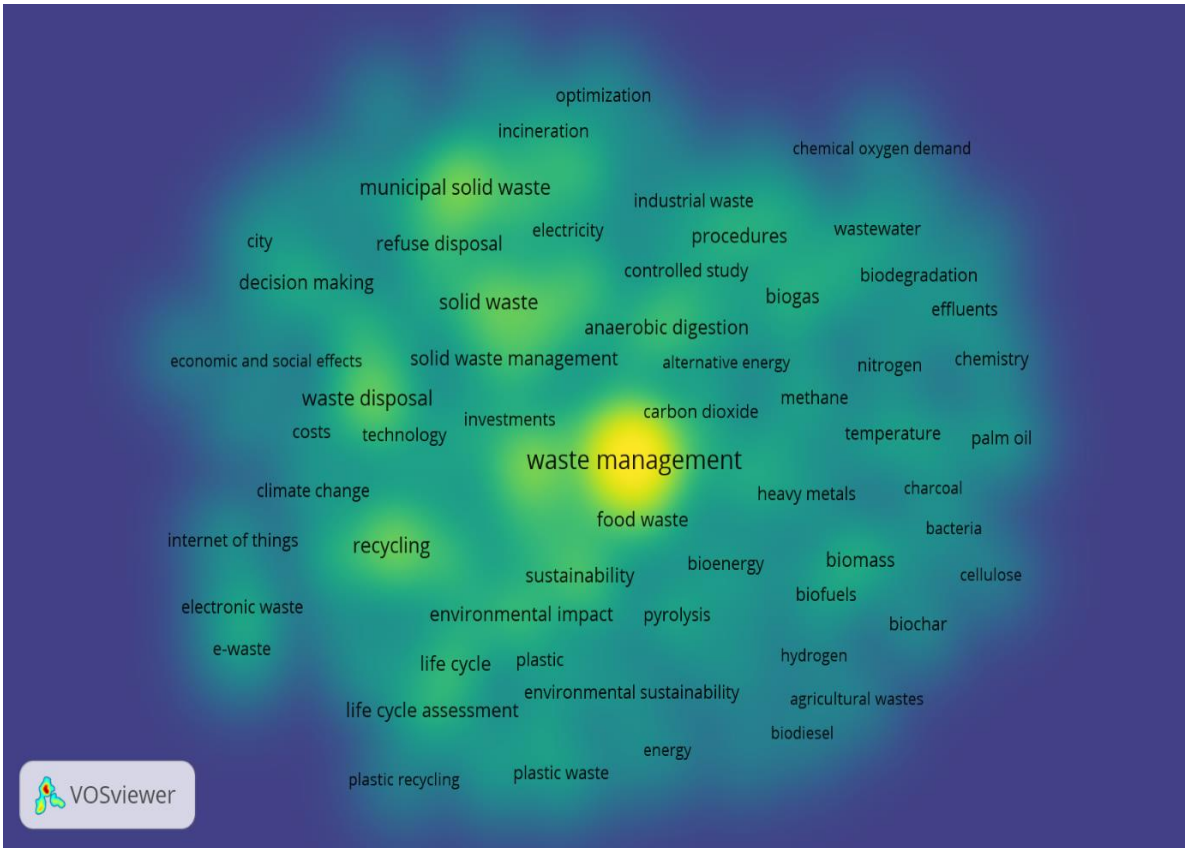

Figure 10. Density visualisation of technology application topics in waste management based on keyword indexing

Discussion

The utilisation of VOSviewer for bibliometric analysis has emerged as a valuable instrument for investigating research trends and contributions across diverse domains. Kirby (2023) and McAllister et al. (2021) emphasise its efficacy in initial research stages and visually representing publication interconnections, specifically within the realm of technology applications in waste management, this software has played a pivotal role in detecting fluctuations in publication figures, signalling an increasing interest in this area. Nonetheless, further inquiry is necessary to comprehend the decrease in recent publications (Rafdhi et al., 2023). Machado et al. (2022) also highlight VOSviewer's potential in identifying research voids, such as the necessity for environmentally-friendly technology in small and medium-sized manufacturing enterprises. This approach enables a comprehensive examination of publication productivity over the decade spanning from 2013 to 2024, revealing distinct fluctuations in publication numbers across different years. An upward trajectory was observed from 2019 to 2023, indicative of heightened interest and research focus in this domain, likely driven by technological advancements and emerging environmental concerns. However, the decline in publications in 2024 may seem unexpected; yet, it's essential to recognise that this data encompasses only the early months of 2024, thus

representing preliminary trends rather than the complete annual pattern. Further investigation and data collection are warranted to ascertain whether this decrease is temporary or indicative of a sustained trend.

Bibliometric analysis facilitates the evaluation of contributions from different countries and institutions in waste management research, offering insights into leading nations and academic entities driving knowledge generation. This comprehensive assessment sheds light on international collaboration dynamics and knowledge dissemination within the research community. The utilisation of VOSviewer in bibliometric analysis provides a nuanced understanding of research trends and contributions in technology application for waste management, aiding in the identification of areas necessitating further attention and understanding of the evolution of research in this domain. The analysis of primary document sources indicates a solid scientific foundation for waste management research, predominantly from scholarly journals spanning disciplines such as environmental science, engineering, and energy. Furthermore, subject area analysis reveals the interdisciplinary nature of technology application in waste management, with research distributed across various disciplines. Visualising document distribution based on subject areas offers a detailed perspective on research distribution across different disciplines. Specific scrutiny of contributions by countries highlights significant involvement from Southeast Asian nations like Malaysia, Indonesia, and Thailand, signalling the region's increasing focus on technology-driven waste management solutions. Visualising publication distribution by country offers a clear overview of the roles played by Southeast Asian countries in advancing research in this area.

A series of bibliometric analyses have illuminated the global landscape of waste management research. Le et al. (2023) and Shi et al. (2021) underscore the growing importance of E-waste and household waste recycling, with China and the British journal 'Waste Management' playing significant roles in these areas. Additionally, Judijanto et al. (2023) and Ndou & Rampedi (2022) highlight the interdisciplinary nature of this research, focusing on environmental sustainability in Indonesia's built environment studies and global and South African trends in municipal solid waste management. Collectively, these studies emphasise the necessity for sustainable solutions and the potential for international collaboration in addressing the challenges of waste management.

A previous bibliometric study, such as the one conducted by Mesdaghinia et al. (2015), examined waste management publications. In this study, the main focus is analysing publication trends regarding technology in waste management across Southeast Asia from 2013 to 2024. We utilised a bibliometric approach to identify institutional contributions, publication trends, and the most popular research topics. On the other hand, Mesdaghinia's research centred on publication trends related to solid waste in Iran from 1982 to 2013. These differences in time frame and geographical coverage offer distinct perspectives in understanding the evolution of waste management research. Meanwhile, the findings from both studies reveal contrasting trends. Our study highlights the highest publication contributions from Malaysia and Singapore and the most popular research topics. In contrast, the study in Iran highlights a decreasing trend in publication numbers and efforts to enhance collaboration among institutions to boost research output in this field. Thus, comparing these two studies provides diverse insights into waste management research trends in the two regions.

Within university affiliations, institutions spanning Malaysia, Singapore, Indonesia, and Thailand emerge as pivotal players in advancing research on technology applications in waste management. Prominent universities from these nations actively contribute to publications in this field, as evidenced by the detailed breakdown in the table showcasing top university affiliations. This underscores the importance of cross-country and cross-institutional collaboration in driving knowledge advancement within this domain. Additionally, noteworthy contributions come from leading authors across various countries, including the Czech Republic, Taiwan, and China, who actively engage in research on technology applications in waste management. Visualisation tools illustrate the significant impact of these authors on knowledge expansion in this area. Moreover, the analysis identifies highly cited publications, underscoring the widespread influence of specific research endeavours. Sure, researchers and authors play pivotal roles in shaping the trajectory and progression of research in this field, highlighting their significant contributions to the scholarly discourse and practical applications of waste management technology.

The most cited document in this bibliometric analysis is a study by Huang et al. (2018), which discusses the management of construction and demolition waste (CDW) in China. CDW accounts for approximately 30-40% of total waste in China, with a recycling rate of only about 5%. The study analyses CDW management in China using the principles of 3R (reduce, reuse, recycle) and discusses existing policies, challenges, and proposed solutions. Highlighted issues include the lack of information exchange between departments, immature recycling technologies, underdeveloped markets for recycled products, and inadequate supervision and management. Proposed strategies include effective circular economic models, strengthening source control, enhancing supervision and management, adopting innovative technologies and market models, and providing

economic incentives to promote CDW reuse and recycling in China. Despite CDW management regulations requiring specific recycling rates for full waste disposal cost recovery, recycling rates in cities like Beijing and Shanghai remain low. Other challenges include the lack of design standards for waste reduction, low disposal costs, improper urban planning leading to high demolition rates, and ineffective systems for CDW material collection, sorting, and reuse. Efforts to promote the principles of reduce, reuse, and recycle (3R) in CDW management in China face various obstacles that must be addressed. The extensive citation of this document is likely attributed to its comprehensive examination of construction and demolition waste management issues in China, offering valuable insights and practical solutions for addressing challenges in the field.

The VOSviewer network visualisation is a valuable tool for understanding the structure and connections among frequently occurring keywords in research, particularly in the domain of technology application in waste management. Through cluster analysis techniques, VOSviewer aids in identifying groups of keywords that commonly co-occur in literature, thereby offering insights into central themes and research trends. VOSviewer network visualisation emerges as a valuable asset in comprehending keyword structures and relationships within waste management research (Gorzeń-Mitka et al., 2020; Han & Gong, 2021; Yalçıntaş et al., 2023; Zhu et al., 2021). This visualisation method enables the identification of keyword clusters, shedding light on primary focuses and evolving research trends within the field. Moreover, the application of VOSviewer reveals clusters of keywords related to waste management technology, waste disposal, and environmental impact analysis, which frequently appear together, indicating the significance of these topics in the literature. Overlay and density visualisations further enrich our understanding of experimental trends and ongoing research focuses. Different colours highlighting annual trends and density levels offer insights into how research interests evolve and where research hubs are situated. For instance, an increase in yellow denotes a growing interest in specific topics in recent research, while blue indicates less-explored areas. This information is pivotal for planning future research endeavours. By comprehending existing research trends and focuses, researchers can pinpoint areas that have been extensively studied and those requiring further attention. For instance, identifying clusters of keywords that have been less explored empowers researchers to delve deeper into those topics and contribute meaningfully to the scientific discourse. Thus, network, overlay, and density visualisations collectively provide a holistic view of research trends and directions in technology application in waste management. Building upon the insights gained from the bibliometric analysis of waste management research, future studies could explore several novel avenues to advance knowledge in this field. One potential area of investigation involves examining the impact of emerging technologies, such as artificial intelligence, machine learning, and the Internet of Things (IoT), on waste management practices. By leveraging these technologies, researchers can develop innovative solutions for optimising waste collection, sorting, recycling, and disposal processes, enhancing efficiency and sustainability.

Furthermore, future research could delve into the socio-economic aspects of waste management, including the role of public awareness, community engagement, and policy interventions in promoting sustainable waste practices. Studies focusing on the socio-economic dimensions of waste management underscore the necessity of adopting a comprehensive approach that encompasses economic viability, public acceptance, and technological progress. The impact of socio-economic status on waste quantity and composition, alongside the significance of public awareness and community involvement, is emphasised (Lakioti et al., 2017). Within healthcare settings, socio-economic and institutional factors emerge as pivotal drivers of sustainable waste management. Additionally, examining the socio-economic ramifications of waste management delves into the interplay between waste practices and sociocultural influences (Tudor, 2007). These investigations highlight the criticality of integrating socio-economic considerations to foster sustainable waste management practices.

Understanding the drivers of waste generation and disposal behaviour among different demographic groups can inform the design of targeted interventions to reduce waste generation, promote recycling, and foster a culture of environmental stewardship. Another promising avenue for future research is the exploration of circular economy principles in waste management. By adopting a circular economy approach, which emphasises the minimisation of waste and the maximisation of resource efficiency, researchers can develop strategies for closing the loop on material flows, reducing reliance on finite resources, and promoting sustainable consumption and production patterns. Additionally, future studies could investigate the environmental and health impacts of emerging waste streams, such as electronic waste (e-waste), plastic waste, and hazardous waste. By quantifying the environmental footprint and health risks associated with these waste streams, researchers can inform policy decisions and industry practices to mitigate their adverse effects on ecosystems and human health. Moreover, interdisciplinary research initiatives that bring together experts from diverse fields, including environmental science, engineering, economics, social sciences, and public health, can facilitate holistic approaches to addressing complex waste management challenges. By fostering collaboration and knowledge exchange across

disciplines, such initiatives can catalyse innovation and drive transformative change in waste management practices.

Future research endeavours in waste management should integrate cutting-edge technologies, socio-economic considerations, circular economy principles, and interdisciplinary collaboration to develop holistic and sustainable solutions for managing waste in an increasingly resource-constrained world. Through these efforts, researchers can contribute to advancing knowledge and developing evidence-based strategies to address the pressing environmental challenges associated with waste management. From the visualisation using VOSviewer, it is evident that waste management technology is still not fully explored in scholarly literature. This indicates that waste management remains a highly complex issue that has been inadequately addressed in various countries. However, from the overlay visualisation, promising opportunities for further development and research in the application of waste management technology can be identified. For instance, researchers are still relatively underexplored in technologies such as pyrolysis, biofuels, biogas, and waste to energy. By harnessing the potential of these technologies, innovative solutions can be developed to address challenges in waste management. Pyrolysis, for example, is a thermal process that can convert organic waste into biochar or biofuel, which can serve as alternative energy sources. Developing biofuels and biogas from organic waste can also help reduce reliance on fossil fuels and mitigate greenhouse gas emissions.

The pressing need for enhanced solid waste management strategies is apparent in existing literature, with studies by Gouveia (2012) underlining the necessity to mitigate environmental and public health risks. These strategies encompass improving recycling methods, reducing waste disposal in landfills, and promoting sustainable consumption habits. Nevertheless, further investigation into the potential health impacts of waste management technologies is warranted whilst acknowledging the significant role of independent waste collectors in sustainable waste management. Developing cost-effective and economically beneficial waste management approaches is also paramount. Furthermore, solid waste management remains relatively unexplored in academic literature despite its critical importance. By formulating efficient technologies and strategies for managing solid waste, we can alleviate its detrimental effects on the environment and public health. This involves enhancing recycling methods, minimising waste disposal in landfills, and advocating for sustainable consumption habits. Considering the findings from VOSviewer and overlay visualisation, it becomes apparent that numerous opportunities exist for further research and advancement in the application of waste management technology. Utilising existing technological capabilities and investigating overlooked areas will be pivotal in addressing waste management challenges and progressing towards a more environmentally sustainable society.

Conclusion

Several key findings can be identified based on the bibliometric analysis using VOSviewer. Over ten years (2013-2024), fluctuations in publication productivity regarding the application of technology in waste management are evident, with an increase in publications from 2014 to 2023 but a decline in 2024. The primary documents are obtained from various sources such as journals, proceedings, book chapters, reviews, and books, with the majority focusing on waste management across various fields such as environmental science, engineering, energy, and psychology. Although most publications originate from Malaysia, Indonesia also plays a significant role in this research trend. Universiti Teknologi Malaysia and the National University of Singapore emerge as the most productive institutions in publications. However, three institutions from Indonesia are also included in the top twenty list. The most relevant author on this topic is Klemes JJ from the Czech Republic. Visualisations with VOSviewer reveal research trends and focuses, with various clusters and patterns emerging, highlighting the most analysed and least studied topics in research. This indicates a strong interest in advancing knowledge about waste management and technology implementation in this field. This research implies that the use of technology in waste management has the potential to yield more effective and sustainable solutions in the future. With a better understanding of research trends and study focuses in this field, researchers and practitioners can identify areas that need further attention and develop innovative technologies. This research also indicates a shift towards a multidisciplinary approach in waste management, emphasising the importance of interdisciplinary collaboration to address complex waste-related challenges. Furthermore, with significant contributions from Southeast Asian countries, the implication is that there is potential to enhance regional cooperation in developing and implementing technological solutions for waste management. Considering the themes revealed in this research, policymakers and stakeholders can prioritise investments in research and technology development that support sustainable waste management, which can contribute to sustainable economic development and environmental protection in the future.

Recommendation

The findings suggest several vital recommendations for improving Southeast Asian waste management practices and research. Firstly, fostering interdisciplinary collaboration among researchers across fields like environmental science, engineering, and social sciences can lead to innovative solutions for complex waste management challenges. Secondly, promoting international cooperation and knowledge sharing can accelerate progress by exchanging best practices and resources. Investing in research capacity building is crucial to cultivating a skilled workforce equipped to tackle emerging challenges. Encouraging open-access publishing ensures wider dissemination of research findings, fostering collaboration and informed decision-making. Prioritising research on emerging technologies like pyrolysis and biogas can unlock sustainable waste treatment solutions. Integrating stakeholder engagement ensures research efforts align with real-world needs, enhancing the relevance of outcomes. Lastly, supporting longitudinal studies enables tracking of evolving trends and assessment of long-term impacts, facilitating informed decision-making for sustainable waste management practices. Implementing these recommendations can lead to more efficient, sustainable, and environmentally friendly regional waste management practices.

Scientific Ethics Declaration

The authors declare that the scientific, ethical and legal responsibility of this article published in EPSTEM Journal belongs to the authors.

Acknowledgements

*This article was presented as an oral presentation at the International Conference on Research in Engineering, Technology and Science (www.icrets.net) held in Tashkent/Uzbekistan on August 22-25, 2024.

*The authors wish to extend their sincere appreciation and gratitude to the Lembaga Pengelola Dana Pendidikan-LPDP (Indonesia Endowment Fund for Education) under the Ministry of Finance of the Republic of Indonesia for their invaluable support in facilitating this publication and fostering collaboration.

References

Adam, M., Okasha, M. E., Tawfeeq, O. M., Margan, M. A., & Nasreldeen, B. (2018, August). Waste management system using IoT. In *2018 International conference on computer, control, electrical, and electronics engineering (ICCCEEE)* (pp. 1-4). IEEE.

Aleyadeh, S., & Taha, A. E. M. (2018, May). An IoT-Based architecture for waste management. In *2018 IEEE International Conference on Communications Workshops (ICC Workshops)* (pp. 1-4). IEEE.

Arancon, R. A. D., Lin, C. S. K., Chan, K. M., Kwan, T. H., & Luque, R. (2013). Advances on waste valorization: new horizons for a more sustainable society. *Energy Science & Engineering*, *1*(2), 53-71.

Boloy, R. A. M., da Cunha Reis, A., Rios, E. M., de Araújo Santos Martins, J., Soares, L. O., de Sá Machado, V. A., & de Moraes, D. R. (2021). Waste-to-energy technologies towards circular economy: A systematic literature review and bibliometric analysis. *Water, Air, & Soil Pollution*, *232*(7), 306.

Malav, L. C., Yadav, K. K., Gupta, N., Kumar, S., Sharma, G. K., Krishnan, S., ... & Bach, Q. V. (2020). A review on municipal solid waste as a renewable source for waste-to-energy project in India: Current practices, challenges, and future opportunities. *Journal of Cleaner Production*, *277*, 123227.

Dinnar, S. H., Islam, S., Singh, M., & Gaba, R. (2022). Future-oriented waste management technology for ward-6, Bogura, Bangladesh–a step towards sustainability. *Geomatics and Environmental Engineering*, *16*(1).

Donthu, N., Kumar, S., Mukherjee, D., Pandey, N., & Lim, W. M. (2021). How to conduct a bibliometric analysis: An overview and guidelines. *Journal of business research*, *133*, 285-296.

Falagas, M. E., Pitsouni, E. I., Malietzis, G. A., & Pappas, G. (2008). Comparison of PubMed, Scopus, web of science, and Google scholar: strengths and weaknesses. *The FASEB journal*, *22*(2), 338-342.

Fatimah, Y. A., Govindan, K., Murniningsih, R., & Setiawan, A. (2020). Industry 4.0 based sustainable circular economy approach for smart waste management system to achieve sustainable development goals: A case study of Indonesia. *Journal of Cleaner Production*, *269*, 122263.

García-Ávila, F., Avilés, A., Cabello-Torres, R., Guanuchi-Quito, A., Cadme-Galabay, M., Gutiérrez-Ortega, H., Alvarez Ochoa, R., & Zhindón-Arévalo, C. (2023). Application of ornamental plants in constructed

wetlands for wastewater treatment: A scientometric analysis. *Case Studies in Chemical and Environmental Engineering*, *7*, 100307.

Gorzeń-Mitka, I., Bilska, B., Tomaszewska, M., & Kołożyn-Krajewska, D. (2020). Mapping the structure of food waste management research: A co-keyword analysis. *International Journal of Environmental Research and Public Health*, *17*(13), 4798.

Gouveia, N. (2012). Solid urban waste: socio-environmental impacts and prospects for sustainable management with social inclusion. *Ciencia & Saude Coletiva*, *17*(6), 1503

Gupta, P. K., Shree, V., Hiremath, L., & Rajendran, S. (2019). The use of modern technology in smart waste management and recycling: artificial ıntelligence and machine learning. *Recent Advances in Computational Intelligence*. https://api.semanticscholar.org/CorpusID:169625832

Ha, C. T., Thao, T. T. P., Trung, N. T., Huong, L. T. T., Dinh, N. Van, & Trung, T. (2020). A bibliometric review of research on STEM education in Asean: Science mapping the literature in scopus database, 2000 to 2019. *Eurasia Journal of Mathematics, Science and Technology Education*, *16*(10).

Hallinger, P., & Suriyankietkaew, S. (2018). Science mapping of the knowledge base on sustainable leadership, 1990-2018. *Sustainability (Switzerland)*, *10*(12), 1–22.

Han, L., & Gong, Z. (2021). Visual analysis of construction waste research based on VOSviewer. *E3S Web of Conferences*.

Hantoko, D., Li, X., Pariatamby, A., Yoshikawa, K., Horttanainen, M., & Yan, M. (2021). Challenges and practices on waste management and disposal during COVID-19 pandemic. *Journal of Environmental Management*, *286*, 112140.

Hoang, N. H., Ishigaki, T., Kubota, R., Yamada, M., & Kawamoto, K. (2020). A review of construction and demolition waste management in Southeast Asia. *Journal of Material Cycles and Waste Management*, *22*, 315-325.

Huang, B., Wang, X., Kua, H., Geng, Y., Bleischwitz, R., & Ren, J. (2018). Construction and demolition waste management in China through the 3R principle. *Resources, Conservation and Recycling*, *129*, 36-44.

Ilyas, S., Srivastava, R. R., & Kim, H. (2020). Disinfection technology and strategies for COVID-19 hospital and bio-medical waste management. *Science of the Total Environment*, *749*, 141652.

Judijanto, L., Lubis, A. F., & Hidayati, N. (2023). A bibliometric analysis of the development of research on environmental ıssues and sustainability in modern society's built environment studies in Indonesia. *West Science Social and Humanities Studies*, *1*(06), 477-486.

Karakus, M., Ersozlu, A., & Clark, A. C. (2019). Augmented reality research in education: A bibliometric study. *Eurasia Journal of Mathematics, Science and Technology Education*, *15*(10).

Karunambiga, Dr. K., & Sathiya, Dr. M. (2023). Technological view on smart waste management. *International Journal of Computer Applications Technology and Research*.

Kho, M. E., & Brouwers, M. C. (2012). The systematic review and bibliometric network analysis (SeBriNA) is a new method to contextualize evidence. Part 1: Description. *Journal of Clinical Epidemiology*, *65*(9), 1010–1015.

Khoo, H. H. (2019). LCA of plastic waste recovery into recycled materials, energy and fuels in Singapore. *Resources, Conservation and Recycling*, *145*, 67-77.

Kinantan, B., Matondang, A. R., & Hidayati, J. (2018). Waste management as an effort to improve urban area cleanliness and community income (journal review). *IOP Conference Series: Materials Science and Engineering*, *309*.

Kirby, A. (2023). Exploratory bibliometrics: using VOSviewer as a preliminary research tool. *Publications*, *11*(1), 10.

Kumari, J., Shrivastava, G., Sinha, A., & Kumar, P. (2019). Role of technology in solid waste management: a review. *Recent Patents on Computer Science*, *12*(4), 338-348.

Lakioti, E. N., Moustakas, K., Komilis, D., Asimina, Domopoulou, E., & Karayannis, V. (2017). Sustainable solid waste management: Socio-economic considerations. *Chemical Engineering Transactions*, *56*, 661–666.

Le, M. H., Lu, W. M., & Chang, J. C. (2023). Recycling E-waste and the sustainable economy: A bibliometric exploration. *Sustainability*, *15*(22), 16108.

Lee, C. T., Mohammad Rozali, N. E., Van Fan, Y., Klemeš, J. J., & Towprayoon, S. (2018). Low-carbon emission development in Asia: energy sector, waste management and environmental management system. *Clean Technologies and Environmental Policy*, *20*, 443-449.

Machado, F., Duarte, N., Amaral, A., & Araújo, M. (2022). Digital transformation in manufacturing SMEs: A bibliometric analysis using VOSviewer. In *Proceedings of the 12th International Scientific Conference on Business and Management* (pp. 627-633).

Maditati, D. R., Munim, Z. H., Schramm, H.-J., & Kummer, S. (2018). A review of green supply chain management: From bibliometric analysis to a conceptual framework and future research directions. *Resources, Conservation and Recycling*, *139*, 150–162.

McAllister, J. T., Lennertz, L., & Mojica, Z. A. (2021). Mapping a discipline: a guide to using vosviewer for bibliometric and visual analysis. *Science \& Technology Libraries*, *41*, 319–348.

Mehmood, Y., Ahmad, F., Yaqoob, I., Adnane, A., Imran, M., & Guizani, S. (2017). Internet-of-things-based smart cities: recent advances and challenges. *IEEE Communications Magazine*, *55*(9), 16 – 24.

Mesdaghinia, A., Mahvi, A. H., Nasseri, S., Nodehi, R. N., & Hadi, M. (2015). A bibliometric analysis on the solid waste-related research from 1982 to 2013 in Iran. *International Journal of Recycling of Organic Waste in Agriculture*, *4*(3), 185–195.

Mongeon, P., & Paul-Hus, A. (2016). The journal coverage of Web of Science and Scopus: a comparative analysis. *Scientometrics*, *106*(1), 213–228.

Ndou, V., & Rampedi, I. T. (2022). Bibliometric analysis of municipal solid waste management research: global and South African trends. *Sustainability*, *14*(16), 10229.

Abhi Rafdhi, A., Soeryanto Soegoto, E., Neni Hayati, E., Saputra, H., Untsa Mega, R., & Ihsan Rifaldi, M. (2023). Economic growth and its influence on environment sustainability: A bibliometric analysis using VOSviewer application. *Journal of Eastern European and Central Asian Research*, *10*(1).

Sadinov, A., & Rajabov, S. (2023). Utilizing digital technologies for waste management. *E3S Web of Conferences*.

Sandeep, P., T.Sreejith, Aravind, G., & Reddy, N. O. (2018). Smart waste management. *International Journal of Advance Research and Innovative Ideas in Education*, *4*, 1078–1085.

Sunyono, S., Een, Y. H., Hariri, H., Ganda Putra, F., Diani, R., Misbah, M., & Umam, R. (2022). Natural disaster education in school: A bibliometric analysis with a detailed future insight overview. *International Journal of Educational Methodology*, *8*(4), 743-757.

Secinaro, S., Brescia, V., Calandra, D., & Biancone, P. (2020). Employing bibliometric analysis to identify suitable business models for electric cars. *Journal of Cleaner Production*, *264*, 121503.

Shi, K., Zhou, Y., & Zhang, Z. (2021). Mapping the research trends of household waste recycling: A bibliometric analysis. *Sustainability*, *13*(11), 6029.

Suprapto, N., Sukarmin, S., Puspitawati, R. P., Erman, E., Savitri, D., Ku, C. H., & Mubarok, H. (2021). Research trend on TPACK through bibliometric analysis (2015-2019). *International Journal of Evaluation and Research in Education*, *10*(4), 1375–1385.

Sweileh, W. M., Al-Jabi, S. W., Sawalha, A. F., & Zyoud, S. E. H. (2016). Bibliometric profile of the global scientific research on autism spectrum disorders. *Springerplus*, *5*, 1-12.

Pallavi Talukdar, P. T., Moonty Baruah, M. B., & Pinky Saikia, P. S. (2018). Waste management for sustainable agricultural production-a brief review. *Asian Journal of Home Science*, *13*(2), 657-659

Tan, S. T., Ho, W. S., Hashim, H., Lee, C. T., Taib, M. R., & Ho, C. S. (2015). Energy, economic and environmental (3E) analysis of waste-to-energy (WTE) strategies for municipal solid waste (MSW) management in Malaysia. *Energy Conversion and Management*, *102*, 111 – 120.

Trivedi, M., Mathur, M., Johri, P., Singh, A., & Tiwari, R. K. (2020). Waste management: A paradigm shift. *Environmental Concerns and Sustainable Development: Volume 2: Biodiversity, Soil and Waste Management*, 337-363.

Tudor, T. L. (2007). The socio-economic, institutional and environmental influences on sustainable waste management practices in the healthcare setting: a UK case study. *The International Journal of Environmental Cultural, Economic and Social Sustainability*, *3*(2), 41-50.

Tun, M. M., Palacky, P., Juchelkova, D., & Síťař, V. (2020). Renewable waste-to-energy in Southeast Asia: status, challenges, opportunities, and selection of waste-to-energy technologies. *applied sciences*, *10*(20), 7312.

van Eck, N. J., & Waltman, L. (2010). Software survey: VOSviewer, a computer program for bibliometric mapping. *Scientometrics*, *84*(2), 523–538. h

Varudandi, S., Mehta, R., Mahetalia, J., Parmar, H., & Samdani, K. (2021). A smart waste management and segregation system that uses ınternet of things, machine learning and android application. *2021 6th International Conference for Convergence in Technology (I2CT)*, 1–6.

Yalçıntaş, D., Oğuz, S., Yaşa Özeltürkay, E., & Gülmez, M. (2023). Bibliometric analysis of studies on sustainable waste management. *Sustainability*, *15*(2), 1414.

Yang, T., Xu, J., Zhao, Y., Gong, T., Zhao, R., Sun, M., & Xi, B. (2021). Classification technology of domestic waste from 2000 to 2019: a bibliometrics-based review. *Environmental Science and Pollution Research*, *28*, 26313-26324.

Yun, L., Linh, D., Shui, L., Peng, X., Garg, A., Le, M. L. P., ... & Sandoval, J. (2018). Metallurgical and mechanical methods for recycling of lithium-ion battery pack for electric vehicles. *Resources, Conservation and Recycling*, *136*, 198-208.

Zhang, Y., Tan, Y. T., Wang, M. J., Li, L., Huang, J. F., & Wang, S. C. (2024). Bibliometric analysis of PTEN in neurodevelopment and neurodegeneration. *Frontiers in Aging Neuroscience*, *16*, 1390324.

Zhu, J. J., Dressel, W., Pacion, K., & Ren, Z. J. (2021). ES&T in the 21st century: A data-driven analysis of research topics, interconnections, and trends in the past 20 years. *Environmental Science & Technology*, *55*(6), 3453-3464.

Zupic, I., & Čater, T. (2015). Bibliometric methods in management and organization. *Organizational Research Methods*, *18*(3), 429-472.

Author Information

Haryanto Haryanto
Universitas Pendidikan Indonesia,
Bandung, Indonesia
Contact e-mail: haryanto10@upi.edu

Sjaeful Anwar
Universitas Pendidikan Indonesia,
Bandung, Indonesia

Rini Solihat
Universitas Pendidikan Indonesia
Bandung, Indonesia

Fadli Agus Triansyah
Universitas Pendidikan Indonesia
Bandung, Indonesia

Ilham Muhammad
Universitas Pendidikan Indonesia
Bandung, Indonesia

Debi S Fuadi
Universitas Pendidikan Indonesia
Bandung, Indonesia

Andika Pratama
Universitas Pendidikan Indonesia
Bandung, Indonesia

Fiza Dora Selpa Pertiwi
Universitas Islam Negeri Fatmawati Sukarno Bengkulu
Bandung, Indonesia

To cite this article:

Haryanto, H., Anwar, S., Solihat, R., Triansyah, F.A., Muhammad, I., Fuadi, D.S., Pratama, A., & Pertiwi, F.D.S. (2024). Technology applications in waste management across Southeast Asia: A bibliometric analysis over the past decades. *The Eurasia Proceedings of Science, Technology, Engineering & Mathematics (EPSTEM)*,*29*,155-172.

The Eurasia Proceedings of Science, Technology, Engineering & Mathematics (EPSTEM)
ISSN: 2602-3199

The Eurasia Proceedings of Science, Technology, Engineering & Mathematics (EPSTEM), 2024

Volume 29, Pages 173-181

ICRETS 2024: International Conference on Research in Engineering, Technology and Science

Computer-Aided System for Customs Fraud Analytics Based on Artificial Intelligence Techniques

Veska Gancheva
Technical University of Sofia

George Popov
Technical University of Sofia

Kamelia Raynova
Technical University of Sofia

Antoaneta Popova
Technical University of Sofia

Ivaylo Georgiev
Bulgarian Academy of Science

Abstract: Globalization has stimulated the opening of the market and the accumulation of huge amounts of data, which consequently leads to an increase in the importance of the control of customs operations. However, customs data is highly imbalanced and this poses challenges in its integration and processing. Therefore, it is of prime importance to find automatic computationally intelligent solutions for customs management. The purpose of the research presented in this paper is to propose a computer-aided system for customs fraud analytics based on artificial intelligence techniques, ensuring the application and verification of methods and algorithms for integration, management, analysis and visualization of data on customs violations. The architecture of the customs violation data analysis system consists of the following components: data sources, data storage, data integration and preprocessing, real-time data flow, modeling, analysis and storage of analytical data, and visualization of the results. A machine learning approach for detecting customs fraud through unstructured data analysis is proposed. An artificial neural network designed for data analysis is designed, and the input data is divided into training data and testing data. A reduced set of statistical records related to the analysis of heterogeneous databases of different institutions, which is stored in a data warehouse, are used as experimental data. The first 80% of the data are used to train the neural network and the remaining 20% to test the trained network. Experimental results show that the calculated accuracy increases with increasing epochs and is higher for the training data and lower for the validation test data. Thus, the trained model can be saved and used to monitor for anomalies. The trained model is applied to the system to calculate new input parameters that were not used in either training or validation.

Keywords: Artificial intelligence, Customs fraud, Computer-aided system, Data analytics, Neural network.

Introduction

Financial fraud is a problem with far-reaching consequences in the financial industry, government, corporate sectors and for ordinary consumers. Increasing reliance on new technologies such as cloud and mobile computing in recent years has compounded the problem. Not surprisingly, financial institutions are turning to automated processes using statistical and computational methods.

Growing volumes of international trade put strain on regulatory oversight, which is faced by customs administration. Regulators thus use data mining to concentrate their little resources on the fraud cases that have the highest likelihood of occurring. Standard learning algorithms are most frequently used in tax studies' fraud detection applications. However, there are new difficulties because of the extreme imbalance in customs data.

Governments and customs administrations realize that the growing demand for free and secure commerce (including e-commerce) requires data standardization. This is the only approach by which governments can fulfill their missions. The World Customs Organization (WCO) Data Model provides an appropriate framework of standard and harmonized data sets and standard electronic messages that are transmitted by trade for customs and other regulatory purposes to complete arrival, departure, transit and release formalities of goods in international cross-border trade. Thus, standardized data sets and electronic messages using international customs code standards are a key mechanism for effective and efficient information exchange between businesses and governments. In practice, through the presented information model, unification of the requirements for data exchange is obtained, and thus it is possible to create a single electronic structure allowing effective exchange of information in a global aspect. The WCO data model also incorporates the data requirements of other government regulatory bodies, enabling a single window environment that allows traders to provide information only once to one official body, preferably customs, to fulfill all regulatory requirements related to import or export.

According to European and international requirements, customs codes are standardized. This standardization, as well as access to information, are regulated by law. Each register is a structured electronic database. The registers contain data provided by economic operators in accordance with European and national customs legislation, and data and circumstances entered by the Customs Service in connection with the implementation of its functions and tasks. Data from the registers are exchanged with the customs authorities of the Member States and the European Commission in cases where the customs legislation requires it, and are determined by the technical specifications of the relevant electronic systems.

Customs administrations lessen the grave risks that smuggling and tax evasion pose to the public through oversight. Customs establishes a set of rules to filter out high-risk goods based on the information provided in import declarations because it is challenging to thoroughly inspect every item given the volume of trade and the limited resources available (budget, officer count, etc.). Implementing an effective customs selection or fraud detection system is therefore essential to accelerating the customs clearance process (Kim S. et al., 2020, 2021, 2023). By predicting potentially fraudulent things, customs authorities can assess each item's level of examination; the most questionable items require a physical inspection by human inspectors. The difficulty is figuring out which set of very suspicious items should be the focus.

An examination of the scientific literature indicates that the application of AI-based methods significantly improves the detection of customs fraud. The Brazilian program, which aims to combat customs fraud, is a well-known example. The system integrates data from many administrative and customs sources to enable more precise and effective control over the import and export of commodities. The system uses a range of artificial intelligence and data analytics techniques to identify anomalies, disparities, and potential fraud (Digiampietri, 2008).

Three steps and three algorithms are used in a proposed approach to identify smugglers from unstructured social media data (Dangsawang & Nuchitprasitchai, 2024). The goal is to locate those who sell goods and services on social media without authorization in order to evade paying taxes levied by the government. The stability and economics of the nation may suffer from this practice. The model classifies imported products using techniques including logistic regression, gated recurrent unit, and long short-term memory by gathering labeling keywords and classifying them into three groups.

The World Customs Organization has implemented information technology in customs operations to identify security dangers resulting from the smuggling of high-risk items, acknowledging the difficulties involved. Using pictures, deep learning algorithms are utilized to automatically identify and discourage the smuggling of commodities into training containers (Jaccard et al., 2016).

The research presented in this paper is part of a scientific project aimed to create artificial intelligence-based solutions for an information system that prevents and detects financial and customs infractions. The system for their detection and prevention must notify users when a violation is being planned, created, and executed in order to put an end to financial and customs violations. If financial customs violations have already taken place,

they should be made public to extract revenge on the perpetrators and create a sense of punishment that will deter similar transgressions in the future.

Method

Computer-Aided System for Customs Fraud Analytics

The architecture of the SOA-based system intended to process different types of customs data is shown in Figure 1. In addition to facilitating the smooth integration and interaction of various applications and data stores, SOA supports the sharing and exchange of data through standardized interfaces, ensuring compatibility between various systems and data sources and enabling the distributed deployment of services in various media and computing environments. Covering different data and functions separately, these services work together to automate complicated tasks. Benefits include cross-compatibility, adaptability, simplicity of maintenance, support for various technologies, and flexibility in response to shifting company needs. It also makes distributed application creation and administration easier.

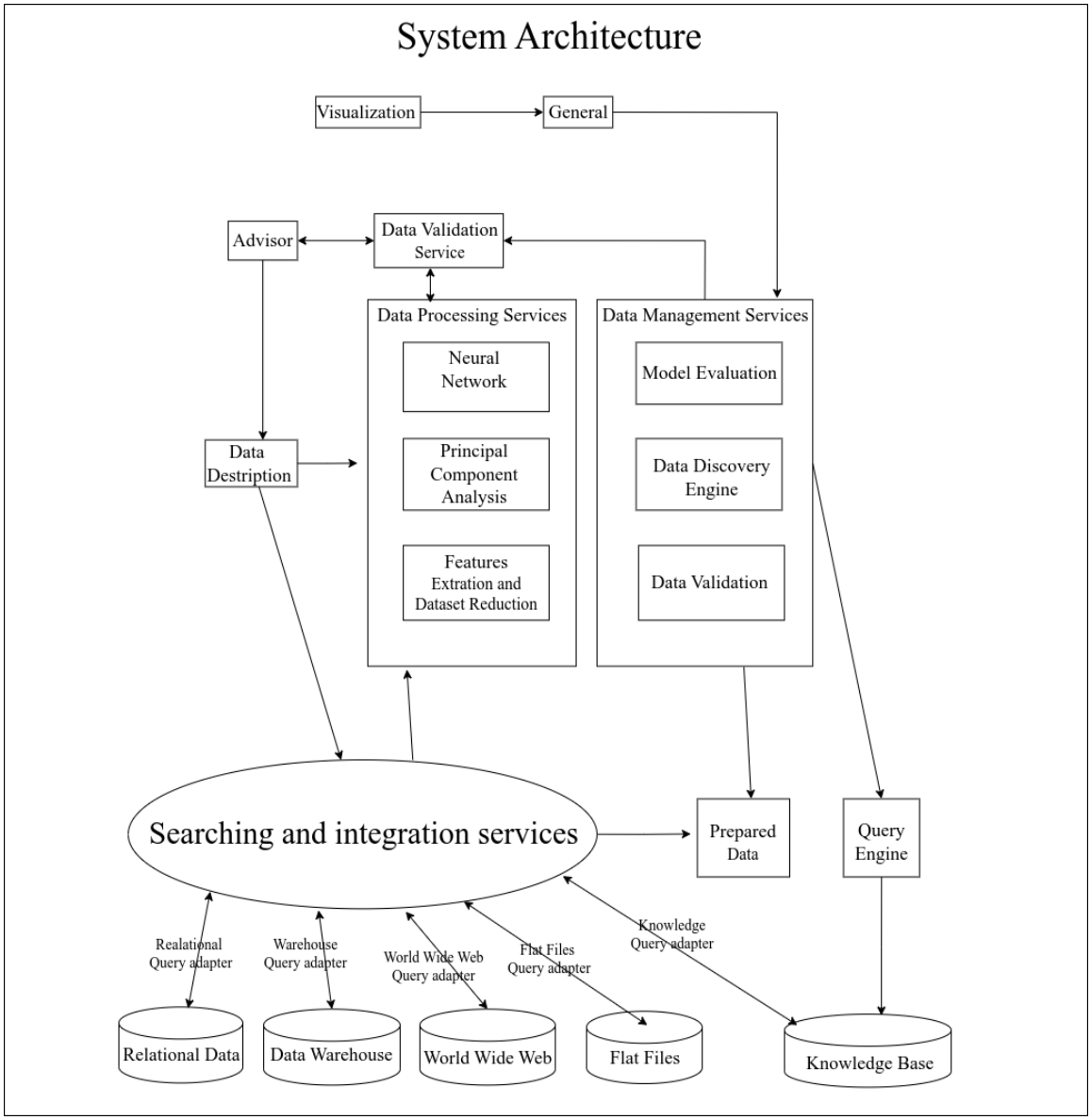

Figure 1. Computer-aided system architecture

In order to facilitate knowledge extraction and decision-making, the system provides intelligent solutions as well as automation of practical techniques, tools, and algorithms for integrating, storing, analyzing, and

visualizing customs data. The system offers an integrated and flexible framework for creating workflows to automate the computational process through a set of software tools. The capabilities encompass the following: 1) a user-friendly interface; 2) interactive tools for executing workflows for custom data analysis; 3) support for various data formats; 4) sharing and reusing workflows; 5) monitoring the outcomes of workflow execution and the steps involved in its creation; 6) the ability to swiftly add, remove, and scale functionalities as services; 7) enhanced speed and efficiency; and 8) the capacity to scale and adaptably increase resources

Essential data management activities are handled by the databases server and data warehouse, guaranteeing that actual data sets are prepared for processing and stored according to their nature. Databases, data warehouses, the Internet, text files, and different papers are examples of data sources. They are all rich in historical information that can be used to effectively extract knowledge. In order to solve the problem of insufficient or unreliable data, data preparation, integration, cleansing, and selection are essential first steps in the knowledge discovery process. It is imperative to apply diverse strategies for cleaning and selection in order to narrow down the extra data generated by multiple sources and select only the pertinent data for the study. The next step in the server's job is to retrieve the relevant data in response to the user's processing request. The system for managing data is created.

One important component is Service Advisor, that helps users choose services and data, helps them upload datasets, and leads them through the inquiry process. Efficient communication with the system is made possible by this module. It enables the wizard to communicate with the system in order to handle, interpret, and analyze different types of data, and it displays the outcomes in an easy-to-use interface.

Rapid handling of massive and diverse data sets in many formats—such as relational databases, NoSQL, and flat files—is made easier by integration services. These services combine information from multiple sources and convert general queries into targeted database queries. The system explores ongoing access to research updates for comparing findings with existing knowledge, and it tackles the difficulties in managing large, diverse, and complicated datasets that can be found in public databases.

By collaborating with the data discovery engine to pinpoint important patterns within the knowledge base, the pattern assessment module evaluates the significance of patterns that are found. A key component of the system, the data discovery engine uses a variety of algorithms to perform tasks such as classification, genetic algorithms, prediction, and clustering, and it consults the knowledge base to produce more dependable and accurate results. While database and data warehouse servers store and manage datasets that are ready for processing, query engines streamline interactions with intricate underlying data sources. By keeping a significant amount of historical data, these servers enable efficient knowledge extraction by retrieving pertinent information from a variety of factual sources in response to user requests.

The knowledge repository stores all identified patterns, models, and rules, supporting the entire knowledge discovery process, particularly in evaluating the significance of outcome models or focusing on specific demands. Preprocessing involves search and optimization techniques for data integration, cleansing, and selection based on relevance and accuracy. Iterative machine learning optimizes feature sets, and post-processing includes verification, validation, visualization, and evaluation of retrieved knowledge through data mining, machine learning, and decision-making methods for high accuracy and precision.

All discovered patterns, models, and rules are kept in the knowledge repository, which aids in the entire process of knowledge discovery, especially when assessing the importance of outcome models or concentrating on particular requirements. Preprocessing includes data integration, cleaning, and selection based on correctness and relevance using search and optimization algorithms. Post-processing comprises verification, validation, visualization, and evaluation of retrieved knowledge through data mining, machine learning, and decision-making procedures for high accuracy and precision. Iterative machine learning optimizes feature sets.

Workflow for Customs Data Analytics

A workflow for creating a neural network-based model for customs data analytics is shown in Fig. 2. The procedure is separated into its principal parts: customs data selection and preprocessing feedforward neural network model creation, model training, model evaluation. The fraud detection problem aims to find the patterns behind the features in predicting the target label Fraud. Data is split into three pieces. We assign the first 12 months of data to the training set, the following three months to the validation set, and the last three months to the test set. Categorical variables are label-encoded and numerical variables are min-max scaled.

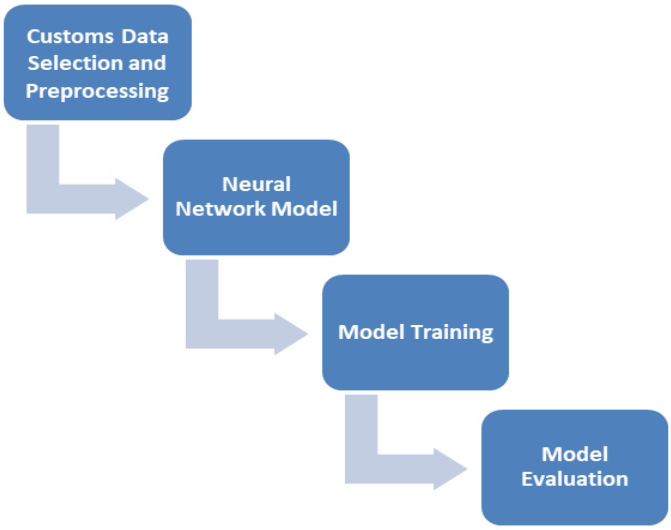

Figure 2. Customs data analytics workflow

Customs Dataset Selection and Preprocessing

Customs data processing covers the electronic submission of customs declarations and/or the provision of paper declarations. Additional documentation related to the implementation of processing procedures leading to the release of goods and the sharing of information with participating parties is also provided. The initial stage of the proposed workflow involves choosing customs data from databases. Preparation of the data for analysis is the aim of this phase. It could involve normalizing and cleaning the data, such as removing outliers and missing numbers. The original data have to be formatted such that the neural network can use it in the categorizing process.

Table 1. Customs dataset parameters

No	Attribute	Description
1	Declaration ID	Primary key
2	Date	Date of the declaration
1	Declaration ID	Primary key
2	Date	Date of the declaration
3	Office ID	Customs office
4	Process type	Declaration process type
5	Import type	Import type code
6	Import use	Import use code
7	Payment type	Determine the type of tariff payment
8	Mode of transport	Nine modes of transport
9	Declarant ID	Person declaring the item
10	Importer ID	Person who imports the product
11	Seller ID	Foreign business associate
12	Courier ID	Provider of delivery services
13	HS6 code	Six-digit code for the product
14	Country of departure	Nation from which a shipment has left or is expected to leave
15	Country of origin	Manufacturing, production, or design nation
16	Tax rate	Tax rate of item
17	Tax type	Tax category of item
18	Country of origin indicator	A means of designating the nation of origin
19	Net mass	Bulk without any packaging
20	Item price	Evaluated worth of a thing
21	Fraud	Dishonest attempt to lower the customs charge
22	Critical fraud	A crucial case that could endanger public safety

An import declaration dataset including 54,000 artificially created transactions with 22 important features that support correlation is used for the experimental validation of the proposed solution (Chaeyoon et al., 2023). The production process reduces the potential identity risk that could be present in trade statistics, and the released data is distributed similarly to the source data, allowing it to be utilized for a variety of purposes. This dataset was synthesized from 24.7 million customs declarations that were reported in the 18 months between 1 January 2020 and 30 June 2021, with the validated (i.e., labelled) part of the reports being used. Every row contains the report for a single item. The data contains 22 typical qualities incl. fraud and critical fraud, among the 62 attributes listed in the import declaration form. The following are full descriptions of the dataset. Table 1 presents the customs dataset parameters. Sample data records are shown in Fig. 3.

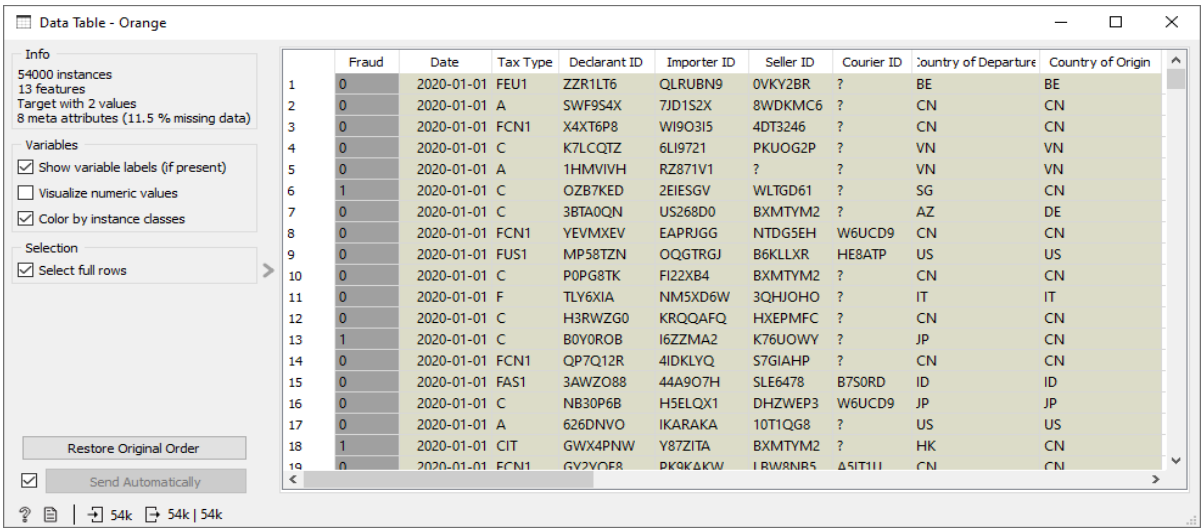

	Fraud	Date	Tax Type	Declarant ID	Importer ID	Seller ID	Courier ID	Country of Departure	Country of Origin
1	0	2020-01-01	FEU1	ZZR1LT6	QLRUBN9	0VKY2BR	?	BE	BE
2	0	2020-01-01	A	SWF9S4X	7JD1S2X	8WDKMC6	?	CN	CN
3	0	2020-01-01	FCN1	X4XT6P8	WI9O3I5	4DT3246	?	CN	CN
4	0	2020-01-01	C	K7LCQTZ	6LI9721	PKUOG2P	?	VN	VN
5	0	2020-01-01	A	1HMVIVH	RZ871V1	?	?	VN	VN
6	1	2020-01-01	C	OZB7KED	2EIESGV	WLTGD61	?	SG	CN
7	0	2020-01-01	C	3BTA0QN	US268D0	BXMTYM2	?	AZ	DE
8	0	2020-01-01	FCN1	YEVMXEV	EAPRJGG	NTDG5EH	W6UCD9	CN	CN
9	0	2020-01-01	FUS1	MP58TZN	OQGTRGJ	B6KLLXR	HE8ATP	US	US
10	0	2020-01-01	C	P0PG8TK	FI22XB4	BXMTYM2	?	CN	CN
11	0	2020-01-01	F	TLY6XIA	NM5XD6W	3QHJOHO	?	IT	IT
12	0	2020-01-01	C	H3RWZG0	KRQQAFQ	HXEPMFC	?	CN	CN
13	1	2020-01-01	C	B0Y0ROB	I6ZZMA2	K76UOWY	?	JP	CN
14	0	2020-01-01	FCN1	QP7Q12R	4IDKLYQ	S7GIAHP	?	CN	CN
15	0	2020-01-01	FAS1	3AWZO88	44A9O7H	SLE6478	B7S0RD	ID	ID
16	0	2020-01-01	C	NB30P6B	H5ELQX1	DHZWEP3	W6UCD9	JP	JP
17	0	2020-01-01	A	626DNVO	IKARAKA	10T1QG8	?	US	US
18	1	2020-01-01	CIT	GWX4PNW	Y87ZITA	BXMTYM2	?	HK	CN
19	0	2020-01-01	FCN1	GY2YOF8	PK9KAKW	LBW8NB5	A5IT1U	CN	CN

Figure 3. Sample customs declaration dataset

Feed Forward Neural Network Model for Customs Data Analytics

Model Creation

Neural Network Model: For this objective, a feed forward neural network model is designed, as seen in Fig. 4. This type of model processes inputs layer by layer as it moves forward. The architecture of the neural network captures the complex correlations that occur between the input features and the intended outcomes. A more nuanced interpretation of the data is made possible by the probabilistic output of the model, where probability acts as a stand-in for forecast certainty. The architecture includes following elements:

- An input layer with eight neurons that match the thirteen input parameters selected from the database.
- A 32-neuron hidden layer that makes it possible to extract more intricate features from the input data.
- An additional hidden layer with 16 neurons to further process the features that the preceding layer had recovered.
- An output layer with two neurons is meant to represent the probability result for a fraud and non fraud, respectively.
- The data is split into training and test data in an 80/20 ratio.

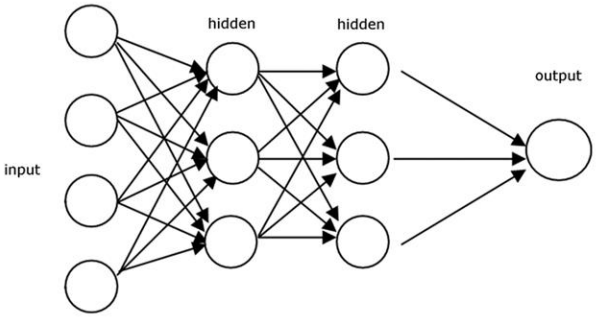

Figure 4. Neural network model

Model Training

Training Process: The neural network is trained in this stage. In order to reduce the discrepancy between the expected and actual results, the network's weights and biases are adjusted throughout training. Usually, backpropagation techniques are combined with an optimization technique to achieve this. The neural network is trained by feeding it training and test vectors; the 200 epochs represent the number of times the network processes the full dataset. The model can progressively learn from the data thanks to this iterative procedure. To avoid underfitting, which occurs when the model learns the data insufficiently, and overfitting, which occurs when the model learns the training data excessively.

Model Validation and Evaluation

Validation: A new, distinct dataset that was not used for training is used to assess performance and usefulness of the model.
Evaluation: Lastly, the performance of the model is evaluated using metrics such as accuracy. Once all training epochs have been read, the accuracy of the model is displayed against the training and validation sets of data (Fig. 5). As expected, accuracy increases with the number of epochs; it is higher for training data and lower for data from validation tests. The trained model can then be saved, loaded onto an alternative system, and checked for weight values.

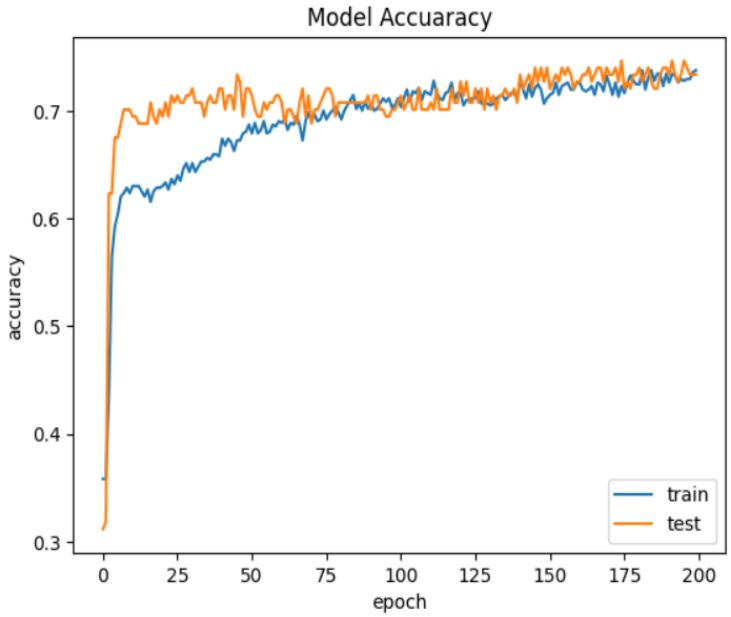

Figure 5. Accuracy of model

This methodology guarantees a rigorous approach to model creation, beginning with data collection and continuing through training and validation to generate a neural network that can assist in customs fraud identification. A solid foundation for creating reliable and effective customs data analytics solutions is laid by the emphasis on careful model design along with adequate training and validation.

As the model quickly learns the underlying patterns in the data, the accuracy increases quickly in the first 50 epochs, as is normal. Following that, test accuracy displays more random variations while training accuracy keeps getting better. This shows that while the model fits the training data well, overfitting or noise in the test data may provide some challenges. Convergence of the training and test accuracy around similar values indicates a strong generalization of the model.

The loss for both training and test data drops very swiftly in the first 50 epochs, suggesting that the model picks up on the underlying patterns in the data quite quickly. Subsequently, the test data loss exhibits a little slower drop and stabilizes early, whereas the training data loss keeps decreasing, albeit more slowly. In the final 50 epochs, both losses even off, with the training loss being marginally greater than the test loss. This suggests that there is little to no overfitting and that the model is well-balanced.

Results and Discussion

The trained model can be deployed in practical situations to assist in detecting customs fraud through several specific applications:

Using the Trained Model

- Handling New Input Parameters: It is crucial that any new data inputs maintain the exact structure and format as those used during the training and validation phases. This requires keeping the input vector's parameters in the same type and order.
- Making Predictions: Once the new input data is properly formatted and entered into the model, the neural network processes it using the learned weights and biases. The model then outputs a probability distribution indicating the likelihood of a customs violation.

Importance of Consistency in Data Format

- Model Accuracy: The accuracy of the model's predictions is heavily influenced by the consistency of the input data format. Neural networks are trained to recognize patterns based on the specific arrangement and type of data. Any deviations in the structure of new input data can lead to inaccurate predictions, as the model may misinterpret the information.
- Streamlined Integration: Keeping a consistent parameter sequence simplifies the integration of the model into automated systems or workflows. This consistency allows experts or automated data collection tools to prepare and input customs data into the model without needing to adjust the data structure for each new case.

Practical Application

- Customs Data Collection: Gathering the necessary customs parameters from new datasets.
- Data Preparation: Ensuring that the collected data adheres to the training format, including the order of the parameters.
- Making Predictions: Inputting the prepared data into the model to obtain a probability distribution indicating the likelihood of customs violations.
- Interpretation of Results: Customs professionals can use the model's output as part of their decision-making process, alongside other assessments and tests, to make informed decisions about potential customs violations.

This use of artificial intelligence and machine learning techniques demonstrates their potential to significantly enhance customs services, particularly in identifying fraud and customs infractions, provided the data is accurately prepared and the model is appropriately used.

Conclusion

The research described in this paper aims to propose a computer-aided system for customs fraud analytics based on artificial intelligence techniques. For the purposes of customs data analysis case study, a feedforward artificial neural network is created. During the training phase, the input data are divided into training and test data. We quantify the training error and show how it affects the neuron weights in the network. A set of statistics on customs data obtained from declaration analysis has been used as experimental data. For the study, 13 attributes from the original database are employed. Additionally, the data is split in a 0.8 to 0.2 ratio. The first 80% of the data are used to train the neural network, and the remaining 20% were used to test the trained network. The calculated accuracy rises with the number of epochs added. As the number of epochs increases, the estimated accuracy decreases for validation test data and increases for training data. The trained model can then be saved, loaded onto an alternative computer, and examined to verify the weight values. To compute new input parameters that are not used during training or validation, the system makes use of the trained model.

Scientific Ethics Declaration

The authors declare that the scientific ethical and legal responsibility of this article published in EPSTEM journal belongs to the authors.

Acknowledgements

* This article was presented as a poster presentation at the International Conference on Research in Engineering, Technology and Science (www.icrets.net) held in Thaskent/Uzbekistan on August 22-25, 2024.

* This research is financially supported by the Bulgarian Ministry of Education and Science, National Science Fund - grant KP-06-N35/12.

References

Dangsawang, B., & Nuchitprasitchai, S. (2024). A machine learning approach for detecting customs fraud through unstructured data analysis in social media. *Decision Analytics Journal*, *10*, 100408.

Digiampietri, L. A., Roman, N. T., Meira, L. A., Jambeiro Filho, J., Ferreira, C. D., Kondo, A. A., & Goldenstein, S. (2008, May). Uses of artificial intelligence in the Brazilian customs fraud detection system. In *DG. O* (pp. 181-187).

Jaccard, N., Rogers, T. W., Morton, E. J., & Griffin, L. D. (2016, November). Automated detection of smuggled high-risk security threats using deep learning. In *7th International Conference on Imaging for Crime Detection and Prevention (ICDP 2016)* (pp. 1-6). IET.

Jeong, C., Kim, S., Park, J., & Choi, Y. (2022). Customs import declaration datasets. *arXiv preprint arXiv:2208.02484*.

Kim, S., Mai, T. D., Han, S., Park, S., Nguyen, D. T., So, J., & Cha, M. (2022). Active learning for human-in-the-loop customs inspection. *IEEE Transactions on Knowledge and Data Engineering*, *35*(12), 12039-12052.

Kim, S., Song, S. K., Cho, M., & Shin, S. H. (2021). Transaction Pattern Discrimination of Malicious Supply Chain using Tariff-Structured Big Data. *The Journal of the Korea Contents Association*, *21*(2), 121-129.

Kim, S., Tsai, Y. C., Singh, K., Choi, Y., Ibok, E., Li, C. T., & Cha, M. (2020, August). DATE: Dual attentive tree-aware embedding for customs fraud detection. In *Proceedings of the 26th ACM SIGKDD International Conference on Knowledge Discovery & Data Mining* (pp. 2880-2890).

Author Information

Veska Gancheva
Technical University of Sofia
Kliment Ohridski 8, Sofia, Bulgaria
Contact e-mail: *vgan@tu-sofia.bg*

George Popov
Technical University of Sofia
Kliment Ohridski 8, Sofia, Bulgaria

Kamelia Raynova
Technical University of Sofia
Kliment Ohridski 8, Sofia, Bulgaria

Antoaneta Popova
Technical University of Sofia
Kliment Ohridski 8, Sofia, Bulgaria

Ivaylo Georgiev
Stephan Angeloff Institute of Microbiology
Bulgarian Academy of Science
Acad. Georgi Bonchev str. 2, blok 26, Sofia, Bulgaria

To cite this article:

Gancheva, V., Popov G., Raynova K., Popova A. & Georgiev I. (2024). Computer-aided system for customs fraud analytics based on artificial intelligence techniques. *The Eurasia Proceedings of Science, Technology, Engineering & Mathematics (EPSTEM), 29*, 173-181.

The Eurasia Proceedings of Science, Technology, Engineering & Mathematics (EPSTEM)
ISSN: 2602-3199

The Eurasia Proceedings of Science, Technology, Engineering & Mathematics (EPSTEM), 2024

Volume 29, Pages 182-191

ICRETS 2024: International Conference on Research in Engineering, Technology and Science

A Graph Database Intrusion Detection and Prevention System

Simona Lyubenova
Sofia University "St. Kliment Ohridski"

Milen Petrov
Sofia University "St. Kliment Ohridski"

Adelina Aleksieva-Petrova
Technical University of Sofia

Abstract: Network threats are perceived as a serious and current problem due to the presence of different types of attacks, the purpose of which is to penetrate the security of a certain system using vulnerabilities and fraud techniques. They can appear anywhere, making them more difficult to detect and prevent. The victims of such type of attacks are constantly increasing, resulting in great losses not only in financial terms, but also in breaches of data privacy and business processes. As a result, protecting confidential information from unpredictable attacks has become a pressing issue and a difficult task that would be impossible without the help of intrusion detection systems (IDS) and intrusion prevention systems (IPS). The goal of the paper is to propose and design general architecture and implement a prototype for protection of an existing network of devices by detecting and preventing threats through the extraction and analysis of information from the devices located in the network, with the necessary data being stored in a graph database offering the possibility of visualization. To implement device network protection, it is necessary to enable software tools that, based on certain rules, impose restrictions on devices on the network and prevent future malicious actions.

Keywords: Graph database, Intrusion detection systems, Intrusion prevention systems, Network security

Introduction

In light of the increasing number and complexity of cyber threats in recent years, timely and efficient detection and prevention of malicious activity is crucial to safeguarding valuable systems and data (Rizvi, 2016). This underscores the need for early detection of cyberattacks. The prevalence of network threats is a major concern in current times, as various attacks aim to exploit vulnerabilities and use deceitful tactics to breach the security of systems. These threats can manifest in various forms and are challenging to identify and thwart.

Intrusion Detection Systems (IDS) and Intrusion Prevention Systems (IPS) are widespread and commonly used (Thapa, 2020). In essence, Intrusion Detection and Prevention Systems (IDPS) are a security measure designed to protect networks from both external and internal threats. By monitoring network activity for suspicious patterns, IDPS can effectively detect and prevent cyberattacks (Birkinshaw, 2019).

The objective of this paper is to propose an architecture and design a graph-based system that can implement protection of an existing network of devices by detecting and preventing threats. The proposed NTDP (Network Threat Detection and Prevention) system implements a real-time collection and monitoring of network traffic, threats, and anomalies, and structure this information in a centralized, easily accessible location. The main contributions of the proposed architecture are (1) the capability of analyzing collected data to detect and prevent network attacks by activating detectors and implementing protective measures automatically and (2) to provide

a dynamic visualization of the network topology, using interactive graphical objects to display device attributes, statuses, and connections, with real-time updates reflecting any changes in the network structure or device conditions.

In order to apply protection to a network of devices, it is necessary to enable software tools that, based on certain rules, enforce restrictions on devices in the network and prevent future malicious actions. For simplicity, we can call these software tools by the short name "detectors". Detectors apply a set of rules on the previously available devices and on those that subsequently join the network, and along with this, some of the information stored in the graph database is modified in order to properly update the visualization.

The paper structure represents the following parts. The first part is introduction, defining the nature of the problem involved and formulates the set goals and tasks for the implementation of the research. The second part introduces related works, including approaches and methods for solving the problem. The third part, the focus falls on the general architecture and the design of its modules. The fourth part describes the experiments set up. The fifth part presents some results and discussion. The sixth part is final and includes a conclusion.

Related Work

To prevent cyber attacks, the analyze packet payloads against malware and intrusions is important part and IDS can accurately detect them. IDS is a process for monitoring and analyzing events that occur on a network and that pose a potential threat to it. IDS is responsible for monitoring data traffic on the network as well as any suspicious actions against its security. While IPS is a network monitoring process that is performed to prevent incoming threats and block ongoing attacks. IPS can be viewed as a combination of IDS and tools that respond to attacks that have occurred by implementing preventive measures (Thapa, 2020).

To address this, researchers are developed a taxonomy covers IDS architectures, detection methods, analysis techniques, responses, data sources, detection ranges, validation strategies, and performance metrics (Quincozes, 2021). Furthermore, authors have provided a comprehensive review of the detection rules used by the latest IDSs and evaluate their resilience against five types of attacks.

The algorithm by Turner (2016) provides an effective solution for determining the enabled and disabled states of rules in a signature-based IDS. By searching through rule sets and creating files to track the status of each rule, the algorithm allows for better management and monitoring of the rules within the IDS. This ultimately contributes to the overall effectiveness and efficiency of the IDS in detecting and responding to security threats.

Several previous studies have supported different approaches for IDPS. For examples, Software-Defined Networking (SDN) are used in IDPS design and implemention (Birkinshaw, 2019). This defense system constantly monitors network traffic for any abnormal or malicious behavior, and actively mitigates potential cyber threats. Also, some researches are developed an IDPS using SDN technology, designed to protect against ARP spoofing and Blacklisted MAC Addresses by adapting SDN's settings in real-time to identify and stop malicious network activity (Girdler, 2021).

To enhance security measures, a hybrid VM-based Honeypot system was implemented in conjunction with a hybrid IDPS (Rizvi, 2016). This setup compensates for any potential decrease in efficiency by focusing on signature-based methods for Network Intrusion Detection and Prevention Systems (NIDPS) and anomaly-based methods for Host Intrusion Detection and Prevention Systems (HIDPS), while still prioritizing the goal of minimizing resource consumption.

After analyzing the utilization of honeypots in corporate networks, virtualization technologies are implemented to decrease the costs associated with configuration, maintenance, and management (Baykara, 2018). The resulting system is an IDPS based on honeypots that visually displays network traffic on servers in real-time animations, allowing for easily accessible system information and the system is capable of detecting zero-day attacks through intrusion detection configuration.

The anomaly-based detection analyzes normal system behavior such as network packet information, operating system data, and system events (Sandhu, 2011). If behavior that differs from normal is observed or a potential threat is detected, the system generates an alert. Unusual activity that is not related to an attack is flagged as intrusive, which can result in a false alert being generated.

System Architecture

The NTDP intrusion detection and prevention system should have the capability to provide the following functionalities:

- Real-time collection of information on network traffic, identified threats and anomalies
- Structure the collected information and store it in a central location providing a means for easy access and management
- Providing secure access to the database through a user authentication and authorization system by managing permissions and roles to limit access to sensitive information
- Analyzing collected information to identify unwanted threats and anomalies with the ability to prevent network attacks by automatically activating detectors and implementing protective measures
- Developing or selecting algorithms to identify threats, detect anomalies and apply appropriate protective measures
- Visualizing the network topology through interactive graphical objects that reflect device attributes, their status, and the connections between them, and the ability to dynamically update as network structure or device status changes

Figure 1 presents an architectural view of the proposed NTDP system.

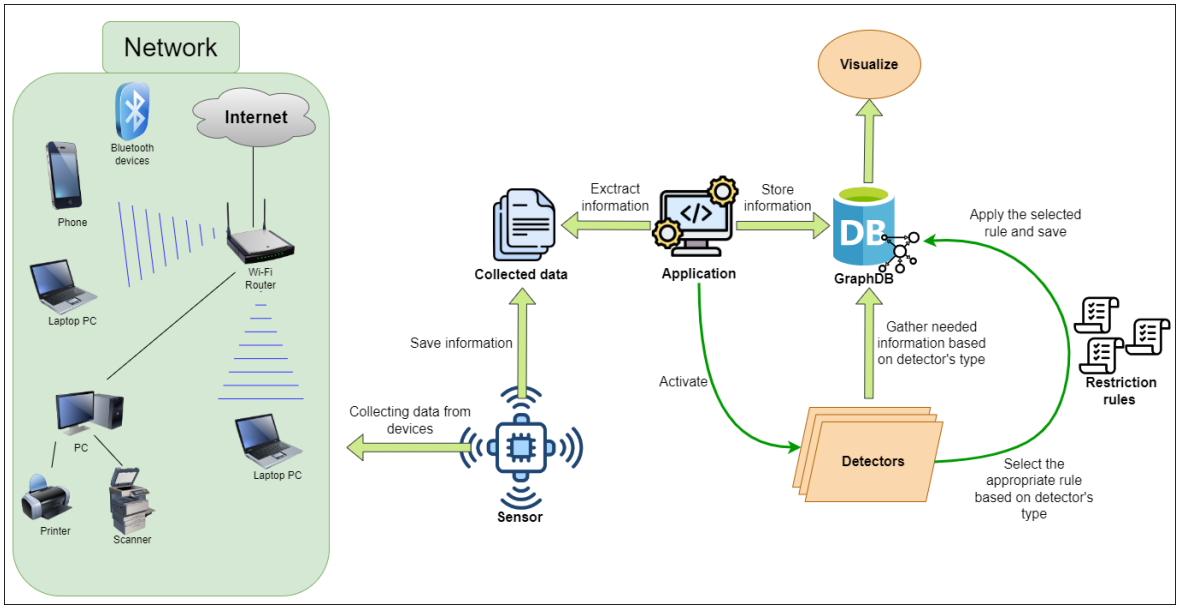

Figure 1. Developed architectural view of NTDP

An architecture is a collection of interacting components that are designed to perform certain tasks or functions (Figure 2).

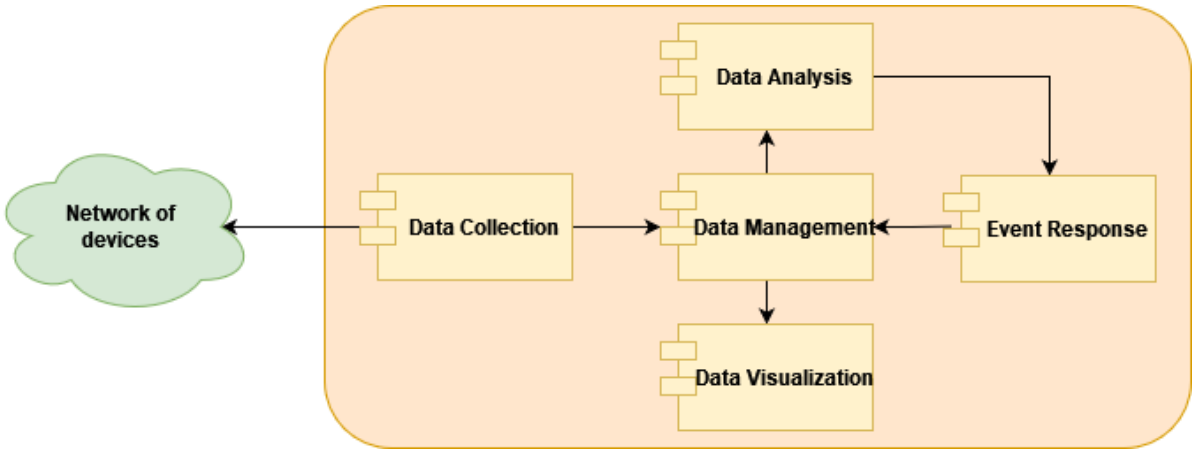

Figure 2. NTDP components architecture

Data Collection Component

The data collection component plays a key role in building an intrusion detection and prevention system. It is responsible for the active extraction, collection, aggregation and conversion into a structured format of information from various sources in the network such as hosts, switches, routers and other network devices. The collected information may include network traffic data, system events, active users, network device statistics, and other important security data.

The tasks of the data collection component include managing connections between network devices, extracting data from them, filtering and processing data, and transferring the collected information to a central storage location. The purpose of the data collection component is to provide a comprehensive overview of the network status and to provide the information necessary for security analysis and incident detection. For this reason, it is an essential element for the effective functioning of a system that includes monitoring and protection because it provides the basis for security-related decision making.

For the purpose of the study, we can assume that a network TAP (Test Access Point) sensor is used to collect information about devices in a network. It plays a key role in the development of the system by actively retrieving data about the network traffic and devices in the network. Similar to a TAP, the sensor allows the monitoring of network traffic without disconnecting devices. This ensures uninterrupted and unchanged access to the data, which is essential for quality system operation.

Data Management Component

The data management component provides the storage, organization and management of data collected from sensors or other sources. It is responsible for the central storage of the collected information and provides a convenient and efficient access to it. The data management component includes databases or other data storage mechanisms that allow for fast searching, filtering and processing of information. Data management is provided with functionalities such as adding, editing and deleting data, as well as their automated updating when necessary. The data management component may also include data protection mechanisms such as encryption and access control to ensure the security and confidentiality of stored information. The data management component in the development of the paper includes the selected graph database which provides various functionalities that satisfy the necessary requirements.

Data Analysis Component

The data analysis component provides functionalities to process, clarify and extract useful information from the collected data. It is designed to analyze the collected information to detect potential threats and anomalies in network behavior. The component applies various algorithms to detect anomalies, identify threats and extract important patterns from the data.

The data analysis component includes various analytical tools such as machine learning, statistical methods, graph algorithms that are used to process the information. It includes integration with other systems and modules that provide the necessary information to apply analysis. The data analytics component plays an important role in real-time event monitoring as well as incident response by providing important data for analysis to administrators to understand the current state of the network and take necessary measures to protect it.

The data analysis component in the development of the paper involves the activation of detectors that periodically monitor devices on the network at a specified interval and inspect them according to set criteria described in clearly defined detector rules. If the devices in the network match the set criteria, then the described response actions are applied by the activated detectors.

Data Visualization Component

The data visualization component aims to provide an intuitive and easy-to-understand way to visualize the network topology and device interactions on the network. It provides a graphical representation of the sensor data collected and processed by the other modules of the system. The data visualization component is connected

to the selected graph database, which contains as functionality the ability to visualize the stored data. It uses the device data in the network that is stored in the graph database to create a visual view of the connections and interactions between them. This can include connections between hosts, switches, routers, and other network components. Users are able to interact with the visualization to view details about individual devices, explore their connections, and analyze network data. This can include the ability to zoom in and out on portions of the graph, filter data to more easily discover key aspects of the network, select colors of different device types on the network, and options to add additional data and attributes to the visualization. The data visualization component provides a means to intuitively understand the network infrastructure and the interactions within it, which proves to be essential in order to quickly and effectively respond to potential threats and issues.

Event Response Component

The Event Response component is responsible for automated or manual action as a result of detected events or threats on the network. It has the ability to be configured to automatically respond to certain types of threats or events, which includes automatically blocking certain network connections, terminating services, or performing other actions to reduce the risk of attacks. Users have the ability to manually manage detected threats through the provided system visualization. Actions can include manually blocking selected network devices or connections, viewing detailed information about detected threats, and taking additional measures to prevent attacks. The event response component in the development of the study involves the activation of detectors that use clearly defined rules to respond if devices are detected that meet the set conditions described in the rules.

Setup of Experiments

For the purpose of the study, we will use off-the-shelf data collected from a network TAP sensor provided by a cybersecurity product development company, which will be used in the construction of the network topology. The devices present in the network are:

- a collection of computers, laptops, phones, and other devices that are under the common name Host;
- a set of network switches (switches), which are under the common name Switch;
- a collection of routers, which are collectively referred to as a Router.

In order to visualize a network topology with the collected data of devices of the listed types, it is necessary to load into the graph database CSV files that contain information about the fields of each object and information about the connections between the objects. The choice to represent objects, their attributes and relationships in the form of relational tables is to provide a clearer view of the properties of the objects and the relationships between them. Each table in Figure 3 represents a separate CSV file that contains the described fields. The graph database needs to be loaded with all CSV files to visualize the network topology. The Hosts, Switches, and Routers tables represent the nodes in the graph database, and the HostsToSwitches, SwitchesToRouters, and RoutersToRouters tables represent the connections between nodes in the graph database.

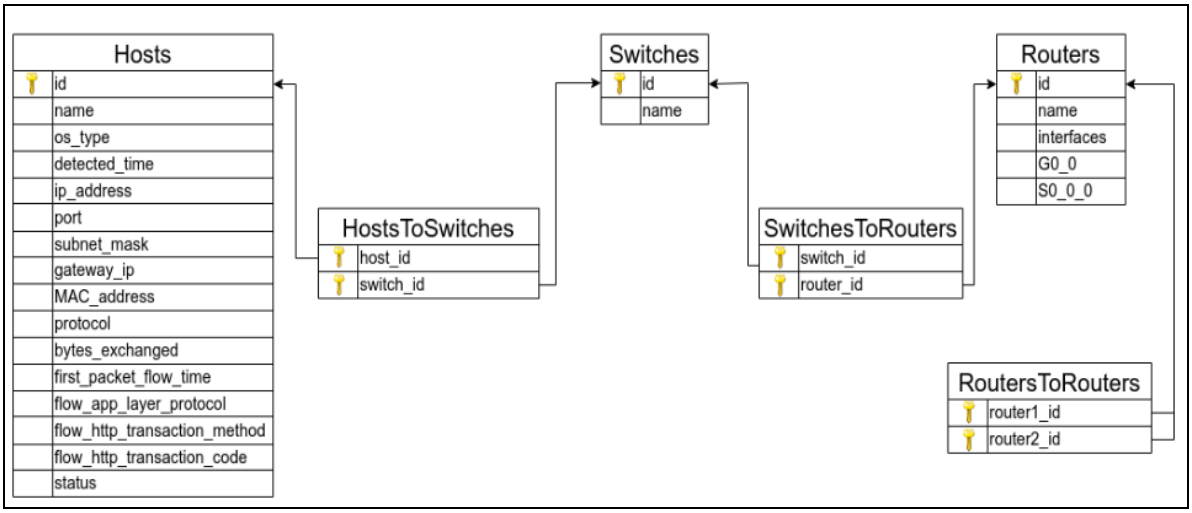

Figure 3. Representation of object types, their attributes and relationships as relational tables

Figure 4 presents some sample data for Host type devices to load into the graph base.

	A	B	C	D	E	F	G	H	I	J	K	L
1	id	name	os_type	detected_time	ip_address	port	subnet_mask	gateway_ip	MAC_address	protocol	bytes_exchanged	first_packet_flow_time
2	15969631	PC-12	WINDOWS	2024-04-01 05:53:24.000	192.168.1.2	59918	255.255.255.0	192.168.1.1	08:bb:64:3b:bc:1d	PROTO_TCP	0	2024-04-01 05:55:04.251
3	10185084	PC-13	MACOS	2024-04-01 07:01:13.000	192.168.1.3	135	255.255.255.0	192.168.1.1	32:ae:1e:2d:c7:7a	PROTO_TCP	2091	2024-04-01 07:01:22.593
4	20847490	PC-14	WINDOWS	2024-04-01 05:49:56.000	192.168.1.4	64427	255.255.255.0	192.168.1.1	ec:bf:6b:12:38:56	PROTO_TCP	15982	2024-04-01 05:51:44.840
5	20847491	PC-15	WINDOWS	2024-04-01 05:49:56.000	192.168.1.5	64427	255.255.255.0	192.168.1.1	60:49:10:b0:1b:da	PROTO_TCP	2781	2024-04-01 05:51:44.840
6	20848490	PC-16	LINUX	2024-04-01 05:45:54.000	192.168.1.6	63949	255.255.255.0	192.168.1.1	70:6a:ef:eb:74:b0	PROTO_TCP	0	2024-04-01 05:46:56.993
7	20847450	PC-17	WINDOWS	2024-04-01 05:45:54.000	192.168.1.7	63949	255.255.255.0	192.168.1.1	bf:97:da:d8:c7:1e	PROTO_TCP	20871	2024-04-01 05:46:56.993
8	20846490	PC-18	WINDOWS	2024-04-01 05:45:58.000	192.168.1.8	63961	255.255.255.0	192.168.1.1	5c:43:d0:45:2a:67	PROTO_TCP	0	2024-04-01 05:46:56.993
9	21847490	PC-19	MACOS	2024-04-01 05:45:58.000	192.168.1.9	63962	255.255.255.0	192.168.1.1	54:57:d3:cd:b3:42	PROTO_TCP	220	2024-04-01 05:46:56.993
10	20947490	PC-110	WINDOWS	2024-04-01 05:45:58.000	192.168.1.10	63963	255.255.255.0	192.168.1.1	71:75:77:42:20:c8	PROTO_TCP	0	2024-04-01 05:46:56.993
11	10183990	PC-111	LINUX	2024-04-01 05:48:05.000	192.168.1.11	54742	255.255.255.0	192.168.1.1	60:89:df:bf:12:48	PROTO_TCP	0	2024-04-01 05:48:25.073
12	10183999	PC-112	MACOS	2024-04-01 05:48:05.000	192.168.1.12	55742	255.255.255.0	192.168.1.1	45:ea:ab:96:78:6c	PROTO_TCP	8790	2024-04-01 05:48:25.073
13	11183990	PC-113	WINDOWS	2024-04-01 05:48:06.000	192.168.1.13	55748	255.255.255.0	192.168.1.1	71:58:7a:35:fe:d9	PROTO_TCP	0	2024-04-01 05:48:25.073
14	15183990	PC-114	WINDOWS	2024-04-01 05:48:06.000	192.168.1.14	55749	255.255.255.0	192.168.1.1	40:dd:ad:b1:1d:dc	PROTO_TCP	8920	2024-04-01 05:48:25.073
15	16183990	PC-22	LINUX	2024-04-01 05:48:06.000	192.168.2.2	55750	255.255.255.0	192.168.2.1	5c:71:20:d9:6f:16	PROTO_TCP	0	2024-04-01 05:48:25.073
16	17183990	PC-23	WINDOWS	2024-04-01 05:48:06.000	192.168.2.3	55751	255.255.255.0	192.168.2.1	c8:82:86:27:c5:03	PROTO_TCP	3245	2024-04-01 05:48:25.073
17	18183990	PC-24	WINDOWS	2024-04-01 05:48:06.000	192.168.2.4	55752	255.255.255.0	192.168.2.1	a2:8e:9e:f3:68:1b	PROTO_TCP	0	2024-04-01 05:48:25.073
18	19183990	PC-25	MACOS	2024-04-01 05:48:06.000	192.168.2.5	52753	255.255.255.0	192.168.2.1	d3:9e:e2:3e:46:6f	PROTO_TCP	1144	2024-04-01 05:48:25.073
19	10283990	PC-26	WINDOWS	2024-04-01 05:48:06.000	192.168.2.6	55756	255.255.255.0	192.168.2.1	5a:e1:55:41:0e:97	PROTO_TCP	3209	2024-04-01 05:48:25.073
20	10383990	PC-27	WINDOWS	2024-04-01 05:48:06.000	192.168.2.7	55757	255.255.255.0	192.168.2.1	08:52:79:12:bb:33	PROTO_TCP	0	2024-04-01 05:48:25.073
21	18602532	PC-28	LINUX	2024-03-30 05:38:09.000	192.168.2.8	59571	255.255.255.0	192.168.2.1	eb:d2:6d:7b:8f:ba	PROTO_TCP	3211	2024-03-30 05:38:09.000

Figure 4. Some sample data for Host devices

Sample data for Switch-type devices are presented in Figure 5 and Figure 6 presents sample data for Router-type devices.

	A	B
1	id	name
2	1	Switch-1
3	2	Switch-2

Figure 5. Representation of object types, their attributes and relationships as relational tables

	A	B	C	D	E
1	id	name	interfaces	G0_0	S0_0_0
2	1	Router-1	G0_0,S0_0_0	192.168.1.1/24	10.1.1.1/30
3	2	Router-2	G0_0,S0_0_0	192.168.2.1/24	10.1.1.2/30

Figure 6. Representation of object types, their attributes and relationships as relational tables

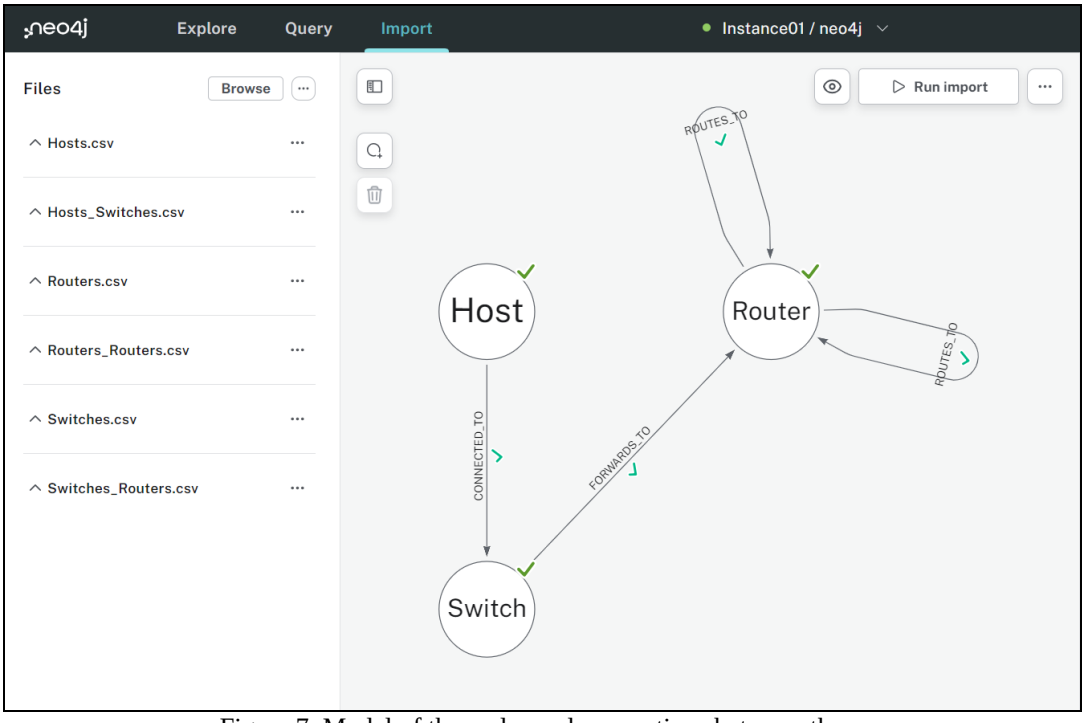

Figure 7. Model of the nodes and connections between them

The system is based on objects in Neo4j that need to be modelled against sample data. In the graph base, the model of the devices in the network infrastructure and their way of communication look like the one presented in Figure 7, which is a final view of the created nodes and their interconnections with collected data from loaded CSV files. A node labeled Router has two connections labeled ROUTES_TO to itself because in the created network, routers exchange information with each other and its transmission is bidirectional.

Rows to nodes and tables to label names:

- Each row from the Hosts relational table and the Hosts.csv file becomes a node in our graph labeled Host.
- Each row from the Switches table and from the Switches.csv file becomes a node in our graph labeled Switch.
- Each row from the Routers table and from the Routers.csv file becomes a node in our graph labeled Router.

Connections between nodes:

- The connection between nodes labeled Host and Switch is done with the relational table HostsToSwitches, represented as the file Hosts_Switches.csv, which is a connection labeled CONNECTED_TO.
- The connection between nodes labeled Switch and Router is accomplished with the SwitchesToRouters relational table, represented as the file Switches_Routers.csv, which is a relationship labeled FORWARDS_TO.
- The connection between nodes with Router and Router labels is implemented with the RoutersToRouters relational table, represented as the Routers_Routers.csv file, which is a relation with the ROUTES_TO label.

The data analysis component and the event response component are key in the development of an intrusion detection and prevention system. In a network, it is necessary to analyze information about the devices in the network and detect potential threats and anomalies in the network behavior that are present, against which protective measures can be taken to respond to the emerging threats. In this research, the two components are unified by the use of detectors that load specific rules from yaml files to filter the data of devices in the network according to set criteria and take actions towards them. The final step aims to simulate a working intrusion detection and prevention system. In the beginning, a network topology is created from devices with ready data loaded. We will use the network topology from Figure 8.

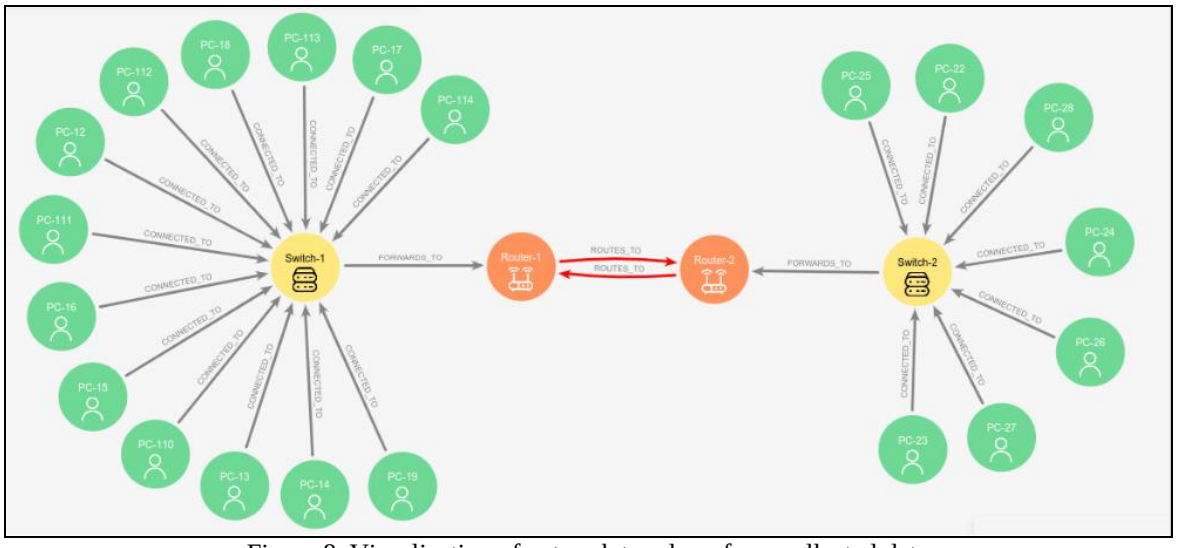

Figure 8. Visualization of network topology from collected data

Results and Discussion

When the simulation starts, devices from an additional CSV file that contains data for devices outside the network begin connecting to the network periodically. In parallel, both types of detectors are activated, which load their intended rules and apply restrictions on devices that are on the network as well as those that are

joining it. To accomplish this, two threads are created, one to add devices to the network and one to periodically activate the detectors. Results of the simulation execution can be observed through the outputted logs as well as the visualization (Figure 9). The displayed logs help to track the actions on the network if there is a problem with the preview or if a moment is missed.

```
Activated detector AppLayerProtocolDetector: Host-10185261,PC-211,FREE->SUSPEND.
Connected Host-23879925,PC-116.
Packet check before sending: Host-20947490,PC-110,SUSPEND :---> Host-23879925,PC-116,FREE.
Packet check before sending: Host-20947490,PC-110,SUSPEND <---: Host-23879925,PC-116,FREE.
Packet not sent: Host-10185084,PC-13,BLOCK x---> Host-23879925,PC-116,FREE.
Packet not sent: Host-10185084,PC-13,BLOCK <---x Host-23879925,PC-116,FREE.
Activated detector PortDetector: Host-23879925,PC-116,FREE->BLOCK.
Deactivated detector AppLayerProtocolDetector: Host-15969631,PC-12,SUSPEND->FREE.
Deactivated detector AppLayerProtocolDetector: Host-10185084,PC-13,BLOCK->FREE
```

Figure 9. A sample of the logs from the execution of the simulation

A visualization of the network topology during the simulation is presented in Figure 10. The color of devices labeled Host is determined by their status - green devices are in FREE status, red devices are in BLOCK status, and the rest are in SUSPEND status. The status change is carried out by the activated detectors, which apply actions from the loaded rules according to the criteria described in them. The devices with the FREE status are those that do not threaten the network in relation to the activated detectors, and the rest are those that in some way pose a threat to it. Figure 11 (a, b) shows a data visualization for devices with a BLOCK state enforced by both types of detectors, and Figure 11 (c) shows a data visualization for a device with a SUSPEND state enforced by the AppLayerProtocolDetector.

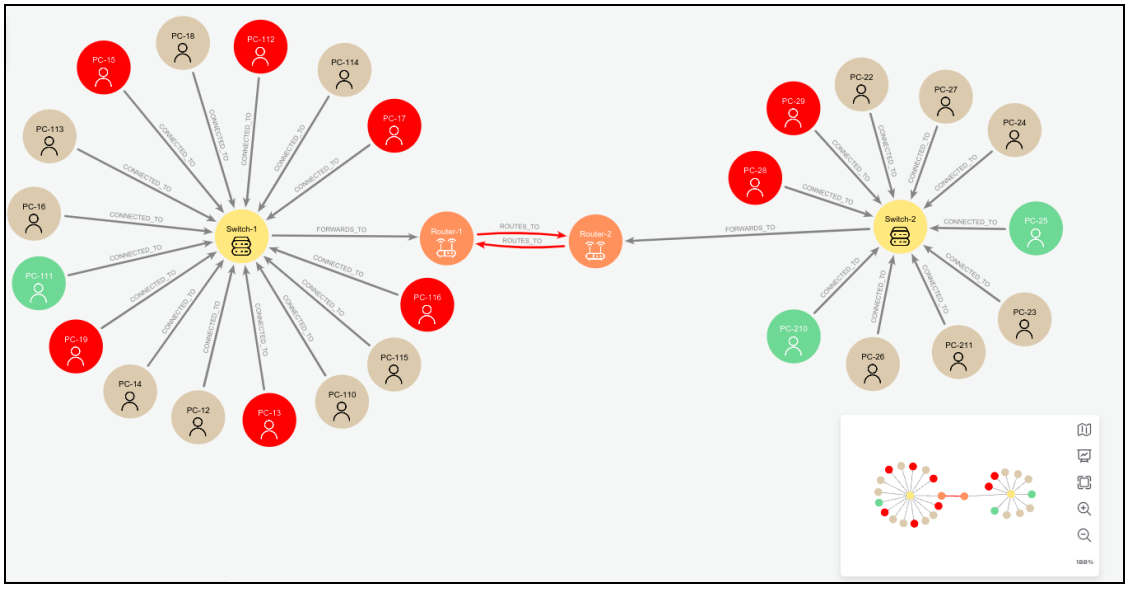

Figure 10. Visualization of the network topology during simulation execution for a working system

A new detector_name attribute has been added, indicating the name of the detector that applied a rule on the corresponding device. Both devices are of BLOCK status, the main difference between them being the values of the detector_name attribute - one device is limited by AppLayerProtocolDetector and the other is limited by PortDetector.

The status of the device in Figure 11 (c) is SUSPEND, the difference with the devices in Figure 10 being the changed color after applying rules by detectors. The detector that applied constraints to PC-110 in Figure 11 (c) is the AppLayerProtocolDetector that also applied constraints to PC-15 in Figure 11 (a). The detector applied different constraints to the two devices and the main difference between them is the status and changed color after the constraints are applied. The preview offers the possibility to observe the created network and to manually impose changes on it. The technologies used lay the foundations for future scalability and portability of the system. The developed modules are designed so that they can be easily extended by adding new functionalities to them. Visual and log-tracing testing has been performed to show that the system meets the requirements and is ready for use.

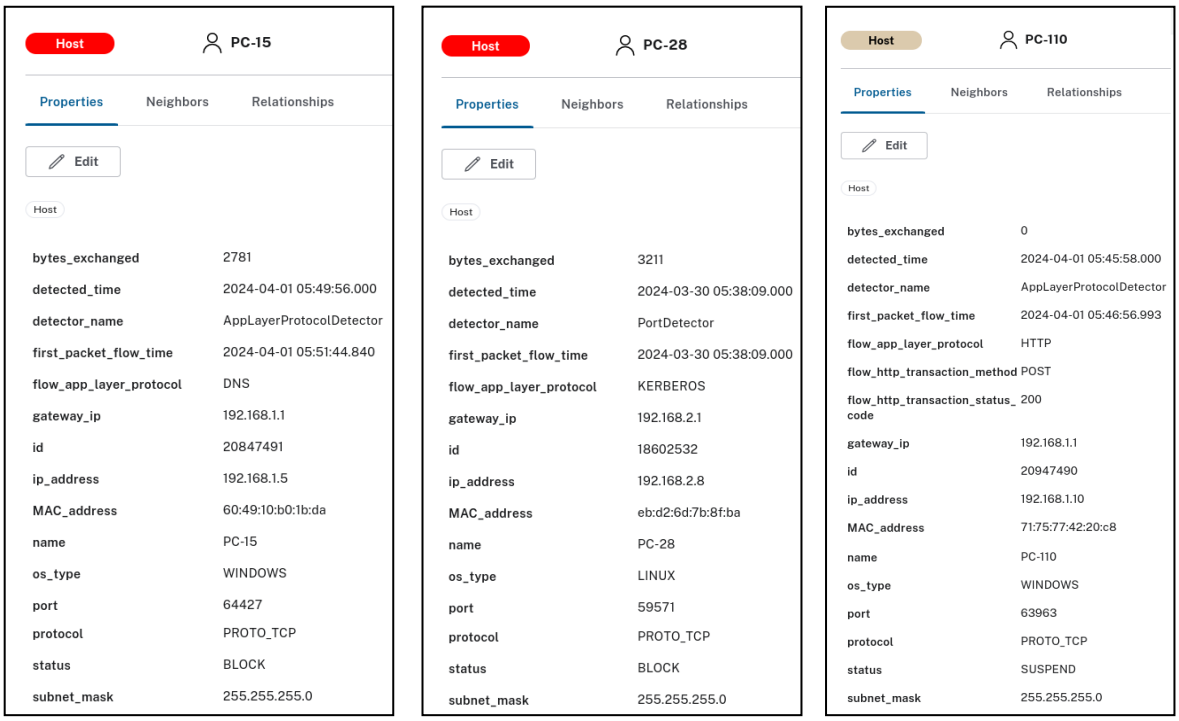

(a) (b) (c)

Figure 11. Data preview for devices labeled Host with (a, b) BLOCK status and (c) SUSPEND

The NTDP intrusion detection and prevention system is scalable, i.e. the system supports the addition and removal of devices as well as network expansion without loss of efficiency and performance. As a result, the system can process a minimum of 10,000 events per second when new devices are added or when the network expands, and keeps the event processing time below 1 millisecond regardless of the number of connected devices in the network. Performance metrics include monitoring resource usage such as CPU and memory under varying network load and expansion. In terms of efficiency, the system provides a quick response in data processing and threat response. Performance metrics include measuring system response time when operations such as adding new devices to the network or when a change occurs to the network. For example, when adding a new device to the network, a response time of less than 1 second was achieved, and the maximum allowable response time was 3 seconds.

A system using enabled detectors monitors the behavior of devices on a network and implements protective measures using restriction rules to prevent future malicious actions. This results in improved network security and provides continuous control and protection against potential threats from both current and those devices that will subsequently join the network. The construction of such a system represents an initial step, providing basic mechanisms for data processing and application of protective measures. This initiative serves as a foundation for further development and refinement of network security. The expected benefits of the implementation include better control and visibility over network activities, which will lead to greater stability and reliability of the built infrastructure through fewer work interruptions, faster recovery from incidents and better management of security risks to prevent unwanted events and losses from potential network threats.

Conclusion

This paper proposed a general architecture and presented the individual modules in the system (data collection module, data management module, data analysis module, data visualization module and event response module) and data model. As a result, objects with their attributes and relations were modeled and loaded with data in the graph base for building a network topology. The originally set objectives for the implementation of the present experiment have been fulfilled. Sample device data has been collected, using which a sample network topology has been built. The data is stored in a graph database, providing the possibility of visualization. Functionalities have been created to join a new device to the available network, to remove an existing device and its connections, and to change properties of an existing device. The system offers options for activating and deactivating detectors that monitor the behavior of devices in the network according to the loaded rules and impose restrictions on the threatening part of them.

The performed simulation shows that the developed system based on the proposed intrusion detection and prevention architecture works according to our expectations, being able to load a large volume of data in real time, which helps to effectively detect and prevent threats. Both visual results of it and results in the form of logs are provided. The system meets the requirements set for it and provides the necessary results.

Scientific Ethics Declaration

The authors declare that the scientific ethical and legal responsibility of this article published in EPSTEM journal belongs to the authors.

Acknowledgements

* This article was presented as a poster presentation at the International Conference on Research in Engineering, Technology and Science (www.icrets.net) held in Thaskent/Uzbekistan on August 22-25, 2024.

* The research reported here was funded by the project "Research and application of machine learning algorithms in the analysis and development of highly secure software", fund with contract KP-06-N57/4 from 16.11.2021 by Bulgarian National Science.

References

Baykara, M., & Das, R. (2018). A novel honeypot based security approach for real-time intrusion detection and prevention systems. *Journal of Information Security and Applications, 41, 103*-116.

Birkinshaw, C., Rouka, E., & Vassilakis, V. G. (2019). Implementing an intrusion detection and prevention system using software-defined networking: Defending against port-scanning and denial-of-service attacks. *Journal of Network and Computer Applications*, *136*, 71-85.

Girdler, T., & Vassilakis, V. G. (2021). Implementing an intrusion detection and prevention system using Software-Defined Networking: Defending against ARP spoofing attacks and Blacklisted MAC Addresses. *Computers & Electrical Engineering*, *90*, 106990.

Quincozes, S. E., Albuquerque, C., Passos, D., & Mossé, D. (2021). A survey on intrusion detection and prevention systems in digital substations. *Computer Networks*, *184*, 107679.

Rizvi, S., Labrador, G., Guyan, M., & Savan, J. (2016). Advocating for hybrid intrusion detection prevention system and framework improvement. *Procedia Computer Science*, *95*, 369-374.

Sandhu, U. A., Haider, S., Naseer, S., & Ateeb, O. U. (2011). A survey of intrusion detection & prevention techniques. In 2011 *International Conference on Information Communication and Management*, IPCSIT, *16*, 66-71.

Thapa, S., & Mailewa, A. (2020, April). The role of intrusion detection/prevention systems in modern computer networks: A review. In *Conference: Midwest Instruction and Computing Symposium (MICS)*, *53*, 1-14.

Turner, C., Jeremiah, R., Richards, D., & Joseph, A. (2016). A rule status monitoring algorithm for rule-based intrusion detection and prevention systems. *Procedia Computer Science*, *95*, 361-368.

Author Information

Simona Lyubenova
Sofia University "St. Kliment Ohridski"
5, James Bourchier Blvd., Sofia, Bulgaria

Milen Petrov
Sofia University "St. Kliment Ohridski"
5, James Bourchier Blvd., Sofia, Bulgaria
Contact e-mail: *milenp@fmi.uni-sofia.bg*

Adelina Aleksieva-Petrova
Technical University of Sofia
8, Kliment Ohridski St., Sofia, Bulgaria

To cite this article:

Lyubenova, S., Petrov, M. & Aleksieva-Petrova, A. (2024). A graph database intrusion detection and prevention system. *The Eurasia Proceedings of Science, Technology, Engineering & Mathematics (EPSTEM), 29*, 182-191.

The Eurasia Proceedings of Science, Technology, Engineering & Mathematics (EPSTEM)
ISSN: 2602-3199

The Eurasia Proceedings of Science, Technology, Engineering & Mathematics (EPSTEM), 2024

Volume 29, Pages 192-209

ICRETS 2024: International Conference on Research in Engineering, Technology and Science

Laplace Method for Calculate the Determinant of Cubic-Matrix of Order 2 and Order 3

Orgest Zaka
Agricultural University of Tirana

Armend Salihu
Universum International College

Abstract: In this paper, as a continuation of our work on the determinants of cubic matrices of order 2 and order 3, we have investigated the possibilities of developing the concept of determinants of cubic matrices with three indexes, as well as the possibility of calculating them using the Laplace expansion method. We have observed that the notion of permutation expansion, which is used for square determinants, and the concept of the Laplace expansion method, which is used for square and non-square (rectangular) determinants, may be applied to this novel concept of 3D determinants. In this research, we demonstrated that the Laplace expansion approach is also applicable to cubic matrices of the second and third orders. These results are presented simply and with extensive proof. The findings are also supported by illustrated cases. In addition, we provided an algorithmic explanation for the Laplace expansion approach applied to cubic matrices.

Keywords: Cubic-matrix determinant, Laplace expansion method, Permutation method, Computer algorithm.

Introduction

Linear Algebra, Abstract Algebra and Geometry are very intertwined fields. The applications of these fields are very important and useful. Considering that matrix theory has very important applications in *Computer Graphics*, *Game-Theory*, *Graph-Theory*, *Imagery*, *different problems from informatics*, *Partial differential equations*, etc., which are very important in many vital fields! We are trying to develop this further, introducing the concept of a 3-dimensional matrix and step by step to first study the determinants for a 3-dimensional matrix. More specifically, in this paper, we study the determinants of the cubic-matrix for order 2 and order 3. Based on the determinant of 2D square matrices presented in (Artin, 1991; Bretscher, 2018; Schneide et al., 1973; Lang, 2010), as well as the determinant of rectangular matrices presented in (Salihu & Marevci, 2021, Amiri et al., 2010; Radić, 1966; Radić, 2005; Makarewicz et al., 2014) we have come to the idea of developing the concept of the determinant of 3D cubic matrices in (Salihu-Zaka, 2023b), also in papers (Salihu-Zaka, 2023b) and (Salihu-Zaka, 2023a) we have studied and proved some basic properties related to the determinant of cubic-matrix of order 2 and 3. Also during this paper, we consider the results obtained in the papers (Amiri et al., 2010; Radić, 1966; Radić, 2005; Makarewicz et al., 2014; Salihu et al., 2022; Milne-Thomson, 1941; Gago et al., 2022; Kuloğlu et al., 2023), but also the results presented in books (Artin, 1991; Bretscher, 2018; Schneide et al., 1973; Lang, 2010; Poole, 2006; Rose, 2002). The history of Determinants and Linear Algebra, in general, is quite beautiful, for this we invite you to look (Eves, 1990; Grattan-Guinness, 2003) and some classic and very rich texts with knowledge about determinants, such as (Lang, 2002; Leon et al., 2021; Lay et al., 2022; Meyer, 2023; Muir, 1933; Price, 1947).

In this paper, we study the properties of the determinants of the cubic-matrix of orders 2 and 3, related to the Laplace expansion method, our concept is based on the permutation expansion method. Encouraged by geometric intuition, in this paper, we are trying to give an idea and visualize the meaning of the determinants for the cubic-matrix. Our early research mainly lies between geometry, algebra, matrix theory, etc., (see (Peters-Zaka, 2023; Zaka & Peters, 2024; Zaka, 2019a; Zaka-Filipi, 2016; Filipi et al., 2019; Zaka, 2017; Zaka, 2018; Zaka, 2016; Zaka & Peters, 2019a; Zaka & Peters, 2019b; Zaka & Mohammed, 2020a; Zaka & Mohammed, 2020b). This paper is a continuation of the ideas that arise based on previous research of 3D matrix rings with elements from any whatever field (Zaka, 2017), but here we study the case when the field F is the field of real numbers $\mathbb{R}$ also is a continuation of our research (Salihu & Zaka, 2023b) related to the study of the properties of determinants for cubic-matrix of order 2 and 3. In this paper, we follow a different method from the calculation of determinants of the 3D matrix, which is studied in (Zaka, 2019b). In contrast to the meaning of the determinant as a multi-scalar studied in (Zaka, 2019b), in this paper, we give a new definition, for the determinant of the 3D-cubic-matrix, which is a real-number.

In the papers (Zaka, 2017; Zaka 2019b), have been studied in detail, properties for 3D-matrix, therefore, those studied properties are also valid for 3D-cubic-Matrix. Our point in this paper is to provide a concept of the determinant of 3D matrices using the Laplace concept which is a well-known methodology for calculating the determinant of square and rectangular matrices. Hence, our concept is based on the Laplace method which is used for calculating 2D square and rectangular determinants (Poole, 2006; Rose 2002) also, during this work we take into account the results achieved earlier, see (Rezaifar et al.i, 2007; Koprowski, 2022; Neto, 2015; Dutta & Pal, 2011; Silvester, 2000; Muir, 1906; Sothanaphan, 2018). At the end of this paper, we have also presented an algorithmic presentation for the Laplace expansion method, for the calculation of cubic-matrix-determinants.

Preliminaries

3D Matrix

The following is the definition of 3D matrices provided in 2017 in (Zaka 2017): see Fig.1 for 3-D matrix appearance

Definition 1 *3-dimensional $m \times n \times p$ matrix will call, a matrix which has: m-horizontal layers (analogous to m-rows), n-vertical page (analogue with n- columns in the usual matrices) and p-vertical layers (p-1 of which are hidden).*

The set of these matrices is written as follows:

$$M_{m\times n\times p}(\mathrm{F}) = \{a_{i,j,k} | a_{i,j,k} \in F - field\ \forall i = \overline{1,m};\quad j = \overline{1,n};\quad k = \overline{1,p}\}. \tag{1}$$

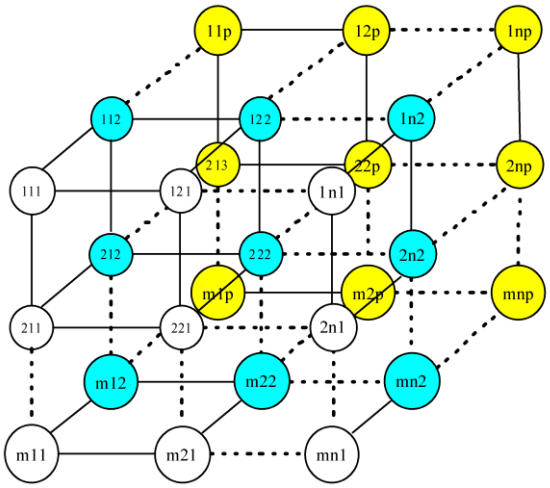

Figure 1. 3D-Matrix view.

The following presents the determinant of 3D-cubic matrices, as well as several properties which are adopted from 2D square determinants.

Cubic-Matrix of Order 2 and 3 and Their Determinants

A 3-dimensional-matrix $A_{n\times n\times n}$ for $n = 2,3,\ldots$, called "cubic-matrix of order n". For $n = 1$ we have that the cubic-matrix of order 1 is an element of F.

Let us now consider the set of cubic-matrix of order n, for $n = 2$ or $n = 3$, with elements from a field F (so when cubic-matrix of order n, there are: n −vertical pages, n −horizontal layers and n −vertical layers). From (Zaka 2017, Zaka 2019b) we have that, the addition of 3D-matrix stands also for cubic-matrix of orders 2 and 3. Also, the set of cubic-matrix of order 2 and 3 forms a commutative group (Abelian Group) related to 3Dmatrix addition.

Determinants of Cubic-Matrix of Order 2 and 3

In a paper (Salihu & Zaka 2023b), we have defined and described the meaning of the determinants of cubic-matrix of order 2 and order 3, with elements from a field F. Recall that a cubic-matrix $A_{n\times n\times n}$ for $n = 2,3,\ldots$, called "cubic-matrix of order n".

For $n = 1$ we have that the cubic-matrix of order 1 is an element of F.
Let us now consider the set of cubic-matrix of order n, with elements from a field F (so when cubic-matrix of order n, there are: n −vertical pages, n −horizontal layers and n −vertical layers),

$$\mathcal{M}_n(F) = \{A_{n\times n\times n} = (a_{ijk})_{n\times n\times n} | a_{ijk} \in F,\ \forall i = \overline{1}, n; j = \overline{1}, n; k = \overline{1}, n\}.$$

In this paper, we define the *determinant of cubic-matrix* as an element from this field, so the map,

$$\begin{array}{ll} \det: \mathcal{M}_n(F) & \to F \\ \forall A \in \mathcal{M}_n(F) & \mapsto \det(A) \in F. \end{array}$$

Below we give two definitions, of how we will calculate the determinant of the cubic-matrix of orders 2 and 3.

Definition 2 *Let $A \in \mathcal{M}_2(F)$ be a $2\times 2\times 2$, with elements from a field F.*

$$A_{2\times 2\times 2} = \left(\begin{array}{cc|cc} a_{111} & a_{121} & a_{112} & a_{122} \\ a_{211} & a_{221} & a_{212} & a_{222} \end{array}\right).$$

The determinant of this cubic-matrix, we called,

$$\det[A_{2\times 2\times 2}] = \det\left(\begin{array}{cc|cc} a_{111} & a_{121} & a_{112} & a_{122} \\ a_{211} & a_{221} & a_{212} & a_{222} \end{array}\right) = a_{111}\cdot a_{222} - a_{112}\cdot a_{221} - a_{121}\cdot a_{212} + a_{122}\cdot a_{211}.$$

The following example is a case where the cubic-matrix, is with elements from the number field $\mathbb{R}$.

Example 1 *Let's have the cubic-matrix, with the element in the number field $\mathbb{R}$,*

$$\det[A_{2\times 2\times 2}] = \det\left(\begin{array}{cc|cc} 4 & -3 & -2 & 4 \\ -1 & 5 & -7 & 3 \end{array}\right).$$

then according to definition 2, we calculate the Determinant of this cubic-matrix, and have,

$$\det[A_{2\times 2\times 2}] = \det\left(\begin{array}{cc|cc} 4 & -3 & -2 & 4 \\ -1 & 5 & -7 & 3 \end{array}\right) = 4\cdot 3 - (-2)\cdot 5 - (-3)\cdot(-7) + 4\cdot(-1)$$
$$\det[A_{2\times 2\times 2}] = 12 - (-10) - 21 + (-4) = 12 + 10 - 21 - 4 = -3.$$

We are trying to expand the meaning of the determinant of cubic-matrix, for order 3 (so when cubic-matrix, there are: 3-vertical pages, 3-horizontal layers and 3-vertical layers).

Definition 3 *Let $A \in \mathcal{M}_3(F)$ be a $3\times 3\times 3$ cubic-matrix with an element from a field F,*

$$A_{3\times3\times3} = \left(\begin{array}{ccc|ccc|ccc} a_{111} & a_{121} & a_{131} & a_{112} & a_{122} & a_{132} & a_{113} & a_{123} & a_{133} \\ a_{211} & a_{221} & a_{231} & a_{212} & a_{222} & a_{232} & a_{213} & a_{223} & a_{233} \\ a_{311} & a_{321} & a_{331} & a_{312} & a_{322} & a_{332} & a_{313} & a_{323} & a_{333} \end{array}\right).$$

The determinant of this cubic-matrix, we called,

$$\det[A_{3\times3\times3}] = \det\left(\begin{array}{ccc|ccc|ccc} a_{111} & a_{121} & a_{131} & a_{112} & a_{122} & a_{132} & a_{113} & a_{123} & a_{133} \\ a_{211} & a_{221} & a_{231} & a_{212} & a_{222} & a_{232} & a_{213} & a_{223} & a_{233} \\ a_{311} & a_{321} & a_{331} & a_{312} & a_{322} & a_{332} & a_{313} & a_{323} & a_{333} \end{array}\right). \quad (2)$$

$$\begin{aligned} \det[A_{3\times3\times3}] = {} & a_{111}\cdot a_{222}\cdot a_{333} - a_{111}\cdot a_{232}\cdot a_{323} - a_{111}\cdot a_{223}\cdot a_{332} \\ & + a_{111}\cdot a_{233}\cdot a_{322} - a_{112}\cdot a_{221}\cdot a_{333} + a_{112}\cdot a_{223}\cdot a_{331} \\ & + a_{112}\cdot a_{231}\cdot a_{323} - a_{112}\cdot a_{233}\cdot a_{321} + a_{113}\cdot a_{221}\cdot a_{332} \\ & - a_{113}\cdot a_{222}\cdot a_{331} - a_{113}\cdot a_{231}\cdot a_{322} + a_{113}\cdot a_{232}\cdot a_{321} \\ & - a_{121}\cdot a_{212}\cdot a_{333} + a_{121}\cdot a_{213}\cdot a_{332} + a_{121}\cdot a_{232}\cdot a_{313} \\ & - a_{121}\cdot a_{233}\cdot a_{312} + a_{122}\cdot a_{211}\cdot a_{333} - a_{122}\cdot a_{213}\cdot a_{331} \\ & - a_{122}\cdot a_{231}\cdot a_{313} + a_{122}\cdot a_{233}\cdot a_{311} - a_{123}\cdot a_{211}\cdot a_{332} \\ & + a_{123}\cdot a_{212}\cdot a_{331} + a_{123}\cdot a_{231}\cdot a_{312} - a_{123}\cdot a_{232}\cdot a_{311} \\ & + a_{131}\cdot a_{212}\cdot a_{323} - a_{131}\cdot a_{213}\cdot a_{322} - a_{131}\cdot a_{222}\cdot a_{313} \\ & + a_{131}\cdot a_{223}\cdot a_{312} - a_{132}\cdot a_{211}\cdot a_{323} + a_{132}\cdot a_{213}\cdot a_{321} \\ & + a_{132}\cdot a_{221}\cdot a_{313} - a_{132}\cdot a_{223}\cdot a_{311} + a_{133}\cdot a_{211}\cdot a_{322} \\ & - a_{133}\cdot a_{212}\cdot a_{321} - a_{133}\cdot a_{221}\cdot a_{312} + a_{133}\cdot a_{222}\cdot a_{311}. \end{aligned}$$

The following example is a case where the cubic-matrix, is with elements from the number field $\mathbb{R}$.

Example 2 *Let's have the cubic-matrix of order 3, with an element from the number field (field of real numbers)* $\mathbb{R}$,

$$\det[A_{3\times3\times3}] = \det\left(\begin{array}{ccc|ccc|ccc} 3 & 0 & -4 & -2 & 4 & 0 & 5 & 1 & 0 \\ 2 & 5 & -1 & -3 & 0 & 3 & 3 & 1 & 2 \\ 0 & 3 & -2 & -3 & 2 & 5 & 0 & 4 & 3 \end{array}\right).$$

Then, we calculate the Determinant of this cubic-matrix following Definition 3, and have that,

$$\det[A_{3\times3\times3}] = \det\left(\begin{array}{ccc|ccc|ccc} 3 & 0 & -4 & -2 & 4 & 0 & 5 & 1 & 0 \\ 2 & 5 & -1 & -3 & 0 & 3 & 3 & 1 & 2 \\ 0 & 3 & -2 & -3 & 2 & 5 & 0 & 4 & 3 \end{array}\right)$$

$$\begin{aligned} & = 3\cdot0\cdot3 - 3\cdot3\cdot4 - 3\cdot1\cdot5 + 3\cdot2\cdot2 - (-2)5\cdot3 + (-2)1(-2) + (-2)(-1)\cdot4 - (-2)2\cdot3 \\ & + 5\cdot5\cdot5 - 5\cdot0\cdot(-2) - 5\cdot(-1)\cdot2 + 5\cdot3\cdot3 - 0\cdot(-3)\cdot3 + 0\cdot3\cdot5 + 0\cdot3\cdot0 - 0\cdot2\cdot(-3) \\ & + 4\cdot2\cdot3 - 4\cdot3\cdot(-2) - 4\cdot(-1)\cdot0 + 4\cdot2\cdot0 - 1\cdot2\cdot5 + 1\cdot(-3)\cdot(-2) + 1\cdot(-1)\cdot(-3) - 1\cdot3\cdot0 \\ & + (-4)(-3)\cdot4 - (-4)3\cdot2 - (-4)0\cdot0 + (-4)1(-3) - 0\cdot2\cdot4 + 0\cdot3\cdot3 + 0\cdot5\cdot0 - 0\cdot1\cdot0 + \\ & + 0\cdot2\cdot2 - 0\cdot(-3)\cdot3 - 0\cdot5\cdot(-3) + 0\cdot0\cdot0 \end{aligned}$$

so,

$$\begin{aligned} \det[A_{3\times3\times3}] = {} & 0 - 36 - 15 + 12 + 30 + 4 + 8 + 12 + 125 + 0 + 10 + 45 + 0 + 0 + 0 + 0 + 24 + 24 + 0 \\ & + 0 - 10 + 6 + 3 - 0 + 48 + 24 + 0 + 12 - 0 + 0 + 0 - 0 + 0 + 0 + 0 + 0 = 326. \end{aligned}$$

Hence,

$$\det\left(\begin{array}{ccc|ccc|ccc} 3 & 0 & -4 & -2 & 4 & 0 & 5 & 1 & 0 \\ 2 & 5 & -1 & -3 & 0 & 3 & 3 & 1 & 2 \\ 0 & 3 & -2 & -3 & 2 & 5 & 0 & 4 & 3 \end{array}\right) = 326.$$

Minors and Co-factors of Cubic-Matrix of Order 2 and 3

In this section, we will present the meaning of Minors and co-factors for the cubic-matrix of order 2 and order 3.

Minors of Cubic-Matrix

Let us start by defining minors.

Definition 4 *Let A_n be a $n \times n \times n$ cubic-matrix (with $n \geq 2$). Denote by A_{ijk} the entry of cubic-matrix A at the intersection of the i −th **horizontal layers**, j −th **vertical pages** and k −th **vertical layers**. The minor of A_{ijk} is the determinant of the sub-cubic-matrix obtained from A by deleting its i −th **horizontal layer**, j −**vertical page** and k −**vertical layer**.*

We now illustrate the definition with an example.

Example 3 *Let's have the cubic-matrix of order 3, with an element from the number field (field of real numbers) $\mathbb{R}$,*

$$A_{3\times3\times3} = \left(\begin{array}{ccc|ccc|ccc} 3 & 0 & -4 & -2 & 4 & 0 & 5 & 1 & 0 \\ 2 & 5 & -1 & -3 & 0 & 3 & 3 & 1 & 2 \\ 0 & 3 & -2 & -3 & 2 & 5 & 0 & 4 & 3 \end{array}\right).$$

Take the entry $A_{111} = 3$, The sub-cubic-matrix obtained by deleting the first-horizontal layer, first-vertical page and first-vertical layer is,

$$\left(\begin{array}{cc|cc} 0 & 3 & 1 & 2 \\ 2 & 5 & 4 & 3 \end{array}\right).$$

Thus, the minor of A_{111} is

$$M_{111} = \det\left(\begin{array}{cc|cc} 0 & 3 & 1 & 2 \\ 2 & 5 & 4 & 3 \end{array}\right) = 0 \cdot 3 - 1 \cdot 5 - 3 \cdot 4 + 2 \cdot 2 = -5 - 12 + 4 = -13.$$

Take the entry $A_{123} = 1$, The sub-cubic-matrix obtained by deleting the first-horizontal layer, 2-vertical page and 3-vertical layer is,

$$\left(\begin{array}{cc|cc} 2 & -1 & -3 & 3 \\ 0 & -2 & -3 & 5 \end{array}\right).$$

Thus, the minor of A_{123} is

$$M_{123} = \det\left(\begin{array}{cc|cc} 2 & -1 & -3 & 3 \\ 0 & -2 & -3 & 5 \end{array}\right) = 2 \cdot 5 - (-3) \cdot (-2) - (-1) \cdot (-3) + 3 \cdot 0 = 10 - 6 - 3 + 0 = 1.$$

Co-Factors of Cubic-Matrix of Order 2 and 3

A co-factor is a minor whose sign may have been changed depending on the location of the respective matrix entry.

Definition 5 Let A_n be a $n \times n \times n$ cubic-matrix (with $n \geq 2$). Denote by M_{ijk} the minor of an entry A_{ijk}. The co-factor of A_{ijk} is

$$C_{ijk} = (-1)^{i+j+k} \cdot M_{ijk}.$$

As an example, the pattern of sign changes $(-1)^{i+j+k}$ of a cubic-matrix of order 3 is

$$\left(\begin{array}{ccc|ccc|ccc} - & + & - & + & - & + & - & + & - \\ + & - & + & - & + & - & + & - & + \\ - & + & - & + & - & + & - & + & - \end{array}\right).$$

Example 4 *Let's have the cubic-matrix of order 3, with an element from the number field (field of real numbers) $\mathbb{R}$,*

$$A_{3\times3\times3} = \left(\begin{array}{ccc|ccc|ccc} 3 & 0 & -4 & -2 & 4 & 0 & 5 & 1 & 0 \\ 2 & 5 & -1 & -3 & 0 & 3 & 3 & 1 & 2 \\ 0 & 3 & -2 & -3 & 2 & 5 & 0 & 4 & 3 \end{array}\right).$$

Take the entry $A_{111} = 3$. The minor of A_{111} is

$$M_{111} = \det\left(\begin{array}{cc|cc} 0 & 3 & 1 & 2 \\ 2 & 5 & 4 & 3 \end{array}\right) = -13$$

and its cofactor is

$$C_{111} = (-1)^{1+1+1} \cdot M_{111} = -M_{111} = -(-13) = 13.$$

Take the entry $A_{123} = 1$. Thus, the minor of A_{123} is

$$M_{123} = \det\left(\begin{array}{cc|cc} 2 & -1 & -3 & 3 \\ 0 & -2 & -3 & 5 \end{array}\right) = 1$$

and its co-factor is

$$C_{123} = (-1)^{1+2+3} \cdot M_{123} = M_{123} = 1.$$

Laplace Expansion for Determinants of Cubic-Matrix of Order 2 and 3

We are now ready to present the Laplace expansion. Following the Laplace expansion method for 2D square-matrix, we are conjecturing this method for 3D cubic-matrix,

Laplace Expansion for Determinants of Cubic-Matrix of Order 2

Laplace Expansion

If we have A a cubic-matrix of order 2 or 3. Denote by C_{ijk} the co-factor of an entry A_{ijk}. Then:

For any '***horizontal laye***r' i, the following 'horizontal layer' expansion holds:

$$\det(A) = \sum_{jk} A_{ijk} \cdot C_{ijk}.$$

For any '***vertical page***' j, the following 'vertical page' expansion holds:

$$\det(A) = \sum_{ik} A_{ijk} \cdot C_{ijk}.$$

For any '***vertical layer***' k, the following 'vertical page' expansion holds:

$$\det(A) = \sum_{ij} A_{ijk} \cdot C_{ijk}.$$

Below we prove that this method is valid for calculating the determinants of the cubic-matrix of order 2.

Theorem 1 *Let A be a cubic-matrix of order 2,*

$$A = \left(\begin{array}{cc|cc} a_{111} & a_{121} & a_{112} & a_{122} \\ a_{211} & a_{221} & a_{212} & a_{222} \end{array}\right).$$

The determinant of this cubic-matrix is invariant into the expansion of three "ways" to Laplace expansion.
Proof. We will prove all three expansion types, L_1, L_2, L_3.
(L_1): For any horizontal layer i ($i = 1,2$), the following 'horizontal layer' expansion holds:

$$\det(A) = \sum_{jk} A_{ijk} \cdot C_{ijk}.$$

If we take $i = 1$, and we consider the meaning of the minors and co-factors for the cubic-matrix of order 2, which we described above, we have:

$$\det[A_{2\times2\times2}] = \begin{pmatrix} a_{111} & a_{121} \\ a_{211} & a_{221} \end{vmatrix} \begin{matrix} a_{112} & a_{122} \\ a_{212} & a_{222} \end{pmatrix}$$
$$= a_{111} \cdot \det(a_{222}) - a_{121} \cdot \det(a_{212}) - a_{112} \cdot \det(a_{221}) + a_{122} \cdot \det(a_{211})$$

so,

$$\det[A_{2\times2\times2}] = a_{111} \cdot a_{222} - a_{112} \cdot a_{221} - a_{121} \cdot a_{212} + a_{122} \cdot a_{211}. \quad (3)$$

This result is the same as that in the Definition 2.
Now similarly we take $i = 2$, and we consider the meaning of the minors and co-factors for the cubic-matrix of order 2, which we described above, we have:

$$\begin{aligned} \det[A_{2\times2\times2}] &= \begin{pmatrix} a_{111} & a_{121} \\ a_{211} & a_{221} \end{vmatrix} \begin{matrix} a_{112} & a_{122} \\ a_{212} & a_{222} \end{pmatrix} \\ &= a_{211} \cdot \det(a_{122}) - a_{221} \cdot \det(a_{112}) - a_{212} \cdot \det(a_{121}) + a_{222} \cdot \det(a_{111}) \\ &= a_{211} \cdot a_{122} - a_{221} \cdot a_{112} - a_{212} \cdot a_{121} + a_{222} \cdot a_{111}. \end{aligned} \quad (4)$$

so,

$$\det[A_{2\times2\times2}] = a_{211} \cdot a_{122} - a_{221} \cdot a_{112} - a_{212} \cdot a_{121} + a_{222} \cdot a_{111}.$$

We see that we have the same result as the Definition 2.
(L_2): for any 'vertical page' j , the following 'vertical page' expansion holds:
We see that we have the same result as the Definition 2.
(L_2): for any 'vertical page' j , the following 'vertical page' expansion holds:

$$\det(A) = \sum_{ik} A_{ijk} \cdot C_{ijk}.$$

If we take $j = 1$, and we consider the meaning of the minors and co-factors for the cubic-matrix of order 2, which we described above, we have:

$$\begin{aligned} \det[A_{2\times2\times2}] &= \begin{pmatrix} a_{111} & a_{121} \\ a_{211} & a_{221} \end{vmatrix} \begin{matrix} a_{112} & a_{122} \\ a_{212} & a_{222} \end{pmatrix} \\ &= a_{111} \cdot \det(a_{222}) + a_{211} \cdot \det(a_{122}) \\ &- a_{112} \cdot \det(a_{221}) - a_{212} \cdot \det(a_{121}) \\ &= a_{111} \cdot a_{222} + a_{211} \cdot a_{122} \\ &- a_{112} \cdot a_{221} + a_{212} \cdot a_{121}. \end{aligned} \quad (5)$$

So we have the same result as the Definition 2.
Now similarly we take $j = 2$, and we consider the meaning of the minors and co-factors for the cubic-matrix of order 2, which we described above, we have:

$$\begin{aligned} \det[A_{2\times2\times2}] &= \begin{pmatrix} a_{111} & a_{121} \\ a_{211} & a_{221} \end{vmatrix} \begin{matrix} a_{112} & a_{122} \\ a_{212} & a_{222} \end{pmatrix} \\ &= -a_{121} \cdot \det(a_{212}) - a_{221} \cdot \det(a_{112}) \\ &+ a_{122} \cdot \det(a_{211}) + a_{222} \cdot \det(a_{111}) \\ &= -a_{121} \cdot a_{212} - a_{221} \cdot a_{112} \\ &+ a_{122} \cdot a_{211} + a_{222} \cdot a_{111}. \end{aligned} \quad (6)$$

So we have the same result as the Definition 2.

(L_3): For any 'vertical layer' k , the following 'vertical layer' expansion holds:

$$\det(A) = \sum_{ik} A_{ijk} \cdot C_{ijk}.$$

If we take $k = 1$, and we consider the meaning of the minors and co-factors for the cubic-matrix of order 2, which we described above, we have:

$$\begin{aligned} \det[A_{2\times2\times2}] &= \left(\begin{array}{cc|cc} a_{111} & a_{121} & a_{112} & a_{122} \\ a_{211} & a_{221} & a_{212} & a_{222} \end{array}\right) \\ &= a_{111} \cdot \det(a_{222}) - a_{121} \cdot \det(a_{212}) \\ &+ a_{211} \cdot \det(a_{122}) - a_{221} \cdot \det(a_{112}) \\ &= a_{111} \cdot a_{222} - a_{121} \cdot a_{212} \\ &+ a_{211} \cdot a_{122} - a_{221} \cdot a_{112}. \end{aligned} \tag{7}$$

So we have the same result as the Definition 2.
Now similarly we take $k = 2$, and we consider the meaning of the minors and co-factors for the cubic-matrix of order 2, which we described above, we have:

$$\begin{aligned} \det[A_{2\times2\times2}] &= \left(\begin{array}{cc|cc} a_{111} & a_{121} & a_{112} & a_{122} \\ a_{211} & a_{221} & a_{212} & a_{222} \end{array}\right) \\ &= -a_{112} \cdot \det(a_{221}) + a_{122} \cdot \det(a_{221}) \\ &- a_{212} \cdot \det(a_{121}) + a_{222} \cdot \det(a_{111}) \\ &= -a_{112} \cdot a_{221} + a_{122} \cdot a_{221} \\ &- a_{212} \cdot a_{121} + a_{222} \cdot a_{111}. \end{aligned} \tag{8}$$

So we have the same result as the Definition 2.
The following example is a case where the cubic-matrix of second order, is with elements from the number field $\mathbb{R}$.

Example 5 *Let's have the cubic-matrix, with the element in the number field* $\mathbb{R}$,

$$A_{2\times2\times2} = \left(\begin{array}{cc|cc} 4 & -3 & -2 & 4 \\ -1 & 5 & -7 & 3 \end{array}\right)$$

then according to Theorem 1, we calculate the Determinant of this cubic-matrix, and have,

$$\det[A_{2\times2\times2}] = \det\left(\begin{array}{cc|cc} 4 & -3 & -2 & 4 \\ -1 & 5 & -7 & 3 \end{array}\right).$$

For $i = 1$, we have:

$$\begin{aligned} \det[A_{2\times2\times2}] &= \left(\begin{array}{cc|cc} 4 & -3 & -2 & 4 \\ -1 & 5 & -7 & 3 \end{array}\right) \\ &= 4 \cdot \det(3) - (-3) \cdot \det(-7) \\ &- (-2) \cdot \det(5) + 4 \cdot \det(-1) \\ &= 4 \cdot 3 - (-3) \cdot (-7) - (-2) \cdot 5 \\ &+ 4 \cdot (-1) = -3. \end{aligned}$$

We see that we have the same result as the Example 1.
For $i = 2$, we have:

$$\begin{aligned} \det[A_{2\times2\times2}] &= \left(\begin{array}{cc|cc} 4 & -3 & -2 & 4 \\ -1 & 5 & -7 & 3 \end{array}\right) \\ &= -1 \cdot \det(4) - 5 \cdot \det(-2) \\ &- (-7) \cdot \det(-3) + 3 \cdot \det(4) \\ &= -1 \cdot 4 - 5 \cdot (-2) - (-7) \cdot (-3) \\ &+ 3 \cdot 4 = -3. \end{aligned}$$

So we get the same result as the Example 1.
For $j = 1$, we have:

$$\begin{aligned}\det[A_{2\times2\times2}] &= \begin{pmatrix} 4 & -3 & -2 & 4 \\ -1 & 5 & -7 & 3 \end{pmatrix} \\ &= 4 \cdot \det(3) + (-1) \cdot \det(4) \\ &-(-2) \cdot \det(5) - (-7) \cdot \det(-3) \\ &= 4 \cdot 3 + (-1) \cdot 4 - (-2) \cdot 5 \\ &-(-7) \cdot (-3) = -3.\end{aligned}$$

So we get the same result as the Example 1.
For $j = 2$, we have:

$$\begin{aligned}\det[A_{2\times2\times2}] &= \begin{pmatrix} 4 & -3 & -2 & 4 \\ -1 & 5 & -7 & 3 \end{pmatrix} \\ &= -(-3) \cdot \det(-7) - 5 \cdot \det(-2) \\ &+4 \cdot \det(-1) + 3 \cdot \det(4) \\ &= 3 \cdot (-7) - 5 \cdot (-2) - 4 \cdot (-1) \\ &+3 \cdot 4 = -3.\end{aligned}$$

So we get the same result as the Example 1.
For $k = 1$, we have:

$$\begin{aligned}\det[A_{2\times2\times2}] &= \begin{pmatrix} 4 & -3 & -2 & 4 \\ -1 & 5 & -7 & 3 \end{pmatrix} \\ &= 4 \cdot \det(3) - (-3) \cdot \det(-7) \\ &+(-1) \cdot \det(4) - 5 \cdot \det(-2) \\ &= 4 \cdot 3 - (-3) \cdot (-7) + (-1) \cdot 4 \\ &-5 \cdot (-2) = -3.\end{aligned}$$

So we have the same result as the Example 1.
For $k = 2$, we have:

$$\begin{aligned}\det[A_{2\times2\times2}] &= \begin{pmatrix} 4 & -3 & -2 & 4 \\ -1 & 5 & -7 & 3 \end{pmatrix} \\ &= -(-2) \cdot \det(5) + 4 \cdot \det(5) \\ &-(-7) \cdot \det(-3) + 3 \cdot \det(4) \\ &= -(-2) \cdot 5 + 4 \cdot 5 - (-7) \cdot (-3) \\ &+3 \cdot 4 = -3.\end{aligned}$$

So we have the same result as the Example 1.

Laplace Expansion for Determinants Of Cubic-Matrix of Order 3

Below we prove that this method is valid for calculating the determinants of the cubic-matrix of order 3.

Theorem 2 *Let A be a cubic-matrix of order 3,*

$$A = \left(\begin{array}{ccc|ccc|ccc} a_{111} & a_{121} & a_{131} & a_{112} & a_{122} & a_{132} & a_{113} & a_{123} & a_{133} \\ a_{211} & a_{221} & a_{231} & a_{212} & a_{222} & a_{232} & a_{213} & a_{223} & a_{233} \\ a_{311} & a_{321} & a_{331} & a_{312} & a_{322} & a_{332} & a_{313} & a_{323} & a_{333} \end{array}\right).$$

The determinant of this cubic-matrix is invariant into the expansion of three "ways" to Laplace expansion.
Proof. We will prove all three expansion types, L_1, L_2, L_3 also for the third order.
(L_1): For any horizontal layer i ($i = 1,2,3$), the following 'horizontal layer' expansion holds:

$$\det(A) = \sum_{jk} A_{ijk} \cdot C_{ijk}.$$

If we take $i = 1$, and we consider the meaning of the minors and co-factors for the cubic-matrix of order 3, which we described above, we have:

$$\det(A) = \det\left(\begin{array}{ccc|ccc|ccc} a_{111} & a_{121} & a_{131} & a_{112} & a_{122} & a_{132} & a_{113} & a_{123} & a_{133} \\ a_{211} & a_{221} & a_{231} & a_{212} & a_{222} & a_{232} & a_{213} & a_{223} & a_{233} \\ a_{311} & a_{321} & a_{331} & a_{312} & a_{322} & a_{332} & a_{313} & a_{323} & a_{333} \end{array}\right)$$

$$= a_{111} \cdot \begin{pmatrix} a_{222} & a_{232} \\ a_{322} & a_{332} \end{vmatrix} \begin{matrix} a_{223} & a_{233} \\ a_{323} & a_{333} \end{pmatrix} - a_{121} \cdot \begin{pmatrix} a_{212} & a_{232} \\ a_{312} & a_{332} \end{vmatrix} \begin{matrix} a_{213} & a_{233} \\ a_{313} & a_{333} \end{pmatrix} + a_{131} \cdot \begin{pmatrix} a_{212} & a_{222} \\ a_{312} & a_{322} \end{vmatrix} \begin{matrix} a_{213} & a_{223} \\ a_{313} & a_{323} \end{pmatrix}$$

$$-a_{112} \cdot \begin{pmatrix} a_{221} & a_{231} \\ a_{321} & a_{331} \end{vmatrix} \begin{matrix} a_{223} & a_{233} \\ a_{323} & a_{333} \end{pmatrix} + a_{122} \cdot \begin{pmatrix} a_{211} & a_{231} \\ a_{311} & a_{331} \end{vmatrix} \begin{matrix} a_{213} & a_{233} \\ a_{313} & a_{333} \end{pmatrix} - a_{132} \cdot \begin{pmatrix} a_{211} & a_{221} \\ a_{311} & a_{321} \end{vmatrix} \begin{matrix} a_{213} & a_{223} \\ a_{313} & a_{323} \end{pmatrix}$$

$$+a_{113} \cdot \begin{pmatrix} a_{221} & a_{231} \\ a_{321} & a_{331} \end{vmatrix} \begin{matrix} a_{222} & a_{232} \\ a_{322} & a_{332} \end{pmatrix} - a_{123} \cdot \begin{pmatrix} a_{211} & a_{231} \\ a_{311} & a_{331} \end{vmatrix} \begin{matrix} a_{212} & a_{232} \\ a_{312} & a_{332} \end{pmatrix} + a_{133} \cdot \begin{pmatrix} a_{211} & a_{221} \\ a_{311} & a_{321} \end{vmatrix} \begin{matrix} a_{212} & a_{222} \\ a_{312} & a_{322} \end{pmatrix}.$$

After expanding further the above determinant based on Theorem 1, we see that this result is the same as the result of Definition 3.

If we take $i = 2$, and we consider the meaning of the minors and co-factors for the cubic-matrix of order 3, which we described above, we have:

$$\det(A) = \det\left(\begin{array}{ccc|ccc|ccc} a_{111} & a_{121} & a_{131} & a_{112} & a_{122} & a_{132} & a_{113} & a_{123} & a_{133} \\ a_{211} & a_{221} & a_{231} & a_{212} & a_{222} & a_{232} & a_{213} & a_{223} & a_{233} \\ a_{311} & a_{321} & a_{331} & a_{312} & a_{322} & a_{332} & a_{313} & a_{323} & a_{333} \end{array}\right)$$

$$= a_{211} \cdot \begin{pmatrix} a_{122} & a_{132} \\ a_{322} & a_{332} \end{vmatrix} \begin{matrix} a_{123} & a_{133} \\ a_{323} & a_{333} \end{pmatrix} - a_{221} \cdot \begin{pmatrix} a_{112} & a_{132} \\ a_{312} & a_{332} \end{vmatrix} \begin{matrix} a_{113} & a_{133} \\ a_{313} & a_{333} \end{pmatrix} + a_{231} \cdot \begin{pmatrix} a_{112} & a_{122} \\ a_{312} & a_{322} \end{vmatrix} \begin{matrix} a_{113} & a_{123} \\ a_{313} & a_{323} \end{pmatrix}$$

$$-a_{212} \cdot \begin{pmatrix} a_{121} & a_{131} \\ a_{321} & a_{331} \end{vmatrix} \begin{matrix} a_{123} & a_{133} \\ a_{323} & a_{333} \end{pmatrix} + a_{222} \cdot \begin{pmatrix} a_{111} & a_{131} \\ a_{311} & a_{331} \end{vmatrix} \begin{matrix} a_{113} & a_{133} \\ a_{313} & a_{333} \end{pmatrix} - a_{232} \cdot \begin{pmatrix} a_{111} & a_{121} \\ a_{311} & a_{321} \end{vmatrix} \begin{matrix} a_{113} & a_{123} \\ a_{313} & a_{323} \end{pmatrix}$$

$$+a_{113} \cdot \begin{pmatrix} a_{221} & a_{231} \\ a_{321} & a_{331} \end{vmatrix} \begin{matrix} a_{222} & a_{232} \\ a_{322} & a_{332} \end{pmatrix} - a_{123} \cdot \begin{pmatrix} a_{211} & a_{231} \\ a_{311} & a_{331} \end{vmatrix} \begin{matrix} a_{212} & a_{232} \\ a_{312} & a_{332} \end{pmatrix} + a_{133} \cdot \begin{pmatrix} a_{211} & a_{221} \\ a_{311} & a_{321} \end{vmatrix} \begin{matrix} a_{212} & a_{222} \\ a_{312} & a_{322} \end{pmatrix}.$$

After expanding further the above determinant based on Theorem 1, we see that this result is the same as the result of Definition 3.

If we take $i = 3$, and we consider the meaning of the minors and co-factors for the cubic-matrix of order 3, which we described above, we have:

$$\det(A) = \det\left(\begin{array}{ccc|ccc|ccc} a_{111} & a_{121} & a_{131} & a_{112} & a_{122} & a_{132} & a_{113} & a_{123} & a_{133} \\ a_{211} & a_{221} & a_{231} & a_{212} & a_{222} & a_{232} & a_{213} & a_{223} & a_{233} \\ a_{311} & a_{321} & a_{331} & a_{312} & a_{322} & a_{332} & a_{313} & a_{323} & a_{333} \end{array}\right)$$

$$= a_{311} \cdot \begin{pmatrix} a_{122} & a_{132} \\ a_{222} & a_{232} \end{vmatrix} \begin{matrix} a_{123} & a_{133} \\ a_{223} & a_{233} \end{pmatrix} - a_{221} \cdot \begin{pmatrix} a_{112} & a_{132} \\ a_{212} & a_{232} \end{vmatrix} \begin{matrix} a_{113} & a_{133} \\ a_{213} & a_{233} \end{pmatrix} + a_{331} \cdot \begin{pmatrix} a_{112} & a_{122} \\ a_{212} & a_{222} \end{vmatrix} \begin{matrix} a_{113} & a_{123} \\ a_{213} & a_{223} \end{pmatrix}$$

$$-a_{312} \cdot \begin{pmatrix} a_{121} & a_{131} \\ a_{221} & a_{231} \end{vmatrix} \begin{matrix} a_{123} & a_{133} \\ a_{223} & a_{233} \end{pmatrix} + a_{322} \cdot \begin{pmatrix} a_{111} & a_{131} \\ a_{211} & a_{231} \end{vmatrix} \begin{matrix} a_{113} & a_{133} \\ a_{213} & a_{233} \end{pmatrix} - a_{332} \cdot \begin{pmatrix} a_{111} & a_{121} \\ a_{211} & a_{221} \end{vmatrix} \begin{matrix} a_{113} & a_{123} \\ a_{213} & a_{223} \end{pmatrix}$$

$$+a_{313} \cdot \begin{pmatrix} a_{221} & a_{231} \\ a_{221} & a_{231} \end{vmatrix} \begin{matrix} a_{222} & a_{232} \\ a_{222} & a_{232} \end{pmatrix} - a_{323} \cdot \begin{pmatrix} a_{211} & a_{231} \\ a_{211} & a_{231} \end{vmatrix} \begin{matrix} a_{212} & a_{232} \\ a_{212} & a_{232} \end{pmatrix} + a_{333} \cdot \begin{pmatrix} a_{211} & a_{221} \\ a_{211} & a_{221} \end{vmatrix} \begin{matrix} a_{212} & a_{222} \\ a_{212} & a_{222} \end{pmatrix}.$$

After expanding further the above determinant based on Theorem 1, we see that this result is the same as the result of Definition 3.

If we take $j = 1$, and we consider the meaning of the minors and co-factors for the cubic-matrix of order 3, which we described above, we have:

$$\det(A) = \det\left(\begin{array}{ccc|ccc|ccc} a_{111} & a_{121} & a_{131} & a_{112} & a_{122} & a_{132} & a_{113} & a_{123} & a_{133} \\ a_{211} & a_{221} & a_{231} & a_{212} & a_{222} & a_{232} & a_{213} & a_{223} & a_{233} \\ a_{311} & a_{321} & a_{331} & a_{312} & a_{322} & a_{332} & a_{313} & a_{323} & a_{333} \end{array}\right)$$

$$= a_{111} \cdot \begin{pmatrix} a_{222} & a_{232} \\ a_{322} & a_{332} \end{vmatrix} \begin{matrix} a_{223} & a_{233} \\ a_{323} & a_{333} \end{pmatrix} - a_{211} \cdot \begin{pmatrix} a_{122} & a_{132} \\ a_{322} & a_{332} \end{vmatrix} \begin{matrix} a_{123} & a_{133} \\ a_{323} & a_{333} \end{pmatrix} + a_{311} \cdot \begin{pmatrix} a_{122} & a_{132} \\ a_{222} & a_{232} \end{vmatrix} \begin{matrix} a_{123} & a_{133} \\ a_{223} & a_{233} \end{pmatrix}$$

$$-a_{112} \cdot \begin{pmatrix} a_{221} & a_{231} \\ a_{321} & a_{331} \end{vmatrix} \begin{matrix} a_{223} & a_{233} \\ a_{323} & a_{333} \end{pmatrix} + a_{212} \cdot \begin{pmatrix} a_{121} & a_{131} \\ a_{321} & a_{331} \end{vmatrix} \begin{matrix} a_{123} & a_{133} \\ a_{323} & a_{333} \end{pmatrix} - a_{312} \cdot \begin{pmatrix} a_{121} & a_{131} \\ a_{221} & a_{231} \end{vmatrix} \begin{matrix} a_{123} & a_{133} \\ a_{223} & a_{233} \end{pmatrix}$$

$$+a_{113} \cdot \begin{pmatrix} a_{221} & a_{231} \\ a_{321} & a_{331} \end{vmatrix} \begin{matrix} a_{222} & a_{232} \\ a_{322} & a_{332} \end{pmatrix} - a_{213} \cdot \begin{pmatrix} a_{121} & a_{131} \\ a_{321} & a_{331} \end{vmatrix} \begin{matrix} a_{122} & a_{132} \\ a_{322} & a_{332} \end{pmatrix} + a_{313} \cdot \begin{pmatrix} a_{121} & a_{131} \\ a_{221} & a_{231} \end{vmatrix} \begin{matrix} a_{122} & a_{132} \\ a_{222} & a_{232} \end{pmatrix}.$$

After expanding further the above determinant based on Theorem 1, we see that this result is the same as the result of Definition 3.

If we take $j = 2$, and we consider the meaning of the minors and co-factors for the cubic-matrix of order 3, which we described above, we have:

$$\det(A) = \det\left(\begin{array}{ccc|ccc|ccc} a_{111} & a_{121} & a_{131} & a_{112} & a_{122} & a_{132} & a_{113} & a_{123} & a_{133} \\ a_{211} & a_{221} & a_{231} & a_{212} & a_{222} & a_{232} & a_{213} & a_{223} & a_{233} \\ a_{311} & a_{321} & a_{331} & a_{312} & a_{322} & a_{332} & a_{313} & a_{323} & a_{333} \end{array}\right)$$

$$= a_{121} \cdot \begin{vmatrix} a_{212} & a_{232} \\ a_{312} & a_{332} \end{vmatrix} \begin{vmatrix} a_{213} & a_{233} \\ a_{313} & a_{333} \end{vmatrix} - a_{221} \cdot \begin{vmatrix} a_{112} & a_{132} \\ a_{312} & a_{332} \end{vmatrix} \begin{vmatrix} a_{113} & a_{133} \\ a_{313} & a_{333} \end{vmatrix} + a_{321} \cdot \begin{vmatrix} a_{112} & a_{132} \\ a_{212} & a_{232} \end{vmatrix} \begin{vmatrix} a_{113} & a_{133} \\ a_{213} & a_{233} \end{vmatrix}$$
$$- a_{122} \cdot \begin{vmatrix} a_{211} & a_{231} \\ a_{311} & a_{331} \end{vmatrix} \begin{vmatrix} a_{213} & a_{233} \\ a_{313} & a_{333} \end{vmatrix} + a_{222} \cdot \begin{vmatrix} a_{111} & a_{131} \\ a_{311} & a_{331} \end{vmatrix} \begin{vmatrix} a_{113} & a_{133} \\ a_{313} & a_{333} \end{vmatrix} - a_{322} \cdot \begin{vmatrix} a_{111} & a_{131} \\ a_{211} & a_{231} \end{vmatrix} \begin{vmatrix} a_{113} & a_{133} \\ a_{213} & a_{233} \end{vmatrix}$$
$$+ a_{123} \cdot \begin{vmatrix} a_{211} & a_{231} \\ a_{311} & a_{331} \end{vmatrix} \begin{vmatrix} a_{212} & a_{232} \\ a_{312} & a_{332} \end{vmatrix} - a_{223} \cdot \begin{vmatrix} a_{111} & a_{131} \\ a_{311} & a_{331} \end{vmatrix} \begin{vmatrix} a_{112} & a_{132} \\ a_{312} & a_{332} \end{vmatrix} + a_{323} \cdot \begin{vmatrix} a_{111} & a_{131} \\ a_{211} & a_{231} \end{vmatrix} \begin{vmatrix} a_{112} & a_{132} \\ a_{212} & a_{232} \end{vmatrix}$$

After expanding further the above determinant based on Theorem 1, we see that this result is the same as the result of Definition 3.

If we take $j = 3$, and we consider the meaning of the minors and co-factors for the cubic-matrix of order 3, which we described above, we have:

$$\det(A) = \det\left(\begin{array}{ccc|ccc|ccc} a_{111} & a_{121} & a_{131} & a_{112} & a_{122} & a_{132} & a_{113} & a_{123} & a_{133} \\ a_{211} & a_{221} & a_{231} & a_{212} & a_{222} & a_{232} & a_{213} & a_{223} & a_{233} \\ a_{311} & a_{321} & a_{331} & a_{312} & a_{322} & a_{332} & a_{313} & a_{323} & a_{333} \end{array}\right)$$

$$= a_{131} \cdot \begin{vmatrix} a_{212} & a_{222} \\ a_{312} & a_{322} \end{vmatrix} \begin{vmatrix} a_{213} & a_{223} \\ a_{313} & a_{323} \end{vmatrix} - a_{231} \cdot \begin{vmatrix} a_{112} & a_{122} \\ a_{312} & a_{322} \end{vmatrix} \begin{vmatrix} a_{113} & a_{123} \\ a_{313} & a_{323} \end{vmatrix} + a_{331} \cdot \begin{vmatrix} a_{112} & a_{122} \\ a_{212} & a_{222} \end{vmatrix} \begin{vmatrix} a_{113} & a_{123} \\ a_{213} & a_{223} \end{vmatrix}$$
$$- a_{132} \cdot \begin{vmatrix} a_{211} & a_{221} \\ a_{311} & a_{321} \end{vmatrix} \begin{vmatrix} a_{213} & a_{223} \\ a_{313} & a_{323} \end{vmatrix} + a_{232} \cdot \begin{vmatrix} a_{111} & a_{121} \\ a_{311} & a_{321} \end{vmatrix} \begin{vmatrix} a_{113} & a_{123} \\ a_{313} & a_{323} \end{vmatrix} - a_{332} \cdot \begin{vmatrix} a_{111} & a_{121} \\ a_{211} & a_{221} \end{vmatrix} \begin{vmatrix} a_{113} & a_{123} \\ a_{213} & a_{223} \end{vmatrix}$$
$$+ a_{133} \cdot \begin{vmatrix} a_{211} & a_{221} \\ a_{311} & a_{321} \end{vmatrix} \begin{vmatrix} a_{212} & a_{222} \\ a_{312} & a_{322} \end{vmatrix} - a_{233} \cdot \begin{vmatrix} a_{111} & a_{121} \\ a_{311} & a_{321} \end{vmatrix} \begin{vmatrix} a_{112} & a_{122} \\ a_{312} & a_{322} \end{vmatrix} + a_{333} \cdot \begin{vmatrix} a_{111} & a_{121} \\ a_{211} & a_{221} \end{vmatrix} \begin{vmatrix} a_{112} & a_{122} \\ a_{212} & a_{222} \end{vmatrix}.$$

After expanding further the above determinant based on Theorem 1, we see that this result is the same as the result of Definition 3.

If we take $k = 1$, and we consider the meaning of the minors and co-factors for the cubic-matrix of order 3, which we described above, we have:

$$\det(A) = \det\left[\left(\begin{array}{ccc|ccc|ccc} a_{111} & a_{121} & a_{131} & a_{112} & a_{122} & a_{132} & a_{113} & a_{123} & a_{133} \\ a_{211} & a_{221} & a_{231} & a_{212} & a_{222} & a_{232} & a_{213} & a_{223} & a_{233} \\ a_{311} & a_{321} & a_{331} & a_{312} & a_{322} & a_{332} & a_{313} & a_{323} & a_{333} \end{array}\right)\right]$$

$$= a_{111} \cdot \begin{vmatrix} a_{222} & a_{232} \\ a_{322} & a_{332} \end{vmatrix} \begin{vmatrix} a_{223} & a_{233} \\ a_{323} & a_{333} \end{vmatrix} - a_{121} \cdot \begin{vmatrix} a_{212} & a_{232} \\ a_{312} & a_{332} \end{vmatrix} \begin{vmatrix} a_{213} & a_{233} \\ a_{313} & a_{333} \end{vmatrix} + a_{131} \cdot \begin{vmatrix} a_{212} & a_{222} \\ a_{312} & a_{322} \end{vmatrix} \begin{vmatrix} a_{213} & a_{223} \\ a_{313} & a_{323} \end{vmatrix}$$
$$- a_{211} \cdot \begin{vmatrix} a_{122} & a_{132} \\ a_{322} & a_{332} \end{vmatrix} \begin{vmatrix} a_{123} & a_{133} \\ a_{323} & a_{333} \end{vmatrix} + a_{221} \cdot \begin{vmatrix} a_{112} & a_{132} \\ a_{312} & a_{332} \end{vmatrix} \begin{vmatrix} a_{113} & a_{133} \\ a_{313} & a_{333} \end{vmatrix} - a_{231} \cdot \begin{vmatrix} a_{112} & a_{122} \\ a_{312} & a_{322} \end{vmatrix} \begin{vmatrix} a_{113} & a_{123} \\ a_{313} & a_{323} \end{vmatrix}$$
$$+ a_{311} \cdot \begin{vmatrix} a_{122} & a_{132} \\ a_{222} & a_{232} \end{vmatrix} \begin{vmatrix} a_{223} & a_{233} \\ a_{323} & a_{333} \end{vmatrix} - a_{321} \cdot \begin{vmatrix} a_{112} & a_{132} \\ a_{212} & a_{232} \end{vmatrix} \begin{vmatrix} a_{123} & a_{133} \\ a_{213} & a_{233} \end{vmatrix} + a_{331} \cdot \begin{vmatrix} a_{112} & a_{122} \\ a_{212} & a_{222} \end{vmatrix} \begin{vmatrix} a_{113} & a_{123} \\ a_{213} & a_{223} \end{vmatrix}.$$

After expanding further the above determinant based on Theorem 1, we see that this result is the same as the result of Definition 3.

If we take $k = 2$, and we consider the meaning of the minors and co-factors for the cubic-matrix of order 3, which we described above, we have:

$$\det(A) = \det\left[\left(\begin{array}{ccc|ccc|ccc} a_{111} & a_{121} & a_{131} & a_{112} & a_{122} & a_{132} & a_{113} & a_{123} & a_{133} \\ a_{211} & a_{221} & a_{231} & a_{212} & a_{222} & a_{232} & a_{213} & a_{223} & a_{233} \\ a_{311} & a_{321} & a_{331} & a_{312} & a_{322} & a_{332} & a_{313} & a_{323} & a_{333} \end{array}\right)\right]$$

$$= a_{112} \cdot \begin{vmatrix} a_{221} & a_{231} \\ a_{321} & a_{331} \end{vmatrix} \begin{vmatrix} a_{223} & a_{233} \\ a_{323} & a_{333} \end{vmatrix} - a_{122} \cdot \begin{vmatrix} a_{211} & a_{231} \\ a_{311} & a_{331} \end{vmatrix} \begin{vmatrix} a_{213} & a_{233} \\ a_{313} & a_{333} \end{vmatrix} + a_{132} \cdot \begin{vmatrix} a_{211} & a_{221} \\ a_{311} & a_{321} \end{vmatrix} \begin{vmatrix} a_{213} & a_{223} \\ a_{313} & a_{323} \end{vmatrix}$$
$$- a_{212} \cdot \begin{vmatrix} a_{121} & a_{131} \\ a_{321} & a_{331} \end{vmatrix} \begin{vmatrix} a_{123} & a_{133} \\ a_{323} & a_{333} \end{vmatrix} + a_{222} \cdot \begin{vmatrix} a_{111} & a_{131} \\ a_{311} & a_{331} \end{vmatrix} \begin{vmatrix} a_{113} & a_{133} \\ a_{313} & a_{333} \end{vmatrix} - a_{232} \cdot \begin{vmatrix} a_{111} & a_{121} \\ a_{311} & a_{321} \end{vmatrix} \begin{vmatrix} a_{113} & a_{123} \\ a_{313} & a_{323} \end{vmatrix}$$

$$+a_{312}\cdot\begin{pmatrix}a_{121} & a_{131}\\ a_{221} & a_{231}\end{pmatrix}\begin{pmatrix}a_{223} & a_{233}\\ a_{323} & a_{333}\end{pmatrix}-a_{322}\cdot\begin{pmatrix}a_{111} & a_{131}\\ a_{211} & a_{231}\end{pmatrix}\begin{pmatrix}a_{123} & a_{133}\\ a_{213} & a_{233}\end{pmatrix}+a_{332}\cdot\begin{pmatrix}a_{111} & a_{121}\\ a_{211} & a_{221}\end{pmatrix}\begin{pmatrix}a_{113} & a_{123}\\ a_{213} & a_{223}\end{pmatrix}.$$

After expanding further the above determinant based on Theorem 1, we see that this result is the same as the result of Definition 3.

If we take $k = 3$, and we consider the meaning of the minors and co-factors for the cubic-matrix of order 3, which we described above, we have:

$$\det(A) = \det\left[\begin{pmatrix}a_{111} & a_{121} & a_{131}\\ a_{211} & a_{221} & a_{231}\\ a_{311} & a_{321} & a_{331}\end{pmatrix}\begin{pmatrix}a_{112} & a_{122} & a_{132}\\ a_{212} & a_{222} & a_{232}\\ a_{312} & a_{322} & a_{332}\end{pmatrix}\begin{pmatrix}a_{113} & a_{123} & a_{133}\\ a_{213} & a_{223} & a_{233}\\ a_{313} & a_{323} & a_{333}\end{pmatrix}\right]$$

$$\begin{aligned}&= a_{113}\cdot\begin{pmatrix}a_{221} & a_{231}\\ a_{321} & a_{331}\end{pmatrix}\begin{pmatrix}a_{222} & a_{232}\\ a_{322} & a_{332}\end{pmatrix}-a_{123}\cdot\begin{pmatrix}a_{211} & a_{231}\\ a_{311} & a_{331}\end{pmatrix}\begin{pmatrix}a_{212} & a_{232}\\ a_{312} & a_{332}\end{pmatrix}+a_{133}\cdot\begin{pmatrix}a_{211} & a_{221}\\ a_{311} & a_{321}\end{pmatrix}\begin{pmatrix}a_{212} & a_{222}\\ a_{312} & a_{322}\end{pmatrix}\\ &-a_{213}\cdot\begin{pmatrix}a_{121} & a_{131}\\ a_{321} & a_{331}\end{pmatrix}\begin{pmatrix}a_{122} & a_{132}\\ a_{322} & a_{332}\end{pmatrix}+a_{223}\cdot\begin{pmatrix}a_{111} & a_{131}\\ a_{311} & a_{331}\end{pmatrix}\begin{pmatrix}a_{112} & a_{132}\\ a_{312} & a_{332}\end{pmatrix}-a_{233}\cdot\begin{pmatrix}a_{111} & a_{121}\\ a_{311} & a_{321}\end{pmatrix}\begin{pmatrix}a_{112} & a_{122}\\ a_{312} & a_{322}\end{pmatrix}\\ &+a_{313}\cdot\begin{pmatrix}a_{121} & a_{131}\\ a_{221} & a_{231}\end{pmatrix}\begin{pmatrix}a_{222} & a_{232}\\ a_{322} & a_{332}\end{pmatrix}-a_{323}\cdot\begin{pmatrix}a_{111} & a_{131}\\ a_{211} & a_{231}\end{pmatrix}\begin{pmatrix}a_{122} & a_{132}\\ a_{212} & a_{232}\end{pmatrix}+a_{333}\cdot\begin{pmatrix}a_{111} & a_{121}\\ a_{211} & a_{221}\end{pmatrix}\begin{pmatrix}a_{112} & a_{122}\\ a_{212} & a_{222}\end{pmatrix}.\end{aligned}$$

After expanding further the above determinant based on Theorem 1, we see that this result is the same as the result of Definition 3.

The following example is a case where the cubic-matrix of the third order, is with elements from the number field $\mathbb{R}$.

Example 6 *Let's have the cubic-matrix, with the element in the number field* $\mathbb{R}$,

$$A_{3\times3\times3} = \begin{pmatrix}3 & 0 & -4\\ 2 & 5 & -1\\ 0 & 3 & -2\end{pmatrix}\begin{pmatrix}-2 & 4 & 0\\ -3 & 0 & 3\\ -3 & 2 & 5\end{pmatrix}\begin{pmatrix}5 & 1 & 0\\ 3 & 1 & 2\\ 0 & 4 & 3\end{pmatrix}$$

then according to Theorem 2, we calculate the Determinant of this cubic-matrix, and have,

$$\det[A_{3\times3\times3}] = \det\left[\begin{pmatrix}3 & 0 & -4\\ 2 & 5 & -1\\ 0 & 3 & -2\end{pmatrix}\begin{pmatrix}-2 & 4 & 0\\ -3 & 0 & 3\\ -3 & 2 & 5\end{pmatrix}\begin{pmatrix}5 & 1 & 0\\ 3 & 1 & 2\\ 0 & 4 & 3\end{pmatrix}\right].$$

For $i = 1$, we have:

$$\det(A) = \det\left[\begin{pmatrix}3 & 0 & -4\\ 2 & 5 & -1\\ 0 & 3 & -2\end{pmatrix}\begin{pmatrix}-2 & 4 & 0\\ -3 & 0 & 3\\ -3 & 2 & 5\end{pmatrix}\begin{pmatrix}5 & 1 & 0\\ 3 & 1 & 2\\ 0 & 4 & 3\end{pmatrix}\right]$$

$$\begin{aligned}&= 3\cdot\begin{pmatrix}0 & 3\\ 2 & 5\end{pmatrix}\begin{pmatrix}1 & 2\\ 4 & 3\end{pmatrix}-0\cdot\begin{pmatrix}-3 & 3\\ -3 & 5\end{pmatrix}\begin{pmatrix}3 & 2\\ 0 & 3\end{pmatrix}+(-4)\cdot\begin{pmatrix}-3 & 0\\ -3 & 2\end{pmatrix}\begin{pmatrix}3 & 1\\ 0 & 4\end{pmatrix}-(-2)\cdot\begin{pmatrix}5 & -1\\ 3 & -2\end{pmatrix}\begin{pmatrix}1 & 2\\ 4 & 3\end{pmatrix}\\ &+4\cdot\begin{pmatrix}2 & -1\\ 0 & -2\end{pmatrix}\begin{pmatrix}3 & 2\\ 0 & 3\end{pmatrix}-0\cdot\begin{pmatrix}2 & 5\\ 0 & 3\end{pmatrix}\begin{pmatrix}3 & 1\\ 0 & 4\end{pmatrix}+5\cdot\begin{pmatrix}5 & -1\\ 3 & -2\end{pmatrix}\begin{pmatrix}0 & 3\\ 2 & 5\end{pmatrix}-1\cdot\begin{pmatrix}2 & -1\\ 0 & -2\end{pmatrix}\begin{pmatrix}-3 & 3\\ -3 & 5\end{pmatrix}+0\cdot\begin{pmatrix}2 & 5\\ 0 & 3\end{pmatrix}\begin{pmatrix}-3 & 0\\ -3 & 2\end{pmatrix}\end{aligned}$$

So

$$\det(A) = 326.$$

After expanding further the minors of the above determinant based on Theorem 1, we see that this result is the same as the result of Example 2.
For $i = 2$, we have:

$$\det(A) = \det\left[\begin{pmatrix}3 & 0 & -4\\ 2 & 5 & -1\\ 0 & 3 & -2\end{pmatrix}\begin{pmatrix}-2 & 4 & 0\\ -3 & 0 & 3\\ -3 & 2 & 5\end{pmatrix}\begin{pmatrix}5 & 1 & 0\\ 3 & 1 & 2\\ 0 & 4 & 3\end{pmatrix}\right]$$

$$= 2\cdot\begin{pmatrix}4 & 0\\ 2 & 5\end{pmatrix}\begin{pmatrix}1 & 0\\ 4 & 3\end{pmatrix}-5\cdot\begin{pmatrix}-2 & 0\\ -3 & 5\end{pmatrix}\begin{pmatrix}5 & 0\\ 0 & 3\end{pmatrix}+(-1)\cdot\begin{pmatrix}-2 & 4\\ -3 & 2\end{pmatrix}\begin{pmatrix}5 & 1\\ 0 & 4\end{pmatrix}-(-3)\cdot\begin{pmatrix}0 & -4\\ 3 & -2\end{pmatrix}\begin{pmatrix}1 & 0\\ 4 & 3\end{pmatrix}$$

$$+0\cdot\begin{pmatrix}3&-4\\0&-2\end{vmatrix}\begin{matrix}5&0\\0&3\end{pmatrix}-3\cdot\begin{pmatrix}3&0\\0&3\end{vmatrix}\begin{matrix}5&1\\0&4\end{pmatrix}+5\cdot\begin{pmatrix}5&-1\\3&-2\end{vmatrix}\begin{matrix}0&3\\2&5\end{pmatrix}-1\cdot\begin{pmatrix}2&-1\\0&-2\end{vmatrix}\begin{matrix}-3&3\\-3&5\end{pmatrix}+0\cdot\begin{pmatrix}2&5\\0&3\end{vmatrix}\begin{matrix}-3&0\\-3&2\end{pmatrix}$$

so

$$\det(A) = 326.$$

After expanding further the minors of the above determinant based on Theorem 1, we see that this result is the same as the result of Example 2.
For $i = 3$, we have:

$$\det(A) = \det\left[\begin{pmatrix}3&0&-4\\2&5&-1\\0&3&-2\end{vmatrix}\begin{matrix}-2&4&0\\-3&0&3\\-3&2&5\end{vmatrix}\begin{matrix}5&1&0\\3&1&2\\0&4&3\end{pmatrix}\right]$$
$$= 0\cdot\begin{pmatrix}4&0\\0&3\end{vmatrix}\begin{matrix}1&0\\1&2\end{pmatrix}-5\cdot\begin{pmatrix}-2&0\\-3&3\end{vmatrix}\begin{matrix}5&0\\3&2\end{pmatrix}+(-2)\cdot\begin{pmatrix}-2&4\\-3&0\end{vmatrix}\begin{matrix}5&1\\3&1\end{pmatrix}-(-3)\cdot\begin{pmatrix}0&-4\\5&-1\end{vmatrix}\begin{matrix}1&0\\1&2\end{pmatrix}$$
$$+2\cdot\begin{pmatrix}3&-4\\2&-1\end{vmatrix}\begin{matrix}5&0\\3&2\end{pmatrix}-5\cdot\begin{pmatrix}3&0\\2&5\end{vmatrix}\begin{matrix}5&1\\3&1\end{pmatrix}+0\cdot\begin{pmatrix}5&-1\\5&-1\end{vmatrix}\begin{matrix}0&3\\0&3\end{pmatrix}-4\cdot\begin{pmatrix}2&-1\\2&-1\end{vmatrix}\begin{matrix}-3&3\\-3&3\end{pmatrix}+3\cdot\begin{pmatrix}2&5\\2&5\end{vmatrix}\begin{matrix}-3&0\\-3&0\end{pmatrix}$$

So

$$\det(A) = 326.$$

After expanding further the minors of the above determinant based on Theorem 1, we see that this result is the same as the result of Example 2.
For $j = 1$, we have:

$$\det(A) = \det\left[\begin{pmatrix}3&0&-4\\2&5&-1\\0&3&-2\end{vmatrix}\begin{matrix}-2&4&0\\-3&0&3\\-3&2&5\end{vmatrix}\begin{matrix}5&1&0\\3&1&2\\0&4&3\end{pmatrix}\right]$$
$$= 3\cdot\begin{pmatrix}0&3\\2&5\end{vmatrix}\begin{matrix}1&2\\4&3\end{pmatrix}-2\cdot\begin{pmatrix}4&0\\2&5\end{vmatrix}\begin{matrix}1&0\\4&3\end{pmatrix}+0\cdot\begin{pmatrix}4&0\\0&3\end{vmatrix}\begin{matrix}1&0\\1&2\end{pmatrix}$$
$$-(-2)\cdot\begin{pmatrix}5&-1\\3&-2\end{vmatrix}\begin{matrix}1&2\\4&3\end{pmatrix}+(-3)\cdot\begin{pmatrix}0&-4\\3&-2\end{vmatrix}\begin{matrix}1&0\\4&3\end{pmatrix}-(-3)\cdot\begin{pmatrix}0&-4\\5&-1\end{vmatrix}\begin{matrix}1&0\\1&2\end{pmatrix}$$
$$+5\cdot\begin{pmatrix}5&-1\\3&-2\end{vmatrix}\begin{matrix}0&3\\2&5\end{pmatrix}-3\cdot\begin{pmatrix}0&-4\\3&-2\end{vmatrix}\begin{matrix}4&0\\2&5\end{pmatrix}+0\cdot\begin{pmatrix}0&-4\\5&-1\end{vmatrix}\begin{matrix}4&0\\0&3\end{pmatrix}$$

So

$$\det(A) = 326.$$

After expanding further the minors of the above determinant based on Theorem 1, we see that this result is the same as the result of Example 2.
For $j = 2$, we have:

$$\det(A) = \det\left[\begin{pmatrix}3&0&-4\\2&5&-1\\0&3&-2\end{vmatrix}\begin{matrix}-2&4&0\\-3&0&3\\-3&2&5\end{vmatrix}\begin{matrix}5&1&0\\3&1&2\\0&4&3\end{pmatrix}\right]$$
$$= 0\cdot\begin{pmatrix}-3&3\\-3&5\end{vmatrix}\begin{matrix}3&2\\0&3\end{pmatrix}-5\cdot\begin{pmatrix}-2&0\\-3&5\end{vmatrix}\begin{matrix}5&0\\0&3\end{pmatrix}+3\cdot\begin{pmatrix}-2&0\\-3&3\end{vmatrix}\begin{matrix}5&0\\3&2\end{pmatrix}-4\cdot\begin{pmatrix}2&-1\\0&-2\end{vmatrix}\begin{matrix}3&2\\0&3\end{pmatrix}$$
$$+0\cdot\begin{pmatrix}3&-4\\0&-2\end{vmatrix}\begin{matrix}5&0\\0&3\end{pmatrix}-2\cdot\begin{pmatrix}3&-4\\2&-1\end{vmatrix}\begin{matrix}5&0\\3&2\end{pmatrix}+1\cdot\begin{pmatrix}2&-1\\0&-2\end{vmatrix}\begin{matrix}-3&3\\-3&5\end{pmatrix}-1\cdot\begin{pmatrix}3&-4\\0&-2\end{vmatrix}\begin{matrix}-2&0\\-3&5\end{pmatrix}$$
$$+4\cdot\begin{pmatrix}3&-4\\2&-1\end{vmatrix}\begin{matrix}-2&0\\-3&3\end{pmatrix}=326.$$

After expanding further the minors of the above determinant based on Theorem 1, we see that this result is the same as the result of Example 2.
For $j = 3$, we have:

$$\det(A) = \det\left[\begin{pmatrix} 3 & 0 & -4 \\ 2 & 5 & -1 \\ 0 & 3 & -2 \end{pmatrix}\begin{vmatrix} -2 & 4 & 0 \\ -3 & 0 & 3 \\ -3 & 2 & 5 \end{vmatrix}\begin{pmatrix} 5 & 1 & 0 \\ 3 & 1 & 2 \\ 0 & 4 & 3 \end{pmatrix}\right]$$

$$= (-4)\cdot\begin{pmatrix} -3 & 0 \\ -3 & 2 \end{pmatrix}\begin{vmatrix} 3 & 1 \\ 0 & 4 \end{vmatrix} - (-1)\cdot\begin{pmatrix} -2 & 4 \\ -3 & 2 \end{pmatrix}\begin{vmatrix} 5 & 1 \\ 0 & 4 \end{vmatrix} + (-2)\cdot\begin{pmatrix} -2 & 4 \\ -3 & 0 \end{pmatrix}\begin{vmatrix} 5 & 1 \\ 3 & 1 \end{vmatrix} - 0\cdot\begin{pmatrix} 2 & 5 \\ 0 & 3 \end{pmatrix}\begin{vmatrix} 3 & 1 \\ 0 & 4 \end{vmatrix}$$

$$+3\cdot\begin{pmatrix} 3 & 0 \\ 0 & 3 \end{pmatrix}\begin{vmatrix} 5 & 1 \\ 0 & 4 \end{vmatrix} - 5\cdot\begin{pmatrix} 3 & 0 \\ 2 & 5 \end{pmatrix}\begin{vmatrix} 5 & 1 \\ 3 & 1 \end{vmatrix} + 0\cdot\begin{pmatrix} 2 & 5 \\ 0 & 3 \end{pmatrix}\begin{vmatrix} -3 & 0 \\ -3 & 2 \end{vmatrix} - 2\cdot\begin{pmatrix} 3 & 0 \\ 0 & 3 \end{pmatrix}\begin{vmatrix} -2 & 4 \\ -3 & 2 \end{vmatrix}$$

$$+3\cdot\begin{pmatrix} 3 & 0 \\ 2 & 5 \end{pmatrix}\begin{vmatrix} -2 & 4 \\ -3 & 0 \end{vmatrix} = 326.$$

After expanding further the minors of the above determinant based on Theorem 1, we see that this result is the same as the result of Example 2.
For $k = 1$, we have:

$$\det(A) = \det\left[\begin{pmatrix} 3 & 0 & -4 \\ 2 & 5 & -1 \\ 0 & 3 & -2 \end{pmatrix}\begin{vmatrix} -2 & 4 & 0 \\ -3 & 0 & 3 \\ -3 & 2 & 5 \end{vmatrix}\begin{pmatrix} 5 & 1 & 0 \\ 3 & 1 & 2 \\ 0 & 4 & 3 \end{pmatrix}\right]$$

$$= 3\cdot\begin{pmatrix} 0 & 3 \\ 2 & 5 \end{pmatrix}\begin{vmatrix} 1 & 2 \\ 4 & 3 \end{vmatrix} - 0\cdot\begin{pmatrix} -3 & 3 \\ -3 & 5 \end{pmatrix}\begin{vmatrix} 3 & 2 \\ 0 & 3 \end{vmatrix} + (-4)\cdot\begin{pmatrix} -3 & 0 \\ -3 & 2 \end{pmatrix}\begin{vmatrix} 3 & 1 \\ 0 & 4 \end{vmatrix} - 2\cdot\begin{pmatrix} 4 & 0 \\ 2 & 5 \end{pmatrix}\begin{vmatrix} 1 & 0 \\ 4 & 3 \end{vmatrix}$$

$$+5\cdot\begin{pmatrix} -2 & 0 \\ -3 & 5 \end{pmatrix}\begin{vmatrix} 5 & 0 \\ 0 & 3 \end{vmatrix} - (-1)\cdot\begin{pmatrix} -2 & 4 \\ -3 & 2 \end{pmatrix}\begin{vmatrix} 5 & 1 \\ 0 & 4 \end{vmatrix} + 0\cdot\begin{pmatrix} 4 & 0 \\ 0 & 3 \end{pmatrix}\begin{vmatrix} 1 & 2 \\ 4 & 3 \end{vmatrix} - 3\cdot\begin{pmatrix} -2 & 0 \\ -3 & 3 \end{pmatrix}\begin{vmatrix} 1 & 0 \\ 3 & 2 \end{vmatrix}$$

$$+(-2)\cdot\begin{pmatrix} -2 & 4 \\ -3 & 0 \end{pmatrix}\begin{vmatrix} 5 & 1 \\ 3 & 1 \end{vmatrix} = 326.$$

After expanding further the minors of the above determinant based on Theorem 1, we see that this result is the same as the result of Example 2.
For $k = 2$, we have:

$$\det(A) = \det\left[\begin{pmatrix} 3 & 0 & -4 \\ 2 & 5 & -1 \\ 0 & 3 & -2 \end{pmatrix}\begin{vmatrix} -2 & 4 & 0 \\ -3 & 0 & 3 \\ -3 & 2 & 5 \end{vmatrix}\begin{pmatrix} 5 & 1 & 0 \\ 3 & 1 & 2 \\ 0 & 4 & 3 \end{pmatrix}\right]$$

$$= (-2)\cdot\begin{pmatrix} 5 & -1 \\ 3 & -2 \end{pmatrix}\begin{vmatrix} 1 & 2 \\ 4 & 3 \end{vmatrix} - 4\cdot\begin{pmatrix} 2 & -1 \\ 0 & -2 \end{pmatrix}\begin{vmatrix} 3 & 2 \\ 0 & 3 \end{vmatrix} + 0\cdot\begin{pmatrix} 2 & 5 \\ 0 & 3 \end{pmatrix}\begin{vmatrix} 3 & 1 \\ 0 & 4 \end{vmatrix} - (-3)\cdot\begin{pmatrix} 0 & -4 \\ 3 & -2 \end{pmatrix}\begin{vmatrix} 1 & 0 \\ 4 & 3 \end{vmatrix}$$

$$+0\cdot\begin{pmatrix} 3 & -4 \\ 0 & -2 \end{pmatrix}\begin{vmatrix} 5 & 0 \\ 0 & 3 \end{vmatrix} - 3\cdot\begin{pmatrix} 3 & 0 \\ 0 & 3 \end{pmatrix}\begin{vmatrix} 5 & 1 \\ 0 & 4 \end{vmatrix} + (-3)\cdot\begin{pmatrix} 0 & -4 \\ 5 & -1 \end{pmatrix}\begin{vmatrix} 1 & 2 \\ 4 & 3 \end{vmatrix} - 2\cdot\begin{pmatrix} 3 & -4 \\ 2 & -1 \end{pmatrix}\begin{vmatrix} 1 & 0 \\ 3 & 2 \end{vmatrix}$$

$$+5\cdot\begin{pmatrix} 3 & 0 \\ 2 & 5 \end{pmatrix}\begin{vmatrix} 5 & 1 \\ 3 & 1 \end{vmatrix} = 326 \implies \mathbf{det(A) = 326.}$$

After expanding further the minors of the above determinant based on Theorem 1, we see that this result is the same as the result of Example 2.
For $k = 3$, we have:

$$\det(A) = \det\left[\begin{pmatrix} 3 & 0 & -4 \\ 2 & 5 & -1 \\ 0 & 3 & -2 \end{pmatrix}\begin{vmatrix} -2 & 4 & 0 \\ -3 & 0 & 3 \\ -3 & 2 & 5 \end{vmatrix}\begin{pmatrix} 5 & 1 & 0 \\ 3 & 1 & 2 \\ 0 & 4 & 3 \end{pmatrix}\right]$$

$$= 5\cdot\begin{pmatrix} 5 & -1 \\ 3 & -2 \end{pmatrix}\begin{vmatrix} 0 & 3 \\ 2 & 5 \end{vmatrix} - 1\cdot\begin{pmatrix} 2 & -1 \\ 0 & -2 \end{pmatrix}\begin{vmatrix} -3 & 3 \\ -3 & 5 \end{vmatrix} + 0\cdot\begin{pmatrix} 2 & 5 \\ 0 & 3 \end{pmatrix}\begin{vmatrix} -3 & 0 \\ -3 & 2 \end{vmatrix} - 3\cdot\begin{pmatrix} 0 & -4 \\ 3 & -2 \end{pmatrix}\begin{vmatrix} 4 & 0 \\ 2 & 5 \end{vmatrix}$$

$$+1\cdot\begin{pmatrix} 3 & -4 \\ 0 & -2 \end{pmatrix}\begin{vmatrix} -2 & 0 \\ -3 & 5 \end{vmatrix} - 2\cdot\begin{pmatrix} 3 & 0 \\ 0 & 3 \end{pmatrix}\begin{vmatrix} -2 & 4 \\ -3 & 2 \end{vmatrix} + 0\cdot\begin{pmatrix} 0 & -4 \\ 5 & -1 \end{pmatrix}\begin{vmatrix} 0 & 3 \\ 2 & 5 \end{vmatrix} - 4\cdot\begin{pmatrix} 3 & -4 \\ 2 & -1 \end{pmatrix}\begin{vmatrix} 4 & 0 \\ -3 & 3 \end{vmatrix}$$

$$+3\cdot\begin{pmatrix} 3 & 0 \\ 2 & 5 \end{pmatrix}\begin{vmatrix} -2 & 4 \\ -3 & 0 \end{vmatrix} \implies \mathbf{det(A) = 326.}$$

After expanding further the minors of the above determinant based on Theorem 1, we see that this result is the same as the result of Example 2.

From Theorem 1 and Theorem 2, we have true the following Theorem,

Theorem 3 *The Laplace Expansion for Determinant calculation, applies to the cubic-matrix of order 2 and the cubic matrix of order 3.*

Algorithmics Implementation of Determinants for Cubic-Matrix of order 2 and 3

In a paper (Salihu-Zaka 2023b) we have presented the pseudo-code of algorithm based on the permutation expansion method as presented in Definition 1. In the following, we have also presented the pseudo-code of the algorithm based on the Laplace method as presented in Theorem 3.

tw]

P 1: Laplace method for determinants of cubic matrices of order 2 and 3

tw]

Step 1: Determine the order of determinants:

$[m, n, o] = size(A);$

Step 2: Checking if the 3D matrix is cubic:

if $m \sim n; m \sim= o; n \sim= o;$

disp('A is not square, cannot calculate the determinant')

$d = 0;$

return

end

Step 3: Checking if the 3D matrix is higher than the 3rd order:

if $m > 3;$

disp('A is higher than the third order, hence can not be calculated.')

$d = 0;$

return

end

Step 4: Initialize $d = 0;$

Step 5: Handling base case.

if $m == 1$

$d = A;$

return

end

Step 6: Select which plan we shall use to expand the determinant:

Horizontal Layer: x1 = 1 or 2 or 3; or

Vertical Layer: x2 = 1 or 2 or 3; or

Vertical page: x3 = 1 or 2 or 3;

Step 7: Calculate the 3D determinant of orders 2 and 3 based on Laplace methodology:

Create a loop from 1 to 2 or 3 (Depending on the order of the cubic matrix):

Create a loop from 1 to 2 or 3 (Depending on the order of the cubic matrix):

If the horizontal layer is selected:

$d = d + (-1)\hat{}(1 + x1 + i + j) * A(x1, i, j) * det\_3DLaplace(A([1{:}x1 - 1x1 + 1{:}m], [1{:}i - 1i + 1{:}n], [1{:}j - 1j + 1{:}m]));$

end

If the vertical layer is selected:

$d = d + (-1)\hat{}(1 + i + x2 + j) * A(i, x2, j) * det\_3DLaplace(A([1{:}i - 1i + 1{:}m], [1{:}x2 - 1x2 + 1{:}n], [1{:}j - 1j + 1{:}m]));$

end

If the vertical page is selected:

$d = d + (-1)\hat{}(1 + i + j + x3) * A(j, i, x3) * det\_3DLaplace(A([1{:}i - 1i + 1{:}m], [1{:}j - 1j + 1{:}n], [1{:}x3 - 1x3 + 1{:}m]));$

end

end

end

Step 8: Return the result of the 3D determinant.

tw]

Conclusions

In this paper, we have continued our work on determinants of cubic-matrices. We have provided that Laplace method which is used on determinants of square and rectangular matrices similarly can be used also for the calculation of determinants of cubic-matrices of order 2 and order 3. In both cases, we have provided the proof

of expanding cubic-matrix in any element, and similar to the determinant of square and rectangular matrices we have used also cubic-minors by removing the horizontal layer, vertical page and vertical layer of the corresponding element. In addition, we have also provided examples for each case, as well as we have provided a computer algorithm that can be used to calculate determinants of cubic-matrices of orders 2 and 3.

We are currently working on: systems of linear and non-linear equations with 3-dimensional representations, presenting them with 3D matrices, this way, we think, significantly reduces the representations and actions of difficult and complex problems, we are also studying '3D-matrix transformations', etc. The understanding and study of determinants for cubic-matrix, we think opens new paths for future research related to cubic-matrix applications.

We think that the concept of 3D matrices can be applied very well, in complex problems of *Game-Theory*, *Graph-Theory*, *Computer Graphics*, *Imagery*, *different problems from informatics*, *Partial differential equations*, etc. Therefore, we recommend that future research, based on this paper but also on other papers that we have for 3D-matrix, focused on the possible applications of 3D-matrices and the Determinants of cubic-matrices.

Declarations

Funding: No Funding.
Authors' contributions: The contributions of the authors are equal.
Data availability statements: This manuscript does not report data.
Conflict of Interest Statement: There is no conflict of interest with any funder.

Scientific Ethics Declaration

The authors declare that the scientific ethical and legal responsibility of this article published in EPSTEM journal belongs to the authors.

Acknowledgements or Notes

* This article was presented as an oral/poster presentation at the International Conference on Research in Engineering, Technology and Science (www.icrets.net) held in Thaskent/Uzbekistan on August 22-25, 2024.

References

Artin, M. (1991). *Algebra*. Prentice Hall, Upper Saddle River.

Amiri, A., Fathy, M., & Bayat, M. (2010). Generalization of some determinantal identities for non-square matrices based on Radic's definition. *TWMS J. Pure Appl. Math*, *1*(2), 163-175.

Bretscher, O. (2018). *Linear algebra with applications (classic version)* (5th ed.). Upper Saddle River, NJ: Pearson.

Dutta, J. & Pal, S. C. (2011). Generalization of a new technique for finding the determinant of matrices. *Journal of Computer and Mathematical Sciences*, *2*(2), 266-273.

Eves, H. (1990). *An intro to the history of mathematics* (6th ed.). Florence, KY: Brooks/Cole.

Filipi, K., Zaka, O., & Jusufi, A. (2019). The construction of a corp in the set of points in a line of desargues affine plane. *Matematicki Bilten*, *43*(1), 27-46.

Gago, E. A., Brstilo, C. L., & De Brito, N. (2022). Computational simulation: Multidisciplinary teaching of dynamic models from the linear algebra perspective. *WSEAS Transactions on Advances in Engineering Education*, *19*, 182-188.

Grattan-Guinness, I. (2002). *Companion encyclopedia of the history and philosophy of the mathematical sciences*. Routledge.

Koprowski, P. (2022). A note on the paper "A new approach for finding the determinant of matrices" by O. Rezaifar and H. Rezaee. *Applied Mathematics and Computation*, *430*, 127245.

Kuloğlu, B., Eser, E., & Özkan, E. N. G. İ. N. (2023). The r-circulant Matrices Associated with k-Fermat and k-Mersenne Numbers. *WSEAS Transactions on Mathematics*, *22*.

Lang, S. (1987). *Linear algebra*. Springer Science & Business Media.

Lang, S. (2002). *Algebra. graduate texts in mathematics*. New York, NY: Springer.

Lay, D. C. (2003). *Linear algebra and its applications*. Pearson Education India.

Leon, S., & Pillis, L. (2021). *Linear algebra with applications, ebook*, Global Edition (10th ed.). London, England: Pearson Education.

Leon, S. J., De Pillis, L., & De Pillis, L. G. (2006). *Linear algebra with applications* (pp. 447-449). Upper Saddle River, NJ: Pearson Prentice Hall.

Makarewicz, A., Pikuta, P., & Szałkowski, D. (2014). Properties of the determinant of a rectangular matrix. *Annales Universitatis Mariae Curie-Skłodowska, sectio A–Mathematica*, *68*(1).

Meyer, C. D. (2023). *Matrix analysis and applied linear algebra*. Society for Industrial and Applied Mathematics.

Milne-Thomson, L. M. (1941). Determinant expansions. *The Mathematical Gazette*, *25*(265), 130-135.

Muir, T. (1890). The theory of determinants in the historical order of its development. *Proceedings of the Royal Society of Edinburgh*, *16*, 389-448.

Muir, T., & Metzler, W. H. (2003). *A treatise on the theory of determinants*. Courier Corporation.

Neto, A. F. (2015). A note on a determinant identity. *Applied Mathematics and Computation*, *264*, 246-248.

Schneider, H., & Barker, G. P. (1989). *Matrices and linear algebra*. Courier Corporation.

Neto, A. F. (2015). A note on a determinant identity. *Applied Mathematics and Computation*, *264*, 246-248.

Peters, J. F., & Zaka, O. (2023). Dyck fundamental group on arcwise-connected polygon cycles. *Afrika Matematika*, *34*(2), 31.

Poole, D. (2015). *Linear algebra: A modern introduction*. Thomson Brooks/Cole

Price, G. B. (1947). Some identities in the theory of determinants. *The American Mathematical Monthly*, *54*(2), 75-90.

Radić, M. (2005). About a determinant of rectangular 2 × n matrix and its geometric interpretation. *Beitrage Algebra Geom, 46*(2), 321–349.

Radic, M. (1966). A definition of the determinant of a rectangular matrix. *Glasnik Matematicki, 1*(21), 17-22.

Rezaifar, O., & Rezaee, H. (2007). A new approach for finding the determinant of matrices. *Applied Mathematics and Computation, 188*(2), 1445–1454.

Rose, H. E. (2002). *Linear algebra. basel,* Switzerland: Birkhauser Verlag AG.

Salihu, A., & Zaka, O. (2023). *Some 3D-determinant properties for calculating of cubic-matrix of order 2 and order 3.* https://www.preprints.org/manuscript/202307.0729/v1

Salihu, A., & Zaka, O. (2023). The determinant of cubic-matrix of order 2 and order 3: Some basic properties and algorithms. *arXiv preprint arXiv:2306.13336*.

Salihu, A., Snopçe, H., Ajdari, J., & Luma, A. (2022, July). Generalization of Dodgson's condensation method for calculating determinant of rectangular matrices. In *2022 International Conference on Electrical, Computer and Energy Technologies (ICECET)* (pp. 1-6). IEEE.

Salihu, A., Snopce, H., Luma, A., & Ajdari, J. (2023, February). Comparison of time complexity growth for different methods/algorithms for rectangular determinant calculations. In *2023 International Conference on Recent Trends in Electronics and Communication (ICRTEC)* (pp. 1-6). IEEE.

Salihu, A., Snopce, H., Luma, A., & Ajdari, J. (2023). Modıfied chıos-lıke method for rectangular determınant calculatıons. *Advanced Mathematical Models & Applications*, *8*(3).

Salihu, A., Snopçe, H., Ajdari, J., & Luma, A. (2022, December). Implementation on a parallel environment of generalized/modified dodgson's method for rectangular determinants calculation. In *2022 32nd International Conference on Computer Theory and Applications (ICCTA)* (pp. 222-226). IEEE.

Salihu, A., Snopce, H., Luma, A., & Ajdari, J. (2022). Time complexity analysis for cullis/radic and dodgson's generalized/modified method for rectangular determinants calculations. *International Jwenal of Computers and Their Applications*, *29*(4), 245-254.

Salihu, A., Snopce, H., Luma, A., & Ajdari, J. (2022). Optimization of Dodgson's condensation method for rectangular determinant calculations. *Advanced Mathematical Models & Applications, 7*(3), 264-274.

Salihu, A., & Marevci, F. (2021). Chio's-like method for calculating the rectangular (non-square) determinants: Computer algorithm interpretation and comparison. *European Journal of Pure and Applied Mathematics*, *14*(2), 431-450.

Salihu, A., & Salihu, F. (2019). A method to calculate determinants, with computer algorithm interpretation. *International Journal of Scientific & Technology Research, 8*(7), 414-416.

Salihu, A., & Marevci, F. (2019). Determinants order decrease/increase for k orders, interpretation with computer algorithms and comparison. *International Journal of Mathematics & Computer Science, 9*(2), 501-518.

Silvester, J. R. (2000). Determinants of block matrices. *The Mathematical Gazette, 84*(501), 460–467.

Sothanaphan, N. (2017). Determinants of block matrices with noncommuting blocks. *Linear Algebra and its Applications*, *512*, 202-218.

Zaka, O., & Peters, J. F. (2019). Isomorphic-dilations of the skew-fields constructed over parallel lines in the Desargues affine plane. *arXiv preprint arXiv:1904.01469*.

Zaka, O. (2017). 3D matrix ring with a "common" multiplication. *Open Access Library Journal*, *4*(5), 1-11.

Zaka, O., & Peters, J. F. (2024). Dyck free group presentatıon of polygon cycles ın the ratıo of collınear poınts ın the desargues affine plane. *Journal of Mathematical Sciences*, 1-26.

Zaka, Orgest. (2019a). Dilations of line in itself as the automorphism of the skew-field constructed over in the same line in Desargues affine plane. *Applied Mathematical Sciences, 13*(5), 231–237.

Zaka, Orgest, & Filipi, K. (2016). The transform of a line of desargues affine plane in an additive group of its points. . *Int. J. Of Current Research. 8,* 34983-34990

Zaka, O. (2017). A description of collineations-groups of an affine plane. Libertas Mathematica, 37, 81-96.

Zaka, O. (2018). Three vertex and parallelograms in the affine plane: similarity and addition abelian groups of similarly n-vertexes in the Desargues affine plane. *Mathematical modelling and applications*, *3*(1), 9-15.

Zaka, O. (2016). Contribution to reports of some algebraic structures with affine plane geometry and applications. *Polytechnic University of Tirana, Tirana, Albania*.

Zaka, Orgest, & Peters, J. F. (2019b). Ordered line and skew-fields in the Desargues affine plane. *Balkan J. Geom. Appl.*. *26,* 141-156.

Zaka, O., & Mohammed, M. A. (2020). Skew-field of trace-preserving endomorphisms, of translation group in affine plane. *Proyecciones (Antofagasta)*, *39*(4), 835-850.

Zaka, O., & Mohammed, M. A. (2020). The endomorphisms algebra of translations group and associative unitary ring of trace-preserving endomorphisms in affine plane. *Proyecciones (Antofagasta)*, *39*(4), 821-834.

Zaka, Orgest. (2019b). The general linear group of degree n for 3D matrices GL(n;n;p;F). Libertas mathematica, *New Series. Lib. Math, 39,* 13–30.

Author Information

Orgest Zaka
Agricultural University of Tirana
Faculty of Economy and Agribusiness
Department of Mathematics-Informatics
1025 Paisi Vodica Street, Tirana, Albania

Armend Salihu
Universum International College
Department of Computer Science
Str. Hasan Prishtina 1,1, Konjuh, Lipjan, 14000, Kosovo
Contact e-mail: *ar.salihu@gmail.com*

To cite this article:

Zaka, O. & Salihu, A. (2024). Laplace method for calculate the determinant of cubic-matrix of order 2 and order 3. *The Eurasia Proceedings of Science, Technology, Engineering & Mathematics (EPSTEM), 29,* 192-209.

The Eurasia Proceedings of Science, Technology, Engineering & Mathematics (EPSTEM)
ISSN: 2602-3199

The Eurasia Proceedings of Science, Technology, Engineering & Mathematics (EPSTEM), 2024

Volume 29, Pages 210-218

ICRETS 2024: International Conference on Research in Engineering, Technology and Science

Organic Waste Valorization through Composting as Part of a Circular Economy

Ayoub Doughmi
Mohammed V University in Rabat

Essediya Cherkaoui
Mohammed V University in Rabat

Mohamed Khamar
Mohammed V University in Rabat

Abderrahman Nounah
Mohammed V University in Rabat

Abstract: Organic solid waste management is a significant challenge given environmental and sustainability concerns. Organic waste, including food residues, plant materials, agricultural waste, and other biological components, makes up a large portion of human-generated waste. Effective management of this waste is a priority for governments and businesses to reduce its ecological footprint and exploit its potential. Composting organic waste is an essential practice with numerous benefits for agriculture and the environment, turning waste into nutrient-rich compost that improves soil structure and health, reduces waste, decreases greenhouse gas emissions, and promotes sustainable agriculture.Olive pomace, the residue from olive oil extraction, is rich in fibers, residual oil, and polyphenols. When composted with other organic materials, it produces compost that enhances soil structure, water retention, and provides essential nutrients to plants. Household organic waste, such as food scraps and fruit and vegetable peelings, decomposes into compost rich in organic matter and nutrients, improving soil quality and structure. Poultry manure, high in nitrogen, phosphorus, and potassium, stabilizes nutrients and reduces pathogens when composted, producing balanced, nutrient-rich compost that enhances soil fertility and promotes healthy crop growth. Green waste, such as leaves and grass clippings, also benefits from composting, producing compost rich in organic matter that improves soil structure, increases water retention, and supplies essential nutrients to plants.Composting organic waste reduces waste, enriches soils, and supports sustainable agriculture by transforming olive pomace, household waste, poultry manure, and green waste into valuable compost. This practice reduces dependence on chemical fertilizers, contributing to sustainable farming and reducing water pollution caused by nutrient runoff. Organic waste valorization through composting is crucial in the circular economy, turning waste into valuable resources, reducing raw material needs, lowering waste management costs, and promoting sustainability. Studies have demonstrated the effectiveness of composts as soil amendments, reducing waste volume and management costs.

Keywords: Composting, Organic waste valorization, Circular economy, Environmental management, Sustainable agriculture.

Introduction

Organic waste valorization is essential in waste management, converting organic components into useful resources with significant environmental and socio-economic benefits. It reduces pollution, greenhouse gas emissions, and promotes responsible management of organic materials. Besides environmental advantages, it

presents economic potential for public entities and businesses, fostering a sustainable and environmentally friendly future (Doughmi et al., 2022).

Managing organic solid waste, such as food residues, plant materials, and agricultural waste, has become a priority for governments and businesses to reduce ecological footprints while exploiting their potential. Transforming organic waste into useful resources decreases the volume of waste destined for landfills, essential for more sustainable waste management (Ministry of Energy Transition and Sustainable Development. Department of Sustainable Development, 2012). This exploration examines common valorization methods, like composting, and their benefits, including reducing greenhouse gas emissions, improving soil fertility, and creating bio-based raw materials. However, it also highlights challenges such as environmental concerns related to incineration, the need for adequate infrastructure, and public awareness (Doughmi et al., 2022; Doughmi et al., 2024).

Composting transforms organic matter into nutrient-rich soil amendments, improving soil quality and reducing the need for synthetic fertilizers. Compost contains essential nutrients for plants and helps to rebalance soil pH, promoting plant growth. It stimulates soil microbial activity, releasing nutrients and suppressing pathogens, thus improving crop health (Hay et al., 1996). Composting reduces the amount of organic waste in landfills and methane emissions. It decreases dependence on chemical fertilizers, contributing to more sustainable agriculture and reducing water pollution. Enriching soils with organic matter and nutrients, composting supports sustainable agriculture, increased productivity, and environmental preservation, promoting healthier soils and more sustainable land use (Zhang et al., 2013).

Moreover, the application of compost in agronomy contributes to soil conservation by diminishing the reliance on synthetic fertilizers. Organic substrates are increasingly utilized in agriculture not only as fertilizers but also as soil ameliorants. Organic matter constitutes a vital component of soil, influencing its physical, chemical, and biological characteristics (Hassink et al., 1997; Herold et al., 2014). Numerous studies have demonstrated the beneficial impacts of organic amendments, particularly when combined with mineral fertilizers, on cultivated soils (Alvarez et al., 1998; Goyal et al., 1999; Blair et al., 2006; Gong et al., 2009; Butler & Hooper, 2010; Evans et al., 2012; Zhou et al., 2013; Cannavo et al., 2014).

In this context, this research emphasizes the valorization of olive by-products. Compost derived from olive pomace could serve as an effective soil amendment, facilitating an environmentally sustainable recycling of waste materials. This approach may enhance the yield of organic emmer production, maintain soil fertility, and mitigate pollution risks associated with landfill disposal (Diacono & Montemurro, 2019). For this, we made six mixtures of different composition based on olive pomace associated with different percentages of organic household waste. Physicochemical and bacteriological characterization of the different mixtures at the initial state at the beginning of the composting process and once the compost is mature at the end of the composting process.

Method

Sampling

Organic wastes including olive pomace, household organic waste, poultry manure, and green waste were collected and prepared for composting. Olive pomace was sourced from a three phase's extraction system olive oil production facility in Tiflet city, household waste from the wholesale market in the city of Salé, poultry manure from a farm located in Tiflet city, and green waste from the higher school of technology in Salé gardening activities. These materials were mixed in appropriate ratios to balance nutrient composition and achieve an optimal C/N ratio. The mixture was placed in a 30 liters composting barrels and regularly turned for proper aeration (Doughmi et al., 2022; Doughmi et al., 2024).

Table 1. Composts mixtures

Mixtures	Signification
Gr	Olive pomace
D	Organic household waste
F	Poultry manure
V	Green waste

Physicochemical and Biological Characterization

Moisture levels were maintained between 40-60% to activate the microbial activity and it was determined by drying the samples at 105 °C until a constant mass is obtained then at 525 °C for 4 hours to determine the organic matter by ignition loss (Rodier et al., 2009). Temperatures were monitored to ensure they remained within the optimal range of 50-65°C. The compost matured over 4 months, during which the organic material stabilized and nutrient availability increased. Upon maturation, the compost was harvested, sieved, and analyzed for nutrient content, pH, moisture content, and microbial activity.

However, the other macro elements were obtained by calcination in the oven at 500 °C for 2 hours to 3 hours; the obtained ashes were dissolved to determine the other mineral elements (Pinta, 1979). Total nitrogen NTK and ammoniacal nitrogen $NH4^+$, total organic carbon and the macro elements (P_2O_5, K_2O, Na_2O, CaO, MgO and Cl^-) were determined by different methods in the Research Unit on Environment and Natural Resource Conservation at the National Institute of Agronomic Research Rabat laboratory (Doughmi et al., 2022). The concentrations of heavy metals (ETM) are measured by Inductively Coupled Plasma Atomic Emission Spectrometry (ICP-AES) at the CNRST in Rabat (Doughmi et al., 2024). Concerning microbiological analyses (fecal pollution indicators: thermotolerant coliforms and *E. coli*) were determined within the microbiology laboratory at the Higher School of Technology of Salé, and were counted by the 3 tube NPP method (Rodier et al., 2009) (Doughmi et al., 2022).

Phytotoxicity Test

This phytotoxicity test involves germinating fenugreek seeds under specific conditions of temperature (25°C), humidity (70%), and light (0% for germination and 1000% for growth). Fifteen fenugreek seeds were placed on filter paper in petri dishes. The dishes were irrigated every 48 hours with 3 mL of compost solutions (Doughmi et al., 2023).

Measured Parameters

- *Germination Rate* = (number of germinated seeds * 100) / number of tested seeds.
- *Germination Index* = (number of germinated seeds in the sample / number of germinated seeds in the control) x (root lengths of germinated seeds in the sample / root lengths of germinated seeds in the control) x 100.
- *Vigor Index* = (Root length + Shoot length) * Germination rate %.

Statistical Analysis

All the parameters analyzed in this study were processed using SPSS software (Statistical Package for the Social Sciences, version 20). The results are presented as mean ± standard deviation and were analyzed using analysis of variance (ANOVA).

Results and Discussion

Physicochemical and Bacteriological Characterization

The composts generated in this study were deemed suitable for agricultural use, featuring a neutral pH across all blends, an ideal C/N ratio around 20, and an electrical conductivity not surpassing the acceptance threshold for use as a soil amendment (3 mS cm^{-1}). Furthermore, the mixtures exhibited a reduction in pollution indicators. These composts are enriched with nutrients, allowing them to act as fertilizers and soil enhancers for mineral-poor soils. Upon completion of the composting process, an optimal C/N ratio was found in the GD2 blend (18.56), with a maximum Na^+ ion concentration of 0.70% and an ammonium nitrogen content below the limit value (400 mg kg^{-1}) (Doughmi et al., 2022) (Table 3). Additionally, the mixtures demonstrated a reduction in pollution indicators. By the conclusion of the composting process, the GF2 blend recorded the lowest C/N ratio (15.85), along with the highest levels of P_2O_5 (0.2606%) and ammoniacal nitrogen (360.74 mg kg^{-1}) below the limit value (400 mg kg^{-1}) too (Doughmi et al., 2024) (Table 3).

The pH of the compost's aqueous solution began to rise from the thermophilic phase onward. This phase's alkalinization results from ammonia, a base, generated through bacterial hydrolysis of proteins and organic nitrogen. During the maturation phase, the pH stays basic but gradually drops over time, eventually reaching neutrality. This pH stability is due to the slow maturation reactions and the buffering capacity of humus (Fauci et al., 1999).

Initially, the electrical conductivity is high, but it decreases over the composting period, ultimately dropping below the threshold of 3 mS cm^{-1} (Soumaré et al., 2002). Throughout the composting process, the level of extractable ammoniacal nitrogen declines as the compost ages, while the nitrate content increases. This transformation from ammonia nitrogen to nitrate nitrogen happens through the mineralization of complex nitrogen compounds into ammonia and amino acids (Table 3).

Ammonium can either be directly utilized in microbial metabolism or oxidized into nitrates and nitrites by nitrogen-fixing organisms (Aylaj & Lhadi, 2008). The changes in the C/N ratio are directly tied to the biodegradation of organic matter, which leads to both the release of carbon as CO_2 and the apparent concentration of mineral elements (N, P, K, etc.). Furthermore, nitrogen is lost as ammonia during the thermophilic phase, which tends to moderate the reduction in the C/N ratio. Similar results have been documented by other researchers (Hafidi, 1996 and Bousselhaj et al., 1996). The C/N ratio serves as another indicator of compost maturity (Lhadi et al., 2004, 2006; Aylaj, 2002; Tazi, 2001; Ozores-Hampton et al., 1998; Mathur et al., 1993).

The properties of the studied mixtures reveal a high concentration of fecal coliforms at the onset of the composting process, which significantly decreased by the end of the treatment. In particular, the GD3 mixture showed a dramatic reduction from 4.19 10^7 TC g^{-1} to 63.3 TC g^{-1}. A notable decrease rate of 76.34% was observed for the thermotolerant coliforms in the GD3 mixture (Doughmi et al., 2022) (Table 3).

The analysis of heavy metals in these compost samples shows that they meet regulatory standards (NF. U 44-051, 2006). They can be safely utilized as organic soil amendments to enhance agricultural soils and support plant growth without the danger of excessive metal contamination. These findings highlight the effectiveness of the composting process employed to create these organic amendments and their appropriateness for environmentally sustainable agricultural use. Nonetheless, it is advisable to maintain regular monitoring of compost quality to ensure its environmental safety and effectiveness in soil enhancement (Doughmi et al., 2022).

In this research, the findings indicate that trace metal concentrations in the compost samples remain below the recommended thresholds for safe agricultural use. The highest levels of heavy metals were observed in poultry manure compost, with post-composting concentrations of Iron (652.62 mg kg^{-1}), Copper (45.34 mg kg^{-1}), Manganese (509.73 mg kg^{-1}), Zinc (364.46 mg kg^{-1}), and Nickel (3.33 mg kg^{-1}) (Doughmi et al., 2024) (Table 2). Conversely, regarding heavy metals, the peak levels after composting were recorded in green waste compost for Chromium (10.40 mg kg^{-1}) and Lead (2.36 mg kg^{-1}), and in poultry manure compost for Cadmium (0.27 mg kg^{-1}) (Doughmi et al., 2024) (Table 2).

Table 2. ETM limit values

ETM	V (mg kg^{-1})	D (mg kg^{-1})	F (mg kg^{-1})	Gr (mg kg^{-1})	ETM limit values (mg kg^{-1}) (NF. U 44-051, 2006)
Cd	0,025 ±0,06	0,19 ±0,16	0,27 ±0,42	0,08 ±0,03	3
Hg	-	-	-	-	2
Pb	2,35 ±0,50	0,75 ±0,84	1,74 ±1,52	0,1125 ±0,19	180
Fe	561,68 ±453,20	287,57 ±44,58	652,62 ±151,77	545,18 ±261,28	-
As	-	-	-	-	18
Mn	91,45 ±27,78	58,62 ±16,66	509,73 ±72,57	28,85 ±7,39	6
Cu	8,46 ±2,50	8,54 ±1,22	45,34 ±8,43	8,30 ±1,93	300
Cr	10,40 ±5,96	6,51 ±2,51	2,75 ±1,19	2,22 ± 2,42	120
Ni	2,68 ±1,14	2,80 ±2,82	3,33 ±1,80	1 ±1,17	60
Se	-	-	-	-	12
Zn	58,57 ±6,47	25,30 ±7,08	364,46 ±41,22	10,88 ±3,92	600

The presence of harmful microorganisms in composted waste can pose a possible risk of infecting crops where compost has been used. Thus, employing composts in agriculture necessitates not only verification of their agronomic effectiveness but also, and more crucially, confirmation of their environmental and health safety (Houot et al., 2009). The presence of pathogenic microorganisms in composted waste poses a potential risk of contaminating crops grown with compost. Thus, the use of composts in agriculture requires not only validation of their agronomic benefits but also assurance of their environmental and health safety (Houot et al., 2009). Composting is essentially a microbiological process that heavily relies on temperature changes within the windrows. The temperature inside the compost mass dictates the rate of many biological processes and influences the evolution and succession of the microbial community (Mustin, 1987).

Table 3. Physicochemical and bacteriological characterization

	Before composting			After composting		
Composts	Gr	D	F	Gr	D	F
pH	5.05 ± 0.53	6.18 ± 0.33	7.52 ± 0.07	7.90 ± 0.29	7.70 ± 0.33	8.00 ± 0.08
EC mS cm^{-1}	1.77 ± 0.10	0.72 ± 0.04	3.33 ± 0.19	1.74 ± 0.08	1.33 ± 0.13	2.66 ± 0.13
Humidité %	26.52 ± 3.46	91.10 ± 3.16	15.73 ± 0.38	15.22 ± 1.47	26.41 ± 2.70	32.86 ± 1.74
OM %	92.35 ± 2.46	89.87 ± 2.38	94.53 ± 1.06	52.62 ± 2.71	44.18 ± 2.70	56.64 ± 5.01
Ash %	7.65 ± 2.46	10.13 ± 2.38	5.47 ± 1.06	47.38 ± 2.71	55.82 ± 2.70	43.36 ± 5.01
TOC %	53.57 ± 1.43	52.13 ± 1.38	54.83 ± 0.62	30.52 ± 1.57	25.62 ± 1.57	32.85 ± 2.90
NTK %	1.27 ± 0.04	1.57 ± 0.02	2.85 ± 0.18	1.06 ± 0.03	1.31 ± 0.09	2.85 ± 0.02
C/N ratio	42.23 ± 1.40	33.28 ± 0.46	19.30 ± 1.20	28.90 ± 0.81	19.68 ± 1.28	11.57 ± 0.72
PO_4^{3-} %	0.0187 ± 0.0013	0.0655 ± 0.0044	0.3259 ± 0.0099	0.0260	0.0875	0.4518
P_2O_5 %	0.007 ± 0.001	0.014 ± 0.002	0.187 ± 0.009	0.0088	0.0194	0.2725
CaO %	0.22 ± 0.007	0.12 ± 0.005	0.63 ± 0.050	0.38	0.22	0.63
MgO %	0.08 ± 0.005	0.14 ± 0.005	0.23 ± 0.030	0.04	0.08	0.43
K_2O %	0.46 ± 0.001	1.52 ± 0.002	1.45 ± 0.087	0.40	0.95	1.92
Na_2O %	0.05 ± 0.001	0.27 ± 0.002	0.24 ± 0.034	0.19	0.51	1.02
Cl^- %	0.0185 ± 0.001	0.0235 ± 0.001	0.0236 ± 0.0004	0.0242	0.0301	0.0291
SO_4^{2-} %	0.0035 ± 0.0006	0.0042 ± 0.0007	0.0120 ± 0.0085	0.0036	0.0035	0.0085
NO_3^- mg kg^{-1}	57.55 ± 10.37	127.32 ± 27.29	379.01 ± 76.92	151.11 ± 14.44	189.29 ± 15.46	779.57 ± 84.48
NH_4^+ mg kg^{-1}	526.01 ± 41.78	728.29 ± 22.31	1116.29 ± 77.37	259.25 ± 19.84	287.93 ± 41.32	586.32 ± 72.00
Thermotolerant coliforms (Log_{10} g^{-1})	8	8	9.2	5.0	5	6.6
E.coli (Log_{10} g^{-1})	7.2	**8**	8.2	2	2	5

Phytotoxicity Test

The first graph shows the germination rate of fenugreek seeds for each type and mixture of compost (Figure 1). Composts made from green waste (V) at 25% (86.67%), 50% (86.67), and 75% (70%) show the highest germination rates, even surpassing the control (63.33%). Composts from poultry manure (F) (73.33% at 25% dilution) and olive pomace (Gr) (80% at 75% dilution) show relatively high germination rates, although slightly lower than green waste. Organic household waste (D) shows the lowest germination rates, particularly at concentrations of 75% and 100% (Figure 1).

The second graph presents the germination index, which takes into account both the germination rate and root growth (Figure 2). The results show that the mixtures of green waste compost (V) have the highest germination indices (at 25% with 305.63%, 50% with 312.62%, and 75% with 210.23%), suggesting not only successful germination but also vigorous root growth. Composts from olive pomace (Gr) and poultry manure (F) follow with moderately high indices. Compost from organic household waste (D) once again shows inferior performance, indicating possible phytotoxicity or nutrient deficiency for germination and growth (Figure 2).

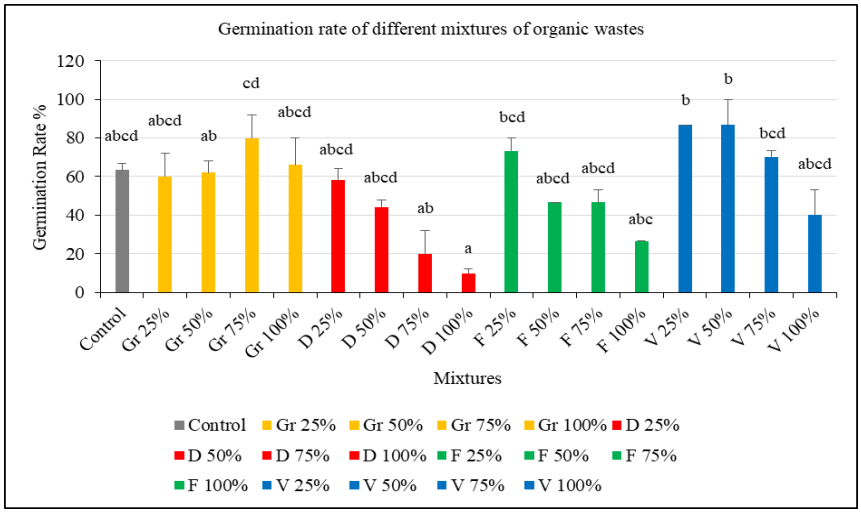

Figure 1. Germination rate of different mixtures of organic wastes

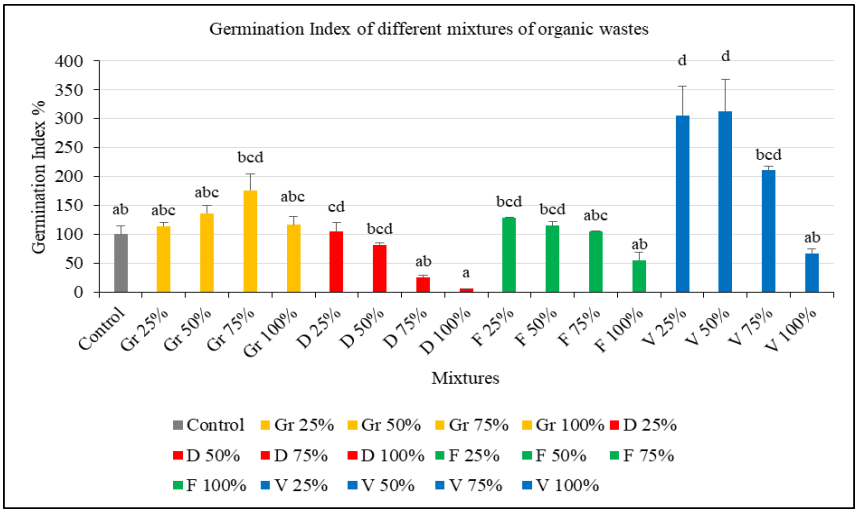

Figure 2. Germination index of different mixtures of organic wastes

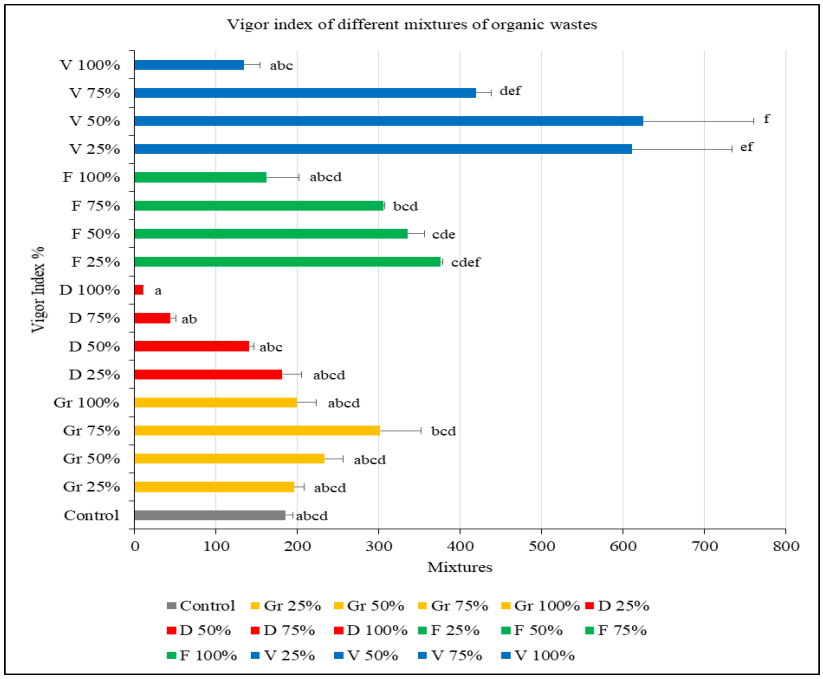

Figure 3. Vigor index of different mixtures of organic wastes

The third graph illustrates the vigor index, a measure that integrates root and stem length as well as the germination rate (Figure 3). Green waste composts (V) dominate once again, particularly at concentrations of 25% (610.58%), and 50% (624.54%), demonstrating robust growth. Composts from poultry manure (F) and olive pomace (Gr) show acceptable vigor indices, but lower than those of green waste. Organic household waste (D) has lower vigor indices, which supports previous results regarding its potential phytotoxicity (Figure 3).

Green waste composts appear to be the most favorable for the germination and growth of fenugreek seeds, indicating their high potential for use as a non-phytotoxic organic amendment. Olive pomace and poultry manure are also effective, although less so than green waste. In contrast, organic household waste composts show signs of phytotoxicity, possibly requiring additional treatment or dilution before application to avoid negative effects on germination and plant growth.

Conclusion

This research focused on the agronomic utilization of various types and sources of organic waste, including olive solid residues (olive pomace from a three-phase continuous extraction system at a milling unit in Tiflet city, Khemisset province, Rabat-Salé-Kénitra region). The olive pomace was mixed in different ratios with other wastes such as organic household refuse, poultry litter, and green waste. These wastes constitute the majority of organic waste in Morocco. The goal of this study was to agronomically utilize these various types of waste through composting. Composting is a biological and ecological breakdown process that reduces waste volume, lowers landfill costs, and converts waste into nutrient-rich bio fertilizers that benefit impoverished soils within a green and circular economy framework.

The composts produced in this investigation were assessed as suitable for agronomic applications, exhibiting a neutral pH across all formulations, an optimal carbon-to-nitrogen (C/N) ratio of approximately 20, and an electrical conductivity that did not exceed the permissible limit for soil amendment usage (3 mS cm^{-1}). Additionally, the mixtures indicated a reduction in pollution metrics. These composts are nutrient-dense, facilitating their role as fertilizers and soil conditioners for mineral-deficient substrates. Upon completion of the composting process, the ammonium nitrogen concentration remained below the threshold value (400 mg kg^{-1}). Furthermore, the mixtures demonstrated a reduction in pollution metrics. In addition, green waste composts are the most effective for germinating and growing fenugreek seeds, making them a valuable non-phytotoxic organic amendment. In contrast, organic household waste composts exhibit phytotoxicity and may require treatment or dilution to avoid negative effects on plant growth.

Recommendations

To valorize organic waste through composting within a circular economy, it is essential to raise awareness among citizens about source separation and establish collection and composting infrastructure. Local authorities should support community and home composting initiatives through grants and training. Promoting the use of compost in agriculture and urban green spaces is crucial, as is the adoption of incentive policies to encourage companies to invest in innovative composting technologies. These measures will transform organic waste into valuable resources, reducing environmental impact and promoting economic and social sustainability.

Scientific Ethics Declaration

The authors declare that the scientific ethical and legal responsibility of this article published in EPSTEM journal belongs to the authors.

Acknowledgements or Notes

* This article was presented as an oral presentation at the International Conference on Research in Engineering, Technology and Science (www.icrets.net) held in Thaskent/Uzbekistan on August 22-25, 2024.

References

Alvarez, C.R., Alvarez, R., Grigera, M.S. & Lavado, R.S. (1998). Associations between organic matter fractions and the active soil microbial biomass. *Soil Biology & Biochemistry, 30*(6), 767–773.

Aylaj, M. (2002). Effect of salinity on sugar beet, agricultural valorization of compost and its effect on improving the tolerance of sugar beet (Beta vulgaris L): Physiological and environmental approach. *Doctoral thesis, Faculty of Sciences, El Jadida, Morocco*. (pp. 146). (In French)

Aylaj, M., & Lhadi, E. K. (2008). Evaluation of the stability and maturity of composts obtained by aerobic biodegradation of a mixture of household waste and chicken waste. *Waste—French Journal of Industrial Ecology*, *50*, 26-32.

Blair, N., Faulkner, R.D., Till, A.R. & Poulton, P.R. (2006). Long-term management impacts on soil C, N and physical fertility: Part I: Broadbalk experiment. *Soil & Tillage Research 91*(1–2), 30–38.

Butler, J. & Hooper, P. (2010). Down to earth: An illustration of life cycle inventory good practice with reference to the production of soil conditioning compost. *Resources Conservation & Recycling 55*(2), 135–147.

Cannavo, P., Vidal-Beaudet, L. & Grosbellet, C. (2014). Prediction of long-term sustainability of constructed urban soil: Impact of high amounts of organic matter on soil physical properties and water transfer. *Soil Use & Management 30*(2), 272–284.

Diacono, M. & Montemurro, F. (2019). Olive pomace compost in organic emmer crop: yield, soil properties, and heavy metals' fate in plant and soil. *Journal of Soil Science and Plant Nutrition 19*(1), 63–70.

Doughmi, A., Benradi, F., Cherkaoui, E., Khamar, M., Nounah, A., & Zouahri, A. (2022). Fertilizing power evaluation of different mixtures of organic household waste and olive pomace. *Agronomy Research*, *20*(S1), 913-937.

Doughmi, A., Elkafz, G., Benradi, F., Cherkaoui, E., Khamar, M., Nounah, A., & Zouahri, A. (2024). Characterization and bioavailability of m etallic trace elements in different organic waste. *Ecological Engineering & Environmental Technology, 25*(3), 133-140.

Doughmi, A., Elkafz, G., Benradi, F., Cherkaoui, E., Khamar, M., Nounah, A., & Zouahri, A. (2023, June). Influence of organic household waste and olive pomace composts on fenugreek seeds germination and growth. In *The scientific conference on Geosciences and Environmental Management (GeoME)* (pp. 3-14). Cham: Springer Nature Switzerland.

Doughmi, A., Elkafz, G., Cherkaoui, E., Khamar, M., Nounah, A., & Zouahri, A. (2024). Evaluation of the compost's maturity of different mixtures of olive pomace and poultry manure. *Ecological Engineering & Environmental Technology (EEET)*, *25*(4).

Evans, C.R.W., Krzic, M., Broersma, K. & Thompson, D.J. (2012). Long-term grazing effects on grassland soil properties in southern British Columbia. *Canadian Journal of Soil Science 92*(4), 685–693.

Fauci, M. F., Bezdicek, D. F., Caldwell, D., & Finch, R. (1999). End product quality and agronomic performance of compost. *Compost Science & Utilization*, *7*(2), 17-29.

Gong, W., Yan, X., Wang, J., Hu, T., & Gong, Y. (2009). Long-term manure and fertilizer effects on soil organic matter fractions and microbes under a wheat–maize cropping system in northern China. *Geoderma*, *149*(3-4), 318-324.

Goyal, S., Chander, K., Mundra, M. C., & Kapoor, K. K. (1999). Influence of inorganic fertilizers and organic amendments on soil organic matter and soil microbial properties under tropical conditions. *Biology and Fertility of Soils*, *29*, 196-200.

Hassink, J., Whitmore, A.P. & Kubat, J. (1997). Size and density fractionation of soil organic matter and the physical capacity of soils to protect organic matter. *European Journal of Agronomy, 7*(1–3), 189–199.

Herold, N., Schoning, I., Michalzik, B., Trumbore, S. & Schrumpf, M. (2014). Controls on soil carbon storage and turnover in German landscapes. *Biogeochemistry, 119*(1), 435–451.

Houot, S., Cambier, P., Deschamps, M., Benoit, P., Bodineau, G., Nicolardot, B., & Lebeau, T. (2009). Compostage et valorisation par l'agriculture des déchets urbains. *Innovations Agronomiques*, *5*, 69-81.

Lhadi, E. K., Tazi, H., Aylaj, M., Genevini, P. L., & Adani, F. (2006). Organic matter evolution during co-composting of the organic fraction of municipal waste and poultry manure. *Bioresource Technology*, *97*(16), 2117-2123.

Lhadi, E. K., Tazi, H., Aylaj, M., Tambone, F., & Adani, F. (2004). Cocomposting separated MSW and poultry manure in Morocco. *Compost Science & Utilization*, *12*(2), 137-144.

Mathur, S. P., Owen, G., Dinel, H., & Schnitzer, M. (1993). Determination of compost biomaturity. I. Literature review. *Biological Agriculture & Horticulture*, *10*(2), 65-85.

Ministry of Energy Transition and Sustainable Development. Department of Sustainable Development. (2012). https://adaptation-undp.org/partners/moroccos-ministry-energy-transition-and-sustainable-development-1

Mustin, M. (1987). Compost, organic matter management. *Waste Management and Research*, *15*, 103-112.

Norm, N. F. U 44-051 (2006) Amendements organiques-Dénominations spécifications et marquage. https://www.boutique.afnor.org/fr-fr/norme/nf-u44051/amendements-organiques-denominations-specifications-et-marquage/fa125064/754

Ozores-Hampton, M. P., Obreza, T. A., & Hochmuth, G. (1998). Composted municipal solid waste use on Florida vegetable crops. *HortTechnology*, *8*, 10-17.

Rodier, J., Bazin, C., Broutin, J. P., Chambon, P., Champsaur, H., & Rodi, L. (2009). *Water analysis*, 9th edit. *Dunod, Paris, France*, *1579*.

Soumaré, M., Demeyer, A., Tack, F. M. G., & Verloo, M. G. (2002). Chemical characteristics of Malian and Belgian solid waste composts. *Bioresource Technology*, *81*(2), 97-101.

Tazi H. (2001). Solid waste: Environmental impact study (soil, groundwater) and treatment by composting. *Doctoral thesis Faculty of Sciences El Jadida, Morocco.* (pp. 224). (In French)

Zhang, L., Sun, X., Tian, Y., & Gong, X. (2013). Effects of brown sugar and calcium superphosphate on the secondary fermentation of green waste. *Bioresource Technology*, *131*, 68-75.

Zhou, Z., Gan, Z., Shangguan, Z. & Zhang, F. (2013). Effects of long-term repeated mineral and organic fertilizer applications on soil organic carbon and total nitrogen in a semi-arid cropland. *European Journal of Agronomy 45*(45), 20–26.

Author Information

Ayoub Doughmi
Civil Engineering and Environmental Laboratory, Water and Environmental Materials Team, Higher School of Technology in Salé, Mohammed V University in Rabat, 11060 Salé, Morocco
Avenue Prince Héritier, Salé 11060, Morocco
Contact e-mail: *ayoub_doughmi@um5.ac.ma*

Essediya Cherkaoui
Civil Engineering and Environmental Laboratory, Water and Environmental Materials Team, Higher School of Technology in Salé, Mohammed V University in Rabat, 11060 Salé, Morocco
Avenue Prince Héritier, Salé 11060, Morocco

Mohamed Khamar
Civil Engineering and Environmental Laboratory, Water and Environmental Materials Team, Higher School of Technology in Salé, Mohammed V University in Rabat, 11060 Salé, Morocco
Avenue Prince Héritier, Salé 11060, Morocco

Abderrahman Nounah
Civil Engineering and Environmental Laboratory, Water and Environmental Materials Team, Higher School of Technology in Salé, Mohammed V University in Rabat, 11060 Salé, Morocco
Avenue Prince Héritier, Salé 11060, Morocco

To cite this article:

Doughmi, A., Cherkaoui, E., Khamar, M. & Nounah, A. (2024). Organic waste valorization through composting as part of a circular economy. *The Eurasia Proceedings of Science, Technology, Engineering & Mathematics (EPSTEM), 29*, 210-218.

The Eurasia Proceedings of Science, Technology, Engineering & Mathematics (EPSTEM)
ISSN: 2602-3199

The Eurasia Proceedings of Science, Technology, Engineering & Mathematics (EPSTEM), 2024

Volume 29, Pages 219-225

ICRETS 2024: International Conference on Research in Engineering, Technology and Science

Intelligent Management of the Pumping System for Irrigation of MBAWAANDE Lands in Podor within the NANN-K Project

Ibrahima Gueye
Université Cheikh Anta Diop

Abdoulaye Kebe
Université Cheikh Anta Diop

Oumar Dia
Université Cheikh Anta Diop

Abdoulahi Sakho
Université Cheikh Anta Diop

Abstract: This article addresses the constraints in exploiting the "MBAWAANDE" lands, particularly the challenges posed by their irrigation system. Currently, the system is powered by a diesel motor pump and a photovoltaic solar system located far apart, leading to inefficiencies and operational difficulties. To mitigate these issues, we propose replacing the motor pump with a generator mounted in parallel with the photovoltaic solar system. This new hybrid configuration, automated by an algorithm, aims to reduce the operational constraints related to distance and minimize diesel consumption, while ensuring continuous and reliable irrigation. The hybrid system integrates the strengths of both power sources, allowing for more flexible and sustainable water pumping. The diesel generator provides backup power during periods of low solar irradiance, ensuring that irrigation needs are met without interruption. Meanwhile, the photovoltaic system takes advantage of renewable energy, reducing dependency on fossil fuels and lowering operational costs. To validate the efficiency and effectiveness of this new configuration, we conducted a simulation using Matlab/Simulink. The results demonstrated that the hybrid system significantly enhances water pumping efficiency with minimal human intervention, ensuring a steady water supply for irrigation. These findings highlight the potential for hybrid systems to improve agricultural practices, especially in remote and resource-constrained areas.

Keywords: Pumping system, Simulink, Photovoltaic solar pumping, Generator, Hybrid configuration

Introduction

The NANN-K project is an ambitious agricultural initiative aimed at exploiting the "MBAWAANDE" lands to ensure food self-sufficiency. The project currently employs two distinct pumping systems: a diesel motor pump and a photovoltaic solar pumping system. However, the distance between these two systems and the operational constraints of using the diesel motor pump present challenges. Therefore, it is imperative to find a more efficient and sustainable pumping solution that eliminates these constraints and ensures continuous irrigation.

Research around the world has explored various pumping systems, assessing their suitability for different regional conditions. Okakwu et al. examined the economic viability of hybrid systems combining photovoltaic (PV), batteries, and diesel generators in Nigeria, highlighting their feasibility (Okakwu, 2023). Dadhich and Shrivastava demonstrated the economic advantages of solar systems over diesel pumps in India (Dadhich, G., & Shrivastava, 2017). Studies by Parajuli et al. in Nepal and Santra et al. in India confirmed the economic benefits of solar pumps for irrigation (Parajuli, 2014; Pande,2016). Alves et al. in Brazil emphasized the long-term

- Selection and peer-review under responsibility of the Organizing Committee of the Conference

profitability of solar pumps despite higher initial costs (Alves,2014), and Shouman et al. highlighted the economic superiority of PV systems in the long run (Shouman, 2016). Ibrahim advocated for the promotion of solar pumps in developing countries, citing their economic, social, and environmental benefits (Ibrahim, 2020).

The novelty of our proposed solution lies in the integration of a generator with a photovoltaic solar system, combined with an automatic switching algorithm to ensure seamless operation. This hybrid system optimizes energy use and minimizes dependency on any single energy source. Unlike previous studies that primarily focused on the economic comparisons of individual systems, our approach emphasizes a practical, real-world application within the context of the NANN-K project. This hybrid configuration addresses the unique challenges of distance and operational constraints encountered in the "MBAWAANDE" lands.

Presentation of the Pumping System Structure

The proposed pumping system combines a generator and an inverter powered by photovoltaic solar panels. When solar energy is available, it is prioritized to power the motor pump through the automatic inverter. When solar energy is insufficient, the generator takes over, ensuring a continuous water supply. This combination offers significant advantages in terms of reliability and energy availability. The schematic diagram below shows the proposed installation, highlighting the placement of the energy management device (automatic inverter) between the generator, the inverter, and the motor pump.

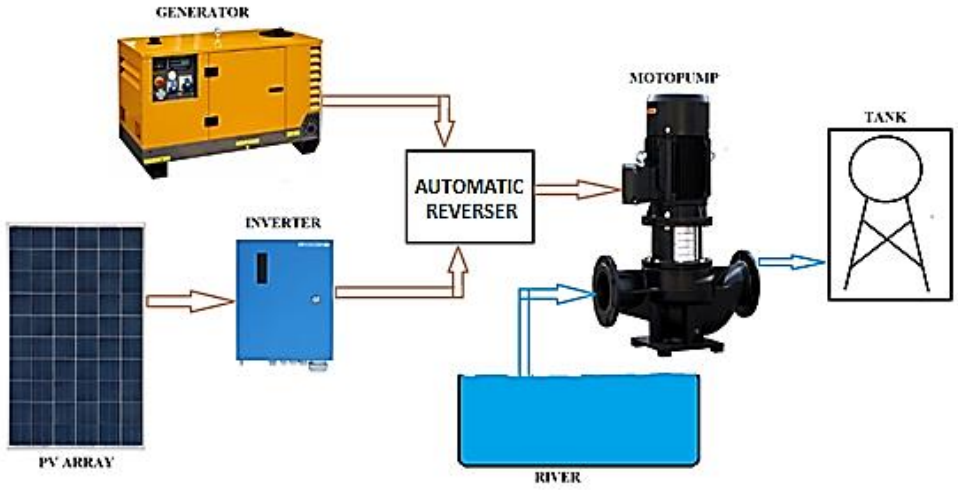

Figure 1. Hybrid pumping system with generator and photovoltaic solar power

This study is based on the exploitation of the "MBAWAANDE" lands in the Podor commune in Senegal. It is related to the NANN-K project and aims for better utilization of these lands by proposing this combination as the best alternative to what is currently on-site.

Modeling of the Essential Components of the System

Modeling of the Boost Converter

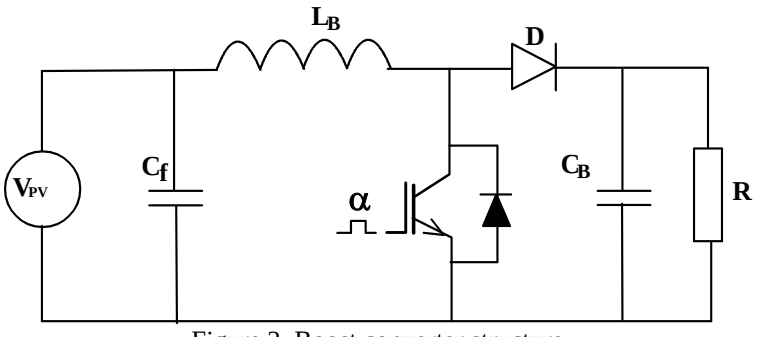

Figure 2. Boost converter structure

A boost converter is used to maintain the voltage within the input range of the inverter with MPPT P&O control. Figure 2 shows the structure of the boost converter, including an ideal IGBT transistor. Similarly, capacitor CB and inductance coil LB are assumed to be perfect.

The voltage transformation ratio of the boost converter is given by (3):

$$M_V = \frac{V_S}{V_{PV}} = \frac{1}{1-D} \quad (1)$$

Where: D is the duty cycle. The values of the inductance L_B and the capacitance C_B are determined in continuous conduction mode according to expressions (2) and (3) as follows:

$$L_B = \frac{(1-D)^2 DR}{2f} \quad (2)$$

$$C_B = \frac{DV_S}{V_r Rf} \quad (3)$$

Where: f is the switching frequency of the transistor, and Vr is the allowable ripple voltage, often estimated at 1% of V_S (Aliane & Zerioul, 2016).

After calculations, the following values are found : L_B = 1.781 mH, Ce = 1000 μF, C_B = 120 μF
In our system, to maintain the power output of the panels at their maximum value under different climatic conditions, a Perturbation and Observation (P&O) MPPT control is used. This control is one of the various techniques used to keep the panels' power at its maximum value. This is achieved by adjusting the duty cycle of the converter. Figure 3 shows the flowchart of the MPPT P&O algorithm.

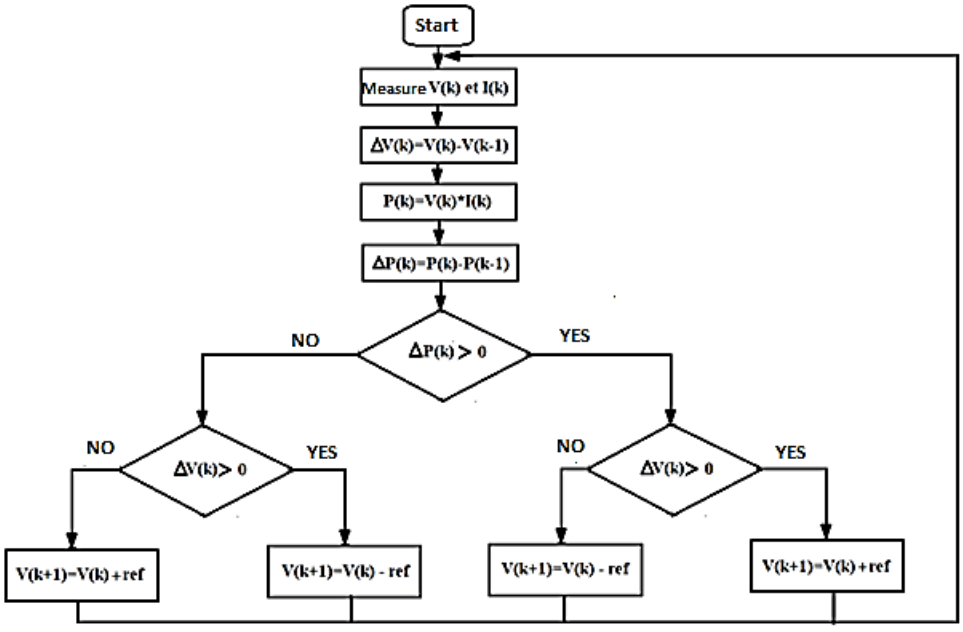

Figure 3. Flowchart of the MPPT P&O algorithm

Automatic Switching Algorithm

This method automates the system by controlling the switching between the photovoltaic solar pumping system and the generator set. This is achieved through an algorithm that allows opening or closing the two circuits. When the irradiation is less than 300 W/m² and the reservoir volume is below its maximum value, the solar circuit is opened and the generator circuit is closed. Conversely, when the irradiation is greater than 300 W/m² and the reservoir volume is below its maximum value, the solar circuit is closed and the generator circuit is opened. However, when the reservoir is full, both circuits are opened. Figure 4 shows the flowchart of the automatic switching algorithm.

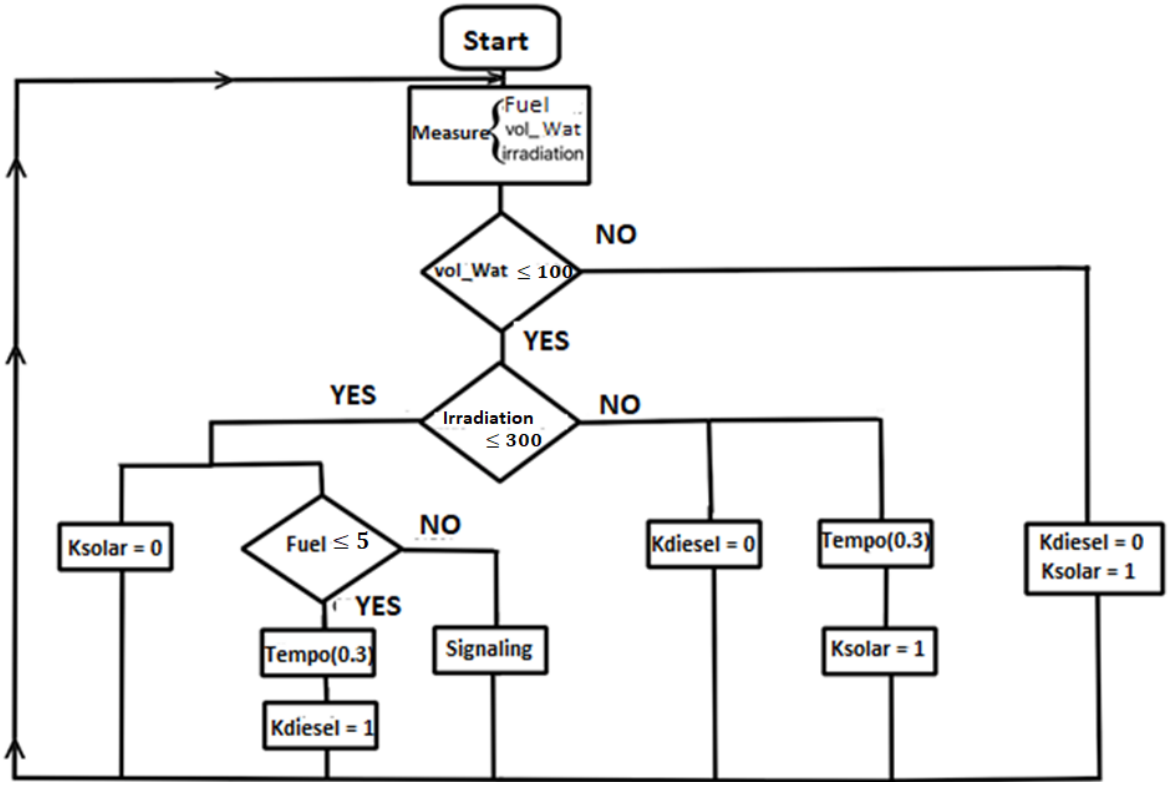

Figure 4. Flowchart of the switch

Results and Discussions

For the simulation in Matlab/Simulink, we used the technical specifications of the equipment installed at the project site. See the tables below. In the context of this simulation in the Simulink environment, the Trinasolar TSM-365DEG14 is used. It's a typical 365W PV module. The module has 72 series of polycrystalline cells connected. The key characteristics are shown in the following table:

Table 1. Characteristics of the solar panel used

Temperature	**T à 25°C**	
Open circuit voltage	V_{OC}	47.1 V
Short circuit current	I_{SC}	9.61 A
Voltage at maximum power	V_{mp}	39.5 V
Current at maximum power	I_{mp}	9.25 A
Maximum power	P_m	365.375 W

An inverter is used to power the asynchronous motor and ensure water pumping across the Senegal River. The input of the inverter corresponds to the voltage provided by the boost converter. In this study, the characteristics of the inverter used are summarized in the following table:

Table 2. The characteristics of the inverter

Input DC	
Umax	850 V DC
Imax	70 A
Output AC	
U	3x380/400/415 V AC 0 à 60 Hz
Pmax	37 kW
Imax	3x65 A

The asynchronous motor converts electrical energy from either the generator or the three-phase inverter into mechanical energy to drive the pump. In this study, the characteristics of the three-phase asynchronous motor used are summarized in the following table.

Table 3. Characteristics of the asynchronous motor of the pump

Designations	Data
Rated power	30 kW
Input voltage	380 V AC
Maximum current	57.6 A
Rotation speed	1470 tr/min
Power factor	0.88
Frequency	50 Hz

The alternator equipped in the generator provides the required power to drive the asynchronous motor of the pump to ensure water pumping. The characteristics of the three-phase alternator used are summarized in the following table.

Table 4. Characteristics of the generator's alternator

Designations	Data
U (Voltage)	400 V
Frequency	50 Hz
Number of phases	3
Delivered current	57.7 A
Active power	32 kW
Apparent power	40 kVA

To validate the hybrid pumping model with automatic switching, a simulation was performed on Matlab/Simulink under temperature conditions of 25°C. The irradiation was initially kept below 300 W/m² to illustrate the operation of the generator set, and then increased above 300 W/m² to simulate solar pumping. Figure 5 shows the structure of the system in Simulink.

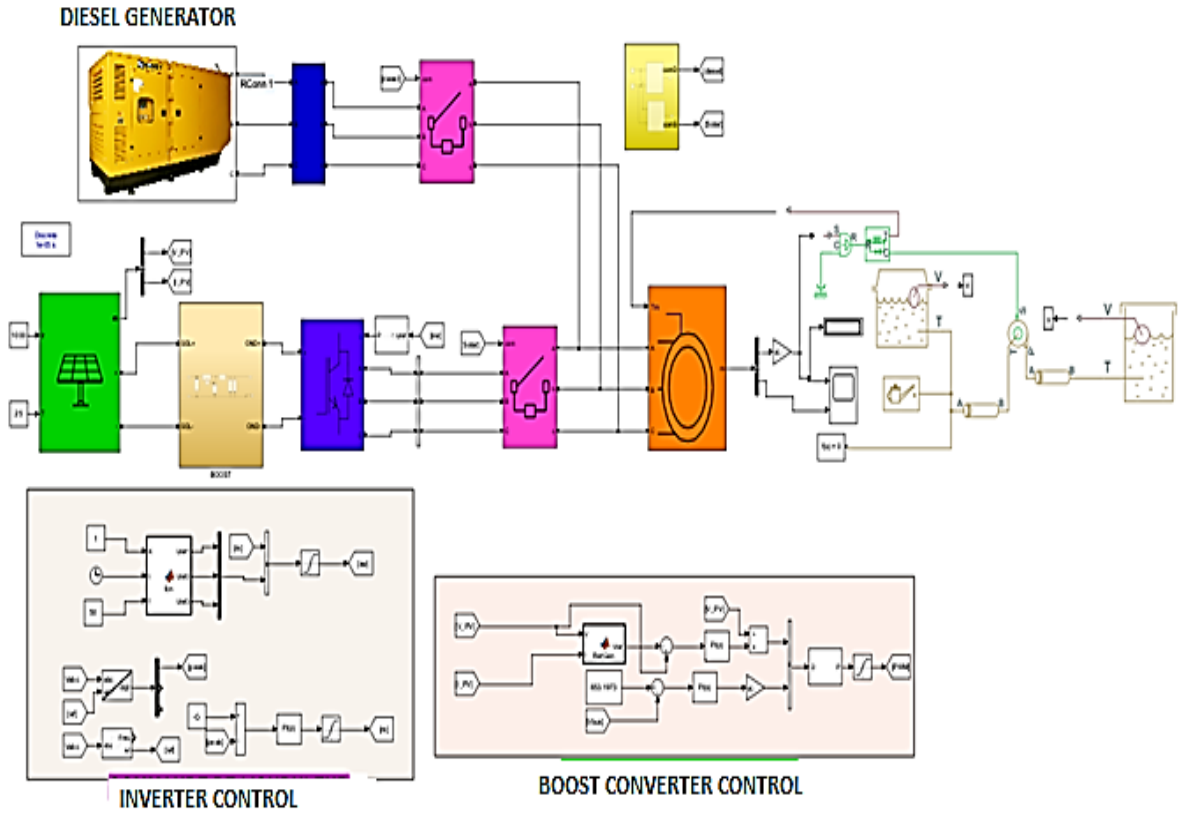

Figure 5. Structure of the solar-generator pumping system in simulink

When irradiation is below 300 W/m² and the reservoir is not full, the automatic inverter switches from solar to generator with a 0.3 s delay, ensuring continuous irrigation. Figure 6 shows the generator-powered water pumping from the river.

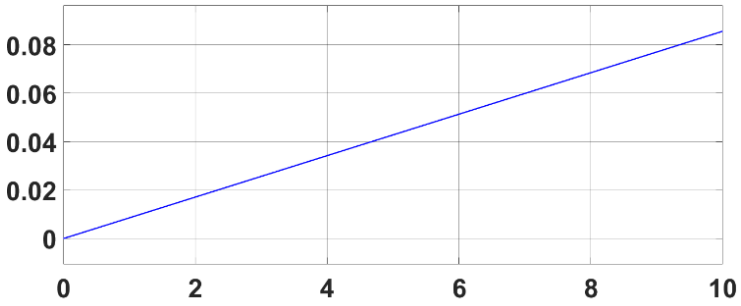

Figure 6. Pumping water from the river by the generator

When powered by the generator, the reservoir fills faster than with solar power for irradiations below 1000 W/m². The automatic inverter effectively manages the switch between systems, ensuring system autonomy and protection. For irradiations above 300 W/m² and when the reservoir is not full, the inverter switches to solar power. Figure 7 shows the solar-powered reservoir filling.

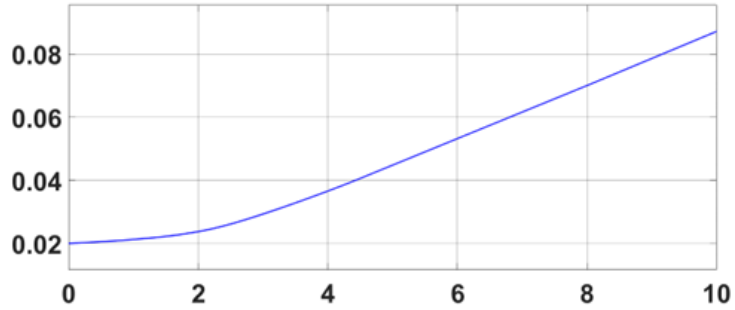

Figure 7. Filling the reservoir with photovoltaic photovoltaic solar power

Figure 8 demonstrates the 0.3s delay during the switch between the generator and the solar system.

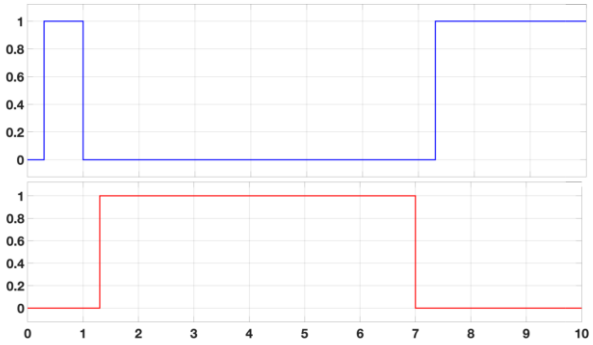

Figure 8. Switching between the generator and the photovoltaic solar system

Conclusion

This article presents a hybrid pumping system combining a photovoltaic solar system and a generator, automated by an algorithm. The Matlab/Simulink simulation demonstrates the system's reliability in ensuring continuous irrigation. Compared to using only a diesel engine pump or a diesel-solar hybrid setup, this solution enhances efficiency and optimizes parallel energy use for additional local applications. This study, part of the NANN-K project in the Podor department, highlights significant economic and operational advantages of our hybrid approach. Furthermore, it emphasizes environmental sustainability by reducing fossil fuel dependency and promoting renewable energy use in agricultural pumping systems. This study underlines the importance of hybrid systems in addressing contemporary challenges in sustainable agriculture and water resource management. To continue this research, integrating energy storage systems to enhance system resilience and conducting field trials to validate the simulation results under real-world conditions would be pertinent. Additionally, a comprehensive economic analysis and environmental impact assessment would provide a better understanding of the long-term benefits of this hybrid configuration.

Scientific Ethics Declaration

The authors declare that the scientific ethical and legal responsibility of this article published in EPSTEM journal belongs to the authors.

Acknowledgements or Notes

* This article was presented as an oral presentation at the International Conference on Research in Engineering, Technology and Science (www.icrets.net) held in Thaskent/Uzbekistan on August 22-25, 2024.

References

Alves, D. G., Pinto, M. F., Damasceno, A. P. A. B., de Fátima Grah, V., & Botrel, T. A. (2014). Cost analysis of water pumping using solar energy and diesel in drip irrigation. *Irriga*, *1*(1), 125-133.

Aliane, C, & Zerioul, A. (2016). *Study of a generator set by numerical simulation (graduation thesis, mouloud mammeri university of Tizi-Ouzou Algeria)*. Master Thesis. Faculty of Electrical Engineering and Computer Science, Département of Electrical Engineering.

Dadhich, G., & Shrivastava, V. (2017, August). Economic comparison of solar PV and diesel water pumping system. In *2017 International Conference on Information, Communication, Instrumentation and Control (ICICIC)* (pp. 1-6). IEEE.

Ibrahim, M. M. (2020*). Performance evaluation and optimal sizing of solar water pumping system compared to convention diesel of remote site in Egypt*. ResearchSquare. https://doi.org/10.21203/rs.3.rs-78887/v1

Okakwu, I. K., Akinyele, D. O., Alayande, A., Olabode, O. E., Ajewole, T. O., Akinyemi, O. O., ... & Oluwasogo, E. S. (2023). Comparative economic viability and sensitivity analyses of a hybrid PV/Battery/Diesel generator for water pumping in Nigeria. *Cankaya University Journal of Science and Engineering*, *20*(2), 76-94.

Parajuli, R., Pokharel, G. R., & Østergaard, P. A. (2014). A comparison of diesel, biodiesel and solar PV-based water pumping systems in the context of rural Nepal. *International Journal of Sustainable Energy*, *33*(3), 536-553.

Pande, P. C., Singh, A. K., & Kumar, P. (2016). Solar PV pumping system for irrigation purpose and its economic comparison with grid-connected electricity and diesel operated pumps. *Indian Journal of Economics and Development*, *4*(4), 1-7.

Shouman, E. R., El Shenawy, E. T., & Badr, M. A. (2016). Economics analysis of diesel and solar water pumping with case study water pumping for irrigation in Egypt. *International Journal of Applied Engineering Research*, *11*(2), 950-954.

Author Information

Ibrahima Gueye
1Laboratoire L3EPI, Ecole Supérieure Polytechnique, Ecole Normale Supérieure d'Enseignement Technique et Professionnel, Université Cheikh Anta Diop, Dakar, Senegal
Contact e-mail: *Ibrahima64.gueye@ucad.edu.sn*

Abdoulaye Kebe
2Laboratoire L3EPI, Ecole Supérieure Polytechnique, Ecole Normale Supérieure d'Enseignement Technique et Professionnel, Université Cheikh Anta Diop, Dakar, Senegal

Oumar Dia
3Ecole Normale Supérieure d'Enseignement Technique et Professionnel,
Université Cheikh Anta Diop, Dakar, Senegal

Abdoulahi Sakho
4Ecole Normale Supérieure d'Enseignement Technique et Professionnel,
Université Cheikh Anta Diop, Dakar, Senegal

To cite this article:

Gueye, I., Kebe, A., Dia, O., & Sakho, A. (2024). Intelligent management of the pumping system for irrigation of MBAWAANDE lands in Podor within the nann-k project. *The Eurasia Proceedings of Science, Technology, Engineering & Mathematics (EPSTEM), 29,* 219-225

The Eurasia Proceedings of Science, Technology, Engineering & Mathematics (EPSTEM)
ISSN: 2602-3199

The Eurasia Proceedings of Science, Technology, Engineering & Mathematics (EPSTEM), 2024

Volume 29, Pages 226-231

ICRETS 2024: International Conference on Research in Engineering, Technology and Science

Fake Accounts and Extended Social Media Use: The Digital Chains of Youth

Mustafa Tevfik Hebebci
Necmettin Erbakan University

Abstract: This study examines students' social media usage patterns and their Technology Addiction Scale (TAS) scores. The research analyzes the relationships between the number of active social media accounts, daily time spent on social media, the use of fake accounts, and technology addiction. The data were evaluated using an independent groups t-test. The findings indicate that students who spend more time on social media have significantly higher technology addiction scores than those who spend less time. Additionally, students who use fake accounts were found to have significantly higher technology addiction scores than those who do not. These findings highlight the significant impact of social media usage duration and the use of fake accounts on technology addiction. Consistent with previous studies, this research supports the notion that increased time spent on social media correlates with higher levels of technology addiction. Furthermore, the findings regarding the influence of fake account usage on technology addiction contribute to the limited body of literature on this topic. The results suggest that young people should manage their social media usage more consciously and avoid using fake accounts to mitigate the risk of technology addiction.

Keywords: Social media, Technology addiction, Digital chains

Introduction

Introduced in a brainstorming event organized by O'Reilly and MediaLive International in 2004, the development of web 2.0 tools has transformed the Internet into more than a communication tool. Web 2.0 is not a structure that can be surfed on the Internet or registered and logged in. It is a concept used to describe more specific resources, websites, and developments (Bartolomé, 2008). Thanks to Web 2.0, one-way communication on the Internet has been replaced with two-way communication with tools such as blogs, wikis, and social media. Thus, users have moved from being just readers to editing and developing roles. Content that used to be developed by developers in Web 1.0 began to be created by users after web 2.0.

Social media (Piotrowski, 2015; Selwyn, 2012), also known as social networking, has deeply affected people's daily and social life with web 2.0. It has also caused many habits of individuals to transform. In this context, social media are internet-based platforms where individuals communicate with each other, create and share their content, and share, like or reshare existing posts (Ellison et al., 2007; Kietzmann et al., 2011). Social media has started to appeal to wider audiences, especially with the development of mobile technologies. One of the most important factors in this sense is the applications developed for mobile devices. Facebook, Twitter, Instagram, and TikTok are some of the social media platforms and applications that are widely used today.

A report published by We Are Social (2022) shows that as of "Digital 2022 Global Overview Report" January 2022, the number of active social media users in the world is 4.62 billion. This number is equal to 58.4% of the total world population. It is seen that the number of active social media users has increased by more than 10% in the last year. The average time of social media use around the world is 2 hours and 27 minutes, corresponding to about 35% of the time spent on the Internet. In terms of monthly time spent on mobile applications, YouTube is used for 23.7 hours, followed by Facebook and TikTok for 19.6 hours, and WhatsApp for 18.6 hours. The report

also indicates that the typical mobile user spends an average of 4 hours and 48 minutes on their phone every day. Considering these data, technology can be said to have a vital place in human life.

In addition to positive effects, such as facilitating human life, technology also brings some negative effects, such as excessive and uncontrolled use. Among these negativities is technology addiction, which is evaluated within the scope of behavioral addictions (Widyanto & Griffiths, 2006). Although technology addiction does not have traumatic symptoms, as in substance addiction, it is known that it negatively affects the mental health of individuals (Karakaya, 2021). In the literature, technology addiction has developed over time into separate forms, such as internet addiction (Young, 1998), digital addiction (Shaw & Black, 2008), social media addiction (Sun & Zhang, 2021), smartphone addiction (Hebebci, 2022), Instagram addiction (Foroughi, 2022), Facebook addiction (Ryan et al., 2008), Twitter addiction (Kircaburun, 2016).

Adolescents and youth are among the groups most prone to technology-related addictions (Yüksel & Yılmaz, 2016). Tsai and Lin (2003) assert that the 12-18 age range is quite critical in terms of internet addiction. Various studies were conducted in the literature covering technology addiction during this period (Anggraeni & Wihardja, 2020; Haug et al., 2015; Jamir et al., 2019). This results from young individuals being more interested in and prone to technology. Arslan (2019) investigated the digital addiction levels of secondary school students in terms of various variables such as gender, class level, and economic status. A similar study was also conducted by Saileela et al. (2020). In Canada, young people's perceptions of smartphone and social media addiction were examined in another research (Adorjan & Ricciardelli, 2021). On the other hand, Jin et al. (2021) investigated the factors correlated with video game addiction.

Various reports around the world suggest that technology use and its components are increasing every year (Ceci, 2022; Dixon, 2022; SRD, 2022). This situation increases the significance of the conscious use of technology even more. Considering that technology use is more common among adolescents and young people (Jasso-Medrano & López-Rosales, 2018), it is anticipated that determining the reasons and consequences of social media use and technology addiction of individuals in this period is expected to contribute to the creation of preventive and intervention programs. It is also essential in terms of being a guide for future studies in this context. In this context, this research aims to determine high school students' social media use and technology addictions. In this direction, the study seeks answers to the following research questions:

1. What is the social media use status of the students?
2. Is there a significant relationship between students' technology addiction scale scores and having a fake account?
3. Is there a significant relationship between students' technology addiction scale scores and the time they spend on social media?

Method

This research was carried out with the screening model, one of the quantitative research methods. The screening model is used to describe the structure of objects, societies, institutions, and the functioning of events (Cohen et al., 2007).

Sample

The sample group of the study consists of 85 high school students of different ages and grades.

Data Collection Tools

The researcher developed the form to collect demographic information such as gender, active social media account, and social media use purpose of the students participating in the research.

TAS is a scale developed by Aydın (2017) to determine the technology addiction levels of students. It consists of four subscales: "Social Network Addiction Scale," "Instant Messaging Addiction Scale," "Online Gaming Addiction Scale," and "Web Site Addiction Scale." Reliability values are 0.786, 0.806, 0.897, and 0.861, respectively.

Data Analysis

The research data were collected by transferring them to the digital environment. SPSS (Statistical Package for the Social Sciences) software was used in the analysis of the obtained data. The data were first examined superficially, and the presence of extreme values was checked. Then, the coefficients of kurtosis and skewness were examined to examine the normal distribution of the data. Parametric tests were used because the kurtosis and skewness coefficients were between -2 and +2 (George & Mallery, 2019). Descriptive values and independent samples t-tests were used in the analysis of the data.

Results

Social Media Use Status of Participants

The social media use status of the participant students was examined in terms of the number of active accounts, the platforms they most frequently used, the time they spent on social media, the purpose of social media use, and the use of fake accounts. In Table 1, the number of active social media accounts used by students based on gender is given.

Table 1. Number of active social media accounts

Account Count	**Female**		**Male**		**Total**	
	f	**%**	**f**	**%**	**f**	**%**
1	14	26.41	12	37.50	26	30.58
2	12	22.64	9	28.12	21	24.70
3	7	13.20	6	18.75	13	15.29
4	10	18.86	3	9.37	13	15.29
5 and more	10	18.86	2	6.25	12	14.11
Total	**53**	**100**	**32**	**100**	**85**	**100**

It is seen that high school students actively use one or two social media accounts. 26.41% of female students have one account, 22.64% have two accounts, and 18.86% have more than five accounts. However, 37.50% of male students have one account.The students were asked how much time they spent on social media platforms daily. The results of this question are shown in Table 2.

Table 2. Distribution of time spent by students on social media platforms by gender

Time	**Female**		**Male**		**Total**	
	f	**%**	**f**	**%**	**f**	**%**
0-2 hours	15	28.30	22	68.75	37	43.52
3-5 hours	38	71.70	10	31.25	48	56.48
Total	**53**	**100**	**32**	**100**	**85**	**100**

Table 2 indicates that students spend a significant part of their days on social media. To this end, it is a notable fact that more than half of the students spend between 3 and 5 hours a day on social media. 70% of females are on social media between 3-5 hours, while the time spent by 68.75% of males on social media is between 0-2 hours.

Examination of TAS Scores by Using Fake Accounts

Table 3 shows the independent groups t-test results applied to determine whether there is a significant difference between students' having fake accounts and their TAS scores.

Table 3. T-test results of TAS scores by using fake account

	N	**$\bar{X}$**	**S**	**df**	**t**	**p**
Using fake account	17	66.76	29.31	83	2.405	0.01
Not using fake account	68	51.96	20.82			

Table 3 suggests there is a significant difference considering the use of fake accounts ($t=(83)=2.405$, $p<.05$).

This finding indicates that the TAS scores of those who use fake accounts ($\bar{X}$=66.76) are significantly higher than those who do not use a fake account ($\bar{X}$=51.96).

Examination of TAS Scores by Time Spent on Social Media

Table 4 shows the independent groups t-test results applied to determine whether there is a significant difference between students' gender, time spent on social media, having fake accounts, and their TAS scores.

Table 4. T-test results of TAS scores by time spent on social media

	N	**$\bar{X}$**	**S**	**df**	**t**	**p**
0-2 hours	37	45.19	20.53	82	-3.464	0.00
3-5 hours	47	61.21	21.43			

Table 4 suggests there is a significant difference considering the time spent on social media (t(82)=-3.464, p<.01). This finding indicates that the TAS scores of who spend more time on social media ($\bar{X}$=61.21) are significantly higher than those who spend less time on social media ($\bar{X}$=45.19).

Discussion and Conclusion

The fact that young people spend more time on social media is one of the determining factors of social media addiction. In this direction, the research findings reveal that spending more than two hours a day on social media increases the technology addiction score. Indeed, excessive use of social media is one of the critical causes of technology addiction (Chou et al., 2005; Savcı et al., 2018). Yüksel and Yılmaz (2016) argue that as the internet use duration increases, the internet addiction level also increases.

There are many studies in the literature that support this result (Aktan, 2018; Demir & Kumcağız, 2019; Sırakaya & Seferoğlu, 2013; Yang & Tung, 2007; Waldo, 2014). It is expected that as the time spent on social media increases, technology addiction also increases. However, this result shows that the time spent on social media exceeds the critical value. The American Academy of Pediatrics (AAP) recommends that children aged 18-24 months not interact with the screen, except for video chat, and adds that children aged 2-5 should get an hour or less of screen time a day. On the other hand, it is advised that adolescents should not spend more than 2 hours a day for entertainment purposes (Tremblay et al., 2011).

Another result of the research is that the technology addiction scores of students with fake accounts are significantly higher than those without fake accounts. The number of studies dealing with the fake account variable in the literature is quite limited. In one of these studies (Köse & Doğan, 2019), it was concluded that the social media addiction of individuals using fake accounts is significantly higher, likewise in this study.

Suggestions

School-age individuals are among the groups most exposed to the negative effects of technology addiction and its types (internet addiction, game addiction, etc.). In order to eliminate the negative effect, preventive and intervening studies should be carried out effectively. In this context, it is of paramount importance to raise awareness and increase consciousness among young people and their families. Alternative activities (sporting, cultural, etc.) should be offered to reduce interaction with technology. Relevant public institutions, especially municipalities, should organize activities in this direction. Apart from this, it is seen that existing studies generally focus on standard variables such as gender, grade level, and duration of use. In this direction, it can be suggested that the studies be designed to cover different variables such as fake accounts, number of followers, and number of accounts in social media.

Scientific Ethics Declaration

The author declares that the scientific ethical and legal responsibility of this article published in EPSTEM journal belongs to the author.

Acknowledgements or Notes

* This article was presented as an oral presentation at the International Conference on Research in Engineering, Technology and Science (www.icrets.net) held in Thaskent/Uzbekistan on August 22-25, 2024.

References

Adorjan, M., & Ricciardelli, R. (2021). Smartphone and social media addiction: Exploring the perceptions and experiences of Canadian teenagers. *Canadian Review of Sociology/Revue Canadienne de Sociologie*, *58*(1), 45-64.

Aktan, E. (2018). Üniversite öğrencilerinin sosyal medya bağımlılık düzeylerinin çeşitli değişkenlere göre incelenmesi [Assessment of social media addiction levels of university students by numerous variables]. *Erciyes İletişim Dergisi*, *5*(4), 405-421.

Aljuboori, A. F., Fashakh, A. M., & Bayat, O. (2020). The impacts of social media on university students in Iraq. *Egyptian Informatics Journal*, *21*(3), 139-144.

Anggraeni, L. D., & Wihardja, H. (2020). Online game, addiction and learning achievement of senior high school students in Jakarta. *IJDS: Indonesian Journal of Disability Studies*, *7*(2), 151-155.

Arslan, A. (2019). Ortaöğretim öğrencilerinin dijital bağımlılık düzeylerinin çeşitli değişkenler açısından incelenmesi: Sivas ili örneği [Determination of the digital addiction levels of students in high school according to various variables: Sivas province sample]. *Gazi Eğitim Bilimleri Dergisi*, *5*(2), 63-80.

Aydın, F. (2017). *Teknoloji bağımlılığının sınıf ortamında yarattığı sorunlara ilişkin öğrenci görüşleri [Student views about relating to the problems in the class environment created by technology addiction]* (Master thesis). Ankara University.

Bartolomé, A. (2008). *Web 2.0 and new learning paradigms*. ELearning papers.

Ceci, L. (2022, October). *Annual number of global mobile app downloads 2016-2021*. Statista. Retrieved from https://www.statista.com/statistics/271644/worldwide-free-and-paid-mobile-app-store-downloads/

Chou, C., Condron, L. & Belland, J. C. (2005). A review of the research on internet addiction. *Educational Psychology Review, 17*(4), 363-388.

Cohen, L., Manion, L., & Morrison, K. (2007). *Research methods in education*. Routledge.

Deniz, L., & Gürültü, E. (2018). High school students' social media addiction. *Kastamonu Eğitim Dergisi*, *26*(2), 355-367.

Dixon, S. (2022, October). *Number of social media users worldwide from 2018 to 2027*. Statista. Retrieved from https://www.statista.com/statistics/278414/number-of-worldwide-social-network-users/

Foroughi, B., Griffiths, M. D., Iranmanesh, M., & Salamzadeh, Y. (2022). Associations between Instagram addiction, academic performance, social anxiety, depression, and life satisfaction among university students. *International Journal of Mental Health and Addiction*, *20*(4), 2221-2242.

George, D., & Mallery, P. (2019). *IBM SPSS statistics 26 step by step: A simple guide and reference*. Routledge.

Goldberg, L. R. (1999). A broad-bandwidth, public domain, personality inventory measuring the lowerlevel facets of several five-factor models. *Personality Psychology in Europe, 7*(1), 7-28.

Haug, S., Castro, R. P., Kwon, M., Filler, A., Kowatsch, T., & Schaub, M. P. (2015). Smartphone use and smartphone addiction among young people in Switzerland. *Journal of Behavioral Addictions*, *4*(4), 299-307.

Hebebci, M. T. (2022). An ınvestigation of smartphone addiction and usage among university students. *MIER Journal of Educational Studies Trends and Practices*, 12(1), 72-88.

Jamir, L., Duggal, M., Nehra, R., Singh, P., & Grover, S. (2019). Epidemiology of technology addiction among school students in rural India. *Asian Journal of Psychiatry, 40*, 30-38.

Jang, K.S., Hwang, S. Y., & Choi, J. Y. (2008). Internet addiction and psychiatric symptoms among Korean adolescents. *Journal of School Health, 78*, 165-171.

Jasso-Medrano, J. L., & López-Rosales, F. (2018). Measuring the relationship between social media use and addictive behavior and depression and suicide ideation among university students. *Computers in Human Behavior*, 87, 183–191.

Jin, Y., Qin, L., Zhang, H., & Zhang, R. (2021, December). Social Factors Associated with Video Game Addiction Among Teenagers: School, Family and Peers. In *2021 4th International Conference on Humanities Education and Social Sciences (ICHESS 2021)* (pp. 763-768). Atlantis Press.

Karakaya, E. N. (2021). *Investigation of technology addiction levels of high school students continuing their education at home during the COVID-19 process*. (Master thesis). Karabuk University.

Kietzmann, J., Hermkens, K., Mccarthy, I., & Silvestre, B. (2011). Social media? Get serious! Understanding the functional building blocks of social media. *Business Horizons, 54*, 241-251.

Kircaburun, K. (2016). Effects of gender and personality differences on Twitter addiction among Turkish undergraduates. *Journal of Education and Practice*, *7*(24), 33-42.

Köse, Ö. B., & Doğan, A. (2019). The relationship between social media addiction and self-esteem among Turkish university students. *Addicta Turk. J. Addict*, *6*, 175-190.

Morahan-Martin, J., & Schumacher, P. (2000). Incidence and correlates of pathological internet use among college students. *Computers in Human Behavior, 16*(1), 13-29.

Pappas, S. (2022, June). What do we really know about kids and screens? *Monitor on Psychology*, *51*(3). https://www.apa.org/monitor/2020/04/cover-kids-screens

Piotrowski, C. (2015). Emerging research on social media use in education: A study of dissertations. *Research in Higher Education Journal*, *27, 1-12*.

Ryan, T., Chester, A., Reece, J., & Xenos, S. (2014). The uses and abuses of Facebook: A review of Facebook addiction. *Journal of Behavioral Addictions*, *3*(3), 133-148.

Saileela, K., Lawrence, A. A., & Kalaivani, S. (2020). Technology usage and technology addiction of higher secondary students. *Journal of Xi'an University of Architecture & Technology*, *12*(4), 2588-2602.

Selwyn, N. (2012). Social media in higher education. *The Europa World of Learning*, *1*(3), 1-10.

Sharov, S., Vorovka, M., Sharova, T., & Zemlianska, A. (2021). The impact of social networks on the development of students' social competence. *International Journal of Engineering Pedagogy (iJEP) 11*(3) 84-98.

Sırakaya, M., & Seferoğlu, S. (2013). Öğretmen adaylarının problemli internet kullanımlarının incelenmesi [Investigation of problematic internet usage of teacher candidates]. *Hacettepe Eğitim Fakültesi Dergisi, 28*(1), 356-368.

Statista Research Department [SRD]. (2022, October). *Global number of internet users 2005-2021*. Statista. Retrieved from https://www.statista.com/statistics/273018/number-of-internet-users-worldwide/

Sun, Y., & Zhang, Y. (2021). A review of theories and models applied in studies of social media addiction and implications for future research. *Addictive Behaviors*, *114*, 106699.

Tremblay, M. S., LeBlanc, A. G., Janssen, I., Kho, M. E., Hicks, A., Murumets, K., ... & Duggan, M. (2011). Canadian sedentary behaviour guidelines for children and youth. *Applied Physiology, Nutrition, and Metabolism*, *36*(1), 59-64.

TUIK [Türkiye İstatistik Kurumu] (2022). *Hanehalkı bilişim teknolojileri (BT) kullanım araştırması, 2022 [Household ınformation technologies (IT) usage survey, 2022]*. Retrieved from https://data.tuik.gov.tr/Bulten/Index?p=Hanehalki-Bilisim-Teknolojileri-(BT)-Kullanim-Arastirmasi-2022-45587

Waldo, A. D. (2014). Correlates of internet addiction among adolescents. *Psychology*, *5*(18), 1999-2008.

We are Social (2022). *Digital 2022: Another year of bumper growth*. https://wearesocial.com/uk/blog/2022/01/digital-2022-another-year-of-bumper-growth-2/

Widyanto, L., & Griffiths, M. (2006). 'Internet addiction': a critical review. *International Journal of Mental Health and Addiction*, *4*(1), 31-51.

Young, K. S. (1998). Internet addiction: The emergence of a new clinical disorder. *Cyberpsychology & Behavior, 1*(3), 237-244.

Yüksel, M., & Yılmaz, E. (2016). Lise öğrencilerinin internet bağımlılık düzeyleri ile problem çözme becerileri arasındaki ilişkinin çeşitli değişkenler açısından incelenmesi [The investigation of the relationship between internet addiction and problem solving skills of high school students in terms of several variables]. *İlköğretim Online*, *15*(3).

Zhang, Y. (2022, April). How psychological factors impact chinese youth Tik Tok addiction. In *2022 International Conference on Social Sciences and Humanities and Arts (SSHA 2022)* (pp. 43-50). Atlantis Press.

Author Information

Mustafa Tevfik Hebebci
Necmettin Erbakan University
Meram, Konya, Türkiye
Contact e-mail: *mhebebci@gmail.com*

To cite this article:

Hebebci, M. T. (2024). Gender differences and technology addiction: The role of social media usage and fake accounts. *The Eurasia Proceedings of Science, Technology, Engineering & Mathematics (EPSTEM), 29,* 226-231.

The Eurasia Proceedings of Science, Technology, Engineering & Mathematics (EPSTEM)
ISSN: 2602-3199

The Eurasia Proceedings of Science, Technology, Engineering & Mathematics (EPSTEM), 2024

Volume 29, Pages 232-244

ICRETS 2024: International Conference on Research in Engineering, Technology and Science

Optimizing Cooling System Design: A Case Study for Innovation Building

Lida Ebrahimi-Vafaei
Near East University

Farzad Zaare-Tajabadi
Near East University

Abstract: This paper presents the design and optimization of a cooling system tailored for innovation building, focusing on maximizing energy efficiency while ensuring optimal thermal comfort for occupants. The proposed cooling system integrates several key components, including chillers, air handling units, distribution systems, and control mechanisms. The system utilizes a combination of centralized and decentralized cooling strategies to efficiently manage thermal loads across different zones within the building. Additionally, advanced control algorithms are employed to dynamically adjust cooling operations based on real-time data, occupant preferences, and external environmental conditions. The optimization process involves comprehensive simulation studies and performance evaluations using building energy modeling software and an Hourly Analysis Program (HAP). Various design parameters such as equipment sizing, layout configurations, air distribution patterns, and control strategies are iteratively refined to achieve the desired balance between energy efficiency, cost-effectiveness, and occupant comfort. The design and optimization of a cooling system for an Innovation building represents a critical step toward achieving sustainable and energy-efficient building operations. By leveraging advanced technologies and innovative design approaches, this cooling system offers a viable solution for addressing the cooling needs of Innovation buildings while mitigating the environmental impact associated with traditional HVAC systems. The proposed design was applied in a case study of an innovation building during the cooling seasons and the results of the optimization demonstrate significant improvements in energy consumption, with substantial reductions in both electricity demand and greenhouse gas emissions compared to conventional cooling systems. Furthermore, the proposed cooling system maintains consistent thermal conditions throughout the building, ensuring a comfortable indoor environment for occupants while minimizing the risk of thermal discomfort and overheating.

Keywords: Energy efficiency, Energy engineering, Cooling system, HVAC systems

Introduction

Studying heat load via the HAP program (Hourly Analysis Program) and air conditioning absorption cycle using chilled water (6°m -12°m) for the Innovation building at Near East University in Nicosia, an area of 2555.7 m^2, which consists of three floors including lecture halls, laboratories, teacher's offices, and Cafe. The building is located in Nicosia with a 35.2 Deg, longitude of 33.3 degrees and elevation of 224m. The summer design dry bulb is 37.2 ℃, the summer coincident wet bulb is 20.6℃ and the summer daily range is 14.4K.

Absorption systems utilize heat energy to generate refrigeration or heating, and sometimes to increase the temperature of waste heat. Aqueous lithium bromide (LiBr) is commonly used to absorb refrigerant and water vapor, resulting in a higher performance coefficient. The modern absorption systems have been categorized as follows: absorption chillers, which use heat energy for refrigeration; absorption chiller heaters, which provide both cooling and heating; absorption heat pumps, which extract heat energy from the evaporator through the absorber, and add it to the heat input in the generator, and release it as hot water in the condenser for heating;

and absorption heat transformers, which elevate the temperature of waste heat to a level higher than any other input fluid stream supplied to the absorption heat transformer (Alefeld & Ziegler, 1985). Absorption chillers have heat exchangers to conserve heat energy input and increase heat transfer efficiency (Gommed & Grossman, 1990). This ensures the transformer is always in the best possible condition for maximum energy efficiency. The level difference also helps to prevent overheating and other potential issues. The heat input for absorption chillers can be derived from other sources than direct-fired burners, such as industrial waste heat or exhaust heat from steam turbines or engines (Grossman, 1982).

Background

In the 1950s and 1960s, central refrigeration plants commonly used centrifugal chillers powered by electric motors and absorption chillers that used steam for summer cooling. Steam was a popular choice because many central plants, which utilized steam for winter heating, had an excess supply during the summer, and energy costs were not a significant concern at that time. However, following the 1973 energy crisis, the natural gas and oil prices needed to fuel steam boilers rose dramatically. The coefficient of performance (COP) in the early model of single-stage, indirect-fired steam absorption chillers was only between the interval of 0.6 to 0.7, making them less energy-efficient and unable to compete with electric centrifugal chillers. Consequently, many absorption chillers were replaced by centrifugal chillers during the late 1970s and 1980s. Moreover, in recent years, absorption chillers have seen a resurgence in popularity due to increased energy efficiency and cost savings. Many modern absorption chillers are now able to achieve COPs of 0.8 or higher, making them competitive with electric centrifugal chillers.

Due to the high costs of building new power plants, electric utility companies began imposing high demand charges and increasing cost-per-unit charges during peak usage periods. Recently, double-effect, direct-fired absorption chillers have been developed in Japan and the United States, achieving a COP of around 1. These chillers are more efficient and have lower operating costs than traditional chillers, making them an attractive option for many businesses. They can also be used to generate electricity during peak usage periods, reducing energy costs even further.

Cost Analysis

A cost analysis is frequently necessary. In the cost analysis, (Aumann,1996) recommended including not only the chiller itself but also the energy and original costs of auxiliaries, such as condenser pumps, cooling towers, and tower fans, given the higher heat rejection in absorption chillers. Auxiliary energy costs can rise to 30% up for absorption chillers compared to ones that use electric power (Aumann, 1996). Additionally, absorption chillers require regular maintenance to ensure that the chiller is performing optimally. This maintenance requires additional labor and materials, which can further increase the overall cost. The absorption chiller has an annual energy cost saving of $20,375 and a simple payback period of about 6 years (ASHRAE,1998). This highlights the importance of considering the total cost of an absorption chiller when analyzing its efficiency. It is also important to consider environmental factors, such as emissions when considering the total cost of an absorption chiller.

Method

Hourly Analysis Program (HAP)

HAP is intended for consulting engineers, design/build contractors, HVAC contractors, facility engineers, and other professionals engaged in designing and analyzing commercial building HVAC systems. The program serves as a robust tool for system design and component sizing. HAP provides users with a comprehensive suite of powerful tools that help them quickly and efficiently model and optimize HVAC systems. It allows users to quickly and accurately analyze system performance and calculate energy consumption. HAP is also compliant with the latest industry standards and regulations.

Carrier's Hourly Analysis Program integrates two powerful tools into a single package: versatile features for designing HVAC systems in commercial buildings and advanced energy analysis capabilities for comparing the

energy consumption and operating costs of different design alternatives. The program helps users identify the most cost-effective system design solution, considering both upfront and operational costs. It allows users to optimize system performance and minimize energy consumption. They are integrating both tools in one package results in significant time savings, as the input data and results from system design calculations can be directly utilized in energy studies. The program helps designers create energy-efficient systems while optimizing system performance. It also helps to identify potential saving opportunities and develop strategies that optimize the energy efficiency of a building.

A. Tools of the Program:

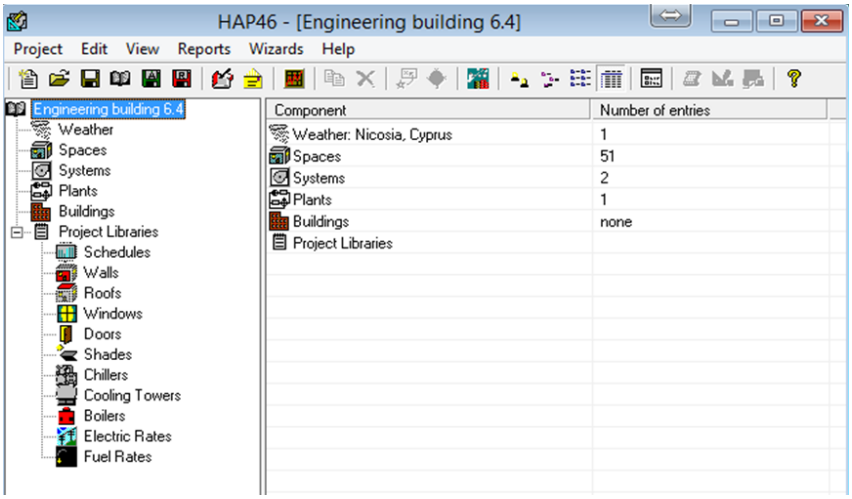

Figure 1. User layout of tools for HAP

B. Weaher:

"Weather Data" encompasses the temperature, humidity, and solar radiation conditions that affect the building and its HVAC equipment. In HAP, this term also includes information about the building's geographical location, local time characteristics, and soil properties. Weather data significantly impacts building loads and equipment operation, making it crucial for load calculations and system performance assessments. Weather data can also be used to assess the energy efficiency of buildings and HVAC systems. İt can also be used to forecast the future performance of a building or system. Finally, weather data can be used to optimize building operations.

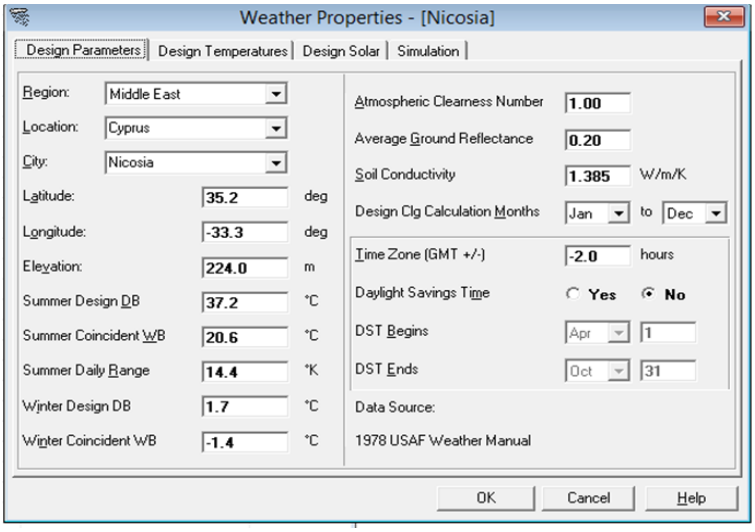

Figure 2. Weather tools layout of the HAP

Calculation

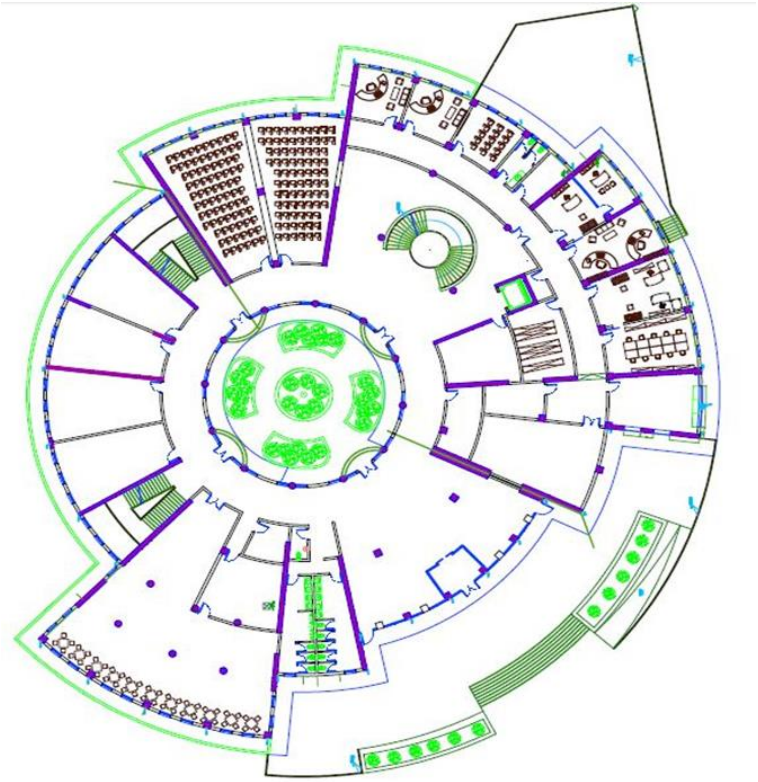

Figure 3. Schematic layout of the innovation building

A. Building load

The building loan entails the data essential for the calculations, the weather inputs, the walls, windows, and roof are all essential load pointers for the calculation required in the design.

Weather Inputs

In the beginning, we selected weather properties of the design area by choosing Region, Location, and City

Table 1. Design parameter of weather inputs

City Name	Nicosia
Location	Cyprus
Latitude	35.2°C
Longitude	-33.3°C
Elevation	224m
Summer design dry-bulb	37.2°C
Summer daily wet bulb	20.6°C
Summer daily range	14.4K
Winter design dry-bulb	1.7°C
Winter design wet bulb	-1.4°C
Atmospheric clearness number	1.00
Average ground reflectance	0.2
Soil conductivity	1.385 W/(m-°K)
Local time zone (GMT +/- N hours)	-2 hours
Consider daylight savings time	No
Simulation weather data	N/A
Current data	1978 USAF Weather Manual
Design Cooling Months	January to December

B. Project Properties

Wall Input

Table 2. Property details of the external wall

Month	**N**	**NNE**	**NE**	**ENE**	**E**	**ESE**	**SE**	**SSE**	**S**
January	68.8	68.8	68.8	307.1	529.0	687.9	784.1	801.0	785.9
February	81.6	81.6	197.7	429.1	640.5	750.1	788.9	754.2	718.4
March	95.8	95.8	345.8	556.3	691.6	762.8	720.1	641.5	591.2
April	109.9	240.4	453.0	629.0	709.4	692.8	610.0	480.6	412.2
May	119.4	340.4	517.3	655.5	696.6	632.7	514.7	354.4	278.9
June	153.3	373.5	542.0	660.4	681.1	600.0	469.1	300.2	229.2
July	121.9	333.6	520.3	647.7	679.1	620.0	499.6	341.0	268.5
August	115.0	232.4	447.1	608.8	679.4	672.2	586.3	462.0	397.1
September	99.7	99.7	315.5	530.4	658.7	724.4	696.2	620.7	578.9
October	84.9	84.9	182.8	426.2	594.4	730.1	753.0	726.4	704.4
November	70.5	70.5	79.0	278.2	522.8	682.5	769.3	783.7	780.6
December	63.5	63.5	63.5	245.4	480.6	647.5	766.7	801.6	799.9
Month	**SSW**	**SW**	**WSW**	**W**	**WNW**	**NW**	**NNW**	**HOR**	**Mult**
January	800.7	782.6	691.4	524.8	309.7	68.8	68.8	496.6	1.00
February	753.9	788.5	751.9	640.0	426.3	199.0	81.6	632.1	1.00
March	644.6	726.1	762.2	701.5	542.4	347.7	95.8	754.9	1.00
April	483.2	608.2	701.7	705.4	617.2	465.4	231.1	830.8	1.00
May	354.7	509.3	641.8	686.9	653.6	534.9	331.6	859.4	1.00
June	300.2	461.8	609.4	668.2	661.2	554.8	363.2	860.4	1.00
July	341.8	493.9	625.8	668.6	646.2	527.0	324.4	846.0	1.00
August	465.9	586.2	676.5	680.2	596.9	452.4	229.5	813.5	1.00
September	625.4	701.4	713.2	670.9	525.7	307.6	99.7	734.4	1.00
October	727.2	754.4	729.5	592.6	427.1	180.8	84.9	627.7	1.00
November	780.1	765.5	686.0	518.0	292.7	76.8	70.5	500.5	1.00
December	795.5	756.9	661.6	472.1	249.1	63.5	63.5	441.8	1.00

Wall Details

Outside Surface Color: Light
Absorptivity: 0.450
Overall U-Value: 1.958W/(m²-°K)

Table 3. Wall layer details (inside to outside)

Layers	**Thickness mm**	**Density kg/m³**	**Specific Ht. kJ / (kg - °K)**	**R-Value (m²-°K)/W**	**Weight kg/m²**
Inside surface resistance	0.000	0.0	0.00	0.12064	0.0
20 mm plaster	19.990	1858.1	0.84	0.02599	37.1
203mm common brick	203.200	1922.2	0.84	0.27954	390.6
20 mm plaster	20.000	1858.1	0.84	0.02599	37.2
Outside surface resistance	0.000	0.0	0.00	0.05864	0.0
Totals	**243.190**	**-**	**-**	**0.51079**	**464.9**

Roof Input

Outside Surface Color: Dark
Absorptivity: 0.900
Overall U-Value: 0.601W/(m²-°K)

Table 4. Roof layer details (inside to outside)

Layers	**Thickness mm**	**Density kg/m³**	**Specific Ht. kJ / (kg - °K)**	**R-Value (m²-°K)/W**	**Weight kg/m²**
Inside surface resistance	0.000	0.0	0.00	0.12064	0.0
200 concretes	250.000	2242.6	0.84	0.11579	448.5
Leveling concrete 70mm	70.000	400.0	0.84	0.12000	28.0
RSI-1.2 board insulation	25.400	32.0	0.92	1.22299	0.8
Asphalt roll	1.588	1121.3	1.51	0.02698	1.8
Outside surface resistance	0.000	0.0	0.00	0.05864	0.0
Totals	**346.988**	**-**	**-**	**1.66503**	**479.1**

Windows Input

Glass window
Window Details
Detailed Input: Yes
Height: 2.40m
Width: 1.00m
Frame Type: Aluminum without thermal breaks
Internal Shade Type: Roller Shades - Light - Translucent
Overall U-Value: 3.353W/(m²-°K)
Overall, Shade Coefficient: 0.334

Table 5. Glass details (gap type 13mm air space)

Glazing	**Glass Type**	**Transmissivity**	**Reflectivity**	**Absorptivity**
Outer Glazing	6mm blue-green reflective	0.282	0.295	0.423
Glazing #2	6mm clear	0.792	0.079	0.129
Glazing #3	not used	1.000	0.000	0.000

Air System Input

1. General Details

Air System Name: Default System
Equipment Type: Chilled Water AHU
Air System Type: Single Zone CAV
Number of zones: 1

2. System Components

Ventilation Air Data

Airflow Control: Constant Ventilation Airflow
Ventilation Sizing Method: Sum of Space OA Airflows
Unocc. Damper Position: Closed
Damper Leak Rate: 0%
Outdoor Air CO2 Level: 400ppm

3. Dehumidification Data

Maximum RH Setpoint: 50%
Heating Source: Hot Water

4. Central Cooling Data

Supply Air Temperature: 14.4°C

Coil Bypass Factor: 0.100
Cooling Source: Chilled Water
Schedule: JFMAMJJASOND
Capacity Control: Cycled or Staged Capacity - Fan On

5. Supply Fan Data

Fan Type : Forward Curved
Configuration: Draw-thru
Fan Performance: 0Pa
Overall Efficiency: 54%

6. Duct System Data

Supply Duct Data

Duct Heat Gain: 0%
Duct Leakage: 0%

7. Return Duct or Plenum Data

Return Air via *Ducted Return*

8. Thermostats and Zone Data

Zone: All
Cooling T-stat: Occ: 23.0°C
Cooling T-stat: Unocc:. 25.0°C
Heating T-stat: Occ: 21.1°C
Heating T-stat: Unocc:. 18.3°C
T-stat Throttling Range: 0.83°K
Diversity Factor: 100%
Direct Exhaust Airflow: 0.0L/s
Direct Exhaust Fan kW: 0.0kW
Thermostat Schedule: fan
Unoccupied Cooling is: Available

9. Supply Terminals Data

Zone: All
Terminal Type: Diffuser
Minimum Airflow: 0.00L/s/person

10. Zone Heating Units

Zone: All
Zone Heating Unit Type: None
Zone Unit Heat Source: Hot Water
Zone Heating Unit Schedule: JFMAMJJASOND

Systems Design Report

Air System Information

Air System Name: Default System
Equipment Class: CW AHU
Air System Type: SZCAV
Number of zones: 1
Floor Area: 2545.5 m²
Location Nicosia: Cyprus

Sizing Calculation Information

Zone and Space Sizing Method

Zone L/s Sum *of space airflow rates*	Calculation Months: Jan to Dec
Space L/s Individual *peak space loads*	Sizing Data: Calculate

Central Cooling Coil Sizing Data

Total coil load:	554.1kW	Load occurs at	Aug 1500	
Sensible coil load:	469.8kW	OA DB / WB:	37.2 / 20.6°C	
Coil L/s at Aug 1500:	26424L/s	Entering DB / WB:	27.1 / 17.8°C	
Max block L/s:	26424L/s	Leaving DB / WB:	11.9 / 11.1°C	
The sum of peak zone L/s:	26424L/s	Coil ADP:	10.3°C	
Sensible heat ratio:	0.848	Bypass Factor:	0.100	
m²/kW:	4.6	Resulting RH:	50%	
W/m² :	217.7	Design supply temp.	14.4°C	
Water flow @ 6.0 °K rise:	22.10L/s	Zone T-stat Check	1 of 1	OK
		Max zone temperature deviation:	0.0°K	

Central Heating Coil Sizing Data

Max coil load:	214.3Kw	Load occurs at	Dec 0800
Coil L/s at Dec 0800:	26424L/s	W/m²:	84.2
Max coil L/s :	26424L/s	Ent. DB / Lvg DB:	11.5 / 18.4°K
Water flow @ 11.1 °K drop:	4.62L/s		

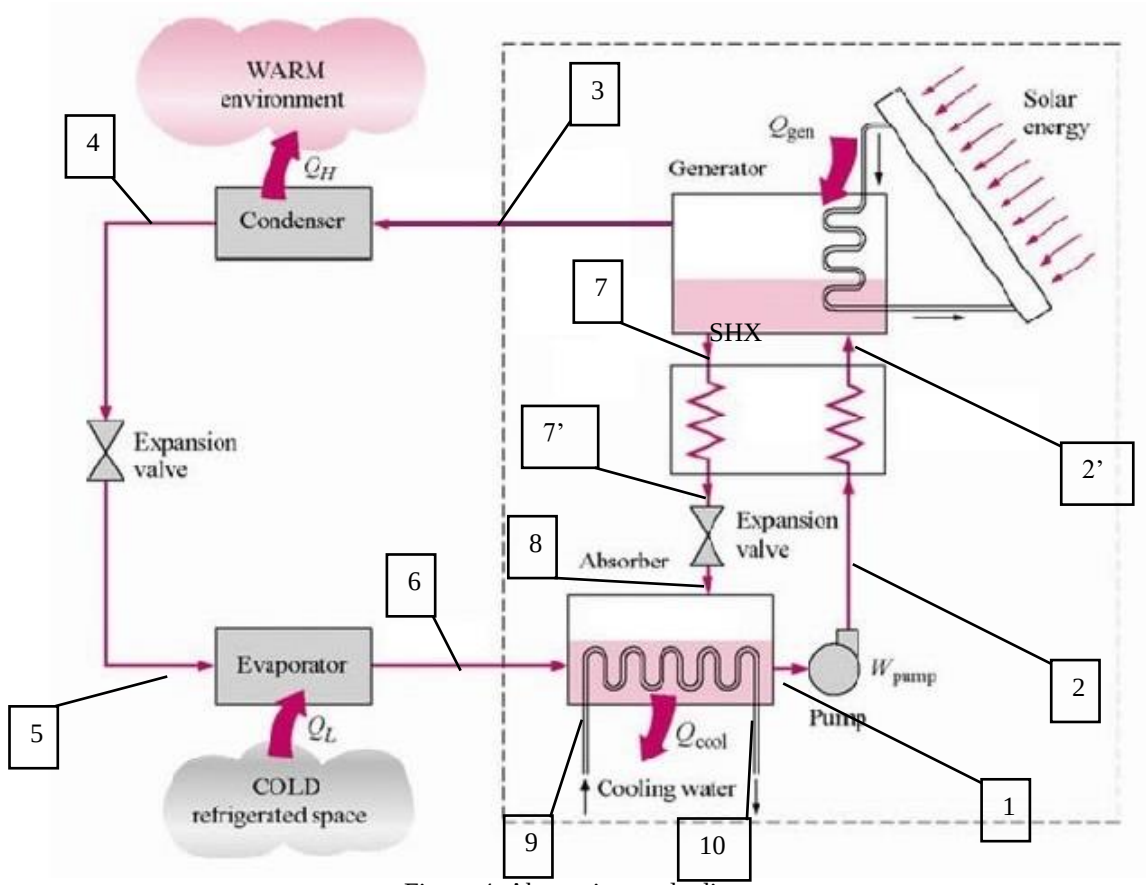

Figure 4. Absorption cycle diagram

Supply Fan Sizing Data

Actual max L/s: 26424L/s
Standard L/s: 25730L/s
Actual max L/(s-m²): 10.38L/(s-m²)

Outdoor Ventilation Air Data

Design airflow L/s: 6568L/s
L/(s-m²): 2.58L/(s-m²)

Evaporator Load of Absorption Cycle

Load [Kw]: 555
Chilled Water Flow: (6°C - 12°C) [L/s] 22.1

Absorption Cycle Calculations

$\dot{m}$=22.134 kg/sec

1. at $T_e = 5\ ℃ \rightarrow P_e = 0.9432\ [kpa]$ low pressure

2- at $T_c = 30\ ℃ \rightarrow P_c = 4.246\ [kpa]$ high pressure

From chart:

3- $P_7 = 4.246[kpa], T_7 = 85\ ℃ \rightarrow x_7 = 65\%\ rich\ solution\ consentrate$

4- $P_1 = 0.9432[kpa], T_1 = 30\ ℃ \rightarrow x_1 = 51.5\%\ poor\ solution\ consentrate$

5- Find enthalpy for outlet point of consider # 4

$T_4 = T_c = 30\ ℃ , \rightarrow x_4 = 0 \rightarrow$ h chart $h_4 = 129\ \frac{kJ}{kg}$

6- Find enthalpy for the outlet point of the evaporator # 6

$T_6 = 6\ ℃ , \rightarrow h_6 = 2487.6\ \frac{kJ}{kg}$

7- calculate the mass flow rate of the refrigerant:

- $Q_t = \dot{m}.(h_6 - h_5) \rightarrow \dot{m}_3 = \frac{\dot{Q}}{h_6 - h_5} = \frac{555}{2487.6-129}$

Where $h_5 = h_4$

$\dot{m}_6 = \dot{m}_5 = \dot{m}_4 = \dot{m}_3 = 0.235$ kg/sec

8- calculate the mass flow rate of the poor solution at point # 7 :

$\dot{m}_{in} = \dot{m}_{out} \rightarrow \dot{m}_{\acute{2}} = \dot{m}_3 + \dot{m}_7 ------ (1)$

From the mass balance equation of LiBr

$x_{\acute{2}} . \dot{m}_{\acute{2}} = x_3 . \dot{m}_3 + x_7 . \dot{m}_7 , \ x_3 = 0 ------ (2)$

$\rightarrow x_{\acute{2}} . (\dot{m}_3 + \dot{m}_7) = x_7 . \dot{m}_7$

$\rightarrow \dot{m}_7 = \frac{x_{\acute{2}} . \dot{m}_3}{x_7 - x_{\acute{2}}} = \frac{0{,}515 \ .0{,}235}{0{,}65-0{,}515} = 0{,}896$ kg/sec

9- calculate the mass flow rate of the rich solution at point # $\acute{2}$:

$\dot{m}_{\acute{2}} = \dot{m}_3 + \dot{m}_7 = 0{,}235 + 0{,}896 = 1.131$ kg/sec

10- calculate circulation factor:

Cf = $\frac{\dot{m}_{\acute{2}}}{\dot{m}_3} = \frac{1{,}131}{0{,}235} = 4{,}812$

That means if we want to generate 1 kg of refrigerant, we have to pump 4,812 kg of solution,
Increasing desorbed temperature causes an increasing mass flow rate of refrigerant then Q_E &Cf

Cf = $\frac{x_7}{x_7 - x_{\acute{2}}} = \frac{0{,}65}{0{,}65-0{,}515} = 4{,}8148$

11-find desorbed outlet enthalpy # 3:

at $T_4 = 85\ ℃$ *vapor* ,

super-heated vapor chart: $h_{3\ =2642,71}$ kJ/ kg

12- find the desorber outlet enthalpy of the liquid solution # 7:

$T_7 = 85\,℃\ ,\ x_7 = 65\,\% \rightarrow (h-x)\ diagram\ of\ LiBr \rightarrow h_7 = 225$ kJ/ kg

13- find a secondary heat exchanger outlet enthalpy # 7´:

$T_{7'} = 60\,℃$ (assuming), $x_{7'} = 0{,}65 \rightarrow (h-x) chart\ h_{7'} = 180\ \ kJ/kg$

14- find absorber outlet enthalpy # 1 :

$T_1 = 30\,℃\ ,\ x = 0{,}515 \rightarrow (h-x) chart\ h_1 = 60\ \ kJ/kg$

15- find pump outlet enthalpy # 2 :

$\dot{W}_{pump} = \dot{E}_{mech} + \dot{E}_{loss} = \dot{m}.v.(p_c - p_E) + \dot{m}.(u_2 - u_{1)}$

$\eta_{pump} = \frac{\dot{E}_{mech}}{\dot{W}_{pump}} = 0{,}7$ (assuming)

$\dot{E}_{mech} = 1{,}131 .10^{-3}(4{,}246 - 0{,}9432) = 3{,}735.\ 10^{-3}[KW]$

$\dot{W}_{pump} = 5{,}33 .10^{-3}[KW]$

$\dot{W}_{pump} = \dot{m}_{1(} h_2 - h_{1)} \rightarrow h_2 = h_1 + \frac{\dot{W}_{pump}}{\dot{m}_1}$

$h_2 = \ 60{,}0047\ \ kJ/kg\ \approx h_1$

16- $h_{2'}$=

$\dot{Q} = \dot{m}_{7(} h_7 - h_{7'}) = \dot{m}_{2(} h_{2'} - h_2) \rightarrow h_{2'} = h_2 + \frac{\dot{m}_7}{\dot{m}_2}(h_7 - h_{7'})$

$h_{2'} = 60 + \frac{0{,}896}{1{,}131}(225 - 180) = 95{,}65\ \ kJ/kg$

17- $T_{2'}$ =??

$x_{2'} = 51{,}5\ \%\ ,\ h_{2'} = 95{,}65 \rightarrow (h-x) \rightarrow T_{2'} = 45\,℃$

18- calculate the thermal capacity of the desorbed:

$\sum \dot{E}_{in} = \sum \dot{E}_{out}$

$\dot{Q}_D + \dot{m}_{2'}.h_{2'} = \dot{m}_3.h_3 + \dot{m}_7.h_7 \rightarrow$

$\dot{Q}_D = 0{,}235 .2642{,}71 + 0{,}896 .225 - 1{,}131 .95{,}65 \rightarrow \dot{Q}_D = 714\ ,45\ [KW]$

19- thermal capacity of absorber:

$\dot{Q}_A + \dot{m}_2.h_2 = \dot{m}_6.h_6 + \dot{m}_{7'}.h_{7'} \rightarrow \dot{Q}_A = 0{,}235 .2487{,}6 + 0{,}896 .180 - 1{,}131 .60 \rightarrow$

$\dot{Q}_A = 678\ [KW]$

20- calculate the thermal capacity of the condenser:

$\dot{Q}_C = \dot{m}_3.h_3 + \dot{m}_4.h_4$

$\dot{Q}_C = 0{,}235\ (2642{,}71 - 129)$

$\dot{Q}_C = 590{,}72\ [KW]$

21- Energy Balance Equation for cycle:

$\sum \dot{E}_{in} = \sum \dot{E}_{out}$

$\dot{Q}_E + \dot{Q}_D + \dot{W}_{pump} \overset{?}{\Leftrightarrow} \dot{Q}_A + \dot{Q}_C$

$555 + 714{,}45 + 5{,}33.\ 10^{-3} \overset{?}{\Leftrightarrow} 678 + 590{,}72$

$1269{,}45 \overset{?}{\Leftrightarrow} 1268{,}72$

Not the difference is quite small, that is acceptable.

22- The coefficient of performance $[COP]$:

$COP = \frac{\dot{Q}_E}{\dot{Q}_D + \dot{W}_{pump}} = \frac{\dot{Q}_E}{\dot{Q}_D + 0} = 0{,}7768$

23-calculate mass flow rate of cooling water for A&C:

$\dot{Q}_A + \dot{Q}_C = \dot{m}_{10} .C_{p10} .(T_{10} - T_9)$

$\dot{m}_{10} = \frac{678+591}{4{,}18(25-20)} : (25-20) assuming \rightarrow \dot{m}_{10} = 60{,}71$ kg/sec

24- $h_{10} = C_{p10} .T_{10} = 4{,}18\ (25+273) = 1245{,}64$ kJ/kg

25 - $h_9 = C_{p9} .T_9 = 4{,}18\ (20+273) = 1224{,}74$ kJ/kg

Table 6. The results of the absorption cycle

#	Temperature [°C]	Concentration %	Enthalpy [Kj/kg]	Mass Flow [kg/sec]
1	30	51.5	60	1.131
2	30	51.5	60	1.131
2'	45	51.5	95.65	1.131
3	85	pure	2642.71	0.235
4	30	pure	129	0.235
5	30	pure	129	0.235
6	6	pure	2487.6	0.235
7	85	56	225	0.896
7'	60	65	180	0.896
8	60	65	180	0.896

Table 7. Fix data for selected collectors in the innovation building

Collector data	A_c [m^2]	$\tau\alpha$	U_L [w/m^2K]	T_i [C]	T_a [°C]	F_R
	2.24	0.8645	4	40	10	0.8

By the using of the data from Table 7 and the below equation, we defined the following results in Table 8.

$$q_u = A_C.F_R.[I_t.\tau\alpha - U_L.(t_i - t_a)]$$

Where:

q_u = useful energy delivered by the collector, W

A_c = total aperture collector area, m^2

I_t = irradiance, total (direct plus diffuse) solar energy incident on the upper surface of sloping collector structure, W/m^2

F_R = correction factor, or collector heat removal efficiency factor, having a value less than 1.0

U_L = overall heat loss coefficient, $W/(m^2 \cdot K)$

τ = transmittance (fraction of incoming solar radiation that reaches absorbing surface), dimensionless

α = absorptance (fraction of solar energy reaching surface that is absorbed), dimensionless

t_i = temperature of fluid entering collector, °C

t_a = atmospheric temperature, °C

Conclusion

In the case of the constant flow rate of water collectors, we must use 678 collectors with the electrical heater to keep the outlet water temperature at 90°C. In the case of the variable flow rate of water collectors, we must use only 603 collectors without any additional equipment's. The negative values q_u in Table 8 mean that the collectors need more energy to overcome the thermal losses in the collectors. The collectors with more collectors require more energy to maintain the same flow rate. This energy loss can be reduced by using a better collector with more efficient heat transfer. Additionally, the collectors should be strategically located to reduce energy losses due to heat loss. If the Generator temperature falls under 85°C the cooling capacity of the evaporator will decrease. It could be expanded in the study to calculate the surface area of heat exchangers (Condenser, Evaporator), and pipe sizes. The surface area of the heat exchangers can be calculated by using the desired temperature difference and the pressure drop across the exchangers. The pipe size should be chosen based on the desired flow rate and the pressure drop across the pipe. The flow rate and pressure drop can be estimated using the pressure drop equation

Scientific Ethics Declaration

The authors declare that the scientific ethical and legal responsibility of this article published in EPSTEM journal belongs to the authors.

Table 8. Useful energy for 680 collectors in the innovation building

Hour	May	June	July	August	September	October	Average solar irradiance during the day I_Avr [w/m2]	Useful energy delivered by one collector qu [w]	Mass flow rate to get 90C of hot water m [kg/s]	Ti [C]	Cp [w/kg.K]	Outlet water Temperature To [C]	Heater to keep To = 90C Heater [w]	Useful Energy from 680 collectors Q [w]	Collector efficiency η
5.00	83.70	98.70	55.60	5.10	0.00	0.00	40.52	-152.27	0.01	45.00	4180.00	39.21	1336.46	-103545.12	-1.68
6.00	300.00	309.70	265.90	198.70	117.90	41.50	205.62	103.50				48.93	1080.68	70378.67	0.22
7.00	509.80	514.20	475.20	418.30	342.00	253.90	418.90	433.91				61.49	750.27	295060.96	0.46
8.00	693.70	694.20	660.90	613.40	541.50	449.90	608.93	728.31				72.68	455.87	495250.65	0.53
9.00	838.90	837.80	810.20	769.40	698.10	601.80	759.37	961.36				81.53	222.82	653723.91	0.57
10.00	935.60	935.20	913.20	875.90	800.80	698.00	859.78	1116.92				87.44	67.26	759507.36	0.58
11.00	977.30	979.90	962.90	925.40	842.20	731.50	903.20	1184.18				90.00	0.00	805244.43	0.59
12.00	961.10	969.00	956.10	914.80	819.70	700.00	886.78	1158.75				89.03	25.43	787950.37	0.58
13.00	888.10	903.10	893.30	844.80	734.60	605.60	811.58	1042.25				84.61	141.93	708731.30	0.57
14.00	763.40	786.80	778.50	719.90	593.00	455.10	682.78	842.72				77.02	341.47	573047.57	0.55
15.00	595.20	627.70	619.60	548.80	404.80	260.20	509.38	574.09				66.82	610.09	390380.19	0.50
16.00	395.10	436.60	427.10	343.30	185.10	47.10	305.72	258.57				54.83	925.61	175828.53	0.38
17.00	177.90	226.70	214.50	120.60	0.50	0.00	123.37	-23.92				44.09	1208.11	-16267.19	-0.09

Acknowledgements or Notes

* This article was presented as an oral/poster presentation at the International Conference on Research in Engineering, Technology and Science (www.icrets.net) held in Thaskent/Uzbekistan on August 22-25, 2024.

References

Alefeld, G., & Ziegler, F. (1985). Advanced heat pump and air-conditioning cycles for the working pair H2O/LiBr: domestic and commercial applications. *ASHRAE transactions*, *91*(2B), 2062-2071.

Aumann, D. J. (1996). Selecting chillers in the 90s: accounting for hidden costs. *Heating, Piping, Air Conditioning*, *68*(3), 65-67.

Ashrae. (1998). ASHRAE Handbook, refrigeration, ashrae inc., atlanta, ga. ashrae, ashrae/iesna Standard 90.1-1999, Energy Standard for Buildings Except for New Low-Rise Residential Buildings, Atlanta, 1999.

Gommed, K., & Grossman, G. (1990). *Performance analysis of staged absorption heat pumps: water-lithium bromide systems*. American Society of Heating, Refrigerating and Air-Conditioning Engineers.

Grossman, G. (1982). Adiabatic absorption and desorption for improvement of temperature-boosting absorption heat pumps. *ASHRAE Trans.;(United States)*, *8*(2).

Author Information

Lida Ebrahimi Vafaei
Near East University
Near East Boulevard, ZIP: 99138, Nicosia / TRNC
Mersin 10 – Türkiye
Contact e-mail: *lida.ebrahimivefaei@neu.edu.tr*

Farzad Zaare Tajabadi
Near East University
Near East Boulevard, ZIP: 99138, Nicosia / TRNC
Mersin 10 – Türkiye

To cite this article:

Ebrahimi-Vafaei, L., & Zaare-Tajabadi, F. (2024). Optimizing cooling system design: A case study for innovation building. *The Eurasia Proceedings of Science, Technology, Engineering & Mathematics (EPSTEM), 29*, 232-244.

The Eurasia Proceedings of Science, Technology, Engineering & Mathematics (EPSTEM)
ISSN: 2602-3199

The Eurasia Proceedings of Science, Technology, Engineering & Mathematics (EPSTEM), 2024

Volume 29, Pages 245-253

ICRETS 2024: International Conference on Research in Engineering, Technology and Science

Industrial Engineering and Management Applications: Evaluation of Data Integration Tools for Smart Manufacturing

Van Thanh Tien Nguyen
Industrial University of Ho Chi Minh City

Nhut Thi Minh Vo
Shinawatra University

Abstract: This study comprehensively evaluates leading data integration tools for smart manufacturing environments using a hybrid Analytic Hierarchy Process (AHP) and VIseKriterijumska Optimizacija I Kompromisno Resenje (VIKOR) methodology. As Industry 4.0 drives increased automation and data exchange in manufacturing processes, selecting appropriate data integration tools has become critical yet complex. We assessed seven prominent data integration tools across 24 criteria grouped into six main categories: functionality, vendor-related factors, user experience, cost, reliability, and flexibility. Our data collection was informed by expert interviews, vendor documentation analysis, user reviews, and benchmark testing. The AHP analysis revealed functionality and data integration features as the most crucial criteria (weight: 0.2493), followed by user-related factors (0.1814). The VIKOR method then ranked the tools, with Oracle Data Integrator emerging as the top performer (Q=0.0000), followed by Informatica PowerCenter (Q=0.22391). Our findings highlight the importance of cloud-native solutions and user experience in industrial data integration. This research contributes a robust framework for evaluating data integration tools in imaginative manufacturing contexts and offers insights to guide decision-making in Industry 4.0 initiatives.

Keywords: Smart manufacturing, Data integration tools, Multi-criteria decision making, Analytic hierarchy process (AHP), VIKOR method, Industrial engineering

Introduction

The fourth industrial revolution, Industry 4.0, has precipitated a paradigm shift in manufacturing paradigms characterized by unprecedented automation, interconnectivity, and data exchange. Central to this transformative epoch is intelligent manufacturing, which harnesses cutting-edge technological advancements such as the Industrial Internet of Things (IIoT), artificial intelligence, and sophisticated analytics to optimize production processes, augment efficiency, and catalyze innovation. A critical component in realizing the full potential of intelligent manufacturing is the efficacious integration of data from diverse sources across the manufacturing ecosystem.

Data integration within intelligent manufacturing milieus presents unique challenges due to the heterogeneous nature of data sources, the volume and velocity of data generated, and the imperative for real-time processing and analysis. As manufacturing systems become increasingly intricate and interconnected, the demand for robust, scalable, and efficient data integration tools has grown exponentially. These tools must address the technical aspects of data integration and align with the strategic objectives of intelligent manufacturing initiatives.

The selection of an appropriate data integration tool for intelligent manufacturing is a multifaceted decision that necessitates careful consideration of various factors. These include the tool's capacity to support a wide range of

data sources, scalability to handle large data volumes, real-time data processing capabilities, security features, ease of use, and compatibility with existing systems. Moreover, the chosen tool must be adaptable to the rapidly evolving technological landscape of intelligent manufacturing.

Given the complexity of this decision-making process and its potential impact on the success of intelligent manufacturing implementations, a pressing need exists for a systematic and objective approach to evaluating and selecting data integration tools. This study addresses this need by proposing a comprehensive framework for assessing data integration tools specifically tailored to the requirements of intelligent manufacturing environments.

Our research employs a hybrid methodology that combines the Analytic Hierarchy Process (AHP) with the VIseKriterijumska Optimizacija I Kompromisno Resenje (VIKOR) method. This approach allows for a nuanced evaluation of data integration tools, considering both quantitative and qualitative criteria. The AHP component enables structuring the decision problem into a hierarchy and facilitates the determination of criteria weights based on expert judgments. Conversely, the VIKOR method provides a mechanism for ranking alternatives and identifying compromise solutions in the presence of conflicting criteria.

The study evaluates seven leading data integration tools: Microsoft Azure Data Factory, Dell Boomi, Informatica PowerCenter, Talend Data Integration, IBM InfoSphere DataStage, Oracle Data Integrator (ODI), and MuleSoft Anypoint Platform. These tools were selected based on their prominence in the market and potential applicability to intelligent manufacturing contexts. The evaluation criteria encompass many factors, including functionality and data integration features, vendor-related aspects, user-related considerations, cost, reliability, flexibility, and adaptation capabilities. By conducting this comprehensive analysis, our research aims to provide valuable insights for manufacturing organizations seeking to implement or upgrade their data integration capabilities in the context of intelligent manufacturing initiatives. The findings of this study will not only assist decision-makers in selecting the most suitable data integration tool for their specific needs but also contribute to the broader body of knowledge on technology adoption in intelligent manufacturing environments.

Furthermore, this research addresses a significant gap in the existing literature. While previous studies have examined data integration tools in various contexts, more research should focus on the unique requirements of intelligent manufacturing ecosystems. By tailoring our evaluation framework to the specific needs of smart manufacturing, we provide a novel and highly relevant contribution to the field.

In the subsequent sections, we present a detailed literature review, delineate our methodology, describe the data collection and analysis process, present our results, and discuss the implications of our findings. Through this rigorous analysis, we aim to advance the understanding of data integration tool selection in intelligent manufacturing and provide actionable insights for practitioners and researchers in this rapidly evolving field.

Literature Review

Industry 4.0 has ushered in an era of intelligent manufacturing, where data integration is pivotal in optimizing production processes and decision-making. The selection of appropriate data integration tools presents a complex decision-making problem, given the many options available and the diverse criteria to consider. The Analytic Hierarchy Process (AHP) and VIseKriterijumska Optimizacija I Kompromisno Resenje (VIKOR) have emerged as robust multi-criteria decision-making methods suitable for such complex evaluations. The review will first explore the broader context of data integration in intelligent manufacturing, followed by an analysis of studies utilizing AHP and VIKOR for tool evaluation. It will then identify gaps in existing research and highlight potential areas for future investigation.

The Analytical Hierarchy Process (AHP) is a highly esteemed and extensively utilized methodology for decision-making. It systematically involves the comparative evaluation of alternatives against a predefined set of criteria, thereby facilitating the determination of priorities with precision and rigor. This structured approach enhances the clarity and consistency of decision-making processes and ensures that complex decisions are made with a comprehensive understanding of all relevant factors. Leal (2019) introduced an innovative, streamlined adaptation of the Analytical Hierarchy Process (AHP), which significantly reduces the requisite number of comparisons, thereby enhancing the efficiency of the decision-making process. Furthermore, Fuzzy AHP methods have garnered considerable attention and popularity, particularly in contexts where decision-making necessitates the incorporation of subjective judgments. These advancements underscore the adaptability and robustness of AHP methodologies in addressing complex decision-making challenges (Leal, 2020).. Gündoğdu

et al. (2020) advanced the classical Analytical Hierarchy Process (AHP) by developing the Spherical Fuzzy AHP (SF-AHP) method, thereby expanding its applicability and precision. This novel approach was effectively demonstrated through a case study on renewable energy location selection, highlighting its potential to enhance decision-making processes in complex, real-world scenarios (Kutlu Gündoğdu & Kahraman, 2020). The Analytical Hierarchy Process (AHP) has been effectively applied across various fields, underscoring its versatility and utility. Notable applications include the assessment of social vulnerability (Hadipour et al., 2020) the optimization of drinking water harvesting strategies (Khashei-Siuki et al., 2020) and the analysis of collaboration evolution (Yu et al., 2021).

Al-Zibaree et al. (2023) employed the Fuzzy Analytic Hierarchy Process (FAHP) to assess the quality of public bus transport services in Budapest, Hungary, effectively addressing the inherent uncertainties in decision-making processes[6]. This application underscores the method's adaptability in real-world scenarios. Furthermore, the Analytical Hierarchy Process (AHP) has been innovatively extended to integrate advanced concepts such as Proportional Picture Fuzzy Sets, as demonstrated by Kahraman (2024) in the context of waste disposal site selection (Kahraman, 2024). Additionally, Tan et al. (2024) utilized confirmatory factor analysis (CFA) to develop a WELL building model tailored for office environments (Tan et al., 2024). These examples demonstrate the strong ability of AHP to tackle intricate decision-making issues across different settings, confirming its importance as an essential instrument in both scholarly and practical fields.

The VIKOR method has been extensively applied across diverse industry decision-making scenarios. Saqlain (2023) underscored the significance of analyzing interdependencies among decision-making variables to comprehend their collective impact and correlations, advocating for further exploration of methodologies such as AHP and TOPSIS within a neutrosophic framework[9]. In a similar vein, Yadav et al. (2023) employed the VIKOR method to rank dental restorative composite materials, showcasing its efficacy in multi-criteria decision-making (MCDM) techniques (Yadav et al., 2023). Singh et al. (2023) introduced the Picture Fuzzy VIKOR-TOPSIS approach for selecting appropriate adsorbents, highlighting knowledge and accuracy measures (Singh, & Kumar, 2023). Additionally, Vahidinia et al. (2023) utilized a comprehensive evaluation model based on the VIKOR method to assess supply chain smartness, focusing on the Iran Khodro Company as a case study (Vahidinia & Hasani, 2023).

In another context, Dagistanli (2024) extended the VIKOR method to the defense industry for selecting R&D projects, emphasizing defense initiatives' complexity and high-budget nature (Jana et al., 2023). Furthermore, Yu et al. (2024) proposed a safety evaluation method for quayside container cranes using the Best-worst method and Pythagorean hesitant fuzzy VIKOR, thereby enriching theoretical approaches in safety assessment (Yu et al., 2024). These studies illustrate the VIKOR method's versatility and effectiveness, making it a preferred choice for researchers and practitioners seeking robust and reliable decision-making solutions across a spectrum of applications, from material selection to project prioritization and safety evaluations.

There exists a need for more exhaustive, contemporaneous analyses of preeminent data integration tools specifically tailored to the exigencies of innovative manufacturing milieus. The present inquiry endeavors to address these identified gaps by furnishing a comprehensive assessment of data integration tools, encompassing their technical prowess and user-centric, vendor-related, and economic dimensions. By applying a rigorous multi-criteria decision-making framework, this study aspires to provide a more nuanced and holistic comprehension of the tool selection process for data integration within intelligent manufacturing applications.

Methodology

To conduct a comprehensive and objective evaluation of data integration tools for smart manufacturing, we employed a hybrid methodology combining the Analytic Hierarchy Process (AHP) and the VIseKriterijumska Optimizacija I Kompromisno Resenje (VIKOR) method. This approach allows for a systematic assessment of both quantitative and qualitative criteria, providing a robust framework for decision-making in complex environments.

Data Collection:

Our data collection process was designed to capture a wide range of information about seven leading data integration tools: Microsoft Azure Data Factory, Dell Boomi, Informatica PowerCenter, Talend Data

Integration, IBM InfoSphere DataStage, Oracle Data Integrator (ODI), and MuleSoft Anypoint Platform. We employed a multi-faceted approach to data collection:

- Literature Review: We extensively reviewed academic literature, industry reports, and technical documentation to identify key criteria for evaluating data integration tools in smart manufacturing contexts.
- Expert Interviews: Semi-structured interviews were conducted with 15 industry experts, including data integration specialists, smart manufacturing consultants, and IT managers in manufacturing organizations. These interviews helped refine our evaluation criteria and provided insights into the practical considerations of data integration tool selection.
- Vendor Documentation Analysis: We systematically analyzed official documentation, white papers, and technical specifications provided by the vendors of the selected data integration tools.
- User Reviews: To incorporate end-user perspectives, we collected and analyzed user reviews from reputable software review platforms, focusing on user reviews in the manufacturing and industrial sectors.
- Benchmark Testing: Where possible, we conducted standardized performance tests to assess specific technical criteria such as data processing speed and scalability.

Data Analysis

Our analysis followed a two-stage process, leveraging the strengths of both AHP and VIKOR methods:

Stage 1: Analytic Hierarchy Process (AHP)

We employed AHP to determine the relative weights of the evaluation criteria. This process involved:

- Structuring the decision problem into a hierarchy of criteria and sub-criteria.
- Conducting pairwise comparisons of criteria at each level of the hierarchy.
- Calculating the eigenvectors to derive the relative weights of criteria.
- Verifying the consistency of judgments using the Consistency Ratio (CR) to ensure reliability.

Stage 2: VIKOR Method

The VIKOR method was then applied to rank the alternatives based on their performance across all weighted criteria. This stage involved:

- Normalizing the decision matrix to ensure comparability across different criteria.
- Determining the ideal and negative-ideal solutions for each criterion.
- Calculate each alternative's utility measures (S) and regret measures (R).
- Computing the VIKOR index (Q) to provide a final ranking of alternatives.

To enhance the robustness of our analysis, we conducted a sensitivity analysis by varying the weights of criteria and observing the impact on the final rankings. This approach allowed us to identify which criteria had the most significant influence on the results and assess the stability of our findings under different scenarios. Combining AHP and VIKOR methods, our methodology provides a comprehensive and nuanced evaluation of data integration tools, considering multiple criteria relevant to smart manufacturing environments. This approach yields a ranking of alternatives and offers insights into the trade-offs between different criteria, enabling more informed decision-making in selecting data integration tools for smart manufacturing applications.

Data Collection and Analysis

The data collection process for this study was designed to comprehensively evaluate seven leading data integration tools in the context of smart manufacturing. The tools under consideration were Microsoft Azure Data Factory (DTI1), Dell Boomi (DTI2), Informatica PowerCenter (DTI3), Talend Data Integration (DTI4), IBM InfoSphere DataStage (DTI5), Oracle Data Integrator (ODI) (DTI6), and MuleSoft Anypoint Platform (DTI7).

Criteria Selection

Based on an extensive literature review and expert consultation, we identified 24 sub-criteria under six main criteria categories. These criteria were selected to encompass the key aspects of data integration in smart manufacturing environments. The criteria hierarchy is as follows:

1. Functionality and data integration features (C1)
    - Data Sources Supported (C11)
    - Category (C12)
    - Transform data (C13)
    - Loading Performance (C14)
    - Real-Time Data Availability (C15)
    - Security (C16)
    - Compatibility (C17)
    - Support Efficient operations (C18)
    - Provide multiple deployment options (C19)
2. Vendor related (C2)
    - Technical capability (C21)
    - Reputation (C22)
    - Provides permanent service (C23)
3. User Related (C3)
    - Ease of Use (C31)
    - Training (C32)
    - Graphical User Interface (GUI) (C33)
    - Documentation and Support (C34)
4. Cost (C4)
    - Cost of maintenance (C41)
    - Consultant expense (C42)
    - Price (C43)
5. Reliability (C5)
    - Stability (C51)
    - Recovery ability (C52)
6. Flexibility and Adaption (C6)
    - Data Transformations capabilities (C61)
    - Scalability/ Data Volume (C62)
    - Interact with sources and targets (C63)

Data Collection

Data for each criterion was collected through a combination of methods:

1. Expert evaluations: A panel of experts in data integration and smart manufacturing was assembled to provide ratings for qualitative criteria.
2. Vendor documentation: Technical specifications and feature lists were obtained from official vendor documentation.
3. User reviews: Data from reputable software review platforms was collected to incorporate user experiences.
4. Benchmark tests: Where applicable, standardized performance tests were conducted to assess loading performance and scalability criteria.

AHP Analysis

The Analytic Hierarchy Process (AHP) was employed to determine the relative weights of the criteria. Pairwise comparison matrices were constructed based on expert judgments. The consistency of these judgments was verified using the Consistency Ratio (CR), ensuring all CRs were below the acceptable threshold of 0.1.
The resulting normalized weights for the main criteria were:

- Functionality and data integration features (C1): 0.2493
- Vendor related (C2): 0.1527
- User Related (C3): 0.1814
- Cost (C4): 0.1080
- Reliability (C5): 0.1360
- Flexibility and Adaption (C6): 0.1726

Sub-criteria weights were similarly calculated, providing a comprehensive weighting system for the evaluation.

VIKOR Analysis

The VIKOR method was then applied to rank the alternatives based on their performance across all criteria. The process involved the following steps, and calculated results are shown in Table 1:

1. Normalization of the decision matrix
2. Calculation of the ideal and negative-ideal solutions
3. Computation of the utility measure (S) and regret measure (R) for each alternative
4. Calculation of the VIKOR index (Q) for each alternative

Table 1. The VIKOR calculated results

Alternative	S	R	Q
DTI1	0.35187	0.06747	0.38511
DTI2	0.41927	0.07397	0.53400
DTI3	0.41208	0.04579	0.22391
DTI4	0.38133	0.06657	0.41015
DTI5	0.66324	0.09066	1.00000
DTI6	0.23865	0.04395	0.00000
DTI7	0.44326	0.07397	0.56226

Results

Applying the hybrid AHP-VIKOR methodology yielded comprehensive insights into the relative performance of the seven evaluated data integration tools in smart manufacturing. This section presents the key findings of our analysis.

Criteria Weights

The AHP analysis resulted in the following normalized weights for the main criteria:

1. Functionality and data integration features (C1): 0.2493
2. Vendor-related criteria (C2): 0.1527
3. User Related criteria (C3): 0.1814
4. Cost (C4): 0.1080
5. Reliability (C5): 0.1360
6. Flexibility and Adaption (C6): 0.1726

These weights reflect the relative importance of each criterion in selecting data integration tools for smart manufacturing environments. Notably, functionality and data integration features emerged as the most critical factor, followed closely by user-related criteria and flexibility and adaptation capabilities.

VIKOR Analysis Results

The VIKOR analysis ranked the seven data integration tools based on their performance across all criteria. Table 2 presents each alternative's S, R, and Q values, where S represents the utility measure, R is the regret measure, and Q is the VIKOR index.

Table 2: VIKOR analysis results

Alternative	Tool Name	S	R	Q
DTI6	Oracle Data Integrator (ODI)	0.23865	0.04395	0.00000
DTI3	Informatica PowerCenter	0.41208	0.04579	0.22391
DTI1	Microsoft Azure Data Factory	0.35187	0.06747	0.38511
DTI4	Talend Data Integration	0.38133	0.06657	0.41015
DTI2	Dell Boomi	0.41927	0.07397	0.53400
DTI7	MuleSoft Anypoint Platform	0.44326	0.07397	0.56226
DTI5	IBM InfoSphere DataStage	0.66324	0.09066	1.00000

The VIKOR index (Q) provides a comprehensive measure of each tool's performance, with lower values indicating better overall performance. Based on these results, we can draw the following conclusions:

1. Oracle Data Integrator (ODI) emerged as the top-performing tool with the lowest Q value of 0.00000, indicating superior performance across the evaluated criteria.
2. Informatica PowerCenter ranked second with a Q value of 0.22391, demonstrating strong overall performance.
3. Microsoft Azure Data Factory and Talend Data Integration performed similarly, ranking third and fourth, respectively.
4. Dell Boomi and MuleSoft Anypoint Platform performed similarly, occupying the fifth and sixth positions.
5. IBM InfoSphere DataStage ranked last with a Q value of 1.00000, suggesting relatively lower performance than the other tools in the context of smart manufacturing requirements.

Discussion

The results of our comprehensive analysis of data integration tools for smart manufacturing environments reveal several significant insights with far-reaching implications for practitioners and researchers in the field. Firstly, the emergence of Oracle Data Integrator (ODI) as the top-performing tool, followed closely by Informatica PowerCenter, underscores the importance of robust functionality and advanced data integration features in smart manufacturing contexts. These tools' superior performance across multiple criteria suggests that the market is evolving to meet the complex demands of Industry 4.0, where seamless data integration is crucial for realizing the full potential of smart manufacturing initiatives.

The strong performance of cloud-native solutions like Microsoft Azure Data Factory indicates a growing trend toward cloud-based data integration in industrial settings. This trend aligns with the broader shift towards cloud computing in manufacturing, driven by the need for scalability, flexibility, and real-time data processing capabilities. However, the varied performance of cloud-based tools in our analysis suggests that cloud adoption in industrial data integration is challenging, particularly in data security and on-premises integration. Interestingly, our results reveal that user-related criteria, including ease of use and quality of documentation and support, play a more significant role in tool selection than previously acknowledged in the literature. This finding highlights the growing importance of user experience in technology adoption within manufacturing environments, where ease of implementation and user proficiency can significantly impact the success of data integration initiatives.

The relatively lower ranking of well-established tools like IBM InfoSphere DataStage suggests that legacy systems may need help to keep pace with the rapidly evolving requirements of intelligent manufacturing. This observation has important implications for vendors and manufacturing organizations, indicating a need for continuous innovation and adaptation to remain competitive in the Industry 4.0 era. Our analysis also reveals a notable trade-off between cost and performance. While some lower-cost solutions, like Talend Data Integration, performed competitively in certain areas, the overall dominance of more premium solutions suggests that manufacturing organizations are willing to invest in higher-priced tools that offer advanced features and reliability. This finding underscores the strategic importance of data integration in smart manufacturing and the recognition of its value in driving operational excellence and innovation.The strong performance of tools offering flexible deployment options and extensive interoperability features, such as MuleSoft Anypoint Platform, reflects the heterogeneous and often complex nature of manufacturing IT environments. This highlights the need for data integration solutions that seamlessly operate across diverse systems, from legacy on-premises applications to cutting-edge IoT devices and cloud services.

Lastly, the sensitivity analysis revealing the stability of top rankings across various weighting scenarios lends credibility to our findings and provides a robust foundation for decision-making in tool selection. However, the sensitivity of rankings to changes in weights for functionality and user-related criteria emphasizes the importance of carefully considering organizational priorities and use cases when selecting a data integration tool.

Conclusion

This study provides a comprehensive evaluation of leading data integration tools in the context of smart manufacturing, employing a rigorous AHP-VIKOR methodology to assess their performance across multiple criteria. Our findings offer valuable insights for practitioners and researchers in industrial data integration and smart manufacturing.

Key findings of our research include:

1. Oracle Data Integrator and Informatica PowerCenter emerged as top-performing tools, excelling in functionality, reliability, and user-related criteria.
2. Cloud-native solutions are gaining traction in industrial data integration, as evidenced by the strong performance of Microsoft Azure Data Factory.
3. User experience and support have become increasingly critical factors in selecting data integration tools for smart manufacturing environments.
4. There is a clear trade-off between cost and advanced features, with manufacturing organizations willing to invest in premium solutions offering comprehensive capabilities.
5. Flexibility in deployment options and robust interoperability features are crucial for addressing manufacturing IT landscapes' complex and heterogeneous nature.

These findings have significant implications for the field, highlighting the evolving requirements of data integration in smart manufacturing and the need for solutions to address the multifaceted challenges of Industry 4.0.

For future research, we suggest the following areas of investigation:

- Longitudinal studies to track the evolution of data integration tool capabilities and their alignment with smart manufacturing needs over time.
- In-depth case studies of successful data integration implementations in smart manufacturing environments to identify best practices and challenges.
- Exploration of emerging technologies such as artificial intelligence and machine learning in enhancing data integration capabilities for smart manufacturing.
- Investigation of industry-specific requirements for data integration in different manufacturing sectors and their impact on tool selection.
- Analysis of the long-term economic impact of data integration tool choices on smart manufacturing initiatives.

In conclusion, as smart manufacturing continues to evolve, selecting appropriate data integration tools will remain critical in the success of Industry 4.0 initiatives. Our research provides a robust framework for evaluating these tools and offers valuable insights to guide decision-making in this rapidly advancing field. By continuing to investigate and refine our understanding of data integration in smart manufacturing, we can further enhance the effectiveness and efficiency of industrial processes in the digital age.

Scientific Ethics Declaration

The authors declare that the scientific, ethical, and legal responsibility of this article published in EPSTEM journal belongs to the authors.

Acknowledgments or Notes

* The authors thank the Ministry of Science and Technology, Taiwan. We also would like to thank the National Kaohsiung University of Science and Technology and the Industrial University of Ho Chi Minh City for their

assistance. Additionally, we would like to thank the reviewers and editors for their constructive comments and suggestions for improving our work.

* This article was presented as an oral presentation at the International Conference on Research in Engineering, Technology, and Science (www.icrets.net) held in Tashkent, Uzbekistan, on August 22 - 25, 2024.

References

Al-Zibaree, H. K. Y., & Konur, M. (2023). Fuzzy analytic hierarchal process for sustainable public transport system. *Journal of Operations Intelligence*, *1*(1), 1-10.

Hadipour, V., Vafaie, F., & Kerle, N. (2020). An indicator-based approach to assess social vulnerability of coastal areas to sea-level rise and flooding: A case study of Bandar Abbas city, Iran. *Ocean & Coastal Management*, *188*, 105077.

Jana, C., Mohamadghasemi, A., Pal, M., & Martinez, L. (2023). An improvement to the interval type-2 fuzzy VIKOR method. *Knowledge-Based Systems*, *280*, 111055..

Kahraman, C. (2024). Proportional picture fuzzy sets and their AHP extension: Application to waste disposal site selection. *Expert Systems with Applications*, *238*, 122354

Khashei-Siuki, A., & Sharifan, H. (2020). Comparison of AHP and FAHP methods in determining suitable areas for drinking water harvesting in Birjand aquifer. Iran. *Groundwater for Sustainable Development*, *10*, 100328.

Kutlu Gündoğdu, F., & Kahraman, C. (2020). A novel spherical fuzzy analytic hierarchy process and its renewable energy application. *Soft Computing*, *24*, 4607-4621.

Leal, J. E. (2020). AHP-express: A simplified version of the analytical hierarchy process method. *MethodsX*, *7*, 100748.

Saqlain, M. (2023). Sustainable hydrogen production: A decision-making approach using VIKOR and intuitionistic hypersoft sets. *Journal of intelligent management decision*, *2*(3), 130-138.

Singh, A., & Kumar, S. (2023). Picture fuzzy VIKOR-TOPSIS approach based on knowledge and accuracy measures for suitable adsorbent decision making. *Applied Soft Computing*, *147*, 110807.

Tan, C. Y., Rahman, R. A., & Lee, Y. S. (2024). Developing a WELL building model for office environments. *Environmental Science and Pollution Research*, 1-20.

Vahidinia, A., & Hasani, A. (2023). A comprehensive evaluation model for smart supply chain based on the hybrid multi-criteria decision-making method. *Journal of Soft Computing and Decision Analytics*, *1*(1), 219-237.

Yadav, R., Singh, M., Meena, A., Lee, S. Y., & Park, S. J. (2023). Selection and ranking of dental restorative composite materials using hybrid Entropy-VIKOR method: An application of MCDM technique. *Journal of the Mechanical Behavior of Biomedical Materials*, *147*, 106103.

Yu, D., Kou, G., Xu, Z., & Shi, S. (2021). Analysis of collaboration evolution in AHP research: 1982–2018. *International Journal of Information Technology & Decision Making*, *20*(01), 7-36.

Yu, J., Xiao, H., Sun, F., Yan, L., & Liu, M. (2024). Research on the safety evaluation method for quayside container cranes based on the best–worst method–pythagorean fuzzy VIKOR approach. *Applied Sciences*, *14*(3), 1312.

Author Information

Van Thanh Tien Nguyen
Industrial University of Ho Chi Minh City
12, Nguyen Van Bao, Go Vap, Ho Chi Minh City, Vietnam

Thi Minh Nhut Vo
Shinawatra University, Thailand
99 Moo 10, Bangtoey, Samkhok, Pathum Thani 12160 Thailand.
Contact email*: n.vo@ieee.org*

To cite this article:

Nguyen, V.T.T., & Vo, T.M.N.. (2024). Industrial engineering and management applications: Evaluation of data integration tools for smart manufacturing. *The Eurasia Proceedings of Science, Technology, Engineering & Mathematics (EPSTEM), 29*, 245-253.

The Eurasia Proceedings of Science, Technology, Engineering & Mathematics (EPSTEM)
ISSN: 2602-3199

The Eurasia Proceedings of Science, Technology, Engineering & Mathematics (EPSTEM), 2024

Volume 29, Pages 254-259

ICRETS 2024: International Conference on Research in Engineering, Technology and Science

Biodiesel Production by Supercritical Methanol from Jojoba Seeds Harvested in the Mesaoria Plain of Cyprus

Filiz Al-Shanableh
Near East University

Mahmut A. Savas
Near East University

Metin Bilin
Near East University

Abstract: Nowadays, interest in renewable energy sources such as biodiesel is increasing due to the limited resources and environmental impacts of fossil fuels. Jojoba plant (Simmondsia chinensis) is one of the oilseeds with significant potential for biodiesel production. This study investigates the viability of producing biodiesel from jojoba oil extracted from plants grown in the Mesaoria Plain of Cyprus. The Mesaoria Plain, with its favorable climate for jojoba cultivation, presents an ideal location for investigating the usability of this biodiesel feedstock. Supercritical methanol, known for its efficiency in transesterification reactions, offers a novel approach to converting jojoba oil into biodiesel. Through analysis and experiments, this work assesses the crucial variables—temperature, pressure, and reaction time—involved in the supercritical methanol process. Furthermore, the quality attributes of the biodiesel produced, like its fatty acid methyl ester content, viscosity, density, and cetane number, were determined in compliance with international biodiesel standards. In the supercritical methanol transesterification at 240°C and 8.3 MPa, the % achieved conversion in a separate portion of fatty acid esters was 97.8 %. The findings of this research contribute valuable insights into the potential of jojoba-derived biodiesel as a sustainable energy solution in Cyprus and beyond.

Keywords: Biodiesel, Jojoba seeds, Supercritical methanol, Energy engineering

Introduction

The limitation of energy resources, one of today's main problems, requires energy production from sustainable raw materials. Biodiesel, due to its biodegradability, reduced emissions, and compatibility with existing diesel engines, has proven to be a solution to the fuel problem due to its ability to be produced from sustainable energy sources (Knothe, 2010). Biodiesel is produced by a chemical reaction called transesterification, in which vegetable oils or animal fats react against alcohols of low molar weight (Al-Shanableh, 2017). Unlike traditional methods used in the transesterification process, the supercritical methanol method stands out for its higher efficiency and less by-product formation. The supercritical methanol (SCM) method that achieves a faster and more efficient transesterification process is based on the reaction of methanol with oils under supercritical conditions (under high temperature (>200 °C) and pressure (>5 MPa)) (Saka & Kusdiana, 2001; Al-Shanableh & Savas, 2023). Additionally, biodiesel produced by the supercritical methanol method may contain higher purity and fewer contaminants, providing reassurance about the effectiveness of this research.

Jojoba (Simmondsia chinensis), a perennial shrub native to arid regions, is particularly suited for biodiesel production, with its high oil content ranging from 45% to 60% and adaptability to semi-arid climates (Bilin, 2020). Jojoba oil is an oil obtained from the seeds of the Jojoba plant. This oil's chemical and thermophysical

properties include many that are important for its industrial and cosmetic uses. Jojoba oil is an unsaturated liquid wax that is clear, golden and has no greasy or perfumed aftertaste. While the phrase "jojoba oil" is commonly used to refer to it, it is more appropriately called "wax," as it is a mixture of long-chain monounsaturated esters (97–98 weight percent) of fatty acids and fatty alcohols rather than a triglyceride like vegetable and animal fats are (Canoira et al., 2006). According to the standard of the International Jojoba Export Council (IJEC), the significant component of wax esters in jojoba oil with C40 and C42, of which monounsaturated fatty acids should be oleic acid (C18:1), eicosenoic acid (C20:1) and erucic acid (C21:1) (IJEC, 2018). The fatty acid compositions of jojoba oil would vary significantly depending on the soil and climate where the jojoba shrub is grown, when it is harvested and how the oil is processed.

Jojoba oil has the exceptional qualities of a liquid wax with low and consistent viscosity at varying temperatures, good lubricity, and other physicochemical characteristics such as high boiling, smoke, flash point, and low chemical reactivity. In lubricants and other industrial applications, jojoba oil has supplanted whale sperm oil as the primary natural source of liquid wax esters (Lei & Li, 2015). Lubricants, medications, and cosmetics are among the industries that use jojoba oil and its derivatives. Jojoba oil is an excellent lubricant for metal cutting, tool work, and high-speed machinery in the automobile industry. Furthermore, the viability of using jojoba methyl ester for biodiesel on a commercial scale is highly dependent on the added value (about 1.16 $/kg) achieved for the fatty alcohols that are created as a side product during the transesterification process (Bouaid et. al., 2007). Different studies showed jojoba oil was successfully used as a raw or biodiesel in different proportions in diesel engines. Both Canoira et al. (2006) and Bouaid et al. (2007) studied to convert jojoba oil to biodiesel using base catalyst transesterification at moderate operation conditions, and they obtained 97 % and 83.5 % conversion yield of esters, respectively. In 2015, Lei and Li transesterified jojoba oil, an enzymatic lipase catalyst, and the maximum conversion they obtained was 97 %. With the SCM method, Singh et al. (2022) achieved 95.7 % conversion within 23 min at 123 bar and 287 °C. In their work, Selim et al. (2022) mixed raw Jojoba oil in different proportions with diesel fuel, and they showed that the mixture could serve as a fuel for diesel engines without any modifications. The raw Jojoba oil was found to be a suitable, promising alternative to the diesel fuel used in diesel engines with viscosity adjustment.

This study aimed to convert jojoba oil extracted from plants grown in the Mesaoria Plain into biodiesel using the SCM method in a supercritical reactor designed and constructed in previous studies.

Method

Extraction of Jojoba Oil

The jojoba seeds were harvested from the Mesaoria Plain test plantation. A typical jojoba seed was an oblong to oval shape produced by a female jojoba plant. The process of extracting oil involves using a screw machine that applies pressure to the seeds within a cylindrical chamber, causing the jojoba oil to be collected through outlet holes located at the bottom of the chamber by preventing the solid press cake from passing through (Al-Shanableh et al., 2020). The jojoba oil was allowed to settle and precipitate for three days following extraction. Several physicochemical properties of the jojoba oil extracted were also examined and listed in Table 1, as required by IJEC quality standards.

Table 1. Various physicochemical properties of Jojoba oil extracted

Physicochemical characteristics	**Values obtained**	**Method**	**IJEC Standards**
Specific gravity (g/cm^3)	0.86	AOCS Cc 10 a	0.86-0.87
Kinematic viscosity at 40 ˚C (mm^2/s)	24.5	ASTM D 445	-
Kinematic viscosity at 100 ˚C (mm^2/s)	6.45	ASTM D 445	-
Refractive Index	1.47	AOCS Cc 7 25	1.45-1.47
Saponification (mg KOH/g)	92.6	AOCS Cd 3-25	88.0-96.0
Acid Value (mg KOH/g)	0.5	AOCS Ci 4-91	≤1.0
Iodine Value (gram)	88.9 /100	AOCS Cd 1-25	882-87 /100
Peroxide Value ($meqO_2/kg$)	<1.0	AOCS Cd 8-53	≤ 2.0

Table 1 illustrates the fatty acid compositions of the jojoba oil samples produced from the seeds of jojoba shrubs grown on the Mesaoria Plain in TRNC.Jojoba oil is a wax ester comprising esters of fatty acids and fatty alcohols. The predominant constituents found in jojoba oil in this study were the wax esters C40 and C42, which align with the specifications outlined in the IJEC standard (IJEC, 2018). C40 wax ester consists of C22:0

alcohol and C18:1 fatty acid, while C42 consists of C22:0 alcohol and C20:1 fatty acid. Eicosenoic acid, also known as C20:1, emerges as the primary component within the specified limits of the IJEC standard.

Table 2. Fatty acids and wax esters compositions of jojoba extracted

Fatty acid and wax ester composition	%	IJEC Standards Limits
Palmitic acid (C16:1)	1.89	≤3.0
Palmitoleic acid (C16:1)	0.07	≤1.0
Stearic acid (C18:0)	0.46	-
Oleic acid (C18:1)	12.3	5.0-15.0
Linoleic acid (C18:2)	0.21	-
Linolenic acid (C18:3)	0.59	-
Arachidic acid (C20:0)	0.13	-
Eicosenoic acid (C20:1)	71.1	65.0-80.0
Behenic acid (C22:0)	0.18	≤1.0
Erucic acid (C22:1)	11.7	10.0-20.0
Nervonic acid (C24:1)	1.15	≤3.0
Wax Ester Compositions		
C40 wax ester	28.2	26.0-34.0
C42 wax ester	46.3	44.0-56.0
C44 wax ester	8.0	8.0-12.0
C46 wax ester	0.5	0.0-3.0

Experimental Setup for Supercritical Methanol

The experimental set-up consisted of a bench-scale, batch-type reactor designed and manufactured to manage SCM's demanding transesterification process conditions, which are characterized by high temperature and pressure, as depicted in Figure 1 (Al-Shanableh & Savas, 2022). This figure's letters are designated as follows: A: Pressure vessel, B: Electrical external heater, C: Hatch (vessel cover), D: Thermocouple, E: Adjusting lever, F: Extruded fins, G: Reactor pressure gauge.

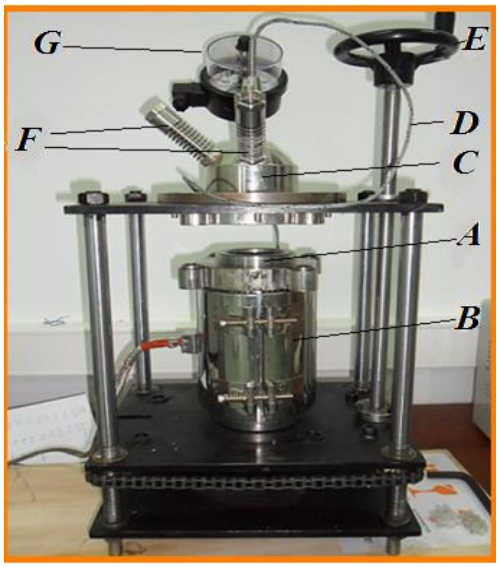

Figure 1. The reactor designed and manufactured for supercritical biodiesel production

The experimental configuration for the one-step supercritical methanol transesterification process was tailored to function effectively under elevated temperatures and pressures. Nitrogen gas was an inert medium to generate pressure, and a pliable high-pressure hose linked the supercritical reactor. This reactor was outfitted with various components, including an external heater, insulating mantle, electromagnetic stirrer, safety valve, pressure gauge, and thermocouple for temperature monitoring. Additionally, a laboratory-grade double-pipe heat exchanger was utilized as the condenser.

Experimental Procedure for Biodiesel Production by Supercritical Methanol

The process of supercritical methanol transesterification of jojoba oil was conducted utilizing the previously outlined experimental arrangement above and adhering to the procedural steps illustrated in the flowchart depicted in Figure 2.

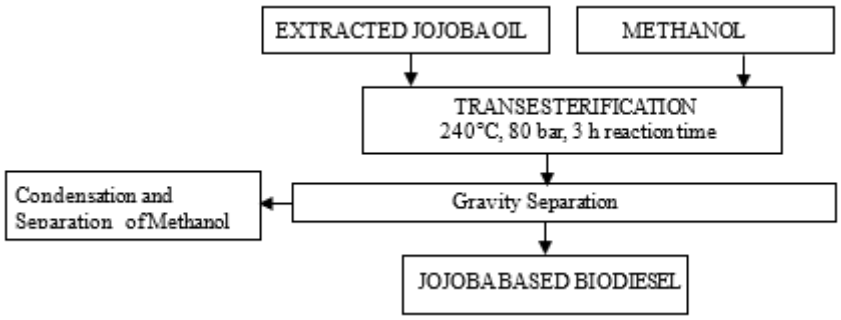

Figure 2. Flowchart for the experimental supercritical methanol procedure of jojoba biodiesel production

The procedure commenced by introducing a blend of extracted jojoba oil and methanol (the oil-to-alcohol molar ratio of 1:41 approximately corresponded to a 1:2 volume ratio) into the supercritical reactor, followed by thorough mixing to achieve a uniform mixture. Subsequently, the reactor was sealed, and temperature and pressure were adjusted to enter the supercritical fluid phase. The reaction duration was arranged as 120 min because this was the optimum duration obtained in the authors' previous study (Al-Shanableh & Savas, 2023). After the designated reaction time was completed, the reaction vessel was removed from the heating jacket to initiate the cooling process. Excess methanol was then transferred to the condenser. At the same time, the product mixture was poured into the distillation column to separate volatile fatty alcohol fraction from fatty acid methyl esters of jojoba (FAME). All other types of vegetable oils/animal fats are made up of triglyceride molecules, so the results of the transesterification process will be glycerol and FAME, unlike the transesterification of jojoba oil. Following the production and separation process, quality assurance measures were implemented to assess the biodiesel's properties, such as viscosity, cloud point, and pour point, following relevant ASTM and EN-ISO standards.

Results and Discussion

Biodiesel Yield by Supercritical Methanol Transesterification

Several physicochemical properties of the end product of supercritical methanol transesterification of jojoba were analyzed to assess its suitability as fuel for diesel engines. Testing methods from ASTM, EN, or ISO standards were employed, and the obtained values for the sample were compared with reference values for biodiesel according to ASTM D6751 and EN 14214. The results are presented in Table 3.

Table 3. Physicochemical fuel properties of the jojoba-biodiesel produced

	Method	**Limits**	**Jojoba based FAME**
Kinematic viscosity at 40 ˚C (mm^2/s)	ASTM D 445	1.9-6.0	5.210
Higher heating value (MJ/kg)	ASTM D 4809	--	44.3
Ester contents (wt %, max.)	EN 14103	96.5	97.8
Linoleic acid methyl esters (wt %, max.)	EN 14103	12.0	0.4
Iodine value (g I_2 / 100 g, max)	EN 14111	120	54
Cloud point (˚C)	ASTM D 2500	--	12
Cold filter plugging point (˚C)	ASTM D 6371	--	10
Pour point (˚C)	ASTM D 97	--	8.6

All measured properties were within the range of ASTM/ EN standards. The authors' previous studies with various vegetable oils have proven that high unsaturated fatty acids content shows low cold flow properties (Al-Shanableh et al., 2023). Three cold flow properties, namely cloud point, cold filter plugging point, and pour point of jojoba-based biodiesel, are relatively high despite having 97% monounsaturated fatty acids content. This is because jojoba oil is a wax, and jojoba-based biodiesel not only contains FAME but is also a mixture of fatty acid methyl esters and fatty alcohols.

Conclusion

Utilizing supercritical methanol to produce biodiesel from jojoba seeds harvested in the Mesaoria Plain of Cyprus offers a promising pathway toward sustainable fuel production, an alternative to traditional diesel. The supercritical fluid approach demonstrated notable efficiency and decreased process time compared to base-catalyzed transesterification. The single-step procedure in the bench-scale reactor achieved considerable conversion rates within a comparatively brief timeframe. These findings suggest that the supercritical method holds promise for scaling up biodiesel production, primarily owing to its abbreviated reaction duration.

Recommendations

Further investigation and fine-tuning of process parameters can elevate conversion rates further and enhance overall efficiency in biodiesel production utilizing supercritical methanol. With adaptability to arid climates and an efficient conversion process, jojoba presents a viable feedstock for biodiesel production in Cyprus. However, successful implementation requires careful consideration of technical, economic, and environmental factors and long-term commitment to sustainable development goals..

Scientific Ethics Declaration

The authors declare that the scientific ethical and legal responsibility of this article published in EPSTEM journal belongs to the authors.

Acknowledgements or Notes

* This article was presented as presentation at the International Conference on Research in Engineering, Technology and Science (www.icrets.net) held in Tashkent/Uzbekistan on August 22-25, 2024.
* The authors would like to express their sincere thanks to Assoc. Prof. Dr. Ali Evcil for his contributions during the reactor design and biodiesel production phase.
* The authors would also like to acknowledge to Eng. Birgul Kaya, and Eng. Muzaffer Kaya for their endless financial and moral support during the manufacturing and testing of the reactor.
* The Near East University Research Fund supported this work under project no. YDU/2010-2-21.

References

Al-Shanableh, F. (2017). *Characterization of cold flow properties of biodiesel transesterified from waste frying oil* (Doctoral dissertation).

Al-Shanableh, F., Bilin, M., Evcil, A., & Savaş, M. A. (2020). Optimization of oil extraction from jojoba seeds of mesaoria plain in screw expelling using Taguchi design. *Management*, *4*(20), 28.

Alshanableh, F., & Savas, M. A. (2022). Material selection of batch type supercritical reactor for biodiesel production. *The Eurasia Proceedings of Science Technology Engineering and Mathematics*, *21*, 477-483.

Alshanableh, F., & Savas, M. A. (2023). Biodiesel production using supercritical methanol in bench-scale reactor. *The Eurasia Proceedings of Science Technology Engineering and Mathematics*, *23*, 19-25.

Al-Shanableh, F., Bilin, M., Evcil, A., & Savas, M. A. (2023). Estimation of cold flow properties of biodiesel using ANFIS-based models. *Energy Sources, Part A: Recovery, Utilization, and Environmental Effects*, *45*(2), 5440-5457.

Bilin, M., Alshanableh, F., Evcil, A., & Savas, M. A. (2018, October). A comparative examination of the quality of Jojoba seed oil harvested on the mesaoria plain of Cyprus Island. In *2018 2nd International Symposium on Multidisciplinary Studies and Innovative Technologies (ISMSIT)* (pp. 1-4). IEEE.

Bilin, M., Al-Shanableh, F., Evcil, A., & Savaş, M. A. (2020, October). Potential of Jojoba Agriculture in Mesarya Plain of Cyprus Island. In *2020 4th International Symposium on Multidisciplinary Studies and Innovative Technologies (ISMSIT)* (pp. 1-4). IEEE.

Bouaid, A., Bajo, L., Martinez, M., & Aracil, J. (2007). Optimization of biodiesel production from jojoba oil. *Process Safety and Environmental Protection*, *85*(5), 378-382.

Canoira, L., Alcantara, R., García-Martínez, M. J., & Carrasco, J. (2006). Biodiesel from Jojoba oil-wax: Transesterification with methanol and properties as a fuel. *Biomass and Bioenergy*, *30*(1), 76-81.

Bilin, M., Alshanableh, F., Evcil, A., & Savas, M. A. (2018, October). A comparative examination of the quality of Jojoba seed oil harvested on the mesaoria plain of Cyprus Island. In *2018 2nd International Symposium on Multidisciplinary Studies and Innovative Technologies (ISMSIT)* (pp. 1-4). IEEE.

Knothe, G. (2010). Biodiesel and renewable diesel: a comparison. *Progress in energy and combustion science*, *36*(3), 364-373.

Lei, Q., & Li, T. (2015). Functional monoesters of jojoba oil can be produced by enzymatic interesterification: reaction analysis and structural characterization. *European Journal of Lipid Science and Technology*, *117*(5), 630-636.

Saka, S., & Kusdiana, D. (2001). Biodiesel fuel from rapeseed oil as prepared in supercritical methanol. *Fuel*, *80*(2), 225-231.

Selim, M. Y., Ghannam, M. T., Abdo, B. N., Attai, Y. A., & Radwan, M. S. (2022). Raw jojoba oil as a sustainable fuel to diesel engines and comparison with diesel fuel. *Energies*, *15*(16), 5770.

Singh, N. K., Singh, Y., & Sharma, A. (2022). Optimization of biodiesel synthesis from Jojoba oil via supercritical methanol: A response surface methodology approach coupled with genetic algorithm. *Biomass and Bioenergy*, *156*, 106332.

Author Information

Filiz Al-Shanableh
Near East University
Nicosia, Mersin 10, Türkiye
Contact e-mail: *filiz.shanableh@neu.edu.tr*

Mahmut A. Savas
Near East University
Nicosia, Mersin 10, Türkiye

Metin Bilin
Near East University
Nicosia, Mersin 10, Türkiye

To cite this article:

Al-Shanableh, F., Savas, M.A. &Bilin, M. (2024). Biodiesel production by supercritical methanol from jojoba seeds harvested in the Mesaoria plain of Cyprus. *The Eurasia Proceedings of Science, Technology, Engineering & Mathematics (EPSTEM), 29*, 254-259

The Eurasia Proceedings of Science, Technology, Engineering & Mathematics (EPSTEM)
ISSN: 2602-3199

The Eurasia Proceedings of Science, Technology, Engineering & Mathematics (EPSTEM), 2024

Volume 29, Pages 260-274

ICRETS 2024: International Conference on Research in Engineering, Technology and Science

Application of Electrical Resistivity Tomography for Improved Blast Movement Monitor Locations Planning

Dimitar Kaykov
University of Mining and Geology "St. Ivan Rilski"

Ivaylo Koprev
University of Mining and Geology "St. Ivan Rilski"

Danail Terziyski
University of Mining and Geology "St. Ivan Rilski"

Abstract: Blast-induced rock movement is a highly variable phenomenon which depends on numerous factors. Rock type and its deriving physical and mechanical properties are among such factors, which are crucial to be available prior to planning the locations where each monitor is placed. Hence, Electrical Resistivity Tomography (ERT) was used to acquire additional rock mass data for several benches of an open-pit mining operation. ERT is considered a valuable tool in mine planning. By providing information about the subsurface electrical resistivity distribution, ERT helps in determination of geological structures, composition of the ground and helps assessing potential hazards. A total of 21 profiles were measured, which allowed for relevant data to be obtained regarding each monitor's location. Results from the study showed that blast movement measurements from different rock-type zones do not differ in a statistically significant manner. However, substantial differences were uncovered regarding the mode of movement vectors by using Kernel density estimation (KDE). These results proved that ERT is a fast and reliable support method for establishing different rock mass zones and for location planning of blast movement monitors and blast design optimization prior to drilling.

Keywords: Blast movement, Electrical resistivity tomography (ERT), Kernel density estimation (KDE)

Introduction

Open-pit blasting is a phenomenon that has been extensively studied during the last 50 years. Certain patterns of blast-induced rock movement have been identified, which supplement the fundamental principles of rock blasting and rock fracturing (Zhang, 1994; Gilbride et al., 1995; Gilbride et al., 1996; Thornton et al., 2005; Thornton, 2009a; Thornton, 2009b; Engmann et al., 2013; Eshun and Dzigbordi, 2016). Some researchers, however, base their conclusions purely on practical experience and a small number of observations under certain conditions (Zlatanov et al., 2008). Robust mathematical or statistical methods are rarely employed for proof of concept. Recent breakthroughs in the use of various numerical methods in the field of blast movement have revealed crucial insights that allow a better understanding of the expected outcome of a blast. Machine learning algorithms based on predictors related to the mechanical characteristics of the rock mass, as well as blast design parameters, have achieved highly accurate prediction results (Yu et al., 2019; Yu et al., 2020; Yu et al., 2021a; Yu et al., 2021b). Deterministic models based on mechanical principles have been extensively investigated (Furtney et al., 2009; Tordoir et al., 2010; Furtney et al., 2016; Preece et al., 2015; Preece et al., 2016), but they have only lately emerged as an accurate modelling tool. DNA Blast Group, Itasca and Orica have also provided commercially viable tools which offer physics-based simulations which achieve superb prediction accuracy (https://dnablast.com/?lang=en; https://www.orica.com/Products-Services/Digital-Solutions/orepro-3d; Fu et al.,

2023). However, the stochastic element in these approaches is limited to some extent for the sake of time required for computations. Alternatively, statistical modelling has also produced sufficient accuracy for interpreting the probable position of post-blast ore zones, which can be further used to calculate appropriate dig lines (Vasylchuk & Deutsch, 2019; Hmoud & Kumral, 2021; Hmoud & Kumral, 2022). In comparison to prior ways of using Kriging, triangulation, or Inversed distance weighing (Taylor & Firth, 2003), these modern approaches give not only a better estimate of the movement or the anticipated losses and dilution, but also statistics indicating the prediction's uncertainty from the simulation of different scenarios. Moreover, latest studies following this modelling framework have introduced the concept of entropy regarding the lack of information with respect to ore zones (Hmoud & Kumral, 2023).

Nonetheless, all these approaches are still limited to providing a complete understanding of the three-dimensional nature of blast movement and its economic implications. The reason behind this is because they are dependent on distinct sets of assumptions regarding the importance of different input or output features for the model. From a statistical standpoint, the horizontal movement vector provides critical information of great value regarding the magnitude and overall direction of the 3D movement vector. Vertical movement, on the other hand, causes "vertical dilution" and should thus be accounted for as accurately as possible.

Three-dimensional models for grade control and muckpile shape prediction have also emerged as a direct result of the improved accuracy regarding modelling blast movement. Hence, to this date they are considered the industry standard for blast movement modelling. Indeed, deterministic physics-based models appear to be more versatile for modelling 3D movement in different scenarios regarding panel shape, spatial configuration of multiple free faces, buffer presence, explosive and booster types, spatial distribution of rock types, etc. In contrast, statistical models based on physical measurements may not always offer a complete picture of the blasting process, since a significant amount of information is needed. Moreover, some parameters are difficult, if not impossible, to assess in-situ. Therefore, in order to gain meaningful insights in terms of empirical measurements, a design of experiments approach and careful planning is required to gather a meaningful amount of information from a reasonable number of shots. Both approaches, indeed have their pros and cons, however, to this date the physics-based approach has emerged as a better choice for commercial use with the addition of empirical measurements. The stochastic approach primarily serves as a pre-processing tool for gaining additional insights, for model calibration and as a topic for academic research. Nonetheless, the authors of this paper believe that a stochastic approach is more suited to the random nature of a blast and hence its implementation is absolutely necessary. Moreover, this approach can be universally applied to both empirical and artificial (simulated) data. Indeed, there can be some scepticism regarding the amount of bias, as well as the precision and accuracy of physical measurements, based on Blast movement monitors (BMMs) developed by Blast Movement Technologies (BMT) (https://hexagon.com/solutions/mine-blast-movement-monitoring). However, to this date they remain a reliable tool for empirical data acquisition.

Studied Conditions

A two-year-long study was conducted on the "Ada Tepe" gold project, an open pit mine in south-eastern Bulgaria (Kaykov & Terziyski, 2023; Koprev et al., 2022, Terziyski et al., 2021). On 5-metre benches, blasting activities were carried out twice a week. For all shots, vertical drillholes with a diameter of 105 mm were used. The operation employed two types of explosives: ANFO and packaged water gel. Furthermore, two types of drilling patterns were commonly used, depending on the rock hardness: 3x3.5 m for medium-hard rock and 3.2 x 3.7 m for softer rock types. The overall blast panel powder factor ranged between 0.34 and 0.46 kg/m³ over the studied period. After blasting, the average rock size was estimated to be roughly 250 mm. All drill patterns are staggered and initiated in an echelon pattern with a NONEL system, with a 42 ms delay between rows and a 17 ms delay within rows. This results in an initiation sequence in which the shot's isochrones are roughly parallel to the front free face of the explosion. Each blast hole is detonated with a bottom charge of either a 450 g cast boosters or 808 g packaged water gel. Due to the nature of the mined commodity, excavators undertake selective mining in two separate flitches for each bench after blasting. Blast Movement Monitors (BMMs) are employed to track blast movement. In the studied conditions, the number of monitors for a single shot can vary up to 8 monitors per flitch depending on the number of pre-blast ore polygons in each flitch. After the blast, a technician utilises a specialised radio frequency detector to locate each BMM’s post-blast location inside the muckpile.

Over 1000 blast monitors were used during the period of the research. For most observations, two monitors are deployed for a single monitoring drillhole. Apart from recalculating the positions of ore polygons after blasting, all of the collected data was used for statistical analyses and predictive modelling. Finally, the gathered data was

used to identify the level of influence for different factors in terms of decomposing the blast movement vectors into their respective components.

With the use of a staggered drilling pattern, BMMs are placed on the boundaries of three Voronoi cells, as shown on the left-hand side of Figure 1. This can be considered a good practice for the studied conditions, especially when the local powder factor of the neighboring Voronoi cells is taken into consideration. It is assumed to be the ratio between the amount of explosive and the volume of the Voronoi cells falling into an arbitrary radius from the assumed BMM location. Hence, zones which have an insufficient or an excessive local powder factor should be avoided for better representativity of the blast movement vector.

The echelon firing pattern allows for ensuring a near-parallel movement direction for all zones of the panel, which follows a direction perpendicular to the isochrone, shown on the right-hand side of Figure 1. Therefore, the choice of a BMM location in terms of movement direction has little to no constraints. Of course, BMMs should not be placed near the boundaries of the blast panel as these locations are edge cases and can significantly differ from other locations near the center of the panel. Placing BMMs near auxiliary drillholes is also considered to be non-representative as its supposedly adjacent Voronoi cells do not follow the uniform shape of the pattern and hence can influence the magnitude of movement. Moreover, the isochrones also change their orientation, which would influence the direction of movement. Such zones which can be considered as constraints can be the ones near drillholes 117 and 92 from Figure 1.

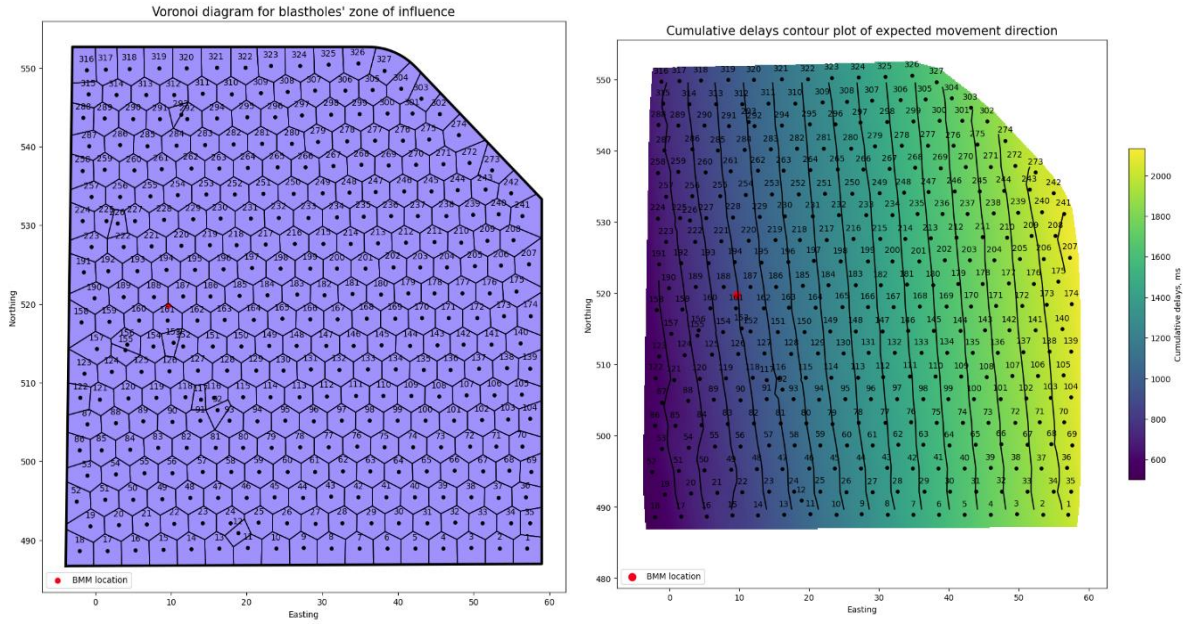

Figure 1. Blast panel conditions influencing the choice of monitoring locations
Left-hand side – Voronoi cells of drillholes' area of effect
Right-hand side – Cumulative delays contour plot

These rules are trivial and are already massively applied in open-pit mines which utilise BMMs. However, little to no information is present (to the authors' knowledge) about how rock mass zones can influence the choice of a BMM's location for the blast panel.

As a result, the purpose of this article is to establish how blast-induced rock movement for both observed flitches can be affected by different rock mass zones. For the purpose Electrical resistivity tomography (ERT) was used as a comprehensive and easy-to-implement method for gathering the necessary data regarding different rock type zones. ERT is considered to be versatile method proving its efficiency in different environments to mining, including acquiring supplementary information regarding the geological composition of blast panels (Grigorova, 2020), quarry's reserves (Grigorova & Koprev, 2019) or for monitoring the saturation level of mine waste facilities (Grigorova, 2023; Tomova & Kisyov, 2023). The total number of used profiles was 21, spanning over a total of 2935 m. The first group of 13 profiles (2 to 14) reached a depth of 25 m, spanning between elevations 445 m and 420 m, while the second group of profiles covered a depth of 15 m, spanning between elevations 470 m and 455 m. Figure 2 represents the studied profiles for the mining operation.

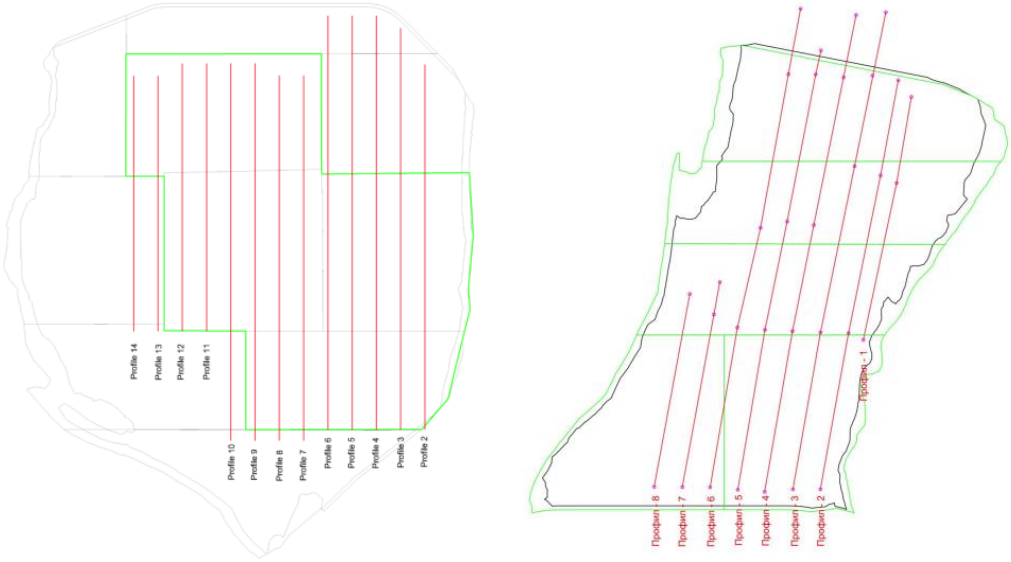

Figure 2. Studied profiles for the mining operation

Upon thorough analysis of the gathered data, it was determined that the electrical resistivity of the rock mass falls within the range of 100 Ωm to 4500 Ωm. The Shavar formation comprises of clay materials, metallic oxides, and sulphide minerals, all of which possess the ability to conduct substantial electrical current through the material itself. Consequently, differentiating between sulphide mineralized rocks and clay materials presented a significant challenge. Following the interpretation process, the researched geoelectrical sections have been classified into four distinct electrical resistivity zones, each characterized by unique lithological features:

- **Zone 1**: This environment is typified by the lowest values of electrical resistivity, ranging from 100 Ωm to 550 Ωm. This zone likely delineates a stratum of Shavar formation sediments, composed of metamorphic clasts and clays.
- **Zone 2:** The zone exhibits relatively higher values of electrical resistivity, ranging from 550 Ωm to 1500 Ωm. Hence, it is assumed that this environment predominantly consists of carbonite breccia and breccia conglomerates.
- **Zone 3:** This zone is marked by nearly the highest electrical resistivity values, ranging between 1200 Ωm to 4000 Ωm. These results show that this environment likely represents siltstones characterized by a high content of quartz or muscovite.
- **Zone 4:** Similarly, featuring high electrical resistivity values, ranging from 2500 Ωm to 4500 Ωm, this zone is attributed to decoupling after blasting in the studied area. Hence, it can be assumed that the zone is a direct consequence of anthropogenic activities.

The conditions of the study include the use of a Wenner electrode array on the ground surface, where the electrodes were placed with a spacing of 5 m. Data was acquired with an automated multi-electrode resistivity meter Terrameter SAS 1000 and was processed via the RES2DINV computer software. An exemplary profile of the studied rock mass can be seen on Figure 3, which was a part of a previous extensive ERT study (Grigorova, 2020).

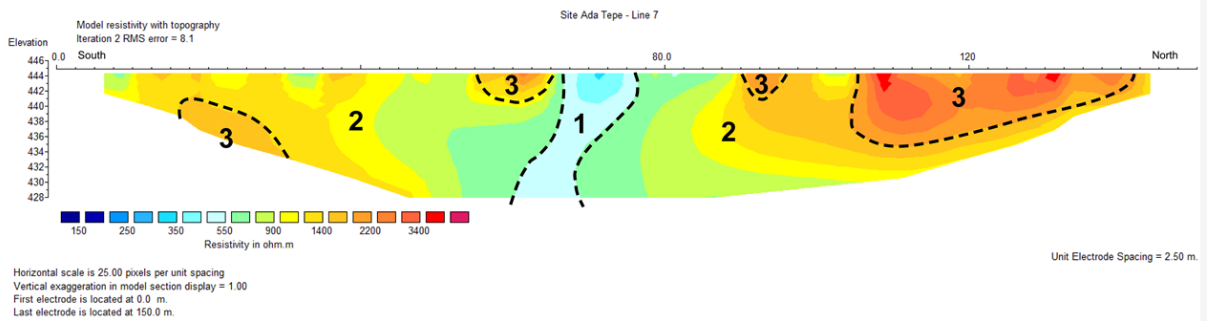

Figure 3. Exemplary ERT profile of the studied rock mass

The covered area by the ERT method allowed for labelling the rock mass zone for a total of 41 blast panels. The obtained data and its relevant interpretations regarding the four rock mass zone classes was used to obtain a sub-sample of the general dataset for those BMMs which were placed in either of the zones. No monitors were placed in Zone 4 and for this reason it was discarded from the analysis. Hence, only zones 1, 2 and 3 were considered as a supplementary categorical variable which was used for further analysis and verifying its influence on the blast movement observations. In order to gain a better understanding of the effect of different rock mass zones, the studied dataset was comprised of observations from shots utilizing only ANFO with a local powder factor value in the interval 0.30-0.40 kg/m³. The reason behind this choice is that the number of observations of shots using a packaged watergel in the cases where ERT data was available were scarce. Hence, they were discarded for this case study. Moreover, the powder factor in the considered range is also representative with the overall powder factor used in most blasts. Hence, these assumed conditions aim to obtain a dataset which closely resembles the conditions of a typical shot. All these conditions used to filter the general dataset led to the use of a sample size of 52 pairs of observations of top and bottom flitch movement. The dataset was further divided into three sub-samples for each rock zone, where 25 pairs of observations were for Rock mass zone 1, 17 for Rock mass zone 2 and only 10 for Rock mass zone 3. Moreover, all observations are based on monitors situated at least 15 m away from the free face and hence they are representative of the blast movement phenomenon for most of the panel, excluding the edge effects.

Methodology

Studied Variables

Each 3D movement vector (M_{3D}) can be decomposed into two main components – the horizontal movement vector (M_H) and the vertical movement vector (M_V). One can also derive the angle of inclination for the 3D movement vector (α_V) and heave effect of the blast, which is calculated as the difference between the elevations of the pre- and post-blast surfaces directly above the monitor. In addition, the azimuth of the movement vector is provided by the report. However, a more rigorous analysis would require the calculation of the ideal angle of horizontal movement relative to the position where the monitor is located, based on the gradient of the cumulative delay field for the blast, as shown via surface plot in Figure 1. As a result, the angle of horizontal deviation can be determined for each monitor as the difference between the ideal direction of horizontal movement and the azimuth of its actual movement. This resulted in the definition of the deviation angle for horizontal movement (α_H). The cumulative delay field and the isochrones for this study were generated from the firing patterns using a Python 3.11 script. Thus, using trigonometric operators, the horizontal movement vector (M_H) is divided into its two components - the horizontal movement in the direction of the free surface (M_{Hff}) and the vector of horizontal deviation towards the first initiated drillhole of the pattern (M_{Hdev}). Both vectors can be estimated via the following equations:

$$M_{H_{ff}} = M_H . \cos \alpha_H \tag{1}$$

$$M_{H_{dev}} = M_H . \sin \alpha_H \tag{2}$$

A visual representation of these variables can be seen on Figure 4.

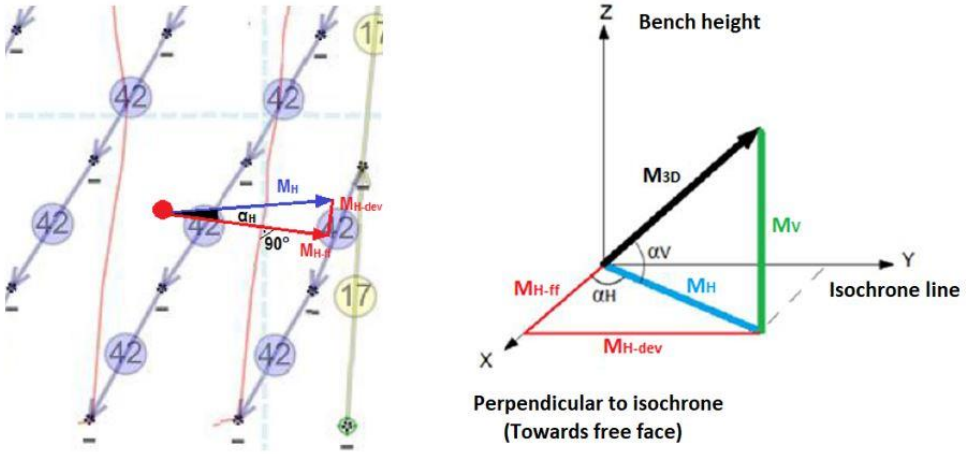

Figure 4. Variables used for the decomposition of 3D blast movement vectors

The components M_{Hff} and M_{Hdev} can assume negative values and they signify the magnitude and direction from the initial position of the BMM. A positive value for the M_{Hff} would indicate perpendicular movement from the isochrone, towards the free face, while a negative value would signify movement opposite the free face. Although these measurements are very rare, such outliers can exist and are interpreted as a potential misinterpretation of the BMM's location. Considering the M_{Hdev} vector component, a positive value signifies movement directed towards the drillhole which was fired first for the echelon pattern, while a negative value indicates the opposite direction. Using both positive and negative values for tracking blast movement can be interpreted as the change of position in the three orthogonal directions from the initial position of the BMM. Therefore, using all three values of M_{Hff} , M_{Hdev} can provide one to estimate the post-blast position of each monitor for an arbitrary location from the blast panel.

As previously discussed, the main groups of factors known to influence blast movement are blast design parameters and rock properties. Numerous writers (Thornton, 2009a; Thornton, 2009b; La Rosa and Thornton, 2011; Poupeau et al., 2019; Yu et al., 2019) have already investigated the impact of these factors on blast movement. D. Thornton (2009a, 2009b) previously explored the difference in flitch movement as well as movement in buffered and free face blasting. Furthermore, Z. Yu et al. (2019, 2020) studied the relationships between the M_{3D}, M_H and M_V variables. The correlations between horizontal movement vectors for several flitches was introduced by Hmoud and Kumral (2021, 2022). However, the relationship between all vector components of both flitches is not thoroughly investigated. Hence, in order to analyse its degree of strength between the vector components for both flitches, a traditional approach was initially used by estimating two non-parametric measures – the Spearman and Kendall correlation coefficients.

Statistical Methods

Conventional descriptive statistics such as mean, median, standard deviation and inter-quartile range (IQR) were obtained. Rock mass type was assumed to be a categorical variable for the purpose of hypothesis testing in order to determine how flitch movement differs in all zones. Due to the non-normal nature of the data, non-parametric tests were performed to investigate blast-induced rock movement under various conditions. As top and bottom flitch movement depend on the same monitoring hole position, all hypothesis tests were performed separately for both flitches. The hypothesis tests which were assumed to be best-suited for this analysis include the Kruskal-Wallis test (Kruskal and Wallis, 1952), Mood's test (Corder and Foreman, 2014) and Levene's test for equality of variances (Levene, 1960). The significance level of the tests is assumed to be 0.05. Should the p-value remain below this threshold, the null hypothesis is to be rejected. Table 1 displays the hypothesis tests that were applied, their purpose, and the stated null hypotheses.

The three considered tests are used for comparing the values of all three vector components. Moreover, if the null hypothesis is rejected in either of the cases, this is an indicator that the central tendency or variance of the investigated movement vector component for at least one rock mass zone is significantly different than the other zones. However, if the null hypothesis is failed to be rejected, this does not indicate that there is no observable difference regarding the variance and central tendency of the vector components' values. On the contrary, the hypothesis should be retained until further evidence suggests otherwise.

Table 1. Applied hypothesis tests

Performed test	**Purpose**	**Null hypothesis (H_0)**
Kruskal-Wallis	Investigate the influence of rock mass zone regarding the central tendency (median) for all vector components	All medians are equal
Mood's test	Investigate the influence of rock mass zone regarding the central tendency (median) for all vector components	All population medians are equal
Levene's test	Investigate the influence of rock mass zone regarding the variances for all vector components	All variances are equal

Kernel Density Estimation

As the provided sample sizes can be a limitation for obtaining accurate results from the hypothesis testing regarding some rock mass zones, an alternative analytical tool was also considered. Kernel Density Estimation

(KDE) is a powerful non-parametric method utilized for the estimation of the probability density function (PDF) of a random variable. Unlike conventional parametric approaches, KDE does not presume any specific underlying data distribution. Instead, it utilizes the data itself to generate a smooth estimation of the distribution. This makes it a versatile tool for data analysis and visualization, especially in the cases where limited number of observations are available and an initial estimation regarding the population's distribution is required. At its essence, KDE involves the placement of a smooth, symmetrical function, referred to as a kernel over each data point. The collective contributions from each kernel are then aggregated to produce a continuous estimate of the density function (Gramacki, 2017). The mathematical formulation of this relationship for a given dataset is as follows:

$$\hat{f}(x) = \frac{1}{nh}\sum_{i=1}^{n} K\left(\frac{x - x_i}{h}\right) \tag{3}$$

where

$\hat{f}$ – estimated density at point x;
K – kernel function;
h – bandwidth;
x_i – i-th observation from the dataset;
n – sample size.

This method provides an estimate of the actual PDF of the data, thereby offering a more precise representation compared to histograms, which may be susceptible to bin widths. Moreover, KDE contributes to establishing intrinsic details of the dataset, which are difficult to be estimated through a parametric approach. Such details can support gathering evidence for the presence of a potential multimodal PDF. Hence, its primary aim is to establish an estimation of the value for a single or multiple modes of the dataset.

The key components of KDE are the kernel function and bandwidth. The **kernel function** denotes a smooth, symmetrical function that integrates to the value of one. Common selections can include the Gaussian (normal) kernel, Epanechnikov kernel, uniform kernel, triangular kernel, etc (Gramacki, 2017). The Gaussian kernel's extensive usage is attributable to its smoothness and mathematical properties. Mathematically, a Gaussian kernel is defined as:

$$K(u) = \frac{1}{\sqrt{2\pi}} e^{-\frac{u^2}{2}} \tag{4}$$

where

$$u = \frac{x - x_i}{h} \tag{5}$$

For the purpose of this case study a Gaussian kernel was assumed, as it was believed to be better suited to the nature and the scale of the data. The purpose of the Gaussian kernel is to simulate the potential presence of random errors regarding the measurements of each BMM's location.

The bandwidth parameter regulates the width of the kernel function and consequently, the level of smoothing in the density estimation process. A smaller bandwidth results in a more intricate estimate with reduced smoothing, leading to more prominent noise, while a larger bandwidth yields a smoother estimate. The selection of an appropriate bandwidth is pivotal as it optimizes the trade-off between bias and variance. Various methodologies, including cross-validation, Silverman's rule of thumb, and Scott's rule, can aid in identifying an optimal bandwidth for each density function. Another general rule for finding the best bandwidth value is to avoid under- and oversmoothing of the PDF, as the aim is to iteratively alter the signal to noise ratio until meaningful interpretations can be made.

This approach, based on KDE, can be considered very well-suited to the stochastic nature of blast movement, especially in cases where different physical and mechanical rock properties are binned under a single rock mass zone category. Moreover, in these cases multimodality is suspected to be present and therefore, a parametric approach could be insufficient. Hence, KDE would allow for one to establish intrinsic details of the potential PDF of each movement vector component for the sake of improving BMM locations planning.

Results

Descriptive statistics for each rock mass zone are provided in tables 2, 3 and 4 respectively. According to the average and median values, movement occurs with a significantly smaller magnitude than other operations of similar bench heights. This can be attributed primarily to the use of a very low powder factor due to the presence of softer rock formations. The smaller amount of explosive utilised, and as a result the smaller amount of produced gas products leads to the observed results.

Table 2. Descriptive statistics of blast movement for Rock mass zone 1

Flitch	Vector	Mean	Std. dev	Median	IQR
TOP	M_{Hff}	0.88	0.30	0.80	0.50
	M_{Hdev}	-0.09	0.27	-0.13	0.34
	M_V	0.45	0.15	0.45	0.15
BOT.	M_{Hff}	0.75	0.38	0.70	0.46
	M_{Hdev}	-0.03	0.30	-0.03	0.31
	M_V	0.13	0.18	0.15	0.19

Table 3. Descriptive statistics of blast movement for Rock mass zone 2

Flitch	Vector	Mean	Std. dev	Median	IQR
TOP	M_{Hff}	1.00	0.37	1.01	0.53
	M_{Hdev}	-0.14	0.26	-0.11	0.20
	M_V	0.42	0.25	0.37	0.22
BOT.	M_{Hff}	0.80	0.39	0.73	0.55
	M_{Hdev}	-0.12	0.28	-0.14	0.43
	M_V	0.08	0.25	0.12	0.19

Table 4. Descriptive statistics of blast movement for Rock mass zone 3

Flitch	Vector	Mean	Std. dev	Median	IQR
TOP	M_{Hff}	0.88	0.47	0.95	0.67
	M_{Hdev}	0.11	0.45	0.00	0.53
	M_V	0.50	0.35	0.42	0.27
BOT.	M_{Hff}	0.73	0.48	0.63	0.84
	M_{Hdev}	0.05	0.34	0.08	0.56
	M_V	0.12	0.20	0.05	0.21

Taking the M_{Hff} vector into account, movement for both flitches and all three rock mass zones exhibit a substantial level of variation. The observable difference between the mean and median values for all movement vectors is a direct result of dealing both with slightly positively and negatively skewed PDFs. Hence, this led to the choice of using the forementioned non-parametric hypothesis tests, instead of the traditionally applied ANOVA and Bartlett's test.

Table 5 displays the results of the applied tests and the decision made with respect to the null hypothesis. Results show that for both flitches and all movement vector components there is no statistically significant difference in the observed results. This can be interpreted as the lack of any practically meaningful difference between movement in each of the studied rock mass zones. Indeed, this interpretation has some reason behind it, as one of the key factors directly influencing the magnitude of blast movement is the powder factor and its respective volume of gas products distributed to the amount of rock mass moved.

Table 5. Results from hypothesis testing regarding differences in the movement vector components on both flitches in different rock mass conditions

Studied flitch		**TOP**			**BOTTOM**		
Vector		M_{Hff}	M_{Hdev}	M_V	M_{Hff}	M_{Hdev}	M_V
Mood's test	*p* value	0.641	0.364	0.129	0.952	0.211	0.779
	Decision	*Retain* H_0	*Retain* H_0	*Retain* H_0	*Retain* H_0	*Retain* H_0	*Retain* H_0
Kruskal-Wallis test	*p* value	0.368	0.276	0.571	0.849	0.319	0.796
	Decision	*Retain* H_0	*Retain* H_0	*Retain* H_0	*Retain* H_0	*Retain* H_0	*Retain* H_0
Levene's test	*p value*	*0.393*	0.185	0.189	0.324	0.690	0.688
	Decision	*Retain* H_0	*Retain* H_0	*Retain* H_0	*Retain* H_0	*Retain* H_0	*Retain* H_0

However, non-parametric tests as robust as they are for non-normally distributed data, could also be prone to Type II error, i.e. failing to reject the null hypothesis. All three tests can be susceptible to small sample sizes and hence, they can be indeed prone to a Type II error. Therefore, this requires for the use of an alternative approach which could provide a more detailed look into the rationale behind the non-obvious difference in blast movement for different Rock mass zones.

As mentioned above, a good alternative in this case is the use of KDE. Assuming a univariate distribution for each vector component for both flitches yielded the results presented in Figures 5 and 6. The choice of bandwidth in all cases were based primarily on a leave-one-out cross validation with the occasional use of Silverman's rule or a custom choice of value, which provided a balance between under- and oversmoothing. Moreover, the median values are also shown in Figures 5 and 6 with dashed lines for each rock mass zone for the sake of comparison with the estimated mode values.

Indeed, results show that the KDE proves to be suitable for these cases where one aims to establish a mode-based measure of the central tendency for the magnitude of movement in different conditions. Moreover, the difference between the modes of M_{Hff} for the top flitch is substantially different in Rock mass zone 1, compared to the other two zones. Furthermore, this difference is more prominent compared to the one observed for the medians in the three rock mass zones. Another key result is that the variance of the vertical movement component M_V also seems to be different to some extent for Rock mass zone 1, compared to zones 2 and 3. This can be attributed to the predominant presence of clasts in clays for zone 1, which would lead to a substantial decrease in the overall magnitude of movement. Interestingly, the PDF of the horizontal deviation vector M_{Hdev} for Rock mass zone 3 differs from the other ones. This deviation in movement could be a result of the resistance put by harder rock inclusions of quartz compared to the zone of softer breccias. In all cases the deviation vector is predominantly affected by the variance in the delays of the NONEL system, however the movement vector in harder rock formations is slightly more likely to redirect compared to the other cases. A reason behind this phenomenon could be the insufficient local powder factor used for all Voronoi cells located in Rock mass zone 3. However, this aspect of the interpretation requires to be further supported by additional observations, as the observed result can be due to "fatter tails" based on the small sample size of Rock mass zone 3.

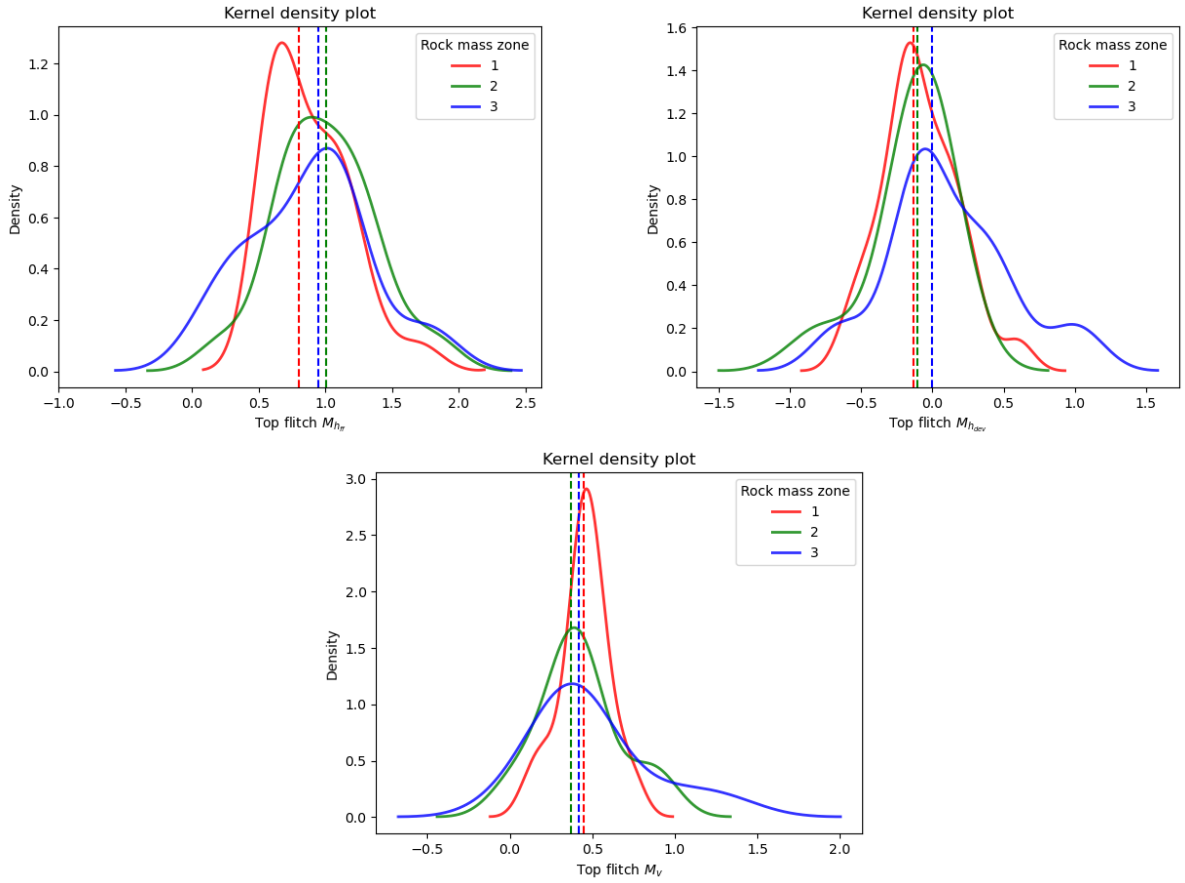

Figure 5. Kernel density plot of blast movement distribution for all three rock mass zones (Top flitch)

An additional insight which was established from the dataset is that there is a substantial difference in the mode value and the PDF of the M_{Hff} vector component for the bottom flitch for Rock mass zone 3, as well (Figure 6). Moreover, there is some evidence suggesting that the observed distribution could be bimodal for Rock mass zone 3. This indicates that an additional factor could be present, but not accounted for in the data associated with the analysed zone. Apart from the discussed key differences, the other movement components for the lower flitch exhibit similarities in their PDFs, which further support the results from the hypothesis tests. As the utilized powder factor and the bench height severely dampen the magnitude of blast movement, it may not be entirely obvious how the use of KDE can be helpful. However, in cases where the difference between the PDF of movement vectors is scaled in magnitude, this can have severe effect on the ore losses, dilution and misclassification.

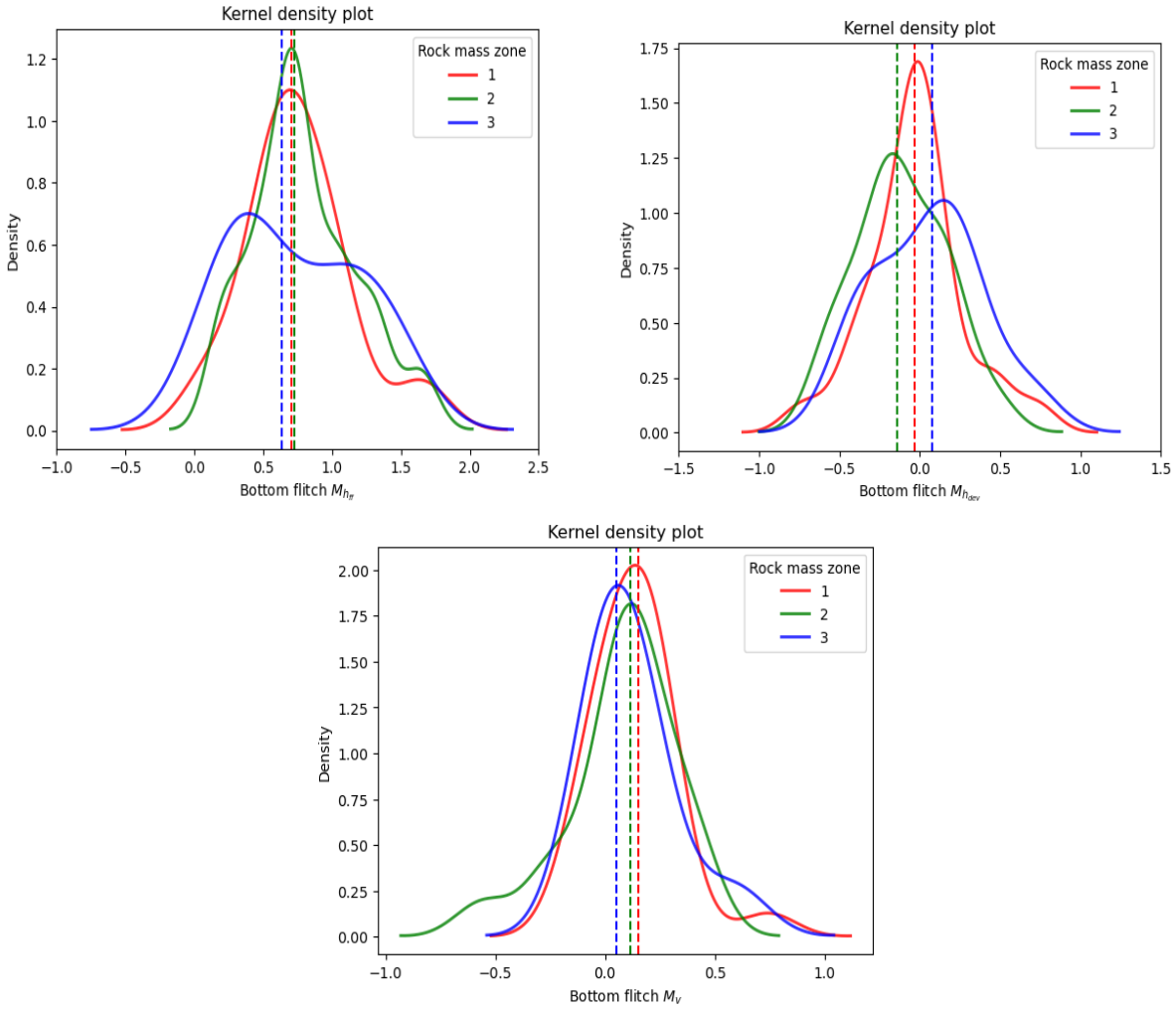

Figure 6. Kernel density plot of blast movement distribution for all three rock mass zones (Bottom flitch)

As blast movement is a complex spatial phenomenon, which is based on multiple dependent variables, it was necessary to extend the univariate PDFs into a higher dimension based on their inter-flitch relationship. The obtained correlation matrices for the three studied rock mass zones are provided below (Figure 7). As the results show, movement vectors on either flitch correlate to a higher degree with their respective vector components on the other flitch. Hence, the dependency of the considered vector components is important for analysing blast movement and should be taken into consideration. Moreover, the established correlation matrices provide an estimate of the differences between the movement component vectors, which are essential for the application of advanced stochastic models, e.g. Monte Carlo or Copula-based simulations.

Therefore, pairing the observations for M_{Hff}, M_{Hdev} and M_V for both flitches can lead to an additional perspective in terms of the joint distribution of each vector component's value based on an arbitrary location of the blast panel. Thus, KDE can also be applied in the case of providing a rough estimation of the bivariate PDF for the top and bottom flitch vector components

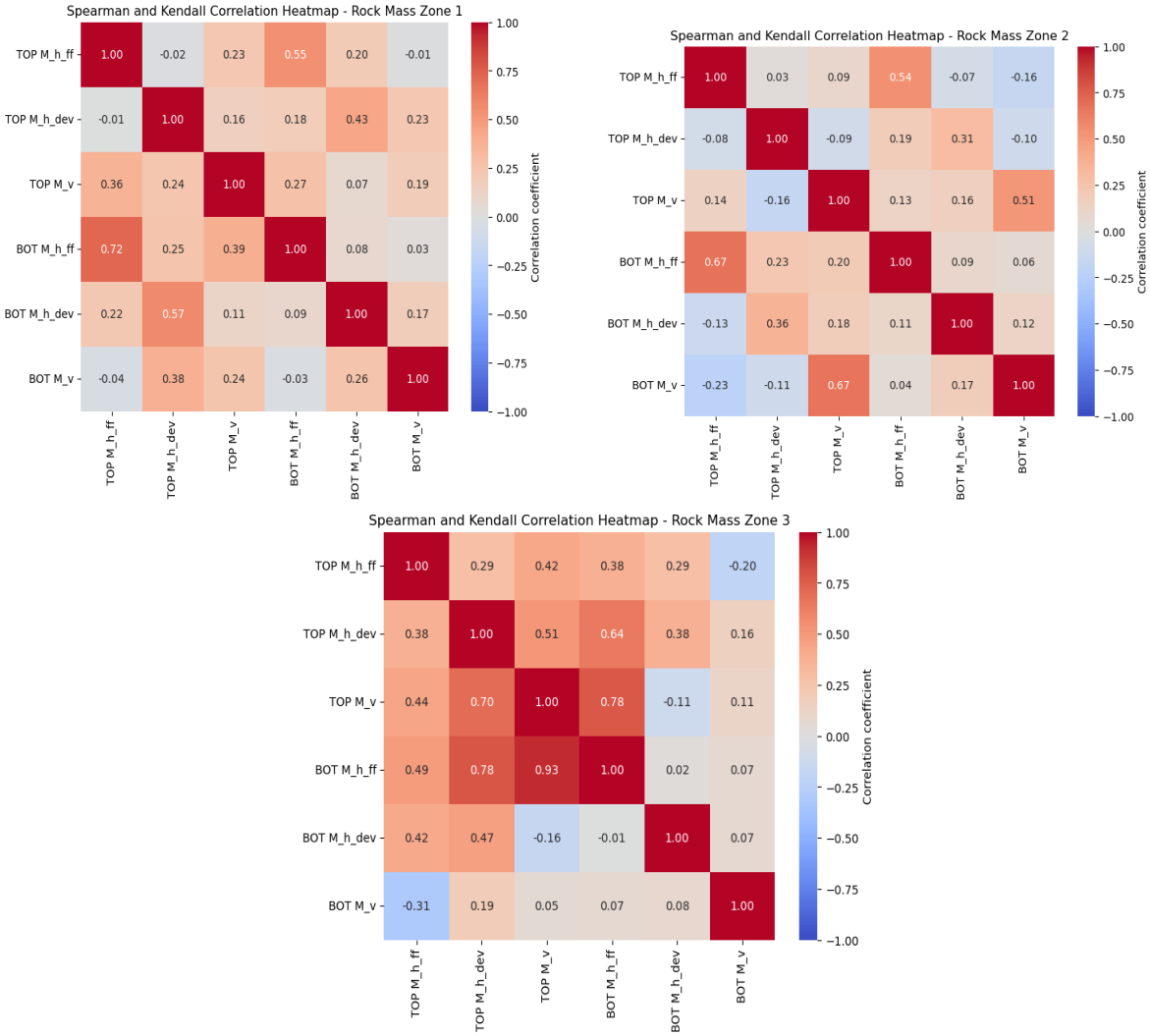

Figure 7. Correlation matrices for all three rock mass zones.
Lower left triangular matrix – Spearman correlation coefficient
Upper right triangular matrix – Kendall correlation coefficient

Figure 8 represents the bivariate PDF for all three movement vector components. The "x"-marks for each distribution are the locations of the median values for each movement vector for both flitches. Once more, KDE has provided a key insight for the central tendency of the joint distribution of the movement vectors for an arbitrary monitoring location. Indeed, the mode and median values can differ significantly, as seen for the M_{Hff} and M_V components in Figure 8. Moreover, the KDE has provided a comprehensive way of establishing several important aspects of the analysis at the same time – the presence or absence of a monotonic relationship between the top and bottom flitch vector components, the strength of this relationship, the inherent variance for the movement vectors in each rock mass zone and the central tendency of their values. Indeed, the estimated bivariate PDFs are not robust, but they provide a more detailed overview of the joint distribution of vector components. This way the difference in terms of variance and central tendency is more evident and hence the shapes of the bivariate distributions contribute to the explanation why the assumed hypothesis tests are not sensitive enough to detect these intrinsic differences.

Therefore, the differences between all movement components for the three rock mass zones are primarily outside the central tendency. Hence, certain movement value ranges are more likely to be observed for each rock mass zone. Furthermore, based on the bivariate PDF for each of the vector components and the established correlation matrices, it can be pointed out that the correlation between the components of Rock mass zones 1 and 2 is observed to be higher than the variance of Rock mass zone 3. These results further support the hypothesized interpretation about the effect of the insufficient local powder factor in significantly harder rock mass zones.

Hence, ERT can prove to be a valuable method for gathering additional data required for improving the results from blasting. This effect is expected to hold true and be magnified in cases where higher bench heights are involved, as well as a higher level of the powder factor. Moreover, even in cases where advanced statistical models are not initially planned to be developed, the initial assumption of each component's PDF shape can prove to be useful when assessing how different points from the ore-waste boundary are expected to behave based on their location in either of the established rock mass zones. Hence, this information is crucial for BMM location planning in order to preserve a maximum level of representativity with respect to the location of the ore-waste contact zones. Last but not least, intrinsic knowledge of the PDF of each vector component, their potential multimodality and their continued updating can be used for uncovering factors which were initially not accounted for and can improve the results regardless of the applied modelling framework (e.g. multivariate Monte Carlo or Copula-based simulations, advanced machine learning models used as surrogate models based on physics simulations, etc.).

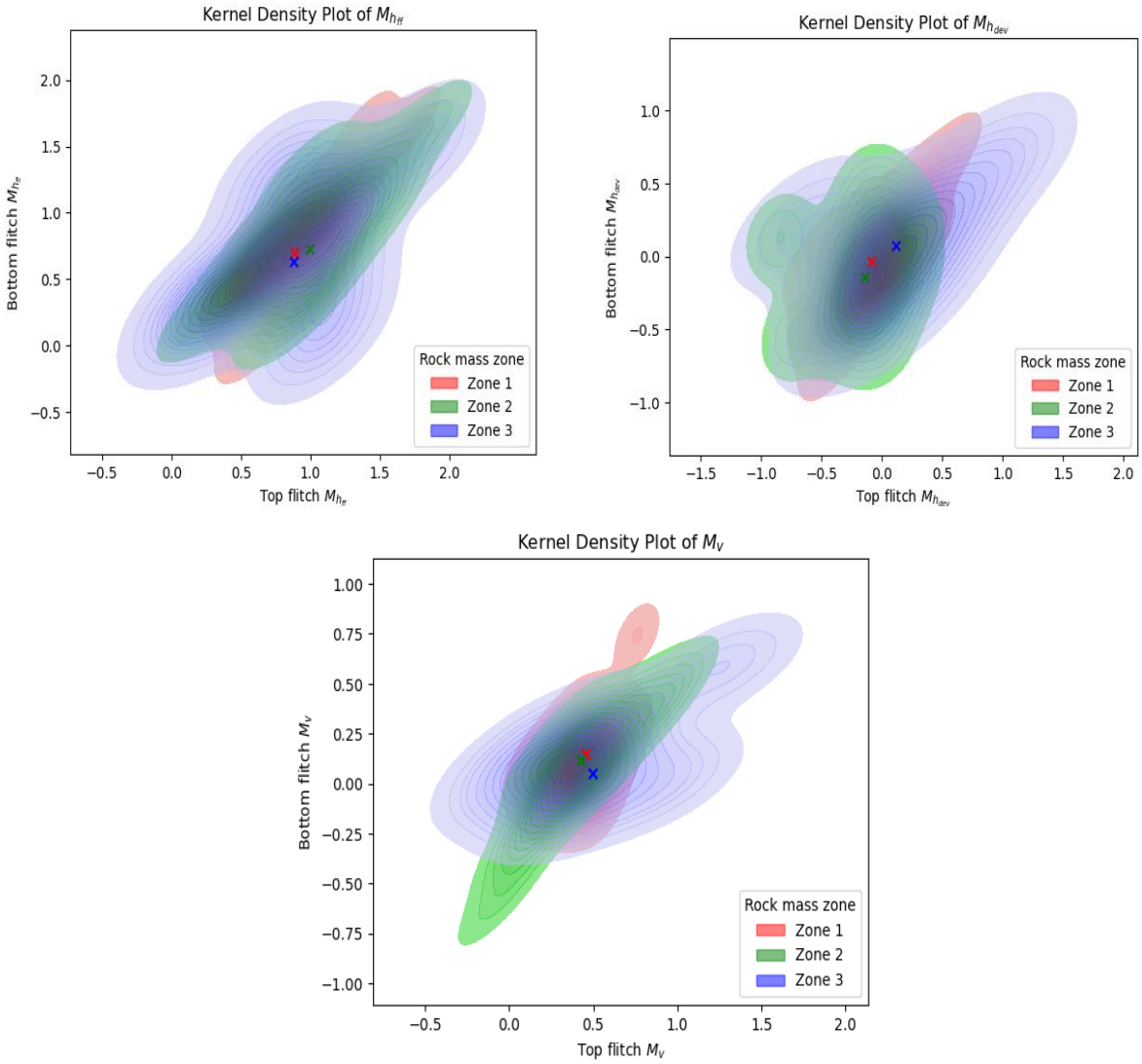

Figure 8. Bivariate distribution of blast movement vectors' components for all three rock types based on KDE

Conclusion

Based on the obtained results from the applied statistical and data mining methods, we conclude that the use of ERT can be beneficial for gaining additional insights regarding the behaviour of blast movement in different environments. Although the applied hypothesis tests fail to detect the presence of notable differences regarding the variance and the median-based central tendency for the blast movement vectors, KDE proves to be a viable instrument for detecting intrinsic details. Indeed, the failure to reject the null hypotheses is due to a high density of observations for all three rock mass zones in the same intervals for both flitches, considering each movement

vector component. However, there are more notable differences between the established modes of the movement vectors compared to the observed difference between their median variables. This is evident mainly for the horizontal movement component directed towards the free face (M_{Hff}).

Furthermore, it was established that a multivariate approach can indeed lead to the detection of certain differences regarding the realization of the 3D movement vector components for both flitches, considering a monitoring drill hole. The joint PDF of the occurring vectors in their respective feature space indeed proves to be crucial and a more powerful tool which complements the use of well-established hypothesis tests. As it was presented for the case study, some notable differences can be observed for the mode values when dealing with the univariate PDF for each vector component in the studied rock mass conditions. However, the difference in their PDFs is more easily observable when the bivariate distribution of each vector component for both flitches is considered. Moreover, by observing the bivariate distribution, one can easily identify the strength of relationship between the top and bottom flitch vectors' components, their variance, as well as the presence of multiple modes for the distribution. Therefore, ERT with a combination of using KDE and hypothesis tests can be used continuously for supplementing one's understanding of blast movement under the influence of different rock mass zones, regardless of the lack of details in terms of their composition.

Scientific Ethics Declaration

The authors declare that the scientific ethical and legal responsibility of this article published in EPSTEM journal belongs to the authors.

Acknowledgements or Notes

* This article was presented as an oral presentation at the International Conference on Research in Engineering, Technology and Science (www.icrets.net) held in Thaskent/Uzbekistan on August 22-25, 2024.

References

Corder, G. W., & Foreman, D. I. (2014). *Nonparametric statistics: A step-by-step approach*. John Wiley & Sons.

Engmann, E., Ako, S., Bisiaux, B., Rogers, W., & Kanchibotla, S. (2013). Measurement and modelling of blast movement to reduce ore losses and dilution at Ahafo Gold Mine in Ghana. *Ghana Mining Journal*, *14*, 27-36.

Eshun, P. A., & Dzigbordi, K. A. (2016). Control of ore loss and dilution at AngloGold Ashanti, Iduapriem mine using blast movement monitoring system. *Ghana Mining Journal*, *16*(1), 49-59.

Fu, W., Furtney, J., & Valencia, J. (2023, June). Blast Movement Simulation Through a Hybrid Approach of Continuum, Discontinuum, and Machine Learning Modeling. In *ARMA US Rock Mechanics/Geomechanics Symposium* (pp. ARMA-2023). ARMA.

Furtney, J. K., Cundall, P. A., & Chitombo, G. P. (2009, January). Developments in numerical modeling of blast induced rock fragmentation: updates from the HSBM project. In *Rock Fragmentation by Blasting-Proceedings of the 9th International Symposium on Rock Fragmentation by Blasting, FRAGBLAST 9* (pp. 335-342). CRC Press.

Furtney, J. K., Andrieux, P., & Hall, A. K. (2016, June). Applications for numerical modeling of blast induced rock fracture. In *ARMA US Rock Mechanics/Geomechanics Symposium* (pp. ARMA-2016). ARMA.

Gilbride, L., Taylor, S., Zhang, S. (1995). Blast-induced rock movement modelling for Nevada gold mines, in *Mineral Resources Engineering, 4*(2)175-193.

Gilbride, L., Taylor, S., DAEMEN, J. K., & Mousset-Jones, P. (1996). Rock movement induced by bench blasting. In *Mining Science and Technology* (pp. 667-676).

Gramacki, A. (2018). *Nonparametric kernel density estimation and its computational aspects* (Vol. 37). Cham, Switzerland: Springer International Publishing.

Grigorova, M. (2020). Geophysical investigations in open pit "Ada Tepe" gold mine In Southeastern Bulgaria, In proc. *International Scientific Conference Geobalcanica* (pp. 47-44).

Grigorova, M., & Koprev, I. (2019, June). Geophysical Investigations in Starite Kolibi Marble Deposit in Central Southern Bulgaria. In *International Scientific Conference Geobalcanica*.

Hmoud, S, Kumral, M. (2021). Simulation of Blast-Induced Movements in Open Pit Mining Benches. *Proc. 10th International Drilling and Blasting Symposium, (*pp. 119-130). Antalya, Turkey.

Hmoud, S., & Kumral, M. (2022). Effect of blast movement uncertainty on dig-limits optimization in open-pit mines. *Natural Resources Research*, *31*(1), 163-178.

Hmoud, S., & Kumral, M. (2023). Spatial entropy for quantifying ore loss and dilution in open-pit mines. *Mining, Metallurgy & Exploration*, *40*(6), 2227-2242.

Kaykov, D. & Terziyski, D. (2023). Possibilities for defining the complexity of blasting conditions for the purpose of blast-induced rock movement prediction. *Proceedings of the XVII International Conference of the Open and Underwater Mining of Minerals*, (pp. 84-91) Varna, Bulgaria.

Koprev, I., Garkov, I., Kaykov, D., & Terziyski, D. (2022). Studying blast induced rock movement in open-pit mining with small benches. In proc.: *Eleventh EFEE World Conference on Explosives and Blasting, European Federation of Explosives Engineers*, (pp. 191-204).

Kruskal, W. H., & Wallis, W. A. (1952). Use of ranks in one-criterion variance analysis. *Journal of the American statistical Association*, *47*(260), 583-621.

Levene, H. (1960). *Contributions to probability and statistics: Essays in honor of harold hotelling*, In I. Olkin et al. (Eds)., Stanford University Press (pp. 278-292).

Poupeau, B., Hunt, W., & La Rosa, D. (2019). Blast induced ore movement: The missing step in achieving realistic reconciliations. In *Proceedings of the 11th international mining geology conference. Australian Institute of Mining and Metallurgy*.

Preece, D., & Silling, S. A. (2016). *Ore Loss and Dilution Studies of Surface Mineral Blasting with 3D Distinct Element Heave Models* (No. SAND2016-1317C). Sandia National Lab.(SNL-NM), Albuquerque, NM (United States).

Preece, D. S., Tawadrous, A., Silling, S. A., & Wheeler, B. (2015). Modelling full-scale blast heave with three-dimensional distinct elements and parallel processing. In *Proceedings of 11th International Symposium on Rock Fragmentation. Carlton Victoria: The Australasian Institute of Mining and Metallurgy*.

Taylor, D. L., & Firth, I. R. (2003). Utilization of blast movement measurements in grade control. *Application of Computers and Operations Research in the Minerals Industry*, 243-247.

Thornton, D. (2009, September). The application of electronic monitors to understand blast movement dynamics and improve blast designs. In *Proceedings of the Ninth International Symposium on Rock Fragmentation by Blasting–Fragblast* (Vol. 9, pp. 287-399).

Thornton, D. (2009, August). The implications of blast-induced movement to grade control. In *Seventh İnternational Mining Geology Conference* (pp. 147-154).

Thornton, D. M., Sprott, D., & Brunton, I. D. (2005). Measuring blast movement to reduce loss and dilution. *Proceedings of the Thirty First Annual Conference on Explosives and Blasting Technique*

Terziyski, D., Aleksandrova, E., & Kaykov, D. (2021). Possibilities for improving rock fragmentation in limestone quarries. *Proceedings of the XVI International Conference of the Open and Underwater Mining of Minerals*, 6 – 10 September 2021, Resort "St. St. Constantine and Elena", Astor Garden Hotel, Varna, Bulgaria (pp. 32-36).

Tomova, M. (2023). Geophysical techniques for monitoring of ıntegrated mine waste storage facility: Case study of Southeastern Bulgaria. *The Eurasia Proceedings of Science Technology Engineering and Mathematics*, *26*, 341-347.

Tomova, M., & Kisyov, A. (2023). Geophysical techniques for determination of areas with increased water saturation in integrated mine waste storage facility. *The Eurasia Proceedings of Science, Technology, Engineering & Mathematics (EPSTEM)*, *26*, 13-18,

Tordoir, A., Weatherley, D., Onederra, I., & Bye, A. (2009, January). A new 3D simulation framework to model blast induced rock mass displacement using physics engines. In *Rock Fragmentation by Blasting-Proceedings of the 9th International Symposium on Rock Fragmentation by Blasting, FRAGBLAST 9* (pp. 381-388). CRC Press/Balkema.

Vasylchuk, Y. V., & Deutsch, C. V. (2019). Approximate blast movement modelling for improved grade control. *Mining Technology*, *128*(3), 152-161.

Yu, Z., Shi, X., Miao, X., Zhou, J., Khandelwal, M., Chen, X., & Qiu, Y. (2021). Intelligent modeling of blast-induced rock movement prediction using dimensional analysis and optimized artificial neural network technique. *International Journal of Rock Mechanics and Mining Sciences*, *143*, 104794.

Yu, Z., Shi, X., Zhou, J., Rao, D., Chen, X., Dong, W., ... & Ipangelwa, T. (2021). Feasibility of the indirect determination of blast-induced rock movement based on three new hybrid intelligent models. *Engineering with Computers*, *37*, 991-1006.

Yu, Z., Shi, X., Zhou, J., Gou, Y., Rao, D., & Huo, X. (2021). Machine-learning-aided determination of post-blast ore boundary for controlling ore loss and dilution. *Natural Resources Research*, *30*, 4063-4078.

Yu, Z., Shi, X., Zhou, J., Chen, X., Miao, X., Teng, B., & Ipangelwa, T. (2020). Prediction of blast-induced rock movement during bench blasting: use of gray wolf optimizer and support vector regression. *Natural Resources Research*, *29*, 843-865.

Zhang, S. (1994). *Rock movement due to blasting and its impact on ore grade control in Nevada open pit gold mines*. University of Nevada, Reno.

Zlatanov, P., & Alexandrova, E. (2008). Technological solutions during and destructions of hard inclusions in the overburden horizons of the East-Maritssa coal basin. *Geology and Mineral Resources, 7-8, 2*-6.

Web References

https://hexagon.com/solutions/mine-blast-movement-monitoring
https://dnablast.com/?lang=en
https://www.orica.com/Products-Services/Digital-Solutions/orepro-3d

Author Information

Dimitar Kaykov
University of Mining and Geology "St. Ivan Rilski"
Sofia, Studentski grad, prof. Boyan Kamenov", Sofia 1700
Sofia, Bulgaria
Contact e-mail: *IvoKoprev@gmail.com*

Ivaylo Koprev
University of Mining and Geology "St. Ivan Rilski"
Sofia, Studentski grad, prof. Boyan Kamenov", Sofia 1700
Sofia, Bulgaria

Danail Terziyski
University of Mining and Geology "St. Ivan Rilski"
Sofia, Studentski grad, prof. Boyan Kamenov", Sofia 1700
Sofia, Bulgaria

To cite this article:

Kaykov, D., Koprev, I. & Terziyski, D. (2024). Application of electrical resistivity tomography for improved blast movement monitor locations planning. *The Eurasia Proceedings of Science, Technology, Engineering & Mathematics (EPSTEM), 29*, 260-274.

The Eurasia Proceedings of Science, Technology, Engineering & Mathematics (EPSTEM)
ISSN: 2602-3199

The Eurasia Proceedings of Science, Technology, Engineering & Mathematics (EPSTEM), 2024

Volume 29, Pages 275-282

ICRETS 2024: International Conference on Research in Engineering, Technology and Science

Investigation of Copper Ores Processing Products

Teodora Yankova
University of Mining and Geology "St. Ivan Rilski"

Ljupcho Dimitrov
University of Mining and Geology "St. Ivan Rilski"

Irena Grigorova
University of Mining and Geology "St. Ivan Rilski"

Abstract: In recent years, the world technics and technologies development in mineral beneficiation has shown significant achievements in the field of mineral separation basic phenomena and regularities. This allows for creation of highly efficient processes and technologies for processing of primary ore with a complex composition, thus providing the metallurgical industry with necessary high-quality concentrates. As well known, the concentrates produced by beneficiation plants are subject to certain requirements for content of valuable components and harmful impurities. In order concentrates to be a commodity product, they must contain valuable components more than minimum permissible content, and harmful impurities must be a lower content than the maximum permissible. The presentation that is summarized in this article focuses on the results of laboratory experimental studies conducted to characterize copper, pyrite and molybdenum concentrates obtained from sulphide copper ores processing. This study also explored copper and pyrite concentrates from sulphide-oxide copper ores and oxide ores productive solutions. Data from concentrates chemical and particle size analysis are presented. Moreover, a brief description of technological studies conducted, their aims, concentrates and productive solutions obtained are presented. All copper concentrates contain gold and silver, as accompanying valuable components. Harmful impurities other than carbon in the molybdenum concentrate have not been detected. We summarize that all copper products are suitable for copper concentrates market.

Keywords: Characterization, Concentrates, Sulphide copper ores

Introduction

Copper ores are characterized by multiple minerals being economically viable to mine. Many of them can occur in the same deposit in different proportions and depths. This fact makes their examination and exploration extremely difficult. Many experts contend the present stage of mineral-raw material industry evolution is describing by mineral deposits with complex mining-geological conditions, difficult for mining, low grade ores with complex processing, which leads to considerable waste quantities formation (Tomova, 2023).

As mentioned by Grigorova (Grigorova, 2020), the heterogeneous nature of the rock varieties complicates the mining process, creating difficulties mainly in the ore comminution. To study the operational porphyry-copper deposits characteristics and the rock varieties detailed mapping, it is appropriate to apply geophysical methods based on the difference composition in the minerals physical properties and the rocks containing them. Despite the metals low content, due to deposits large size, a few valuable components presence and mining carried out by open-pit method, the porphyry-copper deposits exploitation is economically the most effective (Yankova et al., 2021).

The exceptional interest in porphyry-copper deposits, which for the last years have continued to be the subject of intensive and in-depth scientific research and geological studies, is primarily explained by the fact that they contain large copper and copper-molybdenum ores reserves, suitable for open-pit mining, which determines their primary importance in copper and molybdenum mining. As well known the copper sulfide ores must be concentrated before they can be economically transported and smelted. According to Schlesinger & Davenport (2011), the universal technique for concentration is froth flotation (Schlesinger & Davenport, 2011). For copper beneficiation, flotation is the most conventional method that has been used since 1905 (Jena et al., 2022). Flotation, in fact, has allowed mining of the lean and complex ore bodies that would have otherwise been discarded as noneconomic overburdens (Fuerstenau et al., 2007).

Copper concentrates typically contain around 30% of copper, but grades can range from 20 to above 40 per cent. International Copper Study Group reports that the copper concentrate can be processed pyrometallurgically in a smelter to produce matte or hydrometallurgically (pressure leaching) to produce pregnant leach solution, both products requiring further processing to copper metal obtain. In the hydrometallurgical route, copper is extracted from mainly low-grade oxide ores and some sulphide ores, through leaching (solvent extraction) and electrowinning (SX-EW process), (Assofermet, 2023). According to International Copper Study Group copper ores demand and copper concentrates production will undoubtedly continue to grow worldwide. Electric vehicles contain approximately four times more copper than conventional cars (Assofermet, 2023).

Detailed study of estimating copper concentrates benchmark prices under dynamic market conditions by Díaz-Borrego et al., (2021) showed that copper concentrates are traded globally between mines, traders and smelters, constituting the current main source of refined copper (Borrego et al., 2021). Concentrates are produced from copper sulphide ores, occurring naturally in different kinds of deposits, being porphyry deposits the most relevant ones (Borrego et al., 2021). Molybdenum and copper sulphide concentrates are the main source for obtaining one of the most expensive and rare metals of strategic importance - rhenium, which is irreplaceably used in aerospace technologies.

Therefore, searching, validating and developing effective beneficiation technologies for copper recovery is a research focus for many scientists. Due to the depletion of high-grade copper sulphide deposits, the research interest has directed to copper oxide and mixed ore deposits recovery. The aim of this paper is to reports the results of characterize copper, pyrite and molybdenum concentrates obtained from sulphide copper ores processing, sulphide-oxide copper ores and oxide ores, in order to produce saleable concentrates quality.

This article primarily includes the following elements: study of copper, pyrite and molybdenum concentrates from sulphide copper ore processing, study of copper and pyrite concentrates from sulphide-oxide copper ores processing and oxide ores productive solutions obtaining.

Study of Copper, Pyrite and Molybdenum Concentrates from Sulphide Copper Ore Processing

Research and development program has started to establish the technological possibilities for beneficiation of sulfide, sulphide-oxide and oxide copper ores from porphyry-copper deposit in Bulgaria. The technological research aims to develop a technology for copper, pyrite and molybdenum recovery in separate concentrates from the sulphide copper ores.

Copper and Pyrite Concentrate from Sulphide Copper Ores

Technological investigations have been conducted for processing of primary sulphide copper ore from a porphyry-copper deposit (Yankova & Grigorova, 2022). The chemical, mineral and particle size composition, as well as the grindability were studied and analyzed. For copper presence forms determining the phase analysis has been performed. The technological ore sample characterizes the primary sulphide copper ore. The main valuable component in the ore is copper – 0.215%. Sulfur - 0.83 % and molybdenum - 0.0041 % were found as accompanying valuable components with industrial importance (Yankova, et al., 2021). The gold content is 0.06 g/t. Copper in the sample is represented by chalcopyrite (80% relative to total copper), secondary copper sulfides (15.6% relative to total copper) and oxide copper minerals (3.6% relative to total copper).

The sulphide ore beneficiation has been proven by flotation. A selective-bulk flotation flowsheet has been developed, including three cycles - selective flotation, copper-pyrite flotation and pyrite flotation, and the

optimal technological parameters for each individual flotation cycle have been experimentally determined. The selective-bulk flotation flowsheet includes the following operations: ore grinding to 65% fraction "- 0.080 mm"; rougher, cleaner and scavenger flotation; Cu-Py concentrate grinding to 95% fraction "- 0.080 mm"; rougher and scavenger copper-molybdenum flotation; two consecutive cleaner flotation to copper concentrate obtain; copper flotation waste thickening, agitation and dilution; rougher and scavenger pyrite flotation; cleaner flotation to pyrite concentrate obtain.

The results of technological investigations conducted show that the developed selective-bulk flotation flowsheet, with obtaining copper and pyrite concentrate is effective for sulphide copper ores. The technological studies prove that the developed selective-bulk flotation flowsheet with copper and pyrite concentrates production is rational for sulphide ores. According to selective-bulk flotation flowsheet, the following final products and technological indicators were obtained: copper concentrate containing 21.3% copper, 25% sulphur, 0.33% molybdenum and 4.58 g/t gold with copper recovery 88.17%, sulfur - 26.81%, molybdenum 73.4% and gold 69.42%; pyrite concentrate containing 50.2% sulfur, recovery from the total sulfur is 66.5%. Table 1 presents the data from copper concentrate chemical analysis and Table 2 illustrated the data from a particle size analysis with valuable components distribution by fraction for copper concentrate.

Table 1. Copper concentrate chemical composition

Product	Cu, %	Mo, g/t	Au, g/t	S, %	C, %	Na_2O, %	MgO, %	LoI, %
Cu concentrate	21.38	31.00	4.68	25.05	0.42	0.49	0.11	2.03
	Al_2O_3, %	SiO_2, %	P_2O_5, %	K_2O, %	CaO, %	TiO_2, %	Fe_2O_3, %	
	4.19	5.48	0.43	0.50	0.90	0.19	28.04	

Table 2. Particle size analysis with distribution of valuable components by fraction for copper concentrate

Particle size fraction, mm	Yield, %		Grade, %			Recovery, %		
	Mass pull	Cumulative	Cu	S	Mo	Cu	S	Mo
+0.080	7.10	7.10	11.78	17.71	0.199	3.91	5.01	4.72
-0.080 +0.040	31.92	39.02	20.12	25.30	0.310	30.01	32.18	33.03
-0.040 +0.025	20.70	59.72	22.99	26.07	0.379	22.15	21.50	26.15
-0.025 +0.010	19.10	78.82	26.83	28.28	0.038	23.95	21.52	24.10
-0.010	21.18	100.00	20.19	23.45	0.170	19.98	19.79	12.00
Total	100.00	-	21.40	25.10	0.30	100.00	100.00	100.00

Table 3 presents the data from pyrite concentrate chemical analysis and Table 4 illustrated the data from a particle size analysis with distribution of valuable components by fraction for pyrite concentrate.

Table 3. Pyrite concentrate chemical composition

Product	Cu, %	Mo, g/t	Au, g/t	S, %	C, %	Na_2O, %	MgO, %	Al_2O_3, %
Py concentrate	0.17	130	-	50.50	-	0.27	0.04	2.50
	SiO_2, %	P_2O_5, %	K_2O, %	CaO, %	TiO_2, %	Fe_2O_3, %	LoI, %	
	3.10	0.25	0.13	0.20	0.66	71.80	-	

Table 4. Particle size analysis with distribution of valuable components by fraction for pyrite concentrate

Particle size fraction, mm	Yield, %		Grade, %			Recovery, %		
	Mass pull	Cumulative	Cu	S	Mo	Cu	S	Mo
+0.080	22.10	22.10	0.157	42.80	0.005	20.10	18.68	8.30
-0.080 +0.040	42.50	64.60	0.147	53.04	0.008	36.15	44.53	24.15
-0.040 +0.025	19.01	83.61	0.137	52.80	0.014	15.10	19.83	20.10
-0.025 +0.010	8.30	91.91	0.27	52.97	0.036	13.15	8.69	22.03
-0.010	9.09	100.00	0.33	51.74	0.042	15.50	8.27	25.42
Total	100.00	-	0.173	50.62	0.0135	100.00	100.00	100.00

Molybdenum Product from Sulphide Copper Ores

This research study was conducted to illustrate the possibility to obtained molybdenum concentrate from sulphide copper ores. The molybdenite, which accounts for over 90% of the world's molybdenum production, is usually associated with sulfide minerals of other metals, mainly copper. The molybdenum content in ores varies from 0.01 to 0.5%, and in copper-molybdenum sulfide ores it is 0.01-0.05% and reaches 0.12-0.5% in molybdenum sulfide ores. Sulphide molybdenum ores are less common, but due to their large reserves and fact that their molybdenum content is many times higher than in copper-molybdenum ores are important. The molybdenum production from these ores is main activity, and most often the total production costs are covered entirely by the obtained molybdenum concentrate, as opposed to copper-molybdenum ores processing (Kovacheva, 2009).

With steel growth, oil and gas industries and need for corrosion-resistant alloys, the main users of molybdenum, molybdenum-rich ores are being depleted. Molybdenum ores search is a complex process due to the specific conditions of their formation and deposition. Molybdenum ores are extremely unfavorable for direct geological-gephysical prospecting and exploration. With some success, it is possible to apply electrotomography - a method based on the study of the geoelectric section of the studied area, and its geological effectiveness is determined by the differentiation of the environment by specific electrical resistance (Grigorova, 2020). This requires researchers efforts to be directed to study the possibilities for full molybdenum recovery from poor molybdenum-containing ores. Technological investigations were carried out for beneficiation of primary sulphide ore from a porphyry-copper deposit to molybdenum concentrate obtain. The chemical, mineral and particle size composition as well as sulphide copper ore grindability were studied. Phase analysis for copper presence forms determining has been performed.

Selective-bulk flotation flowsheet was developed, including three cycles: bulk flotation, copper-pyrite selection and pyrite flotation, and the optimal technological parameters for each flotation cycle have been experimentally determined. The copper-molybdenum selective-bulk flotation flowsheet includes: copper-molybdenum concentrate thickening up to 50%, conditioning, diluted to 25%, rougher molybdenum flotation and 11 molybdenum refining operations. It was found that molybdenum is represented by molybdenite, mostly associated with chalcopyrite and less frequently with pyrite. With the copper-molybdenum concentrate from the technological sample laboratory experiments were conducted, to determine the optimum values of the main factors, which have a significant effect on molybdenum flotation (Yankova, 2023). Table 5 presents the data from molybdenum concentrate chemical analysis and Table 8 illustrated the data from a particle size analysis with distribution of valuable components by fraction for molybdenum concentrate.

Table 5. Molybdenum concentrate chemical composition

Components	Contents, %	Components	Contents, %
Mo	32.0	MgO	0.38
Cu	1.85	K_2O	0.20
S	24.50	Na_2O	2.01
Fe	2.90	Re, g/t	150
SO_2	2.00	As	0.02
Al_2O_3	2.33	Sb	0.005
CaO	1.02	C	35.00

The molybdenum concentrate chemical analysis shows a significant carbon content – 35% (Table 5). The carbon presence was found in the ore technological sample composition from which copper-molybdenum concentrate was obtained. The ore carbon content was 0.1%, and in the copper-molybdenum concentrate – 0.42%. Since carbon particles have the same hydrophobicity as molybdenite, under the selection conditions of the copper-molybdenum selective-bulk flotation they are extracted together in the molybdenum concentrate.

Based on the chemical analysis, the following minerals composition in the 32 % molybdenum concentrate was calculated: molybdenite - 53.3%, chalcopyrite - 5.3%, pyrite - 2.5%, non-ore minerals 10.9% and 38% carbon products. The obtained results show that copper-molybdenum concentrate selection is performed at a relatively low efficiency. From the molybdenum concentrate particle size analysis presented on the table 6 can be seen that impurities of non-ore minerals and carbon products are concentrated in coarse classes (+0.08 mm).

From the investigated technological ore sample, the highest indicators were obtained when a mixture of sodium sulfide and sodium hydrosulfide in a ratio of 1:1 was used, as a depressant of copper minerals and pyrite. The

final molybdenum product obtained contains 32% molybdenum, and its recovery in an open cycle from the collective concentrate is 64%, and from the ore – 46.7%.

Table 6. Particle size analysis with distribution of valuable components by fraction for molybdenum concentrate

Particle size fraction, mm	Yield, %		Grade, %			Recovery, %		
	Mass pull	Cumulative	Mo	Cu	S	Mo	Cu	S
+0.080	14.40	14.40	5.18	0.77	7.96	3.05	5.80	5.57
-0.080 +0.040	30.25	44.65	28.36	0.85	19.97	35.02	13.50	29.36
-0.040 +0.025	17.40	62.05	39.58	0.98	23.31	28.11	8.96	19.71
-0.025	37.95	100.00	21.83	3.63	24.60	33.82	71.74	45.36
Total	100.00	-	25.50	1.90	20.58	100.00	100.00	100.00

Study of Copper and Pyrite Concentrates from Sulphide-Oxide Copper Ores Processing

İn this section we discused the technological possibilities for beneficiation of sulphide-oxide copper ores from porphyry-copper deposit in Bulgaria. The technological research aims to develop a technology for copper and pyrite recovery in separate concentrates. The laboratory test work started to establish the sulfide-oxide ore beneficiation opportunity and high-quality concentrates obtaining. The research carried out includes full chemical analysis, phase analysis for determining the forms of copper presence in the ore, X-ray diffraction analysis, mineralogical studies of polished sections from ores samples and polished briquettes, prepared from class 2.00-0 mm of the ore, studied through a polarizing microscope in reflected light. The mineral and chemical composition of the studied sulfide-oxide ore determines selective-bulk flotation application, intending to high-quality copper and pyrite concentrates obtain (Yankova, 2023).

Laboratory studies to determine the sulfide-oxide ore grindability at different grinding time (5, 7, 10, 13, 17, 22 min). The ore minerals liberation degree in milled ore different fractions has been determined by microscopic studies. The copper distribution by ore fractions, ground to 65% of the fraction “0.080 mm” has been determined. A laboratory Bond test was performed, and the Bond Work Index was determined. The results of the conducted research show that the studied mixed sulfide-oxide ore is characterized by relatively easy grindability (Yankova & Grigorova, 2023).

The main valuable component in the ore is copper - 0.554%. The ore sample is characterized by a relatively high copper content compared to the samples studied and presented in previous sections. Pyrite sulfur - 1.27 % was found as an accompanying component of industrial importance. The molybdenum and gold contents in the ore are low, respectively: Mo – 0.0029 % and Au – below 0.05 g/t. Copper phase analysis shows the following copper minerals distributions: 19.78% of copper is in the form of oxidized free copper; copper in the form of secondary sulfides amounts to 23.74%; 55.40% of copper is represented by primary copper sulfides.

Obtained results from research conducted could be summarized: the technological flotation studies carried out prove that with a selective-bulk flotation flowsheet for beneficiation of mixed sulphide-oxide ores from porphyry-copper deposit high technological indicators for this ore type are achieved. The following products and parameters were obtained: copper concentrate with 24.64% copper grade, sulfur 28.20%, with 80.21% copper recovery and sulfur 40.19%, pyrite concentrate with 45.26% sulfur grade and 47.10% total sulfur recovery (Yankova et al., 2023).

Table 7 presents the data from copper concentrate chemical analysis and Table 8 illustrated the data from a particle size analysis with distribution of valuable components by fraction for copper concentrate. Table 9 presents the data from pyrite concentrate chemical analysis and Table 10 illustrated the data from a particle size analysis with distribution of valuable components by fraction for pyrite concentrate

Table 7. Copper concentrate chemical composition

Product	Cu, %	Mo, g/t	Au, g/t	S, %	C, %	Na_2O, %	MgO, %	
Cu concentrate	24.65	844	0.54	28.30	0.21	0.65	0.45	
	Al_2O_3, %	SiO_2, %	P_2O_5, %	K_2O, %	CaO, %	TiO_2, %	Fe_2O_3, %	LoI, %
	6.52	10.65	0.39	1.40	0.72	0.18	34.48	1.82

Table 8. Particle size analysis with distribution of valuable components by fraction for copper concentrate

Particle size fraction, mm	Yield, %		Grade, %		Recovery, %	
	Mass pull	Cumulative	Cu	S	Cu	S
+0.10	7.20	7.20	10.96	28.70	3.18	7.31
-0.10 + 0.080	12.35	19.55	18.71	28.06	9.31	12.22
-0.08 + 0.063	20.25	39.80	16.62	28.06	13.56	20.04
-0.063 + 0.040	23.40	63.20	27.53	28.26	25.96	23.32
-0.040 + 0.025	12.20	75.40	32.18	29.47	15.82	12.68
-0.025 + 0.010	15.90	91.30	33.45	30.77	21.43	17.25
-0.010	8.70	100.00	30.64	23.40	10.74	7.18
Total	100.00	-	24.82	28.36	100.00	100.00

Table 9. Pyrite concentrate chemical composition

Product	Cu, %	Mo, g/t	Au, g/t	S, %	C, %	Na_2O, %	MgO, %	LoI, %
Py concentrate	0.27	86	-	45.20	-	0.68	0.25	-
	Al_2O_3, %	SiO_2, %	P_2O_5, %	K_2O, %	CaO, %	TiO_2, %	Fe_2O_3, %	
	6.47	6.83	0.25	0.72	0.86	0.65	55.36	

Table 10. Particle size analysis with distribution of valuable components by fraction for pyrite concentrate

Particle size fraction, mm	Yield, %		Grade, %		Recovery, %	
	Mass pull	Cumulative	Cu	S	Cu	S
+0.125	1.26	1.26	-	-	-	-
-0.125 +0.080	19.72	20.93	0.270	36.94	21.59	17.12
-0.080 +0.063	9.97	30.96	0.231	46.06	8.79	10.17
-0.063 +0.040	33.51	64.46	0.212	47.57	27.09	35.30
-0.040 +0.025	18.49	82.95	0.212	48.53	14.95	19.87
-0.025	17.05	100.00	0.424	46.46	27.58	17.54
Total	100.00	-	0.262	45.16	100.00	100.00

Oxide Ores Productive Solutions Obtaining

Oxide ore bio-hydrometallurgical beneficiation studies were carried out. The results show that copper is mainly represented by oxide copper minerals, soluble in sulfuric acid - 90% of the total copper. Oxide copper occurs in the form of medmontite, chrysocolla, malachite, tenorite and cuprite. Sulphide copper minerals and pyrite are in minor amounts. The host rocks are mainly represented by quartz and feldspars. The high content of oxide copper minerals in the technological sample predetermines sulfuric acid as the main reagent in copper leaching. Table 11 shows the productive solution chemical composition, obtained during the technological studies for copper chemical leaching from the oxide ores.

Table 11. Chemical composition of productive solution from oxide ore beneficiation

Product of leaching	Cu, mg/dm^3	Fe, mg/dm^3	Ca, mg/dm^3	Mg, mg/dm^3	Mn, mg/dm^3
Productive solutions	5319±106	82.9±8.3	566±28	45.4±4.5	15.7±1.6
	Pb, mg/dm^3	Zn, mg/dm^3	As, mg/dm^3	SO_4^{2-} mg/dm^3	Undissolved substances, mg/dm^3
	0.25±0.02	5.6±0.6	0.07±0.01	16665	<6

Conclusion

A technological flowsheet and reagent regime for sulphide copper ores beneficiation have been developed. It has been found that it is possible to quality copper concentrate obtain. The valuable components distribution by copper concentrate fractions shows that copper is mainly concentrated in "-0.080 mm" fraction with a maximum

in "-0.080+0.040 mm" fraction. Technological flotation studies results show that during sulphide ores beneficiation, it is not possible to obtain flotation molybdenum concentrate, which would represent a commercial product. The main reason due to the sulphide ore specific material composition. The ore contains carbon, mostly of organic origin, which reaches over 0.4% in the copper-molybdenum concentrate. Hydrocarbon products are naturally highly hydrophobic and in copper-molybdenum selective flotation they are recovered together with molybdenite in the molybdenum concentrate and contaminate it as harmful impurities.

A technological flowsheet and reagent regime for beneficiation of mixed sulfide-oxide copper ore from a porphyry copper deposit have been developed. It has been established that it is possible to obtain a quality copper concentrate from mixed sulphide-oxide ore. In the experiments with mixed sulphide-oxide copper ore it was found that copper is concentrated mainly in "-0.063 mm" fraction. A flowsheet for oxide ore technological research for productivity solutions production has been developed. The technological regime and forecast indicators of the oxide ore leaching from a copper porphyry deposit in industrial conditions are presented.

Scientific Ethics Declaration

The authors declare that the scientific ethical and legal responsibility of this article published in EPSTEM Journal belongs to the authors.

Acknowledgements or Notes

* This article was presented as an oral presentation at the International Conference on Research in Engineering, Technology and Science (www.icrets.net) held in Tashskent/Uzbekistan on August 22-25, 2024.

References

Assofermet (2023). *The world copper factbook 2023*. https://www.assofermet.it/statistiche/ferramenta/the-world-copper-factbook-a-cura-dell-icsg-international-copper-study-group-di-lisbona/the-world-copper-factbook-2023-dati-2022

Díaz-Borrego, F. J., Escobar-Peréz, B., & del Mar Miras-Rodríguez, M. (2021). Estimating copper concentrates benchmark prices under dynamic market conditions. *Resources Policy*, *70*, 101959.

Fuerstenau, M. C., Jameson, G. J., & Yoon, R. H. (Eds.). (2007). *Froth flotation: a century of innovation*. SME.

Grigorova, M. (2020). Geophysical methods for solving engineering-geological tasks related to increasing efficiency in the conditions of an open-pit mine "Khan Krum", *Geology and Mineral Resources*, 6-7, 3-9.

Jena, S. S., Tripathy, S. K., Mandre, N. R., Venugopal, R., & Farrokhpay, S. (2022). Sustainable use of copper resources: beneficiation of low-grade copper ores. *Minerals*, *12*(5), 545.

Kovacheva, V., Velev, V., Nishkov, I., & Koleva, T. (2009). Molybdenum - a metal with amazing properties and wide application, *Mining and Geology Journal*, *8-9*, 39-42.

Schlesinger, M.E., & Davenport, W.G. (2011). Production of Cu concentrate from finely ground Cu ore. *Extractive metallurgy of copper* (Fifth Edition). Elsevier: Oxford, UK, 51-71.

Tomova, M. (2023). Geophysical techniques for monitoring of integrated mine waste storage facility: Case study of Southeastern Bulgaria. *The Eurasia Proceedings of Science, Technology, Engineering & Mathematics (EPSTEM), 26,* 341-347.

Yankova, T., Angelov, T., Nishkov, I. (2021). Studies on the material composition and physical-mechanical properties of copper porphyry ore, *Annual of the UMG "St. Ivan Rilski", 64*, pp. 103-108.

Yankova, T. & Grigorova, I. (2022). Development of technology for beneficiation of primary sulphide ores, *Annual of the UMG "St. Ivan Rilski", 65*, pp. 55 – 60.

Yankova, T. Grigorova, I. (2024). Beneficiation of sulfide ore from a porphyry-copper deposit. *Journal of International Scientific Publications: Materials, Methods & Technologies, 18,* ISSN 1314-7269 (Online), Retrieved from www.scientific-publications.net

Yankova, T. (2023). Technological studies on beneficiation of sulphide ore to obtain molybdenum concentrate, Annual of the UMG "St. Ivan Rilski", 66, pp. 83-86.

Yankova, T. (2023). Physical composition of mixed sulfide-oxide ores from a copper porphyry deposit, *Annual of the UMG "St. Ivan Rilski", 66*, pp. 78-82.

Yankova, T. & Grigorova, I. (2023). Material composition of mixed type sulfide-oxide ores from a porphyry-copper deposit, *Annual of the UMG "St. Ivan Rilski", 66*, pp. 87-90.

Yankova, T., Dimitrov, L., & Grigorova, I. (2023). Beneficiation of sulfide-oxide ore from a porphyry – copper deposit – technological investigations, *Proceedings of XIX Balkan Mineral Processing Congress, Prishtine, Kosovo 2023*, (pp. 265-270), ISBN 978-9951-9138-0-5.

Author Information

Teodora Yankova
UMG "St. Ivan Rilski"
Prof. Boyan Kamenov Str., Sofia, Bulgaria

Ljupcho Dimitrov
UMG "St. Ivan Rilski"
Prof. Boyan Kamenov Str., Sofia, Bulgaria
Contact e-mail: *ljupcho.dimitrov@mgu.bg*

Irena Grigorova
UMG "St. Ivan Rilski"
Prof. Boyan Kamenov Str., 1700 Sofia, Bulgaria

To cite this article:

Yankova, T., Dimitrov, L. & Grigorova, I. (2024). Investigation of copper ores processing products. *The Eurasia Proceedings of Science, Technology, Engineering & Mathematics (EPSTEM), 29*, 275-282.

The Eurasia Proceedings of Science, Technology, Engineering & Mathematics (EPSTEM)
ISSN: 2602-3199

The Eurasia Proceedings of Science, Technology, Engineering & Mathematics (EPSTEM), 2024

Volume 29, Pages 283-294

ICRETS 2024: International Conference on Research in Engineering, Technology and Science

Statistical Methods for Processing Data on the Impact of Wind Farms on Birds

Vladimir Yeremieiev
Melitopol State University

Valery Siokhin
Melitopol State University

Alexander Matsyura
Melitopol State University

Dmitriy Bukreev
Melitopol State University

Abstract: This article is devoted to the processing and analysis of observational results that make it possible to predict the impact of wind power on the environmental situation; in the course of the work, an algorithm for statistical processing of the results of monitoring the dynamics of ornithocomplexes on the territory of wind power plants (WPPs) is proposed. During the study, it was found that the parameters for the statistical analysis of ornithocomplexes on the territory of the wind farm are: the number of birds, the number of species, the time spent at the recording site and the activity coefficients of individuals of different species at different altitudes. The solution to the most frequently encountered problems in the analysis of bird migration in the wind farm zone is considered: 1) An algorithm has been developed for the primary statistical processing of information obtained by the route counting method and observations in accordance with the recommendations of the Scottish Natural Heritage Foundation. 2) The features of the application of correlation and regression analysis using the Student, Pearson and Fisher criteria are considered. 3) An algorithm for statistical analysis based on the trend approach is proposed. The considered statistical methods were tested on the results of migratory bird census on the territory of the Prymorsk-1 wind farm located on the coast of the Sea of Azov.

Keywords: Wind farms, Statistical processing, Avifauna, Statistical analysis, Birds.

Introduction

The intensive development of wind energy has a significant impact on the avifauna. Numerous observations of researches testify to the need to expand research on the dynamics of ornithocomplexes on the territory of wind farms with the involvement of information technologies and statistical methods of information processing (Ralph, 2009; Felix Liechti & Susanna Commenda-Zehnder, 2013; Bicknell et al., 2019). A large number of studies have been devoted to the study of the wind energy impact on ornithological complexes (Shifeng et al., 2015; Osadchyi et al., 2019; Siokhin et al., 2021; Bernardino et al., 2013). One of the main tasks of monitoring birds on the territory of the wind farms is to obtain data on the dynamics of their quantitative and species characteristics, as well as the height and directionof migration in different seasons (Kunz et al., 2007; Hull & Muir., 2010)

The results of long-term observations over several years make it possible to predict the impactof wind power on the ecological situation associated with changes in the avifauna. Currently, there is an extensive information related to the interaction of birds with wind turbines in various regions, which has been accumulated during the processing of the results of monitoring the territory of wind farms and adjacent regions for several decades (Ralph, 2009; Felix Liechti & Susanna Commenda-Zehnder, 2013; Bicknell et al.,

- Selection and peer-review under responsibility of the Organizing Committee of the Conference

2019; Kunz et al., 2007; Hull &. Muir, 2010). The use of various methods of observation expands the possibility of predicting undesirable impact on the avifauna and taking effective measures to reduce this impact (Kalender & Salih, 2017; Anderson et al., 1999).

When organizing observations, the recommendations of the Scottish Natural Heritage Foundation (*SNH*) (Osadchyi et al., 2019; Anderson et al., 1999; Scottish Natural Heritage, 2014; Yeremieiev et al., 2020) are often used, which provide for the fulfillment of a number of requirements. In particular, it is assumed that monitoring should be carried out in several areas, which in terms of their landscape and biotope characteristics adequately reflect the entire territory of the wind farm. A sufficient amount of time is allocated for observations, covering the main periods of bird migration in the region. Generally, research should be carried out in spring and autumn during the bird migration, as well as during the breeding period and in winter. Observation is carried out simultaneously by several researches (Osadchyi et al., 2019)., Scottish Natural Heritage, 2014; Yeremieiev et al., 2020). During monitoring, the following parameters are recorded:

1. Date, time of the day, species of counted birds and their number at the sites.
2. Direction of flight, flight altitude and type of flight (transit, forage, demonstration).
3. The time spent by each bird flying below the edge of the wind wheel H_1, above its edge H_2 and in the risk zone (*RZ*) of collision with the rotor blades at heights between H_1 and H_2.

The results of observations in accordance with the recommendations of the Scottish Natural Heritage Foundation make it possible to determine the activity coefficient of birds of the j species in the risk zone of collision with turbines at the k site $K^{Risk(k)(j)}$, which is necessary to predict the interaction of birds with rotor blades. Its value is (Osadchyi et al., 2019)

$$K^{Risk(k)(j)} = \sum_i n_i^{Risk(k)(j)} t_i^{Risk(k)(j)} \quad , \tag{1}$$

where $n^{Risk(k)(j)}$ - the number of birds of the j species in the i group recorded in the k site in the *RZ* during the time interval $t^{Risk(k)(j)}$.

In a similar way, it is possible to characterize the activity of birds for other heights, as well as in various monitoring areas and the wind farm territory as a whole. For example, the activity coefficient of birds in the k site is determined by the formula

$$K^{(k)(j)} = \sum_i n_i^{(k)(j)} t_i^{(k)(j)} \quad . \tag{2}$$

An alternative way to obtain information about the behaviour of birds on the territory of the wind farm is the method of route census (*RAM*) Siokhin, et al., 2018). In this case, all birds sitting on the ground and in flight are taken into account. For the last group of birds, the number of individuals of each species, the direction of migration, the height and the type of flight (transit, forage, breeding) are determined. Generally, there are recorded those birds that are located at a distance of no more than 500 m to the left and to the right of the direction of the observer movement along the selected route.

The effectiveness of the analysis of the recorded data largely depends on the adequacy of statistical samples and the correctness of the application of statistical methods. The peculiarity of the processing of primary information in ornithology is associated with the presence of a number of objective reasons, which often make it difficult to obtain reliable conclusions. Therefore, the creation of algorithms that ensure the correct processing of observation results is of great practical importance. This research paper is devoted to the description of the methods of mathematical statistics adapted to the study of the dynamics of ornithocomplexes on the territory of the wind farms.

Results and Discussion

Analysis of Recent Research and Publications

The purpose of the paper is to develop an algorithm for the use of statistical methods in the analysis of the results of monitoring the avifauna on the territory of the wind farms in solving the following problems. Primary statistical processing of information on the number of birds of various species, flight altitude and

time of their stay at the observation sites, obtained by the *SNH* (Osadchyi et al., 2019; Siokhin et al., 2021; Scottish Natural Heritage, 2014) and *RAM* (Siokhin et al., 2021; Siokhin et al., 2018) methods.

1. Correlation and regression analysis to determine the dependence of the number of birds on various factors using the Student, Pearson, Fisher, Irwin criteria.
2. Trend analysis of the results of monitoring the wind farm territory based on the Student, Irwin, Durbin - Watson, Pearson and Fisher criteria.

Work Results

Primary statistical analysis of the observation results

The number of birds that are recorded in the process of monitoring on the territory of thewind farms varies from several dozens to several thousand individuals and more. Therefore, information processing is carried out with the involvement of computer technologies based on mathematical statistics (Osadchyi et al., 2019; Siokhin et al., 2021; Yeremieiev et al., 2020). In this section, we will focus on the traditional methods of primary statistical processing of observational results, which are usually used in the study of avifauna on the wind farm territory.

The following parameters serve as objects of statistical analysis on the wind farm territory: n_x - the number of birds, the number of species, the time spent at the registration site, and the activity coefficients of individuals of various species at different heights, determined by formulas (1), (2). Let $X=x_1, x_2, \ldots x_n$ is the number of values that are obtained during the registration of individuals at one of the registration sites during n days. The degree of scattering of each x_i relative to the average value $x_a=\sum x_i/n_x$ is estimated using the empirical variance $s^2_x=\sum(x_i-x_a)^2/n_x$ or the corrected variance $s^2_x=\sum(x_i-x_a)^2/(n_x-1)$. The average statistical deviation is taken equal to $s_x=\sqrt{s^2_x}$. Statistical data of ornithological research are distinguished by large values of s_x, therefore, in some cases (for example, in the graphical interpretation of the results), a smoothing operation is used. The easiest way to smooth is to convert the original data to new values using the formula

$$x_k=(x_{k-1}+x_k+x_{k+1})/3,\ k=2,3,\ldots,n-1. \tag{3}$$

The weak point of smoothing is the decrease in the number of elements in the original row statistics, which is equal to *n-2* with a single smoothing. Along with the simple operation (1), where the averaging is performed over three elements, other methods of linear and nonlinear transformation are used, which are widely used in economic and sociological research (Fedoseev et al., 1999).

In many cases, there is a problem of comparing monitoring results obtained in different situations, as well as when comparing data at two sites or for different seasons of the year. Let $X=x_1, x_2, \ldots, x_n$ and $Y=y_1, y_2, \ldots, y_n$ are two samples, each consisting of n_x and n_y elements. Let us denote the mean sample values as x_a, y_a. The verification of the hypothesis about the equality of mathematical expectations is carried out in the case of a known random variable distribution law at a given significance level q. Various methods are used to identify the distribution law (V. V. Fedoseev, A. N. Garmash, D. M. and others, 1999; N. Sh. Kremer, 2004) As an example, let's consider the use of the Pearson's criterion (N. Sh. Kremer, 2004) when establishing the normal law of data distribution for the sample $X=x_1, x_2, \ldots, x_n$. Let's dividethe sample into m equal intervals $h=(x_n-x_1)/m$. Let us denote the number of elements in the k interval as n_{xk}. The Pearson criterion is calculated by the formula

$$\chi^2=\sum_{k=1}^{k=m}\frac{(n_{xk}-n'_{xk})^2}{n'_{xk}}, \tag{4}$$

where $n'_k=hn_xp_k/s_x$ - a theoretical value of the number of elements in the k interval, corresponding to the normal random variable distribution law for the analyzed sample, p_k - the probability that the random variable is in the k interval.

In the case of a normal distribution

$$p_k=\exp(-z_k^2/2)/\sqrt{2\pi}, z_k=(x_k-x_a)/s, \tag{5}$$

where x_k - the average value of the elements in the k interval.

If the value of the χ^2 -criterion calculated by the formula (4) is less than the critical value χ^2_{kr} for m-3 degrees of freedom at given significance level q, then the sample obeys the chosen law. For $\chi^2>\chi^2_{kr}$, the hypothesis about the possible use of the normal distribution law is rejected. The normal distribution law is characterized by two parameters - the mathematical expectation a and the general variance σ^2. In practice, instead of a, the average value of x_a, is used, and instead of the general variance, the empirical variance s_x^2 is used.

During the primary processing of row statistics, it is recommended to analyze the possibility of the appearance of anomalous values associated with technical errors in obtaining data or processing the original information. The rejection of erroneous data can be carried out by the Irwin's method. The method is based on determining the coefficients $\lambda_i=|x_i-x_{i-1}|/s_x$, $i=2, 3, ..., n_x$. The values of λ_i are compared with the critical parameter λ_a. If $\lambda_i>\lambda_a$, then the element with the number i of the row statistics is rejected. Parameters λ_a depending on the sample size for the 5% significance level are presented in Table 1.

Table 1. Critical Irwin values λ_a depending on the sample size n

Parameters							
λ_a	2.8	2.3	1.5	1.3	1.2	1.1	1.0
n	2	8	10	20	30	50	100

It should be noted that the rejected element may not be the result of a measurement error, but reflect the influence of an unknown factor. But here mathematics is powerless. The decision on rejection is made by the researcher. Testing the hypothesis about the equality of two mathematical expectations of the average value is performed using the Student's T-test (Bevanger et al., 2009)

$$T=\frac{|x_a-y_a|}{s}\sqrt{\frac{n_x n_y}{n_x+n_y}}, \tag{6}$$

where $s=\sqrt{[(n_x-1)s_x^2+(n_y-1)s_y^2]/(n_x+n_y-2)}$.

If T is less than the critical value T_{kr} for the significance level q for $v=n_x+n_y-2$ degrees of freedom, then the hypothesis of equality of means is true. For $|T| > T_{kr}$, the hypothesis is rejected. Sample values of variances s_x^2, s_y^2 characterizing the scatter of the results of specific measurements generally differ, therefore, before using the formula (6), one should make sure that the general variances $\sigma_x^2=\sigma_y^2$ are equal. Testing the hypothesis about the equality of general variances can be carried out using the Fisher criterion

$$F=\begin{cases}\dot{s}_x^2/\dot{s}_y^2, если\cdot \dot{s}_x^2>\dot{s}_y^2\\ \dot{s}_y^2/\dot{s}_x^2, если\cdot \dot{s}_y^2>\dot{s}_x^2\end{cases}. \tag{7}$$

If the value of F is less than the critical value F_{kr} with a given significance level, then the general variances are equal. Otherwise, the hypothesis of equality of dispersions is rejected. Checking the homogeneity of variances with a large number of samples is carried out using the Duncan method and other methods. As an example, we will make a primary statistical analysis of the monitoring results at three vantage points (VP) belonging to the territory of the Prymorsk-1 wind farm.

Figure 1. The layout of bird counting points on the territory of the Primorsk-1 wind farm

The site sizes of VP1, VP2 and VP3 were respectively 0,50 km^2, 0,86 km^2 and 1,23 km^2, Fig.1. Observations were carried out during the spring period of the bird migration in 2017 (Siokhin et al., 2018). The results of daily registration of the total number of birds $n^{(k)}$ at the k site per 1 km^2, which flew in transit during the spring migration period, are presented in Table 2.

Table 2. The total number of birds flying in transit through the first $n^{(1)}$, second $n^{(2)}$ and third $n^{(3)}$ observation sites on different days

Days	13.03.17	14.03.17	25.03.17	02.04.17	03.04.17	04.04.17	28.04.17
i	1	2	3	4	5	6	7
$n^{(1)}$	74	106	264	102	70	62	238
$n^{(2)}$	43.0	76.7	30.23	25.58	1.26	90.7	59.3
$n^{(3)}$	32.5	39.0	108.9	85.4	23.6	52.0	63.4

Table 3. Values of variances s^2, standard deviations s_x from the mean value x_a and thePearson's criteria χ^2 after rejection of erroneous measurements

Vantage points	VP1	VP2	VP3
n	*7*	*6*	*7*
x_a	131	54.3	57.8
s_x^2	6048	564	800
s_x	77.8	23.7	28.3
χ^2	6.7	2.8	3.1

At the first stage, we reject possible erroneous measurements using the Irwin method. According to Table 1, Irwin's critical value λ_a for the 5% significance level with the number of measurements n=7 is about 2.4. Coefficients λ_i for all row statistics in accordance with the data in Table 3.1.2 is much less than the critical value. The exception is the measurement $n^{(2)}$=1.26, which was carried out on April 3,2017, when λ_i turned out to be 3.1.

The results of variance calculations of s^2_x, standard deviations s_x and the Pearson's criteriaχ^2 according to the data of Table 2, from which the measurement $n^{(2)}$=1.26 obtained on April 3,2017 is excluded, are presented in Table 3 The values of x^2 were calculated for four intervals: m=4. The Pearson's criterion is recommended to apply for large samples. Therefore, the obtained data should be treated with caution. The critical value of the Pearson criterion for m=4 and the 5% significance level at m-3=1 degrees of freedom is 3.8. The calculated value x^2=6.7 for the first area is greater than the critical value, so the first row statistics do not obey the normal random variable distributionlaw.

Checking the homogeneity of variances in the number of birds in different sites using the Fisher's formulas (7) gave the following results for a 5% significance level: F_{23}=1.4 atF_{kr}=5.0, F_{13}=7.6 at F_{kr}=4.3, F_{12}=10.4 at F_{kr}=5.0. Here, the numerical indices in the notation of the F_{ij} criteria refer to the numbers of the monitoring sites. The calculation resultsshowed that the hypothesis about the homogeneity of the variances of the analyzed row statisticscan only be accepted when comparing the number of birds in the second and third sites, where the Fisher criterion F_{23}=1.4 is less than the critical value F_{kr}=5.0. In other cases, the homogeneity hypothesis is not fulfilled.

Let us test the hypothesis about the equality of the average number of birds in the second and third sites. The Student's T -test calculated by the formula (6) is 0.0088, the critical value of T_{kr} for the 5% significance level at 11 degrees of freedom is 2.2. Since the value of T is several times less than the critical value T_{kr}, it can be argued that the mathematical expectations for the number of birds in the second and third sites are the same.

Correlation and Regression Analysis

Methods of correlation and regression analysis are a powerful tool in identifying relationships between different parameters or determining the influence of one factor on another. Let's consider two samples X, Y with the same number of elements n. The presence of a linear correlation between them is determined by the correlation coefficient

$$r_{xy} = (\sum_{i=1}^{i=n} x_i y_i - n x_a y_a) / n s_x s_y \tag{8}$$

where s_x=$\sqrt{s_x^2}$, s_y=$\sqrt{s_y^2}$–standard deviations.

The significance of the coefficient (5) is checked using the Student's *T*-test for $q=n-2$ degrees of freedom:

$$T = |r_{xy}|\sqrt{n-2} / \sqrt{1-r_{xy}^2}. \quad (9)$$

If the value of *T* is greater than the critical value T_{kr} at the chosen signi_cance level *q*, then there is a relationship between the parameters *X* and *Y*. Otherwise, the dependency is considered not installed. The existence of a correlation dependence allows us to represent it in the form of a linear regression equation

$$y=a+bx, \quad (10)$$

where $a=y_a-r_{xy}x_a s_y/s_x$, $b=r_{xy}s_y/s_x$.

The coefficients *a* and *b* can also be found by the least squares method (LSM). The LSM method allows us to find the regression equation in the case of linear and nonlinear multifactorial models in a more general form

$$y(x_1, x_2, \ldots x_n)=a_0+b_1x_1+ b_2x_2+\ldots b_{12}x_{12}+b_{13}x_{13}+\ldots b_{11}x_1^2+\ldots \quad (11)$$

The adequacy of the regression equations (9), (10) is checked using the Fisher criterion, based on a comparison of two variances. One of them $\dot{s}_y^2=\sum(y_i-y_a)^2/(n-1)$ determines the dispersion of the observation results *yi* from the average value *ya*. The second dispersion of adequacy $\dot{s}_{ad}^2=\sum(y_i-\bar{y}_i)^2/(n-2)$ characterizes the degree of deviation of the recorded data y_i from the values calculated using the regression equation at $x=x_i$:

$$F=\dot{s}_y^2/\dot{s}_{ad}^2. \quad (12)$$

If the value of *F* is greater than the critical value F_{kr} with a given significance level *q* with two degrees of freedom equal to *n-1* for the variance s^2y and *n*-2 for the variance s^2_{ad}, then mathematical models (11), (12) adequately describe the situation under study. Otherwise, the equations are not adequate. As an example, we will study the possibility of the existence of a correlation dependence between the activity coefficient $K^{(3)}$ on the total number of birds $n^{(3)}$ per 1 km based on the results of monitoring in the spring migration season in the third site of the Prymorsk-1 wind farm. The initial data are given in Table 4.

Table 4. The number of birds n(k) and their activity coe_cients K(k) in the third site of the wind farm on di_erent days of observation

Days	13.03.17	14.03.17	25.03.17	02.04.17	03.04.17	04.04.17	28.04.17
$n^{(3)}$	32.5	39.0	108.9	85.4	23.6	52.0	63.4
$K^{(3)}$,s	1407.3	1634.0	3669.0	1974.9	894.4	1879.6	2083.8

The correlation coefficient r_{xy} and the Student's *T*-test, calculated by formulas (7), (8), are 0.92 and 5.2, respectively. The critical value of T_{kr} at 5 degrees of freedom for the 5% signifficance level is 2.57. Since the Student's criterion is greater than the critical value of T_{kr}, then the relationship between the statistical samples in Table 3.2.1 exists and we can proceed to the construction of the regression equation (2.3). In the case under consideration, it has the form

$$K^{(3)}=432.9+26.00n^{(3)}. \quad (13)$$

The regression equation (13) is shown in Figure 2.

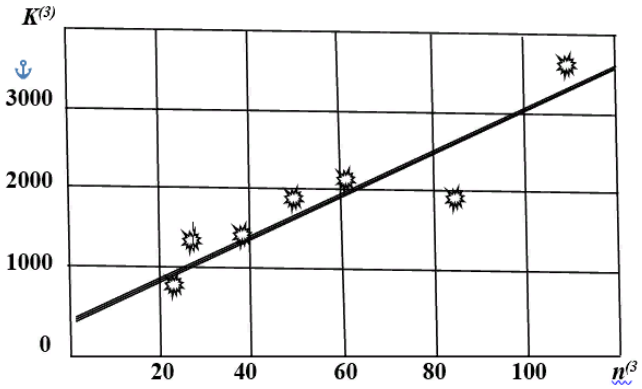

Figure 2. The regression equation (13)

The Fisher criterion calculated by the formula (10) is 5.3, which is greater than the critical value *Fkr*=4.95. The use of the Student's and Fisher's criteria in this case allows us to draw the same conclusion: the mathematical model (13) is adequate.

Trend Analysis

Let us pay attention to the situation, often encountered in the ornithology, when the measured Student's criterion is comparable to or somewhat less than its critical value. In this case, it is recommended to use the following methods of processing observations:

1. evaluate the significance of the regression coefficient b in equation (9);
2. apply the Fisher criterion;
3. use the method of the trend analysis of the study of time series analysis.

Time series differ from row statistics in that the values of its elements depend on the previous elements (Fedoseev et al., 1999). Nevertheless, the trend analysis algorithm, in our opinion, can be extended to the results of ornithological research with some reservations. Of practical interest, for example, is the assessment of the possibility of changing the number of birds in a given region under the influence of anthropogenic factors over time.

The main task of the trend analysis is to identify the trend of changing one factor as another one changes. The mathematical side of the trend model is also expressed by formulas like (8), (9). When identifying a trend in ornithological research, we single out two components: the main one that determines the development trend, called the trend, and the random one e_i, responsible for the deviation from the trend. The deviation value e_i is determined by the difference between the measurement result y_i and the value of functions (8), (9): $e_i=y_i-y(x_i)$. A necessary condition for successful data processing using the trend is the fulfillment of the following requirements (Fedoseev et al., 1999):

1. e_i deviationsions are random;
2. different e_i deviations do not depend on each other, i.e. there is no autocorrelation;
3. deviations obey the normal distribution law.

Let us consider the procedure for carrying out the trend analysis. At the first stage, the randomness of deviations is checked. The randomness is tested using turning points. A turning point is the result of a measurement, for which one of the following conditions is met:

$$y_{i-1}<y_i>y_{i+1} \text{ or } y_{i-1}>y_i<y_{i+1}. \tag{14}$$

If the number of turning points m is greater than the critical value m_{kr}, then the deviations are considered random. The critical value for the 95% confidence level is given by the formula

$$\mathrm{m}_{kr} = \left| 2\frac{(n-2)}{3} - 2\sqrt{\frac{16n-29}{90}} \right|, \tag{15}$$

where n - the number of elements of the row statistics.

Checking deviations for autocorrelation is carried out using the Durbin-Watson test d according to the formula

$$d = \sum_{i=1}^{n-1}(e_i - e_{i+1})^2 / \sum_{i=1}^{n} e_i^2. \tag{16}$$

The calculated value of d is compared with the tabular values d_1 and d_2. There may be two cases here:

1. The value of d does not fall within the interval from 2 to 4. For $d>d_2$, there is no autocorrelation. If $d<d_1$, then there is a relationship between the deviations. When the condition $d_1 \le d \le d_2$ is fulfilled, it is impossible to make an unambiguous conclusion.
2. The value of d falls within the range from 2 to 4. In this case, the parameter $d=4-d$ is determined. Further, the analysis is carried out in accordance with the algorithm given in paragraph (a), where the parameter d is used instead of d.

Checking the compliance of deviations with the normal distribution law is performed using the Pearson's χ^2-criterion (4). In addition to it, the Westergaard method, the *DR* criteri on and other criteria are used (Fedoseev et al., 1999).

When the above conditions are met, the trend analysis is started. The initial data from n measurements are divided into two approximately identical groups. The first group includes the first n_1 measurements, the second - the remaining n_2 elements: $n=n_1+n_2$. Letus introduce the notation for the average values and variances of elements in each group:

$$y^{(1)} = \sum y^{(1)}_i/n_1,\ y^{(2)}=\sum y^{(2)}_i/n_2,\ \dot{s}_{(1)}{}^2=\sum(y^{(1)}_i-y^{(1)})^2/(n_1-1),\ \dot{s}_{(2)}{}^2=\sum(y^{(2)}_i- y^{(2)})^2/(n_2-1).$$

First, the hypothesis about the equality of variances in groups is tested using the Fisher criterion *F* (7). When the value of F is less than the critical value Fkr with a given level of significance, the general variances are equal and it is possible to proceed to assessing the presence of the trend using the Student's *T*-test (7). If the value of T is greater than the critical value of Tkr, then the trend exists. Otherwise, there is no trend. As an example, we will study the possibility of a trend in the number of birds *N* based on the results of n=11 observations in 2010-2011. The initial data are presented in Table 11. The equation for the dependence of the number of birds in thousands on the year of observation *x*, obtained by the LSM method, has the form

$$N=454.5-0.223x. \quad (17)$$

The last line in the Table 5 contains the deviations e_i of the observed values of N_i from the values of $N(x_i)$ obtained using the regression equation (3.4). The standard deviation was s_x = 0.36.

Table 5. The initial data for determining the possibility of existence of a trend in the change in the number of birds N_i in thousands based on the results of n=11 observations from 2000 to 2010

x_i, Year	2000	2001	2002	2003	2004	2005	2006	2007	2008	2009	2010
i	1	2	3	4	5	6	7	8	9	10	11
N_i	9.3	8.7	8.6	8.1	8.5	8.0	7.4	7.7	6.3	7.2	7.3
$e_i=N_i-N(x_i)$	0.30	-0.08	0.041	-0.24	0.09	0.11	-0.27	0.25	-0.92	0.20	0.52

Let us carry out a rejection of possible anomalous values by the Irwin method. The critical value of the Irwin parameter λ_a in accordance with the data in Table 5 equals about 1.5. The maximum value of the parameter λ_i refers to the deviation for number 9 related to measurements in 2008: $\lambda_9=|y_9-y_8|/s_x=|-0.92-0.25|/0.36=3.25$. Since λ_9 is greater than λ_a, the result of the measurement in 2008 should be discarded. In all other measurements, the parameter λ_i is less than the critical value, so they are saved for further analysis. The corrected data after rejection are given in Table 6.

Table 6. Adjusted data to determine the possibility of the existence of a trend in the numberof birds N_i in thousands based on the results of n=10 observations from 2000 to 2010

x_i,Year	2000	2001	2002	2003	2004	2005	2006	2007	2009	2010
i	1	2	3	4	5	6	7	8	9	10
N_i	9.3	8.7	8.6	8.1	8.5	8.0	7.4	7.7	7.2	7.3
$e_i=N_i-N(x_i)$	0.31	-0.10	0.005	-0.31	0.28	0.02	-0.43	0.07	-0.04	0.25

The regression equation obtained by the LSM method for the dependence of the correcteddata has the form

$$N=397.80-0.1944x, \quad (18)$$

where x is the year, N is the number of birds in thousands.

The regression equation (18) is shown in Figure 3. The last line in Table 5 contains deviations e_i of the observed values of N_i from the values of $N(x_i)$ obtained using the regression equation (18). As expected, the mean square deviation of the new model decreased from 0.36 to 0.23 compared to equation (17). At the first stage, we check the requirement for randomness of deviations by the method of turning points. In accordance with condition (1), the turning points are the results of seven deviations (m=7) with numbers 2-5, 7-9 in Table 6.

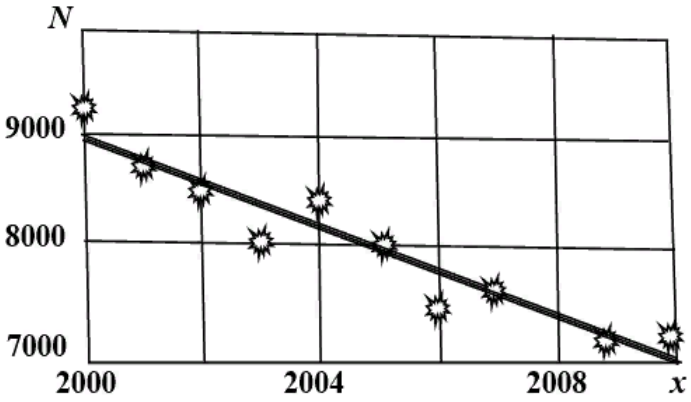

Figure 3. The regression equation (18)

The critical value m_{kr} for ten measurements n=10 is 2.92 according to the formula (12). Since m is less than m_{kr}, the deviations are random. Next, we check the deviations for autocorrelation. The lower and upper critical limits of the Durbin-Watson test for 1% significance are d_1=0.32, d_2=1.30. The Durbin-Watson criterioncalculated by the formula (13) is d=1.95. The value of d is greater than the upper bound of d_2, so there is no autocorrelation.

Let us check the correspondence of deviations to the normal distribution law using the Pearson's χ^2-criterion. Let us break down the sample of n=10 deviations of Table 6 on m=4 intervals of size $h=(e_{max}-e_{min})/m$. From Table 6 it follows that the maximum and minimum values of deviations are equal to e_{max}= 0.31, e_{min}=0.43. Therefore, h=0.185. The Pearson χ^2-criterion calculated by the formula (4) is 2.36. The critical value χ_{kr}^2, for the 5% significance level is 3.8. Since the inequality $\chi^2<\chi^2_{\text{kr}}$ is satisfied, the random variables ek obey the normal distribution law.

All the conditions for the trend analysis are met, so we can proceed to the study of the adequacy of the regression equation (18). The correlation coefficient r_{xy} between the row statistics N and x and the Student's T -test calculated by formulas (7), (8) for the data of Table 6 are -0.93 and 7.54 respectively. The critical value of T_{xy} at 8 degrees of freedom at a 5% significance level is 2.31. Since the Student's criterion is greater than the critical value of T_{kr}, then the relationship between the statistical samples in Table 5 exists.

The Fisher criterion calculated by the formula (11), is equal to 7.20, more than the criticalvalue F_{kr}= 4.95, which indicates the adequacy of the mathematical model (18). In the caseunder consideration, the conclusions obtained using the Student's and Fisher's criteria coincide. Fisher's method is more stringent compared to the Student's method with small correlation coefficients at the level of 0.5-0.7, which can lead to different results. In this case, it is advisable to conduct additional trend studies.

Let us split the datain Table 6 into two identical groups A and B. In the first group A we will include the firstfive measurements, in the second - the remaining measurements. Means and variances in each group are $N^{(1)}$=8.64, $N^{(2)}$=7.52, $s_{(1)}^2$=0.15, $s_{(2)}^2$=0.086. We will check the homogeneity of the variances of the groups under consideration using the Fisher criterion (1.5)F=0.15⁄0.086=1.74. The critical value of F_{kr} for the 5% significance level at 4 degrees of freedom of the numerator and 4 degrees of freedom of the denominator is 6.39. Since $F_{kr}>F$,the variances are homogeneous.

Let us evaluate the presence of the trend using the Student's T-test (4). After substituting the average values of deviations and variances of each group into the formula (4), we have: T=12.9. This value is greater than the critical value T_{kr}=2.31 for 5% significance level at n_1+n_2-2=8 degrees of freedom, so the hypothesis of a trend is accepted. Consequently, the number of birds in the period from 2000 to 2010 is declining. If the average annual number of birds in the first 5 years was estimated at the level of 8640 individuals, then in the last five years it decreased to 7520 individuals. The results of the trend analysis are shown in Figure 4.

Let us compare the results obtained with the help of regression and the trend analyses. Using the regression equation (15), it can be found that the average annual number of birds in the first 5 years of observations was about $N^{(1)}_{Trend}$=8610, and in the last 5 years it was about $N^{(2)}_{Trend}$=6540 individuals. The difference between the two methods for assessing the trend is at the level of 0.3%.

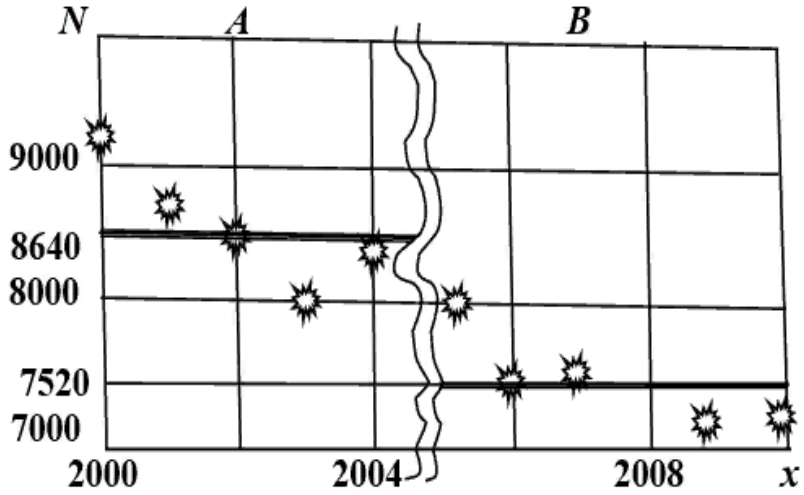

Figure 4. The results of the trend analysis

Development of an Algorithm for Statistical Analysis

Numerous studies of the avifauna on the territory of the wind farms indicate great difficulties in organizing monitoring, collecting information, and in the process of statistical processing of the data obtained (Ralph et al., 2019; Bernardino et al., 2013; Kunz et al., 2007; Hull & Muir, 2010; Kalender & Salih, 2017). The impossibility of duplicating observations under absolutely identical conditions and the influence of uncontrollable factors associated with meteorological and other conditions are partially compensated by long-term observations up to 1-10 years. However, even in this case there are situations when the measured parameters of the dynamics of ornithocomplexes do not fit into the classical schemes of statistical regularities. In this case, it is necessary to pay special attention to rejecting erroneous measurements, identifying individual anomalous data, and careful checking the adequacy of the obtained mathematical models.

The reliability of conclusions based on the results of statistical analysis depends, first of all, on the correctness of the application of the criteria used. The use of each of them requires the fulfillment of certain conditions. For example, the use of the Student's, Irwin's, Durbin -Watson's, Pearson's, Fisher's and other criteria implies the obligatory compliance of the studied sample with the chosen random variable distribution laws. Based on the material presented in this paper and the accumulated experience of statistical studies in a number of publications (Ralph, 2009; Siokhin et al., 2021; Bernardino et al., 2013; Kunz et al., 2007; Anderson et al., 1999; Siokhin et al., 2018; Fedoseev, et al., 1999; Kremer, 2004; Bevanger et al., 2009), we can propose the following algorithm for statistical processing of the results of monitoring the wind farm territory.

Step 1. Selection or development of an information system to ensure the storage of observation results in the form of tables or databases, convenient for systematizing the information received and their subsequent analysis. Examples of such information and computer systems are presented in papers (Osadchyi et al., 2019; Siokhin et al., 2021; Siokhin et al., 2018).

1. Step 2. Primary statistical processing of monitoring results, which consists in determining the average values of row statistics, variances, rejecting the results of erroneous measurements and identifying the random variable distribution law.
2. Step 3. Testing hypotheses about the coincidence of mathematical expectations in a comparative analysis of the number of birds and other parameters, that determine their behavior in different monitoring sites and in different seasons.
3. Step 4. Calculation of correlation coefficients between various parameters that characterize the dynamics of ornithocomplexes depending on the census method, weather, seasonal or other conditions.
4. Step 5. Correlation-regression analysis. Construction of mathematical models, that determine the dependence of one parameter on another parameter.
5. Step 6. Trend analysis to identify the possibility of changes in the number of birds over time or the direction of change in one parameter as another parameter changes.

The proposed algorithm is focused on processing the results of monitoring the dynamics of ornithocomplexes on the territory of wind farms, obtained by the SNH and RAM methods, although they can also be used in the case of other observation methods.

Conclusions

An algorithm for analyzing the results of monitoring the dynamics of ornithological complexes on the territory of wind farms has been developed using statistical methods. The proposed algorithm allows solving the following problems:

1. Carrying out primary processing of information on the number of birds of various species, flight altitude and time spent on observation sites using the Student's *T*-test, Fisher and Pearson criteria.
2. Construction of regression equations that determine the dependence of the number of birds on various factors using the Student's *t*-test, Fisher and Irwin criteria.
3. Trend detection when studying the time dependence of the number of birds or the direction of change of one parameter as another parameter changes using turning points and the Student's *t*-test, Fisher, Irwin and Durbin-Watson tests. The proposed statistical methods have been tested in the analysis of the results of monitoring ornithocomplexes on the territory of the Prymorsk-1 wind farm.

The work was carried out under the state order FRRS-2023-0035 «Assessment of the state of seasonal ornithological complexes and transcontinental migrations at monitoring sites of the Azov-Black Sea region and Sivash, development of software for modeling and managing natural complexes»

Scientific Ethics Declaration

The authors declare that the scientific ethical and legal responsibility of this article published in EPSTEM Journal belongs to the authors.

Acknowledgements or Notes

* This article was presented as an oral presentation at the International Conference on Research in Engineering, Technology and Science (www.icrets.net) held in Tashskent/Uzbekistan on August 22-25, 2024.

* The authors of this paper are grateful to Anastasia Gorlova (Horlova) for translation into English.

References

Anderson, R., Morrison, M., Sinclair, K., & Strickland, D. (1999). *Studying wind energy/bird interactions: a guidance document* (No. NREL/BK-500-27136). National Renewable Energy Lab.(NREL), Golden, CO (United States).

Arikan, K., & Turan, S. L. (2017). Estimation of bird fatalities caused by wind turbines in Turkey. *Fresenius Environmental Bulletin*, *26*(11), 6543-6550.

Bernardino, J., Bispo, R., Costa, H., & Mascarenhas, M. (2013). Estimating bird and bat fatality at wind farms: a practical overview of estimators, their assumptions and limitations. *New Zealand Journal of Zoology*, *40*(1), 63-74.

Bevanger, K., Berntsen, F., Clausen, S., Dahl, E.L, Flagstad, O., Follestad, A., Halley, D., Hanssen, F., Hoel, P.L., Johnsen, L., Kvaløy, P., May, R., Nygård, T., Pedersen, H.C., Reitan, O., Steinheim, Y., & Vang, R. (2009). Pre- and post-construction studies of conflicts between birds and wind turbines in coastal Norway (BirdWind). *Norwegian Institute for Nature Research. Progress Report*. NINA Report 505. (pp. 70). Retrieved from http://www.nina.no/archive/nina/PppBasePdf/rapport/2009/505.pdf

Bicknell, A. W., Sheehan, E. V., Godley, B. J., Doherty, P. D., & Witt, M. J. (2019). Assessing the impact of introduced infrastructure at sea with cameras: A case study for spatial scale, time and statistical power. *Marine Environmental Research*, *147*, 126-137.

Fedoseev, V. V., Garmash, A. N., & Daiitbegov, D. M. (1999). Economic-mathematical methods and applied models. *M., IuNITI*.

Heritage, S. N. (2013). Recommended bird survey methods to inform impact assessment of onshore wind farms. *SNH Guidance. Scottish Natural Heritage, Battleby*.

Hull, C.L., & Muir, S. (2010). Search areas for monitoring bird and bat carcasses at wind farms using a Monte-Carlo model. *Australasian Journal of Environmental Management, 17* (2), 77-87.

Kunz, T. H., Arnett, E. B., Cooper, B. M., Erickson, W. P., Larkin, R. P., Mabee, T., & Szewczak, J. M. (2007). Assessing impacts of wind-energy development on nocturnally active birds and bats: a guidance document. *The Journal of Wildlife Management*, *71*(8), 2449-2486.

Kremer, N. Sh. (2004). *Probability theory and mathematical statistics*. M.: Izd. "Unity-Dana". (pp. 566).

Liechti, F., Guélat, J., & Komenda-Zehnder, S. (2013). Modelling the spatial concentrations of bird migration to assess conflicts with wind turbines. *Biological Conservation*, *162*, 24-32.

Osadchyi, V., Siokhin, V., Gorlov, P., Yeremieiev, V., & Osadcha, K. (2019). Development of the information system for forecasting collision between birds and wind farms. *Eastern-European Journal of Enterprise Technologies*, *4*(2 (100)), 29-40.

Siokhin, V. D., Osadchyi, V. V., Gorlov, P. I., & Yeremieiev, V. S. (2021, June). Identification of "Primorsk-1" wind power plant impact on the ecological situation connected with the behavior of ornithofauna on the azov sea coast. In *Journal of Physics: Conference series*, *1946*(1), 012007. IOP Publishing.

Siokhin, V. D., Horlov, P. I., Polishchuk, I. K., Podorozhny, S. M., Dolynna, O. M., Salnikova-Budenko, I. B., & others. (2018). Conducting modern monitoring studies and developing an expert opinion and a scientific report on the impact of the construction of wind turbines on the natural complexes of the environment, ornithological complexes and migratory birds, bats within the boundaries of Primorye district of Zaporizhzhya region. *Scientific and Industrial Enterprise "Ekoresurs i monitorynh"*,(pp. 149).

Wang, S., Wang, S., & Smith, P. (2015). Ecological impacts of wind farms on birds: Questions, hypotheses, and research needs. *Renewable and Sustainable Energy Reviews*, *44*, 599-607.

Yeremieiev, V., Osadchyi, V., Gorlov, P., & Siokhin, V. (2020). Methodology for calculating the number of migratory birds in the territory of the wind farms of the Azov region using information and communication technology. In *E3S Web of Conferences* (No. 166, pp. 1-8). EDP Sciences.

Author Information

Vladimir Yeremieiev
Professor, Doctor of Technical Sciences
Federal State Budgetary Educational Institution of Higher Education "Melitopol State University". Melitopol., Russia
Contact e-mail: *evs1038@yandex.ru*

Siokhin Valery
Associate Professor, Candidate of Biological Sciences,
Federal State Budgetary Educational Institution of Higher Education "Melitopol State University". Melitopol., Russia

Matsyura Alexander
Professor, Doctor of Biological Sciences
Melitopol State University
Russian Federation, Zaporizhia region, Melitopol, Bohdan Khmelnitsky ave., 18, Melitopol., Russia

Bukreev Dmitriy
Senior Lecturer
Federal State Budgetary Educational Institution of Higher Education "melitopol State University". Melitopol., Russia

To cite this article:

Yeremieiev, V., Siokhin, V., Matsyura, A. & Bukreev, D. (2024). Statistical methods for processıng data on the impact of wind farms on birds. *The Eurasia Proceedings of Science, Technology, Engineering & Mathematics (EPSTEM), 29*, 283-294.

The Eurasia Proceedings of Science, Technology, Engineering & Mathematics (EPSTEM)
ISSN: 2602-3199

The Eurasia Proceedings of Science, Technology, Engineering & Mathematics (EPSTEM), 2024

Volume 29, Pages 295-303

ICRETS 2024: International Conference on Research in Engineering, Technology and Science

Innovations in Cement Production: The Road to Sustainability and A Circular Economy

Vessela Petrova
University of Mining and Geology "St. Ivan Rilski"

Abstract: After water, cement is the most frequently used material on the planet, and the cement industry is critical to any country's economic prosperity. When mixed with water, it produces concrete, which serves as the foundation for buildings, roads, dams, and bridges. According to studies, the cement sector accounts for approximately 8% of global warming carbon dioxide emissions, far more than global carbon emissions from aviation, for example. In this context, the cement industry needs to implement major innovations to ensure sustainability, energy efficiency, and a lower carbon footprint. The scientific publication discusses the most current advances in cement manufacturing, with a focus on methods and technology for achieving sustainability and integrating the cement sector into the circular economy. The study examines the relationship between annual worldwide carbon dioxide emissions and annual global emissions from cement production. The correlation shows that carbon dioxide emissions from cement production have a significant impact on annual worldwide carbon dioxide emissions, emphasising the critical need to apply contemporary, sustainable solutions in this industry.

Keywords: Cement, CO_2, Innovations, Sustainability, Circularity.

Introduction

Cement is an essential construction material that has the potential to greatly contribute to the growing demand for infrastructure due to the increasing global population (GCCA, 2022). According to Grigorova and Koprev the need for raw materials is a prerequisite for their demand on the market and hence for investigations and mining operations. Exploration and mining activities, including sediments mining, are faced with the challenge to ensure both the need for raw materials for the industry and to preserve the fragile ecological balance (Grigorova & Koprev, 2018). Cement production is widely recognised as a significant source of global greenhouse gas emissions (GHGs) (Worrell et al, 2001). It contributes to 7-8% of the total human-caused Greenhouse Gas (GHG) emissions worldwide (Busch et al., 2022).

CO_2 emissions, being a prominent greenhouse gas, provide a substantial contribution to the overall greenhouse effect on a worldwide scale. In 2019, the cement industry released 2.4 gigatonnes (Gt) of carbon dioxide (CO_2), accounting for 26% of total industrial emissions, as reported by the International Energy Agency (IEA, 2020a). Therefore, it is imperative to give high importance to the implementation of low-carbon solutions in the cement business. Cement is manufactured in over 90% of countries and regions worldwide, resulting in a total global production of 4.1 gigatonnes (Gt) in 2019.

The manufacturing of one tonne of cement, on average, emits 0.5-0.6 tonnes of CO_2. The quantity of carbon dioxide released is influenced by several factors, such as the clinker-to-cement ratio, the manufacturing technique, heat recovery methods, and the specific raw materials and fuels employed (Plaza et al., 2020). The reduction of CO_2 emissions from cement production presents challenges primarily because approximately 50% to 60% of CO_2 is produced during the decomposition of limestone (CaCO3) into lime (CaO) (Benhelal et al., 2021). Approximately 30%–40% more carbon dioxide (CO_2) is generated from the combustion of fossil fuels

- Selection and peer-review under responsibility of the Organizing Committee of the Conference

and the indirect discharge of emissions from power generation. The International Energy Agency (IEA) predicts that worldwide carbon dioxide (CO_2) emissions from cement production will decline from 2.4 gigatons (Gt) in 2019 to 0.2 Gt in 2070, based on the sustainable development scenario (SDS).

This reduction is expected to come from a 35% decrease in CO_2 emissions due to reduced demand for cement and a 14% decrease resulting from a lower ratio of clinker to cement. These initiatives are already fully developed and will have a significant impact by 2030. By 2070, CCUS is projected to eliminate over 60% of the total CO_2 emissions, and its function will commence after 2030.

In 2021, China produced 2.36 billion metric tonnes of cement, which represented 56% of global production (DC, 2009). In 2020, the cement industry consumed 175 million tonnes of coal (Wei, 2022). The cement sector generated around 1.375 billion tonnes of carbon emissions, representing over 13.5% of the total emissions in the country (Xinhuanet, 2022). The cement sector has experienced considerable changes in air pollutant emission levels due to the implementation of stricter air pollutant emission limits. Hence, it is crucial to compile a precise emissions inventory for the cement industry.

Various techniques have been identified to reduce the greenhouse gas (GHG) emissions of the cement industry. The initial strategy is the material efficiency plan, which involves enhancing the quality of cement to decrease the required amounts for maintaining its performance. This is also seen as a significant aspect for mitigating climate change. It is advisable to contemplate reducing the amount of cement used in that particular context. Nevertheless, the worldwide increase in population and economic progress indicate that the demand for concrete, and consequently for cement, will continue to rise on a global scale instead of declining.

Method

A comprehensive literature review was conducted to gather existing knowledge on sustainable practices in cement production. Key sources included peer-reviewed journals, industry reports, government publications and conference papers. Search terms included "sustainable cement production," "carbon capture in cement industry," "alternative raw materials for cement," and "circular economy in construction". The relationship between cement production and global CO_2 emissions was analyzed using statistical methods. This involved quantitative analysis of emission data from industry reports and correlation analysis to determine the impact of cement production on overall global CO_2 emissions.

Results and Discussion

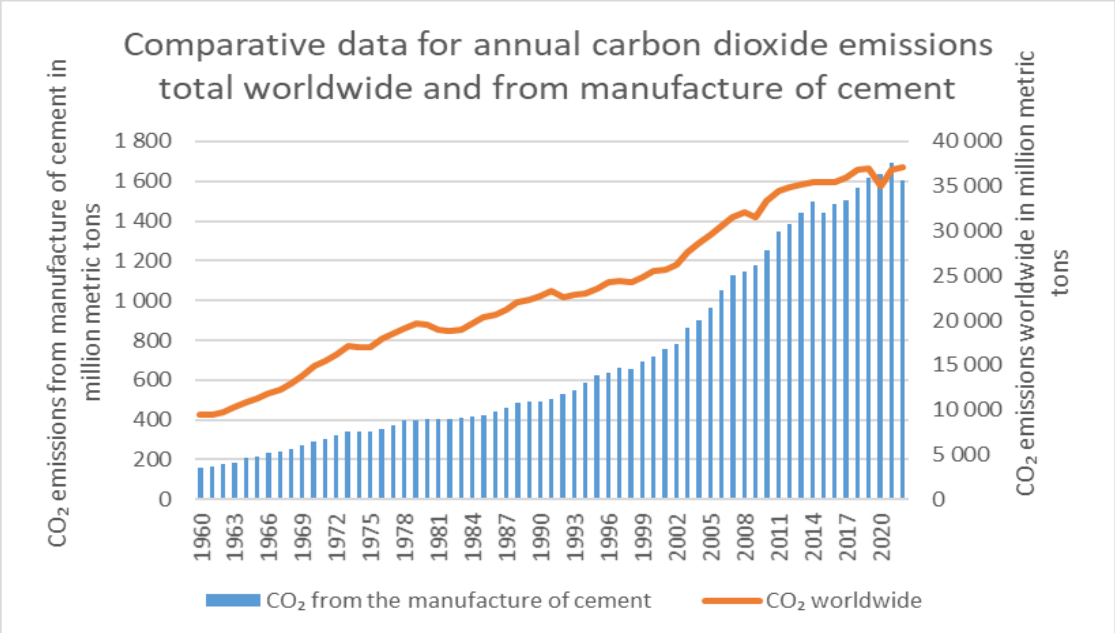

Figure 1. Comparative data for annual carbon dioxide emissions total worldwide and from manufacture of cement

The research in this publication focuses on the comparison between total carbon emissions on a global scale and the carbon emissions caused by cement production. Total Carbon Emissions include all sources of carbon dioxide emissions globally, such as fossil fuel combustion, deforestation, industrial processes and more. Cement Production Emissions specifically refer to carbon dioxide emissions resulting from the production of cement, a significant industrial source of carbon emissions due to the calcination process and energy use. Figure 1 illustrates their development for the period 1960–2022.

Pearson's correlation coefficient was used to determine the linear correlation between the two data sets. Figure 2 demonstrates that carbon dioxide emissions from cement production have a significant impact on annual global carbon dioxide emissions. The equation y=17.078x+11274 describes this dependence. This practically means that an increase in cement production by 1 million metric tonnes will result in an increase in annual carbon dioxide emissions worldwide by more than 17 million metric tonnes, highlighting the urgent need to apply modern purification technologies in this industry. The coefficient of determination, R2, indicates the accuracy of the resulting regression model. Its maximum value can be 1, and the resulting model has been shown to be very accurate.

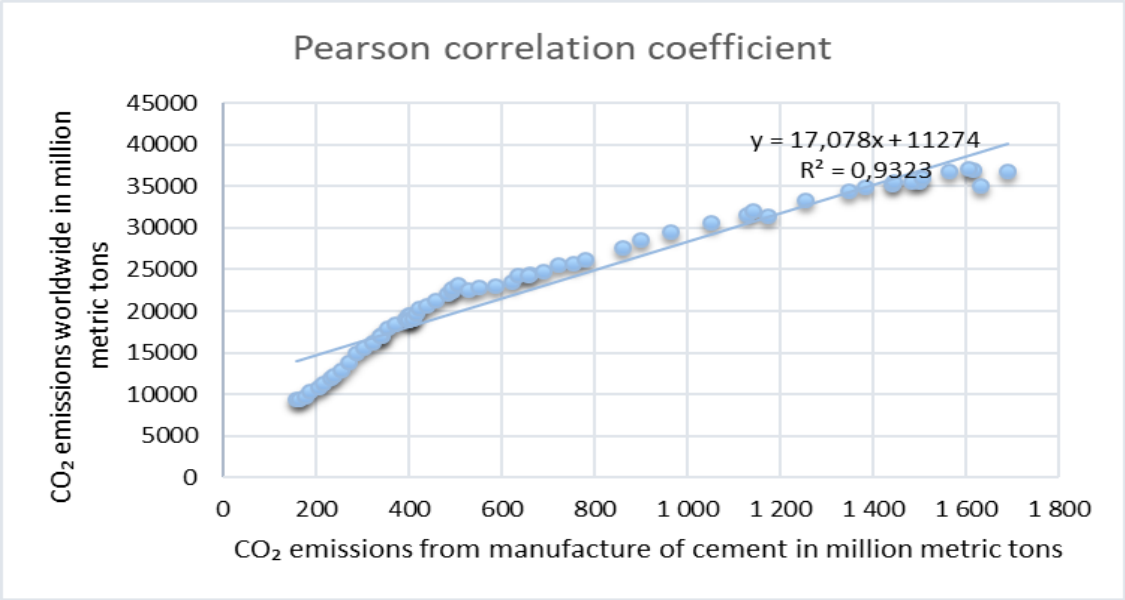

Figure 2. Pearson correlation between annual carbon dioxide emissions total worldwide and the manufacture of cement

The correlation is also evident in population growth, which leads to a higher demand for infrastructure and housing, consequently resulting in increased consumption of construction materials such as cement. The increase in cement usage can be attributed to urban development, industrialisation, and residential construction. As urban areas expand, the demand for additional structures, highways, bridges, and other infrastructure developments also increases.

Principles of Circular Economy in Cement Production

The circular economy model emphasizes sustainability, resource efficiency, waste reduction, and the continual use of resources. In the context of cement production, adopting circular economy principles involves rethinking traditional practices to minimize environmental impact and promote sustainable development. This section explores the key principles of circular economy as they apply to cement production, supported by relevant literature and case studies.

Resource Efficiency

By maximising the utilisation of alternate raw materials, such as industrial by-products like fly ash, slag, and silica fume, the dependence on primary resources can be greatly diminished. Geopolymer cements, which make use of discarded materials, demonstrate this concept.

Waste Minimization

By recycling concrete and utilising demolition waste as aggregate in the creation of new concrete, the amount of trash is reduced and valuable natural resources are conserved (Aleksandrova et al., 2019, Dimov et al., 2020). Smart crushers are advanced technologies that enable the efficient separation and recycling of different components of concrete.

Energy Recovery

Integrating waste heat recovery systems in cement factories enables the capture and reuse of energy, hence enhancing the total energy efficiency. Alternative fuels, such as biomass and fuels obtained from waste, decrease reliance on fossil fuels and decrease carbon emissions.

Product Longevity

Enhancing the longevity and durability of concrete decreases the necessity for frequent repairs and replacements, therefore preserving resources and minimising the environmental footprint over the lifespan of the product.

The Innovations in Cement Production

Low-Carbon Clinker Substitutes

The production of conventional Portland cement clinker significantly contributes to CO_2 emissions due to the high-temperature calcination process required to transform limestone into lime. To address this environmental challenge, several low-carbon clinker substitutes have been developed to reduce carbon emissions associated with cement manufacturing by utilizing alternative materials and methods.

Belite-rich clinkers are a notable example of this innovation. Composed primarily of dicalcium silicate, belite forms at lower kiln temperatures compared to alite, the main component of traditional Portland cement. The production of belite-rich clinkers typically occurs at temperatures around 1250-1350°C, as opposed to 1450°C for alite-rich clinkers. This lower production temperature leads to decreased energy consumption and reduced CO_2 emissions (Buchwald et al., 2019). Additionally, cements with high belite content exhibit superior long-term strength development, although they may demonstrate slower initial strength gain, which can be a disadvantage in applications requiring rapid setting (Gartner, 2004).

Calcium sulfoaluminate (CSA) cements represent another significant advancement in low-carbon alternatives. The production of CSA cements involves mixing bauxite, limestone, and gypsum, with ye'elimite being the primary component of CSA clinker. During hydration, ye'elimite reacts with gypsum to form ettringite and monosulfate, which enhance the cement's strength. CSA cements generate lower CO_2 emissions during production due to reduced limestone content and typically lower calcination temperatures, usually around 1250°C. These cements also set quickly and exhibit high initial strength, making them suitable for fast-track construction projects while demonstrating excellent resistance to sulfate attack (Shi et al., 2011). However, the reliance on specific raw materials, such as bauxite, can pose challenges related to availability and cost (Wang et al., 2020).

Magnesium-based cements, including magnesium oxychloride and magnesium oxysulfate cements, utilize magnesium compounds instead of calcium compounds. A noteworthy variant is magnesium silicate hydrate (MSH) cement, which has the ability to absorb CO_2 during the curing process. This property allows magnesium-based cements to capture and sequester CO_2, thereby reducing net emissions. Additionally, these cements can be produced at lower temperatures compared to traditional Portland cement, leading to energy savings and decreased CO_2 emissions (Meyer, 2009). However, the durability and long-term stability of magnesium-based cements can be compromised in humid environments, and the raw materials required can be more expensive and less accessible than those used for conventional Portland cement (Powers, 2018).

Alkali-activated materials (AAMs), which include geopolymers, are created by activating aluminosilicate materials, such as fly ash or slag, with alkaline solutions. This process eliminates the need for high-temperature

calcination, resulting in significantly reduced CO_2 emissions during production (Davidovits, 1994). AAMs often utilize industrial by-products, which minimizes waste and reduces the demand for virgin raw materials. Furthermore, AAM products demonstrate exceptional durability, including resistance to chemical attacks and high-temperature stability. However, the handling of strong alkaline solutions can present safety challenges, and the lack of standardized production methods can hinder wider acceptance (Van Jaarsveld et al., 2002).

In summary, low-carbon clinker substitutes offer viable solutions for reducing the carbon footprint of cement production. Each alternative presents unique advantages and challenges, and their adoption will depend on regional material availability, cost considerations, and specific application requirements.

Utilization of Industrial By-Products

The utilization of industrial by-products in cement production is a critical strategy for enhancing sustainability and reducing environmental impact. Incorporating materials such as fly ash, slag, and silica fume not only minimizes waste but also improves the performance characteristics of cement (Koprev et al., 2007).

Fly ash, a by-product of coal combustion in power plants, has gained significant attention for its pozzolanic properties. When used as a partial substitute for Portland cement, fly ash can enhance the durability and workability of concrete while reducing overall CO_2 emissions associated with cement production. Studies have shown that incorporating fly ash can lead to improved resistance to sulfate attack and reduced permeability in concrete, contributing to longer service life and reduced maintenance costs (Mehta & Monteiro, 2014).

Similarly, ground granulated blast furnace slag (GGBFS), a by-product from the steel manufacturing process, serves as an effective supplementary cementitious material. The use of slag in cement not only recycles industrial waste but also contributes to the production of low-carbon cements. Slag-based cements exhibit excellent mechanical properties and durability, making them suitable for a variety of construction applications. The hydration products formed with slag lead to increased strength development over time, further enhancing the longevity of concrete structures (Bentz & Stutzman, 2015, Hristova, 2022).

Silica fume, produced during the production of silicon metal or ferrosilicon alloys, is another valuable by-product that enhances the properties of cement and concrete. Its high silica content and fineness improve the density and strength of concrete, making it particularly effective in high-performance applications. The inclusion of silica fume can significantly increase compressive strength and reduce the permeability of concrete, thereby enhancing its durability against environmental stresses (Hooton & Bickley, 2006).
The incorporation of these industrial by-products not only contributes to the circular economy by diverting waste from landfills but also helps in the production of more environmentally friendly cements. By utilizing such materials, the cement industry can significantly reduce its carbon footprint while maintaining or even enhancing the performance of cement and concrete products (Scrivener et al., 2018).

In summary, the utilization of industrial by-products in cement production offers a promising avenue for achieving sustainability goals. By integrating materials like fly ash, slag, and silica fume, the cement industry can promote resource efficiency, reduce environmental impact, and enhance the overall quality of cement and concrete.

Energy Efficiency

Energy efficiency is a crucial aspect of modern cement production, significantly impacting both operational costs and environmental sustainability. The cement industry is inherently energy-intensive due to the high temperatures required for clinker production, making the optimization of energy usage a priority. One effective strategy for enhancing energy efficiency is the implementation of waste heat recovery systems. These systems capture excess heat generated during the manufacturing process, converting it into usable energy for various applications within the plant. By utilizing waste heat, cement producers can reduce their reliance on external energy sources and lower overall production costs (Zhang et al., 2018).

Advanced kiln technologies also play a vital role in improving energy efficiency in cement manufacturing. Innovations such as multi-channel burners and pre-calcination techniques enable more efficient fuel combustion and better thermal management within the kiln. These advancements not only enhance energy efficiency but also contribute to reduced CO_2 emissions. For instance, the use of pre-calcination allows for a portion of the

limestone to be calcined before entering the kiln, which can lower the energy requirements and increase the overall efficiency of the process (Hendriks et al., 2018).

Additionally, optimizing the operation of existing equipment through automation and process control systems can further enhance energy efficiency. By employing real-time monitoring and data analytics, cement plants can fine-tune their operations to minimize energy consumption while maintaining product quality. This integration of digital technologies enables manufacturers to make informed decisions and adopt best practices in energy management (Mourtzis et al., 2020).

Overall, the focus on energy efficiency in cement production not only aids in reducing operational costs but also aligns with the industry's sustainability goals. By implementing waste heat recovery systems, adopting advanced kiln technologies, and optimizing operational processes, cement manufacturers can significantly lower their energy consumption and carbon emissions, contributing to a more sustainable future for the industry.

Carbon Capture and Storage (CCS)

Carbon capture and storage (CCS) is an essential technology for mitigating CO_2 emissions from the cement industry, which is one of the largest industrial sources of greenhouse gases. CCS involves capturing carbon dioxide emissions produced during cement manufacturing and securely storing them to prevent their release into the atmosphere. This process is crucial for achieving climate targets and transitioning towards a low-carbon economy.

One prominent method of CCS is post-combustion capture, where CO_2 is separated from the flue gases after combustion has occurred. This approach utilizes various technologies, such as chemical absorption, to effectively capture CO_2 emissions from cement plants. Research indicates that integrating post-combustion capture systems can significantly reduce overall emissions while maintaining production efficiency (Bui et al., 2018).

Another innovative method within CCS is oxy-fuel combustion, which involves burning fossil fuels in a mixture of oxygen and recycled flue gas instead of air. This process results in a concentrated stream of CO_2, making it easier to capture and store. Oxy-fuel combustion has demonstrated promising results in reducing CO_2 emissions in various industrial applications, including cement production (Zhang et al., 2019). By utilizing this technology, cement manufacturers can potentially achieve higher capture rates while minimizing energy penalties associated with CO_2 capture.

Implementing CCS in the cement industry not only supports emission reduction goals but also aligns with broader sustainability initiatives. By capturing and storing CO_2, cement producers can significantly lower their carbon footprint while maintaining competitiveness in a market increasingly focused on environmental responsibility (IPCC, 2021). Despite the challenges associated with the deployment of CCS, such as high capital costs and the need for extensive infrastructure, ongoing research and development efforts are paving the way for its wider adoption in the cement sector.

In summary, carbon capture and storage is a critical component in the strategy to decarbonize cement production. Through methods like post-combustion capture and oxy-fuel combustion, the cement industry can significantly reduce its greenhouse gas emissions and contribute to global climate goals.

Alternative Fuels

The integration of alternative fuels in cement production is increasingly recognized as a vital strategy for reducing carbon emissions and promoting sustainability. Biomass fuels, such as agricultural residues and wood chips, are particularly significant due to their renewable nature. These materials originate from plant and animal matter, contributing to a carbon-neutral lifecycle. When utilized in cement kilns, biomass fuels release CO_2 that was previously absorbed by plants during growth, thereby maintaining a closed carbon cycle. This approach contrasts sharply with fossil fuels, which release long-sequestered carbon, thereby exacerbating atmospheric CO_2 levels (Gartner, 2004).

Agricultural residues, including straw, husks, and other by-products, can be effectively repurposed as fuel sources in cement manufacturing. This practice not only lowers the carbon footprint of the production process

but also provides an environmentally friendly disposal method for agricultural waste. Additionally, wood chips and forestry by-products serve as valuable energy inputs, further diversifying the fuel mix within the industry (Scrivener et al., 2018).

Waste-derived fuels are equally important in advancing sustainable practices in cement production. Refuse-derived fuel (RDF), which is composed of processed municipal solid waste, significantly aids in diverting waste from landfills while providing a reliable fuel source. The incorporation of RDF into cement production processes enhances energy recovery and reduces dependency on conventional fossil fuels (Worrell et al., 2001). Tire-derived fuel (TDF), produced from shredded tires, is another effective alternative that supports both waste management and energy generation. The utilization of TDF helps cement manufacturers secure a sustainable fuel supply while simultaneously addressing waste disposal challenges (Zhang et al., 2019).

The adoption of these alternative fuels is not only an environmentally responsible choice but also aligns with the principles of the circular economy. By repurposing waste and renewable materials, the cement industry can lower greenhouse gas emissions and improve resource efficiency. This transition represents a strategic move that enhances the resilience and competitiveness of the industry in an evolving market landscape, ultimately contributing to more sustainable cement manufacturing practices.

Digital Technologies

The cement business is being revolutionised by digital technologies, which are improving efficiency, cutting costs, and fostering sustainability. Artificial intelligence (AI) and machine learning (ML) are being more and more used into cement manufacturing processes to enhance operations and enhance decision-making. These technologies facilitate predictive maintenance, wherein algorithms examine past data to identify equipment breakdowns in advance, thereby reducing downtime and operational disturbances. Cement factories can achieve energy consumption optimisation, waste reduction, and improved product quality by utilising artificial intelligence (AI) and machine learning (ML) technologies. This can be accomplished by the use of real-time monitoring and adaptive control systems (Bashir et al., 2020).

The Internet of Things (IoT) is essential for modernising cement production, alongside AI and ML. The Internet of Things (IoT) devices enable the gathering of extensive quantities of data from different phases of the production process, offering valuable insights that can result in enhanced operational efficiency. Embedded sensors in machinery and infrastructure have the capability to monitor performance characteristics in real time. This allows firms to make well-informed decisions using precise and fast information. The connectivity not only improves the visibility of operations but also enables preventive maintenance approaches, resulting in cost reduction and productivity enhancement (Li et al., 2018).

The integration of artificial intelligence (AI), machine learning (ML), and Internet of Things (IoT) has a synergistic impact that enables cement makers to adopt intelligent production systems. For example, the use of AI-powered predictive analytics can enhance the efficiency of the supply chain by accurately predicting demand trends and making necessary adjustments to production schedules. This capacity is especially crucial for effectively managing resources and minimising surplus inventories, which can aid in achieving sustainability objectives (Wang et al., 2020).

Furthermore, the use of these digital technology enables more effective environmental management. Cement plants can achieve substantial reductions in carbon emissions and energy usage by optimising their manufacturing processes and resource utilisation. Aligning with sustainability objectives not only ensures compliance with regulations but also strengthens the competitive edge of enterprises in a dynamic market (Mourtzis et al., 2020).

To summarise, the cement business is being transformed by the implementation of digital technologies such as artificial intelligence, machine learning, and the Internet of Things. These advancements enhance the effectiveness of operations, facilitate preventative maintenance, and encourage environmentally-friendly practices. As the sector increasingly adopts these technologies, there is great potential for improved productivity and decreased environmental impact.

Conclusion

Transitioning to a circular economy in cement production is vital for reducing the industry's environmental impact and aligning with global sustainability goals. Innovations in raw materials, energy efficiency, carbon capture, and recycling provide feasible pathways for achieving this transition. The publication highlights the urgent need to implement modern purification technologies in the cement industry. The publication describes the innovative approaches in the field, namely Low-Carbon Clinker Substitutes, Utilization of Industrial By-products, Energy Efficiency, Carbon Capture and Storage.

By embracing circular economy principles, the cement industry can significantly reduce CO_2 emissions, conserve natural resources, and create a more sustainable future. The path to a sustainable and circular cement industry is paved with innovative technologies and practices that reduce carbon emissions, enhance energy efficiency, and promote the use of alternative materials and fuels. While significant progress has been made, continued efforts are necessary to fully realize the potential of these advancements. By embracing these innovations and integrating them into a cohesive strategy, the cement industry can play a pivotal role in achieving global sustainability goals and mitigating the impact of climate change. The transition to a greener future is not only feasible but imperative for the long-term prosperity of both the industry and the planet.
Continued research, supportive policies, and industry collaboration are essential to drive this transformation.

Scientific Ethics Declaration

The authors declare that the scientific ethical and legal responsibility of this article published in EPSTEM journal belongs to the authors.

Acknowledgements or Notes

* This article was presented as an oral presentation at the International Conference on Research in Engineering, Technology and Science (www.icrets.net) held in Thaskent/Uzbekistan on August 22-25, 2024.

References

Aleksandrova, E., Koprev, I., Balev, V., & Georgiev, D. (2019). Properties and applicability investigation of the overburden solid inclusions as road construction materials in mini Maritsa iztok EAD. *Mining and Geology Magazine*, *8-9*, 41-45.

Bashir, M. A., Lee, S., & Awan, M. A. (2020). Artificial intelligence applications in the cement industry: A review. *Automation in Construction*, *120*, 103401.

Benhelal, E., Shamsaei, E., & Rashid, M. I. (2021). Challenges against CO2 abatement strategies in cement industry: A review. *Journal of Environmental Sciences*, *104*, 84-101.

Bentz, D. P., & Stutzman, P. E. (2015). Properties and durability of concrete incorporating ground granulated blast furnace slag. *Cement and Concrete Research*, 72, 116-123.

Buchwald, A., Voss, K., & Böhme, J. (2019). Performance of belite-rich cements: A review. *Cement and Concrete Research*, 115, 165-174.

Bui, M., Adjiman, C. S., Bardow, A., Anthony, E. J., Boston, A., Brown, S., ... & Mac Dowell, N. (2018). Carbon capture and storage (CCS): the way forward. *Energy & Environmental Science*, *11*(5), 1062-1176.

Busch, P., Kendall, A., Murphy, C. W., & Miller, S. A. (2022). Literature review on policies to mitigate GHG emissions for cement and concrete. *Resources, Conservation and Recycling*, *182*, 106278.

DC, (2009). *Green building' crucial to world's biggest cement producer*. Retrieved from http://www.ch inadaily.com.cn/bw/2009-06/08/content_8257737.htm.

Dimov, E., Bakyrdjieva, R., & Stratiev, N. (2020). The mining industry and the recycling of raw materials as an important element of the Bulgarian economy. *Journal of Mining and Geological Sciences*, 63, 289-292.

Gartner, E. (2004). Industrially interesting approaches to "low-CO_2" cements. *Cement and Concrete Research*, *34*(9), 1489-1498.

GCCA, (2022). *About cement & concrete*. Retrieved from https://gccassociation.org/our-story-cement-a nd-concrete/.

Grigorova, M., & Koprev, I. (2018), Characteristic of the Kriva bara deposit and extraction techniques, *International Scientific Conference Geobalcanica*, 95-100.

Hendriks, C., Worrell, E., & Price, L. (2018). Carbon dioxide emissions from the global cement industry. *Annual Review of Energy and the Environment*, 26(1), 303-329.

Hooton, R. D., & Bickley, J. A. (2006). The use of silica fume in concrete. *Concrete International*, *28*(5), 47-52.

Hristova, T. (2022, June). The place of the blockchain in the recycling of raw materials. In *2022 8th International Conference on Energy Efficiency and Agricultural Engineering (EE&AE)* (pp. 1-4). IEEE.

IEA (International Energy Agency) (2020). Energy technology perspectives. https://www.iea.org/reports/energy-technology- perspectives-2020

Change, I. P. O. C. (2007). Climate change 2007: The physical science basis. *Agenda*, *6*(07), 333.

Koprev, I., & Alexandrova, E. (2007). Potential possibility for displacement of non-productive deposits. *Geology and Mineral Resources, 10*, pp 18-19.

Li, X., Yang, Z., & Zhang, J. (2018). The role of IoT in smart manufacturing: A review. *Journal of Industrial Information Integration*, *10*, 1-12.

Mehta, P. K., & Monteiro, P. (2006). *Concrete: microstructure, properties, and materials*. *https://worksaccounts.com/wp-content/uploads/2020/08/Concrete-Microstructure-Properties-and-Materials.pdf*

Meyer, C. (2009). The greening of the concrete industry. *Cement and Concrete Composites*, *31*(8), 601-605.

Mourtzis, D., Vlachos, D., & Dimitris, K. (2020). Industry 4.0 and digital transformation: The role of smart manufacturing. *International Journal of Production Research*, *58*(1), 1-20.

Powers, M. (2018). The role of magnesium in modern cements. *Cement and Concrete Research*, *112*, 70-76.

Scrivener, K. L., John, V. M., & Gartner, E. M. (2018). Eco-efficient cements: Potential, economically viable solutions for a low-CO_2 cement-based materials industry. *Cement and Concrete Research*, *114*, 2-26.

Shi, C., Wu, Y., & Wang, H. (2011). Properties of calcium sulfoaluminate cements. *Cement and Concrete Research*, *41*(8), 796-801.

Van Jaarsveld, J., van Deventer, J. S. J., & Lukey, G. C. (2002). The characterisation of source materials for alkali-activated cements. *Materials Letters*, *57*(3), 132-139.

Wang, H., & Wang, L. (2020). Advances in calcium sulfoaluminate cement. *Construction and Building Materials*, *261*, 119917.

Wang, Y., Xu, C., & Yan, Y. (2020). Smart manufacturing and big data: A review. *Journal of Manufacturing Systems*, *56*, 102-114.

Wei, Y., (2022). *The ninth China cement energy saving and environmental protection technology exchange conference*. Retrieved from https://www.ccement.com/shidian/V226 27475272205001.html.

Worrell, E., Price, L., Martin, N., Hendriks, C., & Meida, L. O. (2001). Carbon dioxide emissions from the global cement industry. *Annual Review of Energy and the Environment*, *26*(1), 303-329.

Xinhuanet, (2022). *Cement industry: high emission industry in building materials industry*. Retrieved from http://www.xinhuanet.com/science/2022-08/23/c_1310655157.htm (August 24).

Zhang, L., Wu, Z., & Cheng, H. (2018). Waste heat recovery in cement production: A review. *Waste Management*, *76*, 111-119.

Zhang, L., Wu, Z., & Cheng, H. (2019). Oxy-fuel combustion for CO_2 capture in cement production: A review. *Cement and Concrete Research*, *116*, 14-24.

Zhang, L., Wu, Z., & Cheng, H. (2019). Waste tire-derived fuel in cement production: A review. *Waste Management*, *85*, 1-9.

Author Information

Vessela Petrova
University of Mining and Geology "St. Ivan Rilski"
Sofia, Bulgaria.
Contact e-mail: *vessela.petrova@mgu.bg*

To cite this article:

Petrova, V. (2024). Innovations in cement production: The road to sustainability and a circular economy. *The Eurasia Proceedings of Science, Technology, Engineering & Mathematics (EPSTEM), 29*, 295-303.

The Eurasia Proceedings of Science, Technology, Engineering & Mathematics (EPSTEM)
ISSN: 2602-3199

The Eurasia Proceedings of Science, Technology, Engineering & Mathematics (EPSTEM), 2024

Volume 29, Pages 304-310

ICRETS 2024: International Conference on Research in Engineering, Technology and Science

Analysis of Supports Displacements Induced Delamination in Multilayered Indeterminate Beam Structures

Victor Rizov
University of Architecture

Abstract: This theoretical paper is focussed on the problem of delamination in a multilayered beam load-carrying structure that is statically indeterminate. The beam is supported by three supports. The middle support represents a vertical spring. There is no external mechanical loading on the beam. Instead of this, the beam is under vertical displacement of the left-hand support. The main goal of the paper is to investigate the delamination due to the displacement of the left-hand support. Another issue that is under consideration is the effect of the vertical spring. The beam has non-linear elastic mechanical behaviour. The parameters of the non-linear constitutive law that is applied for treating the beam mechanical behaviour vary continuously along the beam length since the beam layers are made of engineering materials that are continuously inhomogeneous in the length direction. Equations for determination of the curvatures and coordinates of the neutral axis in the portions of the beam are constituted. The strain energy release rate (SERR) induced by the support displacement is derived and checked-up by the integral *J*.

Keywords: Support displacement, Multilayered material, Beam, Delamination

Introduction

The problem of delamination of beam load-bearing engineering structures has been investigated mainly for statically determinate beams (Broek, 1986; Dowling, 2007; Rizov, 2018; Rizov, 2021). In the case of statically indeterminate beam structures, the delamination analysis becomes more complicated since the static indeterminacy problem has to be treated first. Also, if the statically indeterminate beams are non-linear elastic, this puts some additional complications in the delamination problem investigation (Rizov, 2019). One of the specific peculiarities that need a detailed examination when studying delamination in statically indeterminate beam structures is the effect of displacements of supports on the SERR.

In this theoretical paper, we give a solution of the SERR for a delamination crack in a multilayered statically indeterminate beam structure on three supports for the case when one of the supports undergoes displacement (we are dealing here with inhomogeneous multilayered beams since multilayered systems are widely used in engineering (Kaul, 2014; Kissiov, 1997; Lloyd & Molina-Aldareguia, 2003; Yu et al., 2003; Rizov, 2005; Rzhanitsyn, 1986; Sy-Ngoc Nguyen et al., 2020; Tokova et al., 2016)). Another issue that is examined in this paper is the influence of the elastic spring on the SERR (it is assumed that the middle support of the beam represents a vertical spring). The SERR solution derived here incorporates both the displacement of the left support and the spring constant of the middle support. Besides, the solution accounts for the non-linear elastic behaviour of the beam structure and the material inhomogeneity of the beam layers along the length. The SERR induced by the support displacement is checked-up by the integral *J*. The analysis leads to results clarifying how the SERR magnitude is influenced by the value of the support displacement and the spring constant.

Analysis

The engineering structure shown in Fig. 1 represents a multilayered beam on three supports in points, H_1, H_3 and H_4.

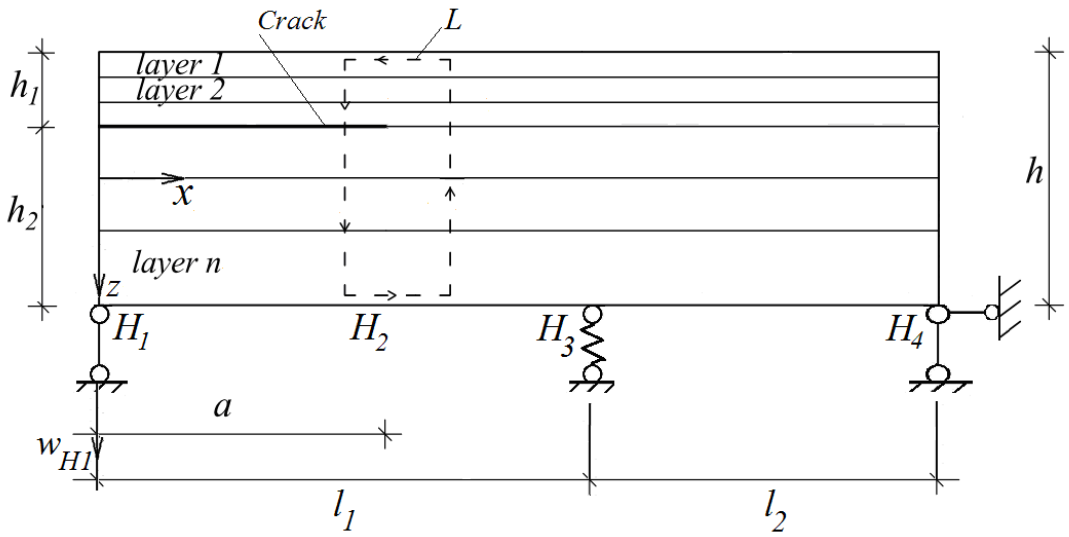

Figure 1. Multilayered beam with delamination.

The support in point, H_3, is a vertical spring with spring constant, C. The beam layers are non-linear elastic. Their behaviour is described by the non-linear constitutive law (1) (Lukash, 1997).

$$\sigma_i = \frac{\varepsilon}{S_i + B_i \varepsilon}, \tag{1}$$

$$i = 1, 2, ..., n, \tag{2}$$

where σ_i is the stress, ε is the strain, S_i and B_i are material properties, n is the number of layers in the beam.

The layers are inhomogeneous along the x axis. Formulas (3) and (4) present the change of material properties along x.

$$S_i = S_{i0} e^{f_i \frac{x}{l_1 + l_2}}, \tag{3}$$

$$B_i = B_{i0} e^{g_i \frac{x}{l_1 + l_2}}, \tag{4}$$

$$0 \le x \le l_1 + l_2, \tag{5}$$

where S_{i0} and B_{i0} are the values of S_i and B_i at the left end of the beam, f_i and g_i are parameters, l_1, l_2 and x are shown in Fig. 1. The support in point, H_1, undergoes vertical displacement, w_{H1}. Our purpose is the derive the SERR for the delamination crack (the latter is located in part, H_1H_2, of the beam (Fig. 1)) with considering w_{H1}. The beam has one degree of static indeterminacy that is treated by the following equations. First, w_{H1} is expressed by integrals of Maxwell-Mohr, i.e.

$$w_{H1} = \int_0^a \kappa_{H1H2} x_1 dx_1 + \int_0^{l_1 - a} \kappa_{H2H3} (x_2 + a) dx_2 + \int_0^{l_2} \kappa_{H3H4} (l_1 + x_3) dx_3 + \frac{w_{H3}(l_1 + l_2)}{l_2}, \tag{6}$$

where κ_{H1H2}, κ_{H2H3} and κ_{H3H4} are the curvatures of the corresponding parts of the beam, x_1, x_2 and x_3 are the local centroidal axes of the beam parts, w_{H3} is the displacement of point, H_3.

The support reaction, R_{H3}, in the spring in point, H_3, is given by

$$R_{H3} = R_{H1}\frac{l_1 + l_2}{l_2}, \tag{7}$$

where R_{H1} is the support reaction in point, H_1.

Formula (8) calculates w_{H3}, i.e.

$$w_{H3} = \frac{R_{H3}}{C}. \tag{8}$$

The next six equations represent conditions for equilibrium of the elementary forces in the cross-sections of the beam parts.

$$N_{H1H2} = b\sum_{i=1}^{i=n_1}\iint_{(A_i)}\sigma_i dA, \tag{9}$$

$$M_{H1H2} = b\sum_{i=1}^{i=n_1}\iint_{(A_i)}\sigma_i z_1 dA, \tag{10}$$

$$N_{H2H3} = b\sum_{i=1}^{i=n}\iint_{(A_i)}\sigma_{H2H3i} dA, \tag{11}$$

$$M_{H2H3} = b\sum_{i=1}^{i=n}\iint_{(A_i)}\sigma_{H2H3i} z_2 dA, \tag{12}$$

$$N_{H3H4} = b\sum_{i=1}^{i=n}\iint_{(A_i)}\sigma_{H3H4i} dA, \tag{13}$$

$$M_{H3H4} = b\sum_{i=1}^{i=n}\iint_{(A_i)}\sigma_{H3H4i} z_3 dA, \tag{14}$$

Where

$$N_{H1H2} = 0, \tag{15}$$

$$M_{H1H2} = R_{H1}x_1, \tag{16}$$

$$N_{H2H3} = 0, \tag{17}$$

$$M_{H2H3} = R_{H1}(a + x_2), \tag{18}$$

$$N_{H3H4} = 0, \tag{19}$$

$$M_{H3H4} = R_{H1}(l_1 + x_3). \tag{20}$$

In equations (9) – (20), b is the beam width, n_1 is the number of layers in the lower delamination arm, N_{H1H2}, N_{H2H3} and N_{H3H4} are the axial forces in the beam parts, M_{H1H2}, M_{H2H3} and M_{H3H4} are the bending moments.

The curvatures and the coordinates of the neutral axes in beam parts, H_1H_2, H_2H_3 and H_3H_4, that are determined from Eqs. (6), (9), (10), (11), (12), (13) and (14) are used to calculate the complementary strain energy, U^*, in the beam via formula (21).

$$U^* = \sum_{i=1}^{i=n_1} \iiint_{(V_i)} u_{0i}^* dV + \sum_{i=1}^{i=n} \iiint_{(V_i)} u_{0H2H3i}^* dV + \sum_{i=1}^{i=n} \iiint_{(V_i)} u_{0H3H4i}^* dV \,, \tag{21}$$

where u_{0i}^*, u_{0H2H3i}^* and u_{0H2H3i}^* are the complementary strain energy densities.
The SERR, G, is given by

$$G = \frac{dU^*}{bda}. \tag{22}$$

The SERR found by (22) is confirmed by the method of the integral *J* (Broek, 1986). This integral is solved along the contour of integration, L, shown in Fig. 1.

Numerical Results

The numerical results for the SERR reported here are for $l_1 = 0.400$ m, $l_2 = 0.300$ m, $a = 0.200$ m, $h = 0.015$ m, $b = 0.008$ m, $n = 5$ and $n_1 = 3$. The results indicating the influence of support displacement, spring constant, and the distribution of the material properties on the SERR magnitude are shown in the next figures. Figure 2 indicates the influence of the support displacement value (the latter is presented by w_{H1}/h ratio) on the SERR magnitude.

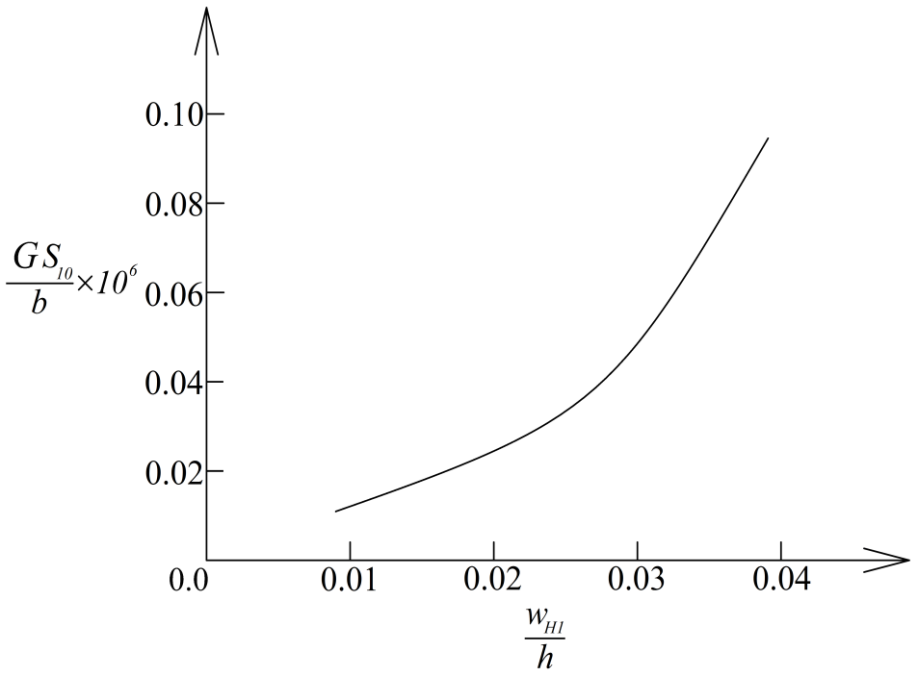

Figure 2. The non-dimensional SERR versus w_{H1}/h ratio.

The rapid growth of the SERR which can be observed in Fig. 2 shows that the support displacements have to be taken into account when analyzing delamination behaviour of statically indeterminate multilayered beam structures.

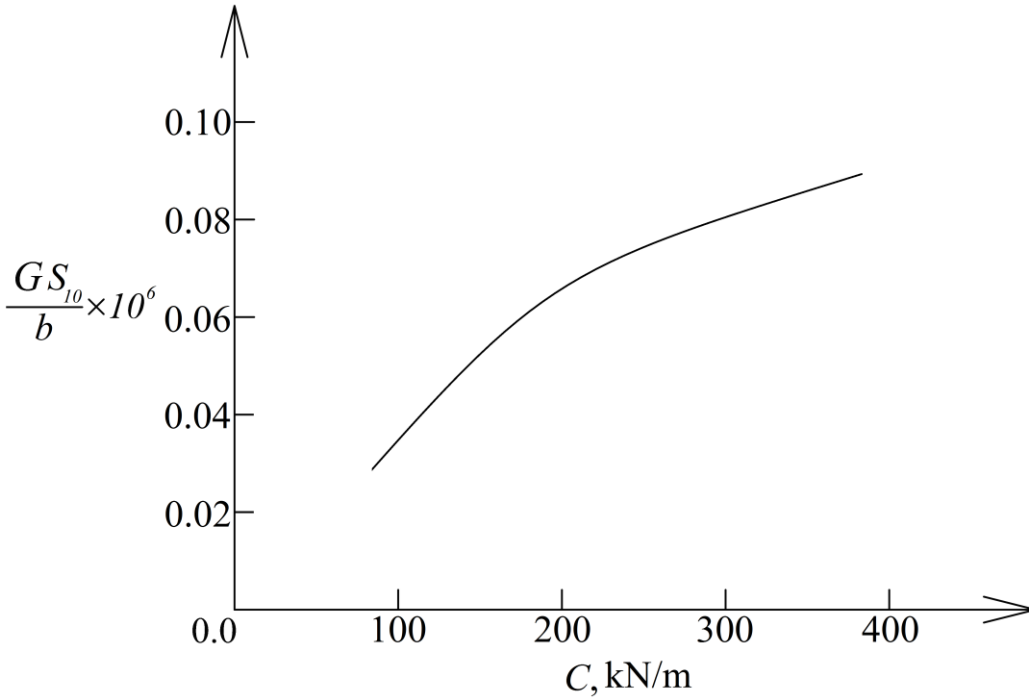

Figure 3. The non-dimensional SERR versus C.

Neglecting the effect of support displacements in delamination studies may have very negative influence on the safety and life of the structures and even may cause structural failure. The curve shown in Fig. 3 illustrates the influence of the value of the spring constant on the SERR magnitude. Since the SERR magnitude changes quickly with rise of the spring constant, it can be concluded that springs have to be considered carefully in the delamination analysis of statically indeterminate multilayered beam structures. The influence of continuous distribution of S_1 along the length of layer 1 of the beam on the SERR magnitude is shown in Fig. 4 (the distribution of S_1 is presented by the parameter, f_1).

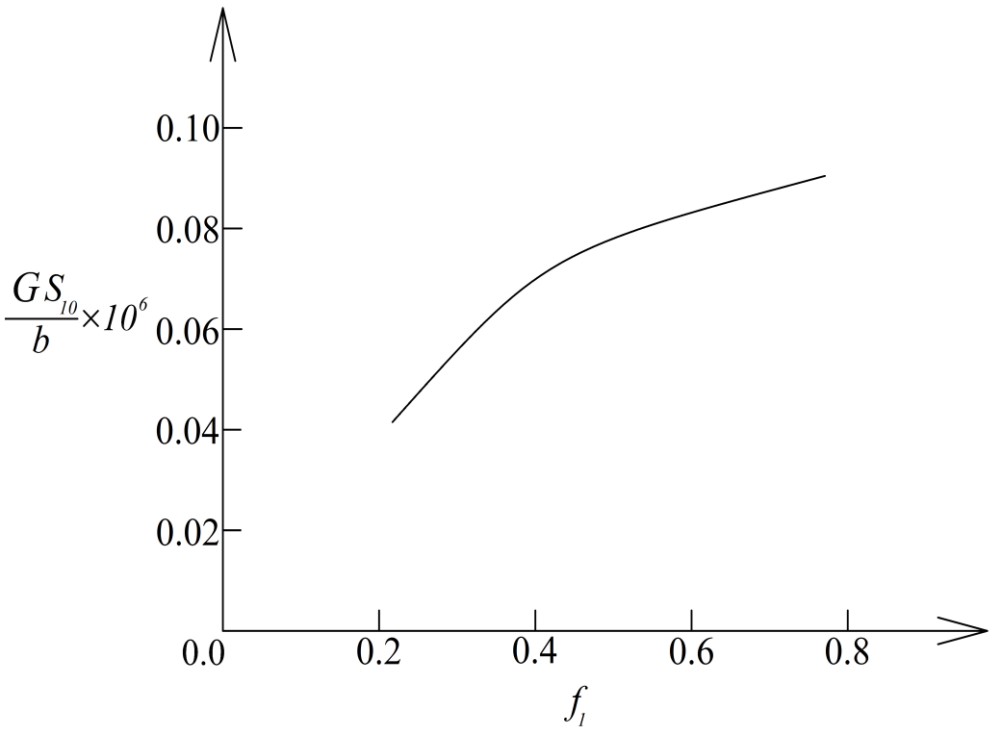

Figure 4. The non-dimensional SERR versus f_1.

From the significant variation of the SERR in Fig. 4 it can be concluded that distribution of S_1 is an important factor for the delamination behaviour.

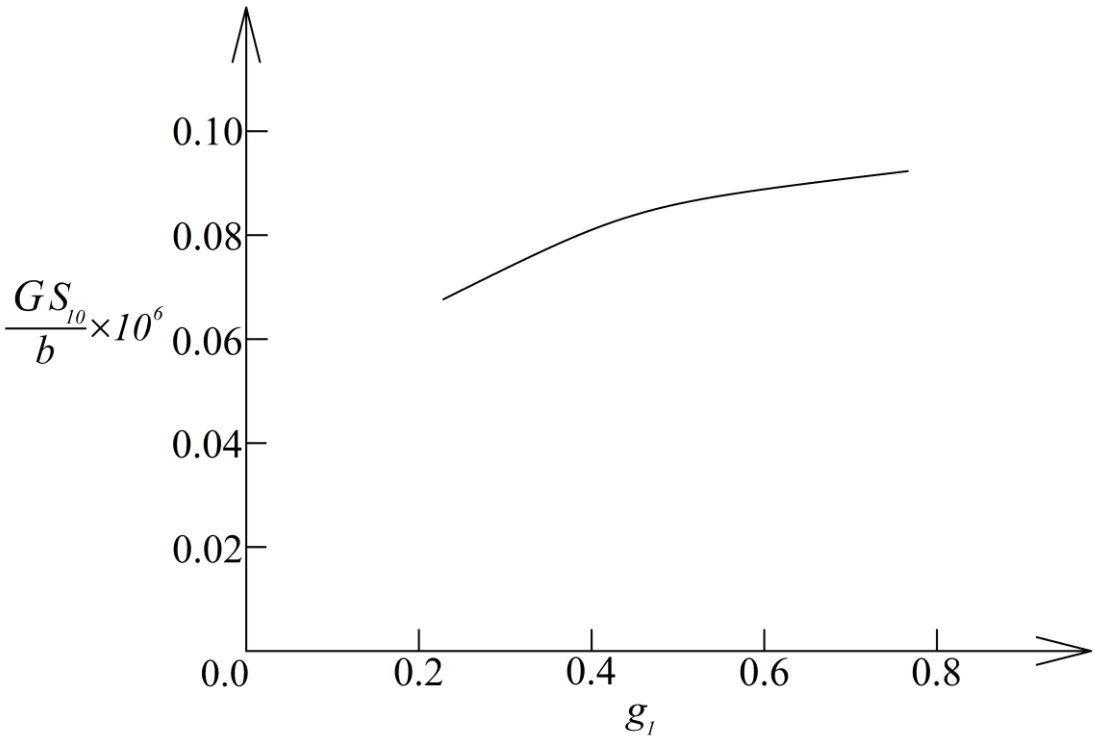

Figure 5. The non-dimensional SERR versus g_1.

Therefore, the S_1 distribution has to be considered in delamination analyses of statically indeterminate beams made of inhomogeneous layers. Another factor whose influence on the delamination is analyzed here is the continuous distribution of B_1 along the length of layer 1 of the beam structure (this distribution is presented by the parameter, g_1). The analysis yielded the curve shown in Fig. 5. It can be seen in Fig. 5 that the distribution of B_1 affects highly the SERR magnitude.

Conclusion

Theoretical study of delamination in a statically indeterminate multilayered beam structure on three supports is carried-out. The main point in the study is that the beam is under support displacement, i.e. delamination is due only to support displacement. Besides, the middle support of the beam is a spring. Thus, the influence of the spring on the delamination in a statically indeterminate beam is also analyzed. The effects of the support displacement and the spring on the delamination are taken into account when deriving the SERR. The study indicates that the SERR magnitude is strongly influenced by the value of the support displacement and the spring constant. A strong influence of the distribution of material properties along the layers length on the SERR magnitude is detected too.

Recommendations

The analytical approach presented in this paper can be recommended also for analyzing support displacements induced delamination in multilayered beams with more degrees of static indeterminacy.

Scientific Ethics Declaration

The author declares that the scientific ethical and legal responsibility of this article published in EPSTEM journal belongs to the author.

Acknowledgements or Notes

This article was presented as an oral presentation at the International Conference on Research in Engineering, Technology and Science (www.icrets.net) held in Tashkent/Uzbekistan on August 22-25, 2024.

References

Broek, D. (1986). *Elementary engineering fracture mechanics*. Springer.

Dowling, N. (2007). *Mechanical behavior of materials*. Pearson.

Kaul, A. B. (2014). Two-dimensional layered materials: Structure, properties, and prospects for device applications. *Journal of Materials Research*, *29*(3), 348-361.

Kissiov, I. (1997). *Strength of materials*. Technics.

Lloyd, S. J., & Molina-Aldareguia, J. M. (2003). Multilayered materials: a palette for the materials artist. *Philosophical Transactions of the Royal Society of London. Series A: Mathematical, Physical and Engineering Sciences*, *361*(1813), 2931-2949.

Lukash, P. (1997). *Fundamentals of non-linear structural mechanics*. Science.

Rizov, V. I. (2005). *Mechanics of composite materials*. BIAP.

Rizov, V. (2018). Non-linear delamination in two-dimensional functionally graded multilayered beam. *International Journal of Structural Integrity*, *9*(5), 646-663.

Rizov, V. (2019). Influence of material inhomogeneity and non-linear mechanical behavior of the material on delamination in multilayered beams. *Frattura ed Integrità Strutturale*, *13*(47), 468-481.

Rizov, V. I. (2021). Delamination analysis of multilayered beams exhibiting creep under torsion. *Coupled Systems Mechanics*, *10*(4), 317-331.

Rzhanitsyn, A.R. (1986). *Built-up bars and plates*. Stroyiizdat.

Nguyen, S. N., Lee, J., Han, J. W., & Cho, M. (2020). A coupled hygrothermo-mechanical viscoelastic analysis of multilayered composite plates for long-term creep behaviors. *Composite Structures*, *242*, 112030.

Tokova, L., Yasinskyy, A., & Ma, C. C. (2017). Effect of the layer inhomogeneity on the distribution of stresses and displacements in an elastic multilayer cylinder. *Acta Mechanica*, *228*(8), 2865-2877.

Yu, J. H., Guo, S., & Dillard, D. A. (2003). Bimaterial curvature measurements for the CTE of adhesives: optimization, modeling, and stability. *Journal of Adhesion Science and Technology*, *17*(2), 149-164.

Author Information

Victor Rizov
Department of Technical Mechanics, University of
Architecture, Civil Engineering and Geodesy
1 Chr. Smirnensky blvd., 1046 – Sofia
Bulgaria
Contact e-mail: *V_RIZOV_FHE@UACG.BG*

To cite this article:

Rizov, V. (2024). Analysis of supports displacements induced delamination in multilayered indeterminate beam structures. *The Eurasia Proceedings of Science, Technology, Engineering & Mathematics (EPSTEM), 29,* 304-310.

The Eurasia Proceedings of Science, Technology, Engineering & Mathematics (EPSTEM)
ISSN: 2602-3199

The Eurasia Proceedings of Science, Technology, Engineering & Mathematics (EPSTEM), 2024

Volume 29, Pages 311-319

ICRETS 2024: International Conference on Research in Engineering, Technology and Science

Design Requirements for the Device for Differentiating Pathological States of Biological Tissues

Volodymyr Sulyma
Dnipro State Medical University

Volodymyr Gaponov
Dnipro State Medical University

Leonid Mescheryakov
Firm KRIPTOIK, Ukraine

Vitaly Kravchenko
Firm KRIPTOIK, Ukraine

Abstract: The appearance of the device for mini-gamma-quantum differentiation of biological tissues, the arrangement of units (research unit and control unit), units (cassette holder, electronic units, etc.) and individual parts (cassette, etc.), as well as control panels (front and rear) have ergonomic indicators that ensure convenience use (preparation for operation – ease of installation of the device on the table, connection to the electrical network and grounding, loading/unloading of biological tissue samples into/from the cassette, etc.); ease of use (ease of working with the control panel and the cassette with the cassette holder); the convenience of preventive maintenance work (cassette disinfection, etc.). The control unit and the research unit are located in different housings of the device: a) control unit – in a high-strength plastic case; b) research unit – in a stainless steel metal case. A measuring device in the form of a scintillation detector is located in the metal case of the research unit, consisting of: a case, a scintillator (crystal, plastic, liquid), a photoelectric multiplier, a power cell, a source of ionizing low-energy gamma radiation in a special protective case that ensures compliance with sanitary requirements and radiation safety standards, and a cassette for biological tissue to be examined (a sample of biological tissue is placed in the biopsies section of the cassette), which is installed in the cassette holder. The design of the cassette holder includes a knife for cutting excess biopsies. The cassette holder is firmly fixed in the housing of the device's research unit. The control unit houses power elements, a microprocessor controller for processing information and maintaining a database, providing communication with peripheral electronic devices. The front panel of the device houses the information monitor and control points. On the back panel there is a device on/off switch, a fuse and places for connecting additional devices. The device has the possibility of applying protective grounding.

Keywords: Device, Mini-gamma-quantum, Differentiation, Tissues

Introduction

Today, modern medicine is used in the treatment of many diseases, from diseases that can be treated on an outpatient basis to diseases that require long-term bed treatment (Sulyma, Bereznytskyy, Duka, &Malinovskyj, 2021; Sulyma & Sulima, 2022; Sulyma, 2022). The quality of the diagnosis of oncological diseases mostly depends on the accuracy of the results of studies that determine the type of neoplasm. The tactics of further examination and treatment of the patient are based on the results of these studies, with the

- Selection and peer-review under responsibility of the Organizing Committee of the Conference

selection of necessary programs of possible complex combined treatment (radiation therapy, chemotherapy, surgery).

An inexpensive instrumental method of differential diagnosis of biological tissues developed by us and currently being implemented in medical practice, which will not only speed up the time of obtaining research results, but also significantly increase their objectivity and reliability on the basis of evidence and fixation of results in physical quantities in a computer program. The developed device is a portable medical apparatus for non-invasive and non-contact differential express diagnostics of normal and pathologically changed tissues of the human body based on the study of biopsies directly during surgical intervention in patients with suspected cancer. The proposed device allows differentiation of biological tissues according to 3 groups:

1. normal biological tissue without pathological formations;
2. biological tissue with non-malignant neoplasms;
3. biological tissue with malignant neoplasms.

Our biological tissue analyzer enables the doctor to establish the nature of the tumor, assess the local or regional spread of the process, determine the boundaries of neoplasms of different localization, assess the extent of surgical intervention and surgical tactics, ensure a negative result at the edges of the resection and reduce the risk of tumor recurrence after its removal.

The industrial production of the developed device will ensure the availability of a tool in every medical organization, which makes it possible to detect cancer early, start quick and high-quality complex combined treatment, reduce the development of complications of the disease and save the lives of patients. Such a device should be in every hospital, every oncology care center, every scientific medical and clinical research center.

The novelty of the proposed solution in the developed small-sized device for express diagnosis of tissues of the human body in the verification of oncological diseases is that the device is a portable medical apparatus for non-invasive and non-contact differential express diagnosis of normal and pathologically changed tissues of the human body based on the examination of biopsies directly during execution surgical intervention.

The main novelty of the development is that the construction of the proposed device is based on the gamma absorption method - a method of elemental analysis based on measuring the degree of attenuation of the gamma radiation flux passing through the biological tissue under investigation, or, in other words, the dependence of the degree of absorption on the biological tissue of a monochromatic beam of gamma quanta with a low energy value ranging from 5 to 17 keB, at which a sample of biological tissue with a thickness of 3 to 5 mm will intensively absorb gamma quanta. At the same time, the weakened flux of gamma quanta, which was not absorbed by the biological tissue and recorded by the device after its irradiation, will have a specific value for a biological tissue, characteristic separately for normal tissues, non-malignant tumors, and tissues affected by a malignant neoplasm.

Irradiation of a tissue sample with a mini-gamma-quantum causes cells to lose their negative charge, thus creating a photoelectric effect (Stoletov effect), which will be strictly individual for tumor, inflammatory and normal tissues. To differentiate various pathological formations, the authors measure the intensity of absorption of gamma quanta by cells, as well as the characteristic emission of microelements present in the tissue. A thallium-NaI (TL) activated sodium-iodine scintillation gamma spectrometric detector converts the energy of gamma quanta entering its sensitive area into flashes of visible light with a brightness proportional to the energy of the gamma quanta.

The current state of differentiation of pathological changes in tissues, and even more so in tumors, requires the use of not only the knowledge, skills and abilities of a pathologist, but also the use of much more informative molecular genetic methods (Kopnyn, 2002). However, the terms of performance of both traditional and modern methods of studying pathologically changed tissues are very significant (from 1 to 7 days), which is especially undesirable in patients with malignant tumors when performing organ-preserving surgical interventions on the biological tissues, which must end with the formation of an any anastomosis .

Usually, the assessment of the state of the ends of the connecting intestine for the presence of parts of the tumor is carried out by the surgeon only visually and by palpation, and only after 5-7 days it is possible to obtain a histological conclusion about the state of the ends of the removed drug. Sometimes, unfortunately, the presence of cancer cells is possible, which leads to a high probability of tumor recurrence in the formed anastomosis

(Sulyma et al., 2007; Сулима et al., 2008). It is important to develop and implement a new instrumental method of differentiation, which will not only speed up the time of obtaining results, but also increase their objectivity and reliability on the basis of evidence and fixation of physical units. There must be a morphological basis for such a method. Normal tissue growth is characterized by two main features: constancy of the cell population (achieved by the balance between proliferation and cell death), and full maturation and differentiation of cells after proliferation (Kopnyn, 2002). With sublethal damage to the genetic material of cells, both fundamental laws of normal tissue growth will be violated. The most frequent types of mutations are translocation, amplification, deletion and point mutations, as a result of which the expression of genes and their products can be excessive (hyperexpression) or suppressed (suppression). This unregulated growth ends with population expansion (cell expansion) and insufficient cell differentiation (Kaz'min & Smirnova, 1989).

Method

One of the main tasks of a surgeon is to determine the extent of surgical intervention in the treatment of colorectal cancer. The choice of the scope of the operation - intestinal resection without restoration of intestinal patency with the formation of a permanent colostomy or sphincter-preserving surgery with restoration of colonic anastomosis patency - depends on the degree of invasion and tumor dissemination (Sulyma, & Malinovskyj, 2021). Since the determination of the borders of the tumor field and the degree of cancer dissemination with carcinoma of the lymphatic and blood vessels is beyond the intraoperative capabilities of the doctor, he relies exclusively on his own experience, intuition, operative findings and the results of preoperative studies.

For radical surgical treatment and to prevent postoperative complications and early recurrences, the surgeon must be sure that the line of bowel resection is not damaged by the neoplastic process. The most common and highly informative diagnostic method is intraoperative express biopsy of intestinal tissue taken from the resection line. When tumor complexes are detected in the line of resection, the surgeon can expand or change the scope of the surgical intervention. Unfortunately, in most hospitals, the method of intraoperative express biopsy is impossible, and even when it is used, the edges of the removed intestine are not completely studied by express examination, but only a few pieces of it, the analysis of which will not give answers about the condition of the ends of the drug. As a rule, the operative material is examined only after the operation, and the doctor receives a conclusion at least a day later, or even 5-7 days after the operation. A modern express method is proposed, which allows determining the extent of tumor spread to neighboring tissues and differentiating tumor and non-tumor processes by means of gamma radiation and residual measurement of samples removed during surgery (Sulyma et al., 2007). The positive achievements of the method consist in the expansion of the surgeon's intraoperative capabilities to determine the type and scope of the operation, which, in the end, is directly related to the improvement of the quality of life of the operated patient.

The method is based on the difference in concentrations of intracellular microelements in tumors and intact intestinal tissues using the phenomenon of the photoelectric effect. Irradiation of the specimens with mini-γ-quanta causes the cells to lose their negative charge, causing a photoelectric effect that is strictly individual for normal, reactively and non-plastically transformed tissues. To differentiate pathological processes of different quality, the intensity of mini-gamma quanta absorption by cells is measured and compared, as well as the characteristic emission of microelements contained in tissues, where the measurement results are represented by the formula.

Biochemical studies of tumors revealed that malignant cells have a different concentration of intracellular ions Na+, K+, and Cl- compared to normal cells. Thus, the concentration of intracellular sodium is increased, while the level of potassium ions is decreased. The ratio of Na+/K+ ions in tumor cells is five times higher than in normal cells. One of the possible explanations for disturbed ion homeostasis of tumor cells is the abnormal activity of Na+/K+-ATP-ase and the altered functioning of the co-transport systems for Na+, K+, Cl- ions, when a shift in the Na+/K+/Ca ion ratio is not only observed in a malignant cell ++, but also their possible influence on the abnormality of the cell shape, its mobility and cellular interactions (Latzkovits et al., 1983; Mtskhvetadze, et al., 1987).

Results and Discussion

Research results indicate that the enzyme Na+/K+-ATPase (sodium pump), in addition to ion transport, is part of the protein complex that transmits growth signals from the extracellular environment to the intracellular

pathway of the replicative signal. The sodium pump acts as a transmembrane receptor for growth factors and is involved in the mechanism of tissue growth, where Na+/K+-ATPase regulates intracellular calcium content (Kaplan,2005).

Changes in metabolism and interactions with Na+/K+-ATPase may be associated with the development of malignant tumors. This is explained by the abnormal activity of Na+/K+-ATPase and its sensitivity in malignant cells, high concentration in the plasma of cancer patients. Na+/K+-ATPase α1-isoform expression is decreased and α3-isoform expression is increased in all colon cancer tissue samples compared with intact colonic mucosa, and poorly differentiated colon carcinomas have reduced Na+/K+-ATPase β1 subunit easy (Espineda et al., 2004;Espineda et al., 2003). These disturbances can explain changes in the level of Na+ and K+ in the cytoplasm of precancerous and tumorous epithelial cells of the colon mucosa (Kometiani et al., 2005).

Determination and fixation of the difference in the concentration of microelements in the tissues of the colon allows to differentiate its states: from normal to damaged by the tumor process. The difference in the composition of pulses for various pathological processes was 30%, which confirms the possibility of differentiating benign, malignant tumors and inflammatory processes of the rectum with the involvement of this energy at a measurement time of 60 seconds (Сулима et al., 2008).

The photomultiplier converts the visible light flashes of the scintillation detector installed opposite the photocathode into electrical pulses with an amplitude proportional to the brightness of the visible light flashes. The pulse amplifier brings the value of the amplitude of electric pulses at the output of the gamma quanta detection unit to several volts, depending on the energy of the output gamma quanta. Thus, the possibility of diagnosing the quality of biological tissue by absorption follows from the fact that the absorption of the same type of radiation will be significantly different in biological tissues of different states. The attenuation of a narrow monoenergetic beam of gamma radiation when passing through biological tissue is described by an exponential law:

$$I = I_0 e^{-\mu_\pi d},$$

where:

I_0 – is the intensity of the gamma radiation beam falling on the biological tissue;
I – is the intensity of the gamma radiation beam that passed through a layer of biological tissue, with a thickness of d cm;
μ_π – is the linear absorption coefficient.

The device developed by us examines mini-samples of biological tissue (biopsies) selected and placed in a special cassette of the measuring part of the analyzer and visually reproduces physical values that are characteristic only for certain tissue states (normal, inflammatory, with non-malignant or malignant growth) with a measurement period from 1 to 6 minutes based on residual characteristic radiation results.

The initial gamma quanta passing through the tissue sample under investigation can receive one of three types of interaction with the electrons of the carbon, nitrogen and oxygen atoms that make up, mainly, the deoxyribonucleic acid molecule, that is, the cell (at the same time, the probability of such a process will be the higher, the more important the density of the study sample will be):

- fluorescent absorption by the electrons of the K- or L-shell of the indicated atoms, while one of the electrons from a more distant orbit, having released excess energy at this time, will move to the vacancy created;
- characteristic radiation, which is cut off by the information processing unit;
- coherent scattering without energy change;
- incoherent scattering with energy change (Compton effect).

The development of a small-sized device for express diagnostics of human body tissues for verification in oncological diseases allowed us to substantiate, manufacture and test a sample of the analyzer, which implements the gamma absorption measurement method using low-energy gamma quanta for differential express diagnostics of the state of normal and pathologically changed tissues of the human body, which are studied during a surgical operation on an oncological patient.

The device allows the doctor to determine the correct and complete volume of surgical intervention when determining the borders of a cancerous tumor, reduces the need to perform a repeat operation (without using the proposed device and method at the edges of the resection, the growth of a cancerous tumor is possible, which will require a new operation), and also provides information on the state of the pathologically changed tissues to confirm the diagnosis.

The main technical parameters that determine the functional, quantitative (numerical) and qualitative characteristics of the developed device.

Functions provided by the proposed device:

1. The device is used in non-invasive, non-contact medical research.
2. The device has such a level of complexity that personnel who have learned only the device's operating instructions are allowed to work with it.
3. The device differentiates the tissues examined according to the following criteria:
- normal biological tissue without pathological formations;
- biological tissue with non-malignant neoplasms;
- biological tissue with malignant neoplasms, and records the obtained results in the form of physical (digital) values.

4. The device has the functional ability to ensure the following actions for express diagnostics:

- calibration with the help of specialized equivalents included in the device package, for working with defined tissue biopsies of a specific part of the human body, as well as re-calibration when switching to another type of biological tissue during operation and in the place of operation of the device using the same equivalents included to the configuration of the device;
- insertion of the biopsy specimen into the cassette of the device's research unit and formation of the defined dimensions of the sample of biological tissue to be examined with the help of the cassette, the cutting mechanism and the cassette holder;
- positioning of the cassette holder with the inserted cassette with the sample to be examined in a molded form in the device's examination unit;
- formation of a low-energy monochromatic collimated stream of gamma radiation with energy from 5 to 17 keV to pass through the research sample;
- measurement of the intensity of the gamma quanta flow after passing through the sample of biological tissue under investigation using a scintillation detector and a photoelectron multiplier;
- perform mathematical processing of the received information;
- display on the monitor the information of the final result in the form of a physical (digital) value and the corresponding category of the state of the biological tissue;
- maintaining a database with the necessary amount of information: numbering of the sequence of research, date, first and last name of the patient, male/female, date of birth, address, digital research result, conclusions based on the research results;
- preservation of the required amount of information;
- communication (wired and wireless) with various electronic devices for data entry;
- transfer of information to a higher-level device for system input of the database and use for official purposes;
- processing of information from the database using artificial intelligence.

Quantitative parameters that determine the device's performance of its functions.

The device must provide the following quantitative parameters:

- distribution of biological tissues, which are studied according to three categories:

a) normal biological tissue without pathological formations;
b) biological tissue with non-malignant neoplasms;
c) biological tissue with malignant neoplasms,

in the form of a physical quantity corresponding to a specific category;
- time of one measurement (exposure time) from 1 to 5 minutes;
- measurement error in comparison with morphological laboratory results studies from 2 to 3%;
- the weight and geometry of the biopsy being studied, which is formed with the help cassette and cutting mechanism: a) weight — from 1.0 g; b) diameter — from 1 to 5 mm;
c) thickness — from 1 to 5 mm;
- the range of measuring the density of the investigated tissues from 1.00 to 1.20 g/cm3;
- use of a low-energy emitting isotope as a source of gamma quanta monochrome flux of gamma radiation with energy from 5 to 17 keV;
- the average working time of the device before failure is not less than 12,000 hours;
- the term of use of the device is at least 10 years.

Design Requirements for the Device.

The device is made in a desktop form with the possibility of moving from one workplace to another depending on the operating conditions (environmental comfort – the microclimate of a medical institution), the workplace – a desk.

The appearance of the device, the arrangement of units (research unit and control unit), units (cassette holder, electronic units, etc.) and individual parts (cassette, etc.), as well as control panels (front and rear) have ergonomic indicators that ensure convenience use (preparation for operation – ease of installation of the device on the table, connection to the electrical network and grounding, loading/unloading of biological tissue samples into/from the cassette, etc.); ease of use (ease of working with the control panel and the cassette with the cassette holder); the convenience of preventive maintenance work (cassette disinfection, etc.).

The control unit and the research unit are located in different housings of the device:
- control unit – in a high-strength plastic case;
- research unit – in a stainless steel metal case.

A measuring device in the form of a scintillation detector is located in the metal case of the research unit, consisting of: a case, a scintillator (crystal, plastic, liquid), a photoelectric multiplier, a power cell, a source of ionizing low-energy gamma radiation in a special protective case that ensures compliance with sanitary requirements and radiation safety standards, and a cassette for biological tissue to be examined (a sample of biological tissue is placed in the biopsies section of the cassette), which is installed in the cassette holder.

The design of the cassette holder includes a knife for cutting excess biopsies. The cassette holder is firmly fixed in the housing of the device's research unit. During the initial period of operation, the device undergoes calibration using equivalents from a set of specialized equivalents included in the device's configuration, for working with certain tissues of various specific areas of the human body.The design of the cassette provides the possibility of heat treatment.The control unit houses power elements, a microprocessor controller for processing information and maintaining a database, providing communication with peripheral electronic devices. The front panel of the device houses the information monitor and control points. On the back panel there is a device on/off switch, a fuse and places for connecting additional devices. The device has the possibility of applying protective grounding.

The core of the presented method is the determination and fixation of different concentrations of trace elements in neoplastically transformed and non-neoplastic tissues using mini-γ radiation. The transformation of a cell from normal to malignant is accompanied by altered expression of the Na+/K+-ATPase enzyme, which is a consequence of both genetic dysregulation of the sodium pump and altered concentration of endogenous agents to which this enzyme is sensitive. Its pumping function decreases, which is manifested by an imbalance of the ionic content of the cell - the concentration of sodium and calcium ions increases, while the level of potassium decreases.

Conclusion

One of the essential characteristic of the malignant tumour is unregulated growth. Two major lows of normal tissue growth - (1) balance between cell proliferation and cell death and (2) complete cell maturation – are

altered as a result of the mutated DNA at the locus of protooncogenes. Various kinds of cancerogenes induce mutations (translocation, point mutation, amplification) in the protooncogenes converting them into oncogenes. The final result of these alterations in the genetic material is abnormal activation of genes responsible for cell proliferation (*sis, ras, abl, myc, N-myc, L-myc, erb,* others) and/or suppression of genes regulated cell death (*Rb, p53, APC, others)* with marked expansion of cellular population.

Well known cell enters cell cycle under the influence of special chemical signals such as hormones, cytokines, and growth factors that bind to correspondent transmembrane receptors on the cell membrane. This extracellular signal transmits via membrane and triggers the intracytoplasmic cascade of reactions of tyrosine kinase phosphorilation - intracellular signaling. In the end of this complex pathway the nucleus receives the signal that creates the expression of growth regulatory genes including *myc, fos, jun,* and pushes the cell to S stage of the mitotic cycle.

Mutation in the genome of somatic cell ultimately leads to activation of growth-promoting oncogenes, alterations of apoptosis-regulated genes, and cancer-suppressor genes with expression of altered genes products and loss of regulatory gene products.The molecular mechanisms by which oncogenes initiate and stimulate tumor growth are: (1) overproduction of the growth factors, (2) increased density of the growth factor receptors on the cell membrane, (3) mutation of the transducer mechanisms, and 4) mutation of the transcription factor.

Precise examination of tumour cell revealed altered concentration of intracellular ions of Na^+, K^+, and Cl^- respect to normal cell. Intracellular sodium is elevated while potassium is depressed. Investigation of this question in urothelial carcinomas discovered the average intranuclear sodium content increased more than three-fold, the potassium content decreased from 32 to 13%, and the chloride level increased too. The Na^+/K^+ ratio were more than five-fold higher in the cancer cells. The possible explanation of such altered ions homeostasis is an abnormal activity of the Na/K-ATPase, as well as an abnormally active Na^+, K^+, Cl^- co-transport systems.

One of the main tasks of the surgeon while carrying out of the resection of colon due to cancer is as more as exact to determine the borders of the intestine resection. Because of the area of tumour spreading and invasion is invisible, the surgeon commonly trusts on self experience and intuition. The histological examination of the frozen tissue samples obtained from the margins of the resection usually sufficient for establishing the presence or absence of complexes of tumour cells.

Although this method is the most reliable and commonly used throughout the world here there is an alternative or additional way that allows determining the precise margins of the resection of the affected colon and differentiation of malignant and non malignant lesions right during surgery. This method is based on the difference in the concentration of the intracellular microelements in tumour and non affected colonic tissue.

The authors use the phenomenon of photoelectrical effect. Radiation of the tissue sample by the mini-γ-quantum induces lost of negative charge by cells thereby creating the photoelectrical effect that will strictly individual for neoplastic and non-neoplastic tissues. For differentiation various pathologic lesions authors measure the intensity of γ-quantum uptake by cells as well characteristic radiation of microelements presence in the tissue.
Thus, the key position of presented method is distinction of the concentration of microelements in malignant and nonmalignant lesions. Taking in account the literature data adduced above this circumstance could be explained by complex and coupled function of sodium pump in cancerogenesis.

The enzyme Na^+,K^+ATP-ase possess unique properties because of combination of so different but interrelated functions – pumping and signalling activity essential for tissue growth. Malignant transformation of a cell accompanies by alterations in functions of this enzyme. So the intracellular concentration of some ions is change together with appearing of disorders of signalling pathway involved in tissue growth.

Presented literature facts regarding participation of Na^+, K^+ATP-ase in tissue growth allow to consider that sodium pump involves in signalling pathway and its acting associated with the expression of protooncogenes. Therefore, the mutated oncogenes caused the abnormal expression and functioning of Na^+,K^+ATP-ase. Some literature sources announced about interdependence between abnormal concentration of intracellular ions and disregulation of the some oncogenes and initiation of malignant transformation of the cell.

This biological tissue analyzer enables the doctor to establish the nature of the tumor, assess the local or regional spread of the process, determine the boundaries of neoplasms of different localization, assess the extent of

surgical intervention and surgical tactics, ensure a negative result at the edges of the resection and reduce the risk of tumor recurrence after its removal.

Recommendations

In the future, the application of the proposed method can objectify and speed up the differential diagnosis of intestinal tumors, and a deep study on other neoplasms of organs and tissues can be the basis of a new direction of instrumental diagnostics in surgery and oncology.

Scientific Ethics Declaration

The authors declare that the scientific ethical and legal responsibility of this article published in EPSTEM journal belongs to the authors.

Acknowledgements or Notes

* This article was presented as an oral presentation at the International Conference on Research in Engineering, Technology and Science (www.icrets.net) held in Tashkent/Uzbekistan on August 22-25, 2024.

References

Сулима В.П., Гапонов В.В., Кравченко В.В., & Мещеряков Л.Г. (2008). *Міні-γ-квантове випромінювання в хірургії та онкології.// 6-а конференція по фізіці високих енергій, ядерній фізіці та прискорювачам.*// Зб. тез. Харків. – 2008. – С. 42.

Espineda, C. E., Chang, J. H., Twiss, J., Rajasekaran, S. A., & Rajasekaran, A. K. (2004). Repression of Na, K-ATPase β1-subunit by the transcription factor snail in carcinoma. *Molecular Biology of the Cell*, *15*(3), 1364-1373.

Espineda, C., Seligson, D. B., James Ball Jr, W., Rao, J., Palotie, A., Horvath, S., ... & Rajasekaran, A. K. (2003). Analysis of the Na, K-ATPase α-and β-subunit expression profiles of bladder cancer using tissue microarrays. *Cancer: Interdisciplinary International Journal of the American Cancer Society*, *97*(8), 1859-1868.

Копнин, Б. П. (2002). Неопластическая клетка: основные свойства и механизмы их возникновения. *Практическая Онкология*, *3*(4), 229-235.

Kaplan, J. H. (2005). A moving new role for the sodium pump in epithelial cells and carcinomas. *Science's STKE*, *2005*(289), pe31-pe31.

Kaz'min, S. D., & Smirnova, I. A. (1989). Cationic control of gene transcription in tumour cells. *Folia Biologica*, *35*(3), 143-151.

Kometiani, P., Liu, L., & Askari, A. (2005). Digitalis-induced signaling by Na+/K+-ATPase in human breast cancer cells. *Molecular Pharmacology*, *67*(3), 929-936.

Latzkovits, L., Torday, C., Jánossy, T., & Erdös, E. (1983). Manifestation of K+ transport alterations in cultured tumour cells of mice. *Acta Chirurgica Hungarica*, *24*(4), 287-294.

McConkey, D. J., Lin, Y., Nutt, L. K., Ozel, H. Z., & Newman, R. A. (2000). Cardiac glycosides stimulate Ca2+ increases and apoptosis in androgen-independent, metastatic human prostate adenocarcinoma cells. *Cancer Research*, *60*(14), 3807-3812.

Mtskhvetadze, A. V., Chillingarov, A. O., & Tushishvili, D. I. (1987). Transmembrane transfer of sodium ions in cell membranes of normal and tumor cells. *Biofizika*, *32*(4), 634-637.

Sulyma V., Gaponov V., Bespyatyj D., & Zelenuk O. (2007). *The method of differentiation with using mini-γ-quantum irradiation as part of Programme for prevention of permanent colostomy*. Electron Microscopy & Microanalysis Conference/Book of Abstract.-Krakow, Poland , (pp.62).

Sulyma, V., & Malinovskyj, S. (2021). Experience in application of mini-invasive methods in proctology. *The Eurasia Proceedings of Health, Environment and Life Sciences (EPHELS)*, *1*, 20-23.

Sulyma, V., Bereznytskyy, Y., Duka, R., &Malinovskyj, S. (2021). General surgery and surgery: Textbooks for training foreign medical students. *The Eurasia Proceedings of Health, Environment and Life Sciences (EPHELS)*, *3*, 29-32.

Sulyma,V.& Sulima, O (2022). Crohn's disease – disease for immunologists, proctologists, gastroenterologists or rheumatologists?. *The Eurasia Proceedings of Health, Environment and Life Sciences (EPHELS), 5*, 84-87.

Sulyma, V. (2022). Variants of modern treatmentof patients with chronic hemorrhoids. *The Eurasia Proceedings of Health, Environment and Life Sciences (EPHELS), 7*, 22-25.

Author Information

Volodymyr Sulyma
Dnipro State Medical University
Vernadskyj Street, 9, Dnipro, 49000, Ukraine
Contact e-mail: *Volodyasulyma2@gmail.com*

Volodymyr Gaponov
Dnipro State Medical University
Vernadskyj Street, 9, Dnipro, 49000, Ukraine

Leonid Mescheryakov
Firm KRIPTOIK
Dnipro, 49000, Ukraine

Vitaly Kravchenko
Firm KRIPTOIK
Dnipro, 49000, Ukraine

To cite this article:

Sulyma, V., Gaponov V., Mescheryakov, L. & Kravchenko, L.(2024). Design requirements for the device for differentiating pathological states of biological tissues. *The Eurasia Proceedings of Science, Technology, Engineering & Mathematics (EPSTEM), 29,* 311-319.

The Eurasia Proceedings of Science, Technology, Engineering & Mathematics (EPSTEM)
ISSN: 2602-3199

The Eurasia Proceedings of Science, Technology, Engineering & Mathematics (EPSTEM), 2024

Volume 29, Pages 320-330

ICRETS 2024: International Conference on Research in Engineering, Technology and Science

Using Queuing Theory and Simulation to Improve Oral Health Program

Ana Paula Lopes
Polytechnic of Porto / ISCAP / CEOS.PP

Ana Cristina Sousa
Polytechnic of Porto / ISCAP

Abstract: Queuing Theory is an important branch of Applied Mathematics which involves the mathematical modelling and analysis of systems where entities, such as customers in a line, arrive at a service facility, wait for service, and then depart after being served. Applied Mathematics provides the tools needed to model and analyze queuing systems. In 2021, the 74th World Health Assembly approved the historic resolution for Oral Health, which, recognizes the need to develop a project and proceed with the launch of a "Global Strategy for Oral Health". In this sense, and for the necessary adaptations to occur in the Portuguese National Health System (PNHS), an in-depth study is necessary specially at the level of human resources, essential for the program to be effectively implemented and the objectives proposals duly achieved. Minimizing patient waiting times is a crucial consideration in healthcare sector management. This work aims to improve and build a discrete event simulation model for modeling patient flow queuing system in an NHS dentist's office, with the purpose of exploring options for designing an effective queuing system. The model of a public dental office is simulated with the help of Arena Software, based on data collected by the Portuguese Dental Association to optimize dental service management. Therefore, through this simulation, the efficiency of this public dental administration can be increased, thus being able to offer oral health care to the entire Portuguese population. The findings of the simulation indicated that little adjustments to the current system could have a significant impact on the use of resources.

Keywords: Arena simulation software, Healthcare logistics, Simulation, Queuing theory, Applied mathematics

Introduction

Queuing Theory is a mathematical approach used to analyze the behavior of queues, which are lines of waiting customers, patients, or other entities requiring service. The fundamental elements of a queuing system include the arrival process (how entities arrive at the queue), the service process (how entities are served), and the queue discipline (the order in which entities are served) (Newton & Medhi, 1992).

In healthcare, Queuing Theory provides essential tools for modeling and analyzing patient flow through various medical facilities, such as hospitals, clinics, and dental offices. Efficient management of these flows is critical to minimizing patient waiting times, optimizing resource utilization, and enhancing the overall quality of care (Green, 2006). Healthcare systems are inherently complex, involving multiple stages of service, varying arrival rates, and diverse patient needs, making Queuing Theory an ideal approach for addressing these challenges (Wallace et al., 2013). Dental offices, use Queuing Theory to streamline patient flow from arrival to departure. By simulating different scenarios, dental offices can identify bottlenecks, optimize appointment schedules, and ensure that resources are allocated efficiently to minimize patient waiting times (Fomundam & Herrmann, 2007).

The Benefits of Queuing Theory in Healthcare are many, such as: by understanding and modeling patient arrival and service processes, healthcare facilities can implement strategies to reduce waiting times, leading to improved patient satisfaction and outcomes (Duguay & Chetouane, 2007; Hall, 2006); queuing models help in determining the optimal number of staff, equipment, and other resources needed at different times, ensuring that resources are used efficiently without overburdening the system(Harper & Shahani, 2002); efficient queuing systems contribute to higher service quality by reducing delays and ensuring that patients receive timely and appropriate care (Kolker, 2008; Rasheed et al., 2012); queuing theory provides a quantitative basis for decision-making, allowing healthcare administrators to make informed choices about resource allocation, staffing, and process improvements (Worthington, 2008; Worthington, 1987).

In 2021, the 74th World Health Assembly (World Health Organization, 2021a)approved a historic resolution for Oral Health, recognizing the critical need to develop a "Global Strategy for Oral Health." This global initiative underscores the importance of oral health and necessitates strategic adaptations in national health systems, including Portugal's National Health System.

The objective of this study is to simulate a queuing model of a public dental office using Arena Software. This simulation aims to enhance the efficiency of the public dental service by evaluating different scenarios and conducting a sensitivity analysis to improve system performance. Ultimately, this research seeks to minimize patient waiting times and ensure the effective delivery of oral health care to the Portuguese population.

Background and Literature Review

Queuing Theory Applications

Queuing Theory is a branch of operations research and applied mathematics that studies the behavior of queues, which are systems where entities wait for service. The fundamental components of a queuing system include the arrival process, the service process, and the queue discipline (Newton & Medhi, 1992). According to Donald Gross (Gross et al., 2011),the key principles of queueing theory are as follows:

- **Arrival Process** - Describes how entities arrive at the service point. It can be deterministic or stochastic. A common stochastic model is the Poisson process, where arrivals are random and independent over time.
- **Service Process** - Explains how entities are served once they reach the service point. This can also be deterministic or stochastic. The exponential distribution is often used to model the time between services.
- **Queue Discipline** - Refers to the rules that determine the order in which entities are served. Common disciplines include First-In-First-Out (FIFO), Last-In-First-Out (LIFO), and priority-based systems.
- **Number of Servers** - The number of parallel service points available. Systems can have a single server or multiple servers.
- **System Capacity** - The maximum number of entities that can be in the system (both waiting and being served) at any time.
- **Population Size** - The size of the population from which entities arrive. This can be finite or infinite.

Originating from the study of telephone call arrivals, Queuing Theory has grown to encompass a wide range of applications, including:

- **Telecommunications** - Managing data packet transmission, call routing, and network bandwidth allocation (Alfa, 2010; Daigle, 2005);
- **Manufacturing**: Optimizing production lines, inventory management, and maintenance scheduling (Bansal & Moses, 2022; Salawu et al., 2020; Xu et al., 2023);
- **Healthcare** - Reducing patient waiting times, optimizing staff levels, and scheduling surgeries or consultations (Kalwar et al., 2021; Mahmudov & Mahmudova, 2022; Nawusu et al., 2020; Santos et al., 2022; Weerakoon et al., 2019);
- **Transportation and Logistics** - Managing traffic flow, scheduling flights, optimizing freight handling, and minimizing delays (Alharbi et al., 2022; Aziziankohan et al., 2017; Jia et al., 2022; Reyes et al., 2023; Zheng et al., 2023);

- **Customer Service** - Staffing call centers, managing checkout lines, and improving customer satisfaction (Brahma, 2013; Feuer & Fallah-Fini, 2020; Gong et al., 2018; Nosek & Wilson, 2001; Preeti & Gupta, 2024; Sakr et al., 2023; Subrayan et al., 2023);
- **Computing and IT** - Allocating computational resources, load balancing in servers, and optimizing cloud services (Fedorova et al., 2023; Han et al., 2023; Kushchazli et al., 2024; Quattrocchi et al., 2024; Sufyan & Banerjee, 2023; Vilaplana et al., 2014; R. Xu et al., 2020).

The main purpose of queuing theory is to improve the efficiency of systems that involve waiting lines, ensuring that resources are utilized effectively while minimizing wait times and costs. By understanding and modeling the behavior of queues, businesses and organizations can make informed decisions about capacity planning, resource allocation, and system design.

Applications in Healthcare

As said before, queuing theory is widely applied in healthcare to improve the efficiency of patient flow, optimize resource utilization, and enhance the quality of care. Some of the key applications in different health fields are:

- **Emergency Departments (EDs) -** Queuing models help manage patient flow in EDs, which often face unpredictable arrival patterns and varying levels of urgency. By optimizing staffing levels and resource allocation, queuing models can reduce patient waiting times and improve care delivery (Alavi-Moghaddam et al., 2012; Cochran & Bharti, 2006; Hajrizi & Berisha, 2019; Samaha et al., 2003). Samaha et al. (2003) used discrete event simulation to analyze and reduce the length of stay in an emergency department. By modeling different scenarios, the study identified optimal staffing levels and process improvements that significantly reduced patient waiting times. Similarly, Cochran and Bharti (2006) applied queuing models to balance bed utilization in obstetrics hospitals, enhancing overall patient flow and resource management.
- **Outpatient Clinics** - Queuing Theory aids in designing appointment systems and managing patient flow in outpatient clinics. Effective scheduling can reduce wait times and enhance patient satisfaction (Cayirli & Veral, 2003; Mtonga et al., 2022; White & Pike, 1964). White and Pike (1964) studied appointment systems in outpatient clinics, focusing on the impact of patient unpunctuality on waiting times. Their work laid the foundation for subsequent studies on outpatient scheduling. Cayirli and Veral (2003) provided a comprehensive review of outpatient scheduling in healthcare, highlighting various queuing models and their applications in reducing patient wait times and improving clinic efficiency.
- **Surgical Units** - In surgical units, queuing models optimize the scheduling of surgeries and the utilization of operating rooms. This helps in minimizing downtime and improving throughput (Ferdinandes et al., 2017; Schulz & Fliedner, 2023; Wang et al., 2020).
- **Pharmacy Services** - Queuing models manage prescription fulfillment processes in pharmacies, ensuring timely service and reducing patient wait times (Adams et al., 2021; Jacobson et al., 2006; Sari et al., 2022; Setiawan & Restiana, 2024).
- **Dental Offices -** Queuing Theory helps dental offices streamline patient flow and optimize appointment schedules, enhancing service delivery and patient satisfaction (Fomundam & Herrmann, 2007; Kakooei, 2022).

The existing literature demonstrates the successful application of queuing models across various medical and dental settings, resulting in reduced waiting times, enhanced service quality, and better overall healthcare outcomes. As healthcare systems continue to face challenges such as increasing demand and limited resources, the application of Queuing Theory will remain crucial in achieving efficient and effective healthcare delivery.

Global Perspective on Oral Health

Oral health is a crucial component of overall health and well-being. It encompasses the health of the teeth, gums, and the entire oral-facial system that allows us to smile, speak, and chew. Poor oral health can lead to significant pain and suffering, impacting an individual's quality of life. It is linked to a range of systemic conditions, including cardiovascular disease, diabetes, respiratory infections, and adverse pregnancy outcomes (Glick et al., 2016; Macdonald, 2000; Petersen & Kwan, 2011).

Globally, oral diseases are among the most common non-communicable diseases (NCDs) and affect people throughout their lifetime, causing pain, discomfort, disfigurement, and even death. The Global Burden of Disease Study 2017 estimated that oral diseases affect half of the world's population (3.5 billion people), with dental caries (tooth decay) in permanent teeth being the most prevalent condition (Kassebaum et al., 2015). Periodontal (gum) disease, which may result in tooth loss, was the 11th most prevalent disease globally (Chang & Chang, 2019; Naqvi et al., 2022).

Oral diseases disproportionately affect the poor and socially disadvantaged in all countries, reflecting significant inequalities. Access to oral health services is limited in many low- and middle-income countries, and even in high-income countries, underserved populations often experience high levels of oral disease (Petersen & Kwan, 2011).

Recognizing the importance of oral health, the 74th World Health Assembly in 2021 approved a historic resolution for oral health, calling for the development of a "Global Strategy for Oral Health." This strategy emphasizes the need for integrating oral health into primary healthcare, improving oral health literacy, and addressing the social determinants of oral health (World Health Organization, 2021b).

Importance of Oral Health in Portugal

In Portugal, oral health has gained increased attention over the past decades. However, despite improvements, there are still significant challenges. The Portuguese population has historically faced high levels of oral diseases, including dental caries and periodontal disease. The prevalence of these conditions remains a public health concern, especially among children and older adults (Portuguese Dental Association, 2021).

The importance of oral health in Portugal is underscored by its impact on individuals' overall health, productivity, and quality of life. Poor oral health can lead to pain, infection, and tooth loss, affecting nutrition, speech, and self-esteem. Additionally, it is associated with chronic conditions such as diabetes and cardiovascular diseases, which are prevalent in the Portuguese population (Carvalho et al., 2016; Costa et al., 2024).

In alignment with global initiatives, Portugal has taken steps to enhance its national oral health strategy. The Portuguese government has launched several programs aimed at improving oral health services, particularly for vulnerable populations. One such initiative is the National Program for the Promotion of Oral Health (PNPSO), which focuses on preventive care, access to dental services, and education (Direção-Geral da Saúde, 2020).

Simulation in Healthcare System

In simulation, the system of interest is replaced with a physical or computational model, resulting in model-based experimentation. Doing field experiments and using this approach are conceptually quite similar. In numerous instances, the technique has shown to be helpful in helping management gain a deeper grasp of their present operations and create better models to address issues. In order to minimize wait times, this method comprises assessing and testing various designs as well as verifying, elucidating, and endorsing simulation results and research recommendations (Alam et al., 2018).

One of the best simulation tools for creating models based on observations and offering different possibilities is Arena Software. Several studies have demonstrated improvements in patient flow, resource utilization, and overall efficiency of health services. These, provide a comprehensive understanding of how Arena Software can be effectively used to enhance dental healthcare delivery (Günal & Pidd, 2010; Kakooei, 2022; Kamali et al., 2022; Mohd Fadilah et al., 2023).

Methodology

Simulation Arena software was used in this study's simulation modeling approach. The data collection process, including dental consultation times in the National Health Service (NHS) were collected from the Order of Dentists, which developed a reference document with the aim of promoting the normative and guiding bases for organizing the consultation, both by dentists and health management planners (Ordem dos Médicos Dentistas, 2021). The model needs information about the number of patients, their arrival time at the dental office as well

as the start and finish times of each procedure, including registration, medical care, dental consultations, prescription fillings, and payment. This study also aims to demonstrate that it is possible to create dental medical offices in the Portuguese National Health System (PNHS) as well as create the careers of dentists and dental assistants, in a planned manner and above all supported by the Primary Health Care (PHC), taking into account the scarcity of resources in the dental health area, so that Portugal can meet the objectives recommended in the Global Action Plan for Oral Health (2023-2030) by the WHO (World Health Organization, 2023). As a way to maximize the profitability of PNHS dental practices, only one dental office is available in a PNHS health unit, it is proposed to use three dentists for every two dental practices, located in different health units, but close to each other; two of the three dentists work full-time, in different offices; and the third dentist fills the gaps between the two offices, alternately between the two offices close to each other, making up a total of 12 hours of continuous daily operation of the dental medical offices in the PNHS health units. Appointments are taken at the dental medical offices from 8:00 am to 8:00 pm, Monday through Friday, excluding holidays. Dentists are always assisted by an assistant, who works equally in terms of hours and rotation, so that they can make the most of available resources and considering the need for permanent care in the PNHS and can cover the greatest number of possible users. There is no Emergency dentist in these PNHS dental offices. Figure 1 shows the flowchart of patients at the local health unit from PNHS, with patient care by the dentist in the specialties: Consultation, Dentistry, Surgery, Endodontics, Periodontics and Prosthetics.

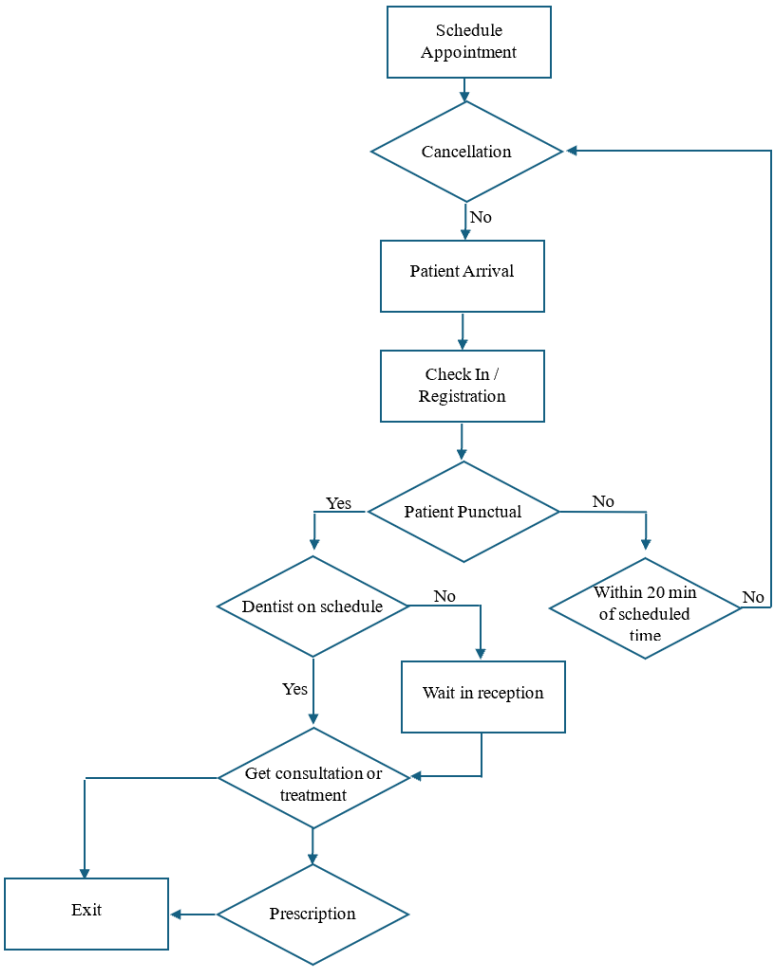

Figure 1. Illustration of the dental office Flowchart in a PNHS health unit

Data regarding dental specialties were taken from the 7th Ed. Oral Health Barometer (Ordem dos Médicos Dentistas (OMD), 2022), which the OMD carries out and publishes annually and only treatments that are included in the National Oral Health Promotion Plan (NOHPP) and according to the goals set out in the Working Group Report – SNS | Oral Health 2.0 (Sistema Nacional da Saúde (SNS), 2023). Among the treatments and respective specialties, Orthodontics was not taken into consideration, as it is not covered by the NOHPP and is not included in the Working Group Report – SNS | Oral Health 2.0. In table 1, there are the percentages of appointments by specialty.

Table 1. Percentages for type of consultation by specialty

Type of Appointment by Specialty	**Percentage (%)**	**Specialty**
Regular visits / Check-Up	26,3%	Consultation
Perform Restorations	14%	Dentistry
Tooth Extraction	9,2%	Surgery
Pain	8,1%	Endodontics
Teeth Cleaning / Gum Problem	27,2%	Periodontics
Placing Prosthetics/Implants	15,2%	Prosthetics

To improve the appointment scheduling process and optimize scarce resources in the PNHS dental practice, the current system was modeled based on data provided by the Dental Association and many years of professional experience. Model performance was evaluated, and output results were compared with those of the current system.

A dental office in a PNHS health unit simulation model was created using Arena simulation software version 16.2, to predict changes in patient waiting time and queue waiting length resulting from variations in the system. Figure 2 shows a screenshot of the existing simulation model in Arena. Seven Discrete Processing modules, Create, Process, Delay, Assign, Route, Station, and Dispose, one Decisions module, Decide, and one Input Output module, Record, with the analysis from the input analyzer, were included in the model.

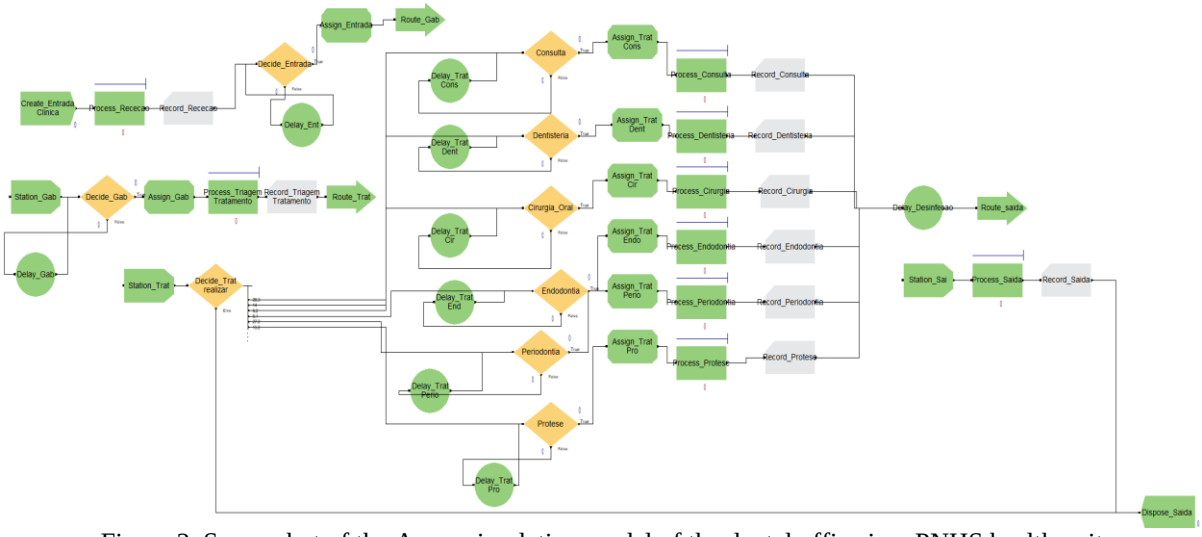

Figure 2. Screenshot of the Arena simulation model of the dental office in a PNHS health unit

The simulation model was executed for ten replications, with each replication simulating a full week of five business days, ensuring the robustness of the results. The dental office operates for 720 minutes (12 hours) each day. Two scheduling scenarios were tested to optimize the appointment scheduling times: Scenario 1 with 30-minute slots and Scenario 2 with 40-minute slots. To evaluate the effectiveness of the processing procedures used in dental offices, a few outputs were tracked. These outputs will be utilized to improve the model. The results are presented in the next section.

Results and Discussion

A simulation model for modeling patient flow queuing system in an Portuguese National Health System dentist's office, with the purpose of exploring options for designing an effective queuing system of a public dental office is simulated by using Arena Software and run it to get the simulation results. The primary metrics tracked were the average processing time for each process and the average number of patients treated for each process.

In Scenario 1, the dental office used 30-minute scheduling slots. The results, as shown in Table 2, indicate the average number of patients treated and the average time spent for each type of appointment by specialty.

Table 2. Average number of patients treated and average time for each process from Scenario 1

Type of Appointment by Specialty (Scenario 1)	Average Number Patients	Average Time (min)
Consultation	29	20,0544
Dentistry	15	44,6888
Surgery	10	31,7800
Endodontics	9	55,2606
Periodontics	30	30,0854
Prosthetics	16	30,1025

In Scenario 2, the dental office used 40-minute scheduling slots. The results, as shown in Table 3, indicate the average number of patients treated and the average time spent for each type of appointment by specialty.

Table 3. Average number of patients treated and average time for each process from Scenario 2

Type of Appointment by Specialty (Scenario 2)	Average Number Patients	Average Time (min)
Consultation	24	20,1947
Dentistry	13	45,0330
Surgery	8	31,6178
Endodontics	7	55,5634
Periodontics	24	30,1713
Prosthetics	13	30,0708

The results from the simulation highlight several important aspects of scheduling effectiveness in the dental office setting:

- **Consultation Appointments**:
    - In Scenario 1, with 30-minute slots, the dental office was able to treat an average of 29 patients per week, with an average processing time of approximately 20 minutes.
    - In Scenario 2, with 40-minute slots, the number of patients treated decreased to 24, while the average processing time remained similar.
- **Dentistry Appointments**:
    - The average number of patients treated in Scenario 1 was 15, with an average processing time of about 45 minutes.
    - In Scenario 2, the number of patients treated decreased to 13, while the average processing time slightly increased.
- **Surgery Appointments**:
    - Scenario 1 allowed for an average of 10 surgeries per week with an average processing time of approximately 32 minutes.
    - In Scenario 2, both the number of surgeries and the average processing time slightly decreased.
- **Endodontics Appointments**:
    - In Scenario 1, an average of 9 patients were treated, with the longest average processing time of 55 minutes.
    - Scenario 2 saw a decrease to 7 patients, with a slight increase in processing time.
- **Periodontics Appointments**:
    - Scenario 1 facilitated the treatment of 30 patients per week, with an average processing time of 30 minutes.
    - Scenario 2 saw a reduction to 24 patients, with a marginal increase in processing time.
- **Prosthetics Appointments**:

- Scenario 1 managed to treat an average of 16 patients per week, with an average processing time of approximately 30 minutes.
- Scenario 2 treated fewer patients (13), but the processing time remained virtually unchanged.

Implications for Dental Office Operations

The analysis suggests that shorter scheduling slots (Scenario 1) generally allow for a higher number of patients to be treated across most specialties, although with marginal increases in processing time for some types of appointments. On the other hand, longer slots (Scenario 2) reduce the number of patients treated but do not significantly impact the average processing time for most appointment types.

Optimizing scheduling times is crucial for balancing the number of patients treated with the quality of care provided. The results indicate that a 30-minute slot scheduling system might be more effective in maximizing patient amount without substantial increases in processing times, making it a potentially better choice for the dental office's queuing system. Future improvements to the model could include additional factors such as patient satisfaction, variability in appointment types, and more detailed tracking of resource utilization to further refine the scheduling system.

Conclusion and Recommendations

This study aimed to optimize the scheduling system of a public dental office within the Portuguese National Health System by simulating patient flow using Arena Software. Two scenarios were analyzed: one with 30-minute scheduling slots (Scenario 1) and another with 40-minute scheduling slots (Scenario 2). The primary metrics evaluated were the average processing time for each process and the average number of patients treated per week. The findings revealed that Scenario 1, utilizing 30-minute slots, generally allowed for a higher number of patients to be treated across various specialties compared to Scenario 2 with 40-minute slots. Specifically, Scenario 1 facilitated a greater patient throughput in consultations, dentistry, surgery, endodontics, periodontics, and prosthetics. Despite the increased patient numbers, the average processing times remained comparable between the two scenarios, indicating that shorter slots did not significantly compromise the time required for each appointment type. This research underscores the importance of optimizing scheduling times to enhance the efficiency of dental office operations. The 30-minute slot scheduling system demonstrated a potential to maximize patient throughput without notably increasing the processing times, suggesting it as a more effective option for the public dental office's queuing system. Implementing such a system could lead to improved patient access to dental care services and better utilization of resources.

Future research could build on these findings by incorporating additional variables such as patient satisfaction, variability in appointment durations, and resource allocation to further refine the model and enhance the effectiveness of the dental office scheduling system.

Scientific Ethics Declaration

The authors declare that the scientific ethical and legal responsibility of this article published in EPSTEM journal belongs to the authors.

Acknowledgements or Notes

* This article was presented as a poster presentation at the International Conference on Research in Engineering, Technology and Science (www.icrets.net) held in Thaskent/Uzbekistan on August 22-25, 2024.

* This work is financed by Portuguese national funds through FCT – Fundação para a Ciência e Tecnologia, under the project UIDB/05422/2020

References

Adams, S., Mulubwa, M., van Huyssteen, M., & Bheekie, A. (2021). Access to chronic medicines: patients' preferences for a last kilometre medicine delivery service in Cape Town, South Africa. *BMC Family Practice*, *22*, 1-12.

Alam, S., Osama, M., Iqbal, F., & Sawar, I. (2018). Reducing pharmacy patient waiting time. *International Journal of Health Care Quality Assurance*, *31*(7), 834-844.

Alavi-Moghaddam, M., Forouzanfar, R., Alamdari, S., Shahrami, A., Kariman, H., Amini, A., ... & Shirvani, A. (2012). Application of queuing analytic theory to decrease waiting times in emergency department: does it make sense?. *Archives of Trauma Research*, *1*(3), 101.

Alfa, A. S. (2010). *Queueing theory for telecommunications: discrete time modelling of a single node system*. Springer Science & Business Media.

Alharbi, E. A., Abdel-Malek, L. L., Milne, R. J., & Wali, A. M. (2022). Analytical model for enhancing the adoptability of continuous descent approach at airports. *Applied Sciences*, *12*(3), 1506.

Aziziankohan, A., Jolai, F., Khalilzadeh, M., Soltani, R., & Tavakkoli-Moghaddam, R. (2017). Green supply chain management using the queuing theory to handle congestion and reduce energy consumption and emissions from supply chain transportation fleet. *Journal of Industrial Engineering and Management (JIEM)*, *10*(2), 213-236.

Bansal, S., & Moses, S. (2022). Reliability characteristics of machining systems and some queueing theory regarding the machine repair problem. *International Journal for Research in Applied Science & Engineering Technology (IJRASET)*, *10(XII)*.

Brahma, P. K. (2013). Queuing theory and customer satisfaction: a review of terminology, trends, and applications to hospital practice. *Asia Pacific Journal of Marketing & Management Review*, *2*(6), 83-89.

Carvalho, C., Manso, A. C., Escoval, A., Salvado, F., & Nunes, C. (2016). Self-perception of oral health in older adults from an urban population in Lisbon, Portugal. *Revista de Saude Publica*, *50*, 53.

Cayirli, T., & Veral, E. (2003). Outpatient scheduling in health care: a review of literature. *Production and Operations Management*, *12*(4), 519-549.

Chang, C. C., & Chang, S. H. (2019). Occupational health nurses promote oral health. *Hu Li Za Zhi*, *66*(1), 14-20.

Cochran, J. K., & Bharti, A. (2006). Stochastic bed balancing of an obstetrics hospital. *Health Care Management Science*, *9*, 31-45.

Costa, H., Lopes, P., Correia, M. J., Couto, P., Silva, A. M., López-Marcos, J. F., & Veiga, N. (2024). Oral health literacy and determinants among an elderly community in Portugal. *International Journal of Environmental Research and Public Health*, *21*(6), 735.

Daigle, J. N. (2005). *Queueing theory with applications to packet telecommunication*. Springer Science & Business Media.

Duguay, C., & Chetouane, F. (2007). Modeling and improving emergency department systems using discrete event simulation. *Simulation*, *83*(4), 311-320.

Fedorova, E., Lapatin, I., Lizyura, O., Moiseev, A., Nazarov, A., & Paul, S. (2023). Queueing system with two phases of service and service rate degradation. *Axioms*, *12*(2), 104.

Ferdinandes, M. G. R. U. K., Lanel, G. H. J., & Samrarakoon, M. A. S. C. (2017). A queuing model to optimize the performance of surgical units. *International Journal of Advanced Engineering Research and Science (IJAERS)*, *4*(5).

Feuer, D., & Fallah-Fini, S. (2020). Call center staffing: An analytical framework for operations improvement at a call center. *Proceedings of the 2016 Industrial and Systems Engineering Research Conference, ISERC 2016*.

Fomundam, S., & Herrmann, J. W. (2007). A survey of queuing theory applications in healthcare. https://drum.lib.umd.edu/items/885228fb-a35f-4c79-b01a-1f70a3c2f08c

Glick, M., Williams, D. M., Kleinman, D. V., Vujicic, M., Watt, R. G., & Weyant, R. J. (2016). A new definition for oral health developed by the FDI World Dental Federation opens the door to a universal definition of oral health. *British Dental Journal*, *221*(12), 792-793.

Gong, J., Jıa, Q. Q., Zhang, J. S., & Yu, M. (2018). Robust program model of human resource management for staffing call centers. *Journal of Northeastern University (Natural Science)*, *39*(1), 20.

Green, L. (2006). Queueing analysis in healthcare. *Patient flow: reducing delay in healthcare delivery*, 281-307.

Gross, D., Shortle, J. F., Thompson, J. M., & Harris, C. M. (2011). *Fundamentals of queueing theory* (Vol. 627). John wiley & sons.

Günal, M. M., & Pidd, M. (2010). Discrete event simulation for performance modelling in health care: a review of the literature. *Journal of Simulation*, *4*(1), 42-51.

Hajrizi, E., & Berisha, D. (2019). Application of discrete events simulation for the department of emergency at peja regional hospital case study Kosovo. *IFAC-PapersOnLine*, *52*(25), 376-381.

Hall, R. W. (2006). Patient flow: the new queueing theory for healthcare. *OR/MS Today*, *33*(3), 36-41.

Han, Y., Xu, Q., Zhao, Q., & Si, F. (2023). Queue-aware computation offloading for UAV-assisted edge computing in wind farm routine inspection. *Journal of Renewable and Sustainable Energy*, *15*(6).

Harper, P. R., & Shahani, A. K. (2002). Modelling for the planning and management of bed capacities in hospitals. *Journal of the Operational research Society*, *53*(1), 11-18.

Jacobson, S. H., Hall, S. N., & Swisher, J. R. (2013). Discrete-event simulation of health care systems. *Patient flow: Reducing delay in healthcare delivery*, 273-309.

Jia, W., Huang, Y. L., Zhao, Q., & Qi, Y. (2022). Modeling taxi drivers' decisions at airport based on queueing theory. *Research in Transportation Economics*, *92*, 101093.

Kakooei, S., Tahmasebi, E., Bahadori, M., Yazdanian, M., Rafiei, E., Mostafavi, M., ... & Modaberi, A. (2022). Application of queuing theory and simulation model to reduce waiting time in dental hospital. *Journal of Oral Health and Oral Epidemiology*, *11*(3), 140-145.

Kalwar, M. A., Marri, H. B., Khan, M. A., & Khaskheli, S. A. (2021). Applications of queuing theory and discrete event simulation in health care units of Pakistan. *International Journal of Science and Engineering Investigations*, *10*(109), 6-18.

Kamali, A. H., Moradi, M., Goodarzian, F., & Ghasemi, P. (2022). A discrete event simulation method for performance analysis of an additive manufacturing in the dental clinic. *The International Journal of Advanced Manufacturing Technology*, 1-31.

Kassebaum, N. J., Bernabé, E., Dahiya, M., Bhandari, B., Murray, C. J. L., & Marcenes, W. (2015). Global burden of untreated caries: a systematic review and metaregression. *Journal of Dental Research*, *94*(5), 650-658.

Kolker, A. (2008). Process modeling of emergency department patient flow: Effect of patient length of stay on ED diversion. *Journal of Medical Systems*, *32*, 389-401.

Kushchazli, A., Safargalieva, A., Kochetkova, I., & Gorshenin, A. (2024). Queuing model with customer class movement across server groups for analyzing virtual machine migration in cloud computing. *Mathematics*, *12*(3), 468.

Macdonald, G. (2000). The evidence of health promotion effectiveness. shaping public health in a new europe. *Health Education Research*, *15*(2).

Mahmudov, S., & Mahmudova, M. (2022, September). Modern Intelligent Health Systems: Queueing, Simulation. In *2022 International Conference on Information Science and Communications Technologies (ICISCT)* (pp. 1-6). IEEE.

Fadilah, N. Z. M., Shahidan, W. N. W., & Sharif, N. (2023). Modeling and simulation analysis of medical and dental clinic system using arena. *Environment-Behaviour Proceedings Journal*, *8*(SI15), 171-178.

Mtonga, K., Gatera, A., Jayavel, K., Nyirenda, M., & Kumaran, S. (2022). Adaptive staff scheduling at outpatient department of ntaja health center in Malawi-A queuing theory application. *Journal of Public Health Research*, *11*(2).

Naqvi, A., Aruna, D. H., Parthi, A., Kamra, M., Nagrale, R. G., Kumar, P., & Chhabra, K. G. (2022). Evaluation of health seeking behaviour of patients with severe periodontitis visiting private dental college and hospital. *Journal of Medical Pharmaceutical and Allied Sciences*, *11*(2).

Nawusu, Y. A. W., Danaa, A. A. A., & Ismail, S. (2020). Queue management during health pandemics: A queuing theory perspective. *Asian Journal of Research in Computer Science*, *6*(4), 18-26.

Newton, J., & Medhi, J. (1992). Stochastic models in queueing theory. *Journal of the Royal Statistical Society. Series A (Statistics in Society)*, *155*(3).

Nosek Jr, R. A., & Wilson, J. P. (2001). Queuing theory and customer satisfaction: a Review of terminology, trends, and applications to pharmacy practice. *Hospital Pharmacy*, *36*(3), 275-279.

Ordem dos Médicos Dentistas. (2021). *Tempos de consulta de medicina dentária no SNS*. Retrieved from Https://Www.Omd.Pt/2021/01/Tempo-Consulta-Dentaria/.

Petersen, P. E., & Kwan, S. (2011). Equity, social determinants and public health programmes–the case of oral health. *Community Dentistry and Oral Epidemiology*, *39*(6), 481-487.

Preeti, & Gupta, N. (2024). Open Jackson queuing networks for waiting time reduction and manpower planning in pharmacy. *International Journal of System Assurance Engineering and Management*, 1-8.

Quattrocchi, G., Incerto, E., Pinciroli, R., Trubiani, C., & Baresi, L. (2024). Autoscaling solutions for cloud applications under dynamic workloads. *IEEE Transactions on Services Computing*.

Rasheed, F., Lee, Y. H., Kim, S. H., & Park, I. C. (2012). Development of emergency department load relief area—gauging benefits in empirical terms. *Simulation in Healthcare*, *7*(6), 343-352.

Reyes, E. G. A., Cangco, G. K. M., Ilagan, S. M. C., Pacunayen, H. P., Piamonte, J. A., & German, J. D. (2023, April). An application of queueing theory on the ticketing booth of light rail transit 1 (LRT-1) Central station. In *Proceedings of the 2023 5th International Conference on Management Science and Industrial Engineering* (pp. 192-198).

Sakr, A., Elzeki, O. M., & El-Bakry, H. (2023). A simulation of mobile-based bank teller application for managing waiting time of customers. *Journal of Computer Science*, *19*(3).

Salawu, G., Bright, G., & Onunka, C. (2020). Performance optimisation on waiting time using queueing theory in an advanced manufacturing environment. *South African Journal of Industrial Engineering*, *31*(4), 9-18.

Samaha, S., Armel, W. S., & Starks, D. W. (2003). The use of simulation to reduce the length of stay in an emergency department. *Winter Simulation Conference Proceedings*, *2*.

Santos, A. B., Calado, R. D., Zeferino, A. C. S., & Bourguignon, S. C. (2022). Queuing theory: Contributions and applications in the field of health service management–A bibliometric approach. *IFAC-PapersOnLine*, *55*(10), 210-214.

Sari, I., Asriwati, A., & Diana, V. E. (2022). The Implementation Evaluation of Drug Demand Plan in Pharmacy Installations of Dr Fauziah Hospital Bireuen Aceh Province. *Journal La Medihealtico*, *3*(4), 343-350.

Schulz, A., & Fliedner, M. (2023). Minimizing the expected waiting time of emergency jobs. *Journal of Scheduling*, *26*(2), 147-167.

Setiawan, D., & Restiana, R. (2024). Perbaıkan sıstem antrıan fasılıtas kesehatan dengan disiplin antrian prıorıtas menggunakan sımulası kejadıan dıskrıt. *Jurnal Disprotek*, *15*(1), 73-80.

Sistema Nacional da Saúde (SNS). (2023). *Relatório do Grupo de Trabalho – SNS | Saúde Oral 2.0*.

Subrayan, M. S., Edward, M. D., & Narayanan, S. V. (2023, June). Application of queuing theory in the ATMs of dutch Bangla bank limited Bangladesh. In *AIP Conference Proceedings* (Vol. 2649, No. 1). AIP Publishing.

Sufyan, F., & Banerjee, A. (2023). Computation offloading for smart devices in fog-cloud queuing system. *IETE Journal of Research*, *69*(3), 1509-1521.

Vilaplana, J., Solsona, F., Teixidó, I., Mateo, J., Abella, F., & Rius, J. (2014). A queuing theory model for cloud computing. *The Journal of Supercomputing*, *69*, 492-507.

Hopp, W. J., & Lovejoy, W. S. (2012). *Hospital operations: Principles of high efficiency health care*. FT Press.

Wang, J., Vahid, S., Eberg, M., Milroy, S., Milkovich, J., Wright, F. C., & Irish, J. (2020). Clearing the surgical backlog caused by COVID-19 in Ontario: a time series modelling study. *Cmaj*, *192*(44), E1347-E1356.

Weerakoon, W. M. N. B., Vasanthapriyan, S., & Ishanka, U. P. (2019, December). A queuing model for outpatient department to reduce unnecessary waiting times. In *2019 14th Conference on industrial and information systems (ICIIS)* (pp. 203-208). IEEE.

White, M., & Pike, M. C. (1964). Appointment systems in outpatient clinics and the effect of patients' unpunctuality. *Medical Care*, *12*(6), 222–230.

World Health Organization. (2021a). *148th Session EB148.R1 - Agenda Item 6 - Oral Health*.

World Health Organization. (2021b). *Seventy-Fourth World Health Assembly. Resolution Wha74.5: Oral health*.

World Health Organization. (2023). *Draft Global Oral Health Action Plan (2023–2030)*.

Worthington, D. (2008). Hospital waiting lists explained. *J. Opt Res.*, *38*(5).

Worthington, D. J. (1987). Queueing models for hospital waiting lists. *Journal of the Operational Research Society*, *38*(5), 413-422.

Xu, R., Wu, J., Cheng, Y., Liu, Z., Lin, Y., & Xie, Y. (2020). Dynamic security exchange scheduling model for business workflow based on queuing theory in cloud computing. *Security and Communication Networks*, *2020*(1), 8886640.

Xu, Y., Wang, Y., & Ji, Z. (2023). Analysis and simulation of blockchain queueing delay in the cloud manufacturing system. *CAAI Transactions on Intelligent Systems*, *18*(3).

Zheng, H., Yang, Y., Gao, G., Yang, K., & Chen, J. (2022). Traffic stream characteristics analysis for roadway linking to pick-up zone of passenger transportation hub: A fundamental diagram derived from threshold queueing theory. *Applied Sciences*, *13*(1), 175.

Author Information

Ana Paula Lopes
Polytechnic of Porto / ISCAP / CEOS.PP
Rua Jaime Lopes Amorim, s/n
4465-004 S. Mamede de Infesta
Portugal
Contact e-mail: *aplopes@iscap.ipp.pt*

Ana Cristina & Sousa
Polytechnic of Porto / ISCAP
Rua Jaime Lopes Amorim, s/n
4465-004 S. Mamede de Infesta
Portugal

To cite this article:

Lopes, A. P. & Sousa, A.C. (2024). Using queuing theory and simulation to improve oral health program. *The Eurasia Proceedings of Science, Technology, Engineering & Mathematics (EPSTEM), 29,* 320-330.